THE STRESS-STRAIN BEHAVIOUR OF BOTHKENNAR CLAY

Kevin McGinty

A Thesis submitted for the degree of Doctor of Philosophy at the University of Glasgow.

Department of Civil Engineering – September 2006

To Kate

Summary

This thesis describes the findings of an experimental and numerical investigation into the mechanical behaviour of a soft clay. The main objectives in the work involve the investigation of the effects of plastic anisotropy and destructuration on natural clay behaviour.

Chapter 1 outlines the need for continued research on soft clay behaviour. The aims and objectives of the work are set out, as well as the structure of the research.

The mechanical behaviour of soft clays has been reported by a large number of researchers and the findings of these are considered in Chapter 2. A review of Bothkennar clay is given.

Chapter 3 sets out the details of two constitutive models, whose purpose is to model the effects of plastic anisotropy and destructuration. A review of previous model validations, both experimental and numerical, is given. Unresolved issues in model validation are explained.

In Chapter 4 the experimental apparatus and procedures used in the testing programme are described. The majority of testing was carried out in triaxial cells and the arrangement of this equipment is detailed. The development of local strain-measuring devices is presented.

In Chapter 5, the main experimental programme is described.

Chapter 6 contains results from triaxial tests on vertically oriented samples. These tests include multi-stage stress path tests and standard drained shearing tests to failure. The initial orientation of the yield surface within the critical state framework is examined and test results are qualitatively compared against the constitutive models described in Chapter 3. Pre-yield behaviour is examined.

Triaxial tests on horizontally oriented samples are presented in Chapter 7. These provide a more generalized assessment of the role of anisotropy and destructuration, aided by the use of local strain measuring devices.

In Chapter 8 tests results on both vertical and horizontal samples are compared with simulations from the constitutive model S-CLAY1 in order to assess how well this constitutive model predicts the stress-strain response of the soil, with particular respect to plastic anisotropy.

Chapter 9 is concerned with the constitutive modelling of both plastic anisotropy and destructuration. In this chapter, experimental results from vertically oriented samples are compared with simulations from the constitutive model S-CLAY1S, which takes these features into account.

In Chapter 10, it is concluded that the constitutive models introduced in Chapter 3 have provided considerably improved predictions of the mechanical behaviour of natural soft clays when compared to commonly used modelling techniques. The experimental data obtained from the experiments has allowed model parameter values to be obtained for Bothkennar clay and the models to be subsequently calibrated.

ACKNOWLEDGEMENTS

I would like to extend my thanks to a number of people who have helped make this thesis possible.

Primarily, I would like to thank my supervisors Professor Simon Wheeler and Dr. Minna Karstunen for inspiration and encouragement throughout the research programme.

Invaluable assistance was provided by the technical support staff within the Civil Engineering Department. In particular, thanks to Tim Montgomery who devoted many hours of time and care to the construction of local strain measuring devices. Thanks to Stewart McLean for guidance on the fabrication of Hall Effect sensors. Thanks also to Alan Yuill and Bobby Boyd for technical support. In addition I would like to thank Ken McColl for assistance on IT matters.

I would also like to thank my friends and colleagues, in particular Lindsay Beevers, Graeme Forbes, Marc Buisson, Domenico Gallipoli, Harald Krenn and Silvia Portas.

I would like to thank my parents, particularly for their support during the latter stages of my work. Finally, I would like to thank Kate for her support and encouragement.

Contents

CHAPTER 1. INTRODUCTION

1.1 Engineering on soft clays

Over the last few decades it has become increasingly necessary for civil engineers to construct on soft clay deposits. In developed countries this is mainly due to sites of favourable ground conditions becoming increasingly rare, whilst social, economic and political issues add further constraints. As a consequence, soft soil deposits have been increasingly used in construction and it has therefore become necessary for engineers to understand more fully their behaviour in order to carry out safe and economical design and construction.

Soft clays occur worldwide and represent a number of difficulties to the engineer. These clays are of low strength and this may cause difficulties when designing against ultimate limit states. Remedial measures may be required, perhaps involving limitation of the load transferred through the clay or improving the stability of the clay. This can typically involve the introduction of lime or cement stabilisation, vibro stone columns, mini-piles or the use of geotextiles. In addition, however, soft soils are usually highly deformable and applications of relatively low loads may results in large ground movements. Soft clays are typically of low permeability and ground movements resulting from additional loading may occur over unacceptably large timescales. This causes major difficulties for design against serviceability limit states. In practice, this means that further ground improvements are required. In order to minimise earthwork settlements during the working life of a structure preloading or accelerated drainage conditions may be required. Alternatively a relatively long period must be allowed to permit primary and secondary consolidation.

Any form of ground improvement will inevitably incur financial penalties due to additional materials, labour and time. However, these additional costs could be minimised if the clay behaviour could be predicted more accurately. Soil models that are commonly used by practicing engineers, such as linear elastic-perfectly plastic with a Mohr-Coulomb failure criterion or elasto-plastic models such as Modified Cam Clay, are simplified and frequently result in predictions that are

inaccurate or over-conservative. This is partly because these models do not incorporate natural features of clay behaviour such as anisotropy, destructuration and creep. Constitutive modelling of clays has developed rapidly since the development of the earliest critical state elasto-plastic models. However, many of the newer models that have attempted to include aspects of natural clay behaviour such as anisotropy and destructuration have involved such complexity that practicing geotechnical engineers cannot readily use them. A particular problem with some models is that the values of the model parameters are difficult to determine from standard laboratory procedures.

The purpose of the present study was to examine a particular soft clay in order to investigate, specifically, the influence of anisotropy and destructuration, and then to examine the performance of two constitutive models which incorporate anisotropy and destructuration. Due to their depositional history, clays tend to have an anisotropic fabric arrangement. Furthermore, subsequent in-situ processes give rise to inter-particle bonding. Subsequent loading will result in changes in the fabric arrangement of the soil (evolving anisotropy) and inter-particle bonds will be destroyed (destructuration). The S-CLAY1 model, developed by Näätänen et al. (1999) and Wheeler et al. (2003) is an extension of the Modified Cam Clay model and has additional components which account for initial anisotropy within the clay and subsequent changes of anisotropy caused by plastic straining under load. A second model, S-CLAY1S, has been proposed by Koskinen et al. (2002). This model retains all of the features of S-CLAY1, but contains an additional component to account for soil bonding and subsequent destructuration. Therefore, a systematic laboratory programme was devised in order to obtain experimental data from the clay and to compare the data with the model predictions of S-CLAY1 and S-CLAY1S.

1.2 Material choice and laboratory programme

Soft clay from the Bothkennar test bed site in Scotland was chosen for testing in the laboratory. There were a number of advantages in using this material. Firstly, Bothkennar clay was expected to exhibit typical natural clay features such as anisotropy and inter-particle bonding and was therefore appropriate for this study. Secondly, a wealth of research into this clay had previously been undertaken and was

detailed in a Géotechnique Symposium-in-Print (Vol. 42, No. 2; 1992). In addition, high quality Laval samples of Bothkennar clay (remaining from the previous research) had been stored at the University of Glasgow. These samples had been carefully extracted and stored and the mechanical behaviour should therefore be closely representative of the soil in its in-situ state.

The laboratory programme involved extensive triaxial testing of Bothkennar clay. The tests were carried out in a Bishop-Wesley triaxial stress path cell and a conventional triaxial cell. Vertically oriented samples (with the sample axis coincident with the vertical direction in the ground) were tested in order to establish the stress-strain-strength characteristics of the clay. The intention was to test these samples under a variety of loading conditions in order to assess the role of plastic anisotropy of the soil and to determine subsequent changes in anisotropy caused by continued loading. The tests were also programmed to obtain information on the effects of destructuration on a natural clay. Horizontally oriented samples (with the sample axis coincident with a lateral direction in the ground) were tested in order to examine the role of anisotropy at more general stress states. The data from these tests were in turn compared directly with equivalent tests on vertically oriented samples.

1.3 Aims and scope of the present study

The main aims of the experimental work were as follows:

- Determination of the initial yield curve shape and size for Bothkennar clay.
- Demonstration of subsequent changes in yield curve shape and size due to continued plastic loading and investigation of the validity of the proposed form of rotational hardening in S-CLAY1 and S-CLAY1S.
- Investigate the role of destructuration in Bothkennar clay.
- Development of local strain-measuring devices so that radial strains on horizontally oriented samples can be recorded.
- Testing of horizontally-oriented samples in order to examine more general stress-strain behaviour for S-CLAY1.

For the theoretical work, the main aims were

- Assess whether the stress-strain behaviour of Bothkennar clay can be modelled by S-CLAY1 or S-CLAY1S.
- Selection of S-CLAY1 and S-CLAY1S model parameter values for Bothkennar clay.
- Examination of the mechanism of plastic deformation, in particular, whether the use of an associated flow rule is appropriate to Bothkennar clay.
- Initial exploration of the more fully generalized S-CLAY1 model through comparison of model predictions with the experimentally observed behaviour of horizontally and vertically oriented samples.

It is hoped the findings of this thesis will ultimately contribute to the solution of practical engineering problems, where design tools such as finite element analyses software are used.

1.4 Structure of the thesis

The main focus of this thesis is an experimental investigation of the stress-strain behaviour of Bothkennar clay in multi-stage stress path tests and the discussion of this behaviour in the context of two new constitutive models. Particular attention is paid to the influence of large strain anisotropy (including changes of anisotropy caused by plastic straining) and the role of destructuration.

The context for the present study is set out in Chapter 2, in which previous experimental and theoretical research on the behaviour of natural and reconstituted soft clays is reviewed in detail. This includes the central themes of anisotropy and destructuration along with other salient features of soil behaviour. Chapter 3 then fully describes the S-CLAY1 and S-CLAY1S constitutive models. This discussion includes comparison with other advanced models described in Chapter 2. In addition, previous comparisons of S-CLAY1 and S-CLAY1S simulations with experimental data from other soft clays are discussed.

Details of laboratory equipment and techniques are set out in Chapter 4, with a specific section on the design, manufacture and application of radial strain measuring devices. Drawing on the conclusions from Chapters 2 and 3, and the technical background in Chapter 4, the experimental programme for Bothkennar clay is detailed in Chapter 5.

The results from all triaxial tests on vertically oriented samples are presented and discussed in Chapter 6 and corresponding tests on horizontally oriented samples are presented in Chapter 7. The conclusions from these experimental results form the basis of numerical model simulations presented in Chapters 8 and 9. The purpose of these simulations is twofold, focussing first on plastic anisotropy (S-CLAY1 simulations in Chapter 8) and then on plastic anisotropy and destructuration (S-CLAY1S simulations in Chapter 9). In each case, the experimental data is directly compared with simulations.

Finally, conclusions and recommendations are given in Chapter 10.

CHAPTER 2. EXPERIMENTAL INVESIGATION AND CONSTITUTIVE MODELLING OF SOFT CLAY BEHAVIOUR

2.1 Introduction

The practical issues of construction on soft clays outlined in Chapter 1 have given rise to the need for a better understanding of soft clay behaviour. The mineralogy of clay soils and the geological processes involved in their formation are discussed in Sections 2.2 and 2.3 respectively. These aspects of clays are of fundamental importance to the resultant mechanical properties and behaviour, as are post-depositional processes discussed in Section 2.4. Therefore, depositional and post-depositional processes are linked to the experimental data obtained by various researchers and form the basis for the constitutive models discussed in Sections 2.6 – 2.8. These models attempt to incorporate the effects of anisotropy, destructuration, small strain behaviour and creep/time-dependency. Discussion of the merits and weaknesses of these models forms the basis of an extensive review of two recent elasto-plastic critical state models in Chapter 3 and the subsequent experimental programme involving Bothkennar clay (see Chapters 4 - 7). Finally, Section 2.10 gives a detailed review of Bothkennar clay, in which the geological history and mechanical behaviour of this soil are considered.

2.2 Clay Mineralogy

Clay particles are derived from the chemical weathering of rock-forming minerals. It is the mineralogy of clays that controls the shape, size and surface properties of the clay particles. In turn this influences the main engineering properties of the clay including plasticity, strength, stiffness and permeability. The main clay minerals are kaolinite, montmorillonite, illite, chlorite and halloysite. Holtz and Kovacs (1981), for example, showed that the plasticity of a clay could vary widely depending on its mineralogy, exemplified by montmorillonites that will tend to have relatively high plasticity (so that the soil is highly deformable) while halloysites tend to have far lower plasticity.

The "fabric" of a clay is defined as the geometrical arrangement of the particles and the inter-particle contacts, and includes the spatial arrangement of the pore spaces. Individual clay particles are the smallest unit of the soil microfabric. Yong and Sheeran (1973) noted that these particles generally occur as aggregated units known as domains, which in turn form clusters. The clusters themselves are aggregated as peds, which may be seen with the naked eye. The interaction of these particle groups is vital to the analyses of fabric described in Section 2.6.1, since the microfabric reflects the history of the clay and controls its behaviour.

2.3 Transportation and sedimentation of clay deposits

The effects of weathering and transportation largely determine the basic nature of the soil (i.e. the size, shape, composition and distribution of the grains). The environment in which deposition takes place, and subsequent geological events that take place there, largely determine the state of the soil, (e.g. void ratio) and the fabric of the soil. This fabric not only includes microfabric (as described in Section 2.2), but also macrofabric (i.e. bedding, stratification, occurrence of joints or fissures, tree roots, voids, etc.). As described by Christoulas et al. (1987), the main environments in which soft clays are deposited are continental (through rivers, swamps and lakes), marine (in off-shore basins or coastal regions due to sea-level rise) or a mixed continental/marine environment, such as deltaic clays.

Due to the one-dimensional strain history of most clay deposits, they are generally cross-anisotropic materials. In general, the clay particles are oriented such that the long axes are perpendicular to the major principal stress direction in the ground (the vertical direction) during deposition (Yu and Axelsson (1994)). As the particles are deposited under gravity and compressed by the deposition of further particles the clay platelets orientate themselves in this way. This means that the material properties are identical in all horizontal directions in the ground, but the properties are different in the vertical direction. This type of fabric is referred to as being "cross-anisotropic". This is an important feature as it is fundamental to the nature of investigations of clay behaviour involving laboratory testing (see Section 2.6.1). In addition, this anisotropy must be acknowledged in numerical modelling of the clay (see Section 2.6.2) if accurate predictions of behaviour are to be obtained.

2.4 Post-depositional processes

After deposition, clay sediments may be subjected to a number of subsequent processes and these will significantly influence the properties of the soil. It is therefore the combination of the clay mineralogy, depositional environment and post-depositional processes which give rise to the clay properties. Both Mitchell (1976) and Burland (1990) used the term "structure" to define the combination of the soil fabric and any interparticle bonding. Structure is a result of clay mineralogy, depositional environment and post-depositional processes.

As a sediment continues to be deposited, the weight of overlying soil increases. This causes water to be expelled and the porosity of the deposit to decrease. After consolidation a number of important processes can begin. Cementation between interparticle contacts can arise due to the precipitation of silica, alumina, iron oxides and various other groundwater precipitates. Chemical weathering will generally affect soft clays. This may be in the form of rainwater, percolating through the soil and oxidising the material. Leaching is an important aspect of soil history and in some cases may be linked to chemical weathering. This process involves the removal of a material (leachate) from a solution, a common example being the removal of salt. In other instances, it may be possible for the aforementioned cement to be leached out of the soil. A soil that has undergone leaching can be extremely hazardous, as in Scandinavia where "quick clays" have formed by deposition under salt-water conditions and then subsequent percolation of freshwater. These clays will deform greatly even under relatively modest stress changes. The effects and implications of these processes are discussed in Section 2.7.

2.5 Soft clays

A short discussion on the classification of clays has been included here in order to appreciate that there are a number of ways in which a clay can be classified and that the criteria for such classification varies regionally.

Fundamentally, soft clays are characterised by low strength and high compressibility. However, the details of each criterion may be specific to the region in which they are

being applied. For example, the Finns may consider a soft clay to have an undrained shear strength c_u of less than 20 kPa, and a maximum overburden stress of, say, 40 kPa (Korhonen and Lojander, 1987). By contrast, samples of clay from Bothkennar, Scotland, (reviewed extensively in Géotechnique (1992) have undrained shear strengths generally in the range 15 to 50 kPa. In the United Kingdom, soft clays are classified according to BS 8004: 1986, which states that soft and very soft clays have values of undrained strength less than 40 kPa. Other means of classification can be used, such as considering representative values of elastic parameters, as explained by Das (1990). In this respect, soft clays are characterized by relatively low values of Young's modulus and shear modulus.

2.6 Anisotropic behaviour of clays

2.6.1 Laboratory evidence

Analyses of fabric anisotropy

If the behaviour of a clay is related to the orientation of its particles, as suggested in Section 2.3, then it is useful to have experimental evidence of fabric anisotropy and how fabric anisotropy changes during straining. It is convenient to make a distinction between the fabric arrangement caused by natural processes in the ground and any subsequent changes in fabric due to engineering works. The geological history of a clay will result in the clay having an "initial" anisotropy. Experimental evidence shall now be discussed, which has shown that further straining can cause this initial fabric to become re-arranged and this is known as "induced" anisotropy.

Collins and McGown (1974) examined the microfabric of a number of clays. They concluded that the fabric can be considered as consisting of individual particle arrangements which are in turn aggregated in units known as domains. The arrangement of these individual particles and their domains is a reflection of the geological history of the soil and influences its mechanical behaviour. Bai and Smart (1997) examined the change of fabric arrangement in reconstituted kaolin samples at various stages of triaxial testing. They consolidated the samples from a slurry such that each sample had an anisotropic stress history (corresponding to one-dimensional

consolidation). After consolidation they sheared each sample under undrained conditions and terminated tests at various levels of shear strain, before and after the peak deviator stresses were reached, so that thin-sections could be obtained for examination using microscopy techniques. They quantified the fabric anisotropy in terms of the preferred orientation of individual particles or groups of particles. It was concluded that during undrained shear, the anisotropy increased at low levels of strain and reached a peak at an intermediate level of straining before reducing again as a critical state was approached. At the critical state, a significant degree of anisotropy still remained. This may due to the fact that at a critical state, the stress-state is highly anisotropic. The peak anisotropy appeared to occur at a level of shear strain of approximately one-half to two-thirds of the strain at peak deviator stress. Sections retrieved from tests involving shearing beyond failure showed that the particles tended to orientate themselves approximately in the direction of the failure plane.

Kuganenthira et al. (1996) examined the effects of shearing in triaxial tests upon the fabric of a clay using microscopy and electrical techniques. Again, they used kaolin samples consolidated under one-dimensional conditions from slurry. They confirmed the expectation that such samples would have a higher electrical conductivity in the horizontal direction than in the vertical direction because the flat platy clay particles tend to align themselves in the horizontal direction (the plane of isotropy) allowing easier flow of current in this direction. Anisotropy was quantified by a coefficient A_e where

$$A_e = \sqrt{\frac{s_h}{s_v}} \tag{2.1}$$

where s_h and s_v are the electrical conductivities in the horizontal and vertical directions respectively and thus the initial anisotropy and any subsequent changes in anisotropy could be quantified. A value of $A_e = 1$ corresponds to an isotropic fabric. In each specimen the initial value of A_e was greater than unity, reflecting the inherent anisotropy in the clay.

Having undergone an anisotropic stress history, each test then involved isotropic compression to a stress level three times greater than the initial stress. It was noted that isotropic loading caused a reduction in A_e, but that in each case A_e did not reduce to unity. However, tests on horizontal samples isotropically compressed to the same stress as the vertical samples showed the stress-strain response in undrained shearing to be almost identical to that of the vertical samples. It seems therefore that the isotropic compression was sufficient to erase the influence of initial anisotropy on the large strain mechanical behaviour of the clay even though the isotropic loading was insufficient to erase all evidence of fabric anisotropy. In tests involving undrained shearing in triaxial compression, it was apparent that there was a significant increase in A_e so that the fabric appeared to be attaining a strongly preferential orientation. Conversely, in undrained triaxial extension, the value of A_e was seen to fall to below unity, suggesting that the fabric arrangement had become radically different from its initial state. This could be explained by the fact that in triaxial extension, the major and minor principal stresses were reversed and that the clay particles would tend to align themselves in this new direction. In this case the stress state was also highly anisotropic. Unlike the evidence of Bai and Smart (1997), there did not seem to be a peak value of anisotropy during the intermediate stages of shearing (whether in triaxial compression or triaxial extension), rather the amount of anisotropy appeared to be increasing even at failure.

Yield characteristics of natural clays

The concept of yielding (the onset of irreversible strains) is widely accepted as a fundamental aspect of the stress-strain behaviour of clays. Yielding is usually accompanied by a marked change in the stiffness of the clay as the material is taken from the elastic domain to the plastic range. It should be noted that the process of yielding is often described in over-simplified terms, however, as explained in Section 2.8, the onset of yield is not simply a sudden transition from an elastic to a plastic domain. Nonetheless, this change in stiffness has implications for analyses of foundations where the change from elastic straining to plastic straining means that the magnitude of straining will be greatly increased. The most common method of locating the yield surface for a particular clay is by identifying this change in the clay stiffness, denoting the onset of plastic straining. This is most easily achieved by

conducting triaxial tests. A number of studies have been carried out to identify the yield surface for various natural clays.

Graham et al (1983) conducted triaxial tests on a natural clay and found that the yield curve could be represented by an inclined ellipse in p'-q space, approximately centred on the K_0 axis, as shown in Figure 2.1. They also showed a number of methods for identifying the yield stresses for each sample including stress-strain and energy plots. These techniques are discussed again in Section 6.5.

Diaz Rodriguez et al. (1992) carried out triaxial tests on Mexico City clay and summarized similar laboratory data from a number of other natural clays. The aim of these tests was to determine the yielding characteristics of natural clays. The tests involved drained stress probes at various values of K (where K is the ratio of radial effective stress to axial effective stress in the triaxial apparatus) so that a yield locus could be established. They concluded that the yield loci for the different clays can be represented in s': t space (where $t = (\sigma'_1 - \sigma'_3)/2$ and $s' = (\sigma'_1 + \sigma'_3)/2$) by an elliptical curve approximately centred on the K_0 axis (see Figure 2.2). This inclined yield curve indicated anisotropy of plastic behaviour, whereas a soil showing isotropic plastic behaviour would have a yield curve centred around the s' axis. Data from other clays showed that these concepts were applicable to a wide range of natural clays with widely varying pre-consolidation pressures and strength characteristics.

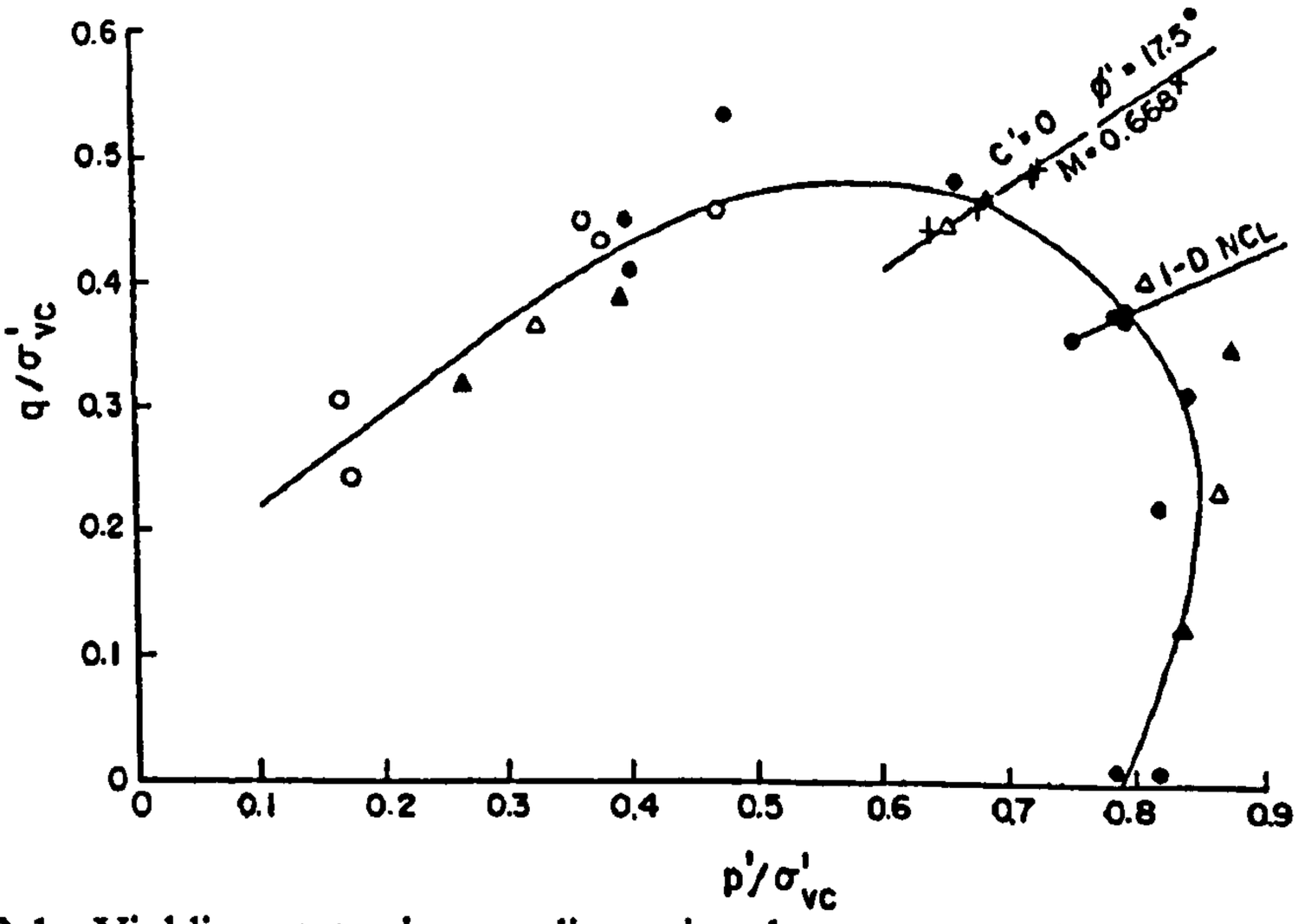

Figure 2.1. Yielding states in non-dimensional stress space (Graham et al., 1983)

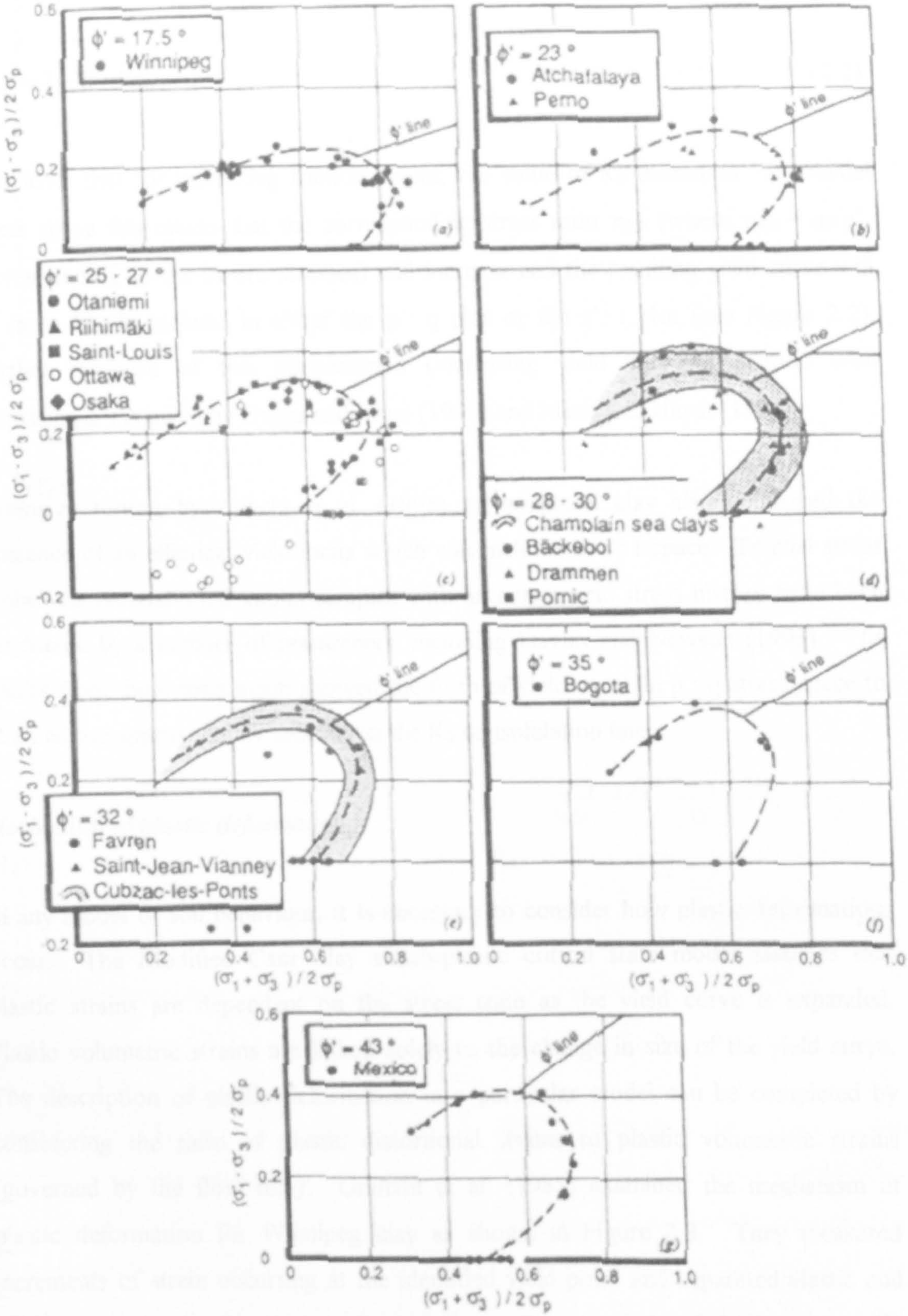

Figure 2.2.Normalized yield curves of natural soft clays (φ=17°-43°) (after Diaz-Rodriquez et al., 1992)

It is widely accepted that in the normally consolidated range, the value of K_0 can be approximated by Jaky's simplified formula

$$K_{0nc} = 1 - \sin\phi' \tag{2.2}$$

It follows that for increasing friction angles, the value of K_0 decreases. In triaxial stress space this means that the corresponding stress ratio η_{K0} (where $\eta_{K0} = q_0/p'_0$ corresponding to the in-situ stresses) will increase and the resulting yield curve will be more highly inclined in either the p': q plot or the s': t plot (see Figure 2.2). Further evidence of this phenomenon (increasing yield curve inclination with increasing ϕ') is given by Garga and Khan (1991) and Mesri and Hayat (1993).

Extensive testing by Adachi et al. (1995) on a natural clay also confirmed the existence of an elliptical yield locus which was inclined in s': t space. Triaxial stress probes on reconstituted kaolin samples with an anisotropic stress history have been conducted by a number of researchers, including Davies and Newson (1993). The results from these tests again showed the form of yield curve in p : q stress space to be an ellipse approximately centred on the K_0 consolidation line.

Mechanism of plastic deformation

In any model of soil behaviour, it is necessary to consider how plastic deformations occur. The Modified Cam Clay elasto-plastic critical state model assumes that plastic strains are dependent on the stress state as the yield curve is expanded. Plastic volumetric strains are linked solely to the change in size of the yield curve. The description of plastic deformation in a particular model can be completed by considering the ratio of plastic distortional strains to plastic volumetric strains (governed by the flow rule). Graham et al. (1983) examined the mechanism of plastic deformation for Winnipeg clay as shown in Figure 2.3. They measured increments of strain occurring at the identified yield point and separated elastic and plastic components of strain in order to estimate the magnitude of plastic strains. By drawing the direction of plastic strain increment vectors in Figure 2.3, they were able to assess the relationship between the ratio of plastic shear and plastic volumetric

strains in relation to the stress state at a given increment of plastic straining. The figure appears to show that the strain increment vectors are approximately normal to the yield surface suggesting that the normality condition for plastic straining is acceptable and that an associated flow rule may be used in the modelling of clays. Triaxial tests by Atkinson and Richardson (1985) on reconstituted specimens of London Clay, Cowden Till and Speswhite kaolin showed conflicting results, where normality appeared to hold under certain loading conditions, but deviated from normality in others.

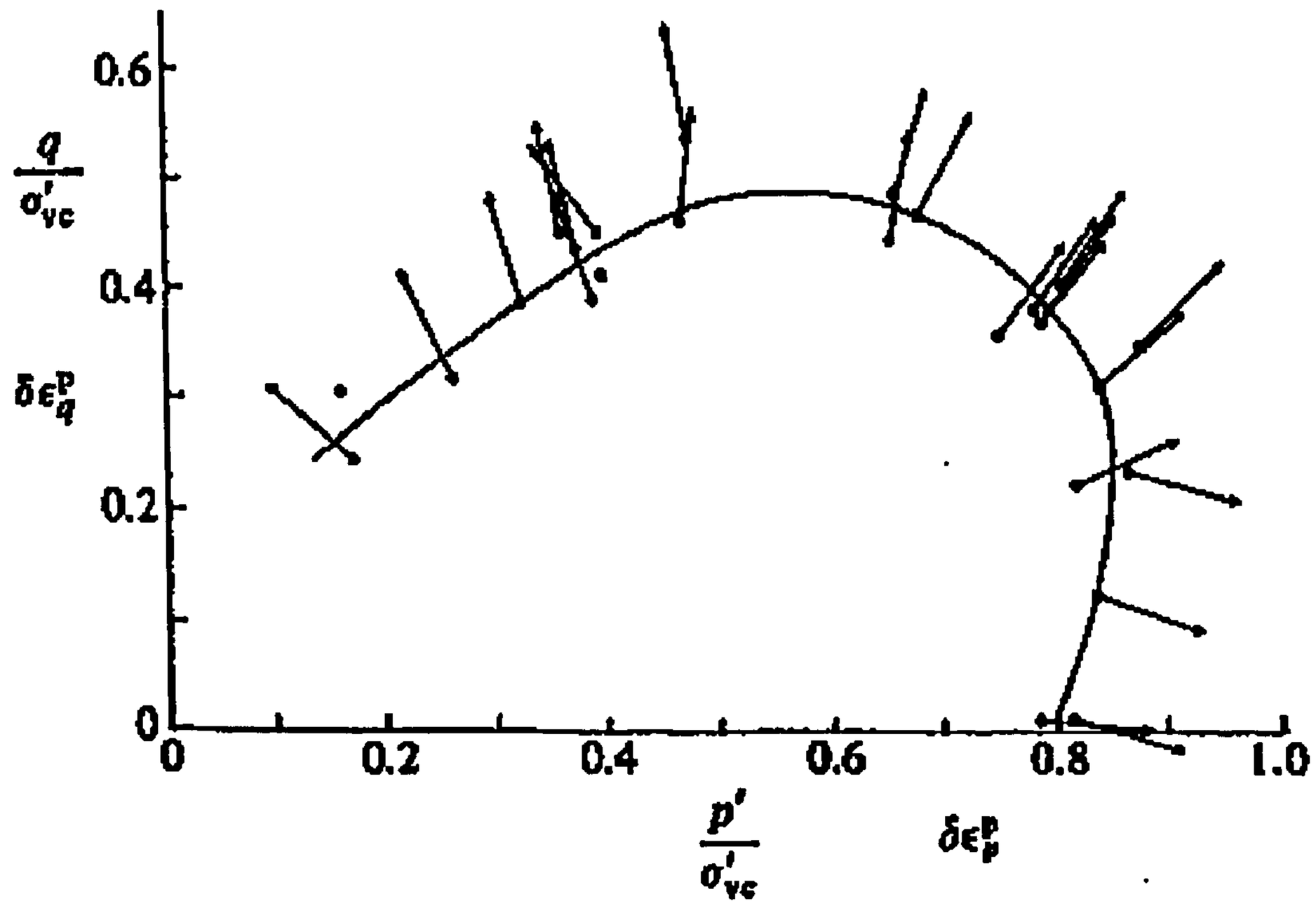

Figure 2.3. Normalized yield curve and plastic strain increment directions (Graham et al., 1983).

Davies and Newson (1993) attempted to identify directions of plastic strain increment vectors using closed stress cycles. Their test results strongly suggested that the relationship between the yield surface and the plastic potential surface was non-associated. Kirkgard and Lade (1993) tested specimens at more general stress states and produced strain increment vectors suggesting that for many cases, the use of an associated flow rule was not appropriate.

Behaviour under generalized stress states

The discussion in Section 2.6.2 is based on studies on vertically oriented samples in a triaxial apparatus, where two of the three principal stresses are equal in magnitude and where the axial stress is applied in a direction normal to the plane of deposition in the ground and therefore normal to the plane of isotropy. In the field, however, the three principal stresses may all be different in magnitude and the directions of the principal stress axes are frequently rotated. It should be noted that this behaviour is common, rather than exceptional. Experimental evidence suggests that stress axis rotation will have a marked effect on the strain response of anisotropic natural soils (Tavenas, 1981). However, an apparent absence of proper investigations means that there is limited knowledge on this effect, perhaps due to experimental difficulties.

Kirkgard and Lade (1993) describe a Cartesian coordinate system in which directions of stress and strain can be defined relative to the principal axes of a cross-anisotropic material (see Figure 2.4 (a)). The Lode angle θ (see Figures 2.4 (b), (c) and (d)), is defined as

$$\tan\theta = \sqrt{3}\frac{\sigma_x - \sigma_z}{(\sigma_y - \sigma_x) - (\sigma_y - \sigma_z)} \tag{2.3}$$

where σ_x, σ_y and σ_z are the three normal stresses and y is the vertical direction in the ground.

If the major, intermediate and minor principal stresses are named σ_1, σ_2 and σ_3 respectively, then the relative magnitude of the intermediate principal stress can be defined by a parameter b:

$$b = \frac{\sigma_2 - \sigma_3}{\sigma_1 - \sigma_3} \tag{2.4}$$

Parameter b must take a value between 0 and 1. It can also be stated that

$$b = \frac{\sigma_x - \sigma_z}{\sigma_y - \sigma_z} \qquad \text{for} \qquad 0^\circ \le \theta \le 60^\circ \tag{2.5a}$$

$$b = \frac{\sigma_y - \sigma_z}{\sigma_x - \sigma_z} \qquad \text{for} \qquad 60^\circ \le \theta \le 120^\circ \tag{2.5b}$$

$$b = \frac{\sigma_z - \sigma_y}{\sigma_x - \sigma_y} \qquad \text{for} \qquad 120^\circ \le \theta \le 180^\circ \tag{2.5c}$$

so that $\theta = 0^\circ$ and b = 0 corresponds to triaxial compression of a vertically oriented sample. $\theta = 180^0$ and b = 1 corresponds to triaxial extension for the vertically oriented sample. Equations 2.5 (a), (b) and (c) show that the value of θ indicates the relative magnitudes of the principal stresses and determines which of the normal stresses corresponds to the major, minor an intermediate principal stresses.

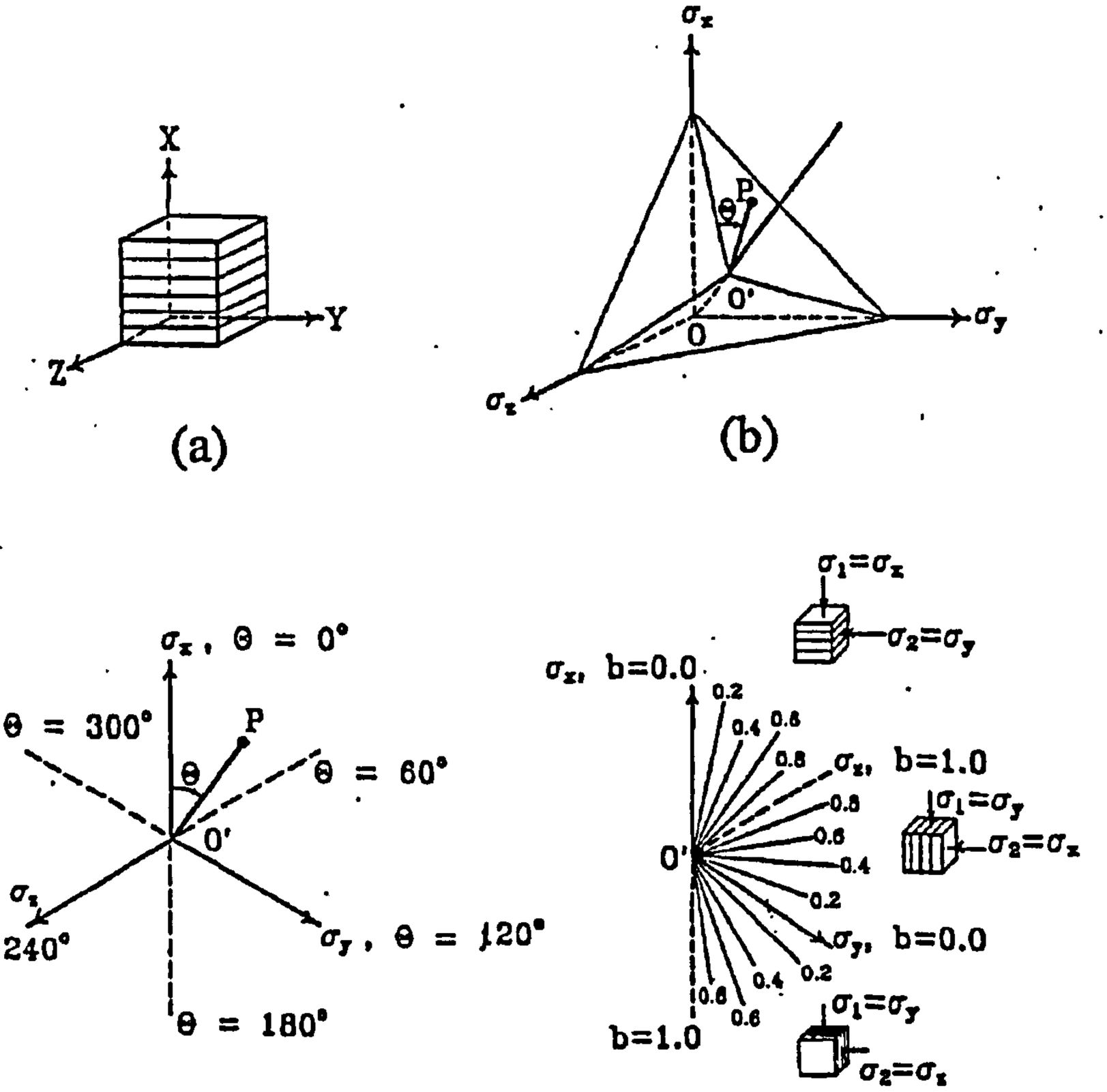

Figure 2.4. Orientation of cross-anisotropic soil relative to (a) Cartesian coordinate system, (b) principal stress space, (c, d) octahedral plane (Kirkgard and Lade, 1993).

Kirkgard and Lade (1993) conducted cubical true triaxial tests on natural San Francisco Bay Mud. In these tests they were able to independently control the three principal stresses. Suites of tests were conducted at various combinations of b and θ. It was found that the measured angle of friction ϕ' was lowest when b = 0. The highest values of θ were found to occur at some intermediate value of b between 0 and 1. It should be noted, however, that M is lowest in triaxial compression (b = 0) as a consequence of the definitions of M and ϕ'.

Comparisons of tests conducted at identical values of b (i.e. the intermediate principal stress has the same relative magnitude in each case), but with different values of θ, show that the measured friction angle is greatest for the case of $\theta = 0^0$ - 60^0 and lowest for $\theta = 120^0$ - 180^0. This suggested that the effective strength characteristics are dependent on how the sample is oriented relative to the vertical direction. These results are consistent with those of Broms and Casbarian (1965), showing that the measured angle of friction was greatest in triaxial compression and reduces to a minimum as the Lode angle is altered. In terms of undrained shear strength, higher strengths were reported by Kirkgard and Lade (1993) for $\theta = 0^0$ - 60^0 and lowest for $\theta = 120^0$ - 180^0. Again, this suggests that the strength characteristics are influenced by the sample orientation relative to the principal stresses.

Atkinson et al. (1987) conducted tests on K_0 normally consolidated samples of reconstituted kaolin clay. They found that the critical state stress ratios M_C in triaxial compression were virtually identical to the critical state stress ratio found in triaxial extension, M_E. As with Kirkgard and Lade (1993), these results implied significant differences (up to 10°) between the Mohr-Coulomb friction angles measured in compression and extension. Adachi et al. (1995) performed unconfined compression tests on a natural clay from Eastern Osaka. Using both vertically and horizontally trimmed samples, they showed that the peak strengths in each test were very similar, but that the strain at which peak strength was obtained was much higher in the horizontal samples. This suggested that the strength characteristics were independent of the value of b but the deformation characteristics were not. This is consistent with the expectation that the yield stress will be dependent on the stress path. However, the paths to critical state will involve the samples undergoing different changes in

fabric anisotropy in these horizontal and vertical samples during the intermediate stages of shearing. Given that the results show the same peak strengths for both sets of results, it appears that the critical state achieved is independent of any stress history.

A hollow cylinder apparatus (HCA) can be used to investigate initial and strain-induced anisotropy by examining the effects of changing parameter b (to any value between 0 and 1) and by inducing principal stress rotation. This is possible because the apparatus allows independent control of axial pressure, radial pressure and torsion, which provides independent control of all 3 principal stress magnitudes and rotation of the two principal stress directions. In a triaxial apparatus, it is only possible to obtain values of b equal to 0 or 1, corresponding to triaxial compression and triaxial extension respectively. Nor is it possible to cause variation in the principal stress directions. The triaxial test therefore cannot represent loading conditions in the ground where stress rotations and intermediate values of b will occur.

Various authors have examined anisotropy of strength using HCA. Tests conducted by Menkiti (1995) show that as the major principal stress direction moves increasingly away from the vertical direction in the ground (at a constant value of b), the observed values of undrained shear strength decrease significantly. Further tests by Zdravkovic (1996) have shown that the observed ultimate friction angle (ϕ'_{ult}) is significantly influenced by principal stress direction, where tests involving σ'_1 parallel with the vertical direction in the ground tend to give higher values of ϕ'_{ult}.

2.6.2 Constitutive modelling of large strain anisotropy

Anisotropic elasto-plastic models with rotational hardening

A number of authors, including Mitchell (1976) and Graham et al. (1983) have indicated that the fundamental concepts of the critical state soil mechanics framework (due to Roscoe et al., 1958) can be applied to the modelling of natural clays. In modelling the behaviour of clay, perhaps the most important family of

models in the last four decades has been the Cam Clay models, developed by Roscoe et al. (1958) and subsequently by Roscoe and Burland (1968). The Modified Cam Clay model (MCC), formulated by Roscoe and Burland (1968), is probably the hardening elasto-plastic model most widely used by practicing geotechnical engineers for numerical predictions. It is the relative simplicity of this model that ensures its popularity, but it has a number of weaknesses in that it ignores the influence of anisotropy (see Section 2.6.1 above), the effects of bonding and destructuration (see Section 2.7 below), the complexities of small strain behaviour (see Section 2.8) and the influence of creep/time-dependency (see Section 2.9).

In p': q space, the Modified Cam Clay yield surface, shown in Figure 2.5 is elliptical and centred on the mean effective stress axis. This form of yield surface is clearly different from the inclined elliptical curves derived from experimentally obtained yield points in Section 2.6.1. It is appropriate for soils with an isotropic stress history, but this will rarely be the case for natural clays due to the one-dimensional strain history of clays. The form of hardening in Modified Cam Clay is isotropic, allowing for changes in size of the yield curve, but no change in yield curve orientation. It therefore cannot account for any changes in the anisotropy of the soil fabric. The laboratory evidence described in Section 2.6.1 suggests, however, that the yield surface can change in shape as a result of plastic straining (due to plastic volumetric or plastic shear strains) and therefore a form of kinematic hardening is required to account for this.

Gens and Potts (1987) concluded that, despite its relative simplicity, Modified Cam Clay has proved very useful in numerical analysis of soil boundary value problems, although it has been found that the model is most successful in situations where stress reversals and stress rotations do not occur. However, it is likely that in practice, geotechnical problem will generally involve these aspects of soil behaviour. A particular weakness of Modified Cam Clay is that the combination of the isotropic elliptical yield curve with an associated flow rule results in the overprediction of K_0 values (underprediction of the stress ratio q/p' corresponding to one-dimensional straining) when compared to experimental observations. Another problem arises in

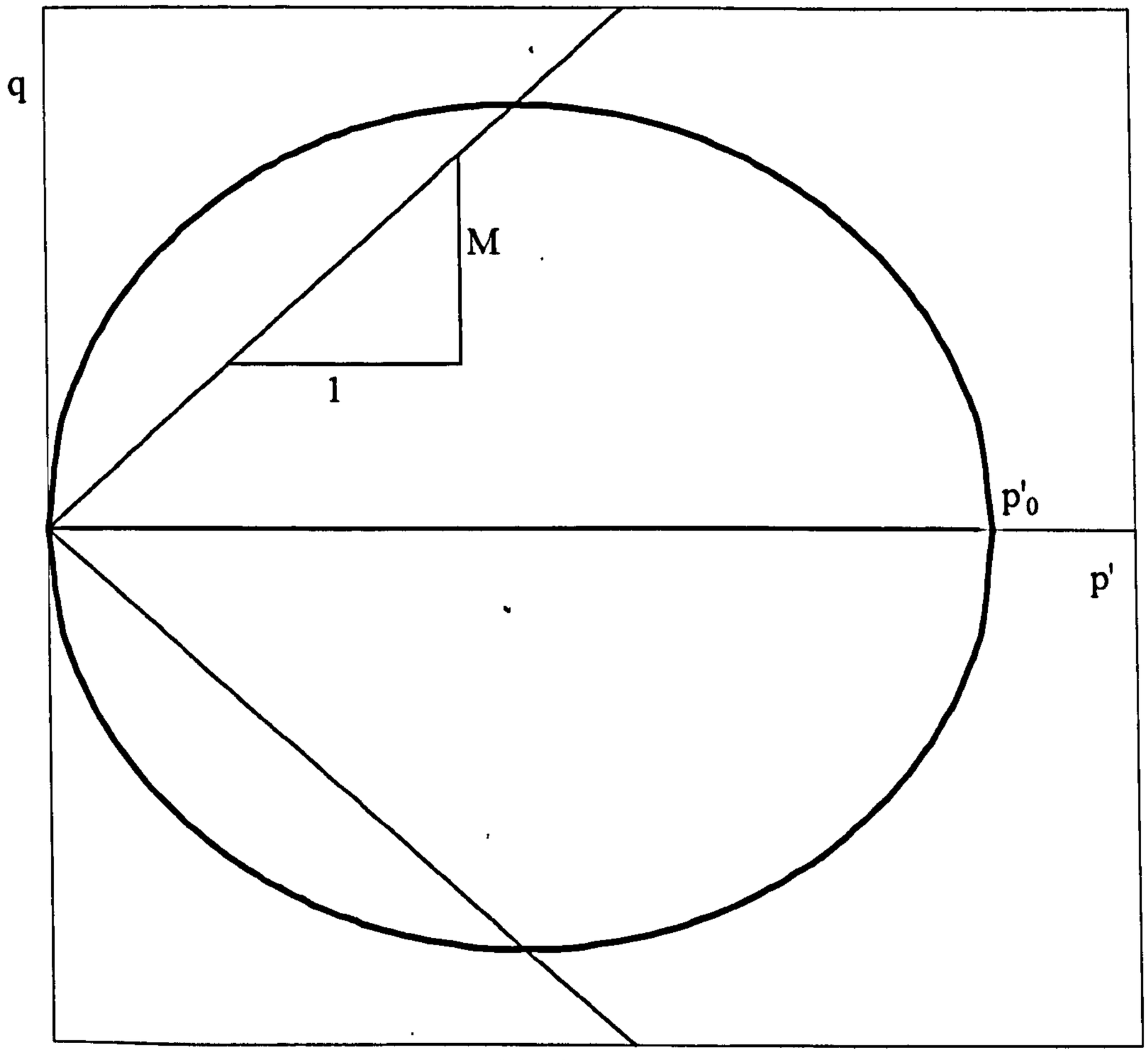

Figure 2.5. Modified Cam Clay yield curve.

predictions involving undrained shearing where the model fails to predict a peak in the stress-strain relationship, a feature commonly observed in experimental data on many natural clays. Davies and Newson (1993) observed that MCC overpredicted values of axial strain in drained shearing, compared to experimental data. Further evidence is given in Chapters 3, 6 and 7 regarding the weaknesses of the Modified Cam Clay predictions. Overall, in the light of the above evidence, it is clear that Modified Cam Clay has significant limitations for modelling of natural clays and more realistic modelling techniques are therefore desirable.

Dafalias (1987) developed an anisotropic model based on Modified Cam Clay. For the simplified case of triaxial tests on vertically oriented samples, the proposed yield function was

$$f = (q - \alpha p')^2 - (M^2 - \alpha^2)(p'_m - p')p' = 0 \qquad (2.6)$$

where the additional parameter α defines the orientation of the sheared elliptical yield curve as shown in Figure 2.6. In this form of yield curve, tangents to the ellipse are vertical at the origin and at point A (where $\eta = \alpha$) and horizontal at B (where $\eta = M$).

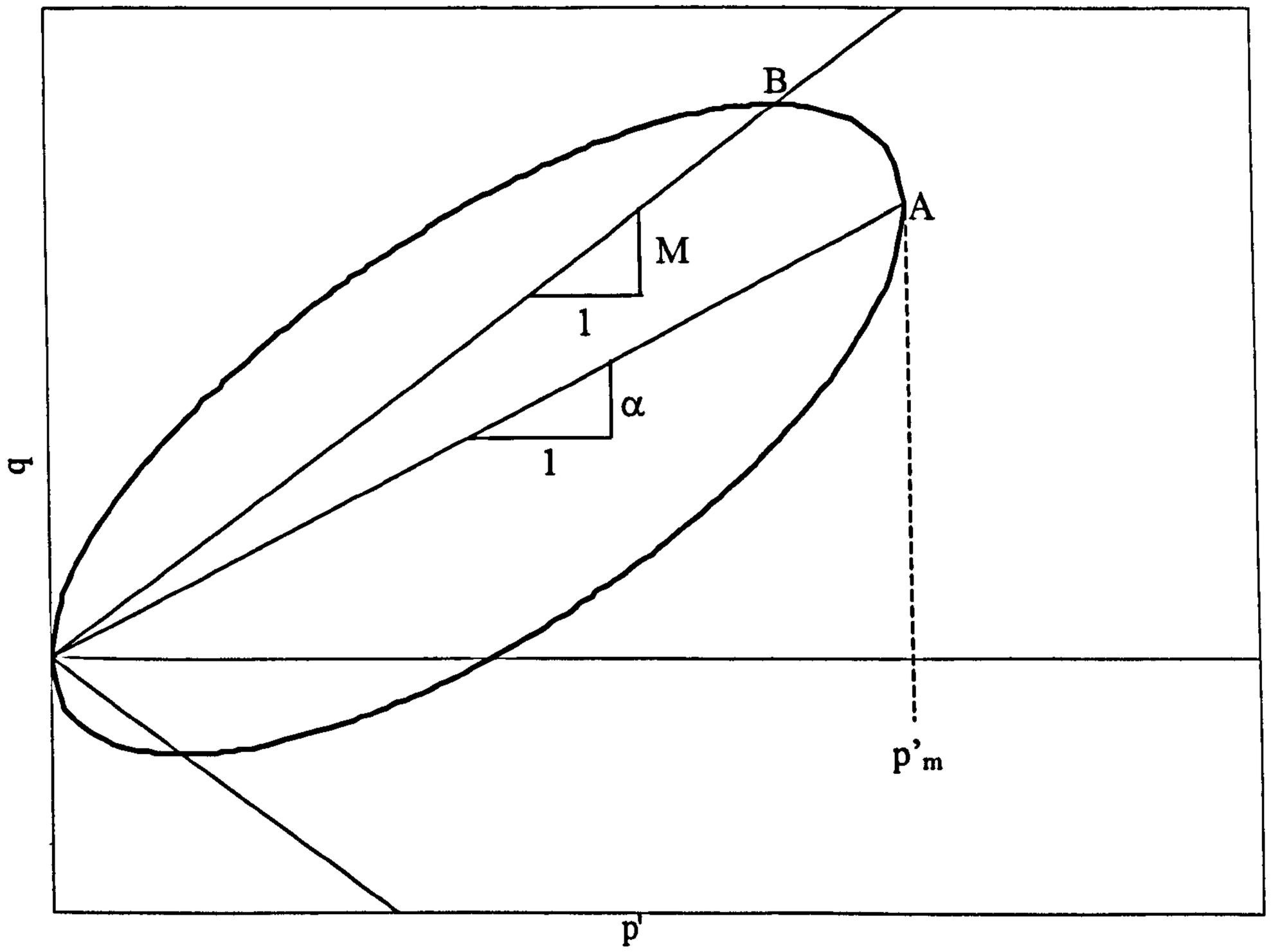

Figure 2.6. Yield curve proposed by Dafalias (1987).

The size of the yield curve (its horizontal width) is defined by p'_m. The aspect ratio (the ratio of the vertical height of the sheared ellipse, measured at $p' = p'_m/2$ to its horizontal width, p'_m) is given by $(M^2 - \alpha^2)^{1/2}$. This form of yield curve is identical to that proposed independently by Korhonen and Lojander (1987).

The model of Dafalias (1987) retained the associated flow rule from Modified Cam Clay and the change in size of the yield curve (defined by p'_m) was linked only the plastic volumetric strain, as in Modified Cam Clay. A component of rotational hardening was, however, introduced by Dafalias to account for the development or erasure of anisotropy with plastic straining. The rotational hardening component

attempts to align the yield curve towards a target value of α during plastic straining. The law is given by

$$d\alpha = k\frac{vp'}{p'_m}\left(\frac{\eta}{x}-\alpha\right)\left|d\varepsilon_v^p\right| \tag{2.7}$$

where k and x are soil constants, v is the specific volume and $d\varepsilon^p_v$ is the increment of plastic volumetric strain. Equation 2.7 shows that plastic volumetric strains (both positive and negative) rotate the yield curve so that α moves towards a target value of η/x.

The merits of the Dafalias (1987) model lie in the relative simplicity of its equations. However, the absence of any dependency on plastic shear strains in the rotational hardening law is physically unreasonable and creates a problem in the model predictions (see Karstunen and Wheeler, 2002). In Figure 2.7 (a) the Dafalias yield curve is shown again. A soil sample has a stress history involving isotropic loading to a stress level A, so that the yield curve has rotated to $\alpha = 0$ (and the yield function has effectively reduced to the Modified Cam Clay form). The sample has then been isotropically unloaded to an overconsolidated state at point B and sheared at constant mean effective stress to a critical state at point C. In Figure 2.7 (b) an identical sample has undergone an anisotropic stress history involving loading to point D, so that the yield curve is oriented with $\alpha > 0$. The sample has then been unloaded to a stress point E, identical to point B in Figure 2.7 (a). Finally, the sample is sheared, again at constant p', to a critical state at F. At points C and F, on the critical state line, with an associated flow rule, only plastic shear strains are generated. Without dependence of the rotational hardening on plastic shear strains it is impossible for further rotation of the yield curve to occur. As a consequence, a critical state can be achieved in both cases, but this will occur with $\alpha = 0$ in Figure 2.7 (a) (isotropy of the soil) and $\alpha > 0$ in Figure 2.7 (b) (anisotropy of the soil). The final degree of anisotropy at a critical state is therefore predicted to be dependent on the initial anisotropy and on the stress path followed to a critical state. This appears physically unreasonable, given that indefinite plastic shear straining at a critical state would be

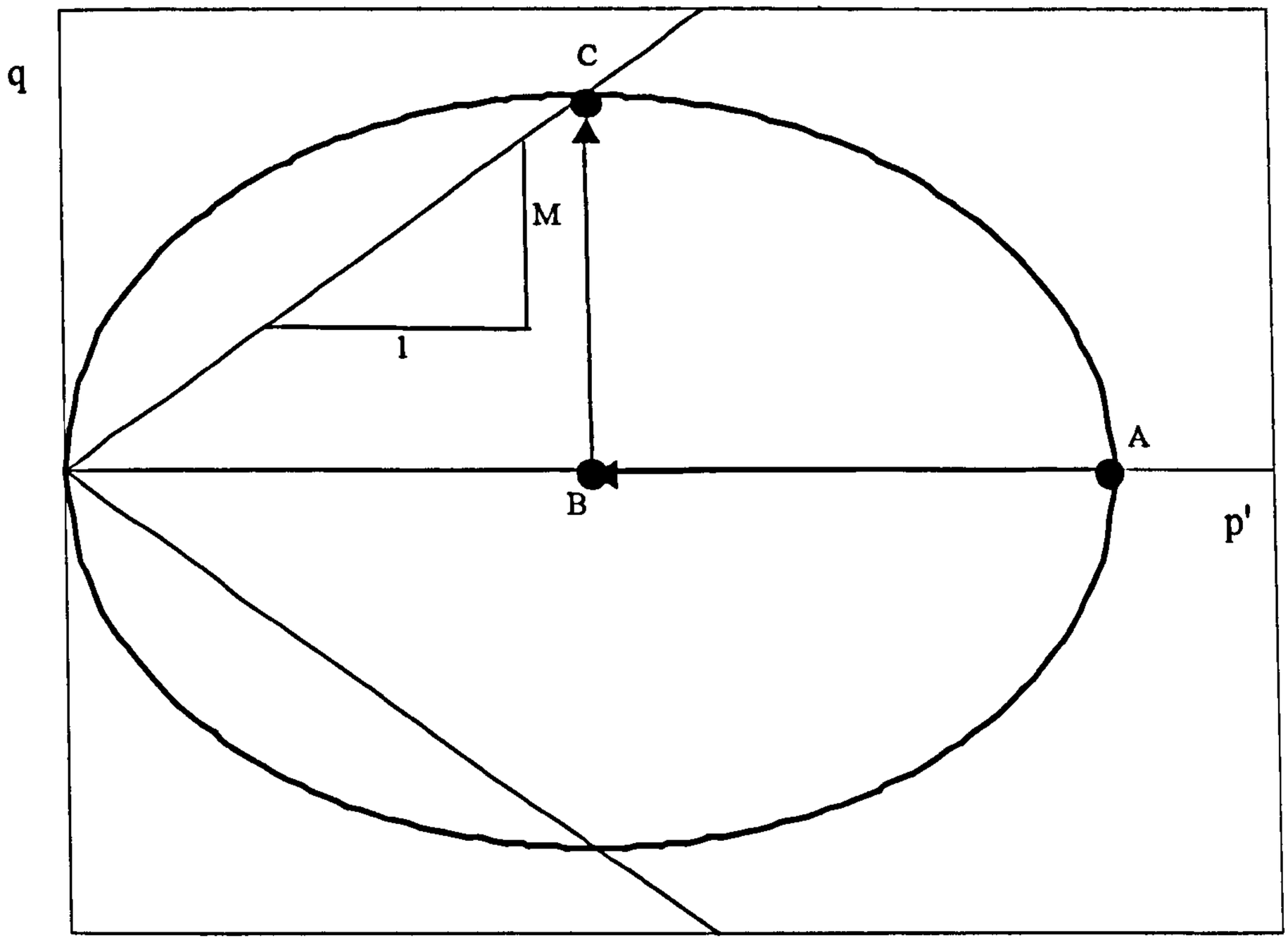

(a)

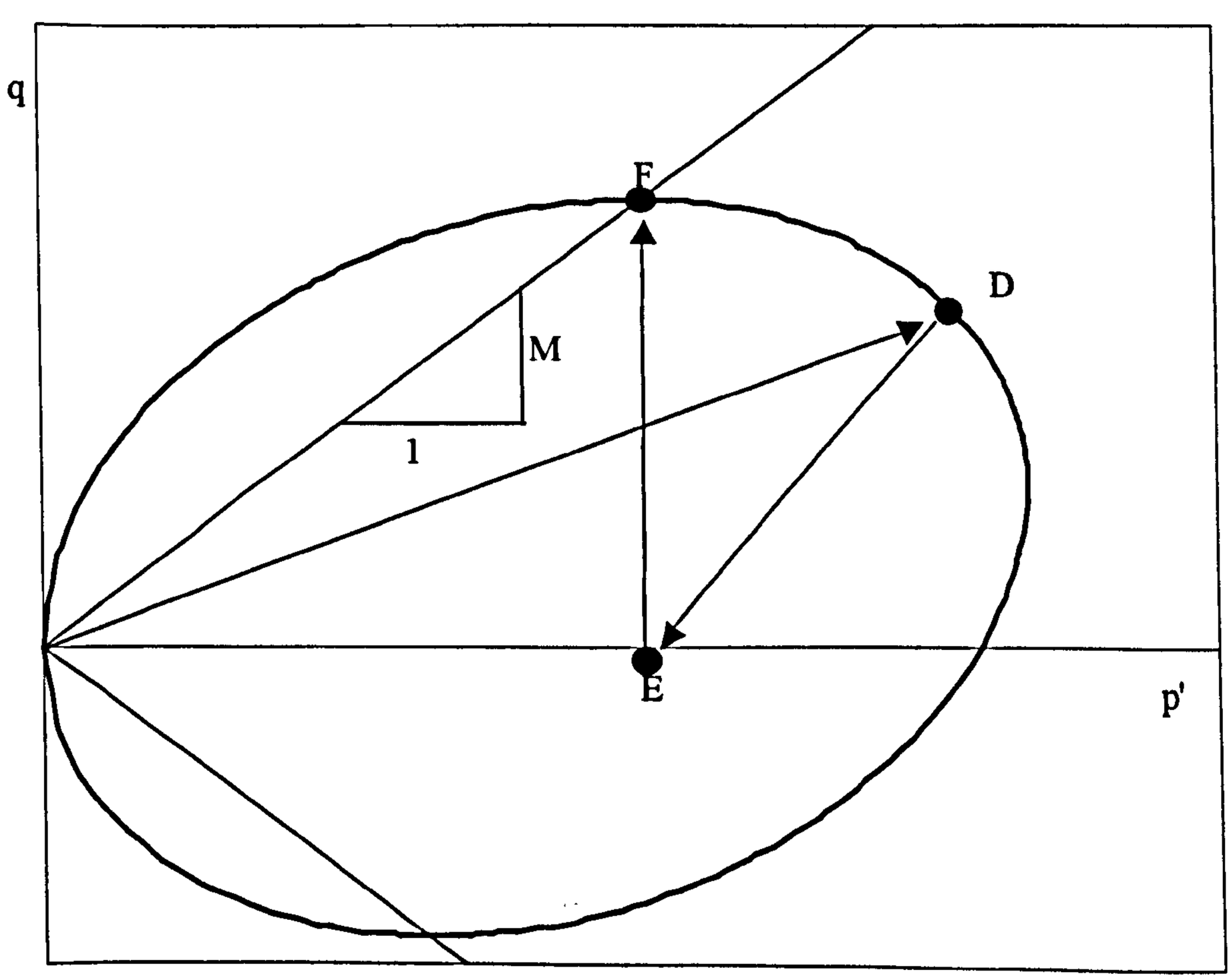

(b)

Figure 2.7. Model predictions for Dafalias model; (a) isotropic stress history, (b) anisotropic stress history.

expected to erase any influence of initial anisotropy. The final size of the yield curves are also different in Figures 2.7 (a) and 2.7 (b), and as a consequence the values of specific volume v are different at points C and F. Again, it seems unreasonable that critical state values of v at a given value of p' should be dependent on the initial anisotropy and on the stress path taken to a critical state.

A model proposed by Banerjee and Yousif (1986) also used an inclined yield curve in the form of a sheared ellipse and a rotational component of hardening. The yield curve, shown in Figure 2.8 can be written as:

$$\left(q-\frac{2}{3}\eta_0 p'\right)^2-\frac{1}{9}p'p'_0\eta_0^2-\mathrm{M}^2p'\left(p'_0-p'\right)=0 \qquad (2.8)$$

where p'_0 and η_0 define the size and inclination of the yield curve, but these are defined at a point B (see Figure 2.8) rather than the vertical tangent point A. Noting that α, the gradient to the vertical tangent point A, is related to η_0 as follows:

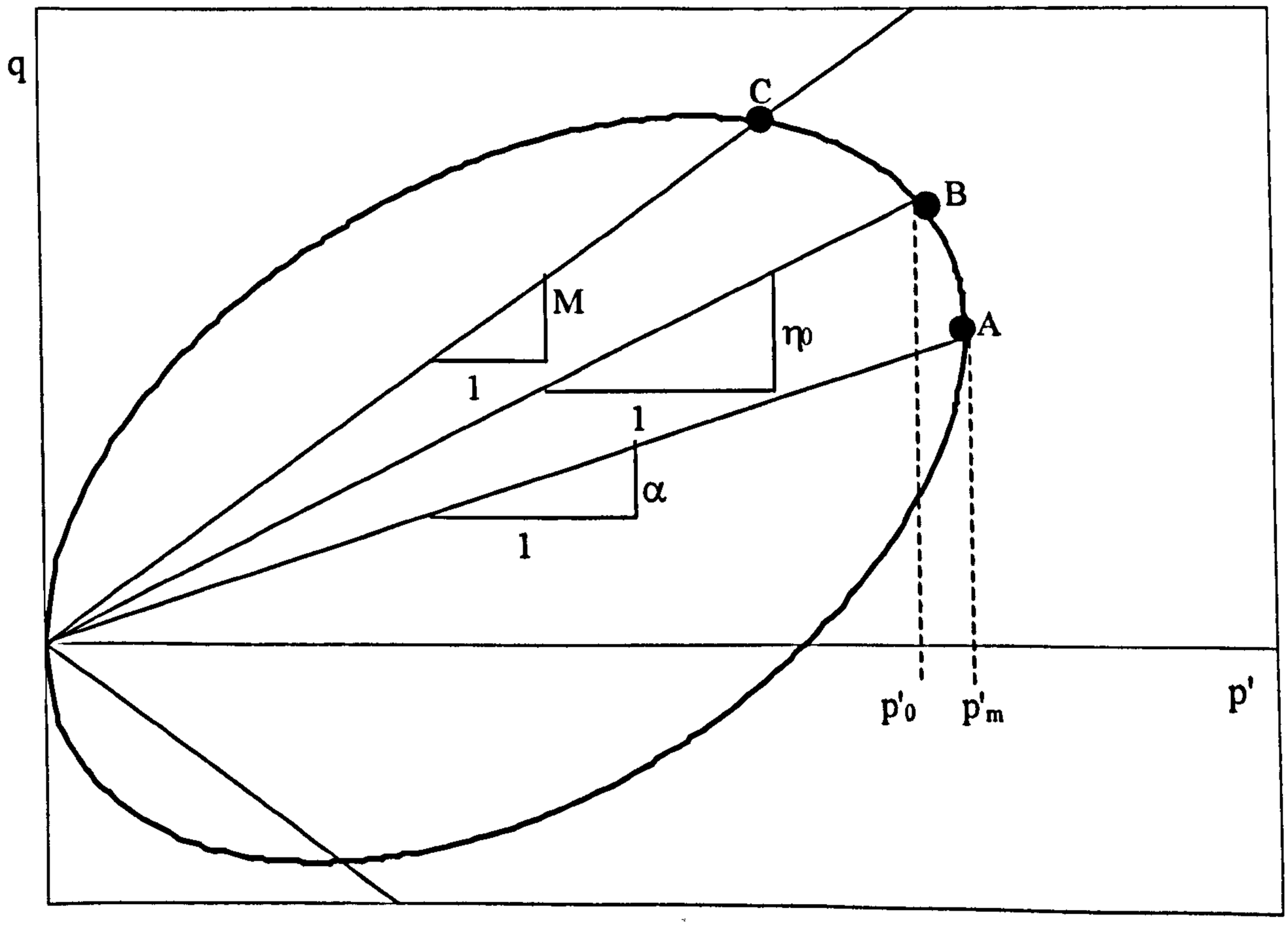

Figure 2.8. Yield curve proposed by Banerjee et al. (1986).

$$\alpha = \frac{2}{3}\eta_0 \tag{2.9}$$

the yield curve expression of Banerjee et al. (1986) can be expressed as:

$$(q - \alpha p')^2 - \mathrm{M}^2 p'(p'_m - p') = 0 \tag{2.10}$$

where

$$p'_m = p'_0\left(1 + \frac{\alpha^2}{4\mathrm{M}^2}\right) \tag{2.11}$$

The only difference therefore with the yield curve of Dafalias (1987) (see Equation 2.6) is that the aspect ratio of the sheared ellipse is M rather than $(M^2 - \alpha^2)^{1/2}$. A consequence is that in the Banerjee and Yousif (1986) model the yield curve is not horizontal where it intersects the critical state line (see point C in Figure 2.8), thereby incurring the need for a non-associated flow rule and the complications that this may bring. Again, the Banerjee and Yousif (1986) model incorporates a rotational hardening law which depends only on plastic volumetric strains (no dependency on plastic shear strains).

Davies and Newson (1993) also developed a constitutive model incorporating a sheared elliptical yield curve and a rotational hardening law. The proposed yield function in triaxial stress space can be written as

$$(q - \alpha p')^2 - \left(\frac{M - \alpha}{1 - \frac{\alpha^3}{\mathrm{M}^3}}\right)^2 (p'_m - p')p' = 0 \tag{2.12}$$

Comparisons with Equations 2.6 and 2.8 show that the aspect ratio of the elliptical yield curve is $(M - \alpha)/(1 - \alpha^3/M^3)^{1/2}$ in the Davies and Newson model. Again this means that the yield curve is not horizontal where it intersects the critical state line (see point C in Figure 2.9) and a non-associated flow rule is therefore employed in

the model. The rotational hardening law in the model of Davies and Newson (1993) is given by

$$d\alpha = \pm\left(1-\left(\frac{\eta_s}{M}\right)^2\right)\cdot\Delta p^*\cdot\exp(\eta_s-\alpha_s) \tag{2.13}$$

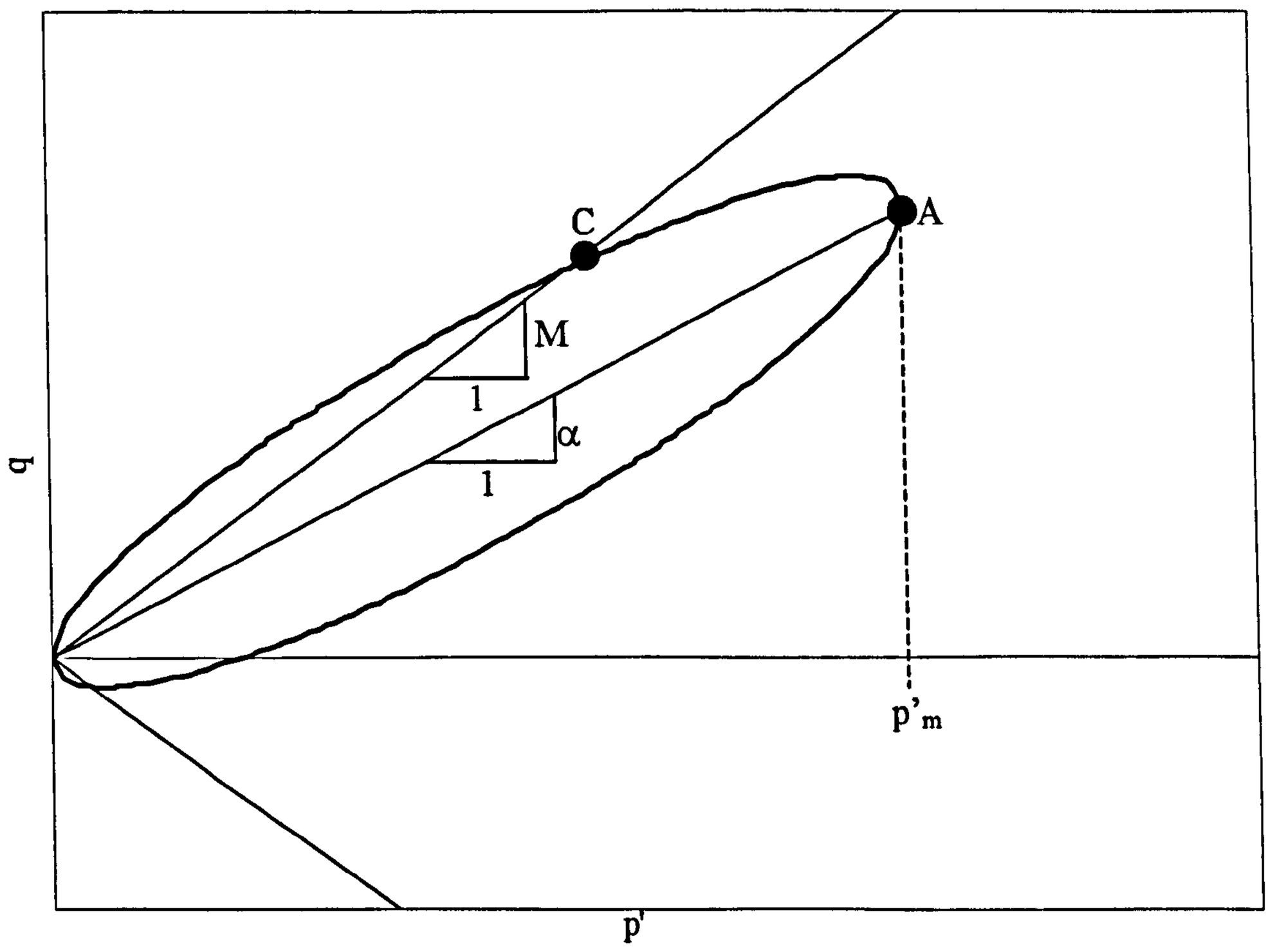

Figure 2.9. Yield curve after Davies and Newson (1993).

where α_s is the rotation of the ellipse at the start of an increment of loading and η_s is the stress ratio at the start of the increment. Δp^* is related to $\Delta\eta$, the change of stress ratio during an increment of loading, with $\Delta p^* = 0$ for $\Delta\eta = 0$ and non-zero values for Δp^* when $\Delta\eta$ is non-zero (see Davies and Newson (1993) for full definition of Δp^*). A feature of this rotational hardening law is therefore that when loading at a constant value of stress ratio η, no rotation of the yield curve will occur. In reality, this is physically unreasonable, such as in the case of an isotropic soil ($\alpha = 0$) loaded anisotropically (η = constant $\neq 0$), or anisotropic soil ($\alpha \neq 0$) loaded isotropically (η = constant = 0). Another weakness of this rotational hardening law is the influence of the exponential term in Equation 2.13. This means that very large values of $d\alpha$ can be predicted when α is less than η_s (unless $\Delta p^* = 0$), whereas small values of $d\alpha$

are predicted when α is more than η_s. Finally, upon shearing to the critical state stress ratio, where η_s/M tends to unity, the model will predict no rotation of the yield curve. As with the models of Dafalias (1987) and Banerjee et al. (1986), the Davies and Newson (1993) model therefore predicts that the degree of anisotropy on reaching a critical state stress ratio is dependent on the initial anisotropy and on the stress path to the critical stress state.

In three-dimensional stress space, the Modified Cam clay yield curve is an ellipsoid centred on the p' axis, as shown in Figure 2.10 (a). If the yield curve for natural soils in triaxial stress space is really inclined away from the p'-axis then the ellipsoidal yield surface will be similarly inclined (see Figure 2.10 b). In general, the soil will have undergone one-dimensional history where the y-direction corresponds to the vertical direction in the ground. The S-CLAY1 and S-CLAY1S models (described in Chapter 3) are examples of models that have been developed to account for fully generalized stress states.

Multilaminate modelling

As an alternative to the rotational hardening models described above, anisotropy can be modelled using a multilaminate framework. This framework was introduced into soil modelling by Zienkiewicz and Pande (1977) and Pande and Sharma (1983). Within this framework, the soil is assumed to be a large homogenous isotropic element behaving elastically (at macroscopic level) and this block is intersected by a number of randomly oriented sampling planes upon which plastic straining may occur (at microscopic level). Each sampling plane is defined in terms of the normal effective stress (σ'_n) and the shear stress (τ). For a soil with an isotropic stress history, the yield curves on each of the sampling planes will be of identical size. Under an isotropic stress state, the stresses on all sampling planes are identical. If a soil is subjected to an anisotropic stress state, different stress states will arise on each of the sampling planes. For a soil with an anisotropic stress history, the yield curves on each of the sampling planes will be of different size. Therefore, this type of framework can incorporate the effects of anisotropy without the need for any additional parameters. Zentar et al. (2002a) have shown that a particular

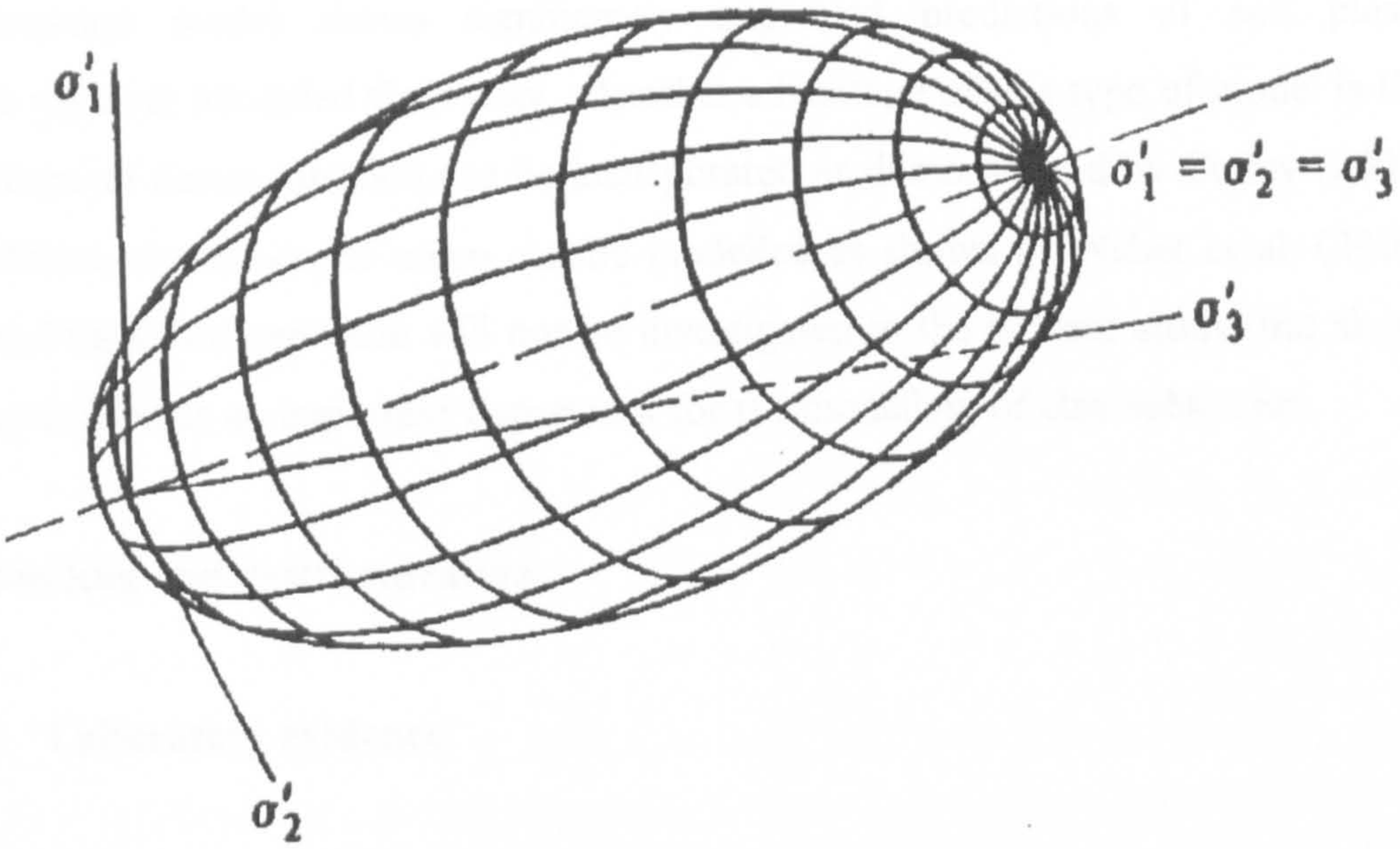

(a)

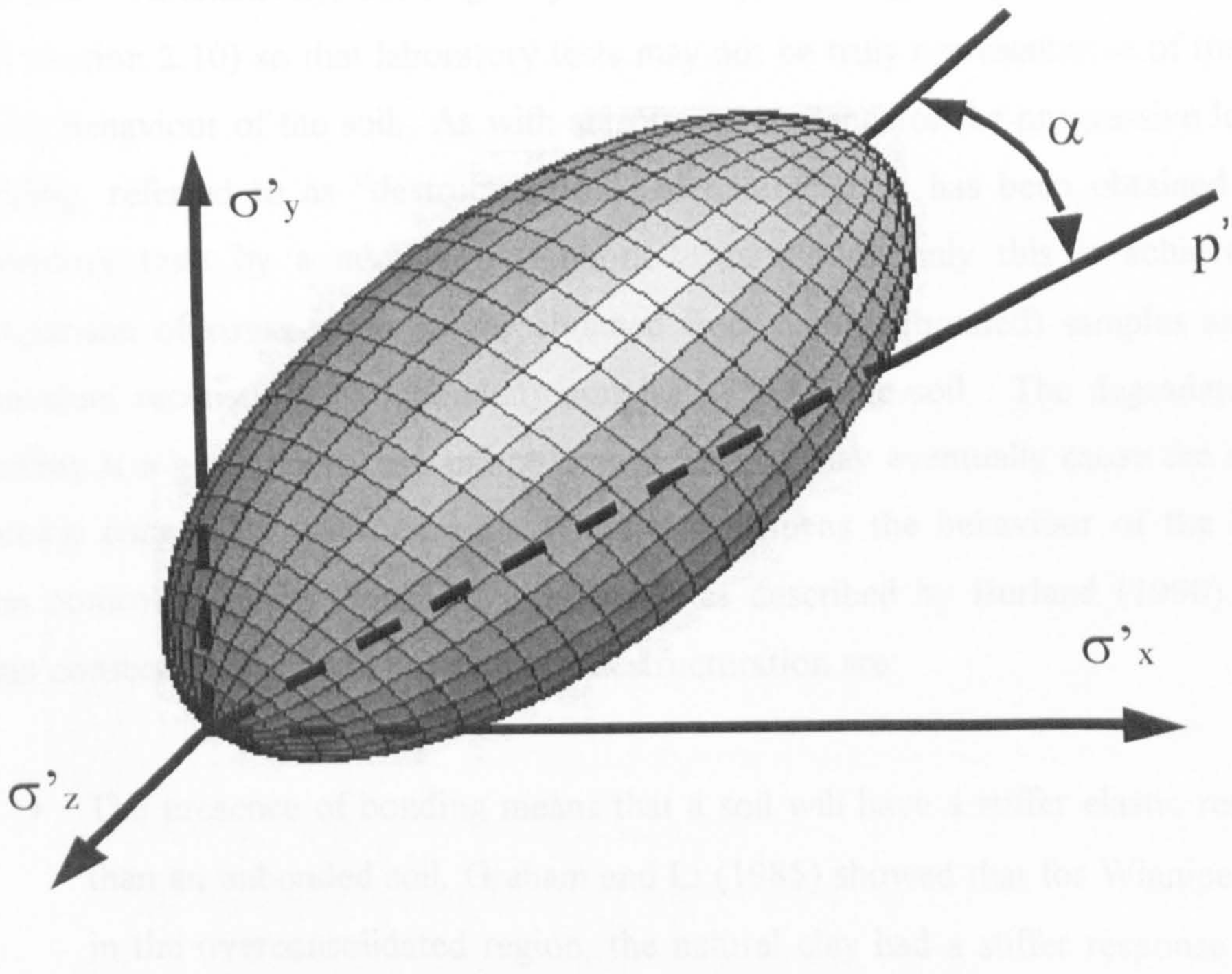

(b)

Figure 2.10 (a) Modified Cam Clay yield surface in general stress space, (b) anisotropic yield surface (Dafalias, 1987) in general stress space.

multilaminate model shows significantly improved predictions of soil plastic anisotropy over Modified Cam Clay. Another advantage of this type of model is that the effects of destructuration can be incorporated as demonstrated by Cudny (2003). In addition, the effects of creep can be modelled as shown by Neher et al. (2001). The multilaminate approach will not be investigated in the present study, but should be appreciated as an important framework for the modelling of clay behaviour.

2.7 Bonding and destructuration

2.7.1 Laboratory evidence

Soil bonding is the cementation between particles (or aggregates of particles) and strongly influences its mechanical behaviour. Bonding may be destroyed as a consequence of straining and this causes significant changes in its mechanical response. Alternatively, bonding may be destroyed during the process of sampling (see Section 2.10) so that laboratory tests may not be truly representative of the true in-situ behaviour of the soil. As with anisotropy, evidence of the progressive loss of bonding, referred to as "destructuration", in natural clays has been obtained from laboratory tests by a number of authors. Most commonly this is achieved by comparison of stress-strain curves obtained from natural (bonded) samples and the equivalent reconstituted (unbonded) samples of the same soil. The degradation of bonding is a gradual process and continued loading may eventually cause the soil to become completely unstructured. When this happens the behaviour of the soil is then controlled by its "intrinsic" properties, as described by Burland (1990). The main consequences of soil bonding and destructuration are:

- The presence of bonding means that a soil will have a stiffer elastic response than an unbonded soil. Graham and Li (1985) showed that for Winnipeg clay, in the overconsolidated region, the natural clay had a stiffer response than a corresponding reconstituted clay.
- A bonded soil will have a greater peak shear strength than the equivalent unbonded soil and destructuration will cause a reduction in this strength. The increase in strength given by soil structure has been observed experimentally.

A comparison of results from undrained triaxial tests on intact and destructured natural clays presented by Leroueil and Vaughan (1990) indicated that the destructured clay was initially less stiff than the bonded clay and reached a lower peak strength at a higher strain level. Undrained shear tests performed on natural and reconstituted Eastern Osaka clay by Adachi et al. (1995) showed that the peak strength of the reconstituted clay was much smaller than that of the disturbed clay, but that the strength of the reconstituted clay at very large strains was similar to the residual strength of the intact clay.

- The presence of bonding gives a soil additional resistance to yielding. Figure 2.11 shows the normal consolidation of a natural (structured) clay soil and that of a corresponding reconstituted soil. The compression curve α- α marks the intrinsic compression line for the soil (as defined by Burland, 1990), where the void ratio decreases during sedimentation. After deposition, further processes may then occur, such as cementation and thixotropic hardening and the soil attains interparticle bonding. Therefore, for the structured soil p'_{y1} is the mean effective stress at which yielding begins and Δv is the difference in void ratio between the natural and reconstituted clay at this stress as a result of the apparently higher yield stress in the bonded soil. The bonded sample would produce a compression curve which would lie above that of a corresponding reconstituted material. The presence of bonding therefore permits the bonded material to exist in states where the reconstituted material cannot.

- Evidently from Figure 2.11 the post-yield compression gradient of the structured soil (λ) is different to that of the reconstituted soil (λ_i). As a bonded soil undergoes post-yield compression the initial post-yield gradient of the natural soil is much greater than that of the reconstituted soil. As the soil is destructured and there will be a marked decrease of the of the post-yield gradient and it eventually decreases to λ_i. . The post-yield compression curve for the bonded material will eventually converge with the post-yield compression curve for the unbonded soil. It was noted by Kenney et al. (1967) and Leroueil and Vaughan (1990) that when the "bond strength" of

the cement is exceeded, and bonds begin to break, there is an abrupt increase in compressibility. This is illustrated in Figure 2.11 where the post-yield compression curve for the bonded soil is initially much steeper than that of the intrinsic curve. Diaz Rodriguez et al. (1992) and Tavenas and Leroueil (1978) noted that for a variety of natural clays, the slope of the post yield compression curve increases as the stress ratio q/ p' increased.

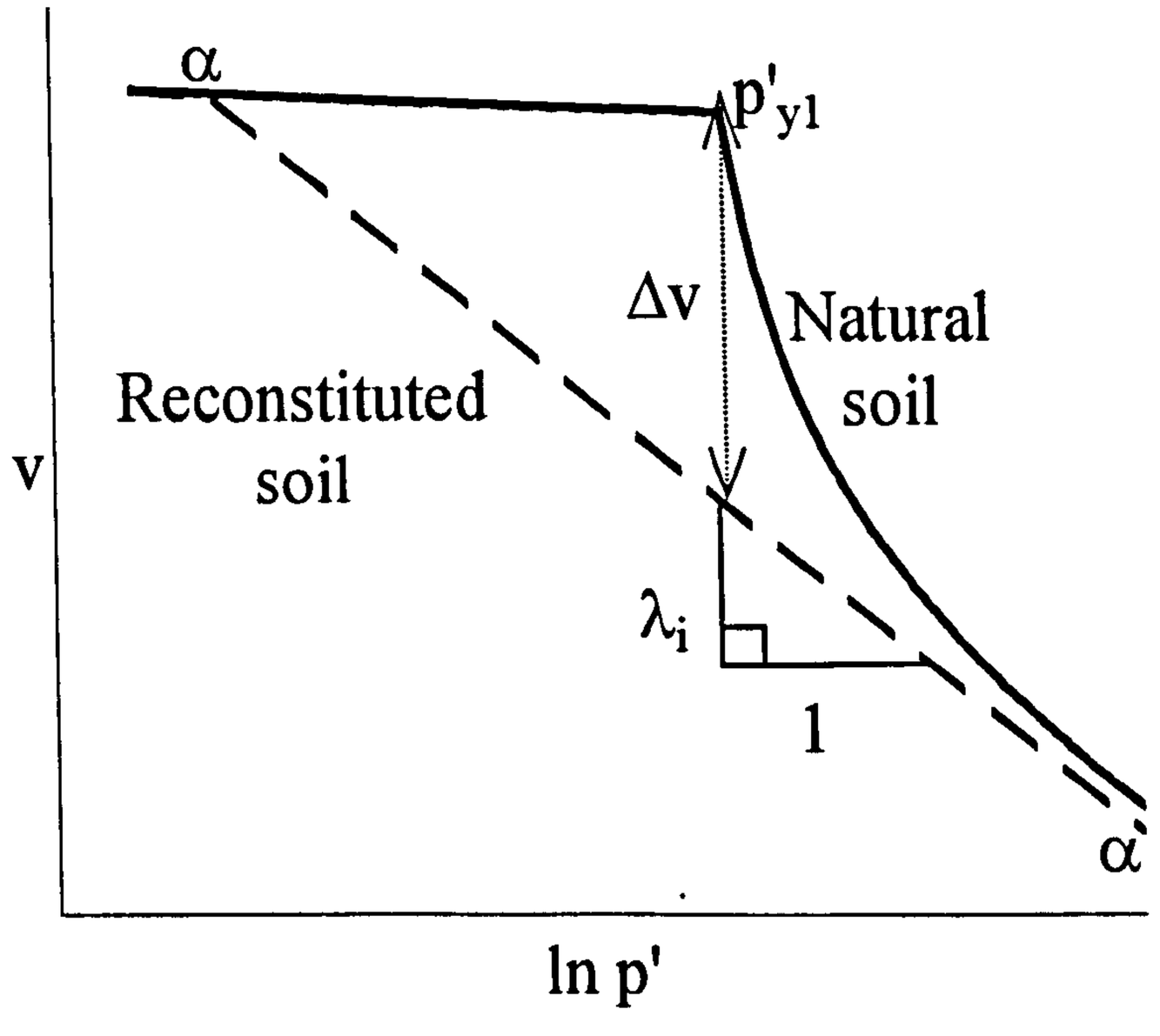

Figure 2.11. Compression curves for natural and reconstituted soils.

The depositional and post-depositional processes described in Sections 2.3 and 2.4 determine the initial structure of a clay, including any presence of bonding. Chemical weathering of a clay, as discussed by Bjerrum (1967), causes a change in the strength, plasticity and compressibility of the clay. Generally, this will involve an increase in the stiffness, the pre-consolidation pressure, and the soil strength. In contrast, leaching causes an increase in compressibility and a decrease in the undrained shear strength.

The degree to which natural clays are structured can be characterised in a number of ways, including:

- Comparison of the strength of the natural clay and the strength of the equivalent reconstituted clay, at the same void ratio (sensitivity),

- State, by examining differences in void ratio of natural and reconstituted clay at the same stress state, and comparison of the yield stress of natural and reconstituted clays.

Bonding or cementation is an important feature of natural clays. Bjerrum (1967) made a distinction between cemented clays and non-cemented clays. He stated that the strength of non-cemented clays (e.g. reconstituted clays) may be comprised of both a component of friction and a component of cohesion, but cemented clays have additional resistance as a result of post-depositional processes. Cementation imparts an increase in peak undrained shear strength and causes an apparent increase in the preconsolidation stress p'_c. Cementing can be removed in a number of ways. Plastic strains (involving slippage at inter-particle contacts during either compression or swelling) cause a progressive breakdown of these bonds. In addition the cementing agents can be removed by leaching. Evidence of the effects of thixotropic hardening has been reported by a number of authors. Results show that there is a similar response to cementing, with an increase in peak shear strength and reduced compressibility.

2.7.2 Constitutive modelling of destructuration

A number of authors have attempted to model the effects of soil bonding and destructuration and some of these models are now discussed.

Gens and Nova (1993) adapted constitutive laws appropriate for unbonded materials that could be modified to account for bonding and destructuration. They stated that after the onset of yield, plastic straining caused a gradual monotonic degradation of the particle bonds. Figure 2.12 (a) shows compression lines for materials with various constant degrees of bonding. For an unbonded soil, states to the right of the intrinsic compression line A-A are impossible. The degree of bonding can be characterized by the difference in void ratio (Δe) between the bonded and unbonded soils at the same stress level. The proposed yield curves are shown in Figure 2.12 (b). Curve A corresponds to the unbonded soil and its size is given as p_c. Curve B represents a bonded material and curve C a material with a greater degree of bonding

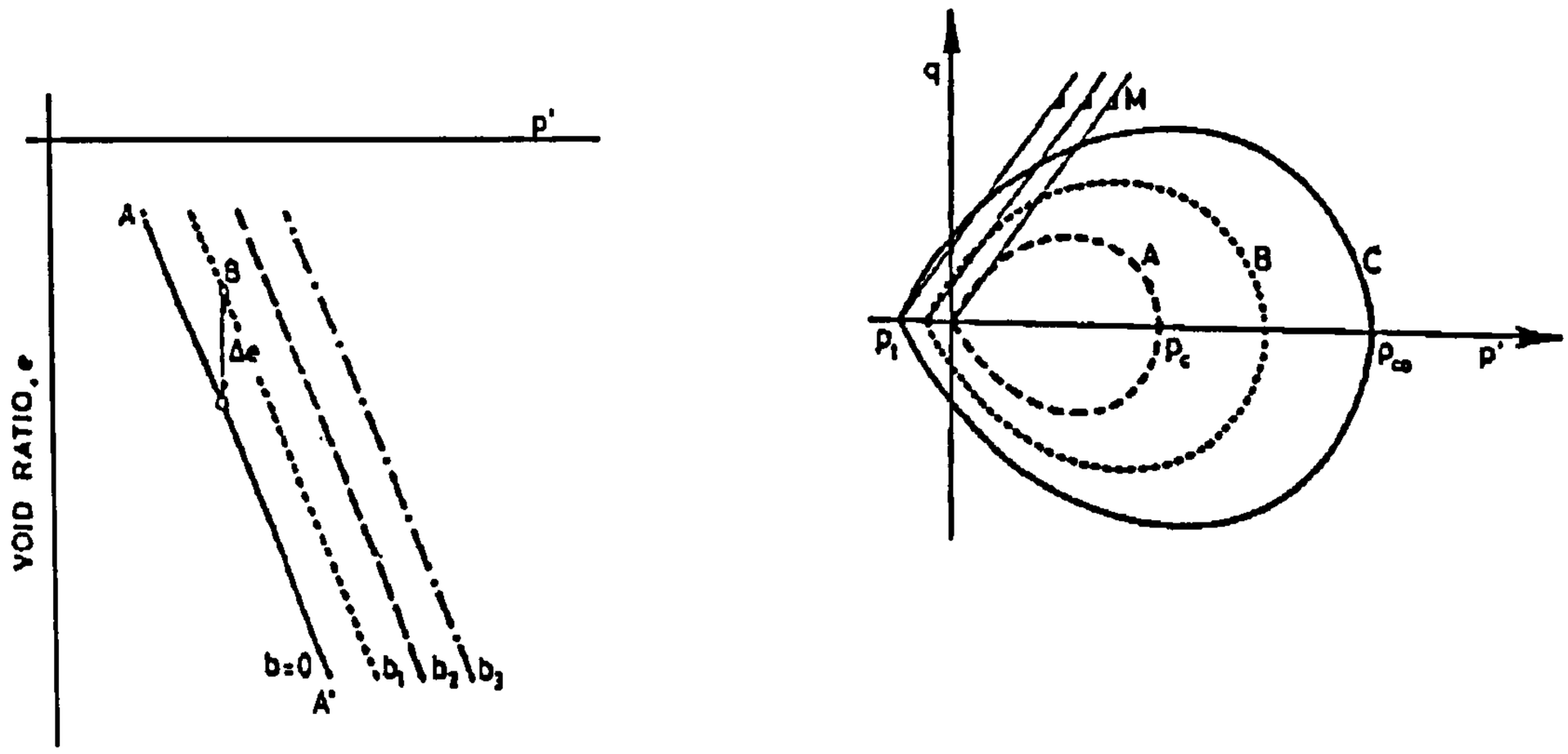

Figure 2.12 (a) Consolidation lines for various degrees of bonding; (b) Yield curves for various degrees of bonding (Gens and Nova, 1993).

than B, so that as the amount of bonding increases, greater stress can be applied to the material before it yields. The size of the yield curve for a bonded soil (curves B or C) is given by p'_{c0}. Bond degradation will cause the ratio of p_{c0}/p_c to decrease and this ratio will be equal to unity when all bonding has been destroyed. Curves B and C indicate that a bonded material, according to Gens and Nova (1993), will have a tensile strength (and therefore cohesion), the magnitude of which is defined by p_t.

Changes in size of the yield curve in Figure 2.12 (b) are governed by two mechanisms. The first mechanism is by conventional hardening (or softening) of the unbonded material. Gens and Nova (1993) assumed that this hardening was isotropic and therefore any anisotropy of the clay behaviour (as described in Section 2.6) is ignored. The second mechanism is caused by destructuration and Gens and Nova suggested that bonds are destroyed as a result of both plastic shear and plastic volumetric strains. This includes dilatant plastic volumetric strains since these have a tendency to overcome bond strength. In this model, the amount of damage caused to the soil bonds is expressed by an additional hardening law (sometimes called a destructuration law):

$$dx = -x\left(h_1\left|d\varepsilon_d^p\right| + h_2\left|d\varepsilon_v^p\right|\right) \tag{2.14}$$

where x is the current degree of bonding, $d\varepsilon_d^p$ and $d\varepsilon_v^p$ are the increments of plastic shear strain and plastic volumetric strain, and h_1 and h_2 are soil constants governing the relative influence of plastic shear and plastic volumetric strains in the destructuration process. The modulus signs in Equation 2.14 ensure that bonding will be destroyed irrespective of the direction of plastic straining. Comparisons by Gens and Nova (1993) of computed triaxial tests results for an unbonded material and a bonded material for a variety of loading directions showed that their model could qualitatively predict the features of a natural soil. However, the model lacks the ability to incorporate the evolution of anisotropy.

Rouainia and Muir Wood (2000) formulated a model capable of representing a soil with an initial degree of structure which could then become destructured. Again the model is an extension of Modified Cam Clay, but incorporates three yield surfaces as shown in Figure 2.13. The reference surface represents the behaviour of the completely remoulded soil. The inner "bubble surface" represents the boundary between elastic and plastic states and will move according to the current stress point. At the onset of plastic straining, destructuration will occur and the "structure surface" will collapse towards the reference surface. The use of multiple yield surfaces in this model provides not only representation of destructuration but better characterisation of small strain behaviour (see Section 2.8.4). The model assumes that the damage to the bonds is due to plastic volumetric and plastic shear strains. Therefore, the destructuration law is dependent on both and is given by

$$dx = -x\left[(1-A)(d\varepsilon_v^p)^2 + A(d\varepsilon_d^p)^2\right]^{\frac{1}{2}} \tag{2.15}$$

where x again represents the amount of bonding and A is a scaling parameter controlling the relative contributions of plastic shear strains and plastic volumetric strains. Clearly, Equation 2.15 is similar in form to the destructuration law of Gens and Nova (1993) (Equation 2.14). Rouainia and Muir Wood (2000) presented model simulations and claimed that if the correct model parameters can be established, then predictions can match the experimental data closely. An advantage of the triple yield surface is that as the bubble approaches the structure surface, the model predicts a reduction in the stiffness of the soil. This is consistent with experimental

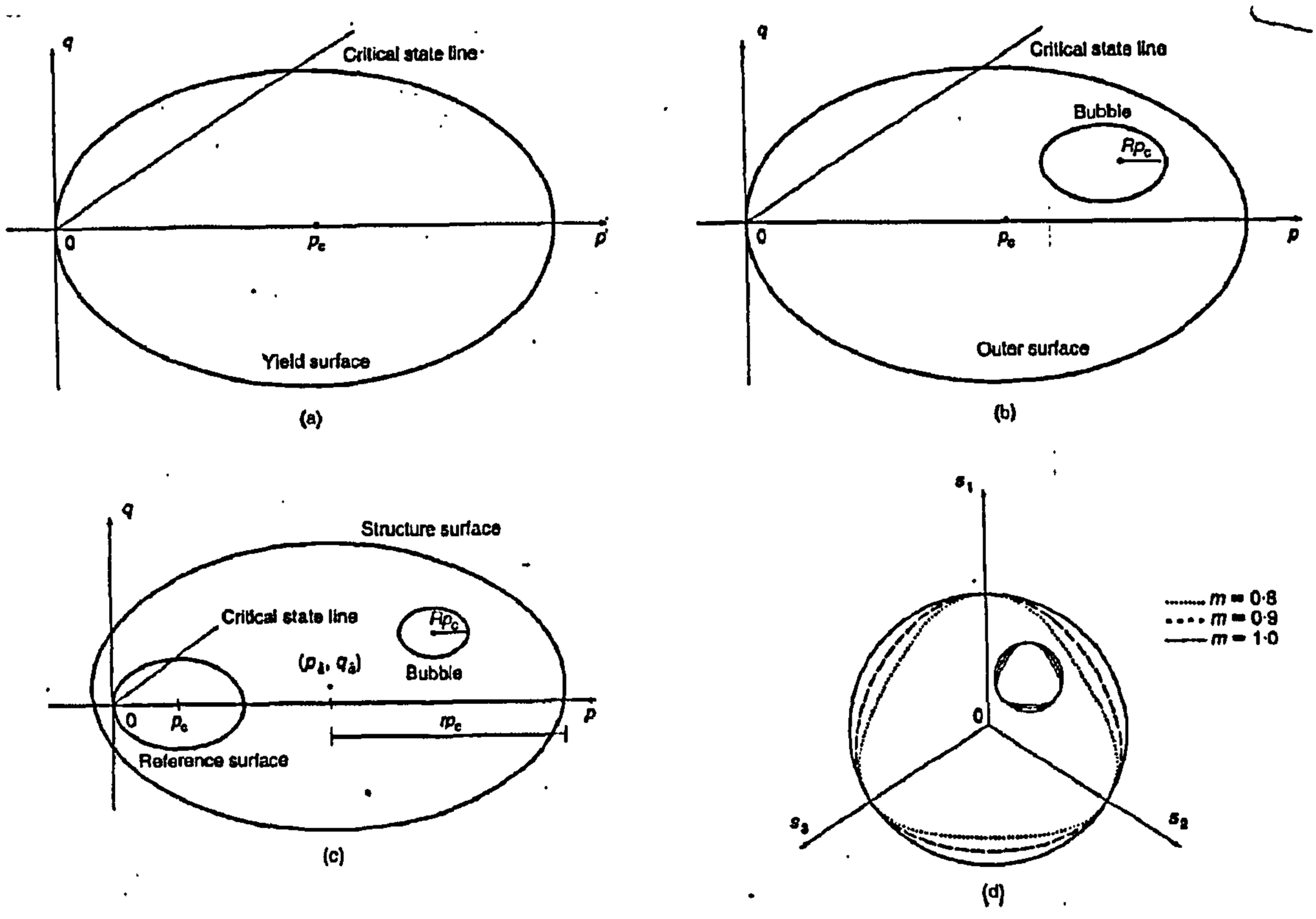

Figure 2.13. Yield surfaces proposed by Rouainia and Muir Wood (2000).

observations and indicates that the onset of plastic strains is a gradual phenomenon. This type of behaviour would not be predicted by Modified Cam Clay in which yield is an instantaneous phenomenon. One disadvantage of this model is that large strain anisotropy is assumed to be solely due to the effects of bonding and that the effects of anisotropy disappear once the destructuration process is complete. Experimental evidence shows that this is unrealistic and that clay fabric orientation may continue to evolve regardless of whether bonding is present or not (see, for example, tests on reconstituted clay by Koskinen et al., 2002b). Another potential disadvantage of this model is that a substantial suite of high quality triaxial tests would be necessary in order to estimate the soil parameters for a particular clay.

Liu and Carter (2000 and 2002) proposed a new framework for modelling destructuration again extended from Modified Cam Clay. Soil behaviour is defined by a single yield surface (that of Modified Cam Clay) and hardening is purely isotropic. The model assumes that plastic volumetric straining is comprised of two components:

$$d\varepsilon_v^p = \left(\lambda^* - \kappa^*\right)\frac{dp_0'}{vp_0'} + b\Delta e\left(1 + \frac{\eta}{M^* - \eta}\right)\frac{dp_0'}{vp_0'} \tag{2.16}$$

where * denotes the intrinsic properties of the soil and λ^* and κ^* are intrinsic post-yield compression and elastic swelling gradients respectively for the reconstituted soil. Δe is the difference in void ratio between a structured soil and a corresponding reconstituted soil. Post-yield compression is therefore comprised of two parts, the first associated with the intrinsic soil properties and the second with soil bonding and destructuration. The parameter b controls the amount of additional compression due to destructuration. The inclusion of the stress parameter η means that at higher stress ratios (and hence greater amounts of plastic shear strains), the rate of destructuration will be more rapid. Model simulations presented by Liu and Carter (2002) claimed that the model can be calibrated to match clay behaviour for a wide variety of soils. However, at time of writing, this model has not been developed to account for the effects of anisotropy.

In Section 3.3, an alternative elasto-plastic critical state model, proposed by Wheeler et al. (2003), is presented. The model, S-CLAY1S, incorporates the effects of large strain anisotropy and destructuration.

2.8 Small strain behaviour

The models described in Sections 2.6.2 and 2.7.2 assume that behaviour inside the yield surface is elastic and isotropic. The models presented in Chapter 3 have also been developed under this assumption. Experimental evidence has shown however, that this is not necessarily the case.

2.8.1 Non-linearity of small strain behaviour

Many classical soil models assume that pre-yield deformation of geomaterials occurred in an elastic fashion. This may be in the form of linear elasticity or, as in the case of Modified Cam Clay, non-linear elasticity. Advances in laboratory testing techniques, particularly in the last 25 years, have provided greater insight into small

strain behaviour. Tests by a number of authors including Jardine et al. (1984) have shown that the so-called "pre-yield" behaviour is highly non-linear. It is widely reported that shear stiffness decreases significantly as stress or strain is increased. This is still the case for stress paths which occur inside the yield surface of classical elasto-plastic models. Atkinson et al. (1990) have shown that soil stiffness is dependent on its recent stress history, which includes both the previous stress path and the time spent at constant stress before this stress path was applied. A wide body of research has shown that the range of constant soil stiffness only occurs over a very short space within the state boundary surface. Further research by Stallebrass (1990) (where strains smaller than 0.005% were measured) has shown that this dependency on recent stress history decreases as the soil is loaded, eventually becoming almost negligible. Importantly, this work also indicated that the strains recorded in these tests were irrecoverable, which led to the conclusion that the strains were inelastic.

Smith et al. (1992) conducted undrained and drained triaxial tests on samples of Bothkennar clay (limited to a depth range of 5.3 - 6.3 m) in order to determine the yielding characteristics of Bothkennar clay. They found that the soil behaviour was highly anisotropic and they interpreted their experimental data within a multi-yield surface framework as proposed by Jardine et al. (1991). Their work is presented in the context of triaxial stress space with 3 yield curves inside the bounding curve as shown in Figure 2.14. In Figure 2.14 the innermost yield (Y_1) represents the boundary of Zone 1 in which behaviour was thought to be linear and elastic (although not necessarily isotropic). As the stress level progresses to Zone 2, behaviour becomes non-linear (but still elastic) and stiffness reduces rapidly. The boundary of Zone 2 (Y_2) represents the onset of permanent (plastic) straining. Both Y_1 and Y_2 are kinematic surfaces that are dragged as the current stress point is moved through stress space. The boundary of Zone 3 (Y_3) represents the conventional yield surface where large plastic strains are developed.

Zone 1 was difficult to map as it involves the measurement of very small strains (typically resolvable at strains within 0.002 %). However, the limits of Zone 1 were thought be confined to a shear strain increment of approximately $\Delta\varepsilon_s = 0.01$ %. Smith et al. (1992) successfully mapped the development of Y_2, within which the soil

behaviour was nonlinear elastic (see Figure 2.14). Mapping of the third surface (Y_3) is discussed in Section 2.10 in the context of large-strain anisotropy.

In terms of more general stress states, Kirkgard and Lade (1993) noted that during undrained shear, the initial stiffness of the clay (at small strains) increased as the influence of the intermediate stress was increased.

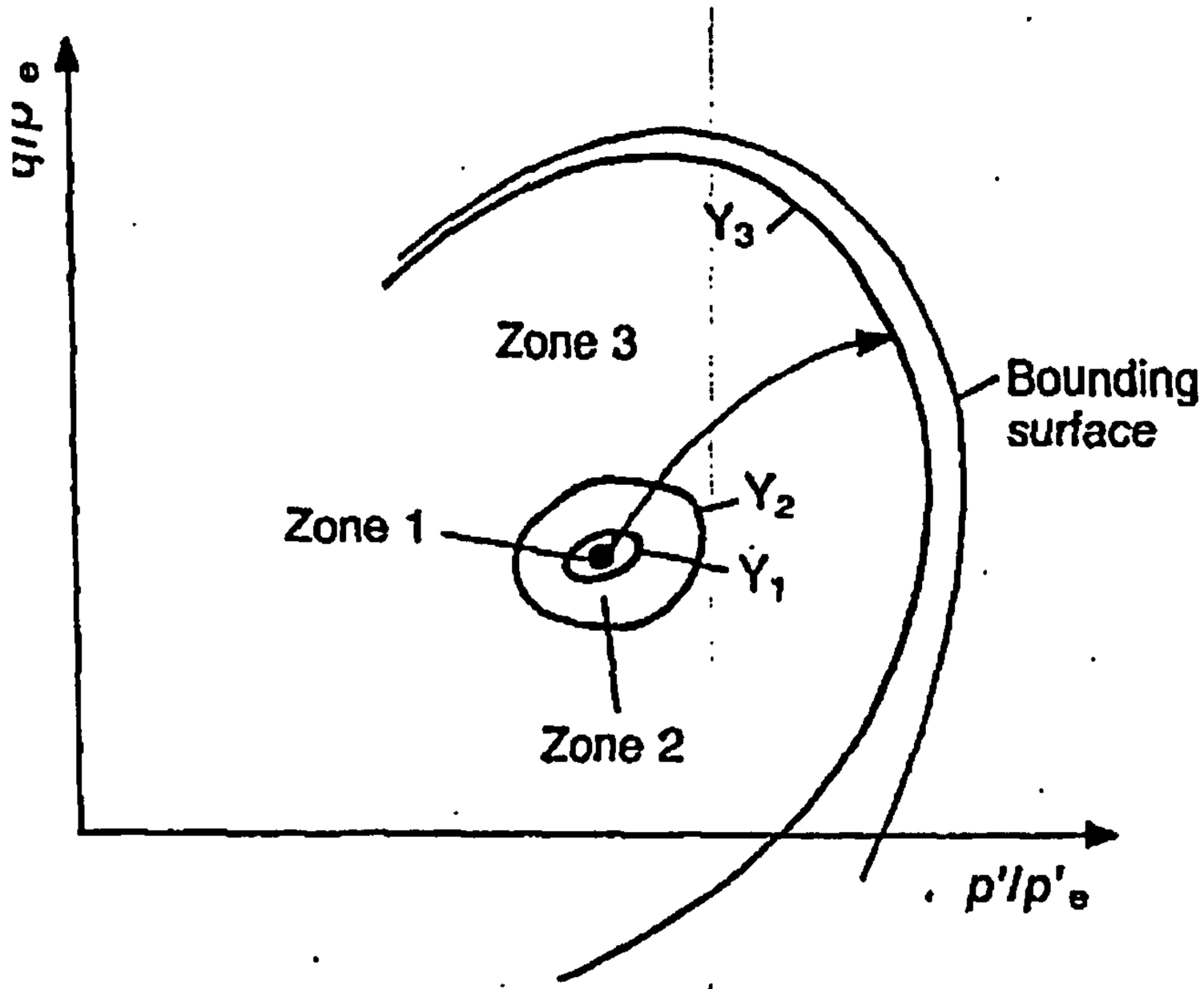

Figure 2.14. Scheme of multiple yield surfaces (Jardine, 1992).

2.8.2 Anisotropy of small strain behaviour

As with plastic anisotropy, small strain anisotropy is a consequence of the previous history that produces an anisotropic fabric within clay. A fully anisotropic elastic material can be described by 21 elastic constants. However, a cross-anisotropic material such as a natural clay exhibits a number of symmetries, and therefore the number of elastic constants required to describe such a material reduces to 5 as described by Muir Wood (1990). Two Young's modulii are required, E_h and E_v. These represent stiffnesses corresponding to the stress-strain response of the clay in the horizontal and vertical directions in the ground respectively. The strains in each horizontal direction are linked to increments of vertical stress by Poisson's ratio ν_{vh}. Similarly, strains in the vertical direction caused by increments of stress in the horizontal direction are linked by Poisson's ratio ν_{hh}. Finally, the modulus of shear deformation in the vertical plane is given by G_{vh}. The stress-strain relationship for

the cross-anisotropic elastic material (in which y is the vertical direction in the ground) is:

$$\begin{Bmatrix} \delta\varepsilon_x \\ \delta\varepsilon_y \\ \delta\varepsilon_z \\ \delta\gamma_{xy} \\ \delta\gamma_{yz} \\ \delta\gamma_{zx} \end{Bmatrix} = \begin{bmatrix} \frac{1}{E_h} & -\frac{\nu_{vh}}{E_v} & -\frac{\nu_{hh}}{E_h} & 0 & 0 & 0 \\ -\frac{\nu_{vh}}{E_v} & \frac{1}{E_v} & -\frac{\nu_{vh}}{E_v} & 0 & 0 & 0 \\ -\frac{\nu_{hh}}{E_h} & -\frac{\nu_{vh}}{E_v} & \frac{1}{E_h} & 0 & 0 & 0 \\ 0 & 0 & 0 & \frac{2(1+\nu_{hh})}{E_h} & 0 & 0 \\ 0 & 0 & 0 & 0 & \frac{1}{G_{vh}} & 0 \\ 0 & 0 & 0 & 0 & 0 & \frac{1}{G_{vh}} \end{bmatrix} \begin{Bmatrix} \delta\sigma_x \\ \delta\sigma_y \\ \delta\sigma_z \\ \delta\tau_{xy} \\ \delta\tau_{yz} \\ \delta\tau_{zx} \end{Bmatrix} \quad (2.17)$$

A variety of research techniques have been used in order to obtain values for these five constants. Pennington et al. (1997) conducted bender element tests in a triaxial cell on Gault clay in order to compare the shear stiffness in the vertical plane (G_{vh}) with the shear stiffness in the horizontal plane (G_{hh}) (note that G_{hh} corresponds to $Eh/(2(1+\nu_{hh}))$ in Equation 2.17, but this is unused to demonstrate that only five parameters are required to fully define the cross-anisotropic material). Results from these tests strongly indicated that the shear stiffness of this material was highly anisotropic. In addition it was also shown that the degree of anisotropy was dependent on the stress state.

The foregoing work suggests that pre-yield behaviour of most natural clays is anisotropic (corresponding to an anisotropic stress history). Atkinson and Richardson (1985) conducted tests on three reconstituted clays. They showed that the unloading and reloading behaviour for these clays were essentially elastic and isotropic. These samples had undergone an isotropic stress-strain history to a stress level approximately eight times the consolidation stress. These results may suggest that such a history has resulted in isotropy of elastic behaviour.

2.8.3 Effects of bonding on small strain behaviour

Evidence shows that the strain to yield is higher for structured soils than for corresponding unstructured soils. Leroueil et al. (1990) suggested that the strain to

yield for the structured clay is double that of the unstructured material, although this may not be the case for all soft clays as discussed in Chapter 3.

2.8.4 Constitutive modelling of small strain behaviour

A model developed by Al-Tabbaa and Wood (1989) has some improvements over Modified Cam Clay. It has an internal bubble (of the same shape as the Cam Clay surface, but a fixed smaller ratio), which marks the onset of plastic behaviour. The internal bubble experiences kinematic hardening and the model incorporates an associated flow rule.

A model developed by Stallebrass (1990) and subsequently by Baudet and Stallebrass (2004) incorporates three-surface kinematic hardening. Model simulations have shown some success in representing small-strain non-linearity.

2.9 Creep and time-dependency

2.9.1 Laboratory evidence

Creep and time-dependency are acknowledged as being highly important factors in soft clay behaviour. Creep (or secondary compression) is apparent in soils where deformations continue despite no changes occurring in the effective stress of a soil sample. This phenomenon is particularly important in normally consolidated soils including clays, clayey silts and peats.

The rate of straining significantly affects the undrained shear strength, the yield stress and the compression curve of a clay. In incrementally loaded oedometer tests by Crawford (1964) and Bjerrum (1967) it was shown that the "apparent" preconsolidation pressure of a clay reduces as the time interval between load increments is increased. Tavenas et al. (1978) also showed that during constant rate of strain tests, the apparent preconsolidation pressure reduces as the rate of straining in a test is reduced. Extensive triaxial testing by Boudali et al. (1994) has shown that the yield curve of a clay appears to shrink as a result of a decrease in the rate of testing.

2.9.2 Constitutive modelling

Although no attempt has been made to model creep effects in the present study, this is an important facet of soil behaviour. Indeed, it is thought that non-trivial creep effects may have been present during triaxial testing of Bothkennar clay (see discussion in Section 6.4.4).

Stolle et al. (1997) describe a constitutive model which takes creep effects into account. The model predicts conventional elastic strains and a component of viscoplastic or creep strains. Yin and Graham (1999) and Neher at al. (2001) also developed an elastic viscoplastic model in an attempt to model the time-dependent behaviour of soils. Neher et al. (2002) describe a multi-laminate based creep model which also incorporates the effects of anisotropy. They report simulations on experimental data from a hollow cylinder apparatus. The simulations generally gave a good match to the soil stress-strain-time response. Although no attempt is made in this study to assess the time-dependent behaviour of Bothkennar clay, it became apparent from test results (see Section 6.4.4) that, despite efforts to minimise secondary effects, creeps strains were present during the triaxial testing programme.

2.10 Bothkennar clay

2.10.1 Introduction

The present study involves an experimental investigation of the mechanical behaviour of a natural soft clay from Bothkennar. The samples used were obtained from the national soft clay test bed site in Bothkennar, details of which are given extensively in the Géotechnique Symposium-in-Print (1992). The main advantage of utilizing this soil is that a large number of researchers have conducted extensive testing of Bothkennar clay. However, the intention in this study was to conduct laboratory tests on Bothkennar clay with the particular aims of exploring the roles of anisotropy (of large strain behaviour) and destructuration. Bothkennar clay is a soft recently deposited marine clay and is situated at Bothkennar in Scotland on the Forth River estuary. Paul et al. (1992) showed that the clay profile consisted of four distinct beds, namely weathered, bedded, laminated and mottled facies.

2.10.2 Classification test data

Table 2.1 summarises the properties of Bothkennar clay, appropriate to a depth range of 10.5 - 11.7 m (the depths from which the samples used in this study were taken). The values in Table 2.1 are based on the data obtained by various authors. Key profiles associated with this data are shown in Figure 2.15. The PSD curves agree with the visual description; in the depth range considered, there is typically around 30 – 40 % clay content, 50 – 60 % silt content and a small amount of sand. Loss on ignition indicates that the organic content is significant, at around 3-4%. The field undrained shear strengths vary from around 25 to 35 kPa, which is fairly typical for soft clays in the UK. The relatively low shear strength indicates that the Bothkennar clay can be classified as a soft clay. In planning the triaxial test programme, this data was used as an approximation only, because there may be natural variation within a given clay stratum.

Test	Range of values	Source(s)
σ'_{v0} (in-situ stress)	70-88 kPa	Nash et al. (1992a)
w_L (liquid limit)	68-71 %	Nash et al. (1992a)
w_P (plastic limit)	24-26 %	Nash et al. (1992a)
I_P (plasticity index)	45-46 %	Nash et al. (1992a)
w (water content)	56-70 %	Nash et al. (1992a)
G_s (specific gravity)	2.65-2.72	Nash et al. (1992a)
c_u (undrained shear strength)	25-35 kPa	Nash et al. (1992b)
c_{ur} (remoulded vane strength)	10-12 kPa	Nash et al. (1992b)
c_v (coefficient of consolidation)	1-1.5 m^2/year (normally consolidated conditions)	Nash et al. (1992b)
Bulk unit weight	17 kN/m^3	Clayton et. al (1992)
Clay fraction	30-40 %	Leroueil et. al (1992)
Organic fraction	3-4 %	Leroueil et. al (1992)

Table 2.1. Data obtained from Bothkennar clay (interpolated for depth range 10.5-11.7m).

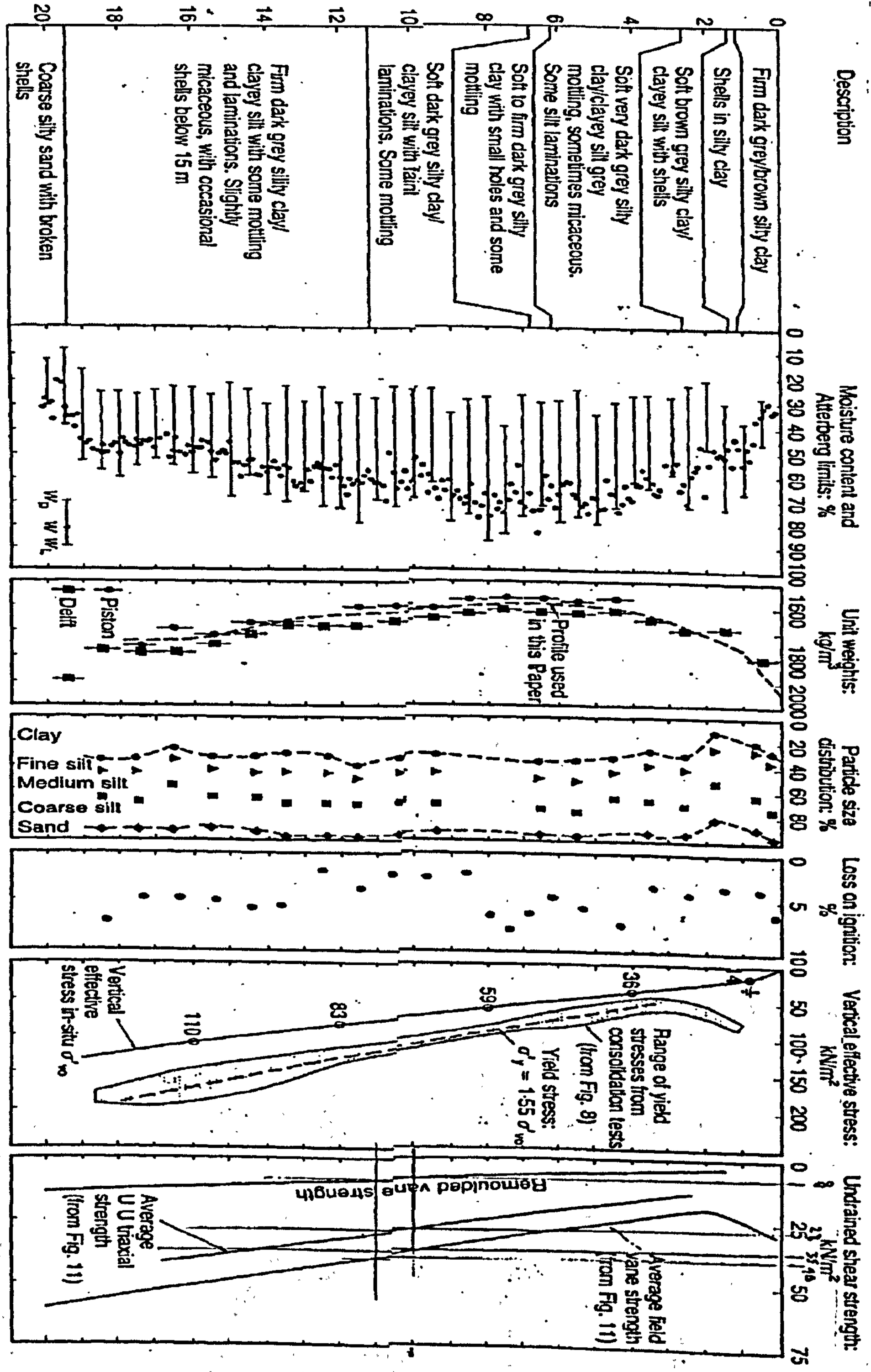

Figure 2.15. Key profiles for Bothkennar clay (Nash et al., 1992).

2.10.3 Yield surface and plastic anisotropy

Following the scheme of Jardine (1992), shown in Figure 2.16, Smith et al. (1992) attempted to map the Y_3 yield surface. As shown in Figure 2.16 (a), this surface was found to be highly inclined with a positive inclination in triaxial stress space approximately centred on the K_0 axis. The form of this surface confirmed that plastic anisotropy existed within Bothkennar clay. However, the tests did not allow the evolution of plastic anisotropy with further straining to be fully explored. This is an aspect of Bothkennar clay which will be examined closely in the present study. Smith et al. (1992) also showed that the shape and size of the Y_3 surface was sensitive to the choice of sampling technique. Figure 2.16 (a) suggests that sampling using the Laval sampler causes a greater degree of disturbance than the Sherbrooke sampler.

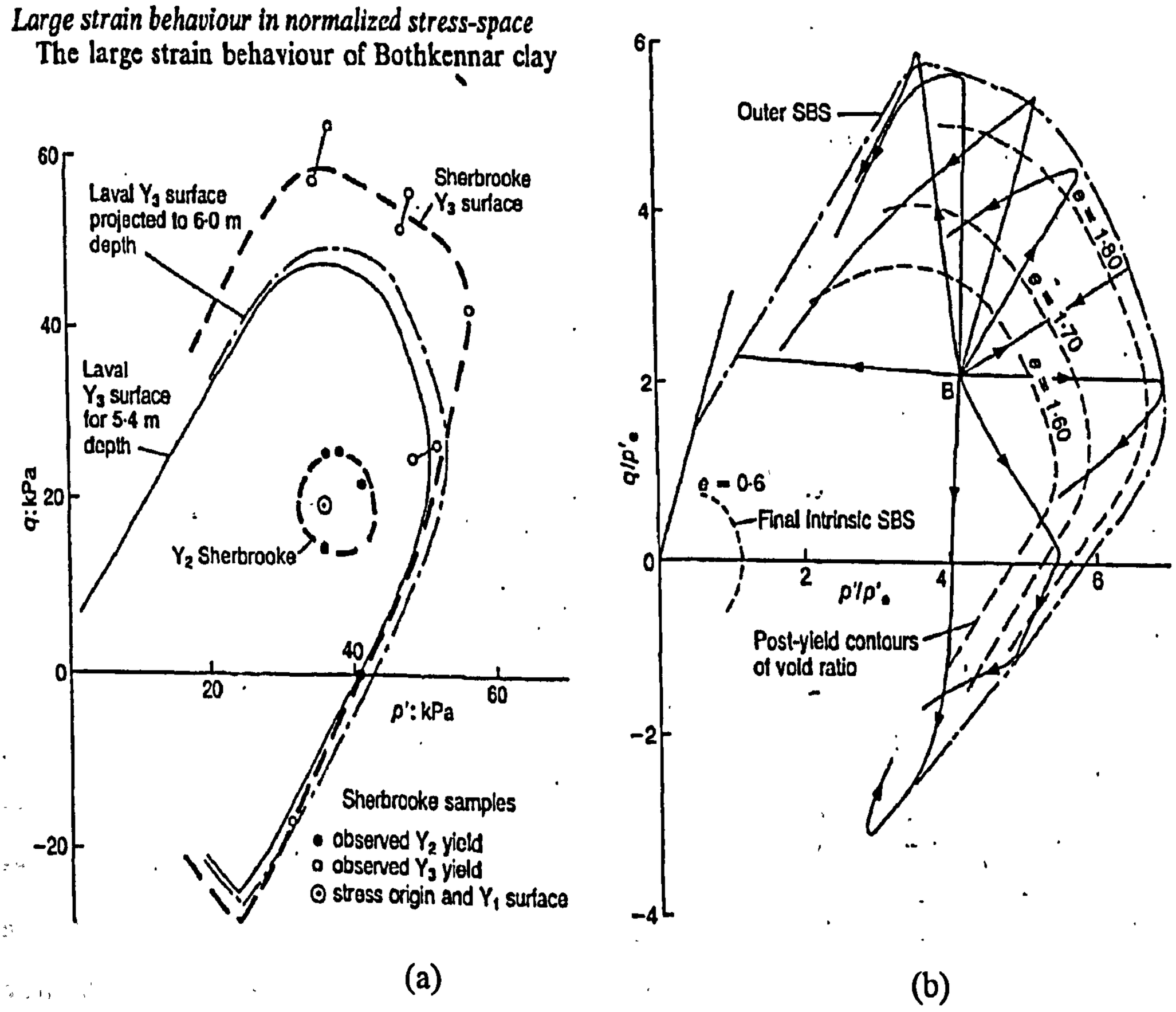

Figure 2.16. Experimental yield surfaces, proposed by Smith et al. (1992).

In Figure 2.16 (b), data from drained stress paths by Smith et al. (1992) have been normalised by p'_e (where p'_e is the corresponding mean effective stress at the same void ratio on the intrinsic compression line). An intact (outer) state boundary surface (SBS) is shown to lie far beyond the intrinsic surface. Drained stress probes moved outwards to the outer SBS and then re-directed inwards. The void ratio contours in Figure 2.16 (b) show that the outer SBS contracts inwards as the void ratio reduces.

Smith et al. (1992) conducted consolidated undrained triaxial tests on Bothkennar clay and noted marked differences in the values of peak deviator stress (q_{max}) and critical state stress ratios in triaxial compression (M_C) and triaxial extension (M_E). They found that q_{max} and M were significantly greater in triaxial compression than in triaxial extension. This aspect of behaviour is also considered in the present study (see Sections 6.2 and 7.2). Results from index and in-situ tests indicated that the within the depth range tested, the material was relatively homogenous.

2.10.4 Bonding and Destructuration

Smith et al. (1992) conducted oedometer tests on Bothkennar clay from 5 to 6m depth. In comparing the compression curves to the corresponding compression curve for the reconstituted clay (the intrinsic compression line), the yield stress for the natural sample were found to be 1.5 times greater than that of the reconstituted samples at the same void ratios. Clayton et al. (1992) conducted triaxial tests on natural Bothkennar clay from a depth range of 6.5 - 8.5m, incorporating three distinct facies. Testing was conducted using local axial and radial strain gauges. Results from tests on Laval samples showed that the breakdown of bonding is progressive, with the stress-strain response suggesting a stick-slip phenomena where the soil structure undergoes a series of collapses, as particle bonds are destroyed, followed by stiffer behaviour (see Figure 2.17). They also showed that the outer yield surface (structure surface) of the soil collapses towards the stable state boundary surface for the reconstituted material. In addition, results indicated that upon plastic straining, the virgin compression line asymptotically approaches the intrinsic compression line, as expected for a structured material. The authors tentatively suggested that plastic volumetric strains were more influential than plastic shear strains in the destructuration of this soil.

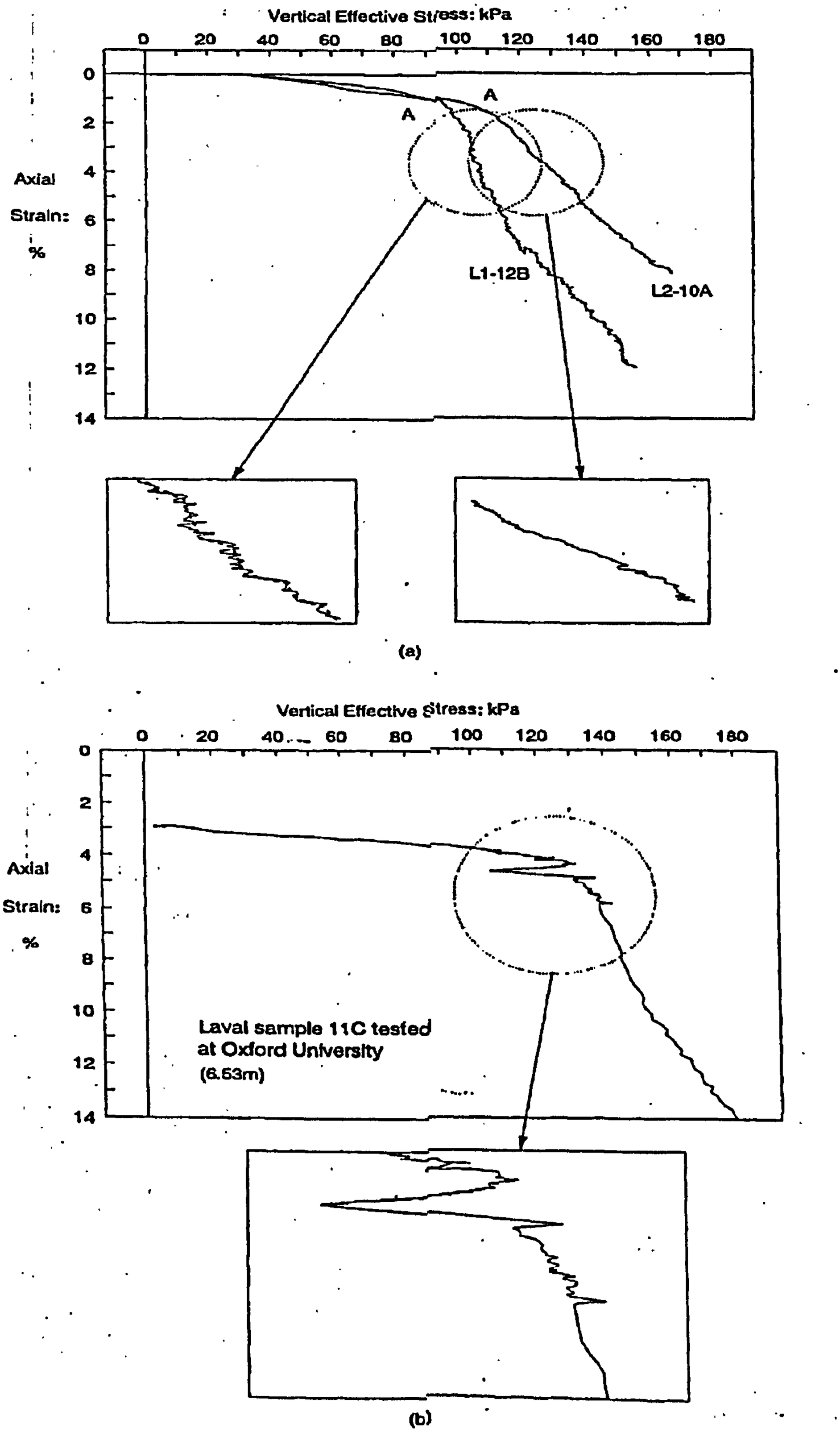

Figure 2.17. Results from triaxial tests conducted by Clayton et al. (1992).

The experiments of Clayton et al. (1992) also gave an indication of the influence of sampling techniques on soil structure. It was noted that sampling techniques thought to cause greater disturbance caused a reduction in the initial stiffness and the peak undrained shear strength and caused a general shrinking of the yield surface. The Sherbrooke samples appeared to retain more structure than equivalent Laval samples, although both of these samplers retain much more structure than conventional tube samplers. In the present study Laval samples were used exclusively, due to availability of material.

2.10.5 Creep behaviour and rate effects

Nash et al. (1992a) observed creep behaviour of Bothkennar clay during incrementally loaded oedometer tests. They noted that creep effects were most prevalent immediately after yield, and suggested that this was associated with the structural breakdown during yield. Although the tests in the current study were not specifically designed to examine creep effects, it may be expected that some secondary compression will have occurred and will have some bearing on the test results. Nash et al. (1992a) also demonstrated that the yield stress observed in oedometer tests was strongly dependent on the applied strain rate, with higher yield stresses resulting from faster strain rates.

2.11 Summary

The behaviour of a natural clay is complex due to various depositional and post-depositional processes that it will have undergone. As a consequence, if constitutive models are required to give accurate representations of soil behaviour it may be necessary to include some of these features of natural soil behaviour. However, this requires the inclusion of an increasing number of soil parameters and can incur penalties such as over-complexity at the expense of common applicability in engineering practice.

At present, there is no single constitutive model that incorporates all the main aspects of soil behaviour, whilst attaining widespread use. In this study, the effects of anisotropy (of large strain behaviour) and destructuration were examined through

laboratory experimentation using a natural soft clay, namely Bothkennar clay. As discussed in Sections 2.6 and 2.7, these are two highly significant facets of soft clays and ignoring their effects can lead to highly inaccurate predictions and potentially unsafe or unreasonably conservative design.

In Chapter 3 a constitutive model incorporating large-strain anisotropy and destructuration is described in detail. This model is an extension of Modified Cam Clay and as such, is not overly complex. The intention was to obtain data from triaxial tests on Bothkennar clay and compare test results with simulations generated by the new model. The previous studies on Bothkennar clay, as discussed in Section 2.10, strongly indicate that this is a highly appropriate material for this study. Small-strain behaviour, although important as discussed in Section 2.8, was not investigated in this study, although some findings arose from the tests performed. The models presented in Chapter 3 assume that elastic behaviour is isotropic and only slightly non-linear (as is the case in Modified Cam Clay). In the context of study involving large straining of a soft normally consolidated clay, the small strain behaviour is thought to be relatively unimportant. As discussed in Section 2.9, creep has an important role in natural clay behaviour. Again, however, this aspect of soil behaviour was not targeted in the present study, but some information has arisen from the test data nonetheless.

CHAPTER 3: CONSTITUTIVE MODELS S-CLAY1 AND S-CLAY1S

3.1 Introduction

In the light of previous studies on the behaviour of natural soft clays (Sections 2.3 and 2.4) and the increasing need to carry out safe and economical design on soft clay sites, Wheeler et al. (1999) and Näätänen et al. (1999) proposed a new anisotropic elasto-plastic model named S-CLAY1 (see Wheeler et al. (2003b) for further details). The model is formulated in the critical state framework and is an extension of the isotropic elasto-plastic Modified Cam Clay model. The model incorporates an inclined yield surface and a rotational hardening law. The intention of the model is to represent the effects of the development and erasure of anisotropy during plastic straining. A fundamental feature of S-CLAY1 is that it predicts a unique critical state line in q: p': v space. This is achieved by ensuring that the orientation of the proposed yield curve at a critical state is independent of the stress path taken to the critical state. Therefore, the predicted level of anisotropy at a critical state is independent of any initial anisotropy and of the stress path taken to a critical state. In this respect, S-CLAY1 does not have the same drawbacks as models previously discussed (see Section 2.3) such as Banerjee and Yousif (1986) and Davies and Newson (1993).

The model is based on an original proposal by Wheeler (1997), which was subsequently modified in the light of experimental data obtained from triaxial tests on a natural soft Finnish clay (Näätänen et al. 1999). Test results and model simulations relating to this clay suggested that S-CLAY1 modelled anisotropy very well, but a number of weaknesses in the modelling were identified. It was considered that the main weaknesses of the model were attributable to the effects of destructuration (Burland 1990). A subsequent model named S-CLAY1S was proposed (Koskinen et al. 2002a, Wheeler et al. 2003a), where all of the components of the S-CLAY1 model were retained, but the influence of destructuration was also incorporated.

One of the underlying aims in the development of the S-CLAY models was to retain a degree of simplicity so that there would be a realistic chance of widespread

understanding and application of the models by practicing geotechnical engineers. Models that attempt to include additional aspects of soil behaviour tend to involve greater complexity and parameters that may not be readily deduced from standard laboratory tests or have no apparent physical meaning. Inevitably, such models will also require a high level of understanding from the practicing geotechnical engineer.

3.2 S-CLAY1 model formulation in triaxial stress space

The S-CLAY1 model can be considered in the simplified triaxial test stress space in terms of the mean effective stress p' and the deviatoric stress q (assuming that the soils is cross-anisotropic) and that its plane of isotropy is normal to the vertical direction in the triaxial test cell.

3.2.1 Elastic behaviour

Elastic behaviour is assumed to be isotropic, although as discussed in Section 2.8, this is unlikely to be the case for natural clays. However, S-CLAY1 was developed with the intention of modelling normally or lightly overconsolidated soils where plastic strains are dominant and elastic strains are relatively unimportant, so that the assumption of isotropic elasticity is sufficient for design purposes. This avoids the introduction of additional complexities into the model. The assumed form of isotropic elastic behaviour is identical to that of Modified Cam Clay. Increments of elastic volumetric strain are given by

$$d\varepsilon_v^e = \frac{\kappa dp'}{vp'} \tag{3.1}$$

where κ is the slope of elastic swelling lines in the v : ln p' plane and v is the specific volume. Increments of elastic deviatoric strain are given by

$$d\varepsilon_d^e = \frac{dq}{3G'} \tag{3.2}$$

where G' is the shear modulus. A constant value of G' can be assumed, or, alternatively, G' can be calculated from an assumption of a constant value of Poisson's ratio ν':

$$G' = \frac{3(1-2\nu')}{2(1+\nu')}\frac{vp'}{\kappa} \tag{3.3}$$

3.2.2 Yield curve

The S-CLAY1 yield curve is the same as proposed by Dafalias (1987) and Korhonen and Lojander (1987) (see Section 2.6.2) and is in the form of a sheared ellipse. It is therefore given by:

$$f = (q-\alpha p')^2 - (M^2-\alpha^2)(p'_m - p')p' = 0 \tag{3.4}$$

where M is the critical state value of stress ratio η (η = q/p'), α defines the orientation of the yield curve and p'_m the size of the yield curve (see Figure 3.1). Therefore, p'_m and α are hardening parameters. The value of α is a measure of the anisotropy of the plastic behaviour, so that with α = 0, the soil behaviour is isotropic and Equation 3.4 is identical to that of Modified Cam Clay. As discussed in Section 2.6.2, soils with a K_0 stress history will have an initial value of α greater than zero. The tangent to the yield curve is horizontal at the point where the critical state line intersects the curve, while the tangents are vertical at the origin and at point C in Figure 3.1 (where η = α and $p' = p'_m$).

The S-CLAY1 form of yield curve has a number of advantages over the Modified or Original Cam Clay formulations. Experimental evidence suggests that the yield stresses for a natural clay will result in an anisotropic yield curve approximating to this shape (see Section 2.6.1 and fuller comparisons in Section 3.2.6), so that predictions using the Cam Clay yield curves would mean that yield stresses for certain stress paths would be badly predicted. One example of this would be the case where a soil sample with an anisotropic stress history (and hence an inclined yield curve as in Figure 3.1) such that the sample exists at a stress point A on the S-

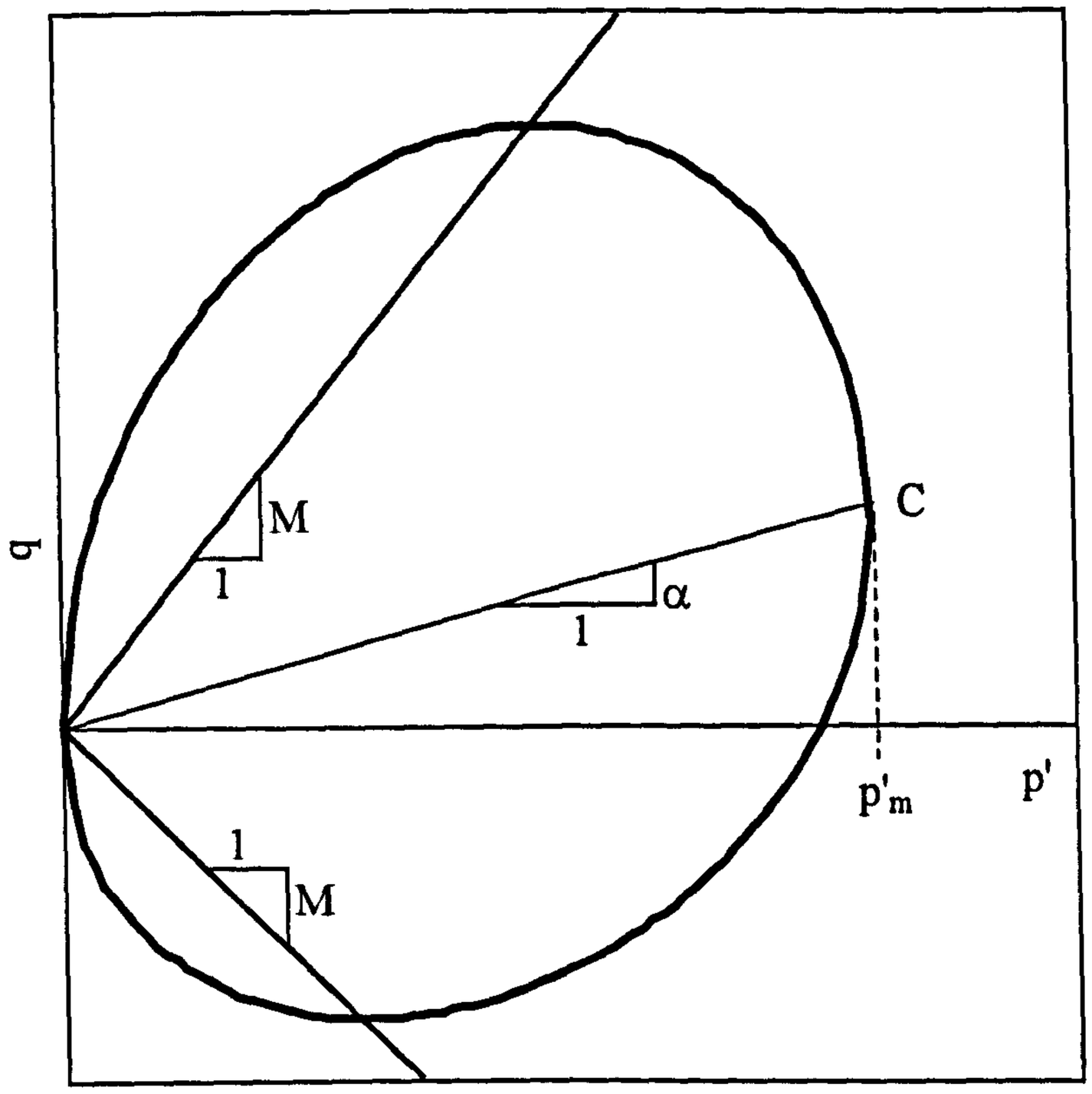

Figure 3.1. S-CLAY1 yield curve.

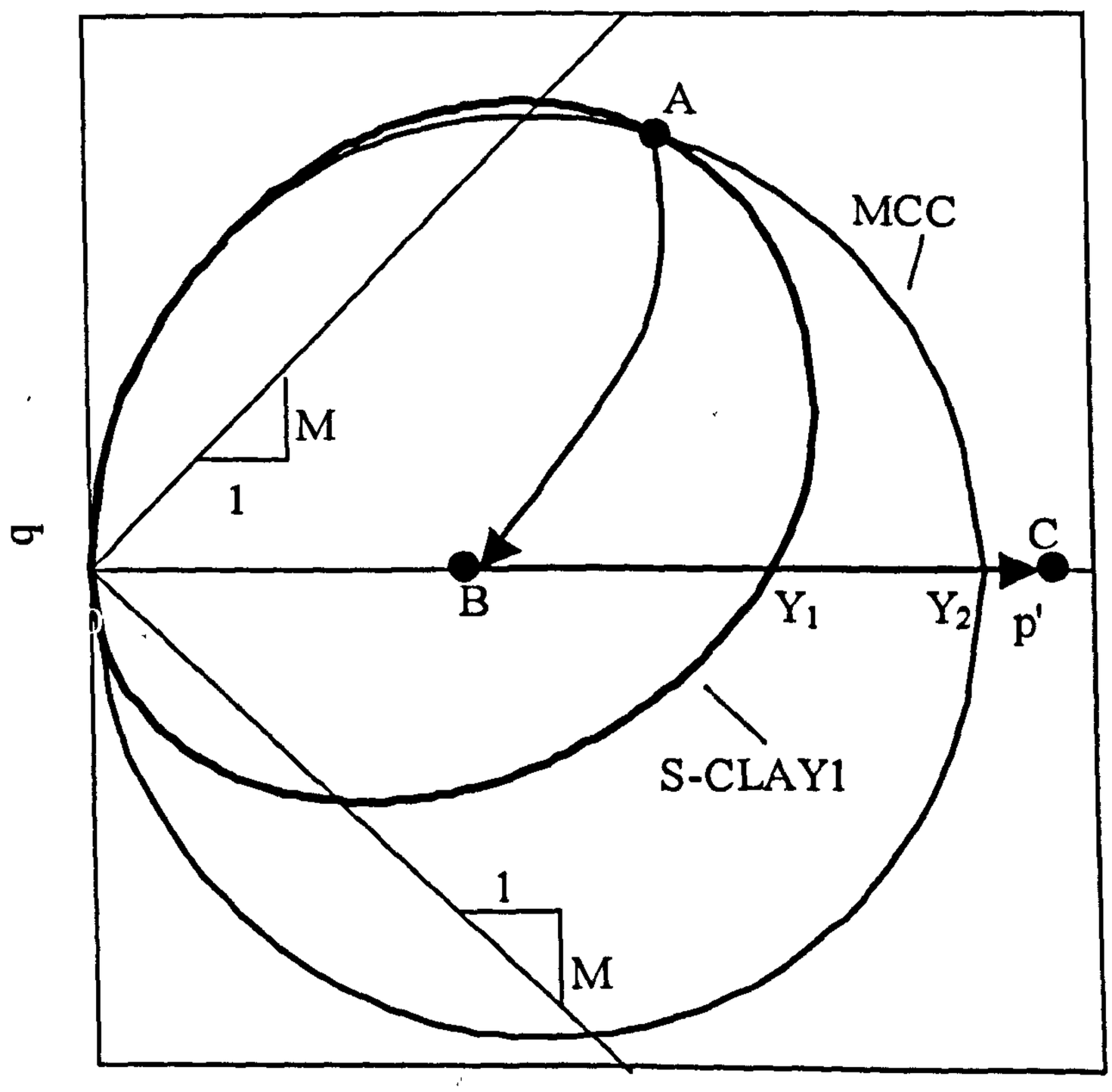

Figure 3.2. S-CLAY1 and MCC yield curves.

CLAY1 yield curve in Figure 3.2. Stress point A also lies on the Modified Cam Clay yield curve in Figure 3.2. If the sample is then unloaded to an overconsolidated state at point B and then reloaded isotropically to a new normally consolidated state C, then S-CLAY1will predict yield occurring at Y_1, at a significantly lower value of p' than that predicted by MCC (Y_2).

The model allows for the possibility that the critical state stress ratio in triaxial extension (M_E) may not be equal to the critical state ratio in triaxial compression (M_C). If the yield curve was oriented about the p'-axis (isotropic) then this could be achieved easily by assuming that when in triaxial extension, with η less than zero, M = M_E in the yield curve expression. However, with a yield curve that will is inclined, this would cause a discontinuity in the yield curve. A more satisfactory approach is to assume that when η is less than α that M takes a value of M_E in the yield curve expression of Equation 3.4, as shown in Figure 3.3.

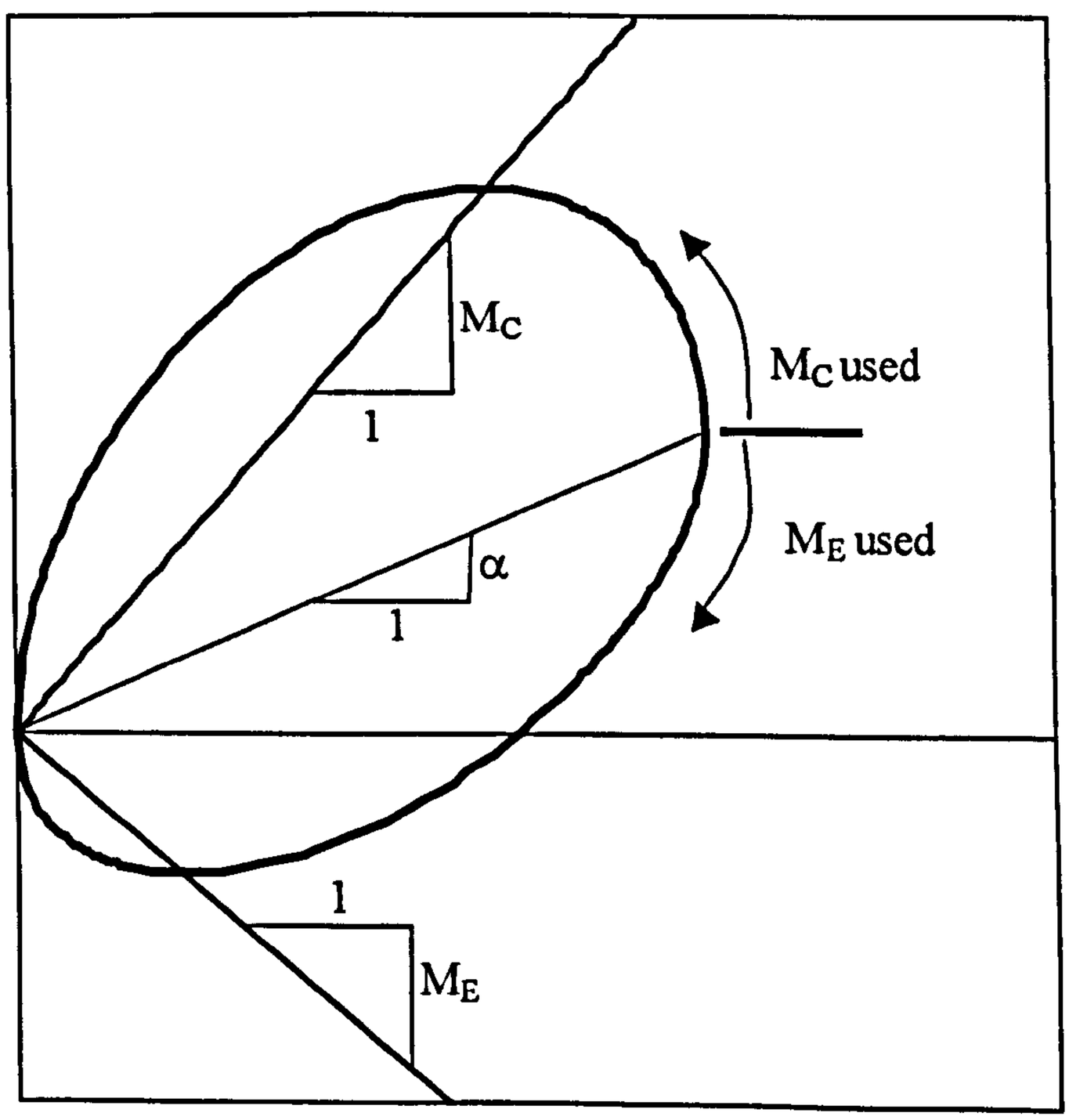

Figure 3.3. S-CLAY1 yield curve incorporating M_C and M_E.

3.2.3 Flow rule

In the light of conflicting evidence regarding the choice of an associated or non-associated flow rule (discussed in Section 2.6.1), and in the interests of maintaining simplicity, an associated flow rule was assumed for S-CLAY1. This is in contrast to Davies and Newson (1993) and Whittle and Kavvadas (1994) who attempted to increase model flexibility by adopting a non-associated flow rule.

The associated flow rule is given by

$$\frac{d\varepsilon_d^p}{d\varepsilon_v^p} = \frac{2(\eta - \alpha)}{M^2 - \eta^2} \tag{3.5}$$

The validity of the associated flow rule is discussed later by comparison of model simulations with experimental results in Section 3.2.7, and Chapters 8 and 9.

3.2.4 Hardening Laws

S-CLAY1 incorporates two hardening laws to account for the changes in size and inclination of the yield curve upon plastic straining. The change in size of the yield curve is assumed to be caused solely by plastic volumetric strains in a hardening law identical to that of Modified Cam Clay:

$$dp'_m = \frac{vp'_m d\varepsilon_v^p}{\lambda - \kappa} \tag{3.6}$$

where λ is the slope of the post-yield compression curve in the v : ln p' plane for a stress path at constant η and with no rotation of the yield curve occurring e.g. isotropic loading of an isotropic sample. It is assumed that only plastic volumetric strains contribute to change of size of the yield curve because it is thought that an increase in yield curve size is due only to re-arrangement of soil particles to a denser packing (or, conversely, looser packing for strain softening).

A second hardening law has been incorporated to account for the change in orientation of the yield curve during plastic straining, where the fabric anisotropy of the soil can be developed or erased. As described in Section 2.6.1, the amount of anisotropy for a soil is not fixed and will, in general, be altered during plastic straining. It is assumed that both plastic volumetric strains and plastic shear strains are effective in changing anisotropy. Plastic volumetric strains and plastic shear strains are each attempting to drag the value of α to an instantaneous target value, which in both cases is a function of the stress ratio η. Plastic volumetric strains drag α towards a target $\chi_v(\eta)$, while plastic shear strains simultaneously drag α towards another target, $\chi_d(\eta)$. The rotational hardening law is

$$d\alpha = \mu\left[(\chi_v(\eta)-\alpha)\left\langle d\varepsilon_v^p \right\rangle + \beta(\chi_d(\eta)-\alpha)\left|d\varepsilon_d^p\right|\right] \tag{3.7}$$

The soil constant β controls the relative effectiveness of plastic shear strains and plastic volumetric strains in rotational hardening, while the soil constant μ controls the absolute rate at which α heads towards its current target value. With β set to zero in Equation 3.5, plastic shear strains are ineffectual and α heads towards a target value of $\chi_v(\eta)$. With very high values of β the target value for α is dominated by plastic shear strains and the orientation tends towards $\chi_d(\eta)$. In reality it is likely that the value of β will be some finite value so that the overall target value would lie between $\chi_d(\eta)$ and $\chi_v(\eta)$. Evidently, for low values of η, where plastic volumetric strains are generally much greater than plastic shear strains, the target value for α will be close to $\chi_v(\eta)$. Conversely, at high η values, when large plastic shear strains are occurring the target will be closer to $\chi_d(\eta)$. As a result of dependency on both plastic volumetric strains and plastic shear strains, S-CLAY1 predicts a unique critical state value of α. Since plastic shear strains are entirely dominant at the critical state, the critical state value for α is given by $\chi_d(M)$, where $\chi_d(M)$ is the value of $\chi_d(\eta)$ at $\eta = M$. The anisotropy at this critical state is therefore only dependent on the stress conditions at this critical state and does not depend on any previous anisotropy or on the loading history involved in approaching the critical state.

Equation 3.7 adopts a different approach to Banerjee and Yousif (1986) and Dafalias (1987) as reviewed in Section 2.6.1. In both these earlier proposals, it was assumed that any change in yield surface orientation was attributable only to plastic volumetric strains, with no influence of plastic deviatoric strains.

In S-CLAY1, plastic shear strains are assumed to drag α towards the target value $\chi_d(\eta)$ regardless of whether the plastic shear strain increments are positive or negative. Therefore, the modulus symbol is applied to the shear strain increment in Equation 3.7. The Macaulay bracket on the plastic volumetric strain increment is necessary when considering plastic straining on the supercritical side of the yield surface, where $\eta > M$ and $d\varepsilon_v^p$ will be negative. Like the Cam Clay models, S-CLAY1 model predictions are unlikely to be accurate in the supercritical region, but the use of the model in numerical analysis may involve some elements of soil that are yielding on the supercritical side. Without the Macaulay bracket, negative increments of $d\varepsilon_v^p$ would result in nonsensical predictions. If the stress ratio η was greater than M and no Macaulay brackets were included then the increments of $d\varepsilon_v^p$ would be negative and $d\alpha$ would tend away from the target value $\chi_v(\eta)$ at an increasing rate. The inclusion of modulus brackets on the volumetric strain increment would also be unacceptable because this would sometimes cause the value of α to head towards a target value that is greater than M (due to the expression for $\chi_v(\eta)$ proposed in Section 3.2.5). If this were to happen, the aspect ratio of the yield curve (defined by $(M^2-\alpha^2)^{1/2}$ would reduce to zero as α approached a value of M, so that the yield curve would collapse to a single line. This would clearly be unacceptable, as this form of curve no longer represents a yield locus. These problems are avoided by means of using the Macaulay bracket on the plastic volumetric strain increment in Equation 3.7.

3.2.5 Functional forms of $\chi_v(\eta)$ and $\chi_d(\eta)$

In the original publication by Wheeler (1997), he proposed that the function for the target value of the plastic volumetric strains $\chi_v(\eta) = 3\eta/4$. This functional form for increments of plastic volumetric strain is similar to that proposed by Dafalias (1987). Wheeler (1997) also suggested that plastic shear strains tended to produce an

isotropic fabric, denoted by $\chi_v(\eta) = 0$ meaning that plastic shear strains would cause anisotropy to be erased, but not re-developed. Näätänen et al. (1999) conducted triaxial tests on a soft clay from Otaniemi in southern Finland in order to test the validity of the S-CLAY1 model.

The triaxial tests of Näätänen et al. (1999) typically involved first loading a sample from an initially overconsolidated stress state along a constant η stress path to a stress state well beyond the yield stress (typically three times greater than the yield stress). It was expected that the first loading stage would cause expansion and rotation of the initial yield curve to a new size and orientation. The samples were then unloaded at the same stress ratio and then reloaded along a different stress ratio, again to a stress level well beyond the new yield stress. During second loading, another yield point could then be detected on the new yield curve. Using the maximum stress point from the first loading stage and the yield point obtained from the second loading stage, the shape and size of the new S-CLAY1 yield curve could be obtained.

Figure 3.4 shows values of the yield curve inclination α (normalized by M) produced by first loading stages plotted against the stress ratio η in the first loading stages (normalized by M) for a suite of tests involving various stress ratios in the first loading stages (η_1) and second stages (η_2). The experimental data points give an indication of the variation of the equilibrium value of α with the stress ratio. This is assuming that the yield curve had reached is equilibrium orientation for each first loading stage.

S-CLAY1 predicts that for plastic loading along a constant η path, the value of α will tend to a final equilibrium value. This value can be calculated by setting $d\alpha = 0$ in the rotational hardening law (Equation 3.7). Combining this with the flow rule of Equation 3.5 leads to a quadratic equation for α for any stress path at a constant value of η:

$$(\chi_v(\eta)-\alpha)(M^2-\eta^2)=\pm 2\beta(\alpha-\chi_d(\eta))(\eta-\alpha) \tag{3.8}$$

where the positive sign corresponds to stress paths in triaxial compression and the negative sign for triaxial extension. This quadratic expression can be solved to obtain the equilibrium value of α for any value of η (where a soil has specified values of soil constants M and β).

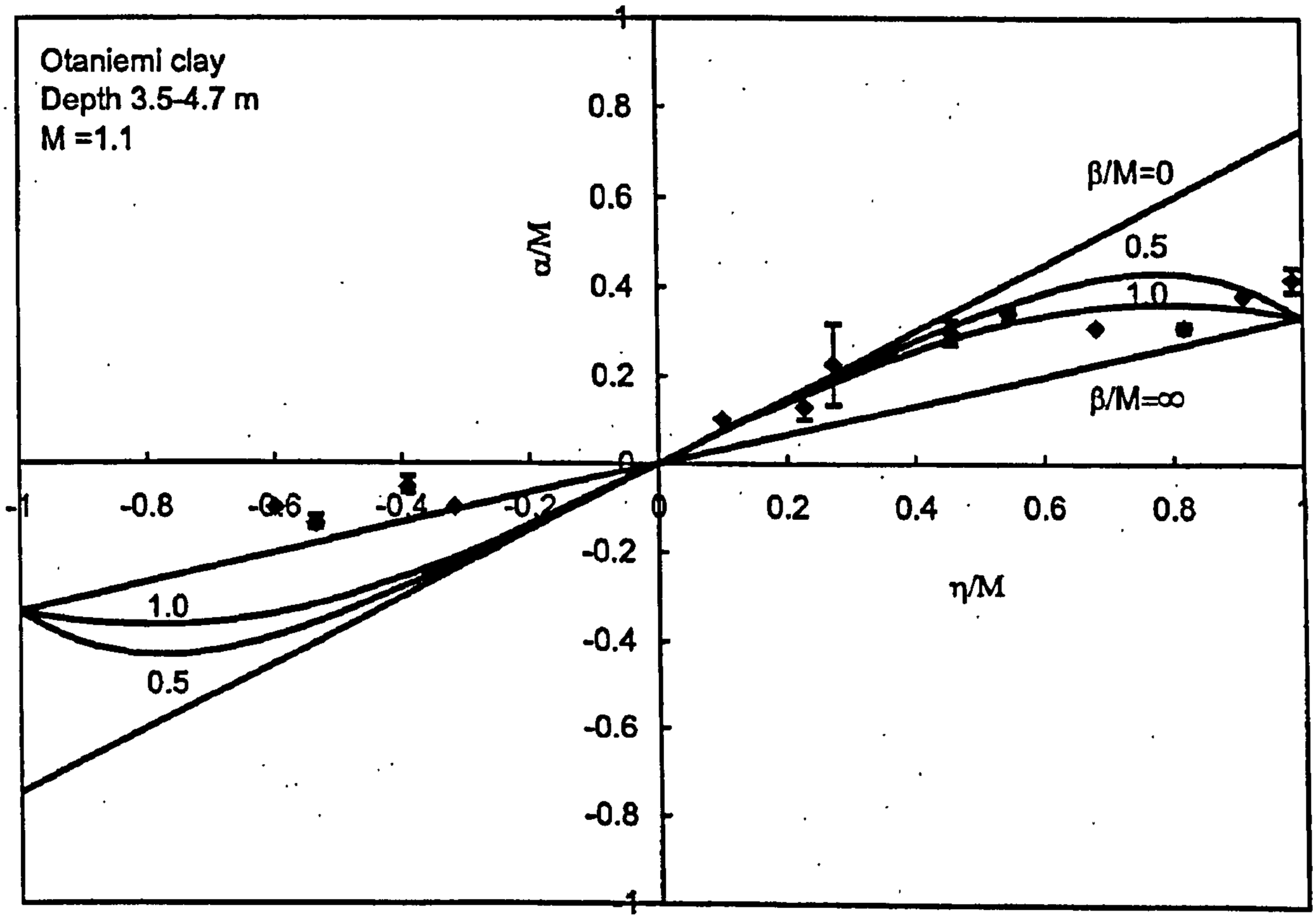

Figure 3.4. Equilibrium values of α/M for radial stress paths on Otaniemi clay Näätänen et al. (1999).

An expression for the function $\chi_v(\eta)$ was estimated by examining the gradient of the curve fitted through the experimental data points at $\eta/M = 0$ (when plastic volumetric strains are dominant) in Figure 3.4. Using the functional form $\chi_v = 3\eta/4$ gives a reasonable fit through the data. A suitable expression for the function $\chi_d(\eta)$ was estimated by considering the experimental data points at values of η approaching M in Figure 3.4. If $\chi_d(\eta)$ was equal to zero, then the data points at high values of η would tend to $\alpha = 0$ as η/M tends to 1. Clearly this is not the case and therefore a significant degree of anisotropy remains at a critical state. Experimental data from

Bai and Smart (1997) and also Kuganenthira et al. (1996) suggested that a significant degree of anisotropy may remain at a critical state (see Section 2.6.1). The solid curves shown in Figure 3.4 were therefore generated by assuming that $\chi_d(\eta) = \eta/3$. Therefore, Equation 3.8 can now be re-written as

$$\left(\frac{3\eta}{4}-\alpha\right)\left(M^2-\eta^2\right)=\pm 2\beta\left(\alpha-\frac{\eta}{3}\right)(\eta-\alpha) \tag{3.9}$$

These curves suggest that not only is there a significant degree of anisotropy at critical state, but that the maximum value of α occurs at some intermediate stage of shearing where $\eta < M$. Theoretical curves calculated by solving Equation 3.9 are shown for 4 different values of β/M in Figure 3.4. Inspection of Figure 3.4 suggested that with $\beta = 0.67$ (derived from the theoretical estimate described in Section 3.3.3) the model predictions are consistent with the data points. With $\chi_v(\eta) = 3\eta/4$ and $\chi_d(\eta) = \eta/3$ the rotational hardening law for S-CLAY1 (Equation 3.7) becomes:

$$d\alpha = \mu\left[\left(\frac{3\eta}{4}-\alpha\right)\left\langle d\varepsilon_v^p\right\rangle+\beta\left(\frac{\eta}{3}-\alpha\right)\left|d\varepsilon_d^p\right|\right] \tag{3.10}$$

3.2.6 Evaluation of S-CLAY1 model parameters

A total of 6 soil constants are required for the S-CLAY1 model. 4 of these are retained from the Modified Cam Clay model. These are κ, λ, M, and G' (or ν'). The Modified Cam Clay parameters can be obtained using relatively simple laboratory procedures (triaxial and oedometer testing). Two additional soil constants μ and β are required for the rotational hardening component of the model. The current state of the soil is completely defined by the values of p', q, v, p'_m and α.

Initial inclination of yield curve, α

Wheeler et al. (1999) showed that an independent procedure could be used to establish the initial value of α, if it can be assumed that the soil was subjected to a

history involving only K_0-loading to a normally consolidated state or K_0 loading and unloading to a moderately or lightly overconsolidated state. An important assumption here is that the soil is not heavily overconsolidated. It is assumed that any elastic unloading to a lightly overconsolidated state will not have influenced the yield curve orientation. If the soil is heavily overconsolidated, its unloading history may involve stress paths that have caused the yield curve to be rotated and expanded. The normally consolidated value of K_0 can be estimated, perhaps from Jaky's simplified formula,

$$K_{0nc} = 1 - \sin \phi'_c \tag{3.11}$$

where ϕ'_c is the friction angle in triaxial compression. The corresponding stress ratio η_{K0} can then be calculated from:

$$\eta_{K0} = \frac{3(1-K_{0nc})}{1+2K_{0nc}} \tag{3.12}$$

When loading at this stress ratio η_{K0} for one-dimensional normally-consolidated states the S-CLAY1 model will predict a target value for the yield curve inclination, which will be denoted as α_{K0}. If it can be assumed that elastic strains are much smaller than plastic strains and that no plastic strains occur in the horizontal direction, then the ratio of plastic volumetric and plastic shear strains at η_{K0} can be approximated by:

$$\frac{d\varepsilon_d^p}{d\varepsilon_v^p} = \frac{2}{3} \tag{3.13}$$

Then combining Equations 3.13 and the flow rule of Equation 3.5, the yield curve inclination which would result from one dimensional consolidation, α_{K0} is given by

$$\alpha_{K0} = \frac{\eta_{K0}^2 + 3\eta_{K0} - M^2}{3} \tag{3.14}$$

where the value of M can be estimated from conventional laboratory tests and can be related to the angle of friction ϕ'_c. Since M and η_{K0} are functions of ϕ'_c, Equation 3.12 suggests that α_{K0} has a unique relationship with ϕ'_c. Wheeler et al. (1999), Näätänen and Lojander (2000) and Wheeler et al. (2003b) showed that for a wide variety of clays there was very good agreement between experimentally derived yield points and the S-CLAY1 yield curve shape with an orientation derived from Equation 3.14.

From Equation 3.4, it can be seen that if α and M are specified, then only one point on the yield curve (defined in terms of p' and q) would be required to calculate an initial value of p'_m. This yield point could be identified from a stress probe in a triaxial test at constant η-value or from one-dimensional consolidation in an oedometer test. In general, however, several triaxial stress path tests at a variety of constant η-values, such as those conducted on the Finnish clays, would be the best method of establishing the initial size of the yield curve. Figure 3.5 shows the yield points identified during the various first loading stages on Otaniemi Clay. The value of α was based on the Equation 3.14 and the value of p'_m was estimated visually. The data from Otaniemi clay shows that there is a significant amount of scatter in the identified yield points. This may be due to natural variability (such as slight variations in depositional history and ageing), but factors such as variation in disturbances caused by sampling and laboratory handling of samples may also contribute. Therefore, the yield curve size can be fitted through this large number of yield points, using visual estimation and/or least squares error technique.

It is clear, however, from Figure 3.5 that the independent procedure for estimating the initial value of α from Equation 3.14 has resulted in a good match with the experimental data. Koskinen et al. (2002a) went on to show that the procedure worked well for reconstituted POKO clay. Näätänen and Lojander (2000) examined the initial inclination for four other natural Finnish clays (ϕ' ranging from 26.5^0 to 36.9^0). Again the procedure gave a reasonably accurate fit in each case.

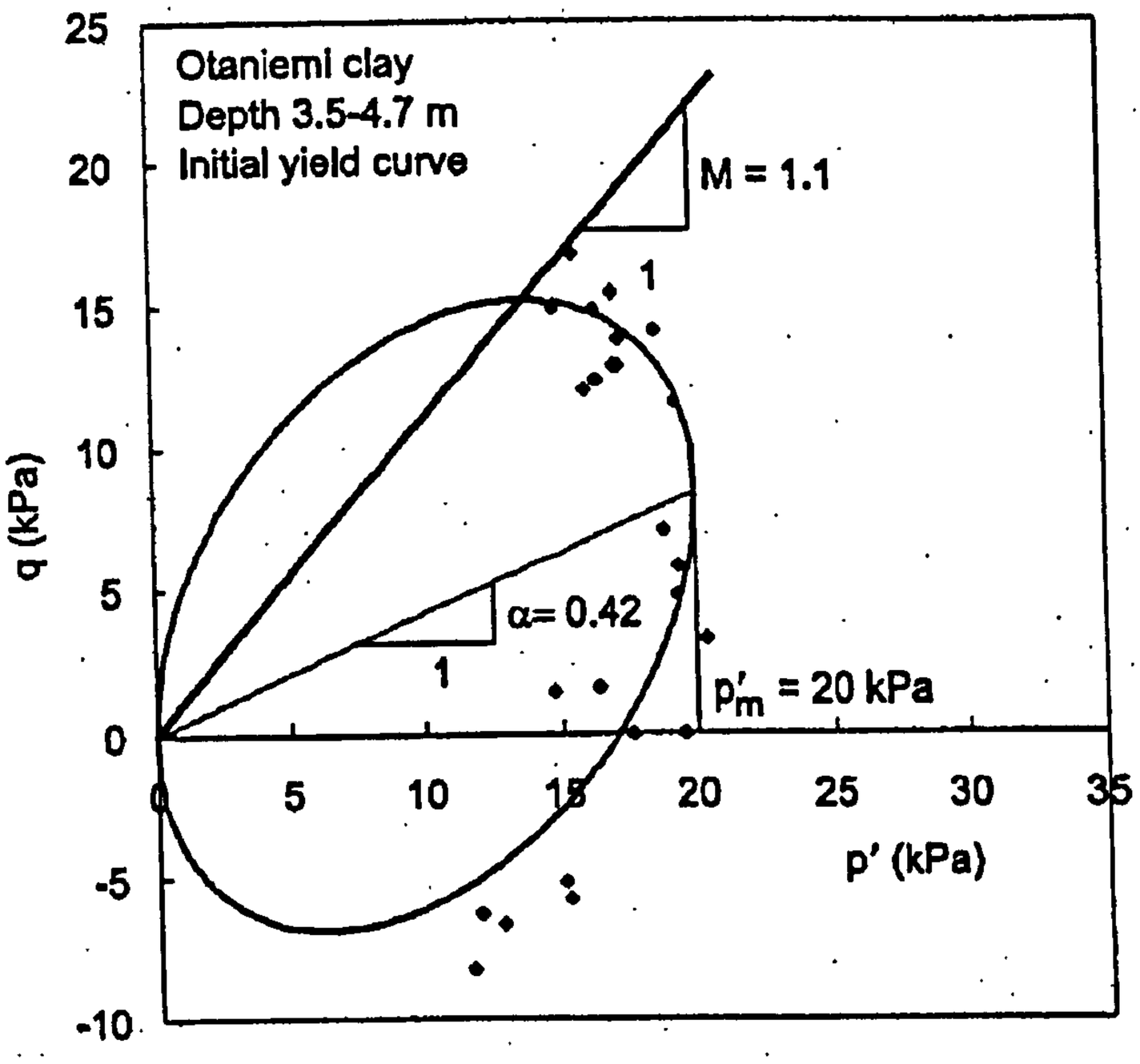

Figure 3.5. S-CLAY1 yield curve and yield points identified for Otaniemi Clay (Wheeler et al. 2003b).

Soil constant β

Wheeler et al. (1999) showed that the value of the soil constant β can be estimated through a simple procedure. Under plastic loading at constant value of η, the yield curve inclination α will eventually reach a final equilibrium value as defined by Equation 3.9. If the soil has undergone a one-dimensional strain history and is normally consolidated or lightly/moderately overconsolidated then Equation 3.9 should result in a yield curve orientation that corresponds to α_{K0} (given by Equation 3.14). From Equation 3.9, it is apparent that only one value of β can produce a value of α corresponding to α_{K0} during loading at η_{K0}. The required value for β for a such a soil can therefore be obtained by combining Equations 3.9 and 3.14:

$$\beta = \frac{3\left(4M^2 - 4\eta_{K0}^2 - 3\eta_{K0}\right)}{8\left(\eta_{K0}^2 - M^2 + 2\eta_{K0}\right)} \tag{3.15}$$

It is apparent that parameter β can be estimated from knowledge of the normally consolidated value of K_0.

Soil constant μ

The soil constant μ controls the absolute rate at which the value of α heads towards its current target value. The parameter μ cannot be easily estimated directly from standard laboratory tests. Instead, μ can be estimated by calibration of the model by conducting model simulations and comparing these to experimental data (see Wheeler et al., 1999 and Wheeler et al., 2003b). The most appropriate experimental tests would be ones involving substantial rotation of the yield curve. Zentar et al. (2002a) noted that there may be an empirical relationship between μ and the gradient of the post-yield compression curve λ. They suggested that the value of μ lies in the range 10/λ to 15/λ. The fact that μ is related to λ appears to suggest that μ is also dependent on stress path (see Section 6.4.3). The use of a number of triaxial tests in conjunction with model simulations in order to estimate μ is discussed in Section 3.2.7.

3.2.7 Triaxial test simulations with S-CLAY1

Stress-strain behaviour of a natural clay

Comparisons of triaxial test data from Otaniemi clay with model simulations (Wheeler et al. 1999, 2003b) highlighted the model strengths and weaknesses and allowed model parameters to be estimated. An example of this work is given in Figure 3.6, in which S-CLAY1 simulations of 3 multi-stage tests on Otaniemi are shown. Corresponding Modified Cam Clay simulations are also shown. Test CAD2251 was first loaded at $\eta = 0.60$ and then unloaded and reloaded at $\eta = 0.10$, test CAD2544 was loaded in extension at $\eta = -0.59$ followed by unloading and reloading in compression at $\eta = 0.51$, and Test CAD2277 was loaded at $\eta = 0.90$ followed by unloading and reloading at $\eta = 0.13$.

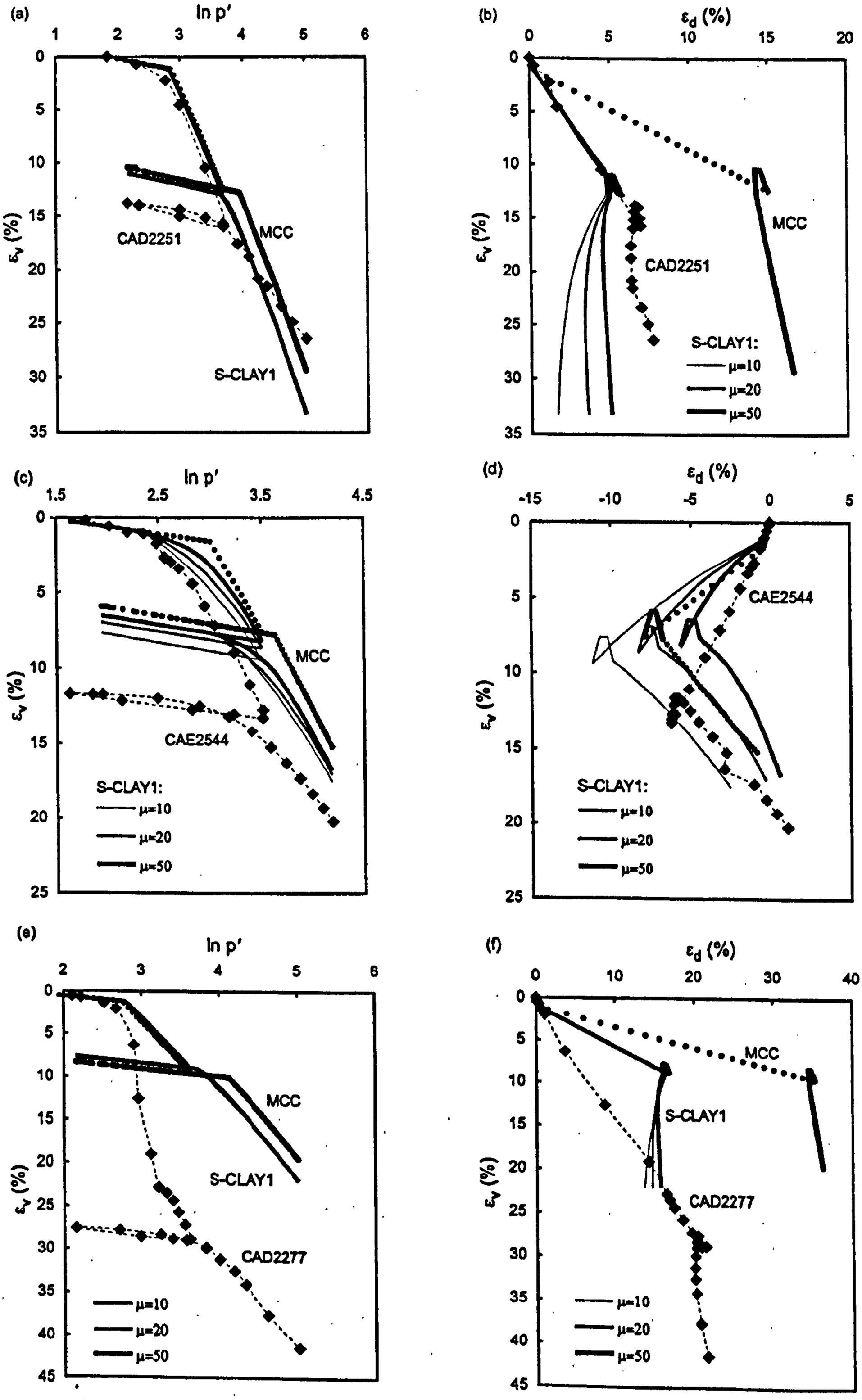

Figure 3.6. S-CLAY1 simulations of Otaniemi clay (Wheeler et al., 2003b).

The results of volumetric strain (ε_v) plotted against the logarithm of mean effective stress (ln p') (see Figures 3.6 (a), (c) and (e)) show that yield stresses are accurately predicted by S-CLAY1. However, volumetric strains are poorly predicted. At low values of η in the first loading stages S-CLAY1 gave generally good predictions in terms of volumetric strains. However at much higher values of η, especially where $\eta >> \eta_{K0}$, the model tended to underpredict the magnitude of volumetric straining. This was because the chosen value of λ was based on oedometer tests (K_0 conditions). At high values of η the "apparent" value of λ is much higher than for η_{K0}. S-CLAY1 also overestimated volumetric strains during the second loading stage and these effects are thought to be due to the effects of destructuration and are discussed more fully in Section 3.3.

Figures 3.6 (b), (d) and (f) show that the pattern of straining (in terms of the ratio of shear and volumetric strains) is better matched by S-CLAY1 than MCC. In most of the tests the ratio of shear and volumetric strains was matched well, but there were discrepancies on loading in triaxial extension and loading at high η values close to the critical state line. The overall suggestion was that the use of an associated flow rule is generally a good assumption, but that discrepancies may occur.

Stress-strain behaviour of a reconstituted clay

Karstunen and Koskinen (2004) conducted triaxial tests on reconstituted Murro clay from Finland, showing that the S-CLAY1 model gave particularly good agreement with the soil behaviour. In model simulations of these tests, volumetric strains were matched extremely well, providing further evidence that the effects of destructuration would need to be represented when modelling a natural clay. Figure 3.7 shows results from a multi-stage triaxial test on reconstituted Murro clay. During the first loading stage ($\eta_0 = 0.99$) both models predict similar amounts of volumetric strain. In the second loading stage ($\eta_1 = 0.21$), S-CLAY1 predicts the volumetric strains and the yield point reasonably well, but MCC overestimates the yield point and therefore underestimates the volumetric strains. Both the volumetric strains and the yielding in the third loading stage with $\eta_2 = 0.92$ are again predicted well with both models. The deviatoric strains, however, are predicted very well with the S-CLAY1 model, in

contrast to the MCC model, which particularly fails in the first and the third loading stages. The pattern of straining (see the ε_v - ε_d plot in Fig. 3.7) is, therefore, predicted extremely well with S-CLAY1, suggesting that the assumption of an associated flow rule in the S-CLAY1 model is justified, and poorly with the MCC model.

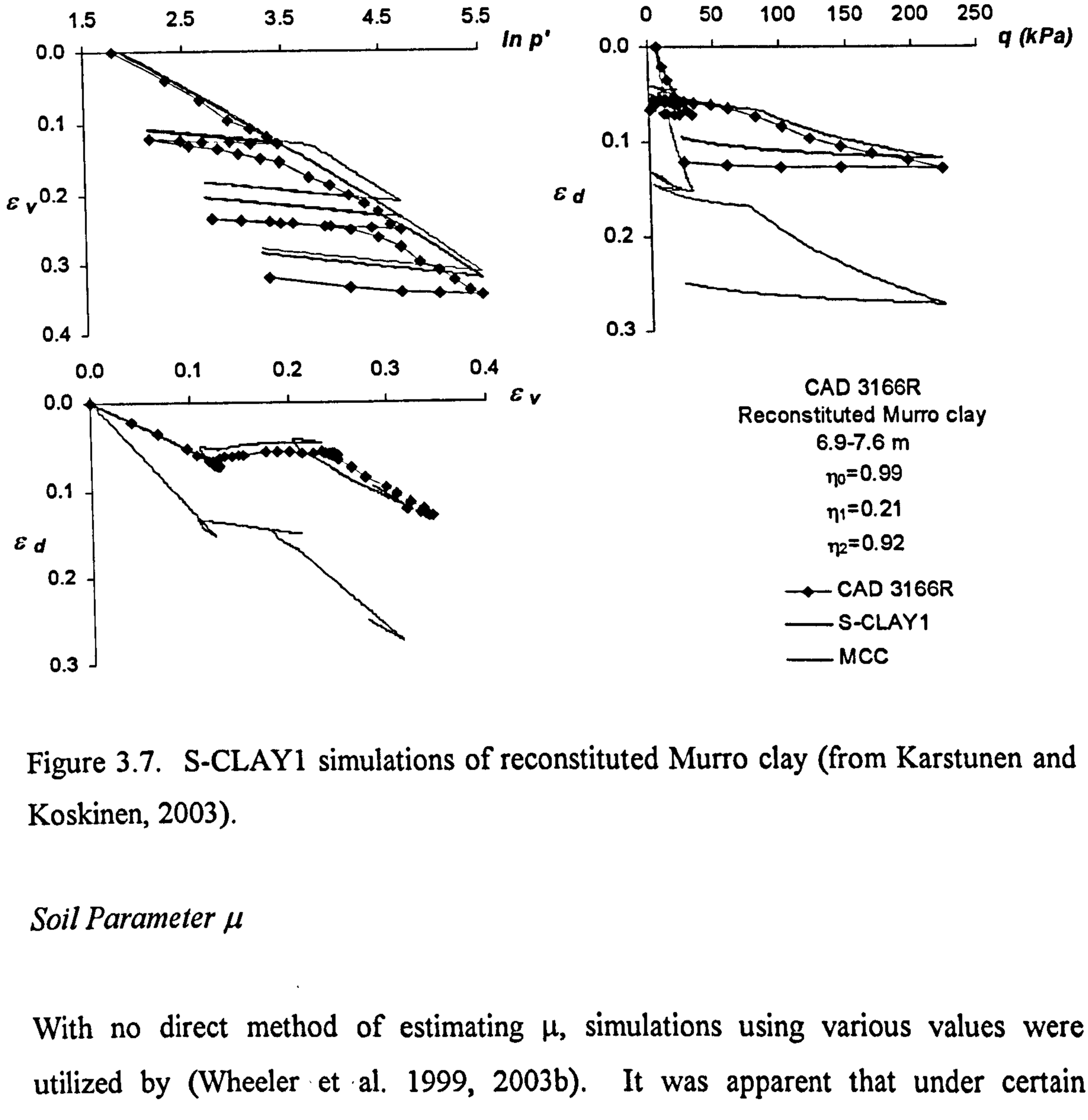

Figure 3.7. S-CLAY1 simulations of reconstituted Murro clay (from Karstunen and Koskinen, 2003).

Soil Parameter μ

With no direct method of estimating μ, simulations using various values were utilized by (Wheeler et al. 1999, 2003b). It was apparent that under certain conditions, the effect of altering μ would be virtually negligible. Obviously, this will occur in cases where there is little or no rotation of the yield curve. In contrast when loading on paths that will cause large rotations of the yield curve, the predictions become sensitive to the choice of μ. The conclusion from the simulations on Otaniemi clay (Wheeler et al. 1999, 2003b) suggested that a value of $\mu = 20$ would be appropriate.

3.3 S-CLAY1S model formulation in triaxial stress space

To account for the effects of destructuration, a modified version of S-CLAY1 was developed and named S-CLAY1S (Soft-Clay1 with Structure,) as described by Koskinen et al. (2002a) and Zentar et al. (2002b). In S-CLAY1S, the yield curve equation for the natural soil with bonding is identical to that of S-CLAY1 (Equation 3.4). However, the effects of inter-particle bonding, described in Section 2.7.1, mean that the bonded soil has an additional resistance to yielding compared to the corresponding unbonded soil. The method of modelling the influence of bonding and destructuration in S-CLAY1S is based on the ideas first suggested by Gens and Nova (1993) (see Section 2.7.2).

3.3.1 Model formulation

As described in Chapter 2 an unbonded soil with the same void ratio and degree of anisotropy as an equivalent bonded soil would yield at lower stresses. Figure 3.8 illustrates how the equivalent unbonded soil is represented by an intrinsic yield curve, of the same orientation α as the true yield curve for the natural soil, but of smaller size, p'_{mi}. The relative sizes of the natural and intrinsic yield curves can be related by a bonding parameter x, so that the size of the natural yield curve is now given by

$$p'_m = (1+x)p'_{mi} \tag{3.16}$$

S-CLAY1S incorporates three hardening laws. The rotational hardening law of Equation 3.10 is retained. The volumetric hardening law in Equation 3.6 is slightly modified and this now accounts for the change in size of the intrinsic yield curve (rather than the yield curve for the bonded soil). This change in size of the intrinsic yield curve is again assumed to be linked exclusively to increments of plastic volumetric strains, $d\varepsilon_v^p$.

$$dp'_{mi} = \frac{vp'_{mi}\,d\varepsilon_v^p}{\lambda_i - \kappa} \tag{3.17}$$

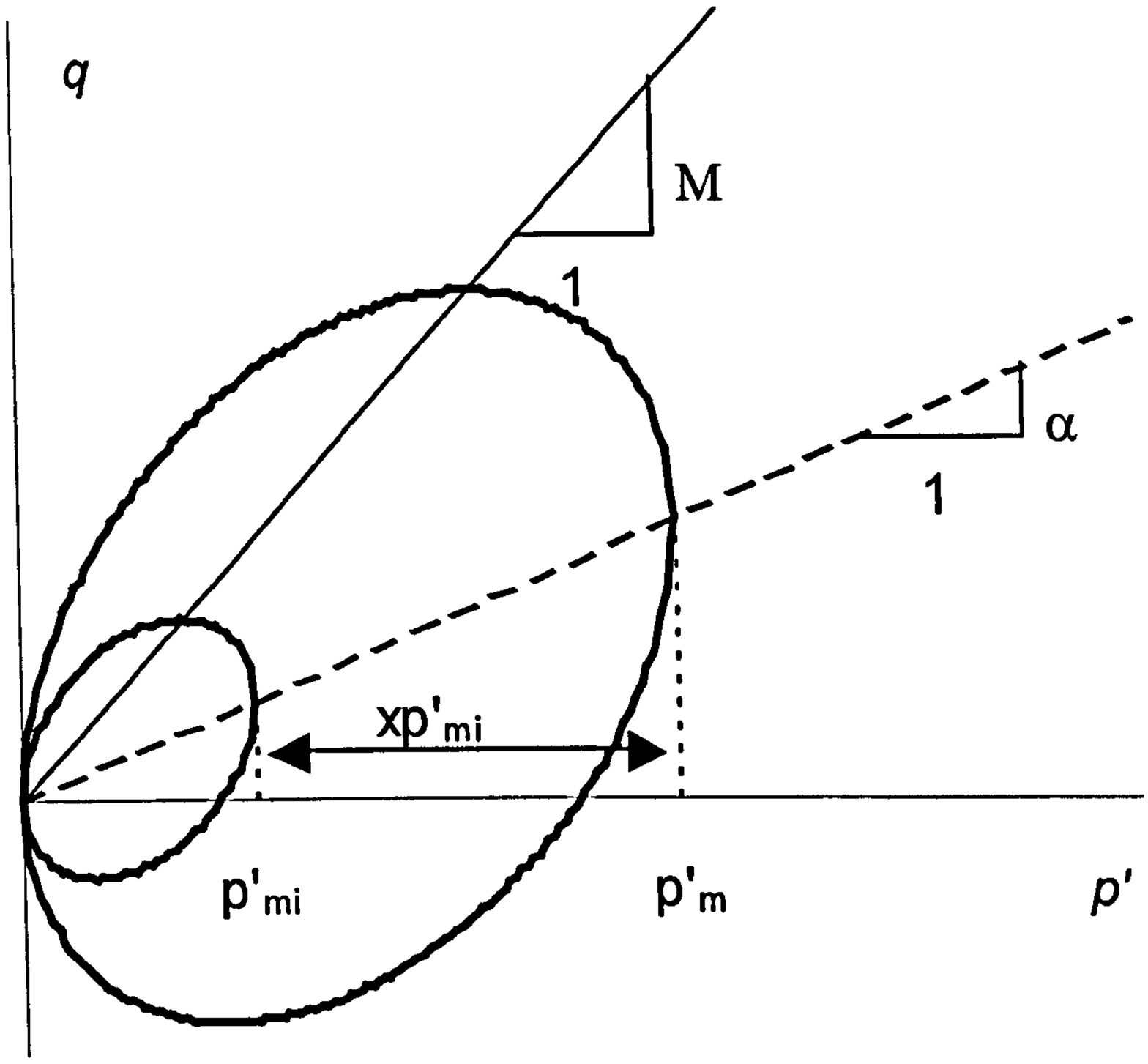

Figure 3.8. S-CLAY1S yield curve.

where λ_i is the slope of the intrinsic compression line in the v: ln p' plane (where no change of anisotropy is occurring). However, by combining Equations 3.16 and 3.17 it can be seen that the increment of plastic volumetric strain now consists of two components

$$d\varepsilon_v^p = \frac{(\lambda_i - \kappa)dp'_m}{vp'_m} + \frac{(\lambda_i - \kappa)(-dx)}{v(1+x)} \tag{3.18}$$

The first component of Equation 3.18 is related to the increase in size of the real yield curve and is identical to the plastic volumetric strain predicted by S-CLAY1 (see Equation 3.6). The second component takes account of the additional plastic volumetric strain caused by destructuration. In Figure 3.9, the behaviour of a natural and reconstituted clay are compared for a constant η loading path, with no change of anisotropy (e.g. isotropic loading of an isotropic sample or K_0 loading of a sample

with a one-dimensional strain history): the reconstituted sample would follow an intrinsic compression line (of gradient λ_i) in the v: ln p' plane. A natural sample would yield at a higher value of effective stress and the compression curve would gradually converge with the intrinsic compression curve. The initial gradient of the post-yield compression curve for the natural sample will be greater than λ_i, due to the additional component of compression from bond degradation.

An additional hardening law is required to account for the effects of destructuration during plastic straining:

$$dx = a[(0-x)|d\varepsilon_v^p| + b(0-x)|d\varepsilon_d^p|] \tag{3.19}$$

or

$$dx = -ax[|d\varepsilon_v^p| + b|d\varepsilon_d^p|] \tag{3.20}$$

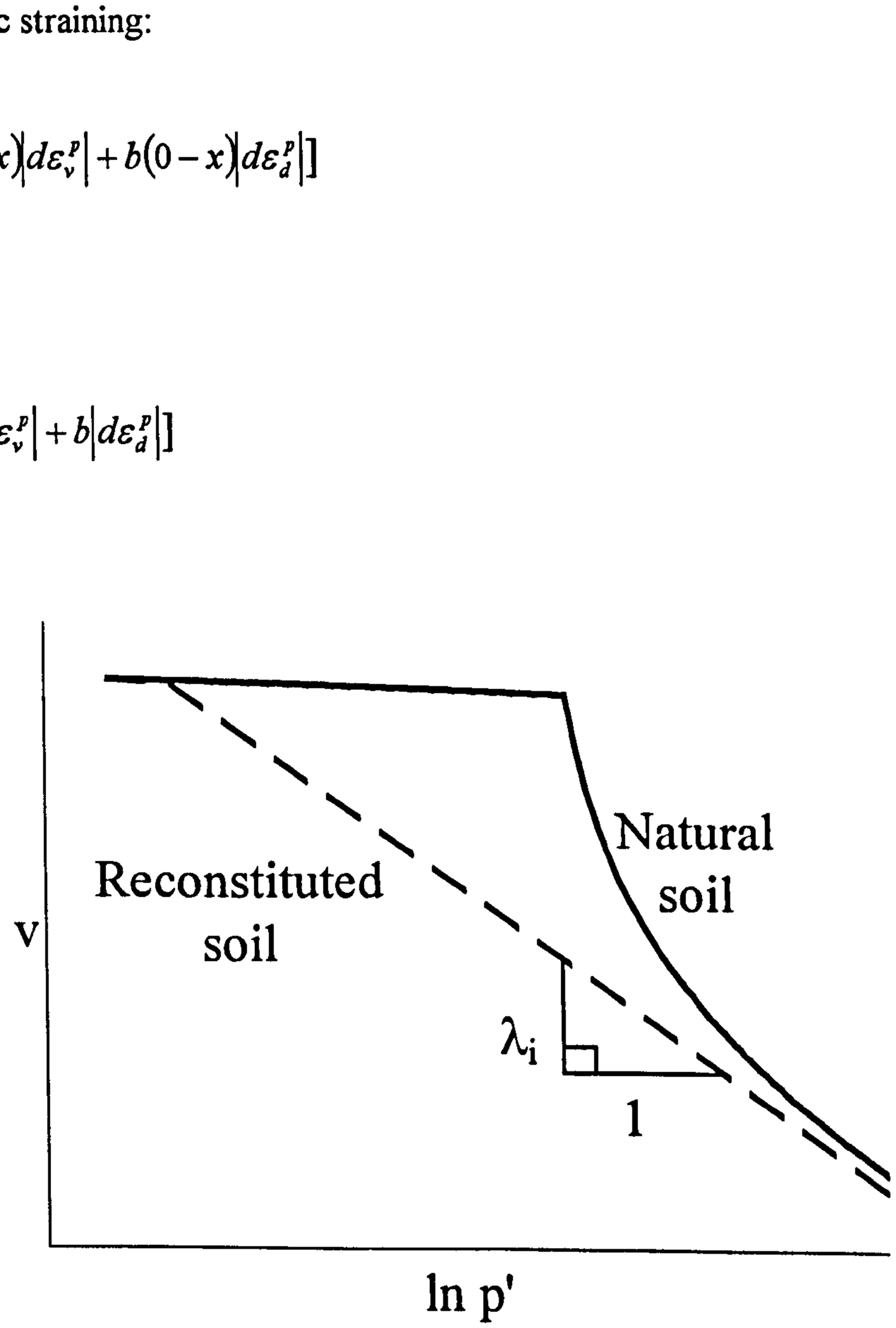

Figure 3.9. Compression curves for natural and reconstituted soil.

This is the same as that proposed by Gens and Nova (1993), (see Equation 2.14).

The function is shown explicitly in Equation 3.19 to emphasise that it is analogous to the rotational hardening law of Equation 3.10. Both plastic volumetric and plastic shear strains are contributing to the bond degradation, and the expanded form of the equation shows that they are both tending to reduce x towards a target value of zero. The soil parameter "a" determines the overall rate at which bonding is destroyed and the parameter "b" governs the relative effectiveness of plastic shear strains and plastic volumetric strains in destructuration. At high value of η, where $d\varepsilon_d^p/d\varepsilon_v^p \rightarrow \infty$, plastic shear strains will be more important in causing destructuration, whereas at lower values of η where $d\varepsilon_d^p/d\varepsilon_v^p \rightarrow 0$, plastic volumetric strains are more influential. Equation 3.20 is identical to that of Gens and Nova (1993) (see Equation 2.14) and Rouainia and Muir Wood (2000) (see Equation 2.15), who also assumed that both plastic shear strains and plastic volumetric strains were influential in bond degradation.

The destructuration law describes only the degradation of bonding with plastic straining. It is assumed that bonding cannot be regained, although this is not necessarily the case in practice. Schmertmann (1991) described the "aging improvement" of soils, which can be due to a variety of processes such as secondary compression, thixotropy, cementation and cold welding. Schmertmann (1991), along with Leonards and Altschaeffl (1964) reported experimental evidence of "restructuring" with time.

In S-CLAY1S, elastic behaviour is represented by Equations 3.1 and 3.2, as for S-CLAY1. Just as it is assumed that elastic behaviour is isotropic, it is also assumed that elastic properties are unaffected by bond degradation. Additionally, it is assumed that elastic strains do not cause destructuration. Although neither of these assumptions are strictly true, it is assumed that, as already discussed in Section 3.2.1, they are acceptable simplifications for soft clays, given the dominance of plastic strains in practical design situations.

3.3.2 Evaluation of S-CLAY1S parameters

The use of S-CLAY1S requires the evaluation of two new soil constants (a and b) and determination of the initial value of an additional state variable x. In addition,

the S-CLAY1 parameter λ has been replaced by the intrinsic compression index λ_i. The value of λ_i can be estimated by tests on reconstituted samples as demonstrated by Koskinen (2001). The initial value of the bonding parameter x_0 can be estimated by referring to data on the sensitivity of the clay. Since sensitivity (S_t) is defined as the ratio of the strength of the natural sample to the strength of a corresponding remoulded sample then it is reasonable to assume that

$$x_0 \approx S_t - 1 \tag{3.21}$$

A more detailed comparison of a reconstituted sample and an undisturbed sample can give an accurate assessment of the initial degree of bonding. If a natural sample is loaded along a certain stress path (η_l), then it will follow a compression curve as shown in Figure 3.10 (a). At a stress level A, inside the real yield curve, the sample exists in triaxial stress space as shown in Figure 3.10 (b).

If p'_m and α are known, then the specific volume at point A is given by

$$v_A = N_i - \lambda_i \ln p'_{mi} - \kappa \ln\left(\frac{p'_A}{p'_{mi}}\right) \tag{3.22}$$

where N_i is the intercept (at p' = 1 kPa) of the intrinsic compression line for a reconstituted sample. Substituting Equation 3.16 in 3.22 gives

$$v_A = N_i - \lambda_i \ln\left(\frac{p'_{m0}}{1+x_0}\right) - \kappa \ln\left(\frac{p'_A(1+x_0)}{p'_{m0}}\right) \tag{3.23}$$

and the initial bonding x_0 can therefore be estimated by re-arranging Equation 3.23 to give:

$$(1+x_0) = p'_{m0} \exp\left[\frac{v_A - N_i + \kappa \ln p'_A}{\lambda_i - \kappa}\right] \tag{3.24}$$

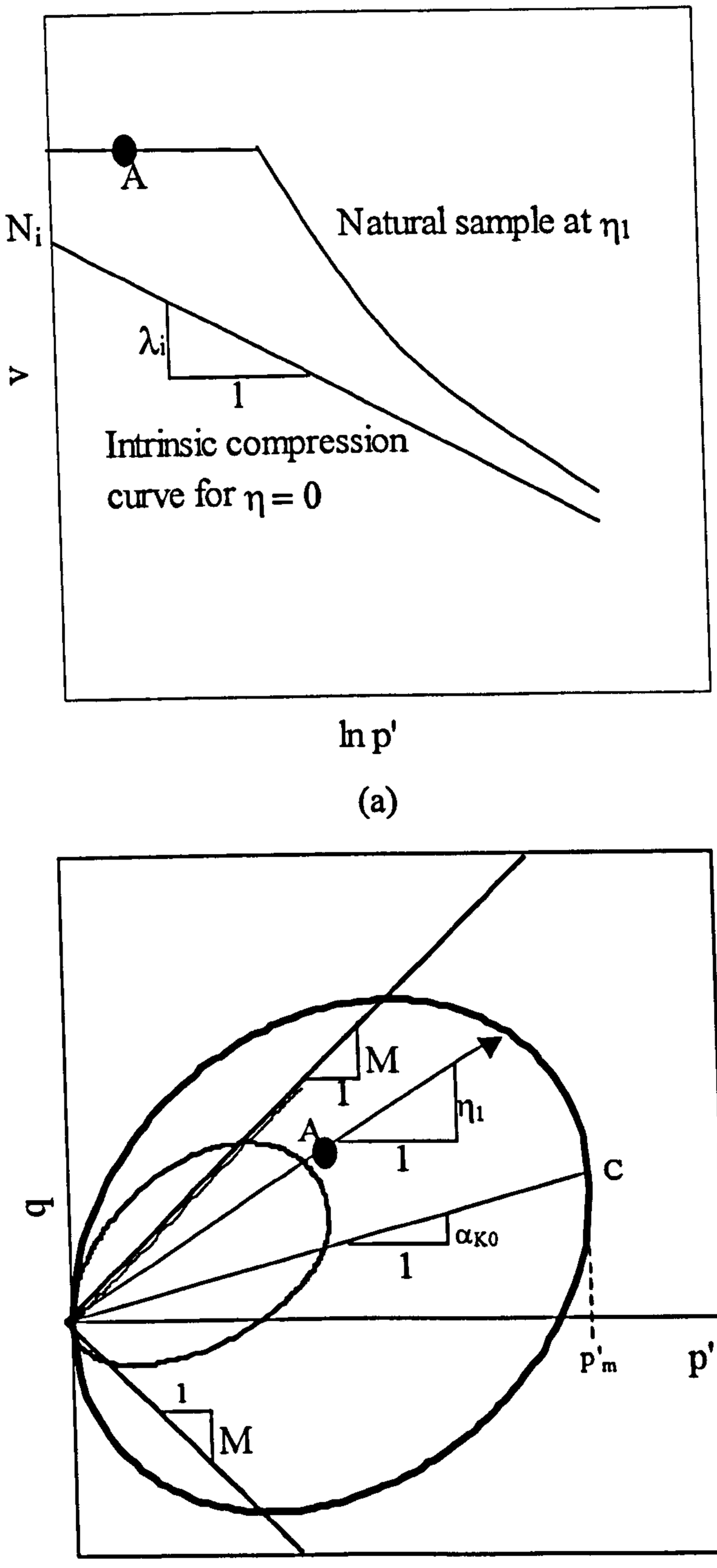

Figure 3.10. Natural sample at stress state A; (a) compression curve, (b) stress state.

The values of N_i and λ_i must be estimated from test data on reconstituted samples, whereas the values of initial yield curve size p'_{m0}, applies to a natural sample, as

does the measured value of specific volume v_A at some initial stress p'_A inside the real yield curve.

The values of parameters a and b can be selected by comparing model simulations with experimental test data in a similar manner to the optimisation of the anisotropy parameter μ. The value of parameter a can be estimated by performing simulations of tests involving very low values of η, in which shear strains are small and the influence of parameter b is minimised. Then, having optimised the value of parameter a, a test simulation involving a high value of η (and therefore significant shear strains) can be used to find an appropriate value for parameter b. Koskinen et al. (2002a) found that a = 9 and b = 0.2 were appropriate for natural samples of POKO clay. Zentar et al. (2002b) suggested similar parameter values for Bothkennar clay (a = 8 and b = 0.3).

3.3.3 Test Simulations using S-CLAY1S model

To validate the S-CLAY1S model, Koskinen et al. (2002a) conducted triaxial tests on POKO clay, a natural soft material from Southern Finland. The test results were compared with model simulations of S-CLAY1S and S-CLAY1. In general, S-CLAY1S shows improved modelling when compared to S-CLAY1.

As an example, simulations from a particular test are shown in Figure 3.11. For the simulations S-CLAY1S test parameters were derived as $\lambda_i = 0.25$ and $x_0 = 14$. For S-CLAY1, the λ value was much higher at 0.75. This value of λ was measured at a stress ratio η_{K0} on a natural sample. The optimisation procedure led to the conclusion that a = 9 and b = 0.2. In this example, the sample had first been loaded at a stress ratio $\eta_1 = 0.95$ to a stress that was approximately three times the yield stress, followed by unloading along the same stress path and then reloading at $\eta_2 = 0.06$. The compression behaviour is shown in Figure 3.11 (a). From the test data it can be seen that the post-yield gradient of the compression curve is relatively steep in the first loading where the η-value was moderately high (given that the M value was 1.20) and the influence of destructuration is strong. This is well represented by S-

CLAY1S, and is also reasonably well represented by S-CLAY1, because of the high value of λ employed.

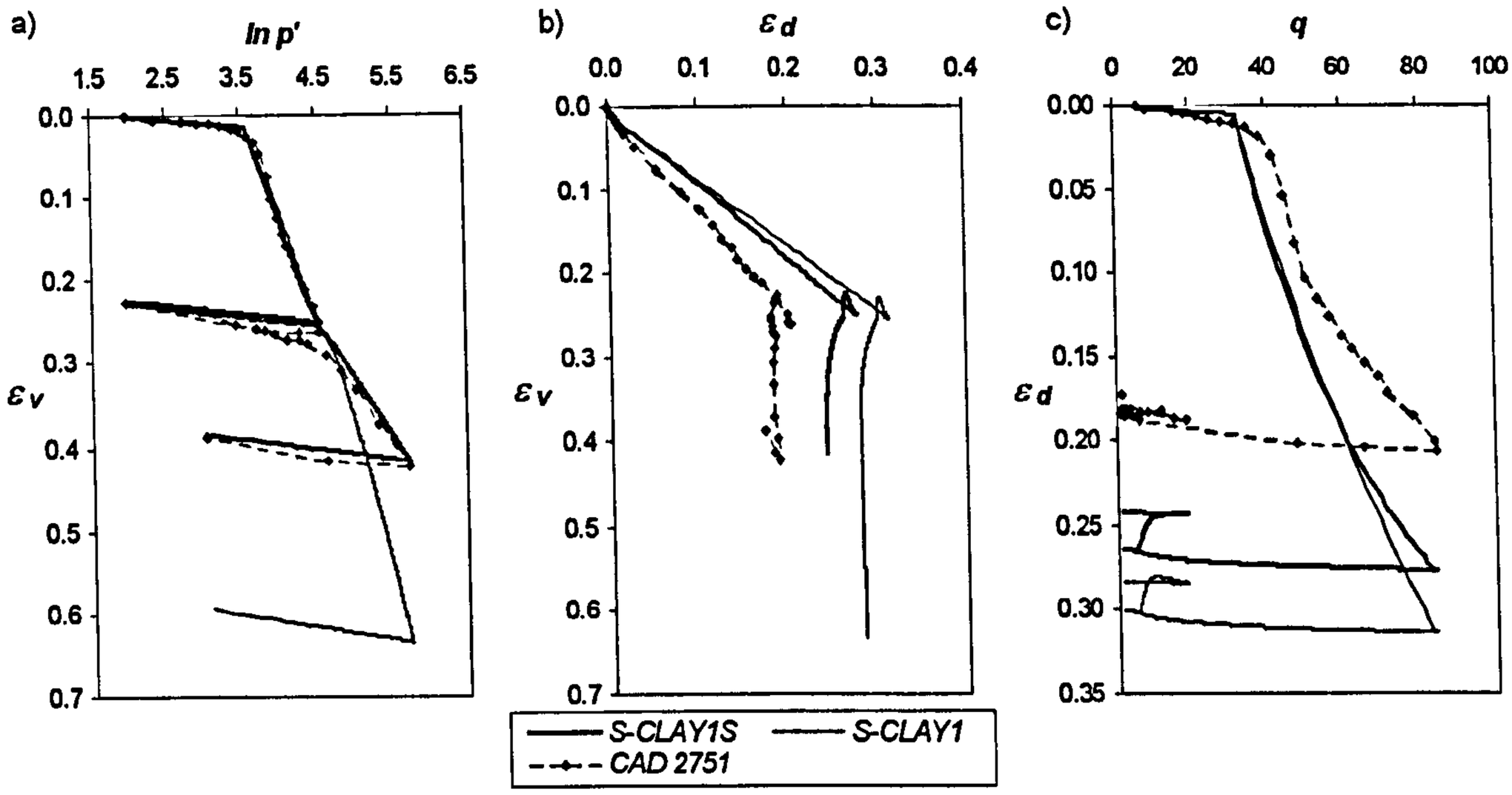

Figure 3.11. Simulation of Test CAD 2751 (Koskinen et al., 2002a).

In contrast, the post-yield gradient of the compression curve is relatively low in the second loading stage. This low gradient is due to two factors. Firstly, the second loading is at a low η-value (almost isotropic), so that the influence of plastic shear strains on destructuration will be minimal. In addition, it is likely that a significant amount of bond degradation has occurred in the first loading stage so that the rate of destructuration in the second stage would be greatly reduced even if it were conducted at the same value of η as the first loading stage. The stress-strain curves are again well represented by S-CLAY1S. In contrast, S-CLAY1 continues to use an elevated value of λ during the second loading stage, and therefore significantly overestimates the magnitude of plastic volumetric strain. Other simulations presented by Koskinen et al. (2002b) showed that while S-CLAY1 was not able to satisfactorily model volumetric strains during certain stress paths, or certain combinations of stress paths, S-CLAY1S generally gave satisfactory predictions of the stress-strain behaviour for this natural soft clay. It was evident that S-CLAY1 may not be able to accurately model stress paths at high η values or stress paths where the sample has been loaded very far beyond the initial yield stress, where the rate of destructuration will eventually tend to zero and λ will tend to λ_i. In addition, inspection of Figures 3.11 (b) indicates that the associated flow rule is not entirely

accurate at this high value of η during the first loading stage, as seen in the overestimation of shear strains.

3.4 Procedure for performing model simulations in triaxial stress space

This section describes how the constitutive relations of S-CLAY1 and S-CLAY1S are used in matrix (or tensor) form in order to be implemented in a computer code to generate model simulations.

The main assumption is that incremental strains can be divided into their elastic and plastic components

$$d\varepsilon = d\varepsilon^{e} + d\varepsilon^{p} \tag{3.25}$$

3.4.1 Elastic strains

The elastic bulk modulus is calculated in the conventional manner:

$$K' = \frac{\nu' p'}{\kappa} \tag{3.26}$$

as is the elastic shear modulus

$$G' = \frac{3K'(1-2\nu')}{2(1+\nu')} \tag{3.27}$$

The elastic stress-strain relationship in triaxial stress space is composed thus:

$$\begin{Bmatrix} d\varepsilon_v^e \\ d\varepsilon_d^e \end{Bmatrix} = \begin{Bmatrix} 1/K' & 0 \\ 0 & 1/3G' \end{Bmatrix} \begin{Bmatrix} dp' \\ dq \end{Bmatrix} \tag{3.28}$$

3.4.2 Plastic strains

With the form of yield function in Equation 3.4 and the associated flow rule of Equation 3.5 we have the plastic compliance matrix:

$$\begin{Bmatrix} d\varepsilon_v^p \\ d\varepsilon_d^p \end{Bmatrix} = \frac{1}{H} \begin{bmatrix} \frac{\partial f}{\partial p'}\frac{\partial f}{\partial p'} & \frac{\partial f}{\partial q}\frac{\partial f}{\partial p'} \\ \frac{\partial f}{\partial p'}\frac{\partial f}{\partial q} & \frac{\partial f}{\partial q}\frac{\partial f}{\partial q} \end{bmatrix} \begin{Bmatrix} dp' \\ dq \end{Bmatrix} \tag{3.29}$$

wherein for the S-CLAY1 model

$$H = -\left(\frac{\partial f}{\partial p'_m}\frac{\partial p'_m}{\partial \varepsilon_v^p}\frac{\partial f}{\partial p'} + \frac{\partial f}{\partial \alpha}\left(\frac{\partial \alpha}{\partial \varepsilon_v^p}\left\langle \frac{\partial f}{\partial p'} \right\rangle + \frac{\partial \alpha}{\partial \varepsilon_d^p}\left| \frac{\partial f}{\partial q} \right| \right) \right) \tag{3.30}$$

For the S-CLAY1S model, Equation 3.29 still holds, but the hardening modulus becomes:

$$H = -\left(\frac{\partial f}{\partial p'_m}\frac{\partial p'_m}{\partial \varepsilon_v^p}\frac{\partial f}{\partial p'} + \frac{\partial f}{\partial \alpha}\left(\frac{\partial \alpha}{\partial \varepsilon_v^p}\left\langle \frac{\partial f}{\partial p'} \right\rangle + \frac{\partial \alpha}{\partial \varepsilon_d^p}\left| \frac{\partial f}{\partial q} \right| \right) + \frac{\partial f}{\partial x}\left(\frac{\partial x}{\partial \varepsilon_v^p}\left| \frac{\partial f}{\partial p'} \right| + \frac{\partial x}{\partial \varepsilon_d^p}\left| \frac{\partial f}{\partial q} \right| \right) \right) \tag{3.31}$$

Expressions for the partial derivatives in Equations 3.29, 3.30 and 3.31 are given in Appendix A.

3.5 S-CLAY1 model formulation in general stress space

In analysis of boundary value problems, soil elements will generally not be under triaxial stress conditions. A generalized version of S-CLAY1 was established by Wheeler et al. (2003b), which was capable of modelling fully 3-dimensional stress states, including rotation of principal stresses. This generalized version of the model is presented in terms of fully general stress and strain tensors, while the scalar anisotropy parameter α is generalized using a fabric tensor.

3.5.1 Definition of stress, strain and anisotropy variables

Stress variables

The mean effective stress is defined as

$$p' = \frac{1}{3}(\sigma'_x + \sigma'_y + \sigma'_z) \tag{3.32}$$

The deviatoric stress tensor can be expressed in vector form $\underline{\sigma}'_d$ and is comprised of six components:

$$\underline{\sigma}'_d = \begin{bmatrix} \sigma'_x - p' \\ \sigma'_y - p' \\ \sigma'_z - p' \\ \sqrt{2}\tau_{xy} \\ \sqrt{2}\tau_{yz} \\ \sqrt{2}\tau_{zx} \end{bmatrix} = \begin{bmatrix} \frac{1}{3}(2\sigma'_x - \sigma'_y - \sigma'_z) \\ \frac{1}{3}(-\sigma'_x + 2\sigma'_y - \sigma'_z) \\ \frac{1}{3}(-\sigma'_x - \sigma'_y + 2\sigma'_z) \\ \sqrt{2}\tau_{xy} \\ \sqrt{2}\tau_{yz} \\ \sqrt{2}\tau_{zx} \end{bmatrix} \tag{3.33}$$

where $\sigma_{x,y,z}$ are the components of normal stress and $\tau_{xy,yz,xz}$ are the corresponding components of shear stress. The scalar value of deviator stress q is related to $\underline{\sigma}'_d$ by:

$$q^2 = \frac{3}{2}\{\underline{\sigma}'_d\}^T\{\underline{\sigma}'_d\} \tag{3.34}$$

Strain variables

The increment of volumetric strain is given by

$$d\varepsilon_v = d\varepsilon_x + d\varepsilon_y + d\varepsilon_z \tag{3.35}$$

where ε_x, ε_y and ε_z are normal strains in the x, y and z directions.

The deviatoric strain increment tensor can be expressed in vector for as:

$$\underline{d\varepsilon_d} = \begin{bmatrix} \frac{1}{3}(2d\varepsilon_x - d\varepsilon_y - d\varepsilon_z) \\ \frac{1}{3}(-d\varepsilon_x + 2d\varepsilon_y - d\varepsilon_z) \\ \frac{1}{3}(-d\varepsilon_x - d\varepsilon_y + 2d\varepsilon_z) \\ \sqrt{2}d\varepsilon_{xy} \\ \sqrt{2}d\varepsilon_{yz} \\ \sqrt{2}d\varepsilon_{zx} \end{bmatrix} = \begin{bmatrix} \frac{1}{3}(2d\varepsilon_x - d\varepsilon_y - d\varepsilon_z) \\ \frac{1}{3}(-d\varepsilon_x + 2d\varepsilon_y - d\varepsilon_z) \\ \frac{1}{3}(-d\varepsilon_x - d\varepsilon_y + 2d\varepsilon_z) \\ \frac{1}{\sqrt{2}}d\gamma_{xy} \\ \frac{1}{\sqrt{2}}d\gamma_{yz} \\ \frac{1}{\sqrt{2}}d\gamma_{zx} \end{bmatrix} \tag{3.36}$$

The scalar value of deviatoric strain increment $d\varepsilon_d$ is related to $d\underline{\varepsilon}_d$ by:

$$d\varepsilon_d^{\,2} = \frac{2}{3}\{d\underline{\varepsilon}_d\}^T\{d\underline{\varepsilon}_d\} = \frac{2}{9}\left[(d\varepsilon_x - d\varepsilon_y)^2 + (d\varepsilon_y - d\varepsilon_z)^2 + (d\varepsilon_z - d\varepsilon_x)^2 + \frac{3}{2}(d\gamma_{xy}^2 + d\gamma_{yz}^2 + d\gamma_{zx}^2)\right] \tag{3.37}$$

Anisotropy variables

In general stress terms, the degree of anisotropy cannot be described by a single scalar parameter α (this is only possible in the special case of a cross-anisotropic sample in a coaxial triaxial stress space). Now anisotropy is described by a fully generalized fabric tensor, with a deviatoric fabric tensor (analogous to the deviatoric stress tensor), which can be expressed in vector form as:

$$\underline{\alpha}_d = \begin{bmatrix} \frac{1}{3}(2\alpha_x - \alpha_y - \alpha_z) \\ \frac{1}{3}(-\alpha_x + 2\alpha_y - \alpha_z) \\ \frac{1}{3}(-\alpha_x - \alpha_y + 2\alpha_z) \\ \sqrt{2}\alpha_{xy} \\ \sqrt{2}\alpha_{yz} \\ \sqrt{2}\alpha_{zx} \end{bmatrix} = \begin{bmatrix} \alpha_x - 1 \\ \alpha_y - 1 \\ \alpha_z - 1 \\ \sqrt{2}\alpha_{xy} \\ \sqrt{2}\alpha_{yz} \\ \sqrt{2}\alpha_{zx} \end{bmatrix} \tag{3.38}$$

The fabric tensor components have the property

$$\frac{1}{3}\left(\alpha_x+\alpha_y+\alpha_z\right)=1 \tag{3.39}$$

and the scalar value of α is related to $\underline{\alpha}_d$ thus:

$$\alpha^2=\frac{3}{2}\{\underline{\alpha}_d\}^T\{\underline{\alpha}_d\} \tag{3.40}$$

A number of features of the fabric tensor are worth discussing. For the case of an isotropic soil ($\alpha = 0$) we have $\alpha_x = \alpha_y = \alpha_z = 1$ and $\alpha_{xy} = \alpha_{yz} = \alpha_{xz} = 0$. If the soil is cross-anisotropic and the vertical direction in the ground is "y" with the two identical in-situ horizontal directions "x" and "z" then we have an initial fabric tensor with $\alpha_x = \alpha_z \neq \alpha_y$ (and also $\alpha_{xy} = \alpha_{yz} = \alpha_{xz} = 0$).

3.5.2 Model formulation

Elastic strains

The elastic stress-strain relationship is

$$d\underline{\varepsilon}^e=\left[\underline{D}^e\right]^{-1}d\underline{\sigma}' \tag{3.41}$$

In fully general stress space the elastic matrix is for an isotropic soil is:

$$\underline{D}^e=\begin{pmatrix} \frac{1}{E'} & -\frac{\nu'}{E'} & -\frac{\nu'}{E'} & 0 & 0 & 0 \\ -\frac{\nu'}{E'} & \frac{1}{E'} & -\frac{\nu'}{E'} & 0 & 0 & 0 \\ -\frac{\nu'}{E'} & -\frac{\nu'}{E'} & \frac{1}{E'} & 0 & 0 & 0 \\ 0 & 0 & 0 & \frac{1}{G'} & 0 & 0 \\ 0 & 0 & 0 & 0 & \frac{1}{G'} & 0 \\ 0 & 0 & 0 & 0 & 0 & \frac{1}{G'} \end{pmatrix} \tag{3.42}$$

where E' is Young's modulus and ν' is Poisson's ratio. and G' = E'/(2(1+ν'))

Yield surface

The yield surface in general stress space is described by

$$f = \{\underline{\sigma}_d - p'\underline{\alpha}_d\}^T\{\underline{\sigma}_d - p'\underline{\alpha}_d\} - \frac{2}{3}\left(M^2 - \frac{3}{2}\{\underline{\alpha}_d\}^T\{\underline{\alpha}_d\}\right)(p'_m - p')p' = 0 \qquad (3.43)$$

For a cross-anisotropic sample in a coaxial triaxial test in triaxial stress space, Equation 3.43 reduces to Equation 3.4. Although Equation 3.4 has been validated by previous authors (see Section 3.2.6, for the specific case of a cross-anisotropic sample in a coaxial triaxial test in triaxial stress space), no attempt had been made to validate the general form of the yield surface expression of Equation 3.43. This validation should include examination of the critical state stress ratio at more generalized stress states (see Section 7.2).

Flow rule

The flow rule for the general case where association is not assumed is expressed

$$d\varepsilon_v^p = \Lambda\frac{\partial g}{\partial p'} \qquad (3.44)$$

$$d\underline{\varepsilon}_d^p = \Lambda\frac{\partial g}{\partial \underline{\sigma}_d} \qquad (3.45)$$

where Λ is a scalar multiplier and g is a potential function. Since the flow rule is associated, the potential function g is equal to the yied function f. The following can therefore be stated

$$d\varepsilon_v^p = \Lambda\frac{\partial f}{\partial p'} \qquad (3.46)$$

$$d\underline{\varepsilon}_d^p = \Lambda \frac{\partial f}{\partial \underline{\sigma}_d} \tag{3.47}$$

The flow rule is therefore

$$\frac{d\underline{\varepsilon}_d^p}{d\varepsilon_v^p} = \frac{\partial f / \partial \underline{\sigma}_d}{\partial f / \partial p'} \tag{3.48}$$

This reduces to Equation 3.5 for a cross-anisotropic sample within a coaxial triaxial test stress space.

Hardening laws

The volumetric hardening law is identical to Equation 3.6 (there are no deviatoric stresses or strains involved) but the rotational hardening law must be generalised thus:

$$d\underline{\alpha}_d = \mu[\{\chi_v(\underline{\sigma}_d, p') - \underline{\alpha}_d\}\langle d\varepsilon_v^p \rangle + \beta \{\chi_d(\underline{\sigma}_d, p') - \underline{\alpha}_d\} d\varepsilon_d^p] \tag{3.49}$$

in which the target value functions, by analogy with the simplified triaxial stress version of the model (see Section 3.2.5), are given by

$$\chi_v(\underline{\sigma}_d, p') = \frac{3\underline{\sigma}_d}{4p'} \tag{3.50}$$

and

$$\chi_d(\underline{\sigma}_d, p') = \frac{\underline{\sigma}_d}{3p'} \tag{3.51}$$

Therefore, the generalized version of the hardening law is:

$$d\underline{\alpha}_d = \mu\left(\left\{ \frac{3\underline{\sigma}_d}{4} - \underline{\alpha}_d \right\} \left\langle d\varepsilon_v^p \right\rangle + \beta \left\{ \frac{\underline{\sigma}_d}{3} - \underline{\alpha}_d \right\} d\varepsilon_d^p \right) \tag{3.52}$$

It is important to note that Equations 3.50 and 3.51 are appropriate to cross-anisotropic samples tested in a coaxial triaxial test, whereas no attempt has yet been made to validate Equations 3.50 and 3.51 for more general conditions. Therefore further experimental data obtained at more general stress states would be necessary to validate the precise functional forms of Equations 3.50 and 3.51.

3.5.3 Procedure for performing model simulations in general stress space

In order to generate model simulations, the consistency equation (or consistency condition) must be satisfied. This states that the stress state must remain in contact with the yield surface during plastic loading via

$$df = \left\{ \frac{\partial f}{\partial \underline{\sigma}_d} \right\}^T d\underline{\sigma}_d + \frac{\partial f}{\partial p'} dp' + \frac{\partial f}{\partial p'_m} dp'_m + \left\{ \frac{\partial f}{\partial \underline{\alpha}_d} \right\}^T d\underline{\alpha}_d = 0 \tag{3.53}$$

Now the relationships for elastic and plastic strains must be considered again. For elastic straining

$$d\underline{\varepsilon}^e = \left[\underline{D}^e\right]^{-1} d\underline{\sigma} \tag{3.54}$$

and for plastic straining

$$d\underline{\varepsilon}^p = \Lambda \frac{\partial g}{\partial \underline{\sigma}'} \tag{3.55}$$

Recalling the additive postulate of Equation 3.25 and substituting in this equation, we have the elasto-plastic strain tensor

$$d\underline{\varepsilon} = \left[\underline{D}^e\right]^{-1} d\underline{\sigma}' + \Lambda \frac{\partial g}{\partial \underline{\sigma}'} \tag{3.56}$$

The flow rule is assumed to be associated and combining this with Equation 3.53 and the hardening laws (Equations 3.6 and 3.52) the plastic multiplier can be solved:

$$\Lambda = -\frac{\dfrac{\partial f}{\partial p'}dp' + \left\{\dfrac{\partial f}{\partial \underline{\sigma}_d}\right\}^T d\underline{\sigma}_d}{\dfrac{\partial f}{\partial p'_m}\dfrac{\partial p'_m}{\partial \varepsilon_v^p}\dfrac{\partial f}{\partial p'} + \left\{\dfrac{\partial f}{\partial \underline{\alpha}_d}\right\}^T \left[\dfrac{\partial \underline{\alpha}_d}{\partial \varepsilon_v^p}\left\langle\dfrac{\partial f}{\partial p'}\right\rangle + \dfrac{\sqrt{2}}{\sqrt{3}}\dfrac{\partial \underline{\alpha}_d}{\partial \varepsilon_d^p}\sqrt{\left\{\dfrac{\partial f}{\partial \underline{\sigma}_d}\right\}^T\left\{\dfrac{\partial f}{\partial \underline{\sigma}_d}\right\}}\right]} \tag{3.57}$$

If we now define the plastic resistance number as H

$$\frac{\partial f}{\partial p'}dp' + \left\{\frac{\partial f}{\partial \underline{\sigma}_d}\right\}^T d\underline{\sigma}_d = H\Lambda \tag{3.58}$$

then H may be defined as

$$H = -\left(\frac{\partial f}{\partial p'_m}\frac{\partial p'_m}{\partial \varepsilon_v^p}\frac{\partial f}{\partial p'} + \left\{\frac{\partial f}{\partial \underline{\alpha}_d}\right\}^T \left[\frac{\partial \underline{\alpha}_d}{\partial \varepsilon_v^p}\left\langle\frac{\partial f}{\partial p'}\right\rangle + \frac{\sqrt{2}}{\sqrt{3}}\frac{\partial \underline{\alpha}_d}{\partial \varepsilon_d^p}\sqrt{\left\{\frac{\partial f}{\partial \underline{\sigma}_d}\right\}^T\left\{\frac{\partial f}{\partial \underline{\sigma}_d}\right\}}\right]\right) \tag{3.59}$$

An equivalent expression may be derived for S-CLAY1S in general stress space. Plastic strains are then calculated via the compliance matrix:

$$\begin{Bmatrix} d\varepsilon_x \\ d\varepsilon_y \\ d\varepsilon_z \\ d\gamma_{xy} \\ d\gamma_{yz} \\ d\gamma_{zx} \end{Bmatrix} = \frac{1}{H}\begin{bmatrix} \frac{\partial f}{\partial \sigma'_x}\frac{\partial f}{\partial \sigma'_x} & \frac{\partial f}{\partial \sigma'_x}\frac{\partial f}{\partial \sigma'_y} & \frac{\partial f}{\partial \sigma'_x}\frac{\partial f}{\partial \sigma'_z} & \frac{\partial f}{\partial \sigma'_x}\frac{\partial f}{\partial \tau_{xy}} & \frac{\partial f}{\partial \sigma'_x}\frac{\partial f}{\partial \tau_{yz}} & \frac{\partial f}{\partial \sigma'_x}\frac{\partial f}{\partial \tau_{zx}} \\ \frac{\partial f}{\partial \sigma'_y}\frac{\partial f}{\partial \sigma'_x} & \frac{\partial f}{\partial \sigma'_y}\frac{\partial f}{\partial \sigma'_y} & \frac{\partial f}{\partial \sigma'_y}\frac{\partial f}{\partial \sigma'_z} & \frac{\partial f}{\partial \sigma'_y}\frac{\partial f}{\partial \tau_{xy}} & \frac{\partial f}{\partial \sigma'_y}\frac{\partial f}{\partial \tau_{yz}} & \frac{\partial f}{\partial \sigma'_z}\frac{\partial f}{\partial \tau_{zx}} \\ \frac{\partial f}{\partial \sigma'_z}\frac{\partial f}{\partial \sigma'_x} & \frac{\partial f}{\partial \sigma'_z}\frac{\partial f}{\partial \sigma'_y} & \frac{\partial f}{\partial \sigma'_z}\frac{\partial f}{\partial \sigma'_z} & \frac{\partial f}{\partial \sigma'_z}\frac{\partial f}{\partial \tau_{xy}} & \frac{\partial f}{\partial \sigma'_z}\frac{\partial f}{\partial \tau_{yz}} & \frac{\partial f}{\partial \sigma'_z}\frac{\partial f}{\partial \tau_{zx}} \\ \frac{\partial f}{\partial \tau_{xy}}\frac{\partial f}{\partial \sigma'_x} & \frac{\partial f}{\partial \tau_{xy}}\frac{\partial f}{\partial \sigma'_y} & \frac{\partial f}{\partial \tau_{xy}}\frac{\partial f}{\partial \sigma'_z} & \frac{\partial f}{\partial \tau_{xy}}\frac{\partial f}{\partial \tau_{xy}} & \frac{\partial f}{\partial \tau_{xy}}\frac{\partial f}{\partial \tau_{yz}} & \frac{\partial f}{\partial \tau_{xy}}\frac{\partial f}{\partial \tau_{zx}} \\ \frac{\partial f}{\partial \tau_{yz}}\frac{\partial f}{\partial \sigma'_x} & \frac{\partial f}{\partial \tau_{yz}}\frac{\partial f}{\partial \sigma'_y} & \frac{\partial f}{\partial \tau_{yz}}\frac{\partial f}{\partial \sigma'_z} & \frac{\partial f}{\partial \tau_{yz}}\frac{\partial f}{\partial \tau_{xy}} & \frac{\partial f}{\partial \tau_{yz}}\frac{\partial f}{\partial \tau_{yz}} & \frac{\partial f}{\partial \tau_{yz}}\frac{\partial f}{\partial \tau_{zx}} \\ \frac{\partial f}{\partial \tau_{zx}}\frac{\partial f}{\partial \sigma'_x} & \frac{\partial f}{\partial \tau_{zx}}\frac{\partial f}{\partial \sigma'_y} & \frac{\partial f}{\partial \tau_{zx}}\frac{\partial f}{\partial \sigma'_z} & \frac{\partial f}{\partial \tau_{zx}}\frac{\partial f}{\partial \tau_{xy}} & \frac{\partial f}{\partial \tau_{zx}}\frac{\partial f}{\partial \tau_{yz}} & \frac{\partial f}{\partial \tau_{zx}}\frac{\partial f}{\partial \tau_{zx}} \end{bmatrix}\begin{Bmatrix} d\sigma'_x \\ d\sigma'_y \\ d\sigma'_z \\ d\tau_{xy} \\ d\tau_{yz} \\ d\tau_{zx} \end{Bmatrix} \tag{3.60}$$

S-CLAY1 and S-CLAY1S model simulations (presented in Chapters 8 and 9) are limited to cases in which the x, y and z directions remain as the principal directions of stress and strain. The soil initially has principal directions of the fabric tensor in the x, y and z directions. Under these conditions, the x, y and z directions remain the principal directions of the fabric tensor ($\alpha_{xy} = \alpha_{yz} = \alpha_{zx} = 0$). The principal directions of the strain increment vector are coincident with those of the fabric tensor so that $\gamma_{xy} = \gamma_{yz} = \gamma_{zx} = 0$. In this case, Equation 3.60 reduces to Equation 8.1 (see Section 8.5).

3.6 Aspects of soft clay behaviour requiring further investigation and validation

In the light of conclusions drawn from previous studies, it is necessary to investigate further the validity of the S-CLAY1 and S-CLAY1S models. The aims of this study, set out in Section 1.3, have evolved from the findings of previous authors, as described in Chapters 2 and 3. The current study involves triaxial testing of a natural clay from Bothkennar in Scotland. As described in Section 2.10, Bothkennar clay is well suited to the testing requirements in this study. The procedure and apparatus employed in these tests are described in Chapter 4, while the methodology and testing programme are described in Chapter 5. Results from these tests were subsequently compared with S-CLAY1 and S-CLAY1S model simulations in an attempt to determine model parameter values for Bothkennar clay and to further explore the validity of the two models (including a limited extension to the fully generalized version of the models).

CHAPTER 4: EXPERIMENTAL APPARATUS AND PROCEDURES

4.1 Experimental objectives

This chapter describes the equipment and procedures used in the experimental investigation of the stress-strain behaviour of Bothkennar clay. The main laboratory work involved testing soil samples in Bishop-Wesley triaxial cell. To meet the specific objectives outlined in Sections 1.3 and 3.6, a number of experimental requirements had to be met, and these are as follows:

(i) A lightly overconsolidated natural soft clay was required for the experimental programme and samples of Bothkennar clay were deemed suitable for testing purposes.

(ii) A series of multi-stage triaxial tests was to be performed, requiring the use of computer controlled stress-path testing in a triaxial cell. The tests involved drained anisotropic loading and unloading at various values of constant stress ratio η (where $\eta = q/p'$) in both triaxial compression and extension. Isotropic loading and unloading ($\eta = 0$) were also required.

(iii) A series of conventional drained shearing tests were required, where soil samples were to be sheared to a critical state in triaxial compression and extension at constant cell pressure.

(iv) The tests outlined in (i) and (ii) were to be performed on both vertically and horizontally oriented samples. The testing of horizontally oriented samples required the design, manufacture and calibration of radial strain measuring devices, capable of monitoring radial strain in the two orthogonal directions.

(v) In preparation for the triaxial tests, a series of supplementary tests was to be carried out. These included oedometer tests, Atterberg limit tests, specific gravity tests and organic content tests.

4.2 Bothkennar clay samples

4.2.1 Choice of material for testing

It was intended to study a natural soft clay, which exhibited anisotropic behaviour and possessed structure. Samples from the Bothkennar test bed site were therefore selected for testing, as explained in Section 2.10. The Bothkennar soft clay test site has been used as a large-scale facility for experimental and field research. A major advantage in exploring this soil was that a vast amount of data from previous test programmes was readily available, most notably from the 8th Géotechnique Symposium-in-Print (1992) in which a broad range of laboratory and field data were obtained and discussed.

High quality Laval samples were available at the University of Glasgow, Department of Civil Engineering, together with a small number of Sherbrook samples. The 200 mm diameter Laval tube samples were obtained from the Bothkennar test site in April 1989 as described by Hight et al., (1992). Each of the Laval samples was originally 530 mm long and they were subsequently cut into shorter lengths of approximately 200 mm prior to storage. The samples had been coated in alternate layers of paraffin wax and clingfilm dipped in wax. After transportation from the site to the University of Glasgow (a 50 km road journey), the samples were stored in temperature and humidity controlled conditions at 17° C and 90 – 100 % relative humidity. Many of these samples have been used for testing by other researchers and the remaining samples are listed in Table 4.1. "Full cylinder" samples of about 230 mm height appeared not to had been sub-sampled or cut in any way since being sealed on site. "Half-cylinder" samples denote samples that have been cut vertically into two pieces with one remaining. Samples whose height was much less than 200 mm also appear to have been opened, cut and re-sealed in wax.

The Sherbrooke samples were limited in number and their original depths were difficult to identify due to poor labelling. The Laval samples were, however, abundant and covered a wide range of the profile and these were therefore used in this investigation.

Sampler	Sample No.	Depth (m)	Diameter (mm)	Height (mm)	Remarks
Laval	?	3.06-3.165	205	65	Half-cylinder
Laval	10A	5.66-5.79	215	130	Half-cylinder
Laval	12B	8.47-8.69	220	230	Half-cylinder
Laval	18A	9.91-10.14	220	230	Half-cylinder
Laval	18B	10.14-10.36	210	225	Cylinder
Laval	19A	10.46-10.59	205	120	Cylinder
Laval	19B	10.59-10.72	205	65	Half-cylinder
Laval	20A	10.95-11.18	210	230	Half-cylinder
Laval	20B	11.18-11.40	210	225	Cylinder
Laval	21A	11.50-11.73	215	235	Half-cylinder
Laval	22B	12.21-12.44	210	225	Cylinder
Laval	24B	13.31-13.53	220	220	Half-cylinder
Laval	26A	14.15-14.24	210	190	Cylinder
Laval	29B	16.00-16.23	220	220	Half-cylinder
Laval	30A	?	210	230	Cylinder
Laval	30B	16.54-16.60	210	235	Cylinder
Laval	31A	16.85-17.07	210	230	Cylinder
Laval	31B	17.07-17.28	220	215	Half-cylinder
Sherb'k	2	0.85-1.25	230	260	Cylinder
Sherb'k	?	?	230	260	Cylinder
Sherb'k	?	?	230	260	Cylinder

Table 4.1. Laval and Sherbrooke samples of Bothkennar clay, stored at the University of Glasgow (Laval samples from Borehole 1).

4.2.2 Preparation of samples: sampling on site

Nash et al. (1992b) described the Bothkennar soil profile in some detail, showing that a highly homogenous region existed from about 8.90-11.70 m depth. This

depth was described as "soft dark grey silty clay/clayey silt". Examining Table 4.1, it was decided to use Laval samples 20A, 20B and 21A as these fell into this region, covering a depth range 10.95 - 11.73 m. This volume of soil provided enough material for approximately 50 triaxial specimens (38 mm diameter, 76 mm height) and various supplementary tests. Samples from deeper in the profile could have been used, but these were under increasing in-situ stresses and below 11.50 m the material is described as "firm dark grey silty clay/clayey silt". The in-situ stresses at these depths were likely to be sufficiently high that certain stress paths would have been compromised (see Section 5.3). A group of samples from a slightly shallower depth (namely Laval samples 18A, 18B, 19A and 19B) were retained for other research purposes.

Although stored since 1989 (more than 10 years before the present experimental programme was started), it was found that the samples sealed on site and the samples that had been subsequently opened and re-sealed (i.e. the half-cylinders 20A and 21A) appeared to have been well re-sealed and there was no significant loss of moisture during storage, when compared to the in-situ values stated by Nash et al. (1992b). Hight et al. (1992) suggested that the effects of long-term storage on Sherbrooke and Laval samples were small.

Hight et al. (1992) showed that sampling had a number of significant effects on the mechanical properties of the soil. They compared the effects of sampling using Sherbrooke, Laval and piston samplers. When compared to piston samples, the Laval samples were found to have retained a much higher effective stress after trimming, suggesting that the sampling process had caused relatively little disturbance to the soil. It was shown that despite its high quality, Laval triaxial specimens produced a bounding surface that was slightly inside the Sherbrooke surface, showing that slightly more disturbance had occurred in the Laval process (perhaps due to varying degrees of destructuration). In drained and undrained triaxial tests, the Sherbrooke sampler showed the highest peak strengths in triaxial compression, with Laval slightly less and the piston sampler significantly less. A similar pattern was observed in triaxial extension and again the differences were thought to be due to destructuration. Overall, the

Sherbrooke sampler produced marginally the highest quality of sample, but both the Sherbrooke and Laval sampler were far superior to the piston sampler.

4.2.3 Preparation of samples: sub-sampling in the laboratory

The bulk of the soil was to be used for triaxial testing, with a small portion retained for oedometer testing and various index tests. Given that each of the three designated Laval samples was 220 mm high (with wax and cling film removed), it was convenient to subdivide each of them into three horizontal layers, with two layers (each 88 mm in height) used for vertically oriented triaxial test samples and one layer (44 mm in height) reserved for the smaller number of tests on horizontally oriented samples (see Chapter 5 for testing programme). It was also possible to obtain additional horizontal samples from the layers designated for vertical samples if required. The trimming of specimens for triaxial testing is described in Section 4.6.3.

4.3 Triaxial stress path equipment

4.3.1 Layout of equipment

Figure 4.1 shows the overall layout of the triaxial cell and the associated equipment. The apparatus was located in a temperature-controlled laboratory ($20^0C \pm 1^0C$). Figure 4.2 shows a schematic diagram of the stress path cell control system. Backpressure and cell pressure were controlled by stepper-motor regulators and deviatoric stress was applied using a constant rate of strain pump. The triaxial apparatus was equipped with a series of transducers linked to a PC allowing feedback control and of the pressure controllers and the constant rate of strain pump. The individual components and their roles are described below.

4.3.2 Bishop Wesley hydraulic triaxial cell

In order to perform stress path tests (at constant η) in Series B, C and E (see Sections 5.3 to 5.5), a hydraulic triaxial apparatus, as developed by Bishop and

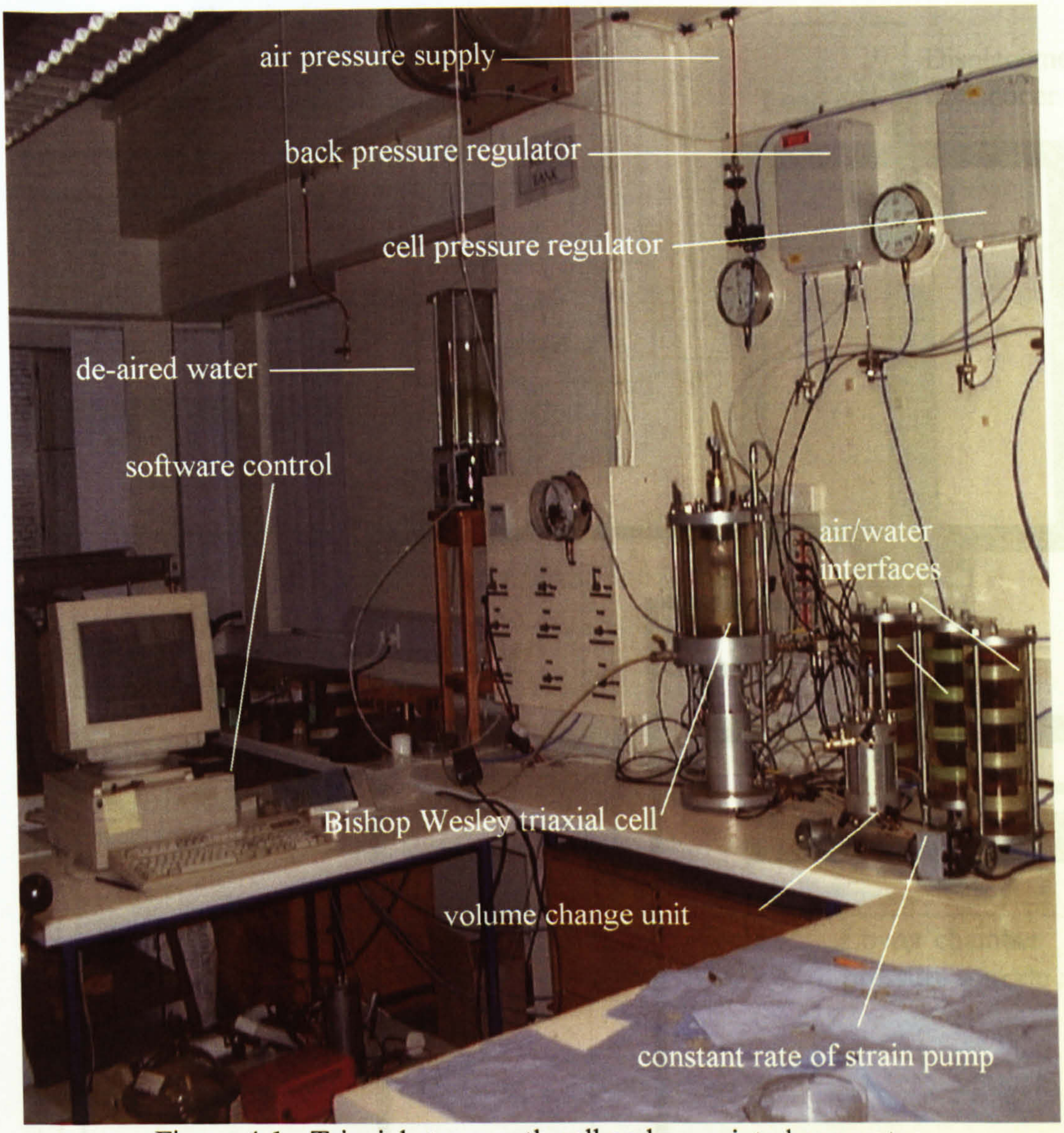

Figure 4.1. Triaxial stress path cell and associated apparatus.

Wesley (1975), was used. Using this apparatus it was possible to carry out the stages described in Section 5.3 and to load and unload the samples at appropriate rates. The layout of the triaxial cell is shown in Figure 4.2. The cell was suitable for testing samples of up to 50 mm in diameter, but was used in this programme for triaxial samples of 38 mm diameter (height 76 mm). Drainage from the sample was provided radially (using filter paper strips) and at both ends against a backpressure, with all drainage expelled from the cell through the base pedestal to a volume change unit. A drainage connection to the top cap was not used. A suction device was fitted to the load cell so that under isotropic loading ($q = 0$) and triaxial extension ($q < 0$) it was possible to maintain contact between the

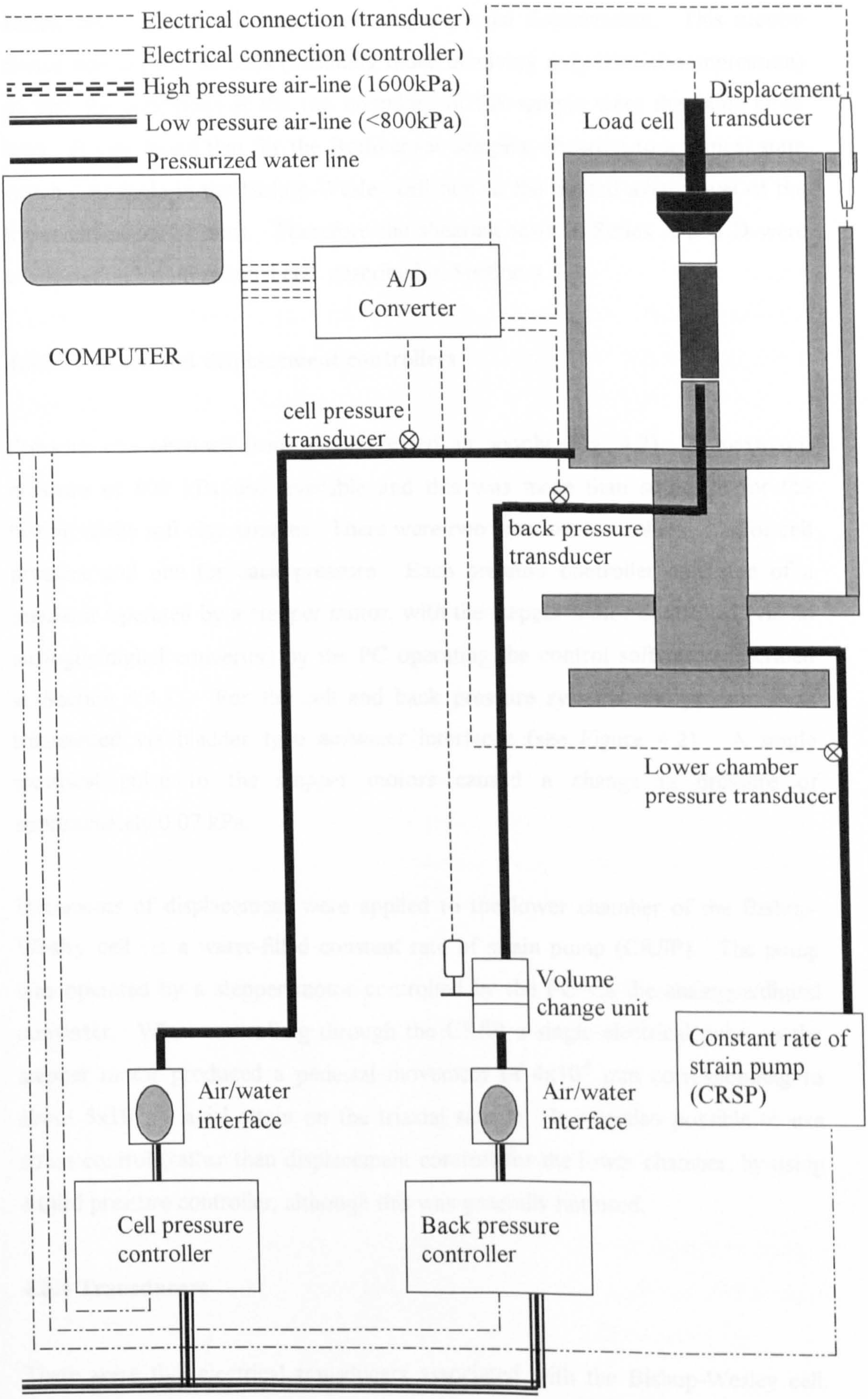

Figure 4.2. Schematic diagram of triaxial stress path equipment.

sample and the load cell in order to measure axial displacement. This suction device was used in all tests (including those involving only triaxial compression) so that the conditions at the top boundary of the sample were the same in all tests. It was found that for the Bothkennar samples, shearing to a critical state was not possible in the Bishop-Wesley cell due to the limited axial travel of the lower chamber (27 mm). Therefore the shearing tests in Series A and D were conducted in a conventional cell, described in Section 4.7.

4.3.3 Pressure and displacement controllers

Pressure was obtained from a compressed air supply (Fig. 4.2). A maximum pressure of 800 kPa was available and this was more than sufficient for the testing of the soft clay samples. There were two pressure controllers: one for cell pressure and one for back pressure. Each pressure controller consisted of a regulator operated by a stepper motor, with the stepper motor controlled (via an analogue/digital converter) by the PC operating the control software (described in Section 4.4.1). For the cell and back pressure systems, the pressure was transmitted via bladder type air/water interfaces (see Figure 4.2). A single electrical pulse to the stepper motors caused a change in pressure of approximately 0.07 kPa.

Increments of displacement were applied to the lower chamber of the Bishop-Wesley cell via a water-filled constant rate of strain pump (CRSP). The pump was operated by a stepper motor controlled by the PC via the analogue/digital converter. When controlling through the CRSP a single electrical pulse to the stepper motor produced a pedestal movement of 4×10^{-6} mm corresponding to about 5×10^{-6} % axial strain on the triaxial sample. It was also possible to use stress control (rather than displacement control) for the lower chamber, by using a third pressure controller, although this was generally not used.

4.3.4 Transducers

There were five electrical transducers associated with the Bishop-Wesley cell. These were an internal load cell (for measuring deviator force on the sample), a

linear variable differential transformer (LVDT) (for externally measuring axial displacement), two pressure transducers (for measuring cell pressure and pore pressure/back pressure) and a volume change gauge (for measuring the flow of water in or out of the sample), as shown in Figure 4.2. A sixth transducer monitoring the pressure in the lower chamber was in operation during testing. This had no role in controlling any of the tests, but was used to monitor pressure to ensure that the lower chamber was working under permissible pressures (greater than atmospheric pressure, but less than 2380 kPa). Additionally, for Test Series E a pair of strain callipers were used to monitor radial displacement in two orthogonal directions (see Section 4.8).

Calibration of all transducers was carried out in the lab in which the tests were to be conducted. The control software (see Section 4.4.1) had a calibration suite, which was used for all calibrations, to log the transducers output, fit a regression line to the calibration data and then store the calibration function for subsequent control and logging.

The internal load cell (Imperial College type) was calibrated using a dead weight calibration rig with axial force applied in increments of 100 N up to a maximum of 1000 N. This range was considered appropriate to the testing of the soft clay. Calibrations were carried out in both compression and tension. This resulted in a linear calibration with a maximum error of 0.01 N.

Axial displacements were recorded using an LVDT mounted on the crosshead arm of the cell as shown in Fig. 4.2. The range of the LVDT was 50mm. Calibration was carried out using a micrometer that was graduated in divisions of 0.002 mm although it was possible to read to 0.001 mm. A linear calibration was achieved over the full range of the device, with a maximum error of 0.005mm.

Cell and back pressure transducers (capacity 1000 kPa) were calibrated using a dead-weight gauge tester. Again a linear calibration was achieved over a range of 800 kPa, with maximum errors of 0.015 kPa and 0.01 kPa respectively.

A 100 cm^3 Imperial College type volume change unit was used to measure fluid flow in and out of the sample. Calibration of the volume change unit was achieved using a burette system as described by Head (1990). The system was flushed with de-aired water prior to calibration and was checked to ensure it was leak-free. It was noted by Head (1990) that erroneous volume change response can be given by the volume change unit due to the internal membrane seals not being fully inflated. Typically a pressure of at least 30 kPa is sufficient to inflate the seals (Head, 1990), but a back-pressure of 100 kPa was used in this calibration, which corresponded to the back-pressure applied during any drained test in the programme. The burette was graduated in divisions of 0.05 cm^3, but could be read to a precision of 0.01 cm^3. The volume change unit was filled in increments of approximately 5 cm^3 up to its full capacity and then drained in similar increments. Transducer readings were recorded and calibrated against the burette readings. It was not possible to obtain an acceptable linear calibration over the full range of the device, so linear calibration over a range of 43cm^3 was accepted. In practice, this was more than sufficient to monitor drainage from the sample (as the initial volume of the sample was 86 cm^3 and volume changes of greater than 40 cm^3 were not expected). Over two calibration cycles, the maximum error observed for this truncated range was 0.05 cm^3.

4.4 Computer control system

4.4.1 Software

The TRIAX software control system (developed by D.G. Toll at Imperial College London and then Durham University) was used to control the triaxial tests in the Bishop-Wesley triaxial apparatus. The software was PC mounted and the logged variables were downloaded to an Excel worksheet. The PC received output signals from the various transducers and, having been calibrated with suitable regression lines fitted to the calibration data, converted these signals into engineering units of force, axial displacement, back pressure, cell pressure and volume change.

4.4.2 Control variables

The software used a calculation routine to convert the raw logged data into triaxial variables to be used in control of the test and plotting of results. During testing, axial and volumetric strains were calculated by TRIAX in terms of engineering or nominal strains. These experimental data were later processed and converted to true strains for the purpose of being consistent with computer generated simulations (see Section 6.1).

The software calculated strains based on the output of the appropriate device and the initial dimensions of the sample. The initial volume of the sample, V_0, was based on the measured initial height (h_0) and diameter (d_0) of the sample at the beginning of the test. A slight correction was required when resetting strains to zero, since all strains were measured from the point where the required stress ratio was achieved (see Section 5.4.1). Cell pressure and back pressure were calculated simply from the output of the cell and back pressure transducers respectively. All strains are positive in compression.

Volumetric strain ε_v

Assuming full saturation (so that volume of air $V_a = 0$), the volumetric strain was calculated by TRIAX thus

$$\varepsilon_v = -\frac{\Delta V}{V_0} \tag{4.1}$$

where ΔV was the measured flow in or out of the sample from the volume change unit and V_0 was the initial volume of the sample, based on the measured initial height (h_0) and diameter (d_0) of the sample.

Axial strains, ε_a

TRIAX calculated axial strains, thus

$$\varepsilon_a = -\frac{\Delta h}{h_0} \tag{4.2}$$

where Δh was the change in height of the sample measured by the external LVDT.

Deviator stress and mean effective stress

During the test the deviator stress q was calculated as

$$q = \frac{F}{A_{curr}} \tag{4.3}$$

where F was the measured deviator force from the load cell and A_{curr} was the current cross-sectional area of the sample. TRIAX calculated this area as

$$A_{curr} = A_0 \frac{(1-\varepsilon_v)}{(1-\varepsilon_a)} \tag{4.4}$$

where A_0 was the initial cross-sectional area of the sample deduced from the diameter, d_0

$$A_0 = \frac{\pi d_0^2}{4} \tag{4.5}$$

The mean effective stress p' was then calculated from

$$p' = \sigma_r + \frac{q}{3} - u \tag{4.6}$$

where σ_r was the cell pressure and u was the pore pressure/back pressure, measured by the respective transducers.

4.4.3 Control instructions

For anisotropic loading at a constant stress ratio η, the CRSP was instructed to increase (or decrease) the value of q at a specified constant rate. Simultaneously, the cell pressure controller was instructed to ensure that the correct stress ratio η was maintained. For example, on a stress path where $\eta = 0.8$ had to be maintained, to load at dp'/dt = 2 kPa/hr, the lower chamber pressure controller was instructed to adjust the lower chamber pressure so that q increased at a rate of 1.6 kPa/hr. A tolerance of 0.1 kPa was imposed on this controller and this was found to be satisfactory in achieving the control. At the same time, the cell pressure controller was instructed to maintain the condition p' - (1.25q) = 0 so the correct stress ratio was maintained. It was found that the strictest tolerance that could be imposed on this controller was 0.3 kPa, but this was found to be satisfactory in keeping the stress ratio to within 0.05 of the required value. It was found that reducing either of these tolerances further caused the system to overshoot or undershoot its target.

One test involved one-dimensional (K_0) straining of a specimen. In this case it was required to load the sample while maintaining zero radial strain. This was achieved by instructing the cell pressure controller to increase the radial effective stress (σ'_r) at a specified constant rate with time while the CRSP was instructed to maintain the radial strain at zero. If the diameter of the sample reduced, an application of axial displacement (driven by the CRSP) caused the sample to expand radially, thereby restoring the required zero radial strain condition. Control was found to be difficult if this procedure was commenced from an isotropic stress state, so the sample was first brought to a stress ratio η_{K0} (see Equation 3.12) using a short shearing stage similar to that used prior to anisotropic loading (see Section 5.4.1).

4.5 Rates of loading

It was essential to ensure that the samples were loaded at a rate that was sufficiently slow so as to allow almost complete dissipation of excess pore

pressures, without leading to excessive test duration. Newson et al. (1997) suggested methods of selecting the rate of loading for drained triaxial stress path tests. Gibson and Henkel (1954) showed that the rate of dissipation of excess pore pressure u for the case of total stress σ increasing linearly with time t (at a constant rate dσ/dt) is given by

$$\frac{\partial u}{\partial t} = c_v \nabla^2 u + \frac{d\sigma}{dt} \tag{4.7}$$

where c_v is the coefficient of consolidation.

The solution of Equation 4.7 for a triaxial sample with drainage to both ends and the cylindrical boundary is

$$\bar{u}[T_v] = \frac{128 u_0}{T_v \pi^2} \cdot \sum_{i=1}^{\infty} \sum_{n=1,3,5} \frac{1}{n^2 m_i^2 \xi} \cdot \left[1 - \exp\left(-\frac{\xi}{4} T_v\right)\right] \tag{4.8}$$

where ū is the average excess pore pressure, $u_0 = t d\sigma/dt = t\dot{\sigma}$ is the excess pore pressure that would occur if no dissipation had occurred, $\xi = n^2\pi^2 + 4\varphi^2 m_i^2$ (where $\varphi = H^2/a^2$, a is the radius of the soil sample and H is the half height of the sample) and m_i are the zeroes of the Bessel function of the first kind and zero order. T_v is the time factor defined by

$$T_v = \frac{c_v t}{H^2} \tag{4.9}$$

Nash et al. (1992a) suggested that, when normally consolidated, Bothkennar clay will have a c_v value of approximately 1 m^2/year. This value was confirmed by oedometer tests on Laval samples 20A, 20B and 21A (see Section 5.2).

Figure 4.3 (a) shows that the excess pore pressure ratio $\bar{u}/u_0 = \bar{u}/\dot{\sigma} t$ (calculated from Equation 4.9) decreases continuously as the time factor T_v increases.

Figure 4.3 (b) shows these results plotted in terms of normalized excess pore pressure $\bar{u}\, c_v/H^2\dot{\sigma}$.

This shows that $\bar{u}$ reaches a limiting value of approximately $0.02H^2\dot{\sigma}/c_v$ for values of T_v greater than about 0.1. This suggests that for a 38 mm diameter sample (H = 38mm) of Bothkennar clay (where $c_v = 1m^2$/year) the loading rate $\dot{\sigma}$ must be limited to about 2 kPa/hour if the average excess pore pressure u is to stabilise at less than 0.5 kPa. This limiting value is reached at around $T_v = 0.1$ (corresponding to t = 76 minutes). Prior to this, the value of $\bar{u}$ should be less than 0.5 kPa.

4.6 Setting up of triaxial tests

4.6.1 De-airing

During each test de-aired water was used in the cell chamber, cell pressure system and the back pressure line. Dissolved air was removed from the water by subjecting it to a vacuum approaching −100 kPa in a Nold deaerator (incorporating a rotating disc to encourage removal of dissolved air). In order to ensure that the drainage line was de-aired, the volume change unit was repeatedly flushed back and forth with de-aired water before each test. The de-aired water was supplied to the volume change unit from a storage chamber where it was held under vacuum. The de-aired water was expelled from the volume change unit alternately via the volume change unit bleed valve and the triaxial pedestal using a small back pressure. The drainage line between the volume change unit and the pedestal was closed in the short period between de-airing and mounting the sample on the pedestal.

The porous ceramic disc used on the triaxial cell base pedestal was boiled in de-aired water immediately before each test and kept under de-aired water until the sample was mounted. Having mounted the soil sample and fitted the rubber membrane, the cell itself was filled with de-aired water. De-ionized water was

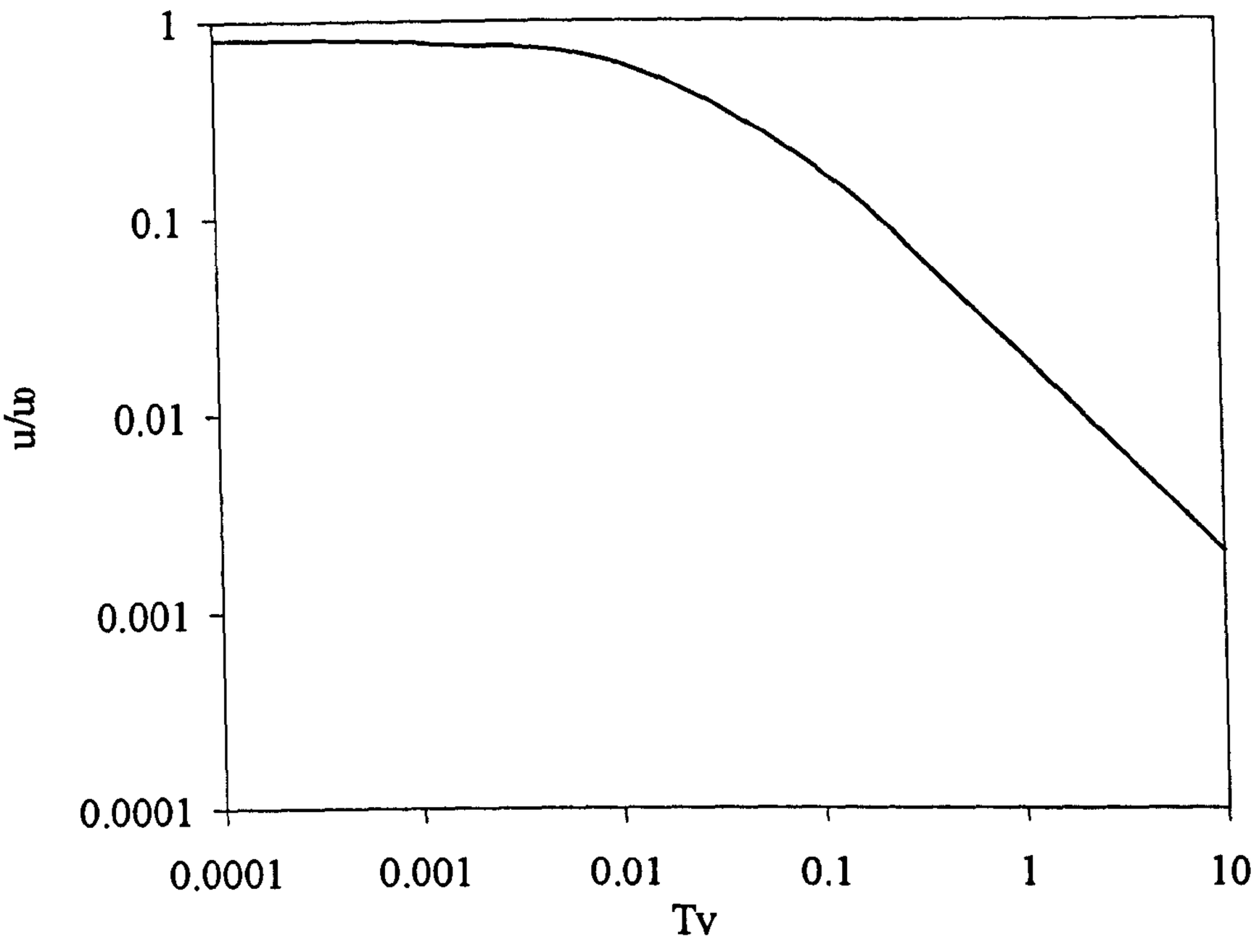

(a)

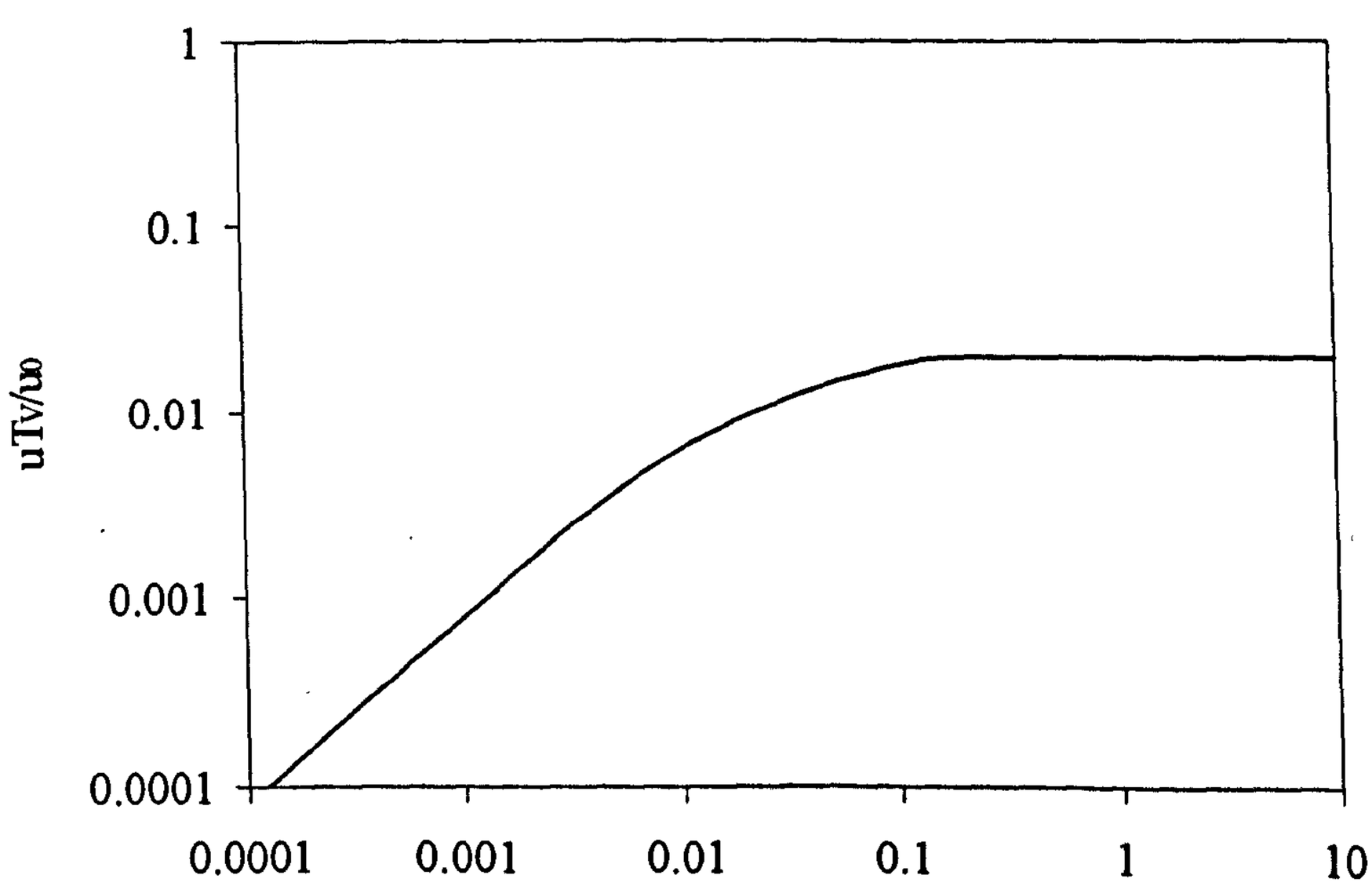

(b)

Figure 4.3. Theoretical one-dimensional consolidation behaviour (a) time dependent loading, (b) excess pore-pressure/rate of loading relationship.

not used in triaxial testing as it may have had a corrosive effect on the membrane and O-ring seals within the cell.

4.6.2 Drainage

Drainage from the samples was provided at both top and bottom ends and radially. Drainage from the bottom of the sample was provided by filter paper (Whatman No.54) and a coarse porous ceramic disc placed on the pedestal. A filter paper was also provided at the top boundary of the sample. A system of equally spaced spiral filter strips was employed to provide drainage at the radial boundary. Gens (1982) found that this arrangement of drains ensured that no correction to the measured deviator force in compression or extension was required. The filter paper strips were applied by placing the filter paper drains on a flat flexible polythene sheet onto which the sample was positioned. The sheet and the drains were then wrapped around the sample. The sheet was then removed from the sample leaving the drains adhering to the soil. The suction from the soil allowed the filter paper to adhere to the sample. The top and bottom of the side drains overlapped with the top and bottom filter papers, to allow a complete drainage circuit. This meant that drainage via a separate top cap drainage line was unnecessary.

4.6.3 Trimming triaxial specimens

All triaxial samples were nominally cylinders of 38 mm diameter and 76 mm in height. Small block samples cut from the large cylindrical Laval samples were reduced to these dimensions using a wire saw and straight-edge with a 38 mm diameter soil-lathe and a wire saw with a 76 mm long cradle. It was desirable to measure the initial diameter and height of the soil immediately after trimming, but this could not be achieved without disturbing the soft clay. It was therefore assumed that the initial dimensions were 38 mm and 76 mm (having carefully checked that these were the precise dimensions of the cradle and lathe). Hight et al. (1992) showed that the disturbance effects of trimming using the wire saw and lathe were much less pronounced than those during tube penetration.

4.6.4 Sample saturation and use of back pressure

Initial tests indicated that the Bothkennar samples were at a degree of saturation of less than 90%. It was essential that samples were brought to a fully saturated state prior to testing. The pore pressure was therefore elevated using a back pressure. The intention was to ensure that any air in the void spaces within the sample was forced into solution. In a trial test in the Bishop-Wesley cell, a back pressure of 80 kPa was found to be sufficient to achieve a B value greater than 0.95, so a standard back pressure of 100 kPa was used throughout the testing programme.

4.7 Conventional triaxial apparatus

In order to carry out triaxial tests involving shearing to a critical state, a conventional triaxial apparatus was used, because the axial travel of the Bishop-Wesley hydraulic triaxial cell was insufficient. The use of a second cell also allowed an increased number of tests to be performed within the time constraints. A cell suitable for testing samples up to 50 mm in diameter was used, but with a pedestal for 38 mm samples.

No feedback-control system was used with this apparatus. Cell pressure and back pressure were supplied from a compressor (capable of 800 kPa output) and were regulated manually. These pressures were transmitted to the cell and the sample via two bladder type air water interfaces. During shearing the axial displacement was applied at a constant rate, using a programmable compression frame. With no ability to alter the cell pressure (other than manual step-loading) all shearing tests were performed at constant cell pressure under the condition $dq/dp' = 3$.

Measurements of deviator force, axial displacement, cell pressure, back pressure and volume change were achieved using transducer devices of the same type and capacity as for the Bishop-Wesley cell. Raw data from these devices was sent to a data logger linked to a PC, which recorded the data at appropriate intervals. Calibration of the transducers was carried out in the same manner as the Bishop-

Wesley cell devices. Linear calibration of the load cell was achieved over a range of 1000 N with a maximum error of 0.015 N. The back pressure and cell pressure transducers were calibrated over a range of 800 kPa and a maximum error of 0.01 kPa and 0.02 kPa resulted respectively. The axial displacement transducer was calibrated over its full range giving a maximum error of 0.01 mm. Again, a linear calibration of the volume change unit could not be achieved over its full range so a linear calibration over a range of 50 cm^3 was accepted giving a maximum error of 0.05 cm^3.

4.8 Radial strain devices

4.8.1 Requirements

During testing of horizontally oriented samples it was expected that, due to the initial anisotropy of the soil, the magnitudes of radial straining would be different for the two orthogonal directions corresponding to horizontal and vertical directions in the ground. It was therefore necessary to monitor both of these radial strains independently. The criteria to be met in the design of appropriate instrumentation were:

(i) the devices had to cause minimal disturbance to the specimen;

(ii) they had to be capable of use in water at pressures up to 800 kPa;

(iii) the range of measurement had to be up to 15 % radial strain, based on experience of testing of vertically oriented samples, and;

(iv) repeatable calibration of the device was essential.

Local strain measuring instruments take measurements from points located directly on the specimen itself. This had several implications for soft clay testing. The attachment of any device to a specimen was expected to cause some specimen disturbance that had to be minimized. When considering the range of the device, it was noted that in Series C, radial expansion at high positive values

of η was as much as 5 mm at the mid-height of the sample, whereas radial compression at high negative values of η was as great as 8 mm.

Available space within the triaxial cell was considered. The Bishop-Wesley cell had an internal diameter of about 160 mm. Deducting the specimen diameter (38 mm) gave a clear space of 66 mm on either side between the sample and the acrylic cell walls. Four ports were available in the base of the triaxial cell through which electrical wiring could be inserted, although modification of these was required to maintain the hydraulic seal. Additionally, since it was required to measure radial strains in two horizontal direction, it was necessary to mount two devices at the same height of the sample. Another consideration was the occurrence of axial deformation during testing, which meant that the radial strain measurement devices had to be free to move axially with the sample.

4.8.2 Choice of device

Prior to design, a number of possible devices were considered. Hird and Yung (1987) used proximity transducers to measure radial strains stating good accuracy (0.001 % strain for 102 mm diameter samples), but these devices had very limited range and were difficult to adapt to large strain deformations.

Jardine et al. (1984) reported on the use of an electro-level device that resolved axial displacements to less than 0.001 mm over a range of 15 mm and could conceivably be adapted for radial strain measurement.

Submersible LVDTs make contact with a sample via radiused pads that may cause sample disturbance. The calliper-type mounting and the size and weight of the two transducers would mean that they could not be easily mounted on a 38 mm diameter sample. These devices are generally used on samples of at least 50 mm diameter. However, they typically have a range of greater than 5 mm and can operate under 2000 kPa water pressure (Dodd, 2000). Lojander (2000) successfully achieved a linear calibration of such a device over 5 mm, with non-linearity thereafter.

Clayton et al. (1989) described Hall effect transducers that have a linear range of 1.5 mm radial deformation measurement, which is about 4 % strain on a 38 mm diameter sample. This range was clearly too small, but the possibility of using non-linear calibration to achieve a larger range was investigated. Importantly, the type of mounting, although via radiused pads like the LVDTs, could be used on 38 mm diameter samples, as these could be manufactured and mounted in a way that was less space consuming.

In order to achieve the requirements outlined above, radial callipers incorporating Hall effect devices were designed and fabricated within the Department of Civil Engineering at the University of Glasgow. It was thought that a device of this type could be designed to fulfil the criteria. The design was similar to that of Clayton et al. (1989), but crucially the device had to be capable of measuring much larger deformations. The Hall effect principle is based on the fact that when a semiconductor or metallic plate, through which current is flowing, is placed in a magnetic field, a voltage is produced across the plate perpendicular to the direction of the current flow.

4.8.3 Construction of Hall effect sensor

The device is shown in Figure 4.4. A radial calliper hinged at point A and restrained by two springs connecting between pins at B and C was attached to the triaxial sample by two radiused pads at points D and E, mounted on hinges at F and G on the calliper. The Hall effect sensor was mounted at point H and the magnet at J. As the sample strained radially, the magnet and sensor moved relative to one another, thus inducing changes in the Hall voltage. Calibration of this motion allowed the subsequent voltage to be interpreted as radial compression or expansion of the sample. The arrangement of the sensor was "single magnet bi-polar slide-by" as described by Clayton et al. (1989). The outer diameter of the device was 88 mm and its overall height was 30 mm.

Choice of materials was important in the construction of the device. The dimensions of the device (rather larger than the dimensions of a similar commercial device used to measure small strains) meant that it was especially

Clayton et al. (1989) described Hall effect transducers that have a linear range of 1.5 mm radial deformation measurement, which is about 4 % strain on a 38 mm diameter sample. This range was clearly too small, but the possibility of using non-linear calibration to achieve a larger range was investigated. Importantly, the type of mounting, although via radiused pads like the LVDTs, could be used on 38 mm diameter samples, as these could be manufactured and mounted in a way that was less space consuming.

In order to achieve the requirements outlined above, radial callipers incorporating Hall effect devices were designed and fabricated within the Department of Civil Engineering at the University of Glasgow. It was thought that a device of this type could be designed to fulfil the criteria. The design was similar to that of Clayton et al. (1989), but crucially the device had to be capable of measuring much larger deformations. The Hall effect principle is based on the fact that when a semiconductor or metallic plate, through which current is flowing, is placed in a magnetic field, a voltage is produced across the plate perpendicular to the direction of the current flow.

4.8.3 Construction of Hall effect sensor

The device is shown in Figure 4.4. A radial calliper hinged at point A and restrained by two springs connecting between pins at B and C was attached to the triaxial sample by two radiused pads at points D and E, mounted on hinges at F and G on the calliper. The Hall effect sensor was mounted at point H and the magnet at J. As the sample strained radially, the magnet and sensor moved relative to one another, thus inducing changes in the Hall voltage. Calibration of this motion allowed the subsequent voltage to be interpreted as radial compression or expansion of the sample. The arrangement of the sensor was "single magnet bi-polar slide-by" as described by Clayton et al. (1989). The outer diameter of the device was 88 mm and its overall height was 30 mm.

Choice of materials was important in the construction of the device. The dimensions of the device (rather larger than the dimensions of a similar commercial device used to measure small strains) meant that it was especially

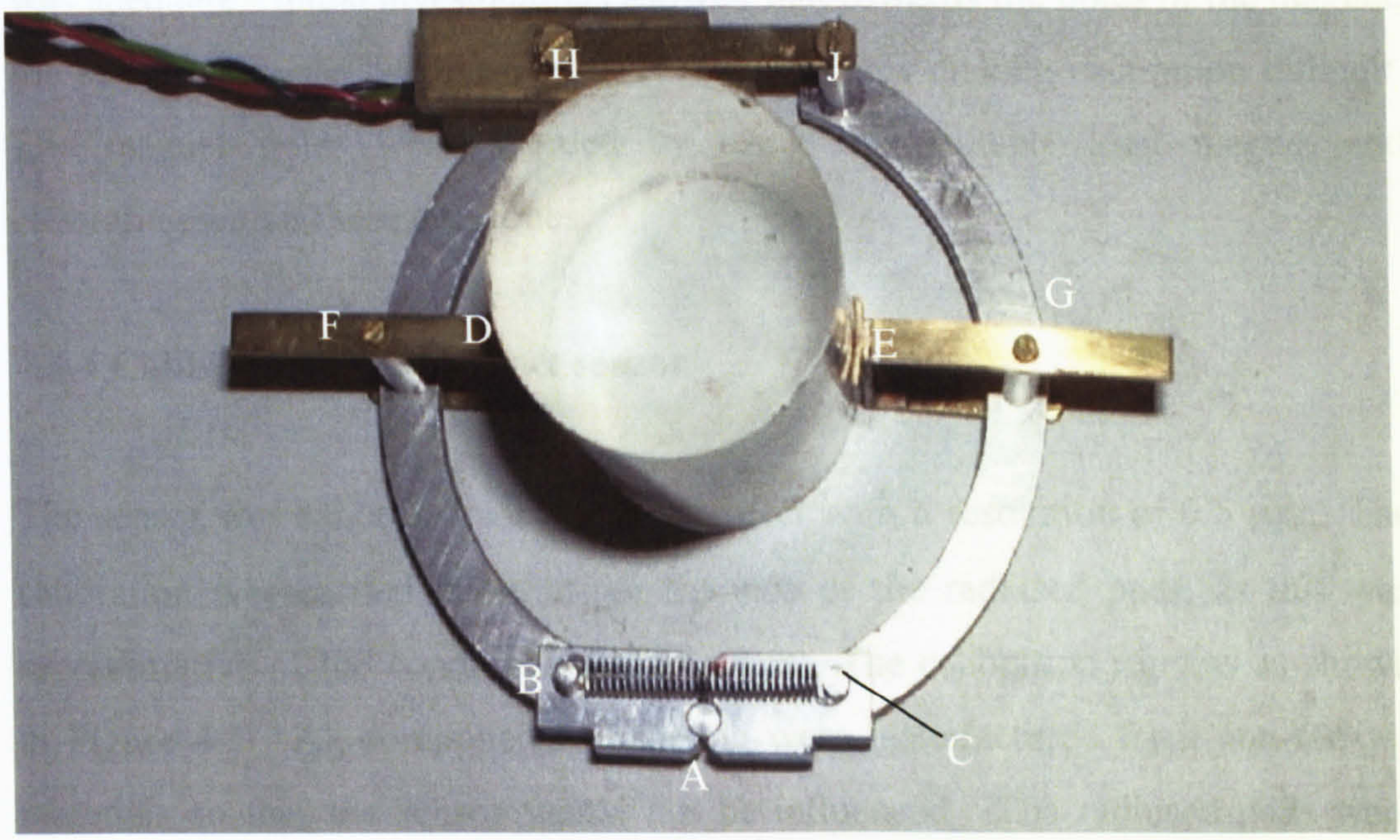

Figure 4.4. Radial calliper and Hall effect device.

important to minimise weight. Additionally, the use of the Hall effect sensor meant that non-ferrous materials had to be used, because the zone of influence of ferrous materials (for the sensors investigated) was found to be typically 60 mm. An attempt was made to construct the device from acrylic, a material of relatively low density (approximately 1100 kg/m^3). It was found that this material was difficult to machine and was too flexible. Aluminium alloy (density approximately 2700 kg/m^3) was therefore used in the fabrication of the calliper ring and spring mountings. The radiused pads and their mountings were made of small pieces of brass (density approximately 8800 kg/m^3), which were well suited to the high temperatures and fine precision required during fabrication.

The Hall effect sensor had to be protected from water ingress and was therefore potted in a polyurethane resin. Included in this pot was a steel concentrator, which focuses the lines of magnetic flux and causes the sensor response to become more linear. The range of the device was limited by the length of the magnet used. The maximum movement between the radiused pads was expected to be 13 mm. This corresponded to a movement of 26 mm of the magnet relative to the sensor. A cylindrical magnet 30 mm long and 4 mm diameter was therefore used. The length of this magnet was such that the range of the device

was adequate. Initial investigations showed that towards the poles of the magnet, the sensor response becomes highly non-linear, thus making calibration difficult. The magnet poles were avoided by using this suitably long magnet and calibrating within these end zones.

4.8.4 Calibration of Hall effect sensor

The sensor was calibrated using a micrometer with a resolution of 0.5 μm. The calibration was carried out through the axis of the radiused pads, as this was representative of the conditions during a test. The calibration rig was as shown in Figure 4.5. All components of the rig were manufactured from non-ferrous materials so that the sensor would not be influenced. The radiused pads were mounted in the recesses at A and B. Point A remained fixed during calibration. Point B was part of an aluminium frame connected to the spindle of a micrometer. The connection was made via a brass shaft at C, which rotated as the micrometer spindle was turned. The rotation of the micrometer spindle caused a flange at point C to pull the aluminium frame so that Point B moved laterally away from (or towards) point A and therefore opened (or closed) the radial calliper. The spring force at the calliper hinge was sufficient to keep the flange in contact with the frame throughout calibration.

The output voltage/displacement relationship is shown in Figure 4.6 for the two devices. The calibration was non-linear over the required range of displacement. This was probably due to the non-linearity of the magnetic field and flux lines (particularly towards the magnetic poles) and the arcing motion of the sensor and magnet as they pass over each other. Various possible forms of regression curve were imposed when examining the data. The relationship was clearly only linear over a very small range and therefore attempts were made to impose higher order polynomial and exponential functions to the data. Fourth and fifth order polynomials (such as the solid lines shown in Figure 4.6) provided calibrations that only gave accuracy of about ±0.1 mm, which is clearly unacceptable for the level of accuracy required in this study. However, calibration errors were found to be best minimized by using a series of short linear splines. This technique

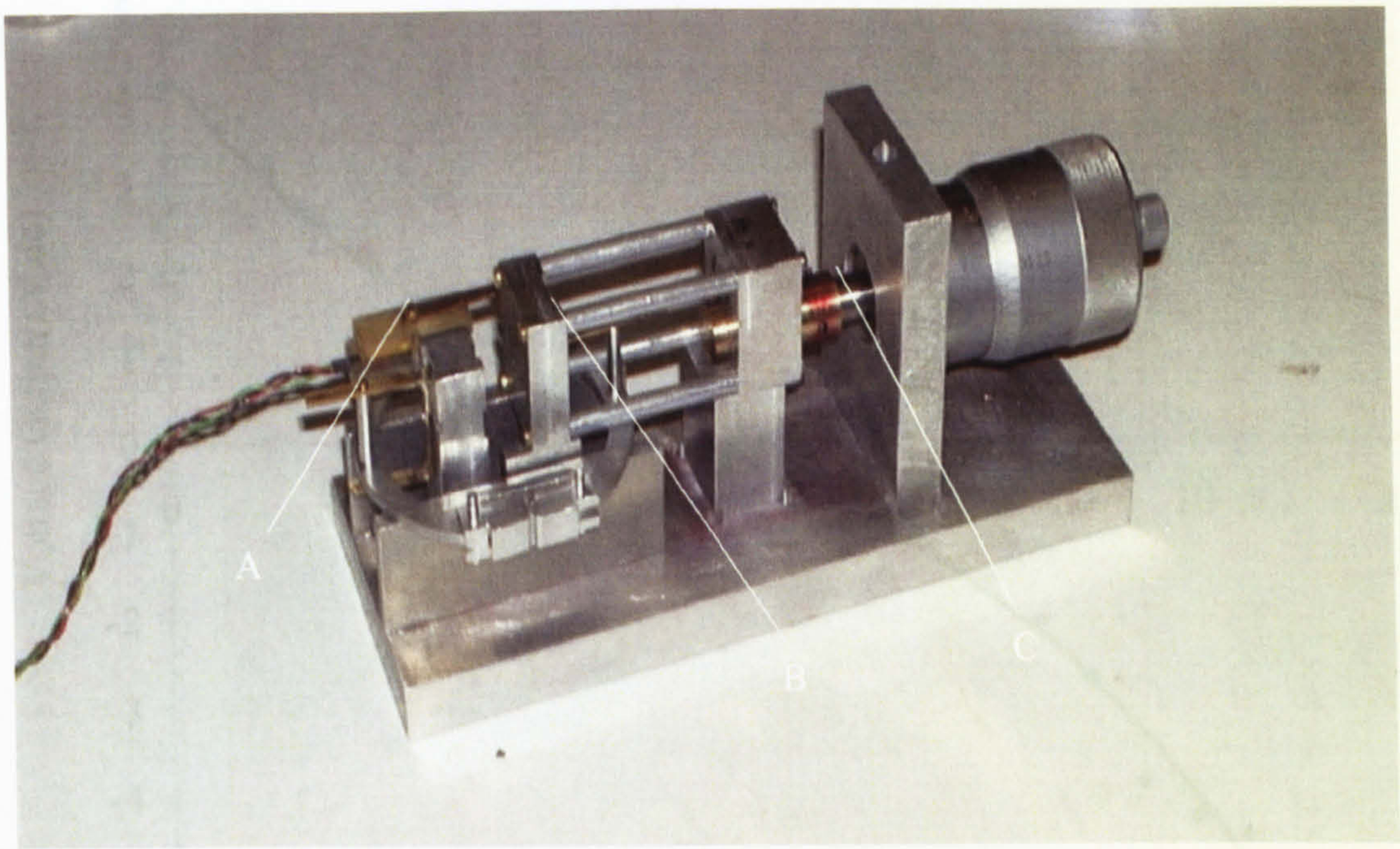

Figure 4.5. Radial calliper calibration rig.

provided a calibration with an accuracy, at worst, of around ±0.005 mm, which was thought to be adequate for the purposes of the testing programme.

4.8.5 Mounting of Hall effect sensors

Sample disturbance had to be minimized when attaching the devices to the sample and during subsequent testing. It was found that the radiused pads could be attached to the sample membrane efficiently and with minimal disturbance using superglue. The springs were designed so that in the working range of the device a small compressive contact force was transmitted to the sample. The locations of the spring attachment points were selected, together with the spring stiffness and unstretched length of the springs, to give an appropriate variation of force on the sample. The spring length was 34 mm, the initial stretch (with a distance of 38mm between the pads) was 1.5mm and the spring stiffness was 0.43 N/mm. The contact force transmitted onto the sample (expressed as a pressure over the area of a radiused pad of dimensions 8 x 7 mm) due to the springs is shown in Fig 4.7. A positive contact pressure was maintained over a

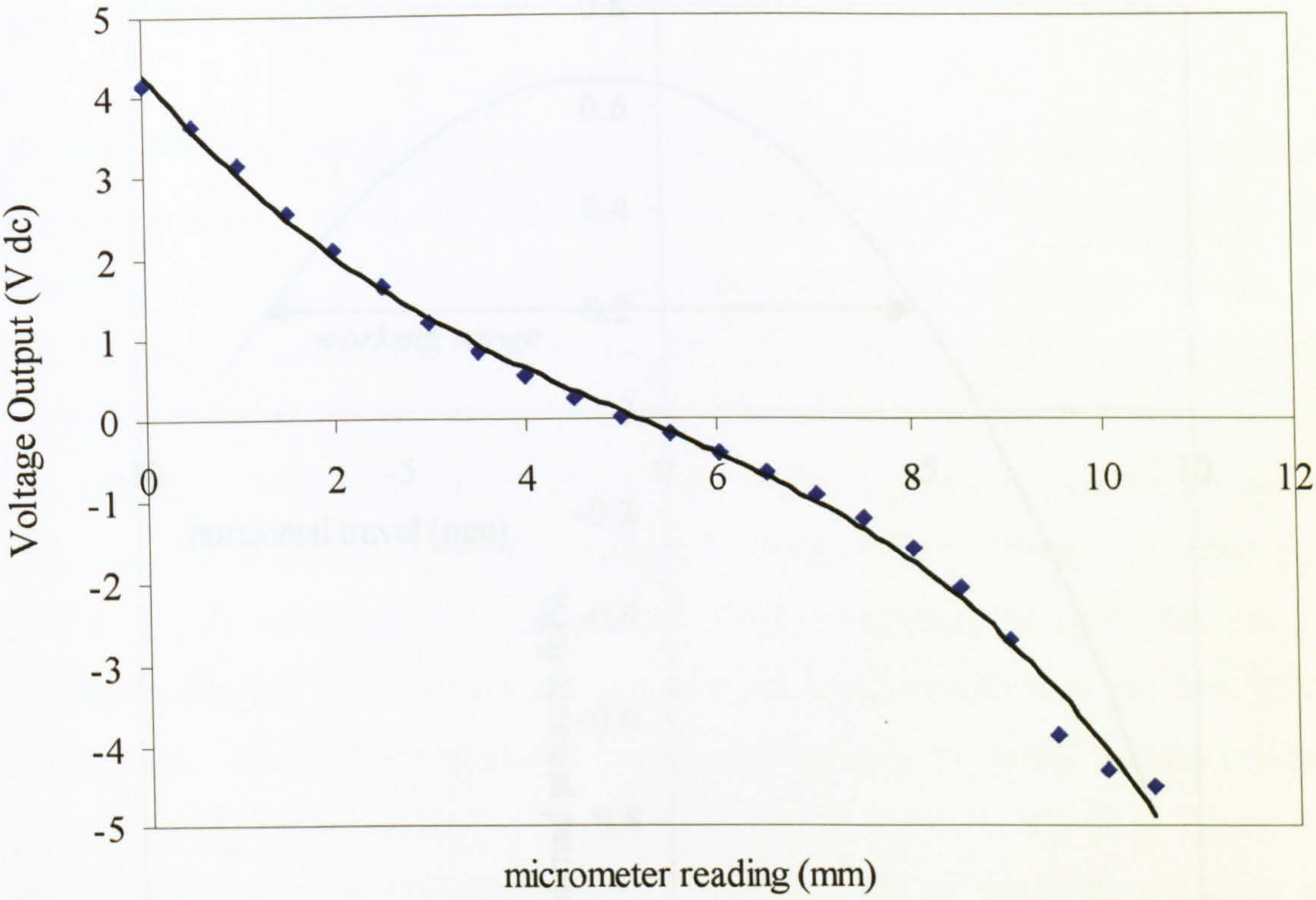

(a)

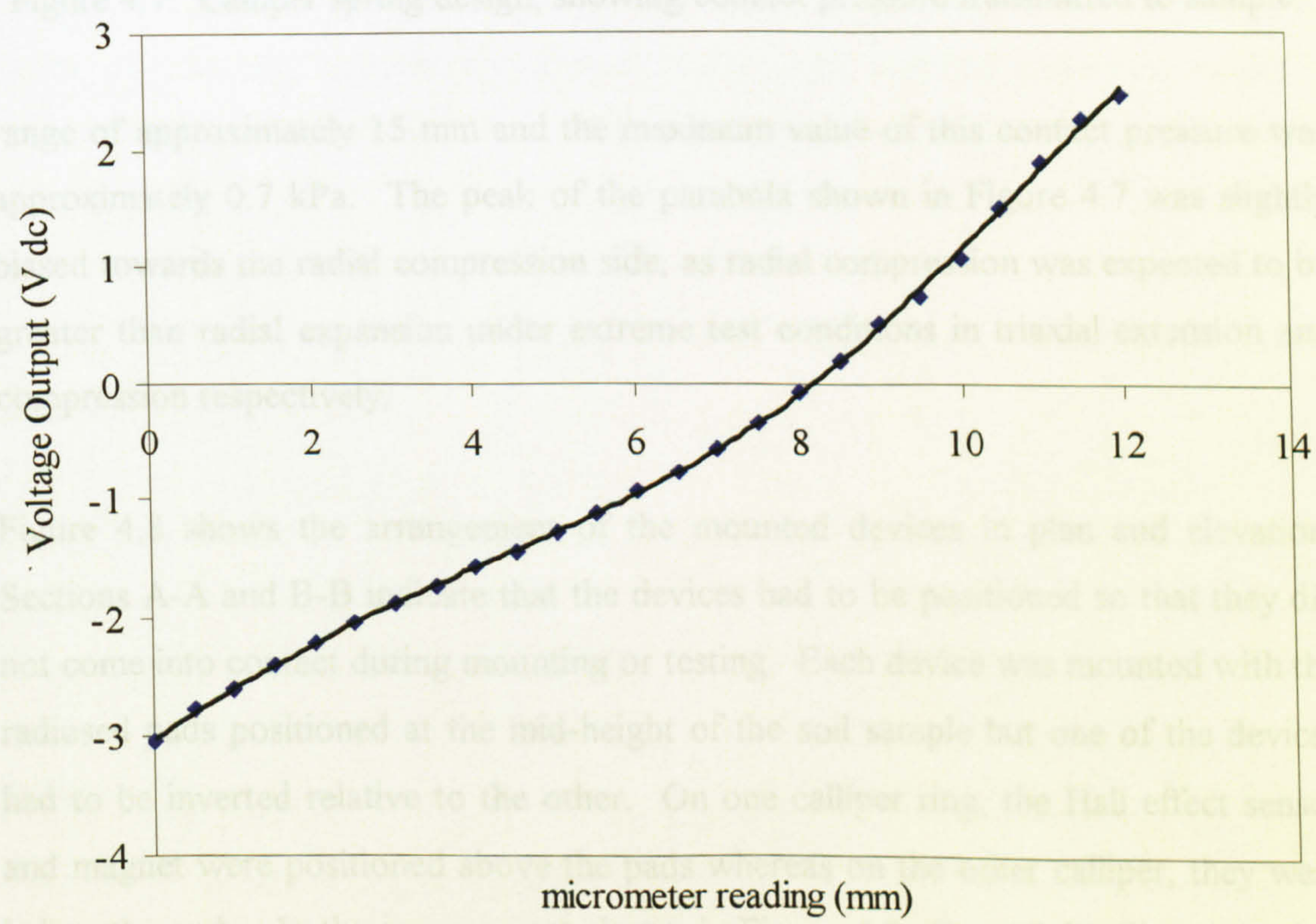

(b)

Figure 4.6. Calibration curves for radial strain devices (a) Gauge 1 (b) Gauge 2.

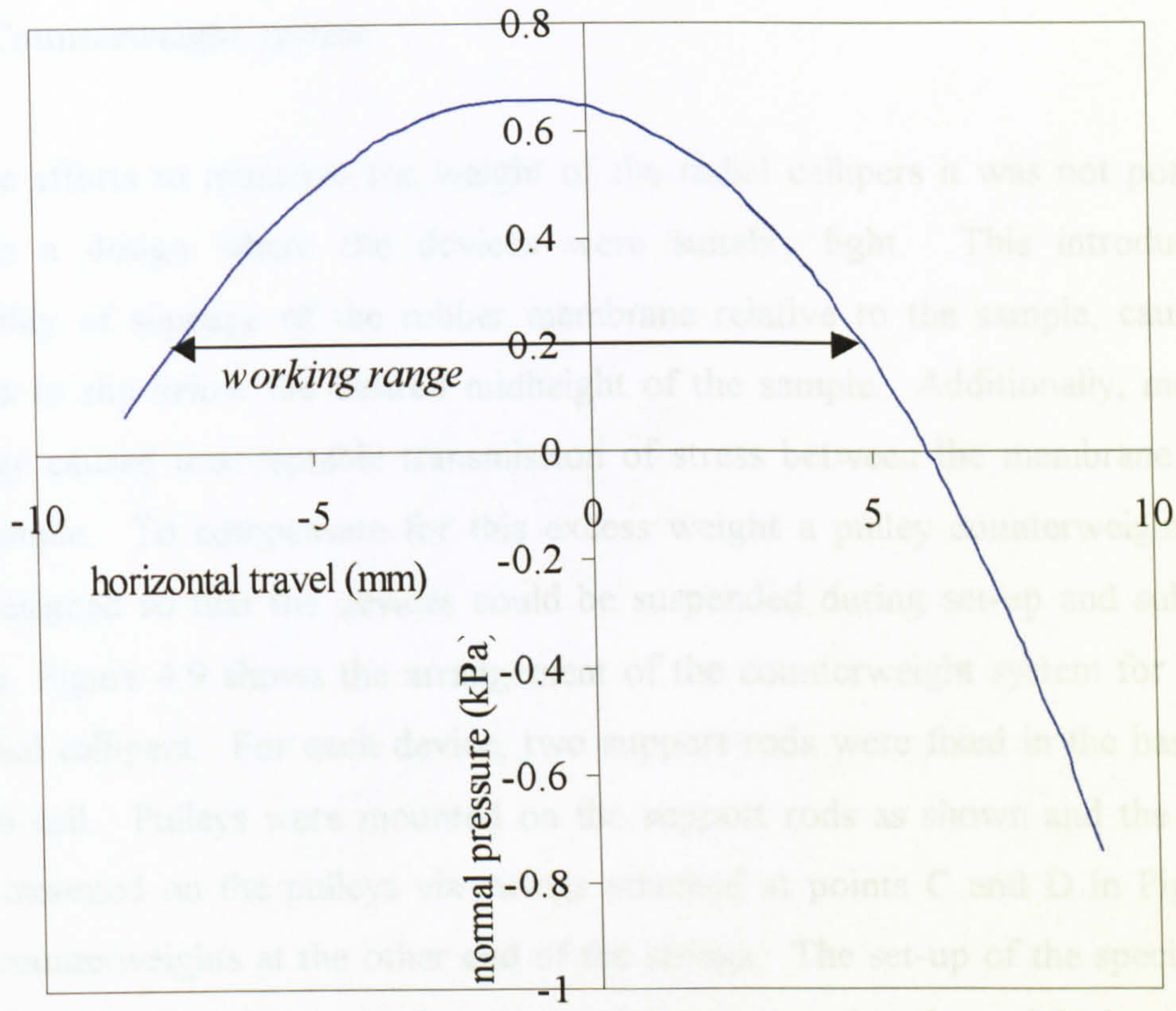

Figure 4.7. Calliper spring design, showing contact pressure transmitted to sample.

range of approximately 15 mm and the maximum value of this contact pressure was approximately 0.7 kPa. The peak of the parabola shown in Figure 4.7 was slightly biased towards the radial compression side, as radial compression was expected to be greater than radial expansion under extreme test conditions in triaxial extension and compression respectively.

Figure 4.8 shows the arrangement of the mounted devices in plan and elevation. Sections A-A and B-B indicate that the devices had to be positioned so that they did not come into contact during mounting or testing. Each device was mounted with the radiused pads positioned at the mid-height of the soil sample but one of the devices had to be inverted relative to the other. On one calliper ring, the Hall effect sensor and magnet were positioned above the pads whereas on the other calliper, they were below the pads. In the arrangement shown in Figure 4.8, the radial callipers are free to expand and contract without coming into contact each other.

4.8.6 Counterweight system

Despite efforts to minimize the weight of the radial callipers it was not possible to achieve a design where the devices were suitably light. This introduced the possibility of slippage of the rubber membrane relative to the sample, causing the devices to slip below the desired midheight of the sample. Additionally, membrane slippage caused unacceptable transmission of stress between the membrane and the soil sample. To compensate for this excess weight a pulley counterweight system was designed so that the devices could be suspended during set-up and subsequent testing. Figure 4.9 shows the arrangement of the counterweight system for one pair of radial callipers. For each device, two support rods were fixed in the base of the triaxial cell. Pulleys were mounted on the support rods as shown and the callipers were mounted on the pulleys via strings attached at points C and D in Figure 4.9, with counterweights at the other end of the strings. The set-up of the specimen was carried out in air, whereas testing was under water, so that the weight in air and the buoyant weight in water of the devices were both considered. The counterweights (made of brass and aluminium) weighed 33.3 g in air and had a buoyant weight in water of 21.3 g. These gave a reasonable match for the corresponding weights of the calliper device.

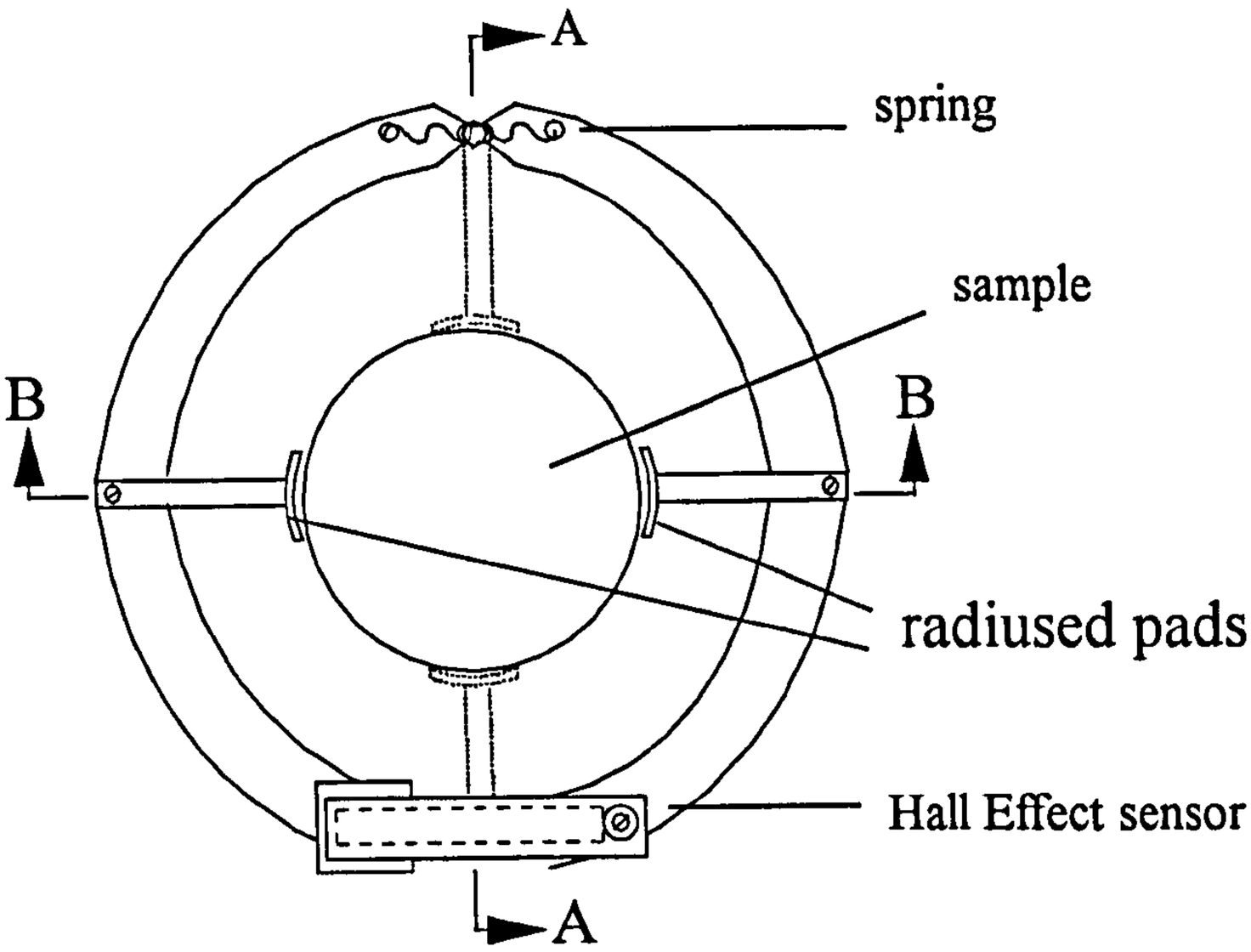

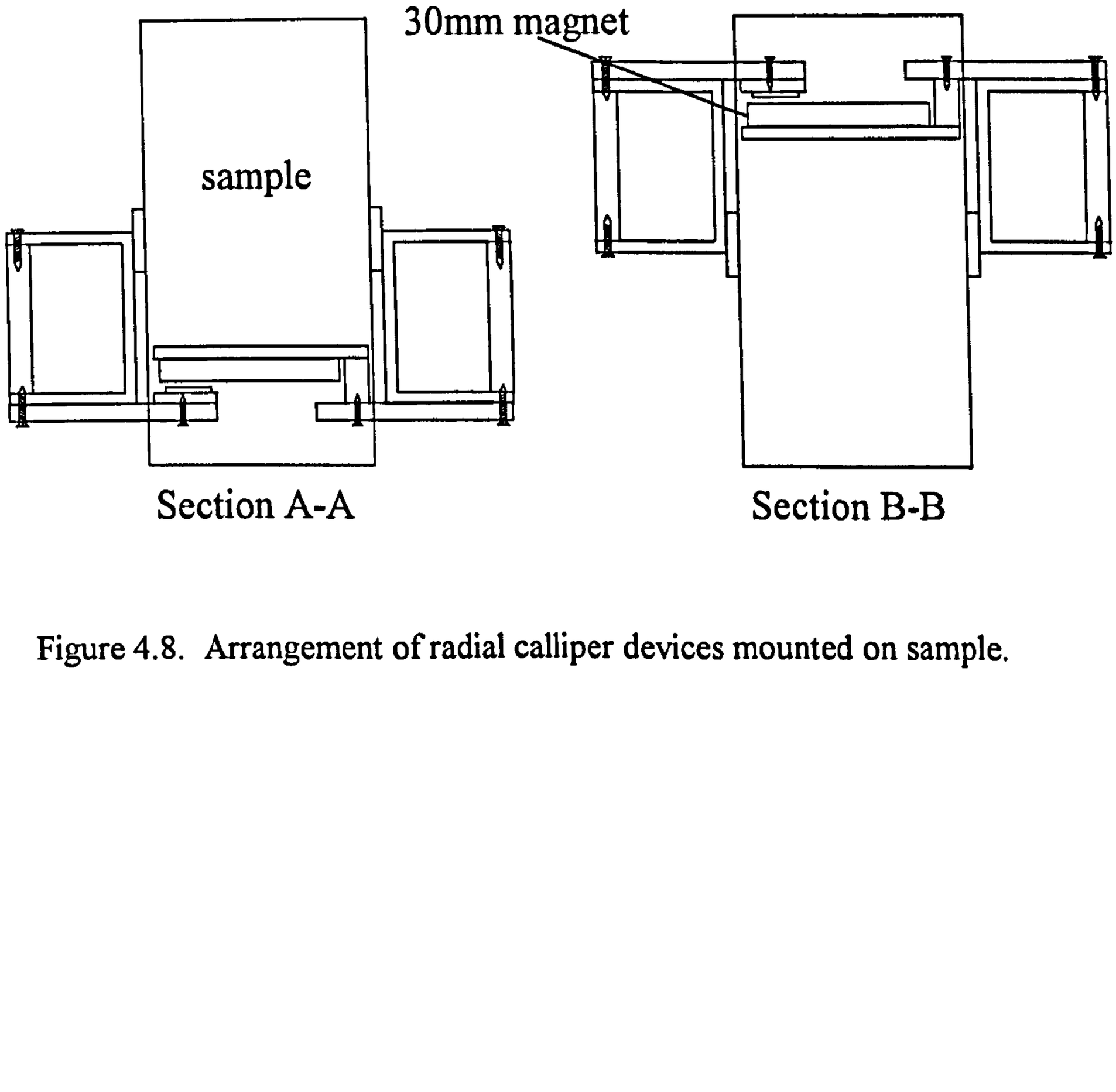

Figure 4.8. Arrangement of radial calliper devices mounted on sample.

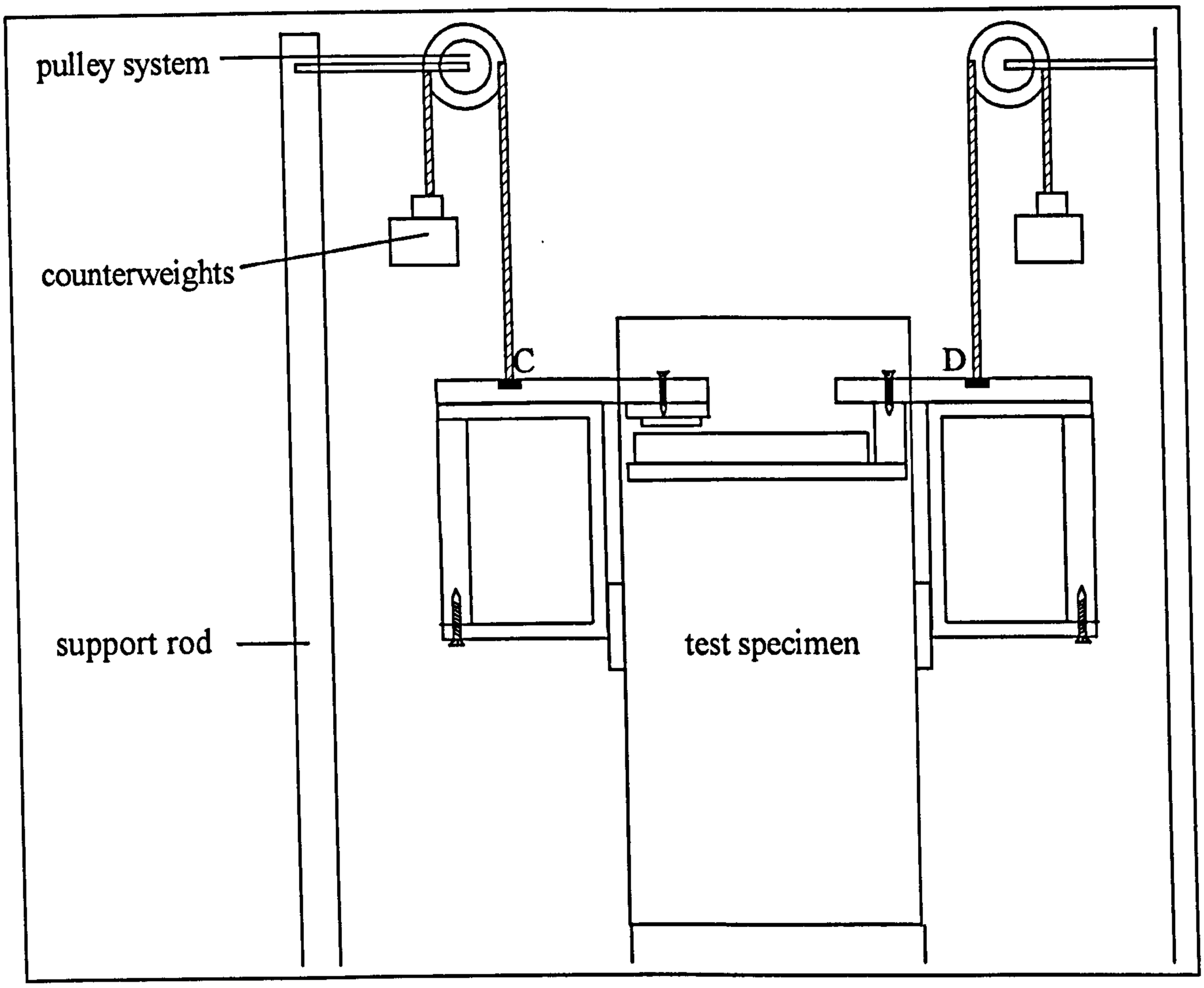

Figure 4.9. Counterweight system for mounting radial calliper devices.

CHAPTER 5: EXPERIMENTAL PROGRAMME

5.1 Introduction

The experimental objectives of the study were set out in Section 1.3. As outlined in Chapter 4, the main body of experimental work involved testing in triaxial cells. The testing programme consisted of three series of tests involving vertical samples (Series A, B and C) and two series of tests involving horizontal samples (Series D and E).

5.2 Preliminary testing

Various preliminary tests were carried out in preparation for the suites of triaxial tests. Oedometer tests on vertically oriented samples suggested a yield stress of approximately $\sigma'_v = 80$ kPa (see Figure 5.1). A c_v value of approximately $1m^2$/year was obtained form the final increment of stress (where the soil had yielded). Specific gravity tests were performed using the density bottle method (BS 1377: 1975, Test 6 (B)), which is appropriate to fine-grained soils. The specific gravity (G_s) of Bothkennar clay was found to be 2.68 (see Table 5.1). Prior to each triaxial test, trimmings from the soil blocks were taken and used to determine the moisture content (w) of the soil. This was found to be in the region 55 – 66 %. The organic content of the soil (through loss on ignition) was found to be 3 – 4 %.

Test 1	G_s (Specimen 1)	G_s (Specimen 2)	G_s (Specimen 3)
1	2.62	2.66	2.73
2	2.69	2.64	2.69
3	2.70	2.69	2.68

Table 5.1. Results from specific gravity tests (BS 1377: 1975, Test 6 (B)).

5.3 Drained shearing tests to failure on vertical samples (Test Series A)

In the first instance it was necessary to establish the critical state stress ratio of the soil. Series A comprised drained shearing tests to failure on vertical samples. 3 tests

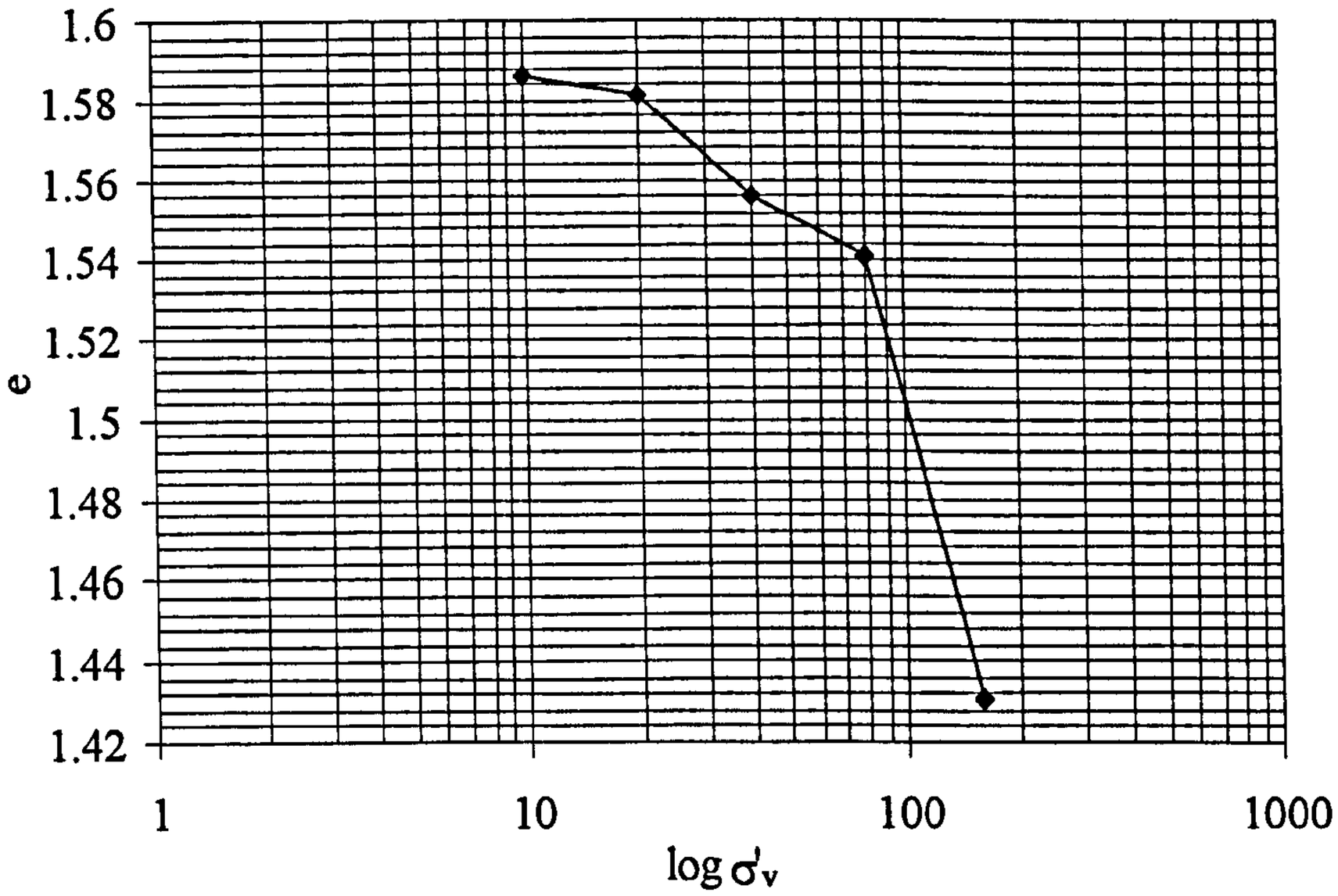

Figure 5.1. Oedometer test on vertical sample of Bothkennar clay.

were carried out in triaxial compression and 3 in triaxial extension since it is widely accepted that the critical state stress ratios in triaxial compression and triaxial extension are generally unequal (see for example Gens, 1982). Table 5.1 gives details of the tests involved in Series A.

Test	direction	σ'_c (kPa)	Laval sample
A1	compression	58	20A
A2	compression	94	20B
A3	compression	150	21A
A5	extension	100	20A
A6	extension	150	20B
A7	extension	171	21A

Table 5.1. Test Series A: Drained shearing tests on vertical samples

In each drained shearing test, the samples were initially consolidated isotropically to a stress σ'_c so that they were normally consolidated or lightly overconsolidated. The isotropic consolidation involved a single step application of load followed by a 24-hour consolidation period to allow dissipation of excess pore pressures. Tests A1,

A2 and A3 were carried out in triaxial compression, with each sample consolidated to a different value of effective cell pressure σ'_c prior to drained shearing. The intention was to determine 3 points on the critical state line to be established from the three data points. Similarly, in triaxial extension, Tests A5, A6 and A7 involved isotropic compression to a different value of effective cell pressure σ'_c before drained shearing to a critical state. Again, with three data sets it was possible to establish the critical state line in triaxial extension. As discussed in Section 6.2, it is possible that the effects of post-peak softening, strain-localisation and destructuration will influence these test results.

5.4 Stress path tests on vertical samples

5.4.1 Objectives

The specific objectives of the stress path tests in Test Series B and C were as follows

- to establish the initial shape and size of the yield curve
- to examine the effects of post-yield straining on yield curve orientation
- to examine the role of destructuration
- to examine the pre-yield and post-yield stress-strain behaviour

An initial test on a vertical sample (Test A4) was carried out in an attempt to establish the K_0 stress ratio. The details of this test are set out in Section 6.2.3.

A typical stress path test is shown in Figure 5.1 involving a first loading stage in triaxial compression at a stress ratio η_1, followed by an unloading stage at η_1 and then a second loading stage at a different stress ratio η_2. Prior to the first loading stage, the sample was loaded isotropically to point A in Figure 5.1 and allowed to consolidate under a back pressure for 24 hours. Monitoring of this stage showed that this allowed the sample to become sufficiently saturated (B > 95 %) prior to stress probing. The mean effective stress level at point A was sufficiently low so as to avoid any possibility of yielding. The sample then underwent a short drained shearing stage at constant cell pressure to point B in order to achieve the required

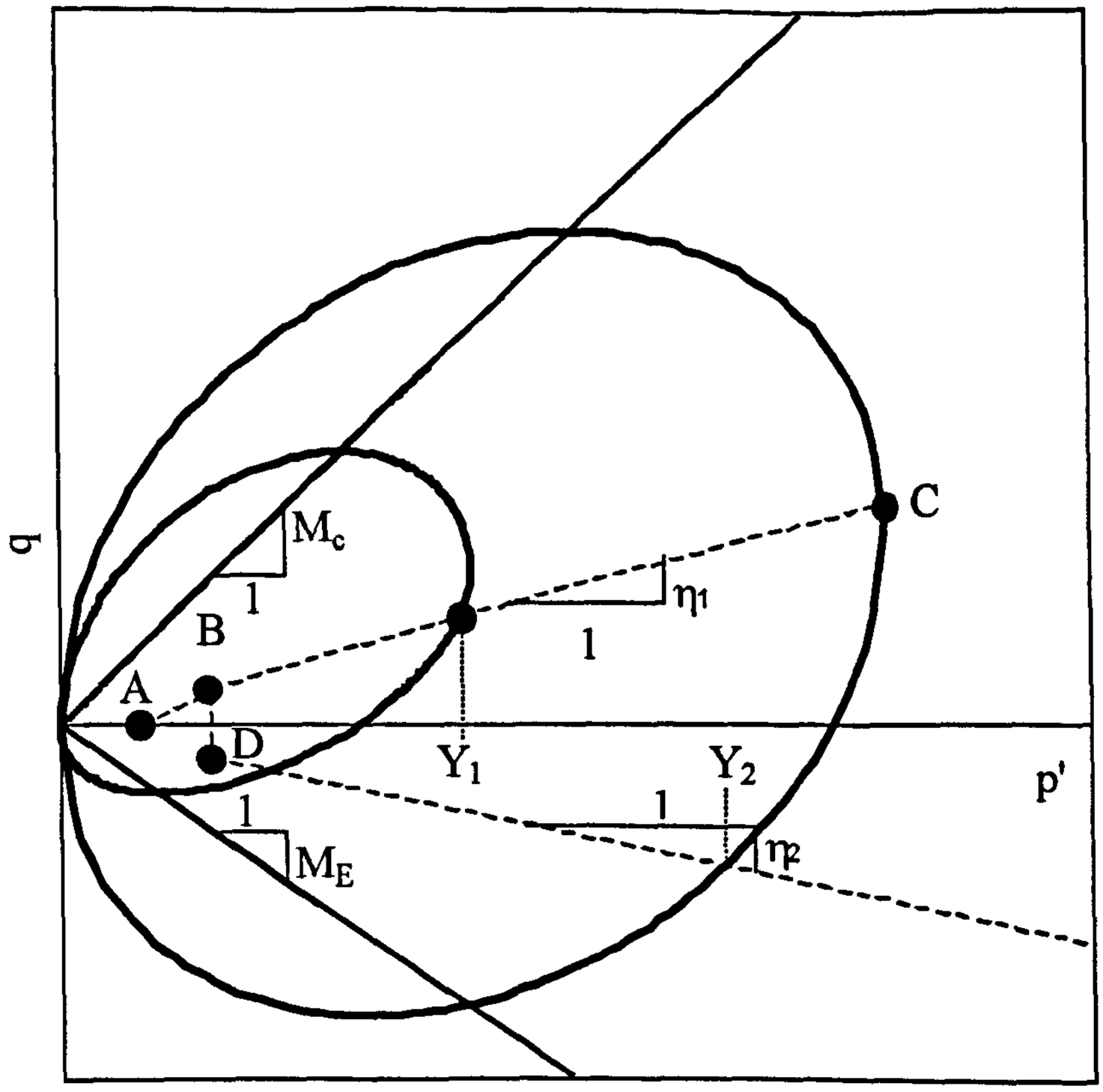

Figure 5.1. Typical multi-stage stress path test on a vertical sample.

stress ratio η_1. In each test in Series B and C, strains were zeroed at point B. The first loading stage at η_1 involved loading to a stress level that was approximately three times that of the yield stress (to point C), expanding and rotating the initial yield curve (yielding at Y_1 in Figure 5.1) to a new size and orientation. Several authors, including Davies and Newson (1993) have suggested that at such a magnitude of stress, the soil fabric arrangement will be significantly altered. As a first approximation, the yield stress could be estimated from Test A4. The location of the yield curve could also be estimated from the oedometer tests described in Section 5.2 and from evidence provided by Nash et al. (1992b) (whose data suggested that the initial yield curve for soil at this depth was thought to have a tip stress (p'_m) at approximately p' = 80 kPa). However, given the fact that yield stresses were expected to be dependent on the value of η, each test had to be monitored individually, so that the required stress level was reached. At point C the sample was allowed to rest for a period of 24 hours in order to allow dissipation of any excess pore pressures.

The unloading stage CB was carried out at the same stress ratio η_1 as the first loading stage. Unloading continued until the stress state returned to point B. Once unloading was completed, the sample was again allowed to rest at point B for 24 hours to allow dissipation of excess pore pressures.

A short shearing stage BD was then required to bring the sample to the correct stress ratio η_2 (at point D) for the second loading stage. The intention in the second loading stage DE was to identify a new yield stress, Y_2, on the yield curve by loading at a different stress ratio η_2 from the first loading stage and to assess both pre-yield and post-yield stress-strain behaviour.

5.4.2 Test Series B

This series involved 9 multi-stage tests on vertical samples (see Table 5.2) each commencing with isotropic loading ($\eta_1 = 0$) in the first loading stage. This was followed by isotropic unloading then a second loading stage at a different stress ratio η_2 (with the exception of Test B7, which also involved isotropic loading in the second loading stage (see Table 5.2)).

Test	η_1	η_2	Laval sample
B1	0.00	-	20B
B2	0.00	0.70	20B
B3	0.00	1.01	20A
B4	0.00	1.30	20A
B5	0.00	-0.40	21A
B6	0.00	-0.70	21A
B7	0.00	0.00	21A
B8	0.00	0.40	20B
B9	0.00	-1.00	20A

Table 5.2. Stress paths in Test Series B.

In each of the first loading stages, it would be expected that by loading to a stress level much higher than the initial yield stress, it would be possible to re-arrange the

soil fabric significantly. This meant that the yield curve orientation would have changed considerably, in this case rotating clockwise towards an inclination centred around the isotropic axis. In addition, following the discussion in Section 2.7, it would be expected that sustained isotropic loading would incur significant destructuration. In the second loading stages, the shape and size of the expanded and re-oriented yield curve could be explored by identifying new yield stresses at various stress ratios. Results from Test Series B are presented in Section 6.3.

5.4.3 Test Series C

Test Series C comprised 9 tests on vertical samples, each involving a different value of η_1 in the first loading stage as shown in Table 5.3. Table 5.3 shows that a wide variety of values of η_1 were chosen. This allowed both pre-yield and post-yield stress-strain behaviour to be examined under diverse loading conditions. The yield points obtained from the first loading stages allowed the initial size and shape of the yield curve to be determined (to the yield points obtained from isotropic loading in Test Series B were also used). Loading to a stress approximately three times greater than the initial yield stress meant that the evolution of post-yield anisotropy and destructuration could be analysed.

Test	η_1	η_2	Laval sample
C1	0.42	1.04	20B
C2	1.11	-0.50	20B
C3	1.30	-0.60	21A
C4	-0.80	0.60	21A
C5	0.80	-0.80	20A
C6	0.20	1.03	20A
C7	0.42	-0.70	20A
C8	0.80	-	21A
C9	-0.50	-0.96	20B

Table 5.3. Stress paths in Test Series C.

As in Test Series B, unloading occurred at the same stress ratio η_1, back to point B in Figure 5.1. Each sample was then reloaded at a stress ratio η_2 that was radically

different from that in the first stage. This allowed the shape and size of the newly expanded and rotated yield curve to be assessed, for each first loading scenario. Results from Test Series C are described in Section 6.4.

5.5 Tests on horizontal samples

5.5.1 Objectives

Generalized versions of S-CLAY1 and S-CLAY1S were presented in Section 3.5. By testing specimens samples horizontally in a triaxial cell (that is with a horizontal direction in the ground now coinciding with the axial direction in the triaxial apparatus; see Section 7.2 for further details) it was possible to examine more fully the anisotropic stress-strain behaviour of Bothkennar clay. As described in Section 4.8, behaviour of these horizontally oriented samples in the triaxial apparatus was expected to produce different values of radial stress in two orthogonal directions. One of these directions corresponded to a vertical direction in the ground and the other to a horizontal direction in the ground.

5.5.2 Test Series D

Four conventional drained shearing tests to failure were conducted on horizontal samples, two in triaxial compression and two in triaxial extension. These were performed in the conventional triaxial cell. Table 5.4 provides details of these tests.

Test	σ'_c (kPa)	direction	Laval sample
D1	100	compression	20A
D2	175	compression	20B
D3	100	extension	20B
D4	65	extension	21A

Table 5.4. Test Series D: Drained shearing tests on horizontal samples

The purpose of these tests was to examine whether the values of critical state stress ratios in triaxial compression (M_C) and triaxial extension (M_E) for horizontal samples

were the same as the corresponding values already obtained for the vertical samples in Test Series A. Radial strains were not recorded in these tests since it was thought that the magnitudes of radial expansion and compression would be well beyond the working range of the calliper devices. This proved to be the case. Results from Test Series D are described in Section 7.2.

5.5.3 Test Series E

As shown in Table 5.5, seven stress path tests were conducted on horizontal samples. In the first loading stages (or single loading stages), the values of η_1 were chosen to coincide with stress ratios chosen for tests on vertical samples. This provided an opportunity to make direct comparisons between horizontal and vertical samples in terms of pre-yield behaviour, the magnitude of yield stress, and post-yield behaviour. The yield stresses obtained in these first loading stages were intended to provide information on a section of the yield surface which was different from that explored when testing the vertical samples. Tests E1, E2 and E4 involved unloading stages (at a constant value of η_1) followed by reloading at a new stress ratio η_2. These additional loading stages allowed further exploration of the effects of destructuration and anisotropy. In each test in Series E, radial strains were measured in two orthogonal directions using Hall Effect transducers (see Section 4.8). This provided additional information and allowed particular aspects of the S-CLAY1 model to be investigated. The results of these tests are presented in Section 7.3.

TEST	η_1	η_2	Laval sample
E1	0.00	0.70	20A
E2	0.41	-0.79	20A
E3	0.80	-	21A
E4	0.41	0.99	21A
E5	1.10	-	20A
E6	-0.81	-	20B
E7	-0.4	-	20B

Table 5.5. Stress path tests on horizontal samples (Test Series E).

CHAPTER 6: TESTS ON VERTICAL SAMPLES

6.1 Introduction

In this chapter, the experimental data from the triaxial tests on vertical samples are presented and discussed. In Section 6.2 the drained shearing tests to failure in Test Series A are presented and discussed. Using this data, the value of the critical state stress ratios in triaxial compression and triaxial extension are calculated. The stress path tests in Test Series B are presented in Section 6.3 and the main features of the stress-strain behaviour in these tests are discussed. Test Series C is presented in Section 6.4. The identification of the yield points from Test Series B and C is addressed in Section 6.5 and this information is used to establish the initial size and orientation of the yield curve in Section 6.6. The evolution of anisotropy during the first loading stages in Test Series B and C is examined in Section 6.7.

All test results are presented in terms of natural strains calculated from

$$\varepsilon = -\ln(1-\varepsilon_n) \tag{6.1}$$

where ε is the natural strain and ε_n is the corresponding nominal (engineering) strain calculated with respect to the initial sample dimensions. This method of presentation is used because the code used to generate model simulations in Chapters 8 and 9 works in terms of natural strains.

6.2 Test Series A: shearing tests to failure

6.2.1 Stress-strain behaviour

Six conventional drained shearing tests to failure (three in triaxial compression and three in triaxial extension) were carried out in order to establish the critical state stress ratios M_C (in triaxial compression) and M_E (in triaxial extension). All of these tests were performed in a conventional triaxial cell, due to the axial strain limit in the Bishop-Wesley cell in which the maximum possible axial travel was 27 mm (or 35.5

% nominal axial strain on a 76 mm high sample). A preliminary test in the Bishop Wesley cell showed that this travel would not be sufficient to shear a sample through to critical state in triaxial compression.

Table 6.1 shows the value of isotropic consolidation stress σ'_c used for each test. The conventional drained shear tests were performed at constant cell pressure and the stress paths are shown in Figure 6.1. The range of values of isotropic consolidation pressure, σ'_c was chosen so that each sample would be normally consolidated prior to drained shearing. The stress-strain behaviour for each test is shown in terms of deviator stress and deviator strain in Figure 6.2 (a) and in terms of volumetric strain and mean effective stress (with p' on a logarithmic scale) in Figure 6.2 (b). Each test was terminated at a magnitude of strain that was significantly greater than the level of strain observed at the peak deviator stress. The points corresponding to peak deviator stress observed during each test are indicated by the open circular data points in Figure 6.2. In triaxial compression tests, this meant shearing to strains of 40 - 50% beyond the peak stress ratio, whilst in triaxial extension this involved going to a strain level 20 - 30% beyond the peak.

Figure 6.2 (a) shows that a significant reduction of deviator stress occurred in all of the compression tests (Tests A1 – A3) after the peak stress was reached. The samples were observed during the test and after the tests for signs of development of a failure plane. In each case no such failure plane could be identified, even upon inspection of the final sample (some of which had been sheared to very high levels of strain). This could however, still mean that deformations were highly non-uniform during post-peak shearing. In triaxial extension (Tests A5 - A7) the deviator stress again reached a peak before steadily decreasing. In Tests A6 and A7, the samples eventually ruptured some time after the peak deviator stress was observed and this is seen as a rapid decrease in observed deviator stress in each case. In Figure 6.2 (b) the peak deviator stress is indicated on the compression curves for each test. In each case the sample continued to compress after the peak deviator stress had been reached.

Test	σ'_c (kPa)	q_{peak} (kPa)	η_{peak}	ε_{dpeak} (%)	ε_{vpeak} (%)	v_{peak}	Laval sample
A1	58	156	1.47	20.90	9.95	2.263	20A
A2	94	207	1.29	36.36	13.35	2.157	20B
A3	150	384	1.39	31.72	20.96	2.021	21A
A5	100	-76	-1.14	-12.1251	1.93	2.384	20A
A6	150	-124	-1.15	-12.25	1.69	2.265	20B
A7	171	-118	-1.03	-5.96	1.02	2.277	21A

Table 6.1. Details of shearing tests to failure on vertical samples.

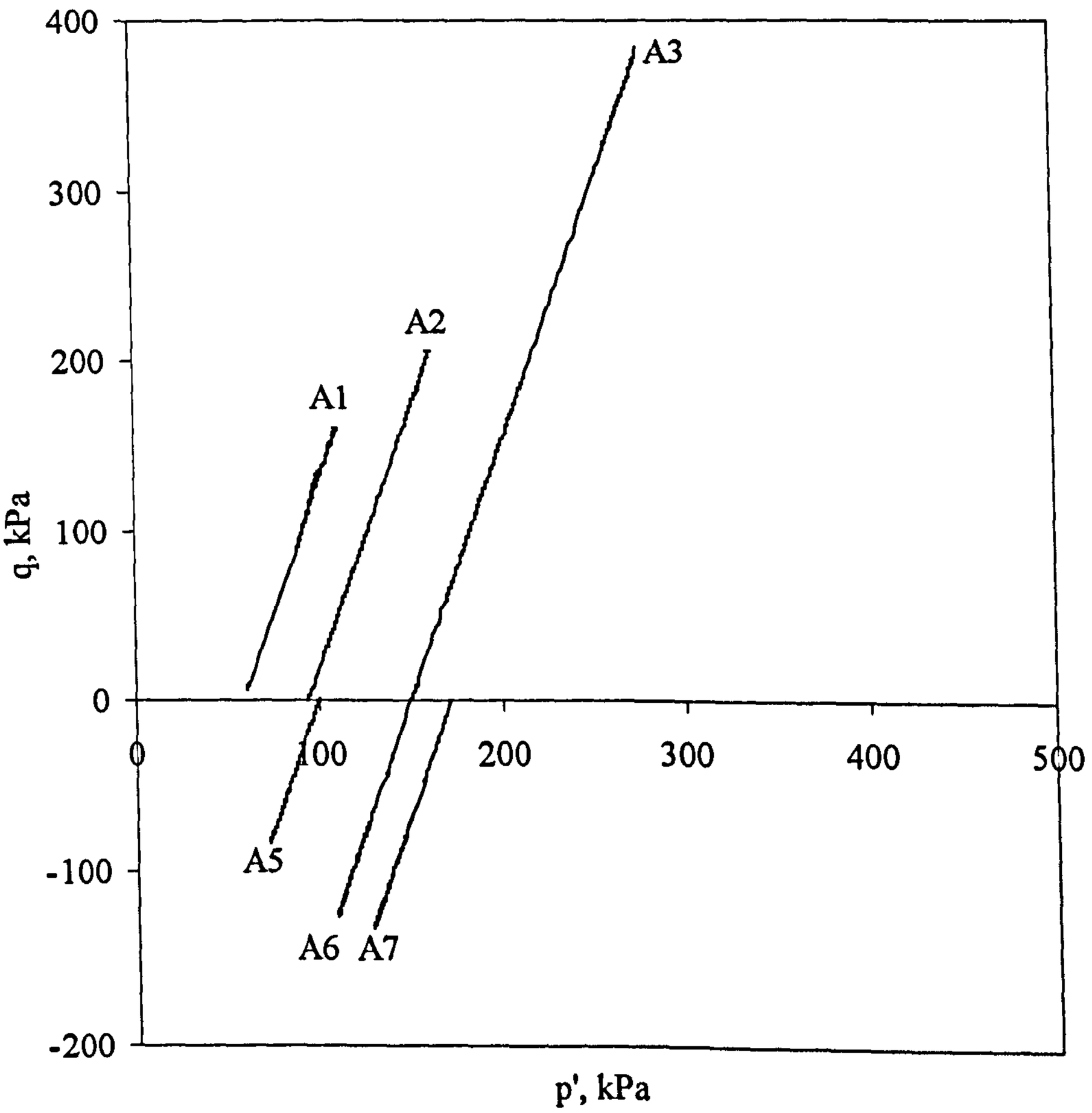

Figure 6.1. Stress paths for drained shearing to failure of vertical samples (Test Series A).

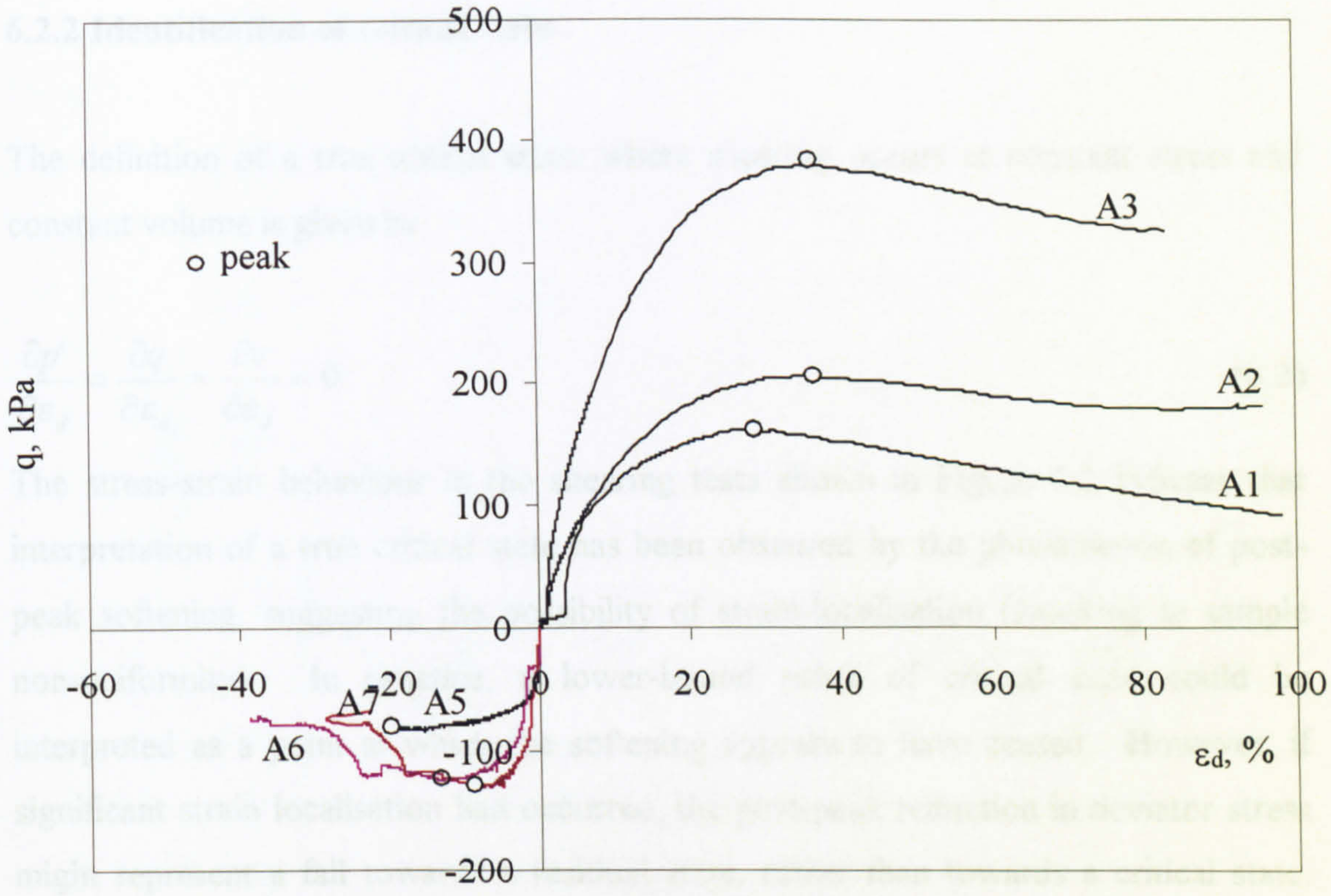

(a)

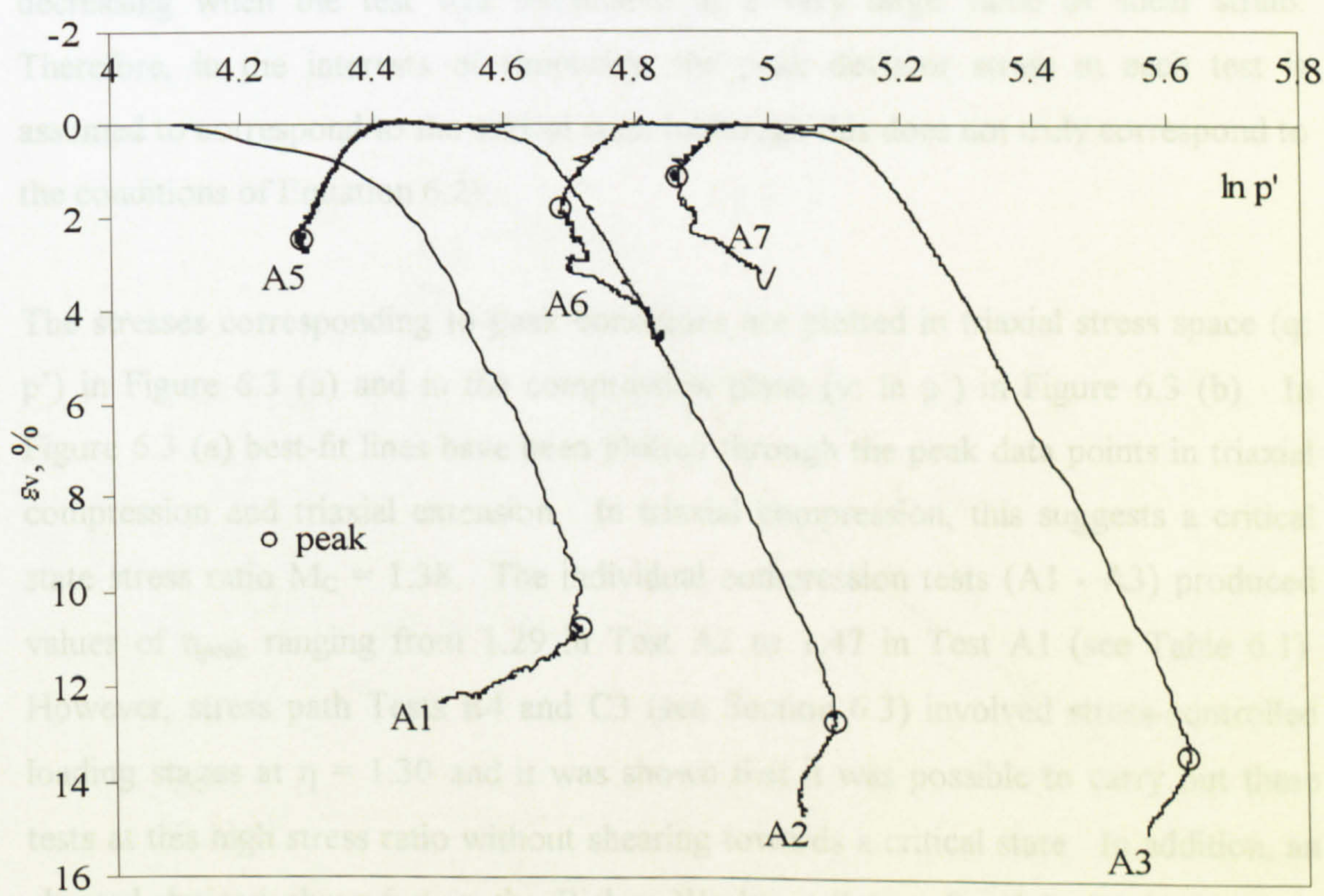

(b)

Figure 6.2. Drained shearing tests to failure on vertical samples; (a) deviatoric stress-strain behaviour, (b) volumetric stress-strain behaviour.

6.2.2 Identification of critical state

The definition of a true critical state, where shearing occurs at constant stress and constant volume is given by

$$\frac{\partial p'}{\partial \varepsilon_d} = \frac{\partial q}{\partial \varepsilon_d} = \frac{\partial v}{\partial \varepsilon_d} = 0 \qquad (6.2)$$

The stress-strain behaviour in the shearing tests shown in Figure 6.2 indicate that interpretation of a true critical state has been obscured by the phenomenon of post-peak softening, suggesting the possibility of strain-localisation (resulting in sample non-uniformity). In practice, a lower-bound value of critical state could be interpreted as a point at which the softening appears to have ceased. However, if significant strain localisation had occurred, the post-peak reduction in deviator stress might represent a fall towards a residual state, rather than towards a critical state. This appeared likely, since in several of the tests the deviator stress was still decreasing when the test was terminated at a very large value of shear strain. Therefore, in the interests of simplicity, the peak deviator stress in each test is assumed to correspond to the critical state (although this does not truly correspond to the conditions of Equation 6.2).

The stresses corresponding to peak conditions are plotted in triaxial stress space (q: p') in Figure 6.3 (a) and in the compression plane (v: ln p') in Figure 6.3 (b). In Figure 6.3 (a) best-fit lines have been plotted through the peak data points in triaxial compression and triaxial extension. In triaxial compression, this suggests a critical state stress ratio $M_C = 1.38$. The individual compression tests (A1 - A3) produced values of η_{peak} ranging from 1.29 in Test A2 to 1.47 in Test A1 (see Table 6.1). However, stress path Tests B4 and C3 (see Section 6.3) involved stress-controlled loading stages at $\eta = 1.30$ and it was shown that it was possible to carry out these tests at this high stress ratio without shearing towards a critical state. In addition, an aborted drained shear test in the Bishop-Wesley cell (not listed in Table 6.1) was carried through until $\eta = 1.36$, but from the stress-strain plots it was obvious that the critical state had not been reached, adding weight to the possibility that Test A2 ($\eta_{peak} = 1.29$) produced an unusually low value of η at the peak. In view of this

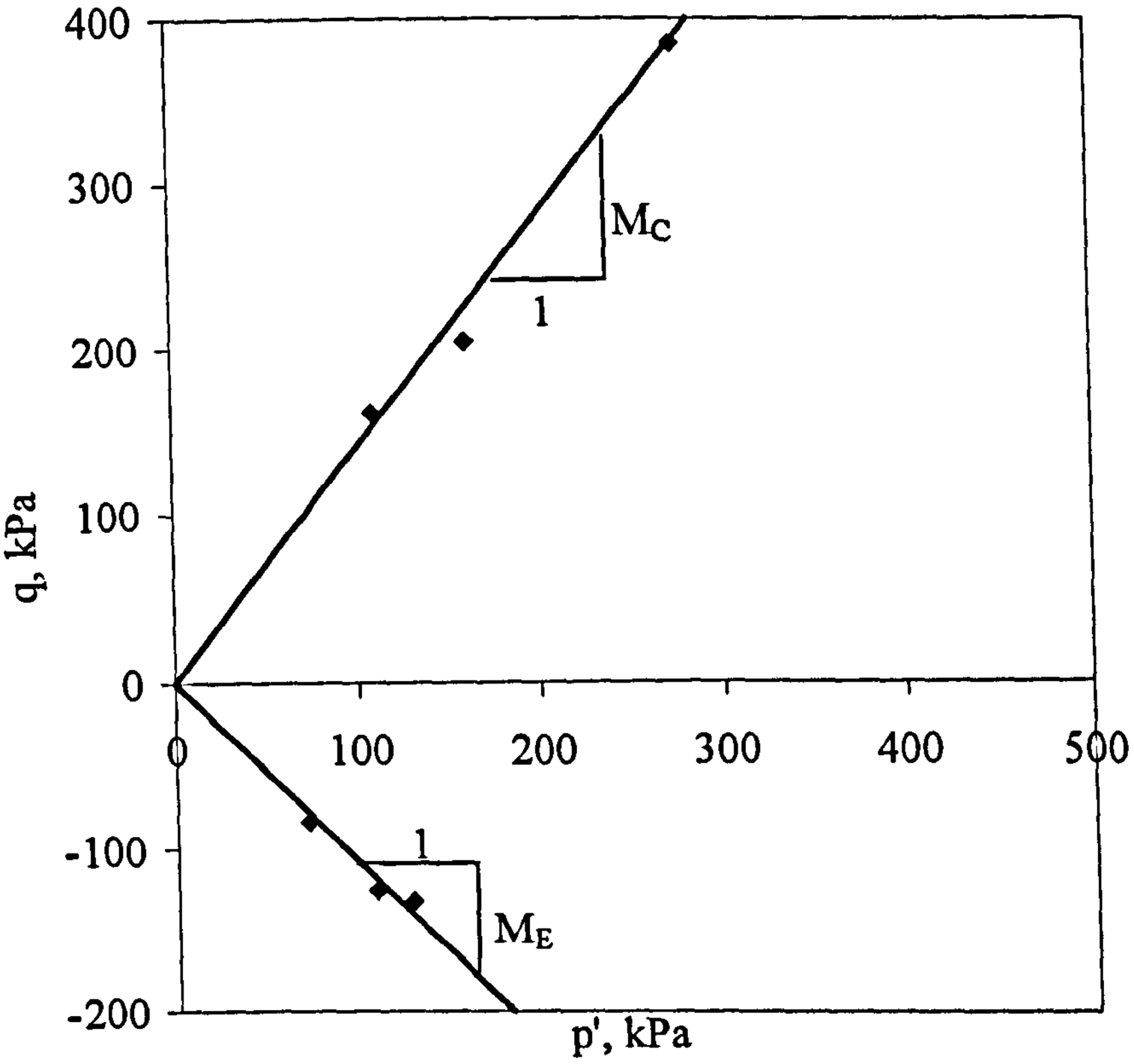

(a)

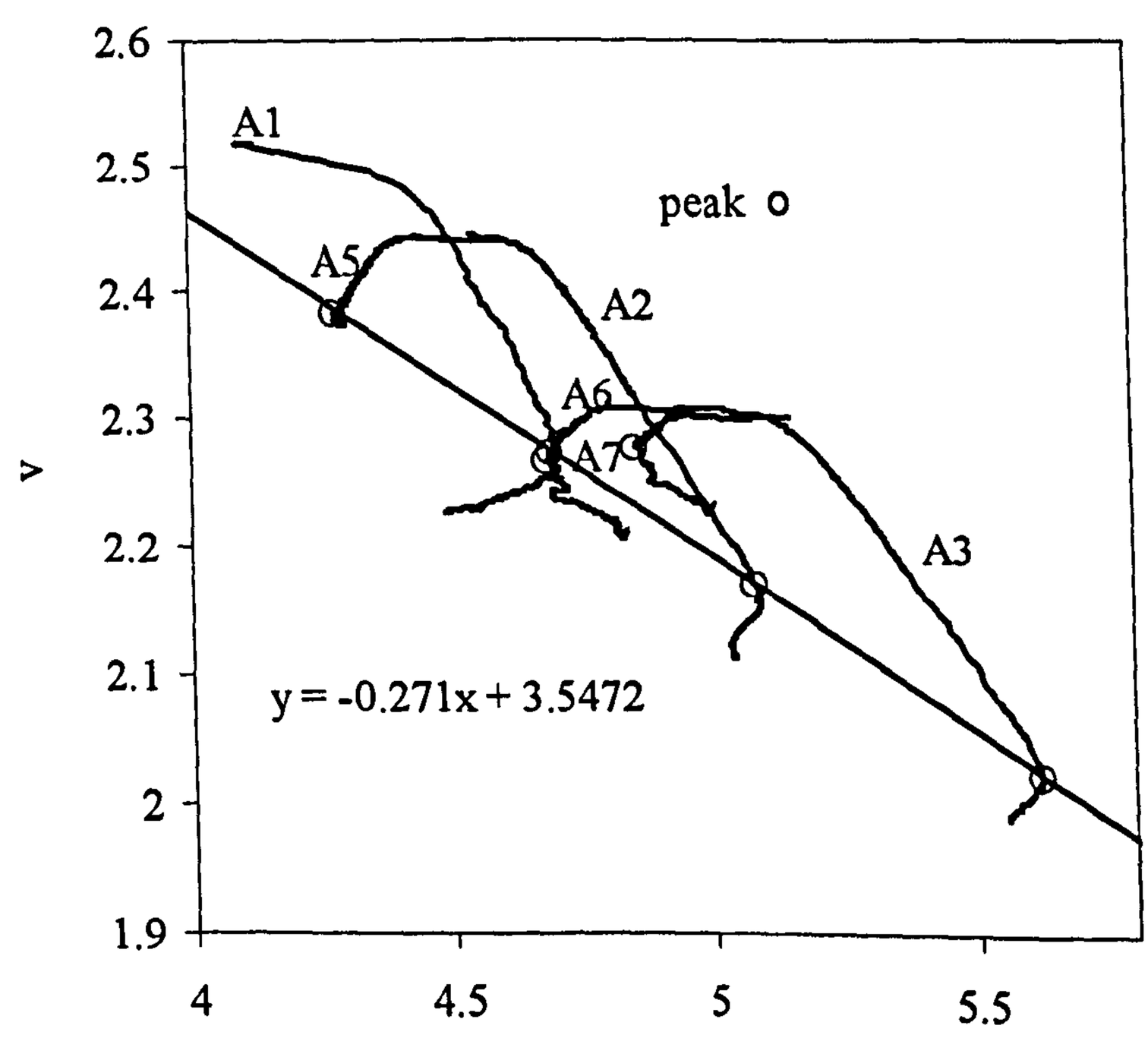

(b)

Figure 6.3. Drained shearing tests to failure on vertical samples: (a) peak stresses, (b) stress paths in v: ln p' plane.

additional information, and given the scatter within the peak data points, it was considered inappropriate to state the value of M_C to a precision better than ± 0.05 and a value of M_C = 1.40 was therefore assumed. In triaxial extension, the peak stress ratios are again widely varied, ranging from –1.03 in Test A7 to –1.15 in Test A6 (see Table 6.1). The best-fit line in Figure 6.3 (a) suggests that M_E = 1.10, with the accuracy again assumed to be ±0.05. Points corresponding to the peak deviator stress are indicated in the ln p': v plots shown in Figure 6.3 (b). The data suggest that there is a unique relationship between the specific volume, v, and the mean effective stress, p', at points corresponding to peak deviator stress. This lends support to the suggestion that the points corresponding to peak deviator stress are a close approximation to critical states, with most of the post-peak reduction in deviator stress corresponding to a fall towards a residual value, rather than towards a critical state. The trend-line applied to the data suggests that the gradient of the critical state line is $\lambda = 0.27$ and the critical state intercept (at p' = 1 kPa) is $\Gamma = 3.54$.

The critical state stress ratio in triaxial compression M_C relates to the corresponding friction angle ϕ'_C thus:

$$\sin \phi'_C = \frac{3M_C}{6+M_C} \tag{6.3}$$

Inserting M_C = 1.40 into Equation 5.2 results in $\phi'_C = 34.6^0$. In triaxial extension:

$$\sin \phi'_E = \frac{3M_E}{6-M_E} \tag{6.4}$$

The suggested value of M_E = 1.10 leads to $\phi'_E = 42.3^0$. Thus, while the results suggest that M_C is greater than M_E, when this is expressed in terms of friction angle it is suggested that ϕ'_E is greater than ϕ'_C. A number of authors including Gens (1982) have noted that the critical state stress ratio M is generally greater in compression and than in extension. A number of undrained triaxial shearing tests were conducted and presented within the 1992 Géotechnique Symposium-in-Print on the Bothkennar soft clay site. Smith et al. (1992) reported values of M_C = 1.40 in

triaxial compression and M_E = 1.04 in triaxial extension from Laval samples taken at around 5.5m depth. Hight et al. (1992) reported M_C = 1.40 from the same depth. Allman and Atkinson (1992) carried out undrained triaxial tests on reconstituted Bothkennar clay and found M_C = 1.38 and M_E = 1.00. The values of M_C and M_E suggested from Test Series A (1.40 and 1.10 respectively) are therefore reasonably consistent with those reported for Bothkennar clay by previous authors, and support the widely reported suggestion that M_C is significantly greater than M_E.

6.2.3 K_0 consolidation test

Test A4 involved anisotropic consolidation with feedback control to maintain zero lateral strain, in an attempt to establish the stress-ratio, η_{K0}, corresponding to one-dimensional consolidation. As a first approximation, the normally consolidated K_0 stress ratio is related to the friction angle by Jaky's simplified formula

$$K_{0nc} = 1 - \sin\phi'_C \qquad (3.11 \text{ bis})$$

Inserting a friction angle of $\phi'_C = 34.6^0$ results in $K_{0nc} = 0.432$. This was converted to a corresponding stress ratio, η_{K0}, as follows:

$$\eta_{K0} = \frac{3(1-K_{0nc})}{(1+2K_{0nc})} \qquad (6.5)$$

resulting in $\eta_{K0} = 0.913$.

The test was carried out in the Bishop-Wesley cell as follows. The sample was isotropically consolidated to p' = 15 kPa (under a standard back pressure of 100 kPa) and allowed to consolidate for 24 hours (at point A in Figure 6.4). A short drained shear stage, at constant cell pressure, was then included until the stress ratio η had increased to the estimated normally consolidated K_0 value η_{K0} = 0.913 (point B in Figure 6.4). At this stage consolidation commenced with feedback control of the cell pressure and axial stress to maintain zero radial strain, ε_r (see Section 4.4.3 for details

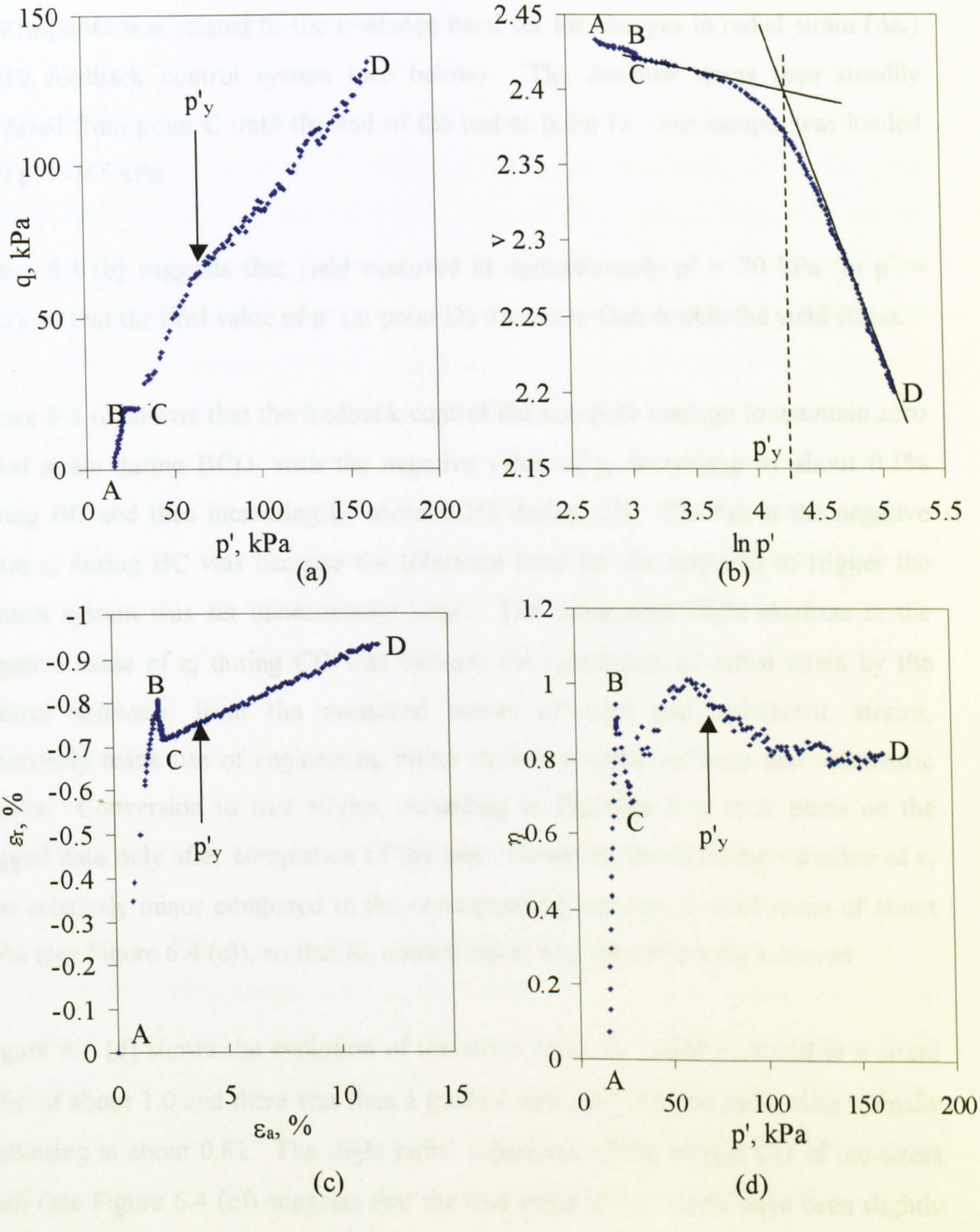

Figure 6.4. K_0 consolidation test; (a) stress path, (b) compression behaviour, (c) axial and radial strain and (d) stress ratio.

of the software control used in this test). Under feedback control, the stress path initially involved almost no change in deviator stress up to point C in Figure 6.4 (a). This response was related to the tolerance band set for changes in radial strain ($\Delta\varepsilon_r$) in the feedback control system (see below). The deviator stress then steadily increased from point C until the end of the test at point D. The sample was loaded until p' = 165 kPa.

Figure 6.4 (b) suggests that yield occurred at approximately p' = 70 kPa (ln p' = 4.25), so that the final value of p' (at point D) was more than double the yield stress.

Figure 6.4 (c) shows that the feedback control did not quite manage to maintain zero radial strain during BCD, with the negative value of ε_r decreasing by about 0.1% during BC and then increasing by about 0.2% during CD. The fall in the negative value ε_r during BC was because the tolerance band for $\Delta\varepsilon_r$ required to trigger the control system was set unnecessarily large. The subsequent slight increase in the negative value of ε_r during CD was because the calculation of radial strain by the control software, from the measured values of axial and volumetric strains, incorrectly made use of engineering rather than true values of axial and volumetric strains. Conversion to true strains, according to Equation 6.1, took place on the logged data only after completion of the test. However, the resulting variation of ε_r was relatively minor compared to the corresponding increase in axial strain of about 10% (see Figure 6.4 (c)), so that K_0 consolidation was approximately achieved.

Figure 6.4 (d) shows the evolution of the stress ratio, η. Yield occurred at a stress ratio of about 1.0 and there was then a gradual decrease of stress ratio, with η finally stabilising at about 0.82. The slight radial expansion during section CD of the stress path (see Figure 6.4 (c)) suggests that the true value of η_{K0} might have been slightly lower than 0.82.

The estimate of η_{K0} = 0.913, based on Jaky's simplified formula (Equation 3.9), therefore appears to slightly overestimate the measured value of η_{K0}.

6.3 Stress-strain behaviour during Test Series B

6.3.1 Summary of sample properties and stress paths

Details of the multi-stage stress paths in Test Series B are given in Table 6.2. The information includes the initial void ratio (e_0), the stress ratio during first and second loading stages (η_1 and η_2), the maximum mean effective stresses in first and second loading stages (p'_{max1}, and p'_{max2}) and the Laval sample from which each triaxial specimen was cut. All the samples in Test Series B were first loaded isotropically to a mean effective stress of 210 kPa. As discussed in Section 5.4, it was intended to first load each sample to a stress level approximately three times beyond the initial yield stress. Examination of the stress-strain behaviour (discussed in detail in Section 6.3.2) showed that this could be achieved by loading to a mean effective stress of 210 kPa. On reloading the intention was to load again to three times the new yield stress, but in Test B4 (where $\eta_2 = 1.30$) this was not possible ($p'_{max2} = 198$ kPa) as the axial deformation at this high value of η meant that the axial travel was exhausted. Again, however, the data obtained was sufficient to observe the post-yield behaviour. Test B1 was terminated prematurely during the second loading stages due to compressor failure. However, the data obtained during first loading and unloading stages was valuable and these results have therefore been included.

The stress-strain behaviour in each of the tests in Series B is presented in Figures 6.5 – 6.13. In each plot, circular data points indicate the start of a loading stage (when the stress ratio for the loading stage is first achieved) and square data points indicate the end of a loading stage. For each test, the compression behaviour has been plotted in linear form (volumetric strain ε_v against the mean effective stress, p') and in semi-logarithmic form (ε_v against ln p'). The other plots included are the deviatoric stress-strain behaviour, plotted in terms of deviator stress (q) and deviator strain (ε_d), and the axial stress-strain response, plotted in terms of axial effective stress (σ'_1) and axial strain (ε_1). The inclusion of axial stress-strain response is useful as the axial strain is measured separately from the volumetric strain and therefore provides an independent measure of the soil behaviour. The compression curves in Figures 6.5 - 6.13 show significant volumetric strains occurring during the 24 hour rest periods at

the end of loading and unloading stages. The significance of these strains during rest periods is discussed later, together with the corresponding results from Test Series C in Section 6.4.4.

Test	e_0	η_1	p'_{max1} (kPa)	η_2	p'_{max2} (kPa)	Laval Sample
B1	1.721	0.00	210	-	-	20B
B2	1.512	0.00	210	0.70	550	21A
B3	1.527	0.00	210	1.01	497	21B
B4	1.484	0.00	210	1.30	198	20B
B5	1.607	0.00	210	-0.40	445	21A
B6	1.571	0.00	210	-0.70	326	21B
B7	1.550	0.00	210	0.00	450	20B
B8	1.514	0.00	210	0.40	450	21A
B9	1.536	0.00	210	-1.02	259	21B

Table 6.2. Summary of stress path tests on vertical samples (Test Series B).

6.3.2 Compression curves

During the first loading stages (all at $\eta_1 = 0$), the onset of yield is generally apparent in the semi-logarithmic plots (ε_v: ln p') in Figures 6.5 (b) - 6.13 (b). Commencing from an initially overconsolidated state, although the compression curves are non-linear right from the start of the loading stage, the gradient of the curve remains relatively low until the onset of yield is indicated by a gradual, but distinct, increase in gradient. When the yield point has been exceeded and plastic straining is fully mobilized, the post-yield compression curve is approximately linear in the ε_v: ln p' plot. The onset of yield is also apparent during second loading stages when using this type of plot (with the exception of Test B1 which was terminated prematurely). Yield points are particularly well defined where the second loading stage involved a high stress ratio in triaxial compression, as was the case in Tests B2, B3 and B4. The yield point is, however, less clearly defined in tests involving second loading in triaxial extension, such as Tests B5, B6 and B9. In each of these tests, the post-yield

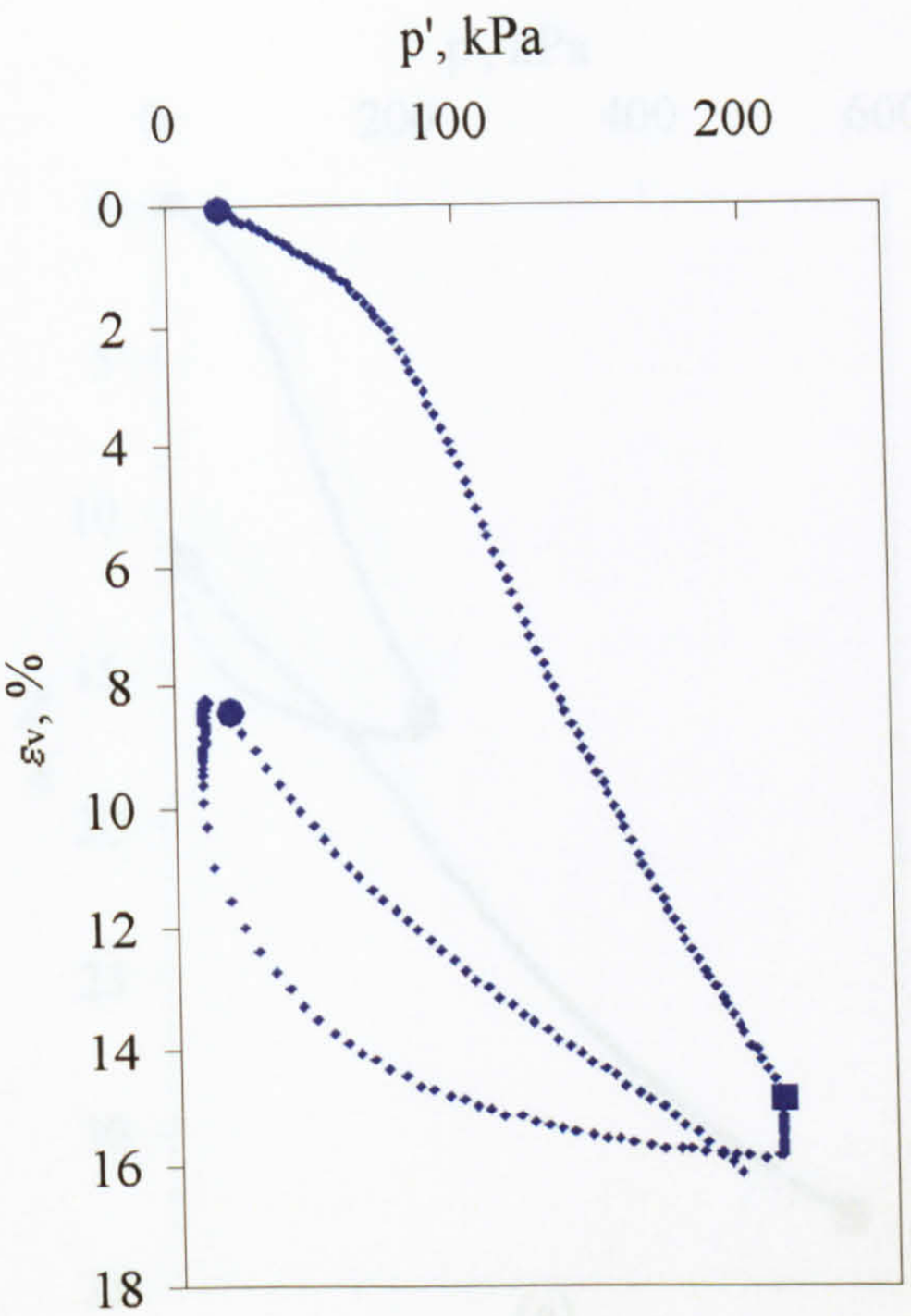

(a)

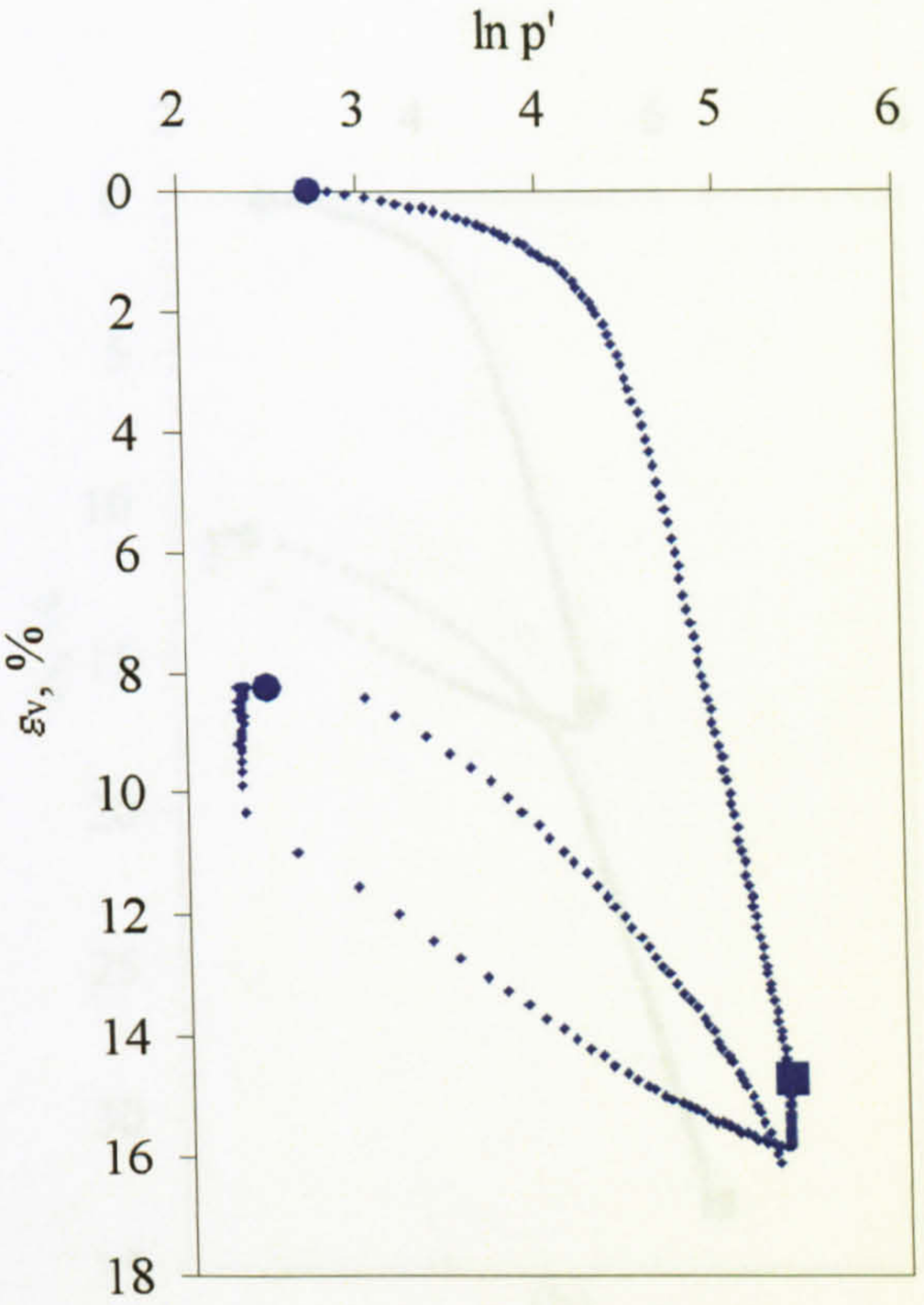

(b)

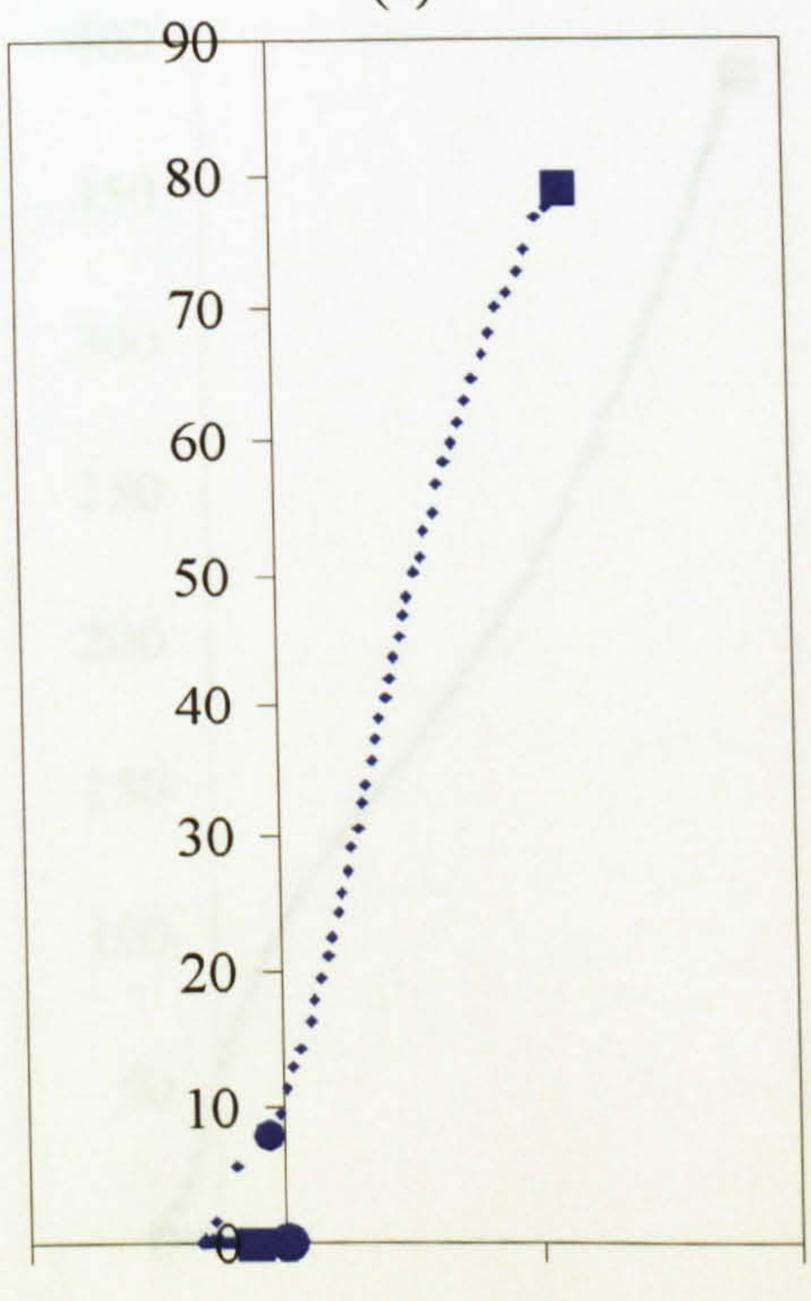

(c)

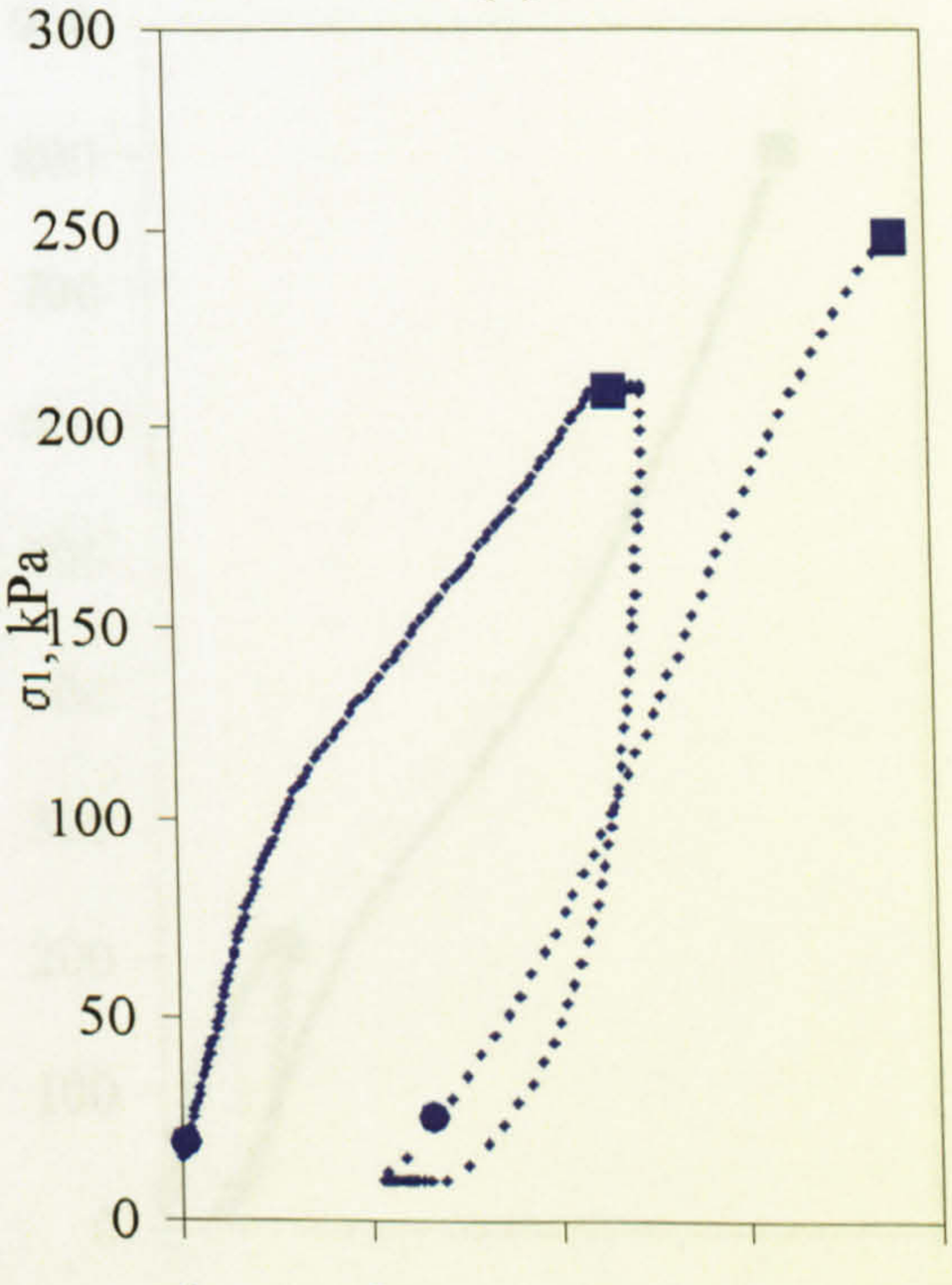

(d)

Figure 6.5. Stress-strain behaviour in Test B1 ($\eta_1 = 0$, $\eta_2 = 0.40$): (a), (b) compression behaviour, (c) deviatoric behaviour and (d) axial behaviour.

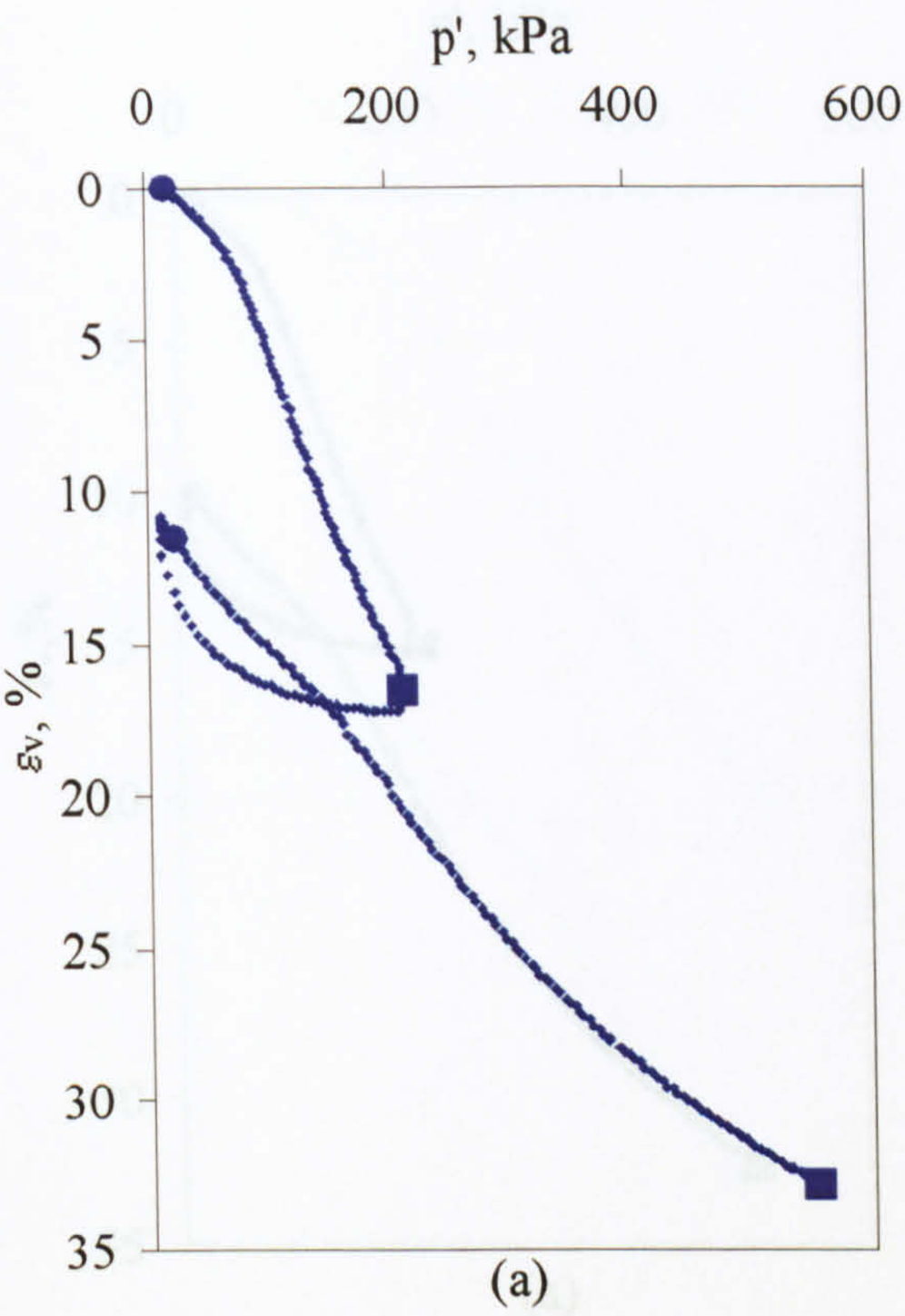

(a)

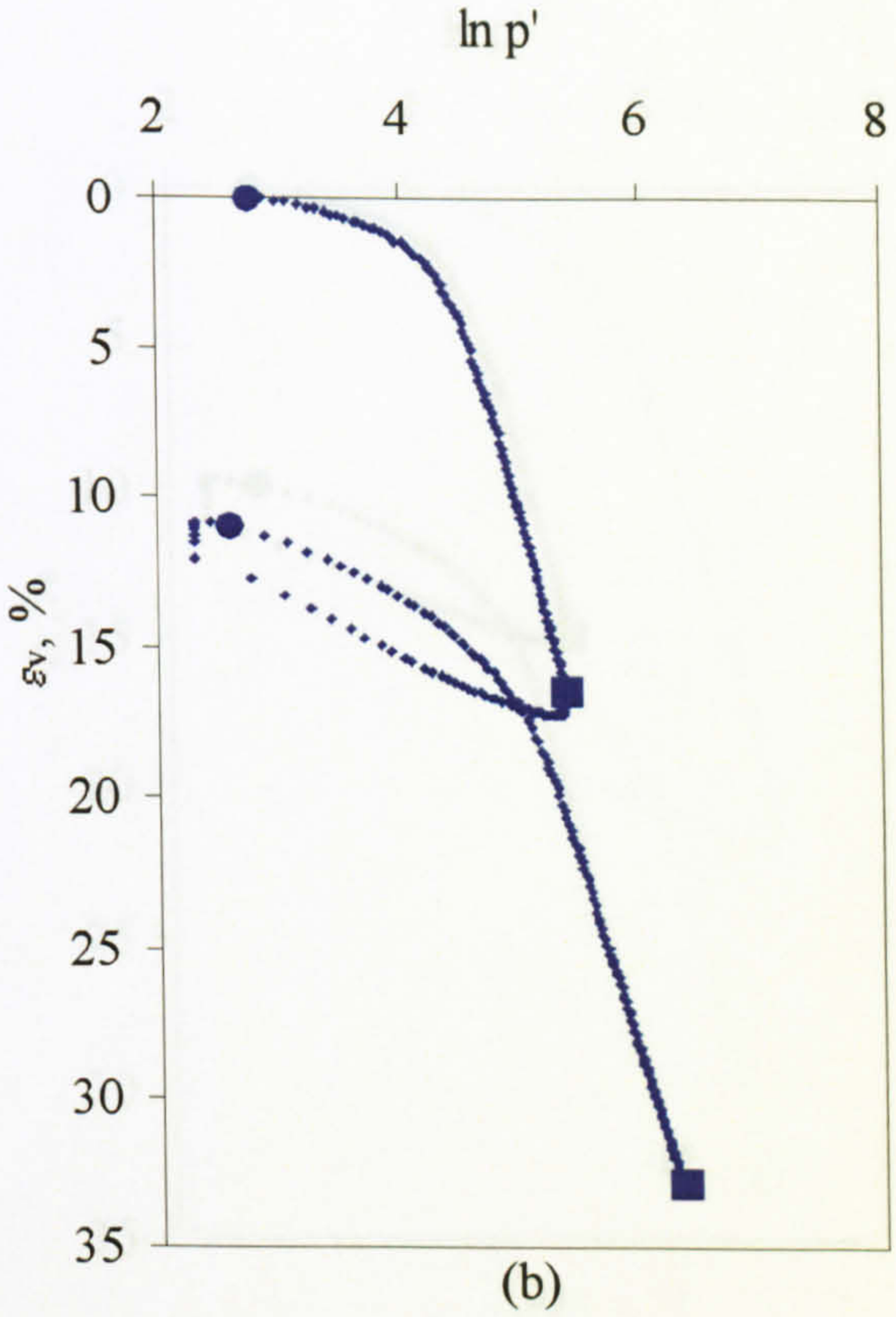

(b)

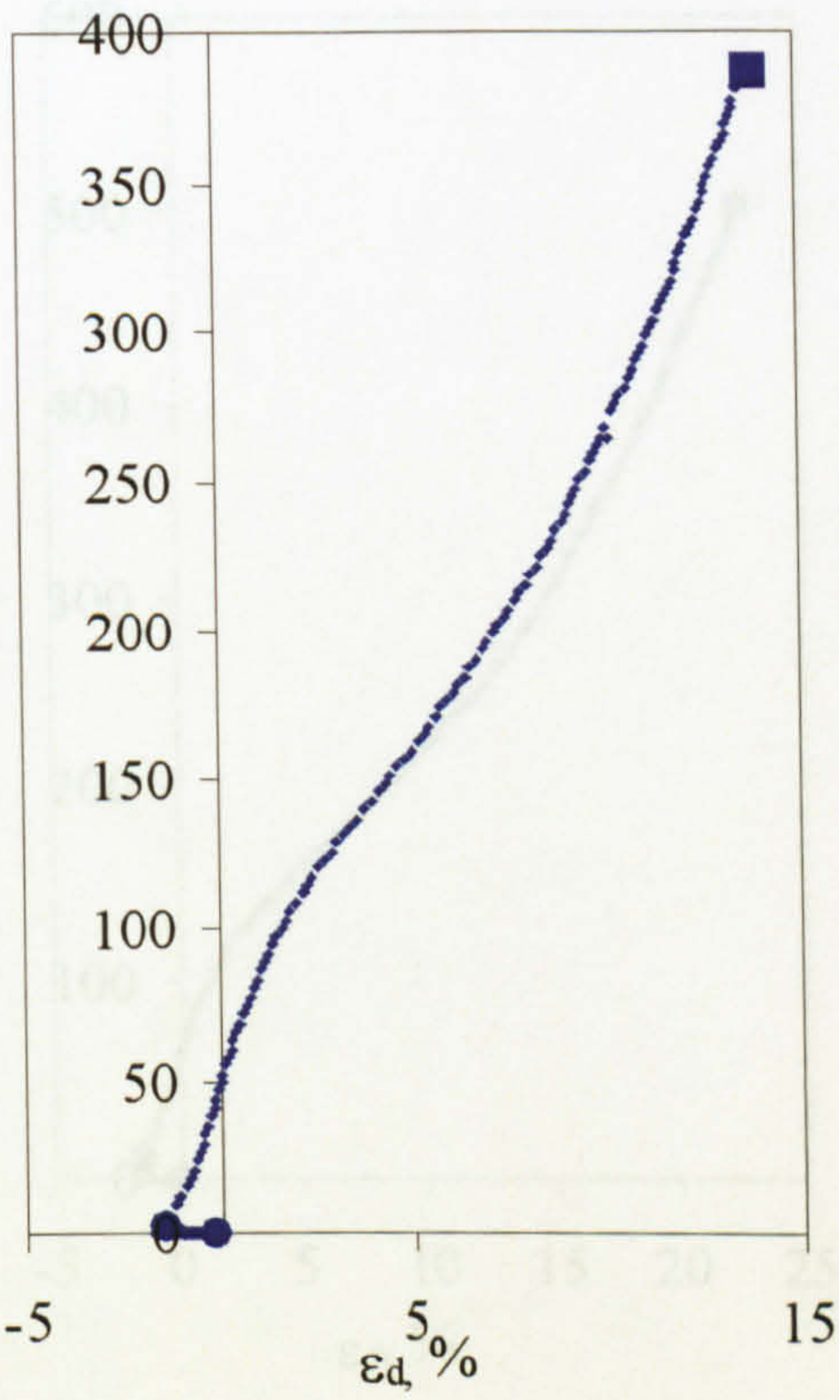

(c)

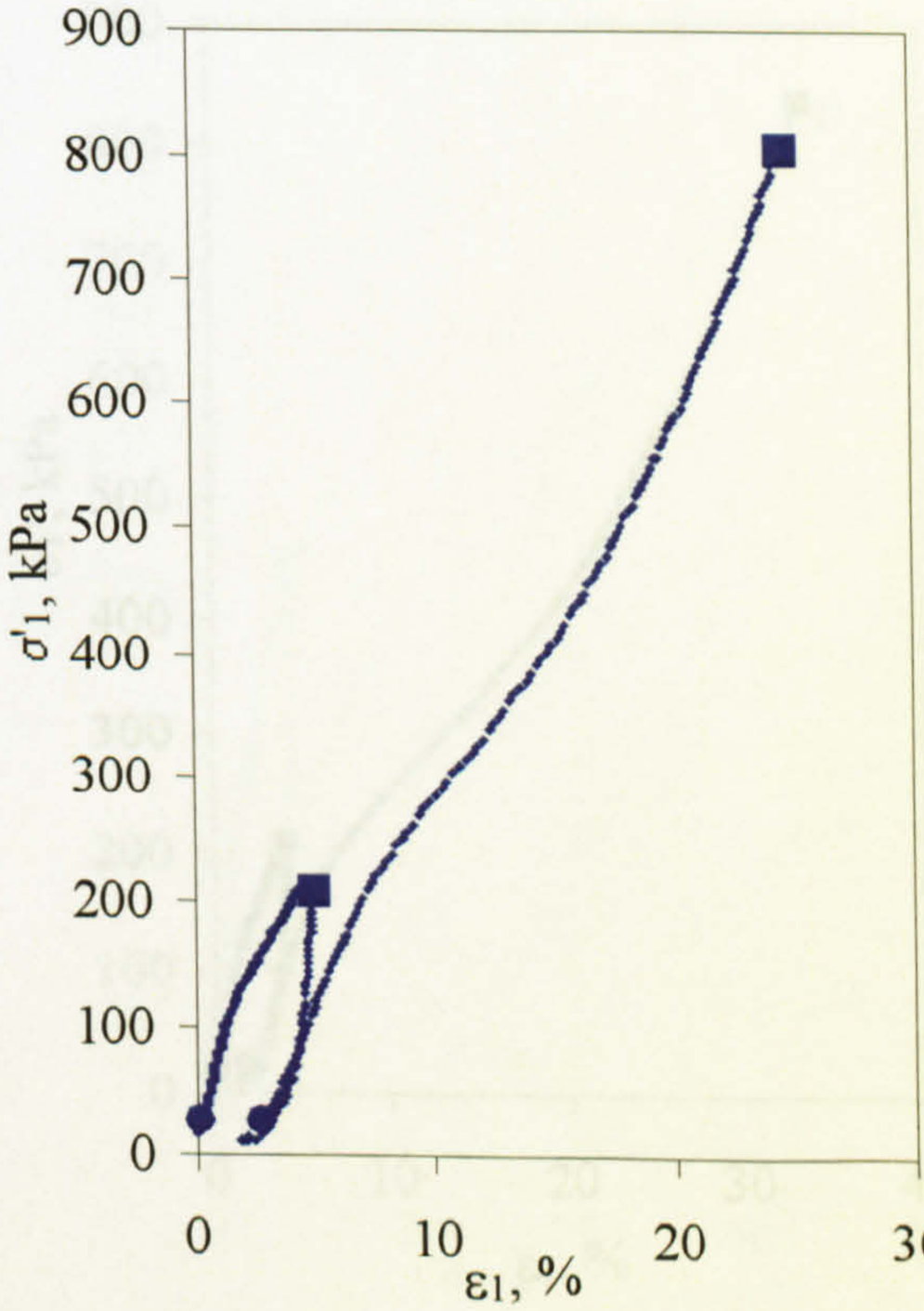

(d)

Figure 6.6. Stress-strain behaviour in Test B2 ($\eta_1 = 0$ and $\eta_2 = 0.70$): (a), (b) compression behaviour, (c) deviatoric behaviour and (d) axial behaviour.

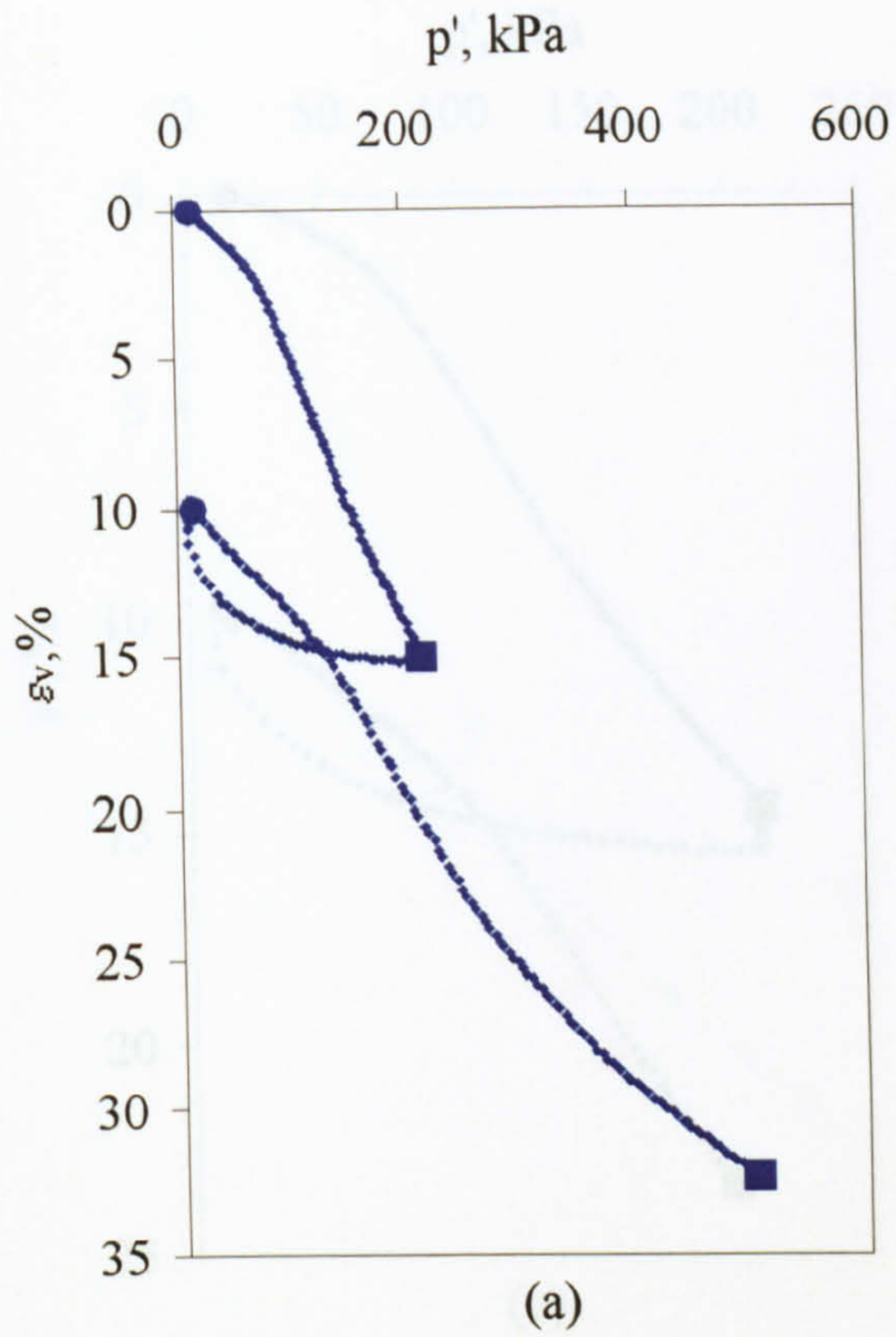

(a)

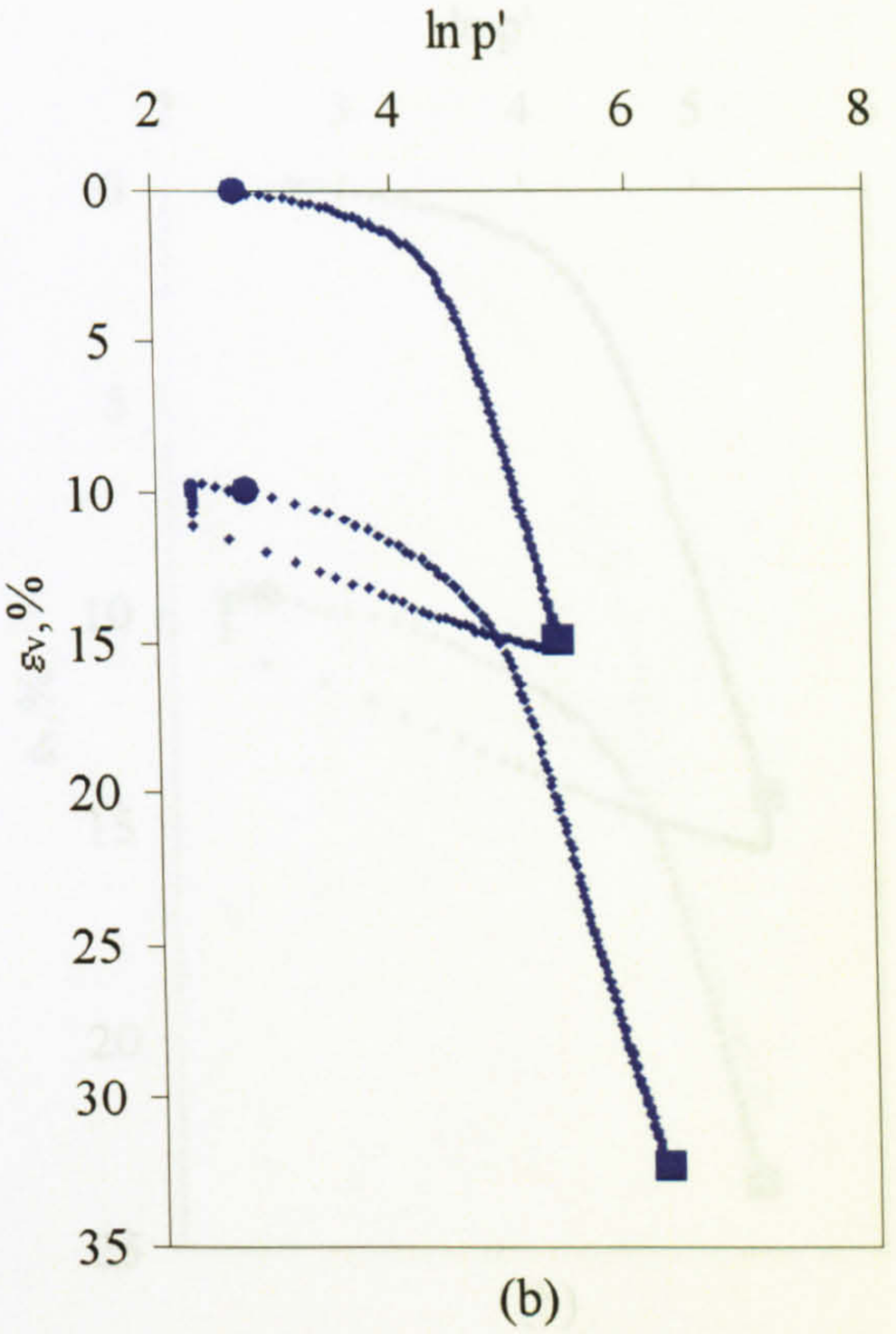

(b)

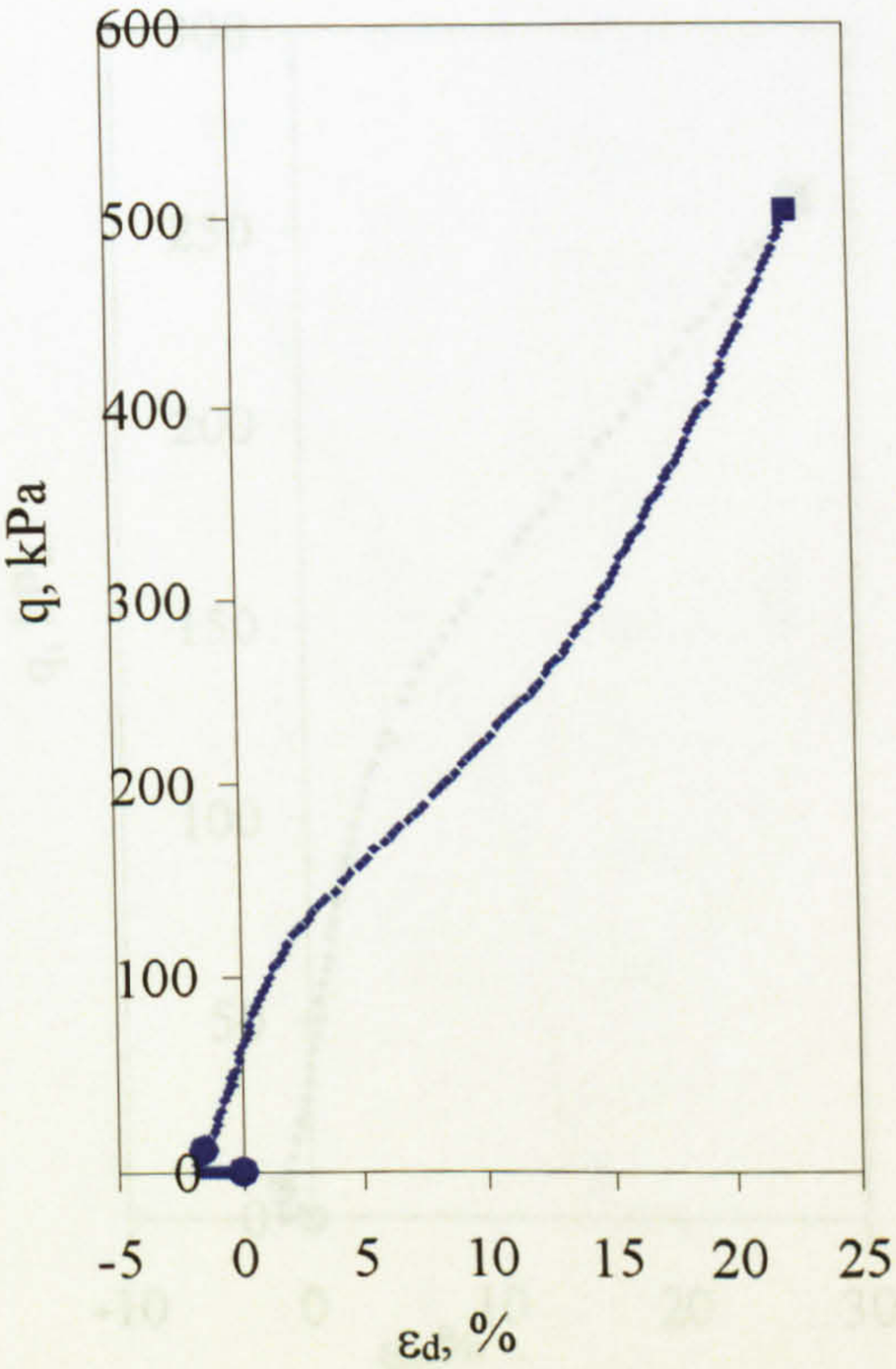

(c)

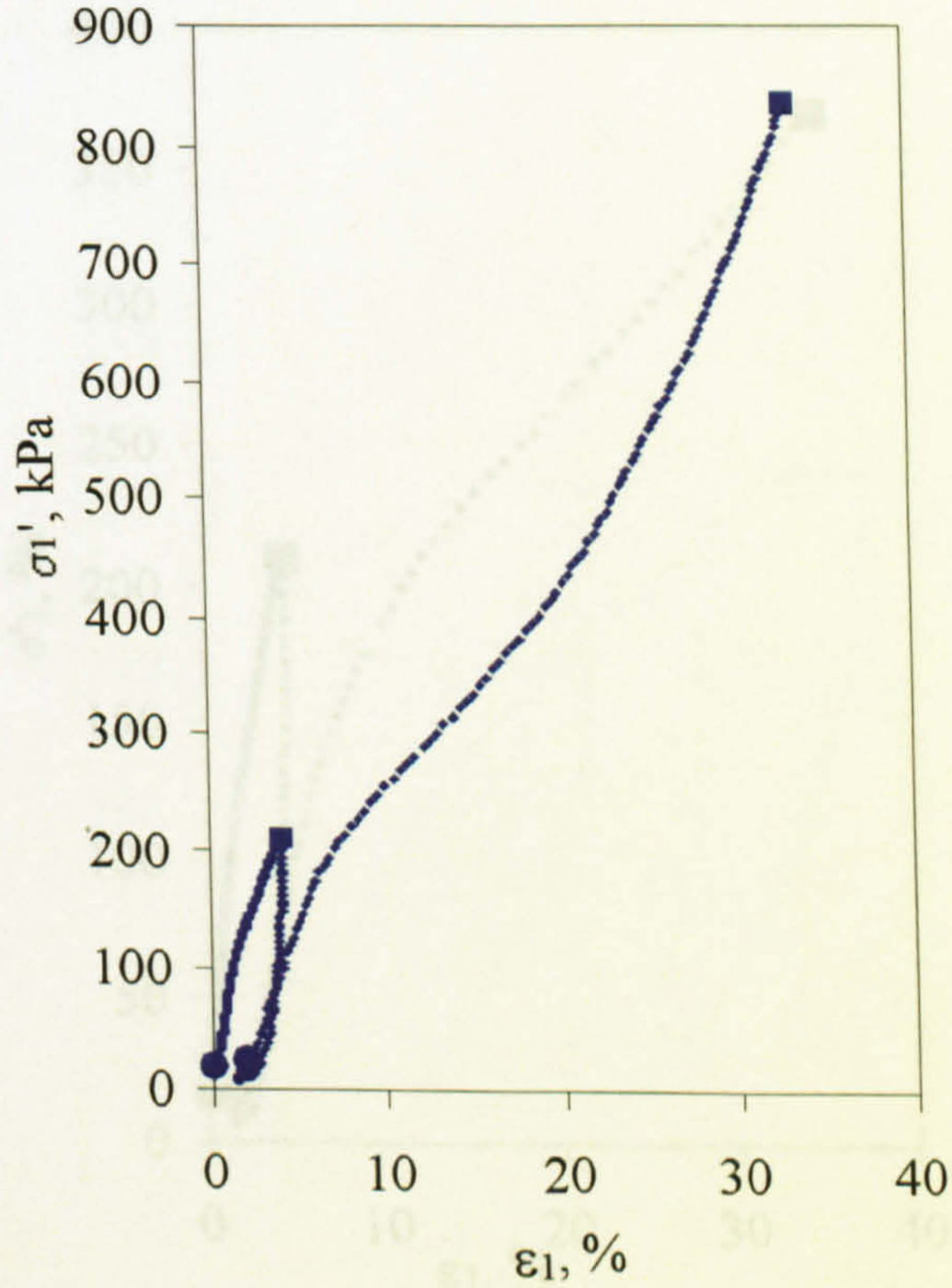

(d)

Figure 6.7. Stress-strain behaviour in Test B3 ($\eta_1 = 0$ and $\eta_2 = 1.01$): (a), (b) compression behaviour, (c) deviatoric behaviour and (d) axial behaviour.

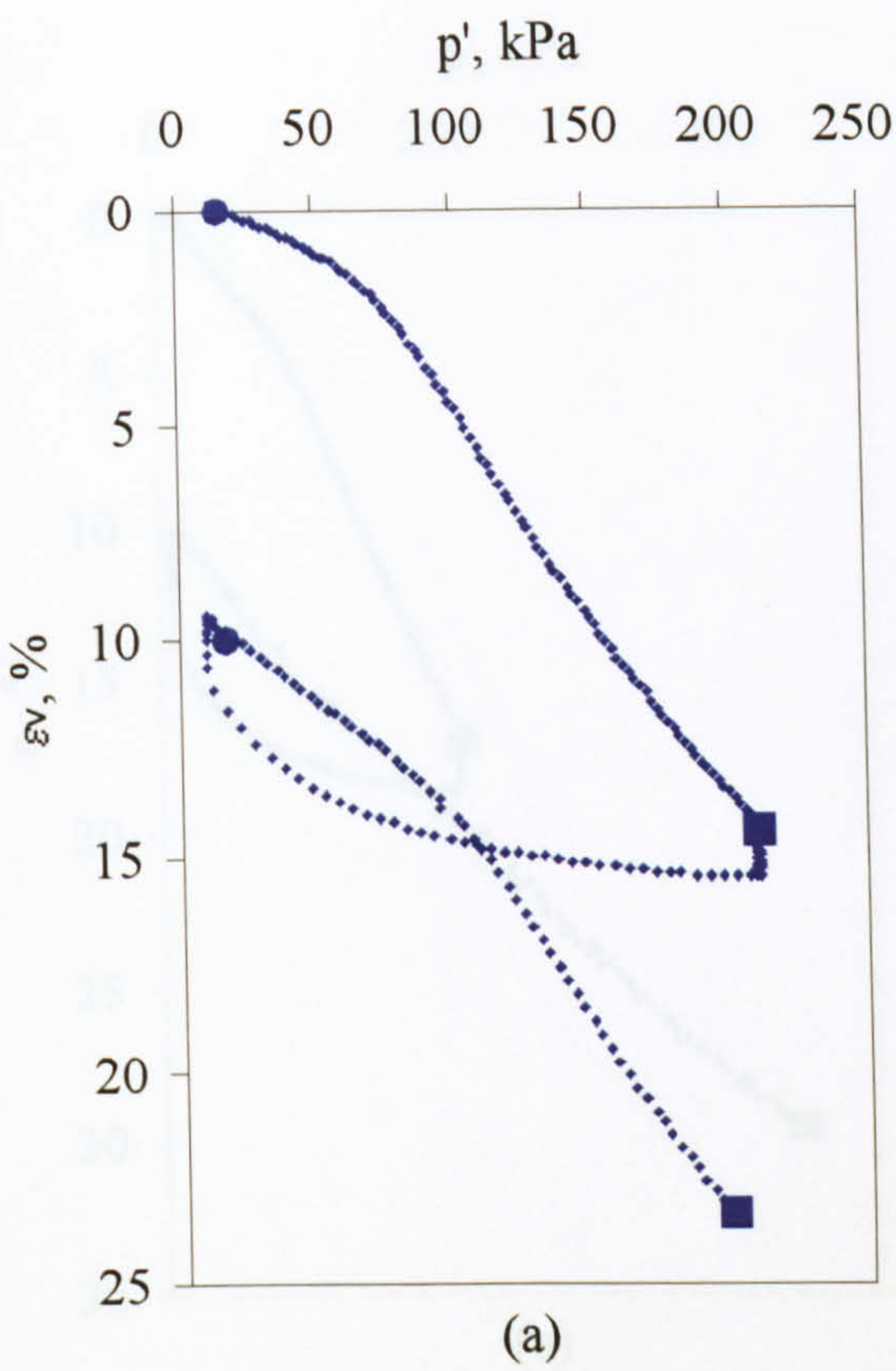

(a)

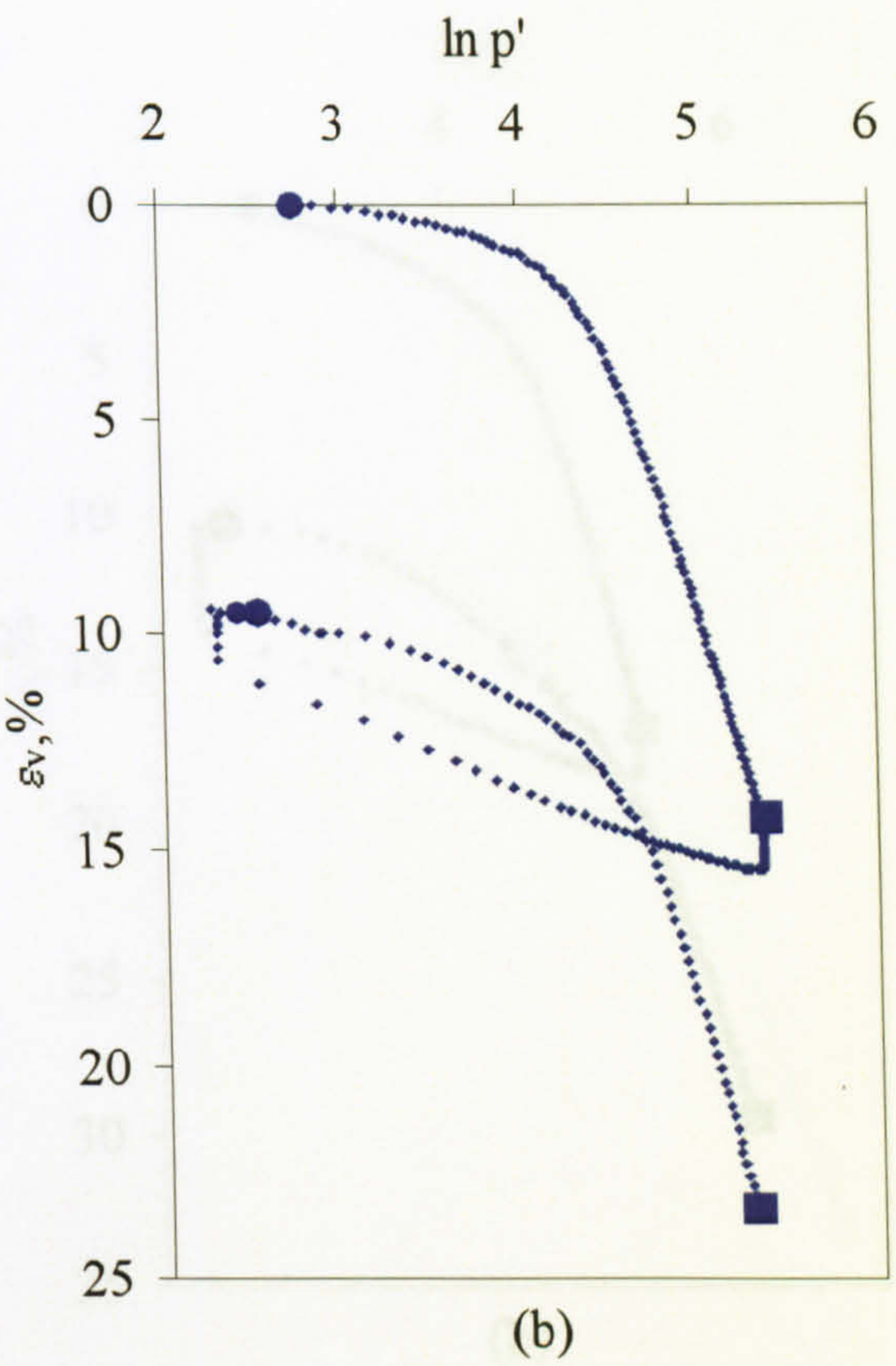

(b)

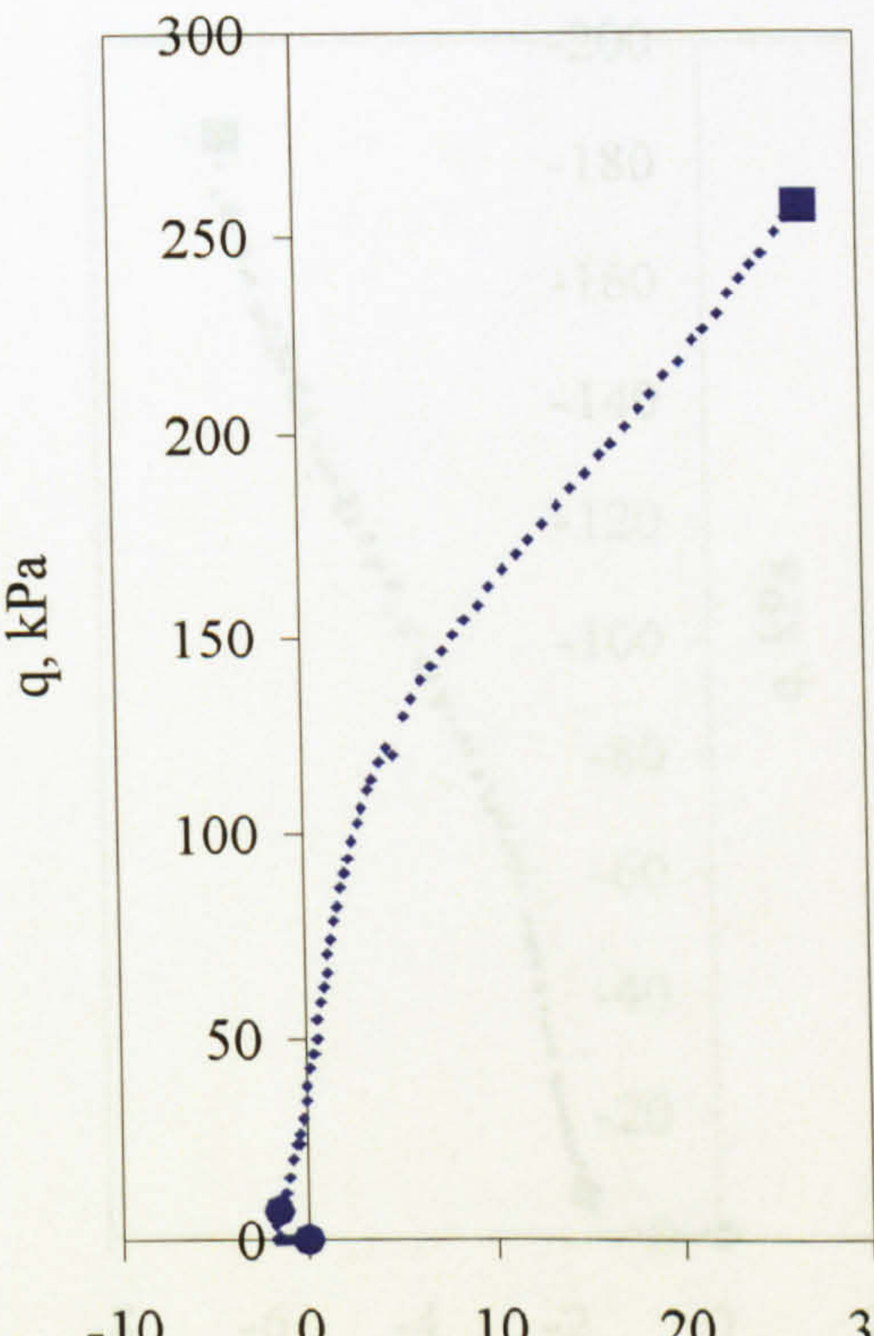

(c)

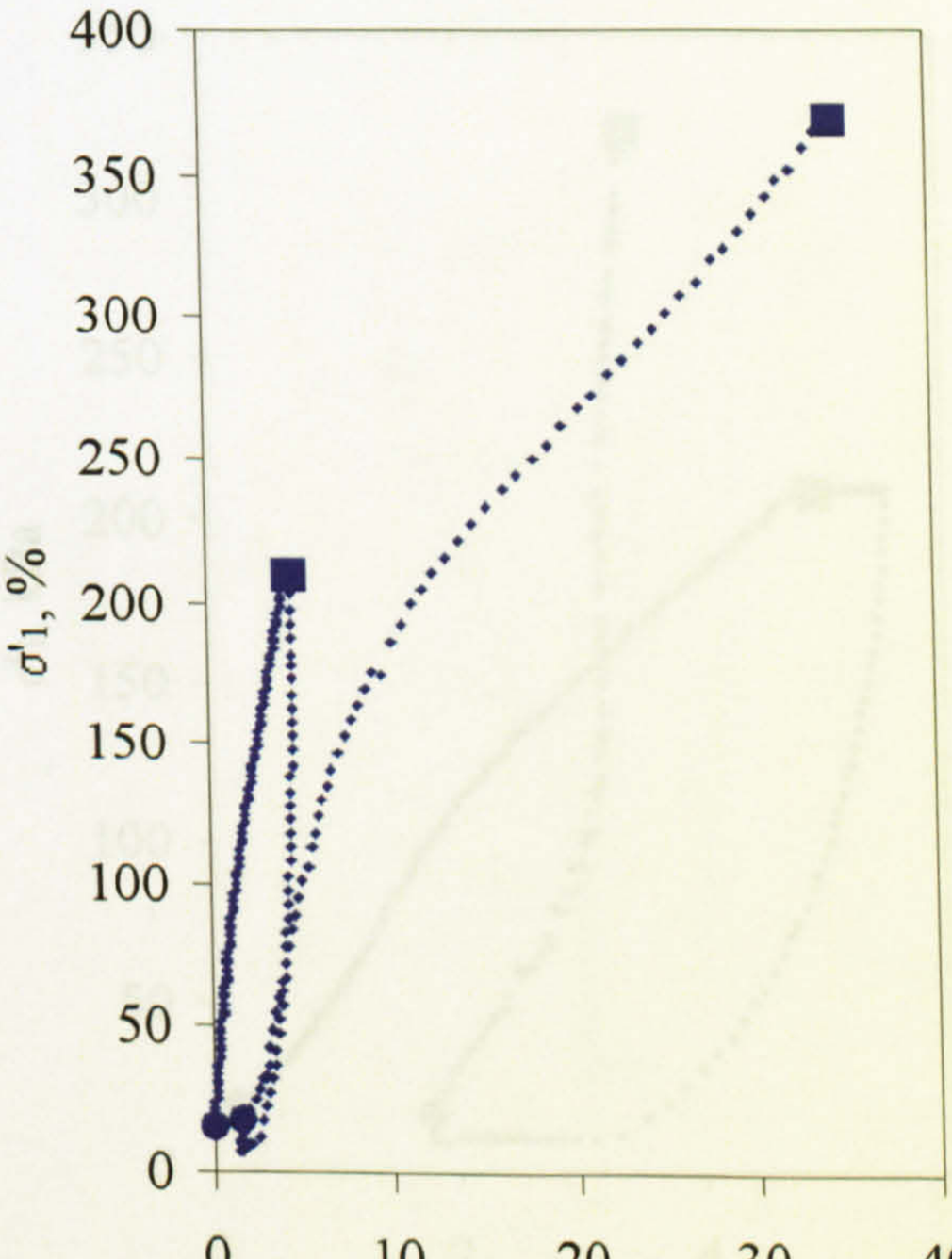

(d)

Figure 6.8. Stress-strain behaviour in Test B4 ($\eta_1 = 0$ and $\eta_2 = 1.30$): (a), (b) compression behaviour, (c) deviatoric behaviour and (d) axial behaviour.

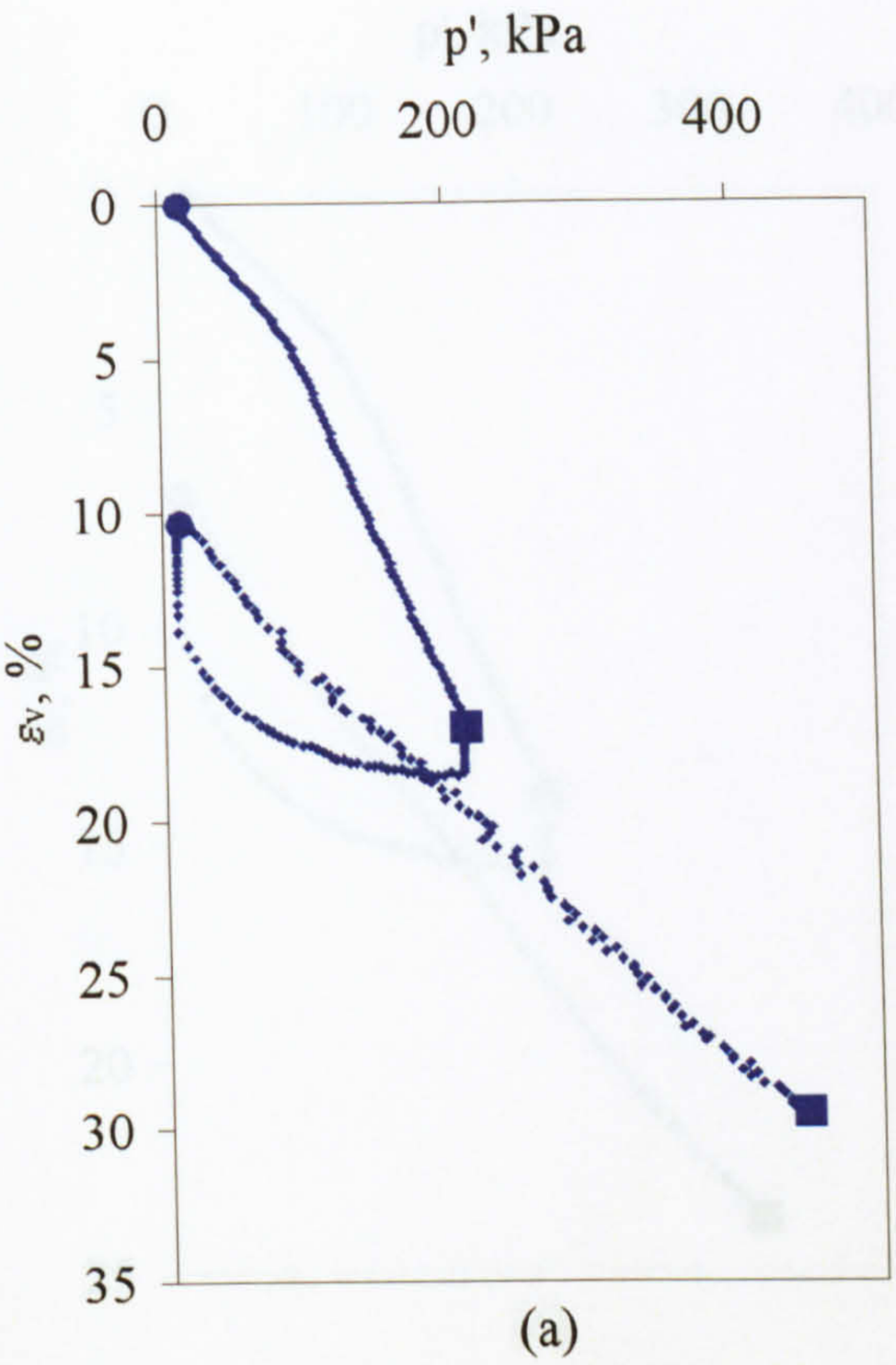

(a)

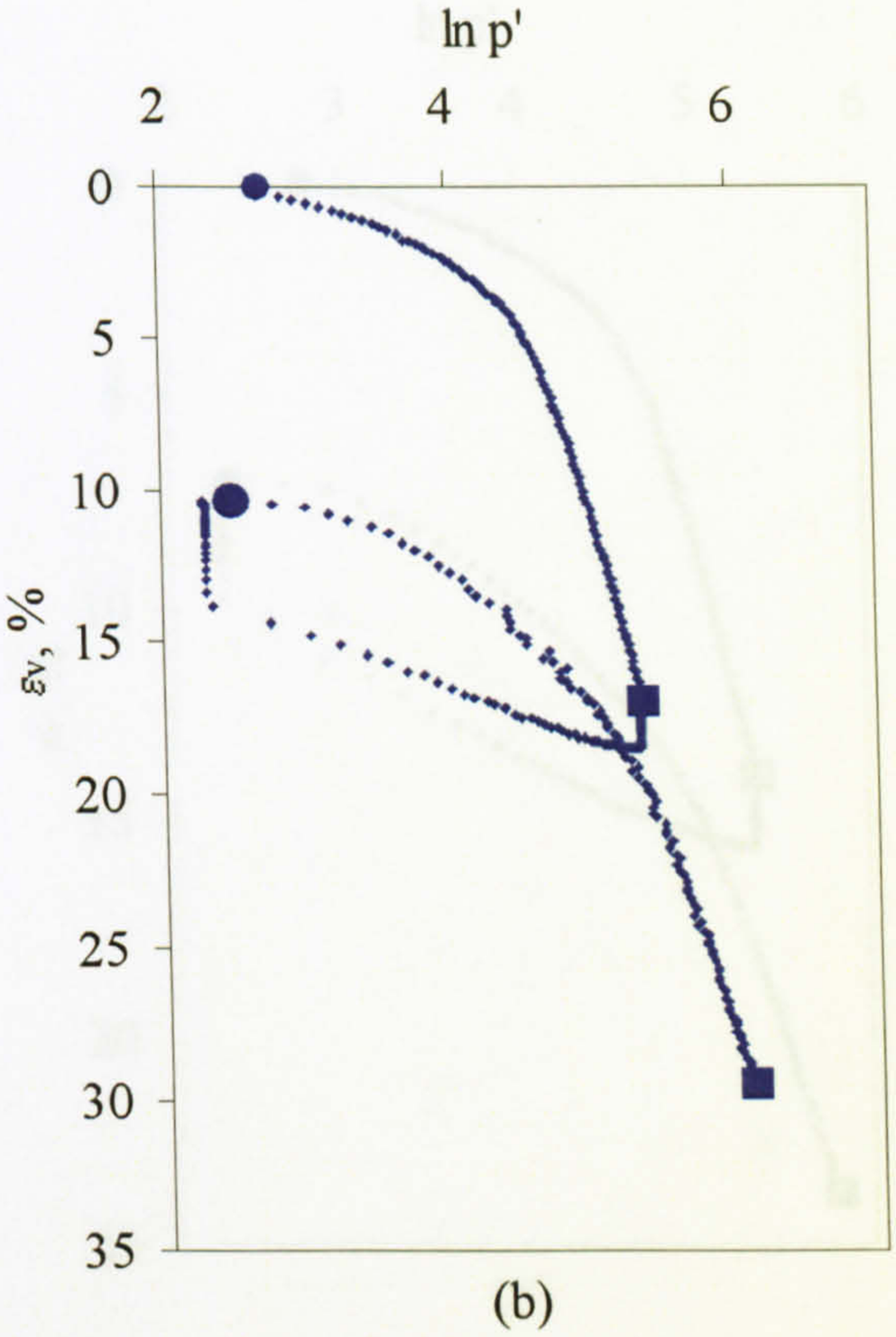

(b)

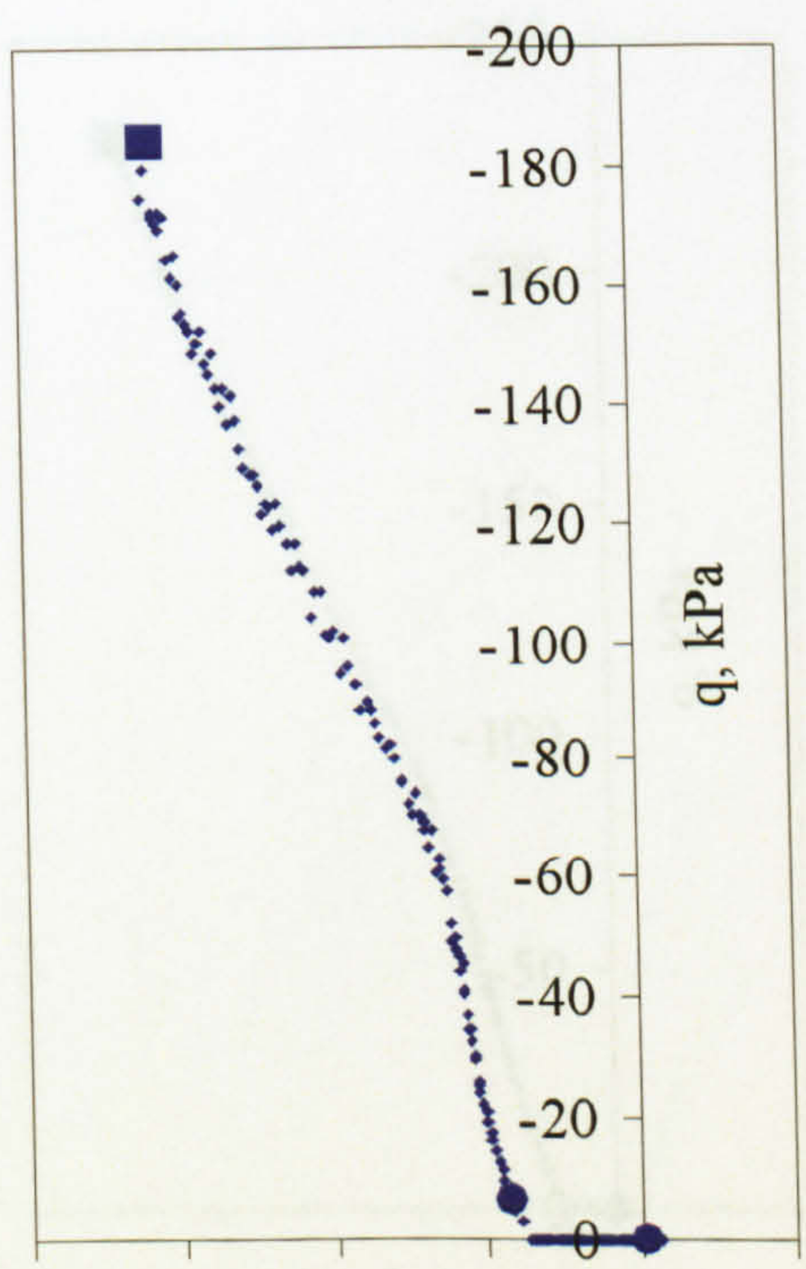

(c)

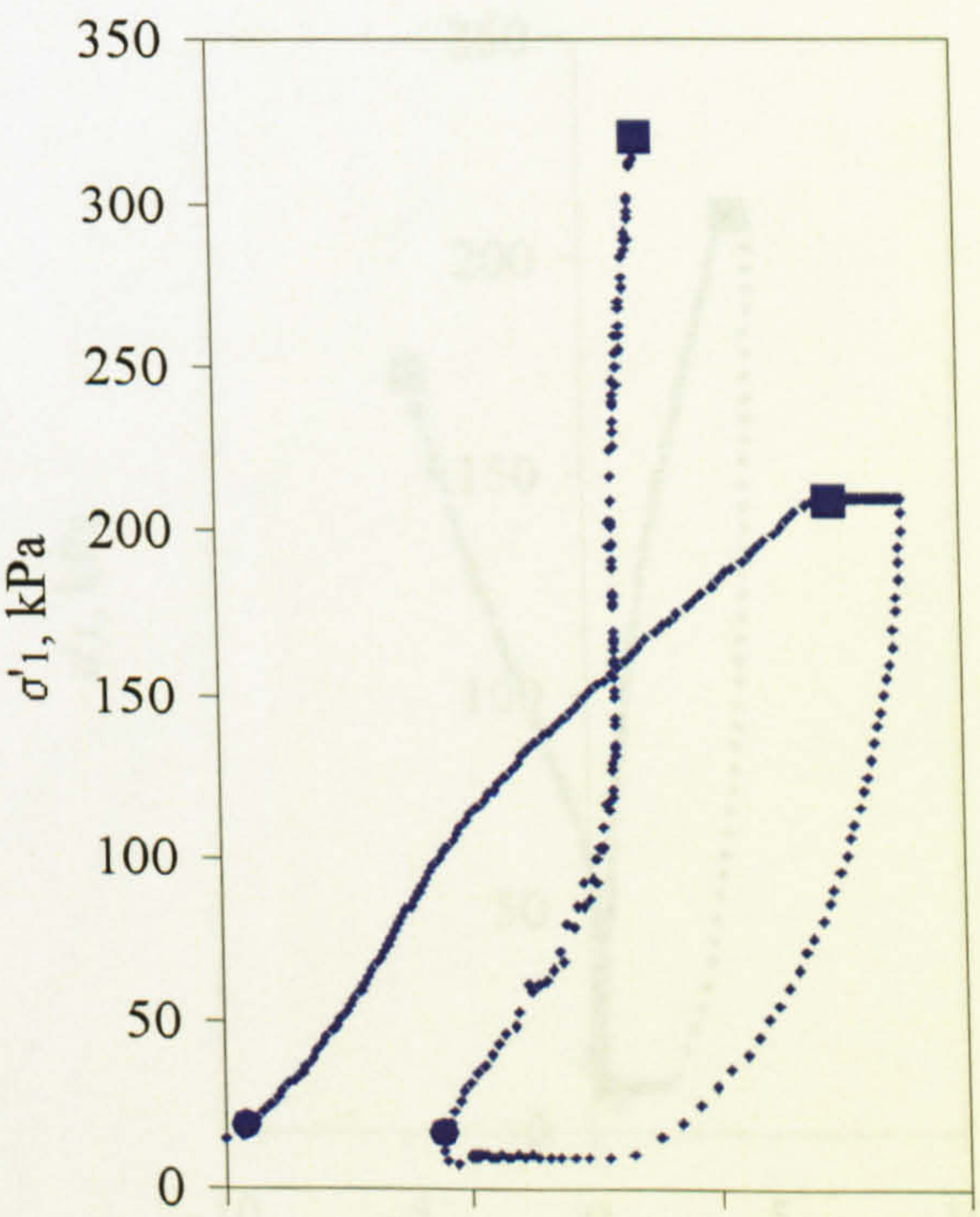

(d)

Figure 6.9. Stress-strain behaviour in Test B5 ($\eta_1 = 0$ and $\eta_2 = -0.40$): (a), (b) compression behaviour, (c) deviatoric behaviour and (d) axial behaviour.

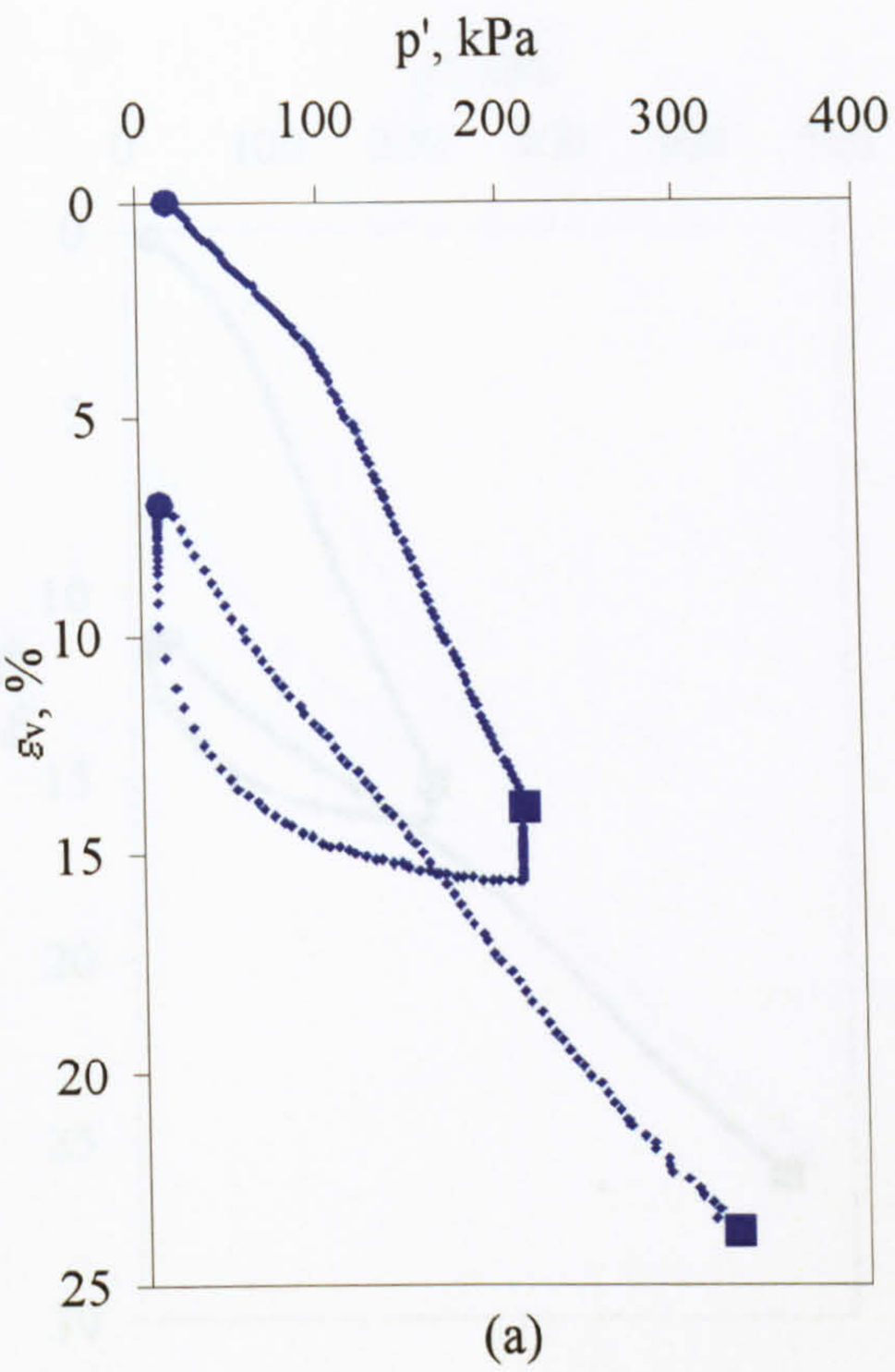

(a)

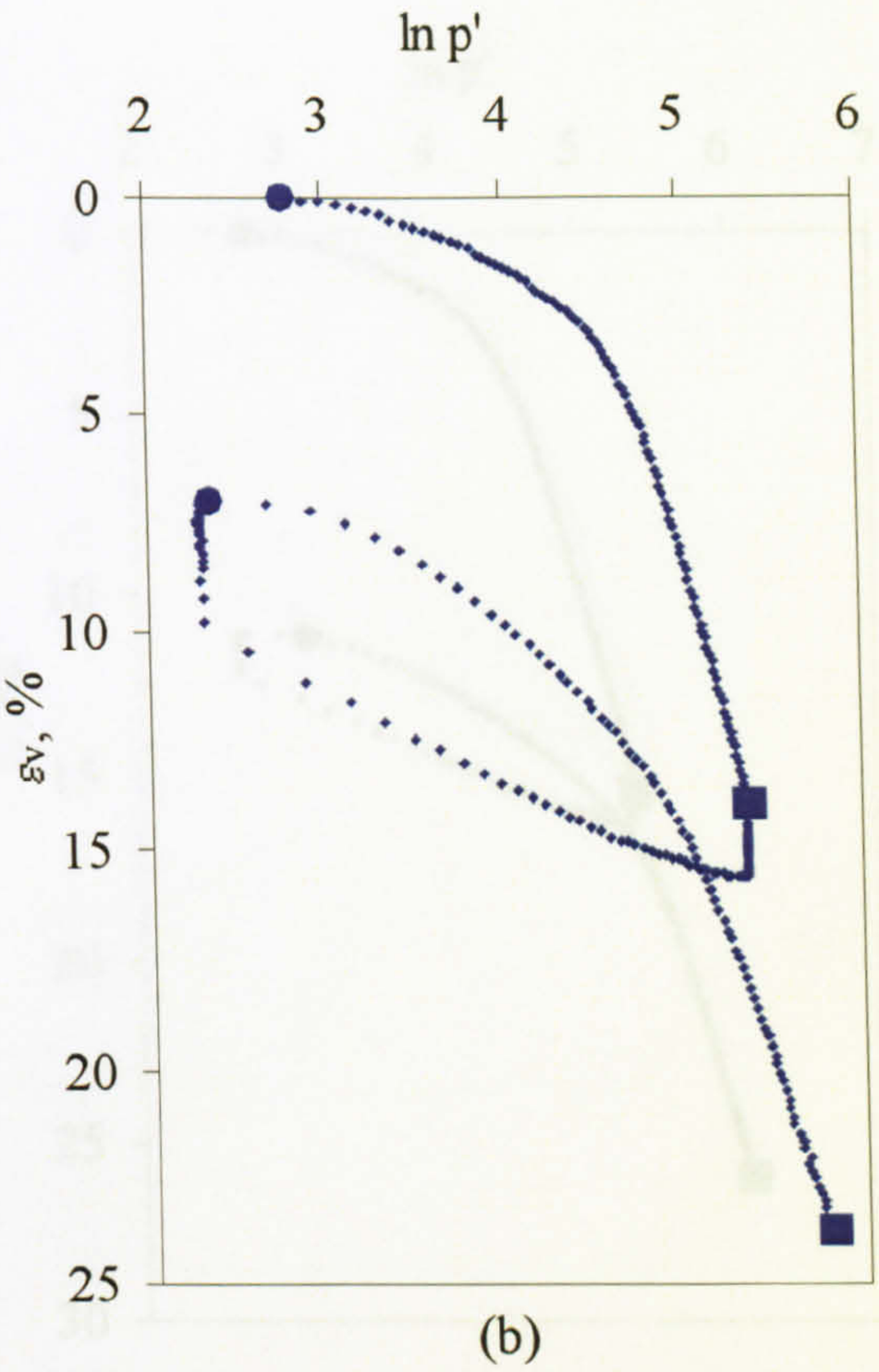

(b)

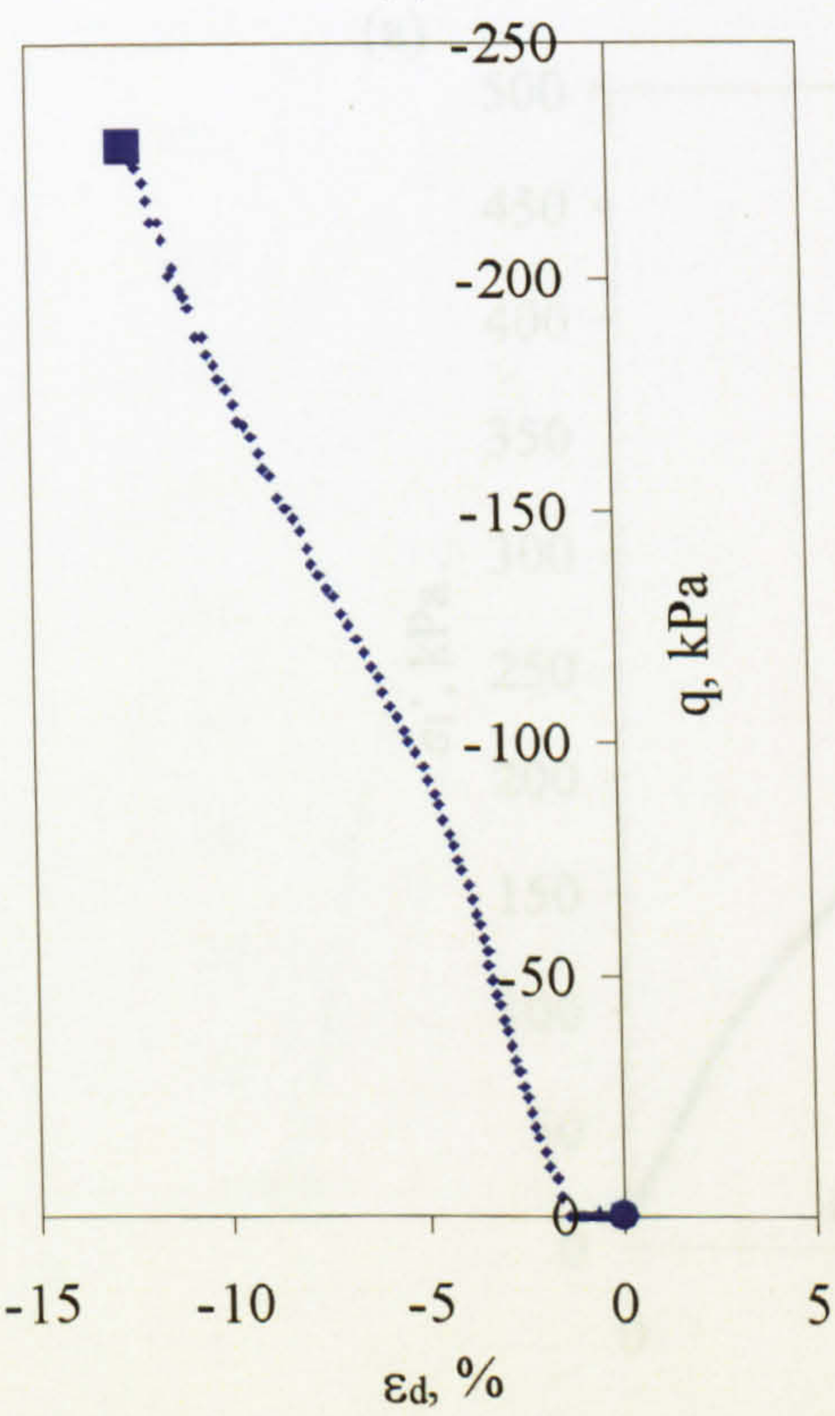

(c)

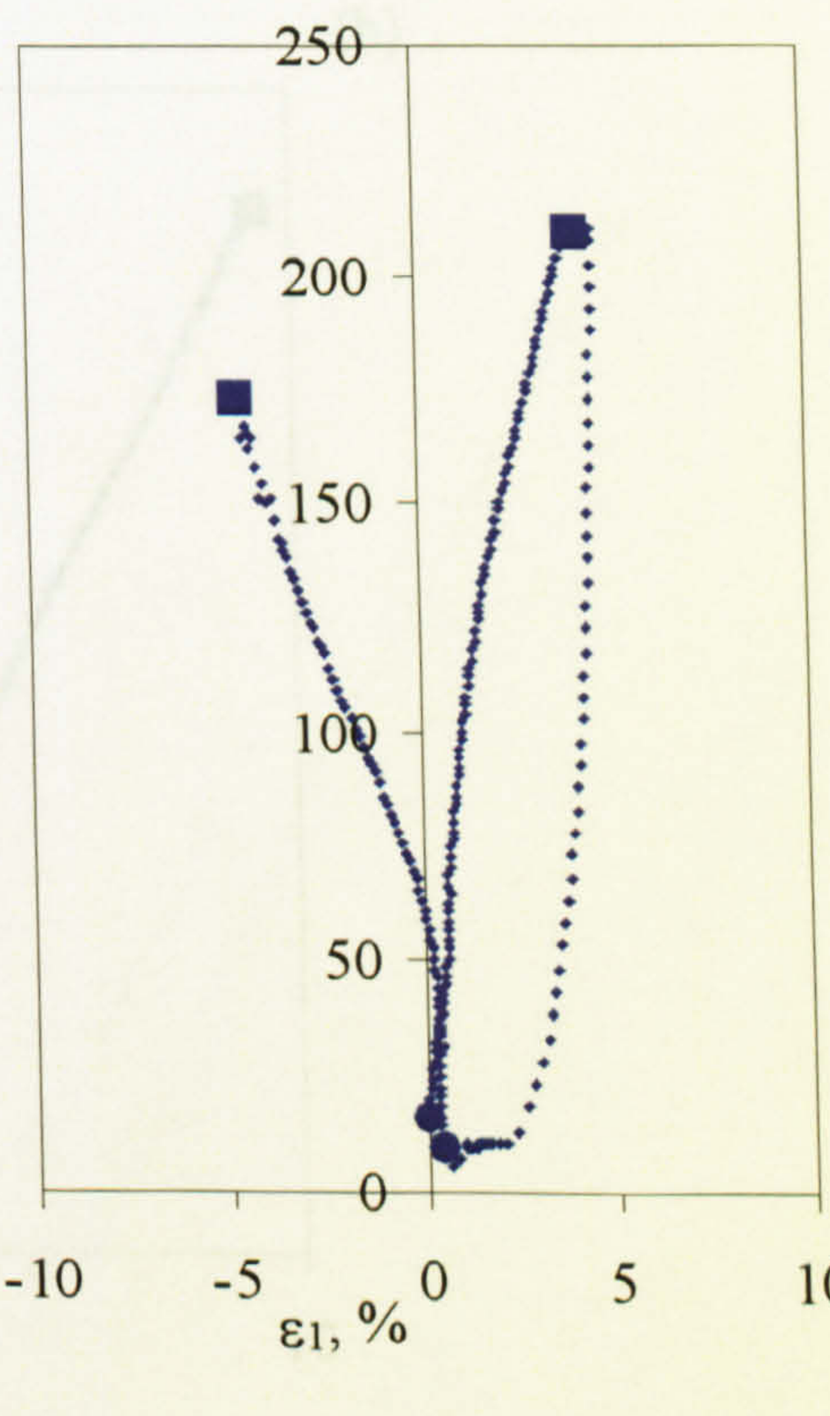

(d)

Figure 6.10. Stress-strain behaviour in Test B6 ($\eta_1 = 0$ and $\eta_2 = -0.70$): (a), (b) compression behaviour, (c) deviatoric behaviour and (d) axial behaviour.

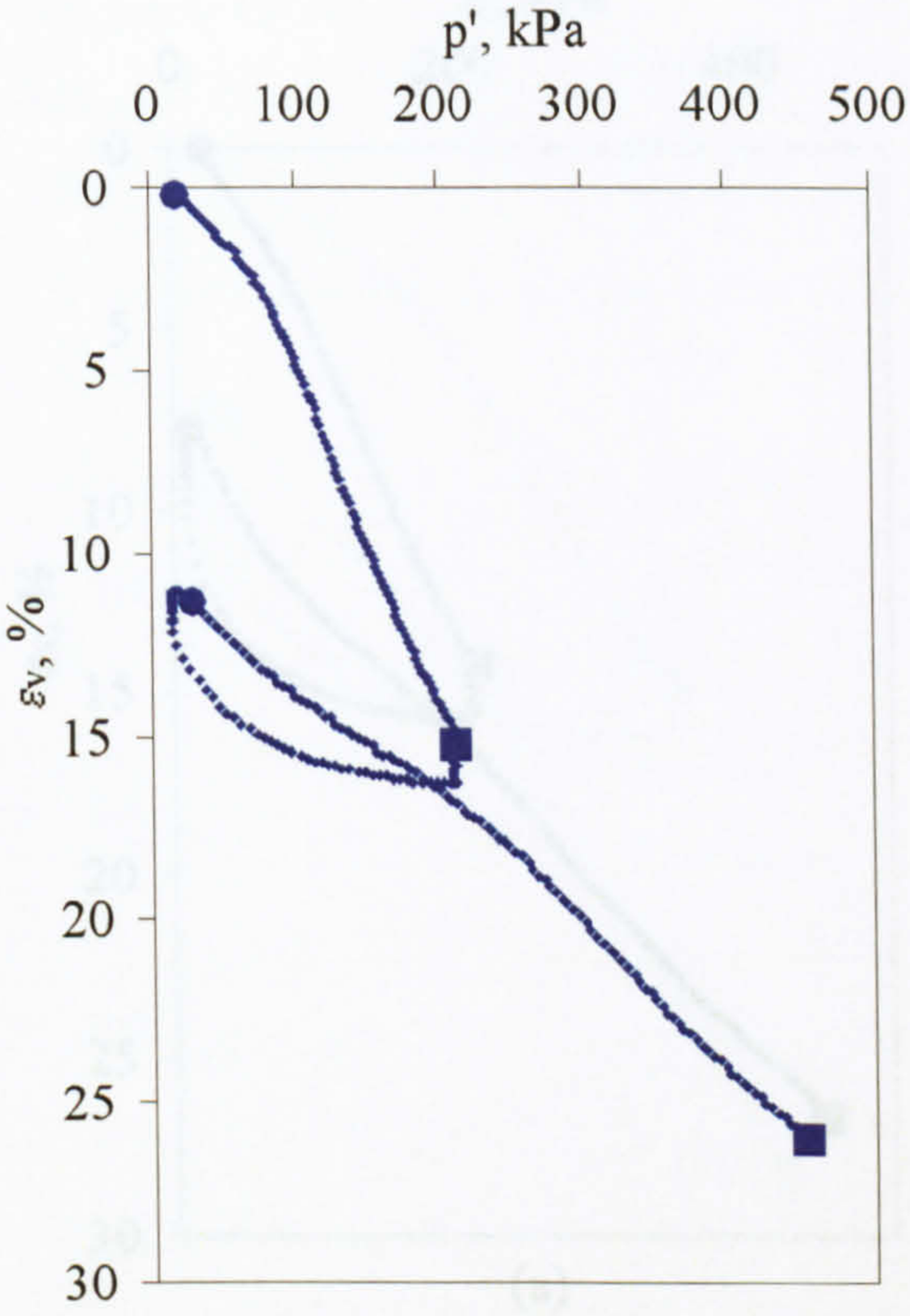

(a)

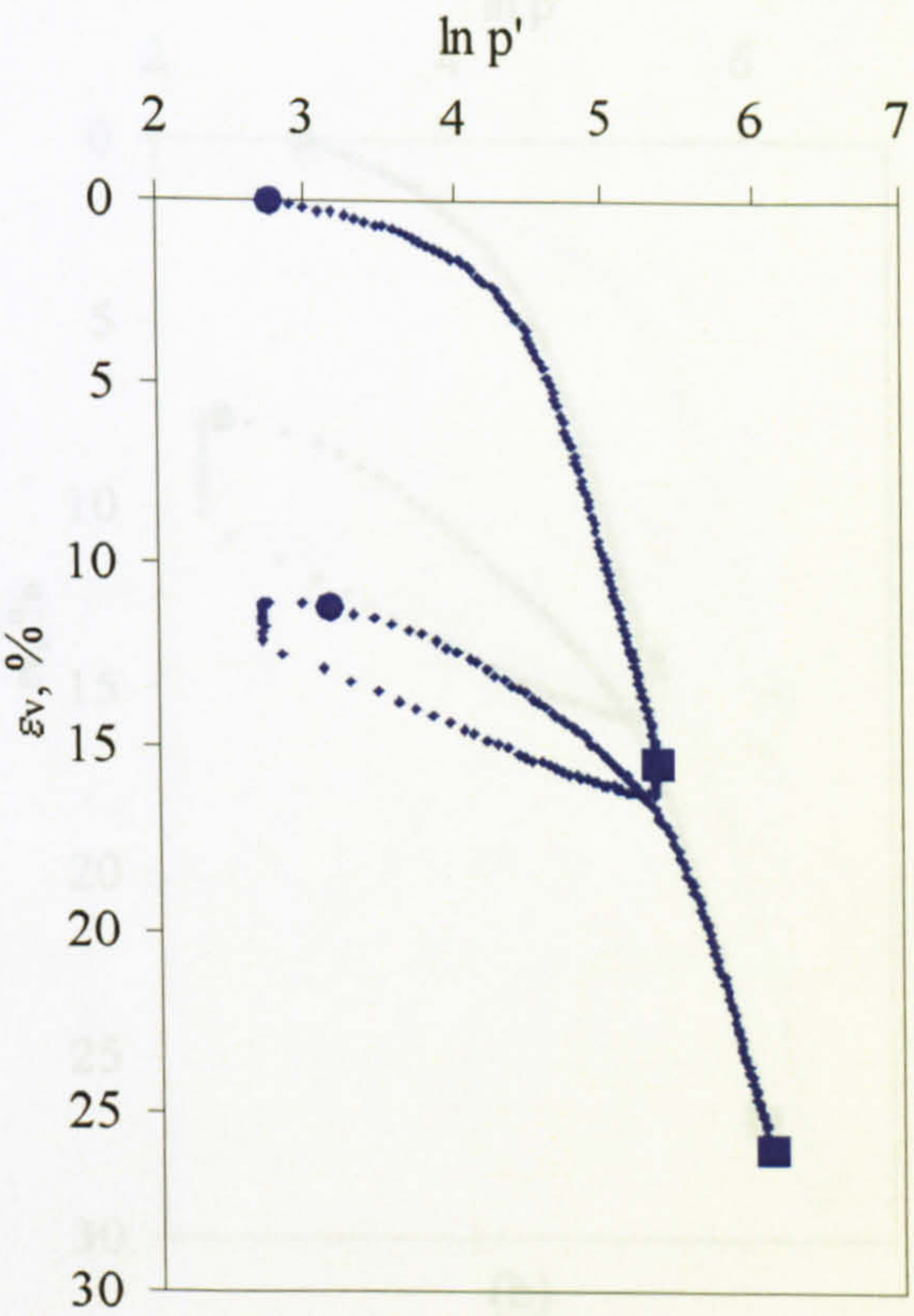

(b)

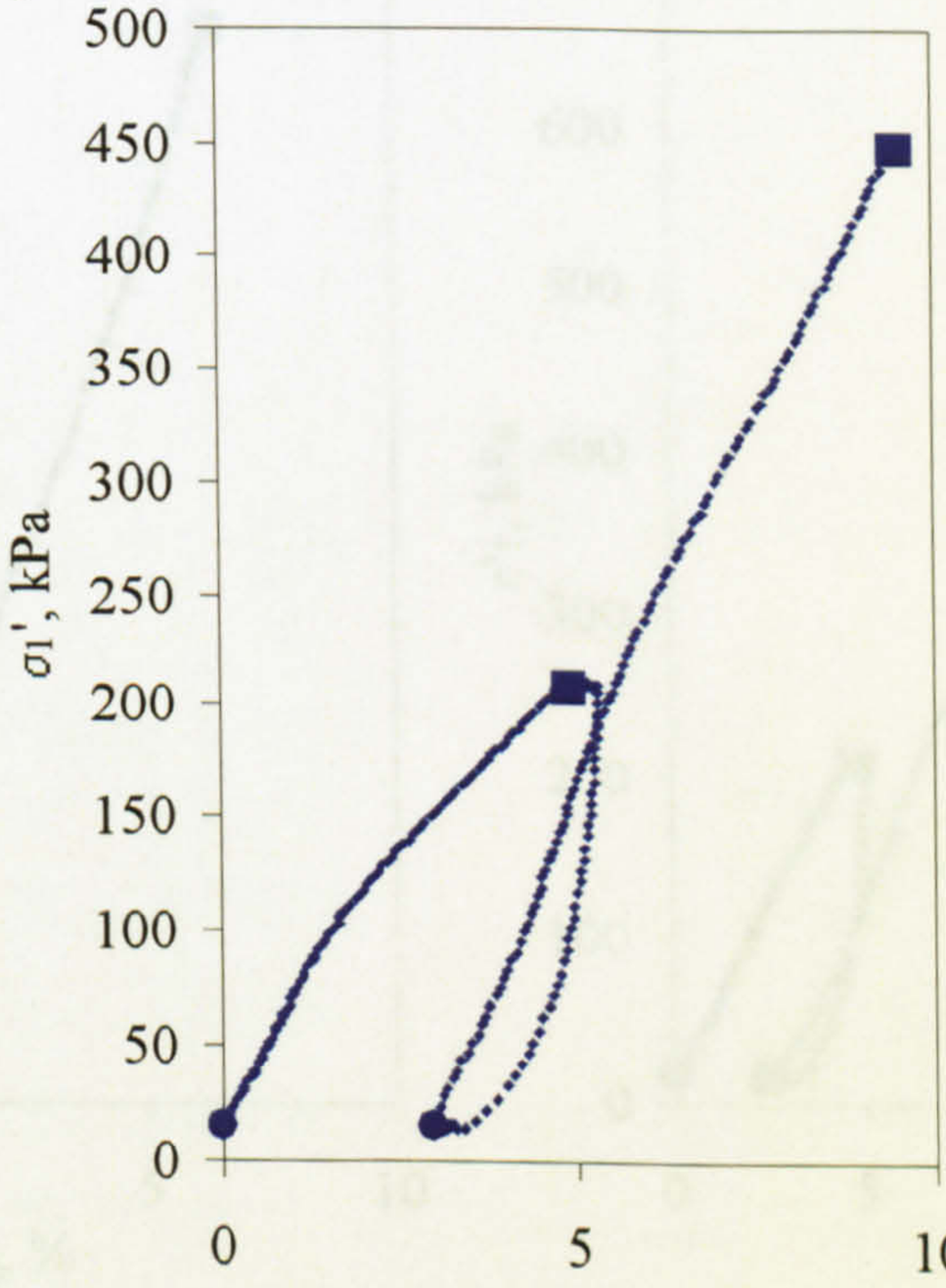

(c)

Figure 6.11. Stress-strain behaviour in Test B7 ($\eta_1 = 0$ and $\eta_2 = 0$): (a), (b) compression behaviour, (c) axial behaviour.

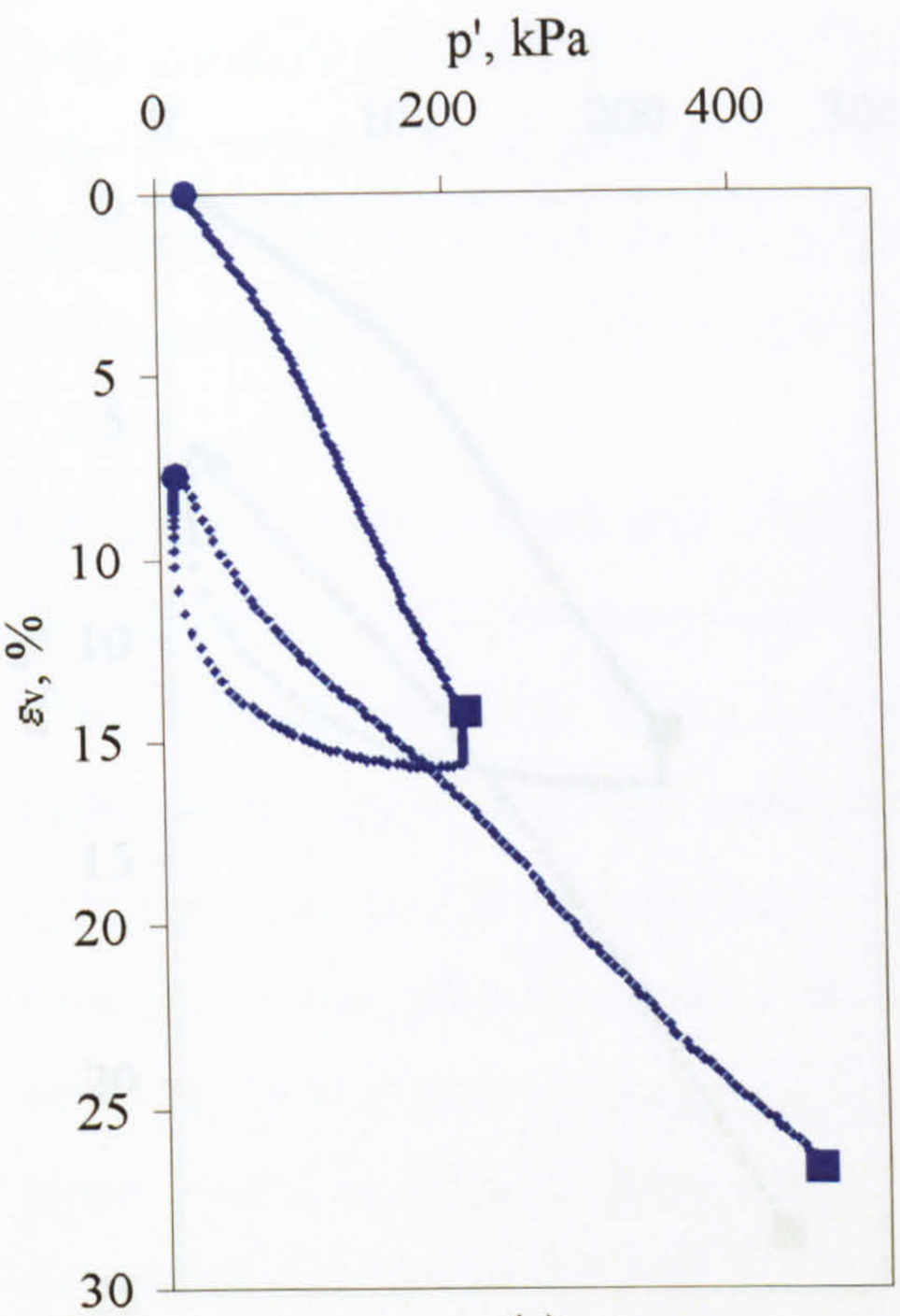

(a)

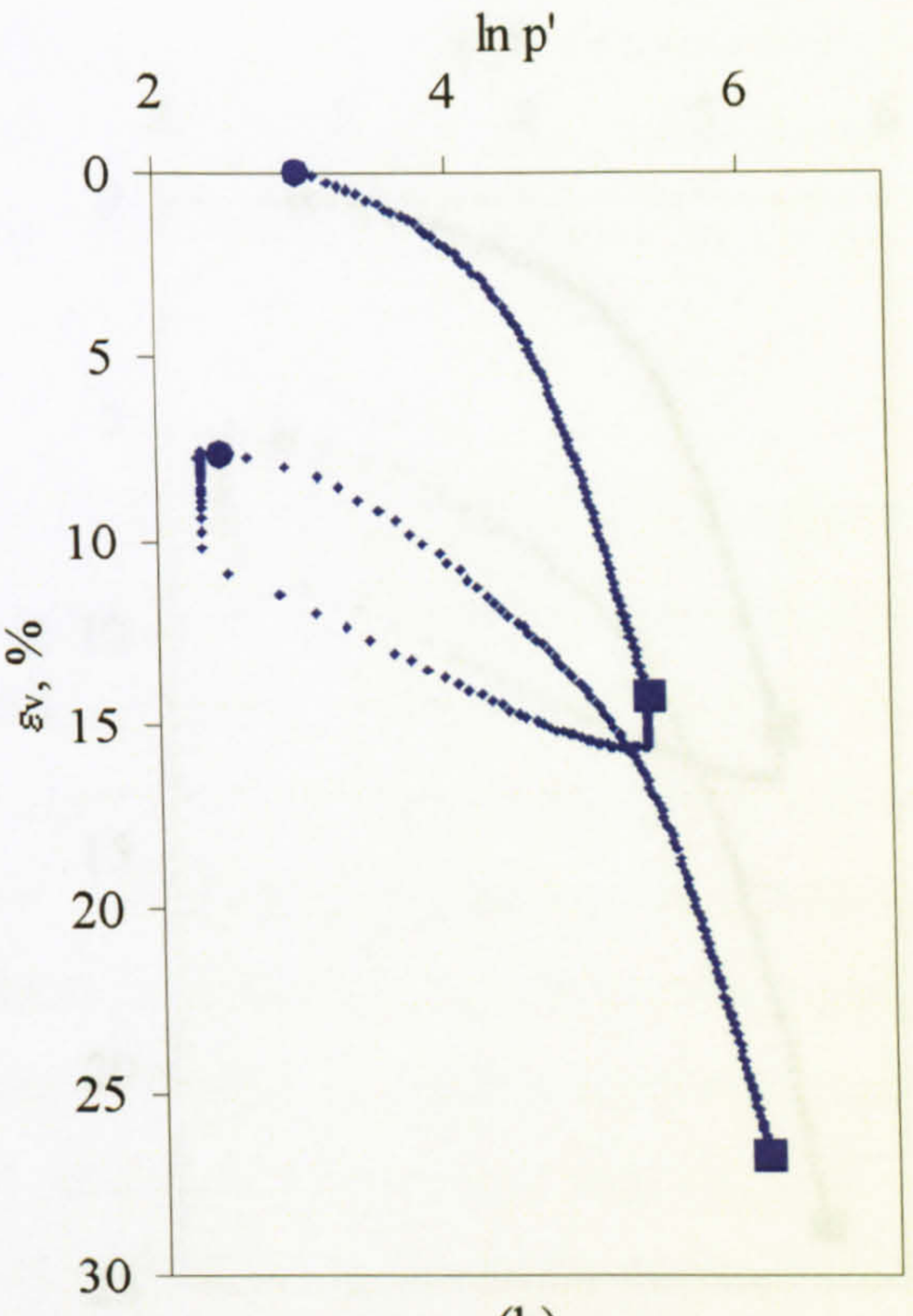

(b)

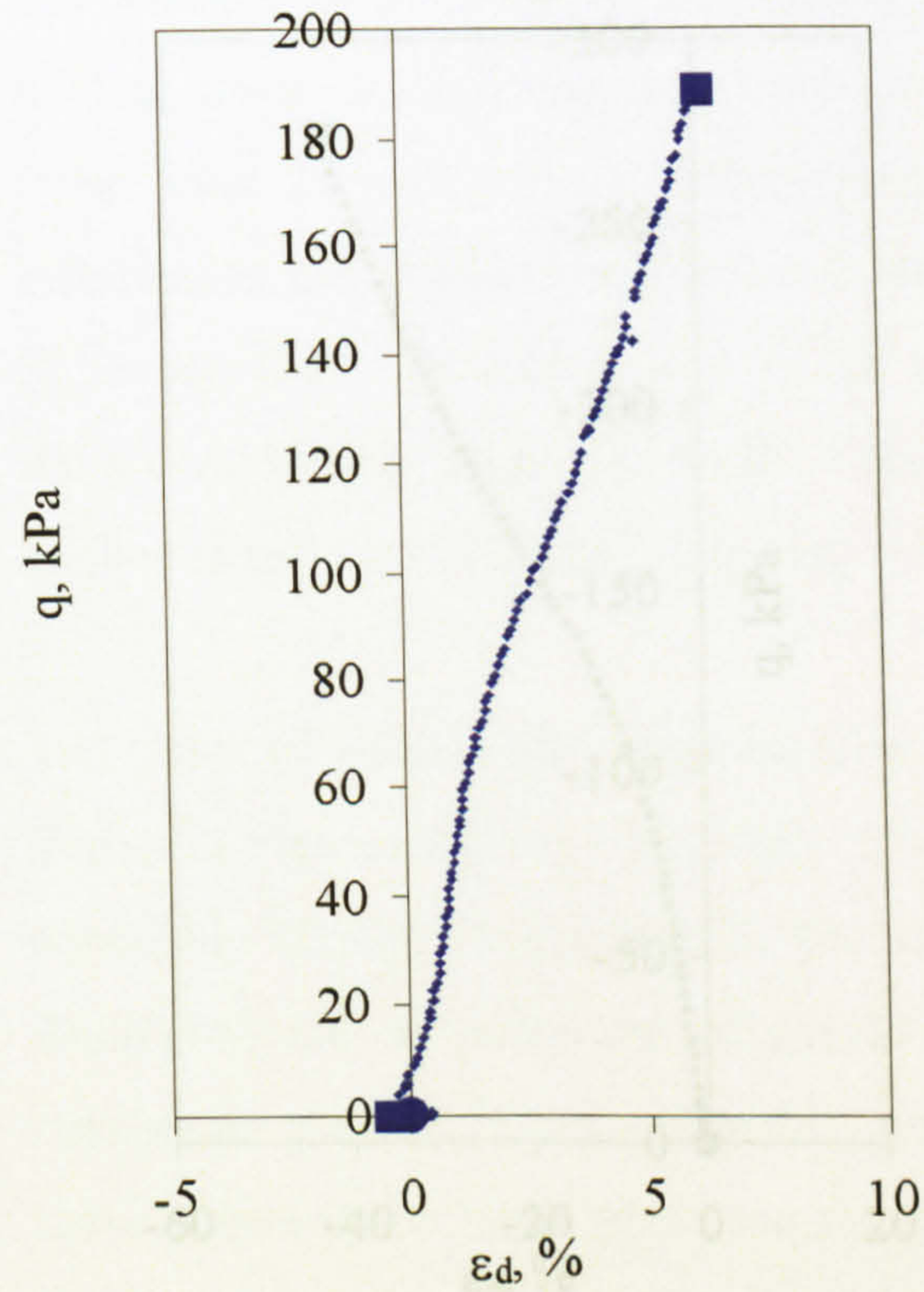

(c)

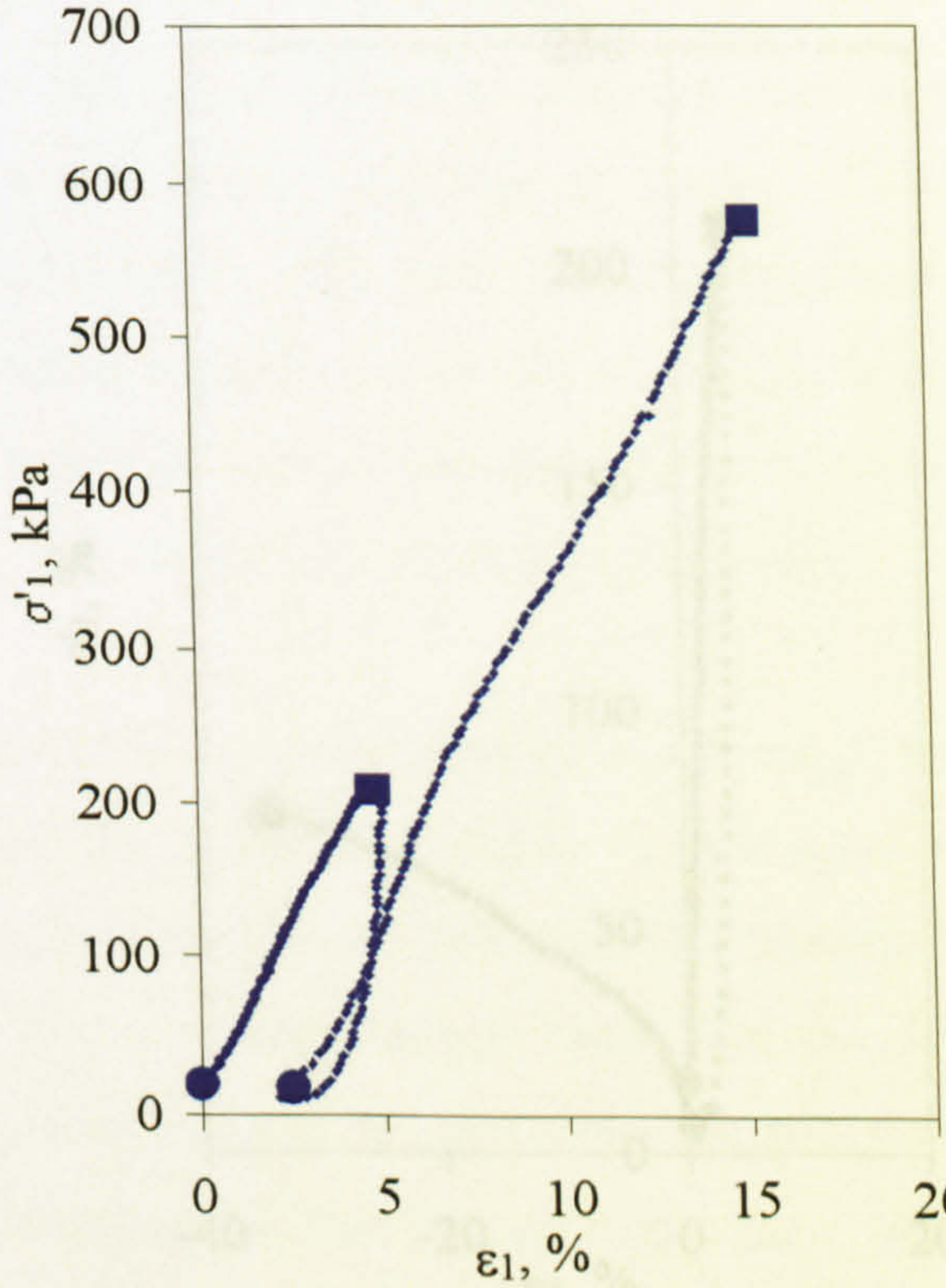

(d)

Figure 6.12. Stress-strain behaviour in Test B8 ($\eta_1 = 0$ and $\eta_2 = -0.40$): (a), (b) compression behaviour, (c) deviatoric behaviour, (d) axial behaviour.

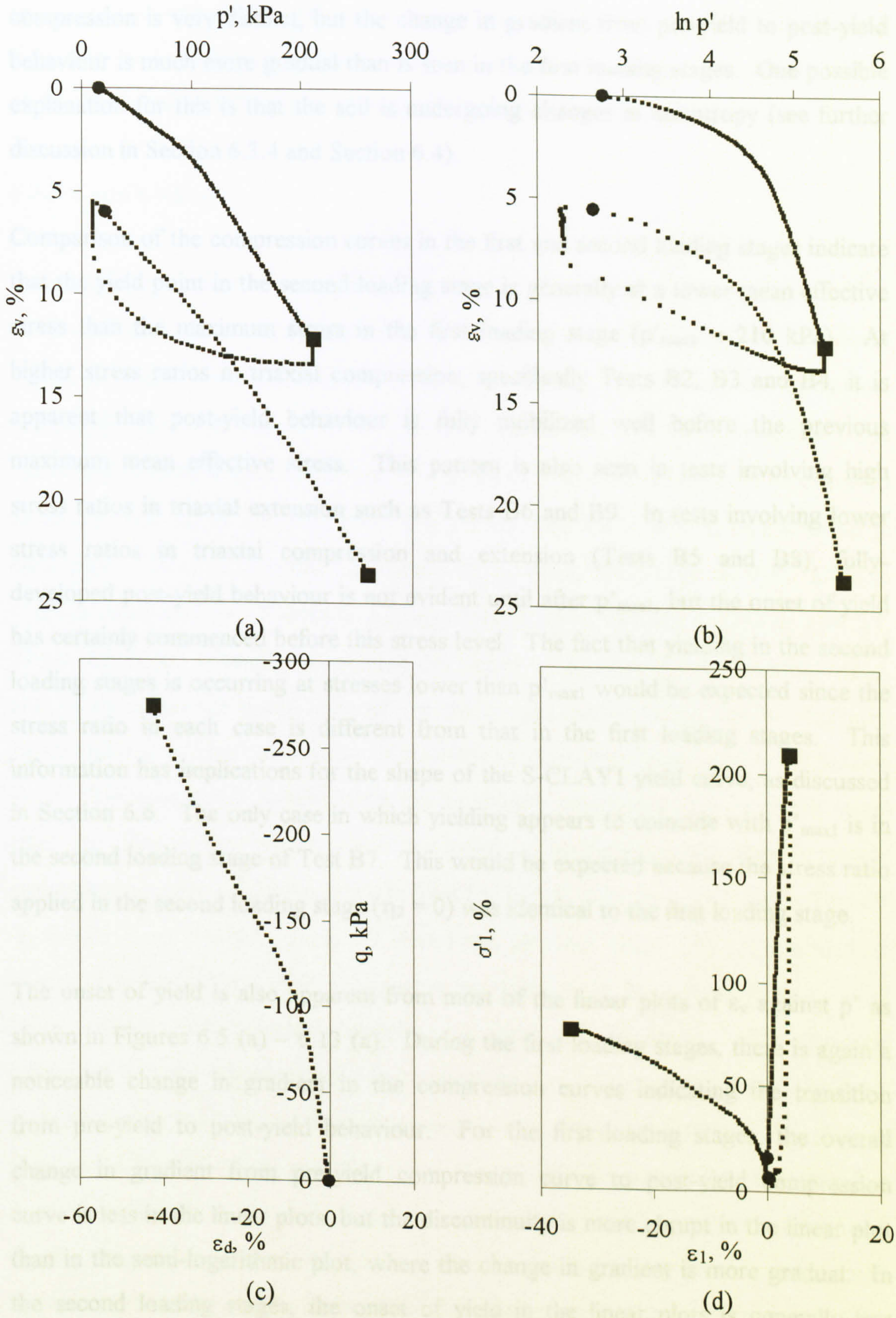

Figure 6.13. Stress-strain behaviour in Test B9 ($\eta_1 = 0$ and $\eta_2 = -1.02$): (a), (b) compression behaviour, (c) deviatoric behaviour, (d) axial behaviour.

compression is very distinct, but the change in gradient from pre-yield to post-yield behaviour is much more gradual than is seen in the first loading stages. One possible explanation for this is that the soil is undergoing changes in anisotropy (see further discussion in Section 6.3.4 and Section 6.4).

Comparison of the compression curves in the first and second loading stages indicate that the yield point in the second loading stage is generally at a lower mean effective stress than the maximum stress in the first loading stage (p'_{max1} = 210 kPa). At higher stress ratios in triaxial compression, specifically Tests B2, B3 and B4, it is apparent that post-yield behaviour is fully mobilized well before the previous maximum mean effective stress. This pattern is also seen in tests involving high stress ratios in triaxial extension such as Tests B6 and B9. In tests involving lower stress ratios in triaxial compression and extension (Tests B5 and B8), fully-developed post-yield behaviour is not evident until after p'_{max1}, but the onset of yield has certainly commenced before this stress level. The fact that yielding in the second loading stages is occurring at stresses lower than p'_{max1} would be expected since the stress ratio in each case is different from that in the first loading stages. This information has implications for the shape of the S-CLAY1 yield curve, as discussed in Section 6.6. The only case in which yielding appears to coincide with p'_{max1} is in the second loading stage of Test B7. This would be expected because the stress ratio applied in the second loading stage ($\eta_2 = 0$) was identical to the first loading stage.

The onset of yield is also apparent from most of the linear plots of ε_v against p' as shown in Figures 6.5 (a) – 6.13 (a). During the first loading stages, there is again a noticeable change in gradient in the compression curves indicating the transition from pre-yield to post-yield behaviour. For the first loading stages, the overall change in gradient from pre-yield compression curve to post-yield compression curve is less in the linear plots, but the discontinuity is more abrupt in the linear plot than in the semi-logarithmic plot, where the change in gradient is more gradual. In the second loading stages, the onset of yield in the linear plots is generally less apparent than during the first loading stages. In tests reloaded at high stress ratios in triaxial compression (Tests B2, B3 and B4), yield is detectable in the change in gradient of the compression curve. However, in tests reloaded at low stress ratios in

triaxial compression (Tests B7 and B8) and in triaxial extension (Tests B5, B6 and B9), there is very little change in the gradient of the compression curve and the onset of yield is therefore difficult to detect from the linear plot.

6.3.3 λ and κ values

Semi-logarithmic plots of specific volume v plotted against ln p' have been used to obtain values of the post-yield compression slope λ, as shown in Figure 6.14. Each value of λ has been determined from the steepest portion of the post-yield compression curve in Figure 6.14. Values of λ from the first loading stage (λ_1) and the second loading stage (λ_2) are listed in Table 6.3. Values of λ_1 would be expected to be the same for all tests in Series B, given that the stress ratio η_1 was identical in each case. Table 6.3 shows that values of λ_1 range from 0.30 to 0.38, with an average value of 0.33. Values of λ_2 range from 0.25 in Test B2 to 0.33 in Test B4. These values are generally lower than the values of λ_1 from the first loading stage. It is possible that the lower value of λ in the second loading stages can be attributed to the effects of destructuration. This issue is examined more closely in Section 6.4.3. There does not appear to be any significant correlation of λ_2 with the stress ratio, η_2. The highest values of λ_2 correspond to the highest stress ratios in triaxial compression and triaxial extension. In Test B4 $\lambda_2 = 0.31$ at $\eta_2 = 1.30$ and in Test B9 $\lambda_2 = 0.33$ at $\eta_2 = -1.00$. Table 6.3 shows that all other values of λ_2 at intermediate values of η_2 lie within a relatively small range (0.25-0.27). Semi-logarithmic ε_v: ln p' plots indicate that pre-yield behaviour is generally non-linear. The pre-yield behaviour actually appears rather more linear in linear ε_v: p' plots than in the semi-logarithmic ε_v: ln p' plots. This is apparent from the ε_v: p' and ε_v: ln p' plots in Figures 6.5 (a) to 6.13 (a) and Figures 6.5 (b) to 6.13 (b) respectively. It is therefore extremely difficult to obtain values of pre-yield compressibility κ from any of these loading stages. In contrast, the swelling curves observed during the unloading stages appear approximately linear in the semi-logarithmic plots, whereas they appear to be non-linear in the linear plots. It was therefore possible to determine values of κ from these swelling lines. These values are listed as κ_{unload} in Table 6.3. The values of κ_{unload} were taken as the average gradient of the swelling line, ignoring any additional

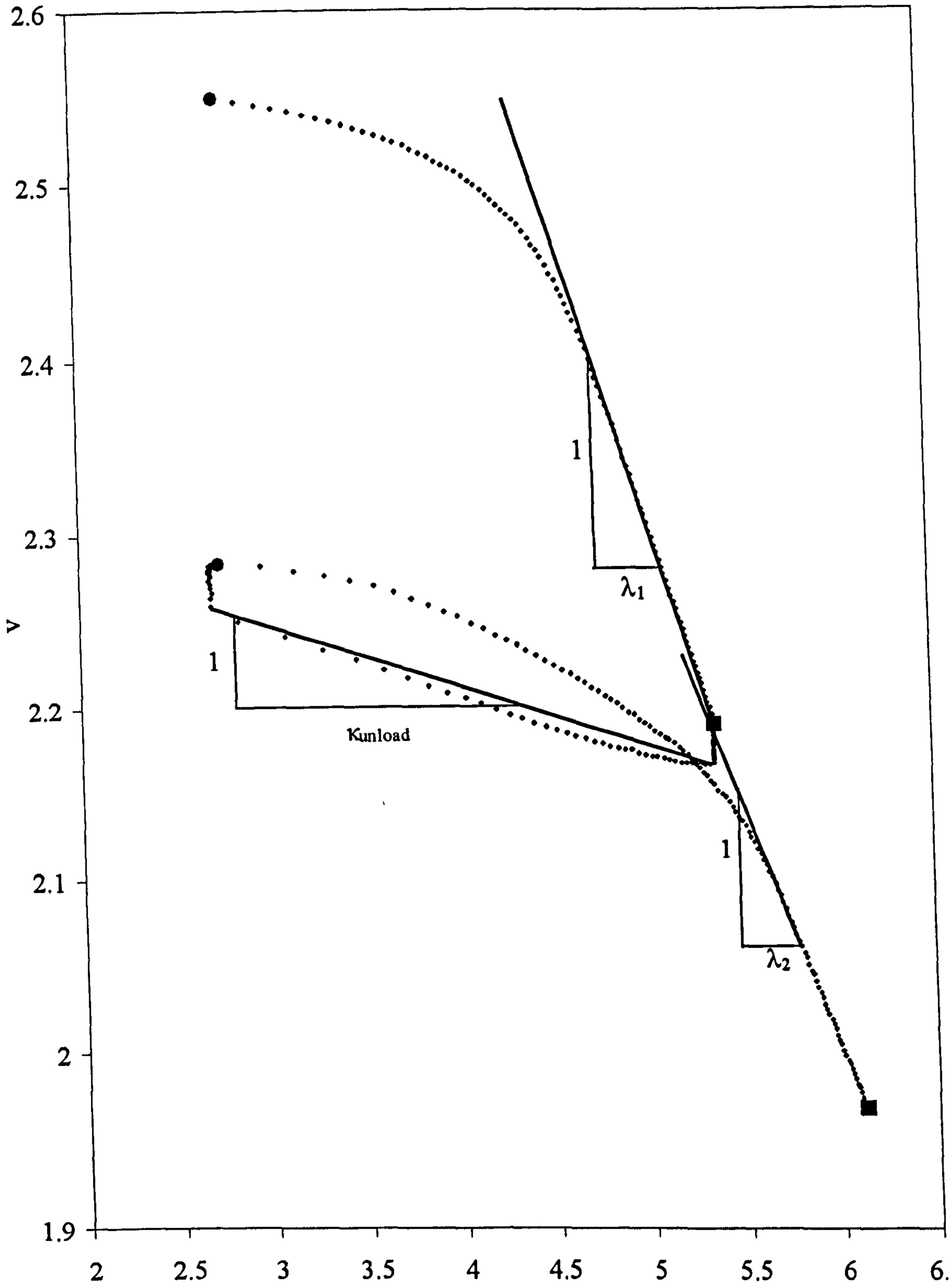

Figure 6.14. Measurement of λ and κ values in Test B7.

TEST	η_1	λ_1	κ_{unload}	η_2	λ_2
B1	0.00	0.34	0.044	-	-
B2	0.00	0.34	0.038	0.70	0.25
B3	0.00	0.31	0.028	1.01	0.27
B4	0.00	0.30	0.035	1.30	0.31
B5	0.00	0.38	0.037	-0.40	0.27
B6	0.00	0.37	0.044	-0.70	0.26
B7	0.00	0.34	0.034	0.00	0.26
B8	0.00	0.30	0.039	0.40	0.27
B9	0.00	0.32	0.039	-1.00	0.33

Table 6.3. λ and κ values observed in Test Series B.

swelling during the 24-hour rest period after unloading (see Figure 6.14; also see Section 6.4.4 for discussion on swelling during rest periods). The average value of κ_{unload} was 0.038, with individual values ranging from 0.028 to 0.044.

6.3.4 Other stress-strain plots

Plots of q: ε_d in Figures 6.5 (c) - 6.13 (c) show that, during second loading stages, yield is relatively clear-cut in tests performed at high stress ratios in triaxial compression (such as Tests B2, B3 and B4). The change in gradient is still noticeable (but less clear-cut) at a lower stress ratio in Test B8. When reloading in triaxial extension (Tests B5, B6 and B9), there is also a change in gradient in the q: ε_d stress-strain curve, but this is much more gradual than in the other tests. Post-yield behaviour is highly non-linear in Tests B2 and B3 (both at high stress ratios in triaxial compression).

σ'_1: ε_1 plots in Figures 6.5 (d) – 6.13 (d) show that yield points are distinct during the first loading stages, again associated with a change of gradient in the stress-strain curve. In the second loading stages, the pattern is similar to the linear ε_v: p' plots. Yield is more clearly defined at high stress ratios in triaxial compression than in tests involving low stress ratios in triaxial compression or tests in triaxial extension.

6.3.5. Strain paths

First loading stages

The strain paths involved in each of the first loading stages in Test Series B have been collated and are presented in Figure 6.15. The yield points identified from v: ln p' plots in the first loading stages (see Section 6.4) ranged from 74 – 86 kPa and this range is marked as p'_{y1} on Figure 6.15. The yield points are coincident with a change in strain path direction. Each curve indicates that a small amount of positive deviatoric strain (0.1 to 0.4 %) has been generated prior to the yield point. This suggests that the pre-yield behaviour is anisotropic, since it would be expected that under isotropic loading, only volumetric strains would be generated for an isotropic soil. A number of authors, including Graham et al. (1983), have shown that the elastic behaviour of natural soils is significantly anisotropic. They have demonstrated that in triaxial stress space, three elastic parameters can be determined from the following relationship:

$$\begin{bmatrix} \delta p' \\ \delta q \end{bmatrix} = \begin{bmatrix} K^* & J \\ J & 3G^* \end{bmatrix} \begin{bmatrix} \delta \varepsilon_v^e \\ \delta \varepsilon_d^e \end{bmatrix} \tag{6.6}$$

where K* and G* are modified values of bulk modulus and shear modulus respectively and the parameter J describes the cross-linkage between shear and volumetric strains. For an isotropic soil, J is equal to zero and it has been shown that for most natural (anisotropic) soils, J is negative (Graham et al. 1983). The possibility of elastic anisotropy is discussed more fully in conjunction with Test Series C (see Section 6.4.), but some initial evidence can be gained in the context of Test Series B.

After the yield point has been exceeded, each curve indicates that negative shear strains are initially developing. This suggests that plastic anisotropy is producing shear strains of the opposite sense to those produced by elastic anisotropy. As each test progresses it can be seen that the plastic anisotropy gradually reduces. As the isotropic stress is increased further, positive shear strains again begin to develop at a

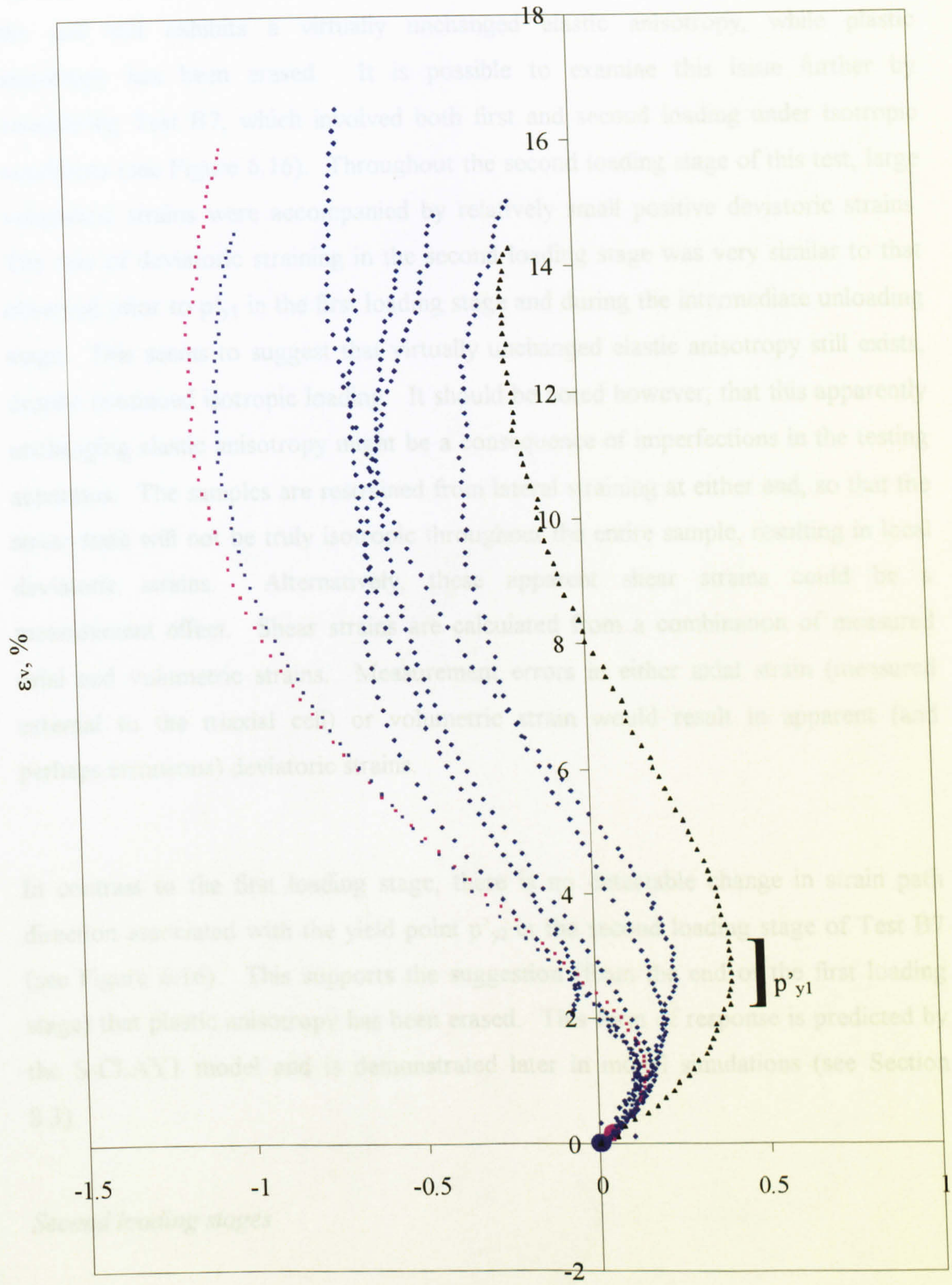

Figure 6.15. Strain paths for first loading stages in Test Series B ($\eta_1 = 0$).

rate that is similar to the pre-yield rate of positive shear straining. This suggests that the soil still exhibits a virtually unchanged elastic anisotropy, while plastic anisotropy has been erased. It is possible to examine this issue further by considering Test B7, which involved both first and second loading under isotropic conditions (see Figure 6.16). Throughout the second loading stage of this test, large volumetric strains were accompanied by relatively small positive deviatoric strains. The rate of deviatoric straining in the second loading stage was very similar to that observed prior to p'_{y1} in the first loading stage and during the intermediate unloading stage. This seems to suggest that virtually unchanged elastic anisotropy still exists, despite continued isotropic loading. It should be noted however, that this apparently unchanging elastic anisotropy might be a consequence of imperfections in the testing apparatus. The samples are restrained from lateral straining at either end, so that the stress state will not be truly isotropic throughout the entire sample, resulting in local deviatoric strains. Alternatively, these apparent shear strains could be a measurement effect. Shear strains are calculated from a combination of measured axial and volumetric strains. Measurement errors in either axial strain (measured external to the triaxial cell) or volumetric strain would result in apparent (and perhaps erroneous) deviatoric strains.

In contrast to the first loading stage, there is no detectable change in strain path direction associated with the yield point p'_{y2} in the second loading stage of Test B7 (see Figure 6.16). This supports the suggestion (from the end of the first loading stage) that plastic anisotropy has been erased. This form of response is predicted by the S-CLAY1 model and is demonstrated later in model simulations (see Section 8.3).

Second loading stages

Strain paths, plotted in terms of deviatoric and volumetric strains, for all test stages in Series B (except Test B1) are shown in Figure 6.17 (in ascending order of η_2). The yield points during second loading, identified from v: ln p' plots (see Section 6.5) are indicated on the plots as open circles and labelled Y_2. The plots show that both pre-yield and post-yield patterns of straining are highly dependent on the stress

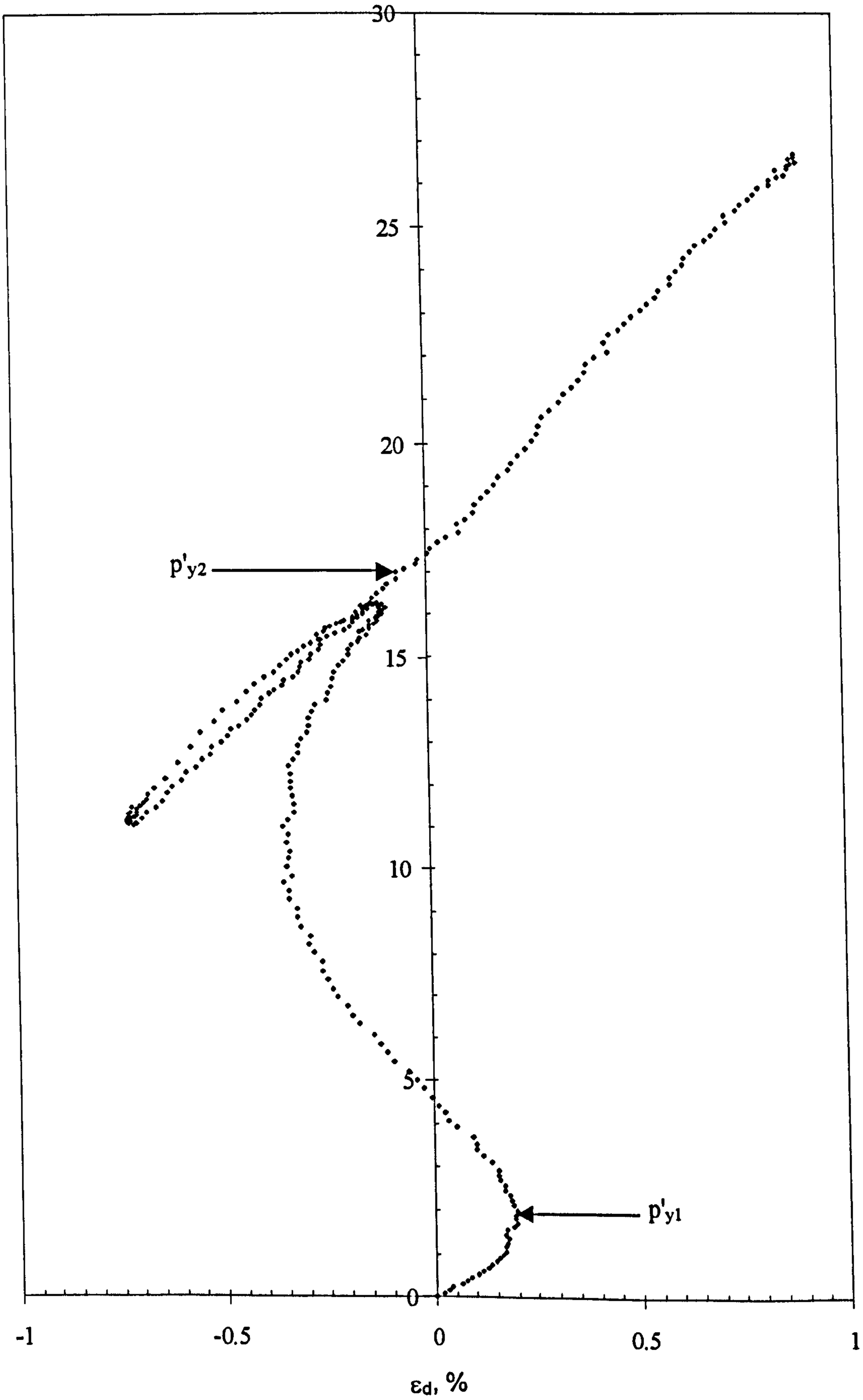

Figure 6.16. Strain path for Test B7 ($\eta_1 = 0$, $\eta_2 = 0$).

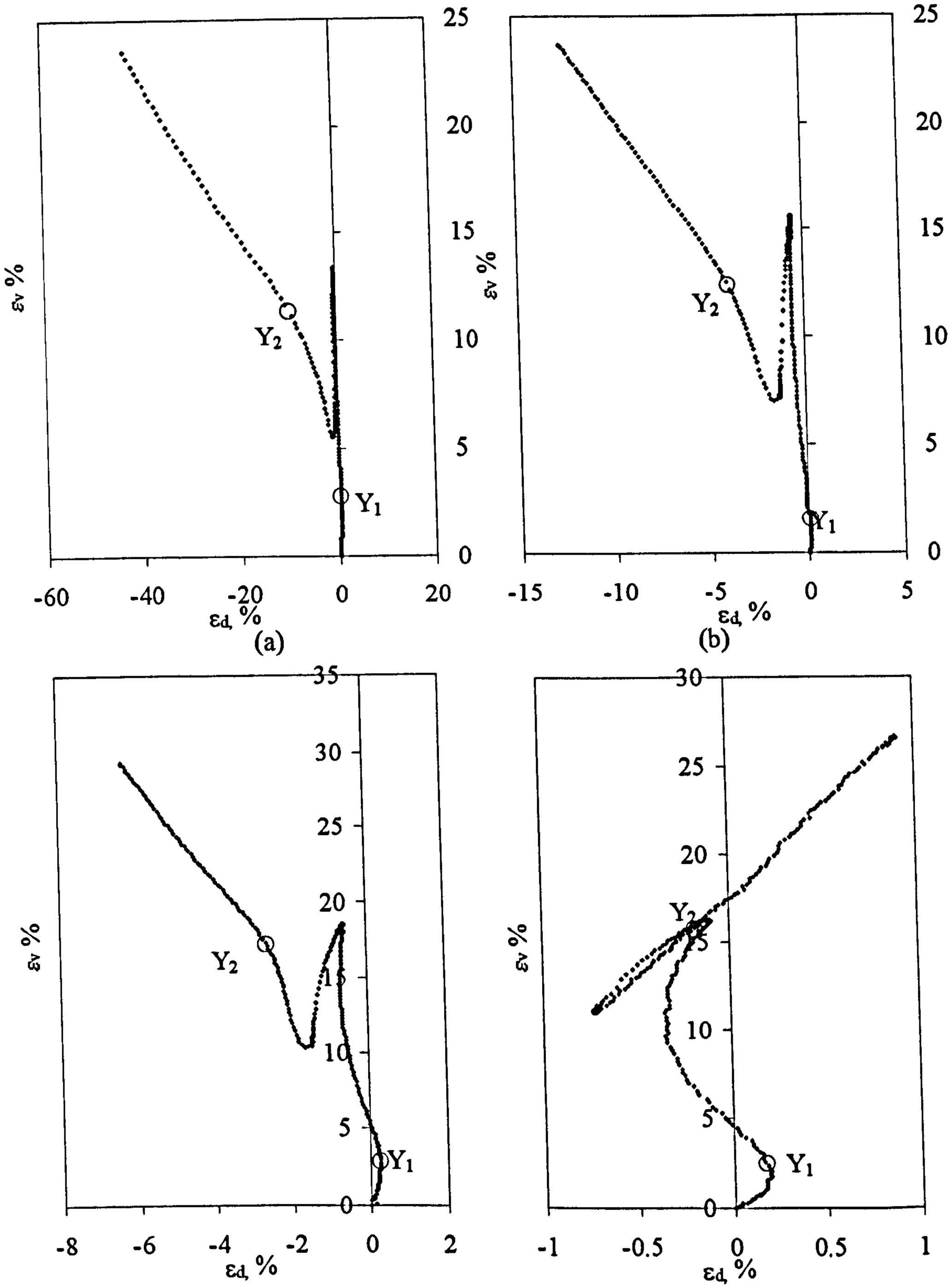

Figure 6.17. Strain paths in Test Series B ($\eta_1 = 0$): (a) Test B9 ($\eta_2 = -1.02$), (b) Test B6 ($\eta_2 = -0.70$), (c) Test B5 ($\eta_2 = -0.40$), (d) Test B7 ($\eta_2 = 0$).

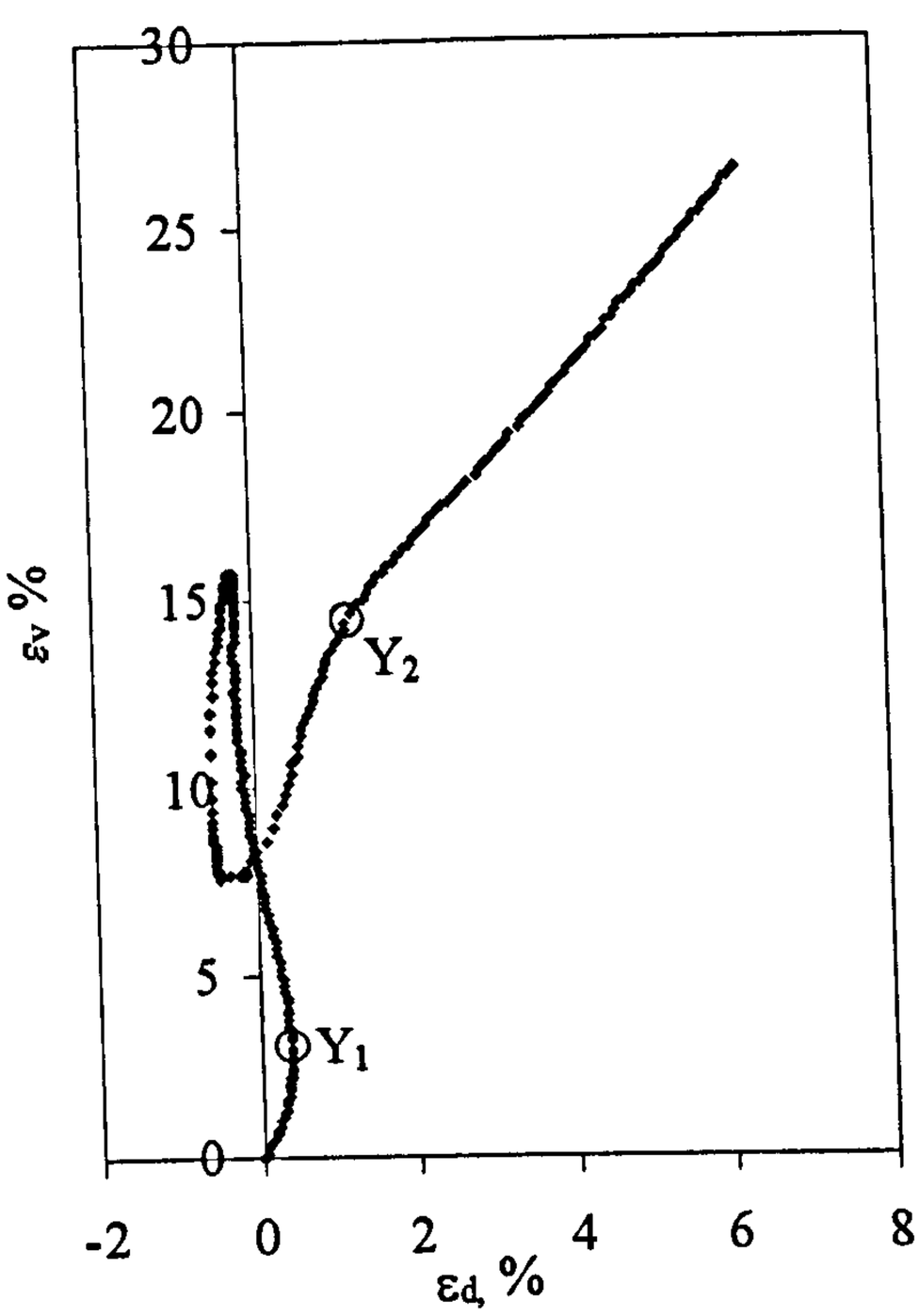

(e)

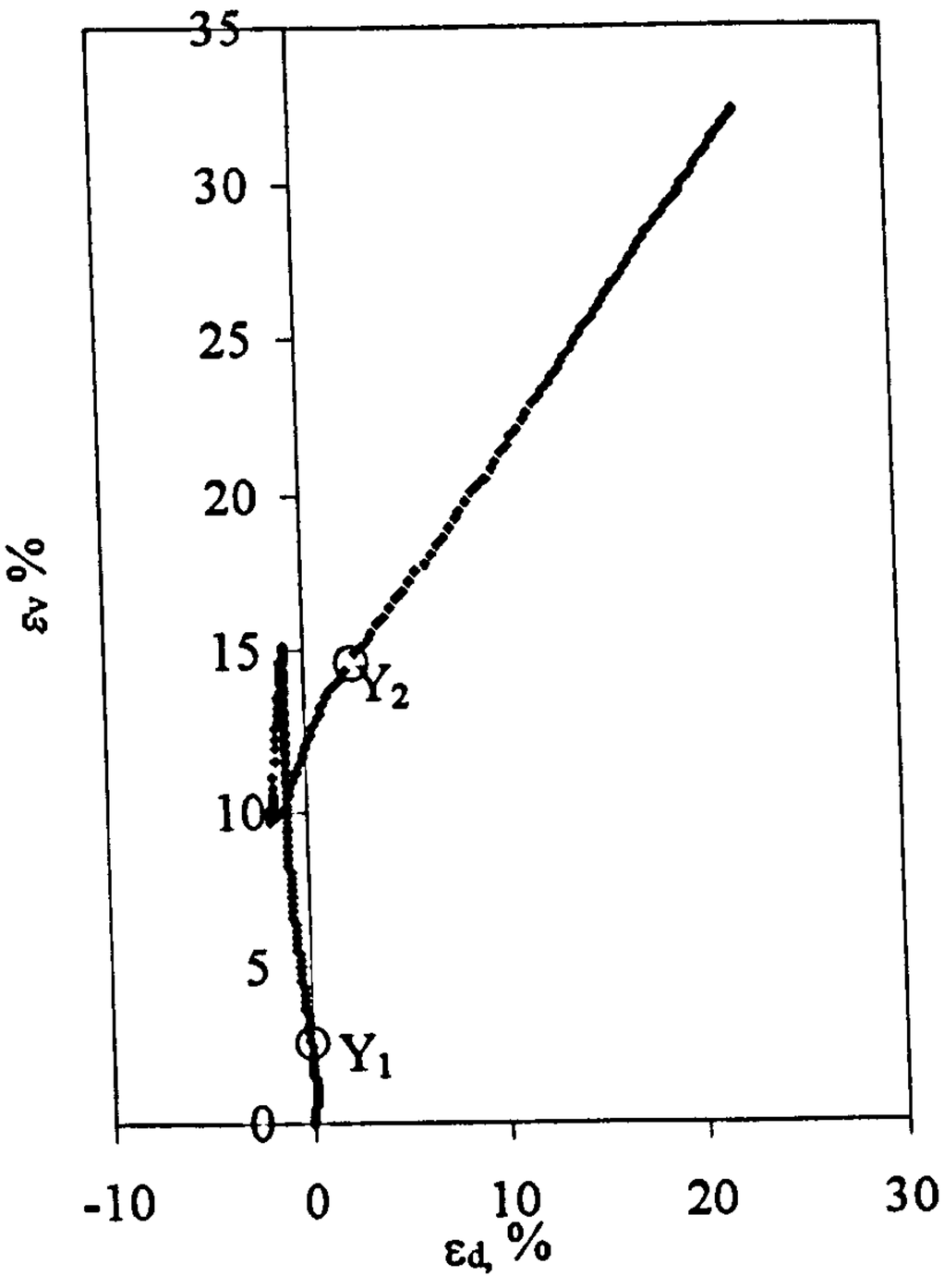

(f)

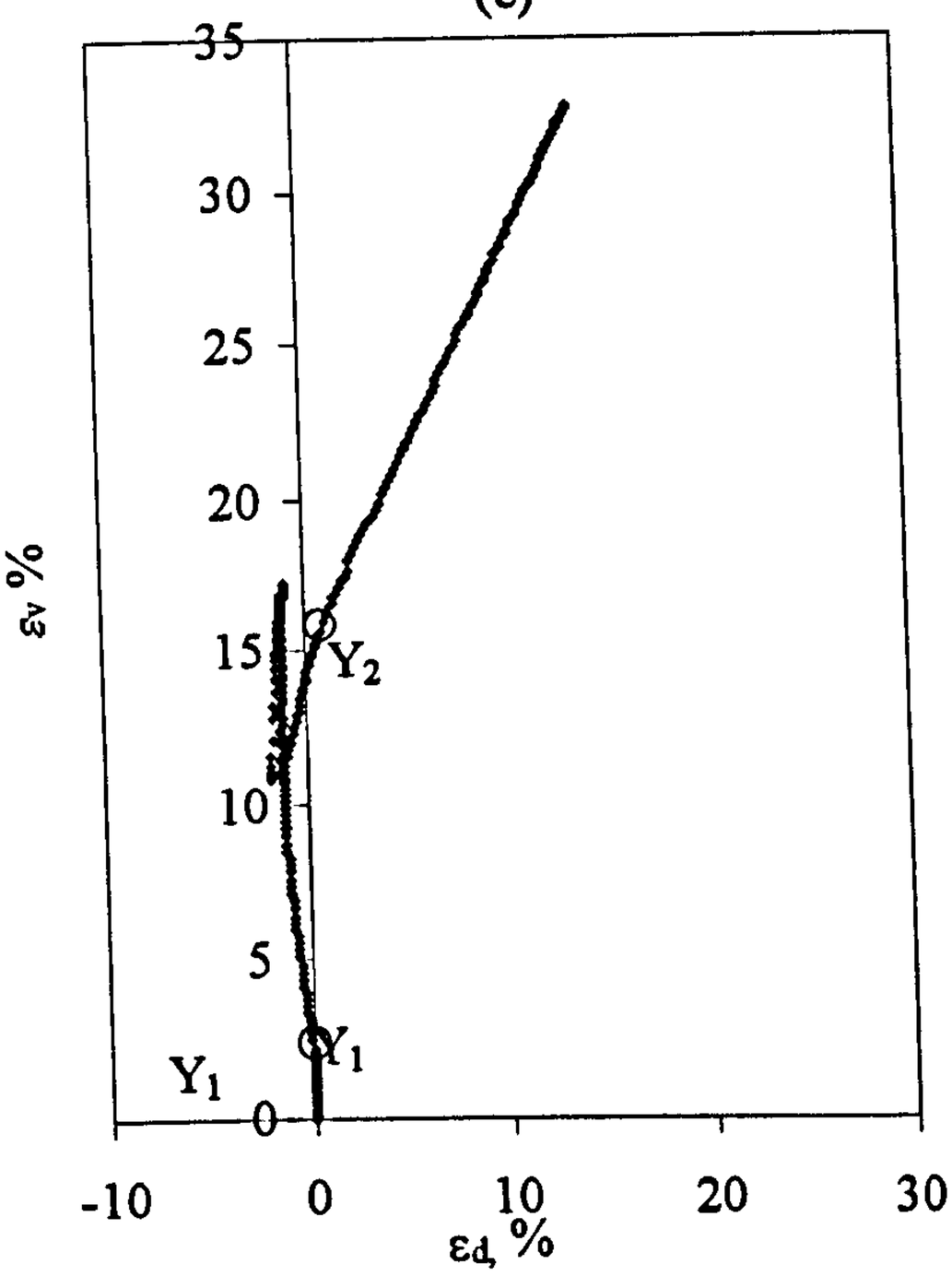

(g)

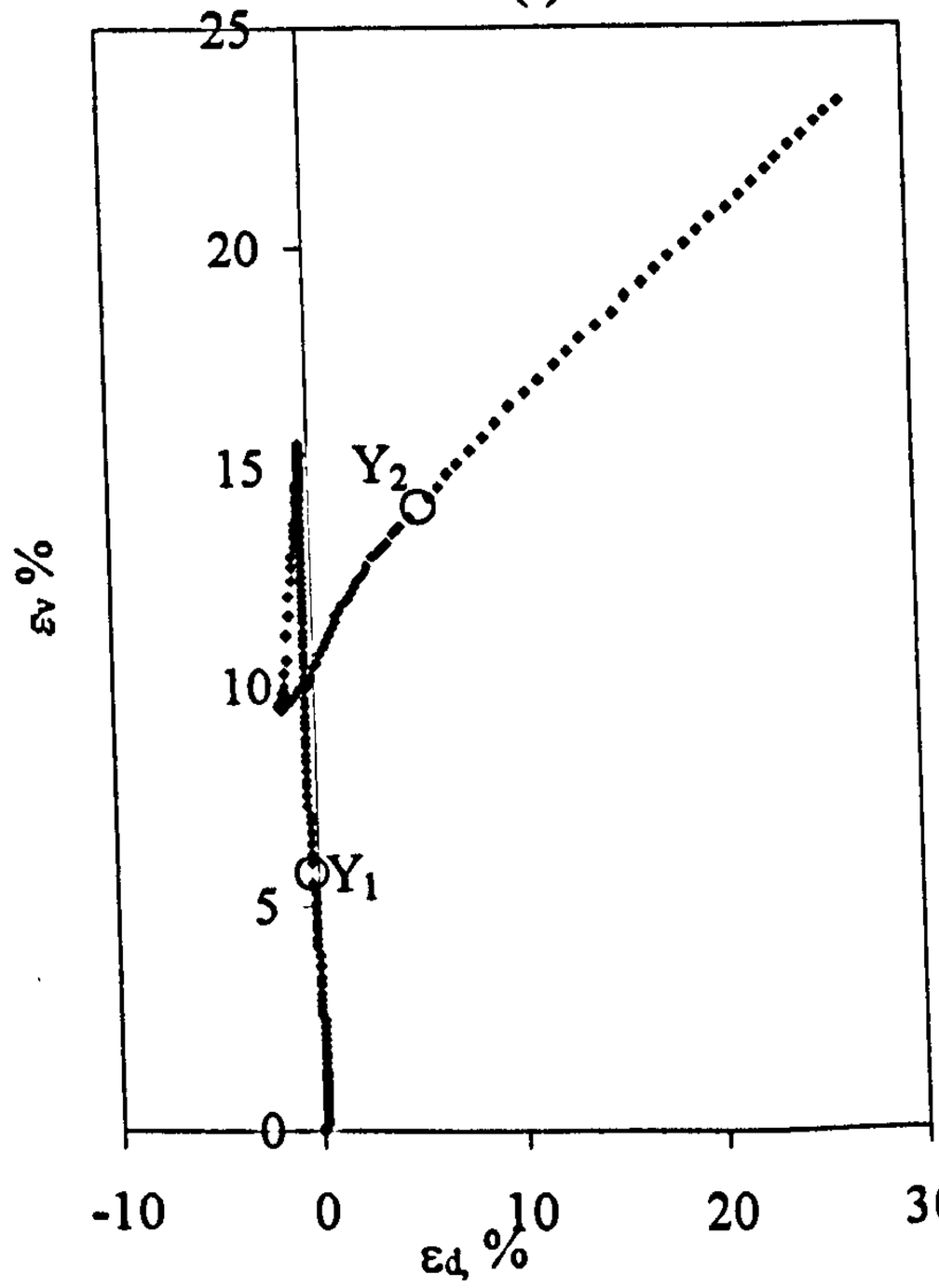

(h)

Figure 6.17. Strain paths in Test Series B ($\eta_1 = 0$): (e) Test B8 ($\eta_2 = 0.40$), (f) Test B2 ($\eta_2 = 0.70$), (g) Test B3 ($\eta_2 = 1.01$), (h) Test B4 ($\eta_2 = 1.30$).

ratio. During second loading, the pre-yield behaviour involves volumetric compression accompanied by positive shear strains for all tests reloaded in triaxial compression (Tests B2, B3, B4 and B8) and Test B7, reloaded isotropically. Positive volumetric strains are accompanied by negative shear strains in Tests B5, B6 and B9 (all involving triaxial extension).

Inspection of Figure 6.17 indicates that yield points during the first and second loading stages (marked Y_1 and Y_2 respectively) are often accompanied by a distinct change of strain path gradient. This would be expected, given that for a constant η stress path the ratio of plastic shear strains to plastic volumetric strains after yielding is not the same as the ratio of elastic shear strains to elastic volumetric strains. At certain values of η, particularly in Tests B2 and B7, elastic and plastic ratios of shear strain to volumetric strain happen to coincide, and for these cases there is no change of strain path gradient at the yield point.

Figure 6.17 shows that post-yield strain paths in both first and second loading stages are reasonably linear. In some stages there is curvature of the strain path immediately after the yield point, as would be expected if a change in anisotropy was occurring, caused by plastic straining at a new value of η (see S-CLAY1 and S-CLAY1S simulations in Chapters 8 and 9 respectively). However, the curvature observed in the post-yield strain paths is not particularly marked in the test data shown in Figure 6.17.

6.4 Stress-strain behaviour during Test Series C

6.4.1 Summary of sample properties and stress paths

Details of the multi-stage stress paths in Test Series C are given in Table 6.4. The information includes the initial void ratio (e_0), the stress ratio during first and second loading stages (η_1 and η_2), the maximum mean effective stresses in first and second loading stages (p'_{max1}, and p'_{max2}) and the Laval sample from which each triaxial specimen was cut. Each sample in Test Series C was first loaded at a stress ratio η_1 to a stress approximately three times greater than the estimated yield stress. At low

to medium values of η_1 (for example Tests C1, C5 and C7) this involved loading to a mean effective stress of 210 kPa (as per Test series B). At higher stress ratios in triaxial compression, such as Tests C2 and C3, yield was expected to occur at a lower mean effective stress and therefore the tests were planned accordingly. In the event, however, the first loading stages in these tests were limited by the available axial travel in the Bishop-Wesley cell, although the length of the post-yield stress path was satisfactory in both cases. In triaxial extension, it was expected that the yield stresses would occur at a lower mean effective stress than in Test Series B. The first loading stage of Test C4 (at η_1 = -0.80) was therefore terminated at p' = 125 kPa. However, Test C9, the final test to be conducted, was carried through to a much higher mean effective stress than any other test in Series B and Series C. It was felt that although yield points could be identified at relatively low stress in triaxial extension, substantially longer stress paths (compared to triaxial compression) were necessary to observe the complete evolution of anisotropy. Test C8 was terminated prematurely due to compressor failure.

Test	e_0	η_1	p'_{max1} (kPa)	η_2	p'_{max2} (kPa)	Laval Sample
C1	1.626	0.42	210	1.04	330	20B
C2	1.607	1.11	198	-0.50	587	20B
C3	1.604	1.30	125	-0.60	236	21A
C4	1.743	-0.80	125	0.60	280	21A
C5	1.619	0.80	210	-0.80	448	20A
C6	1.554	0.20	210	1.03	318	20A
C7	1.631	0.42	210	-0.70	354	20A
C8	1.663	0.80	210	-	-	21A
C9	1.603	-0.50	301	-0.96	505	20B

Table 6.4. Summary of stress path tests on vertical samples (Test Series C).

The stress-strain behaviour in each of the tests in Series C is shown in Figures 6.18 – 6.26. As before, large circular data points indicate the first data point at the specified stress ratio at the start of a loading stage and large square data points represent the end of a loading stage.

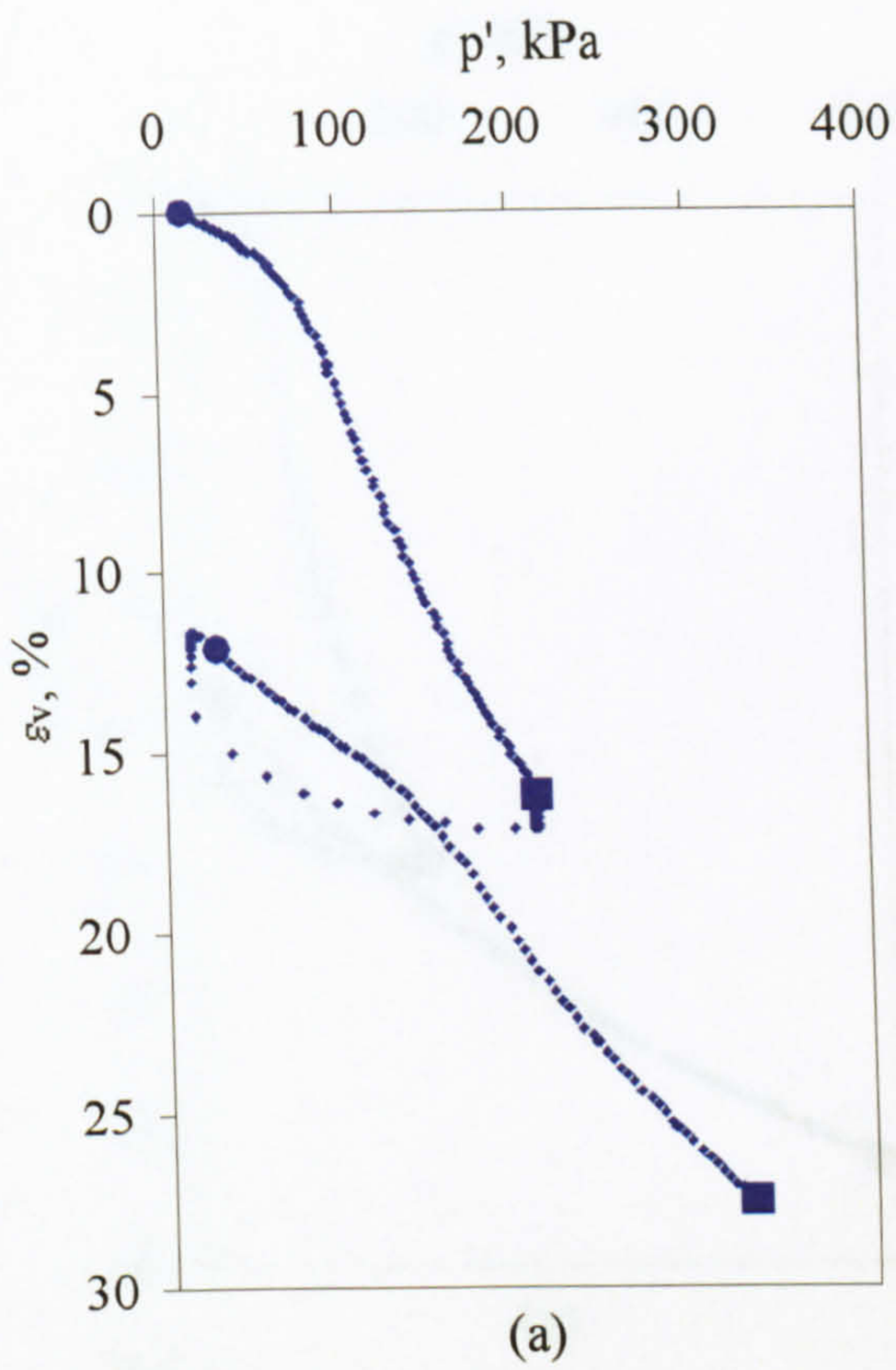

(a)

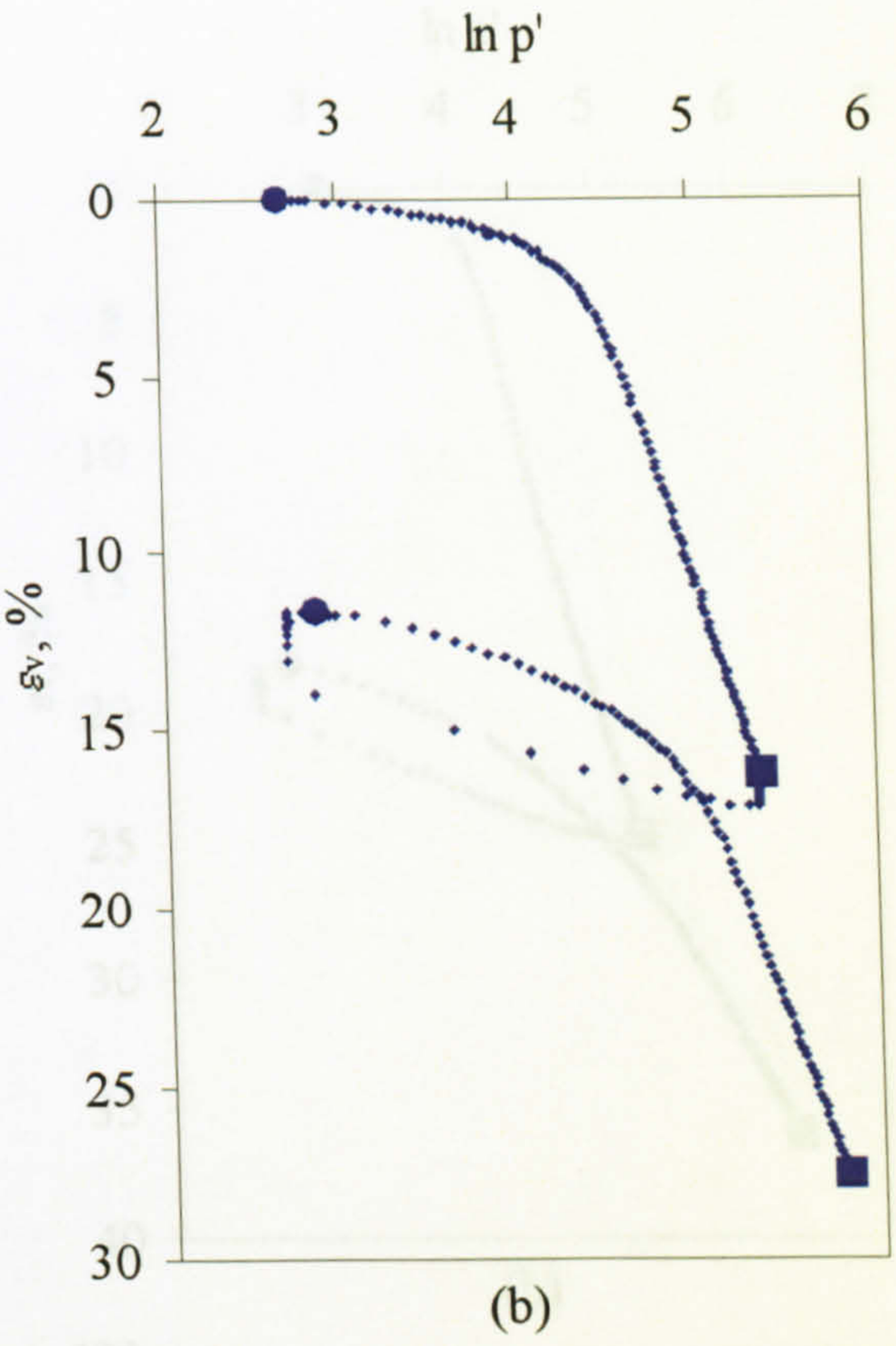

(b)

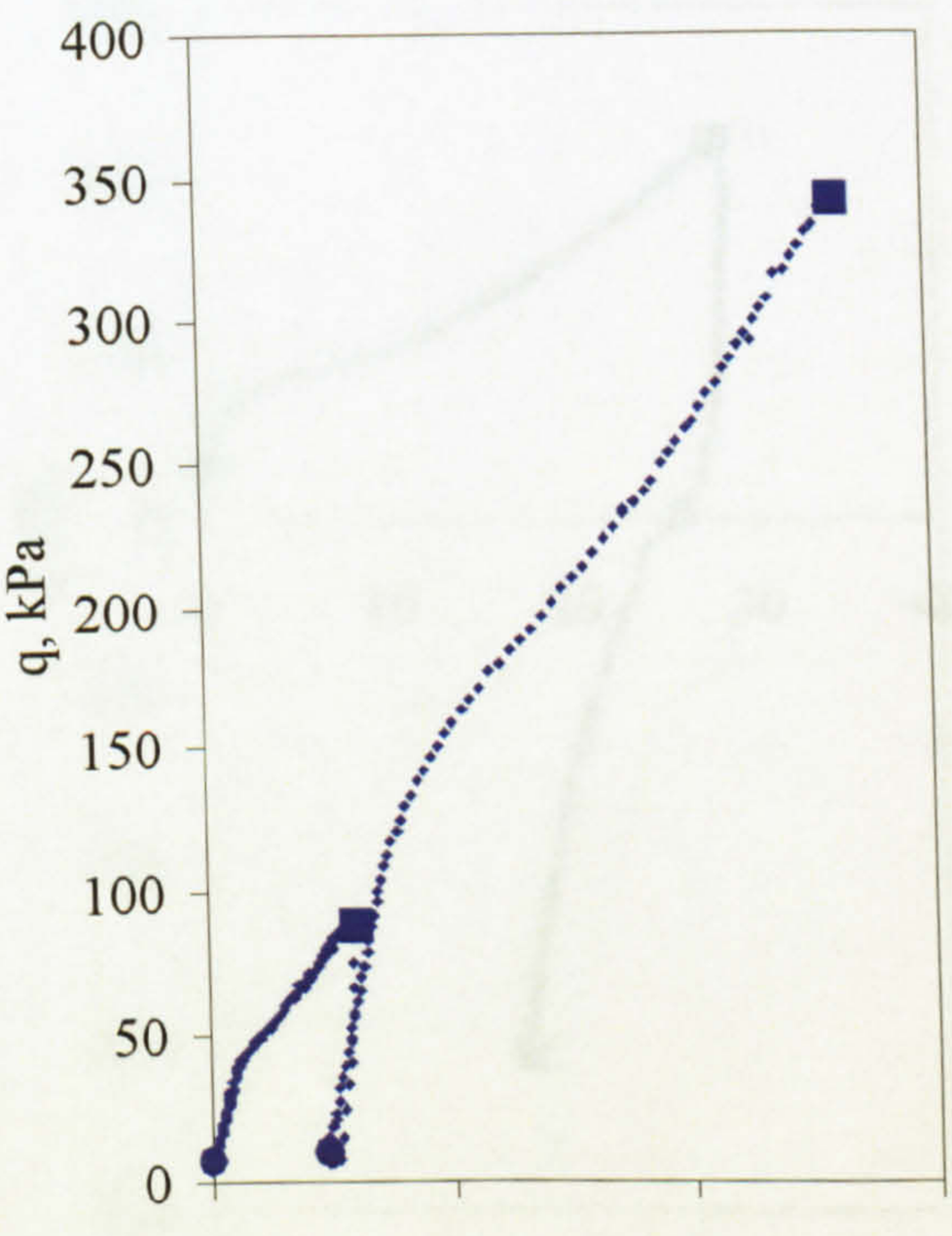

(c)

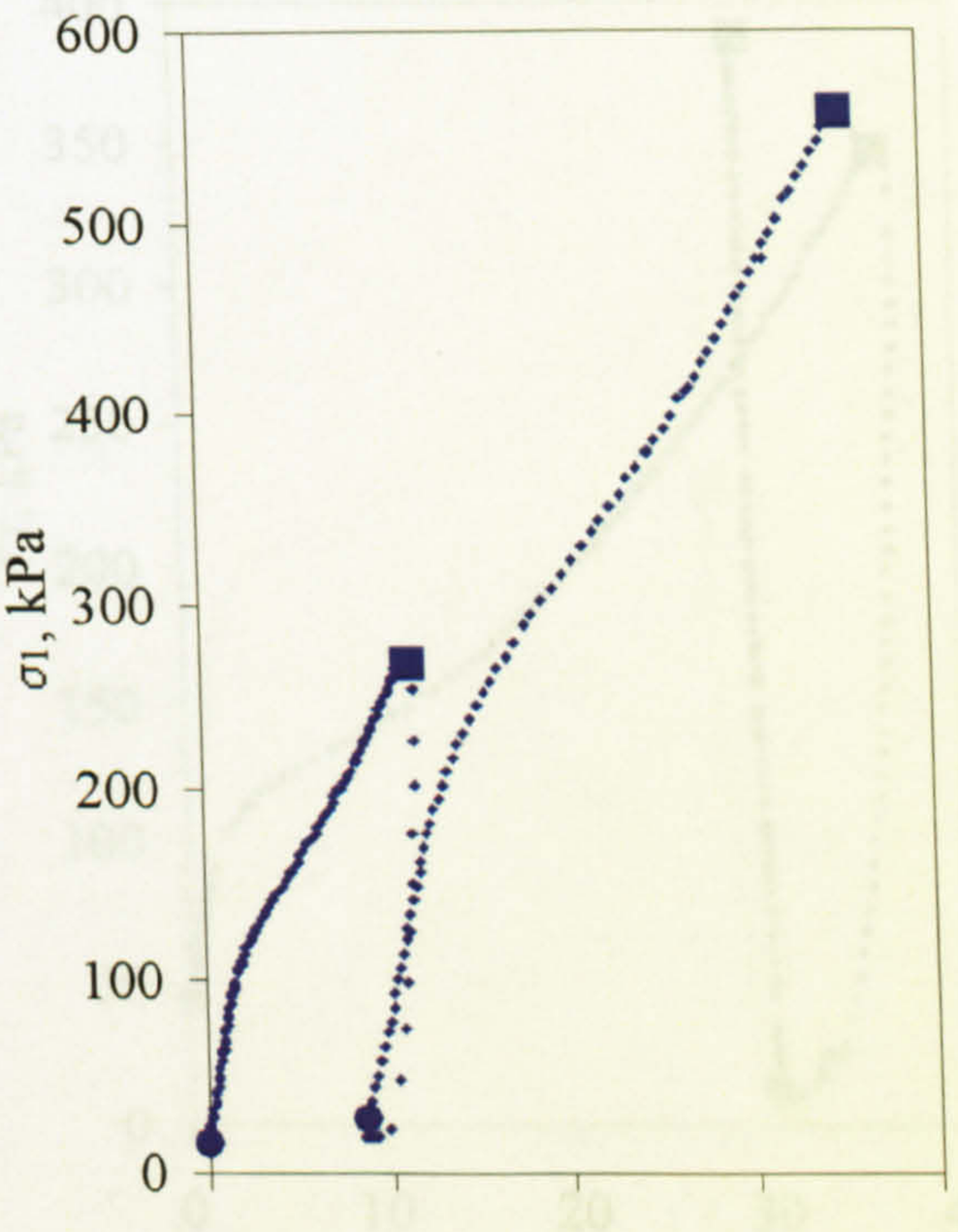

(d)

Figure 6.18. Stress-strain behaviour in Test C1 ($\eta_1 = 0.42$ and $\eta_2 = 1.04$) (a), (b) compression behaviour, (c) deviatoric behaviour and (d) axial behaviour.

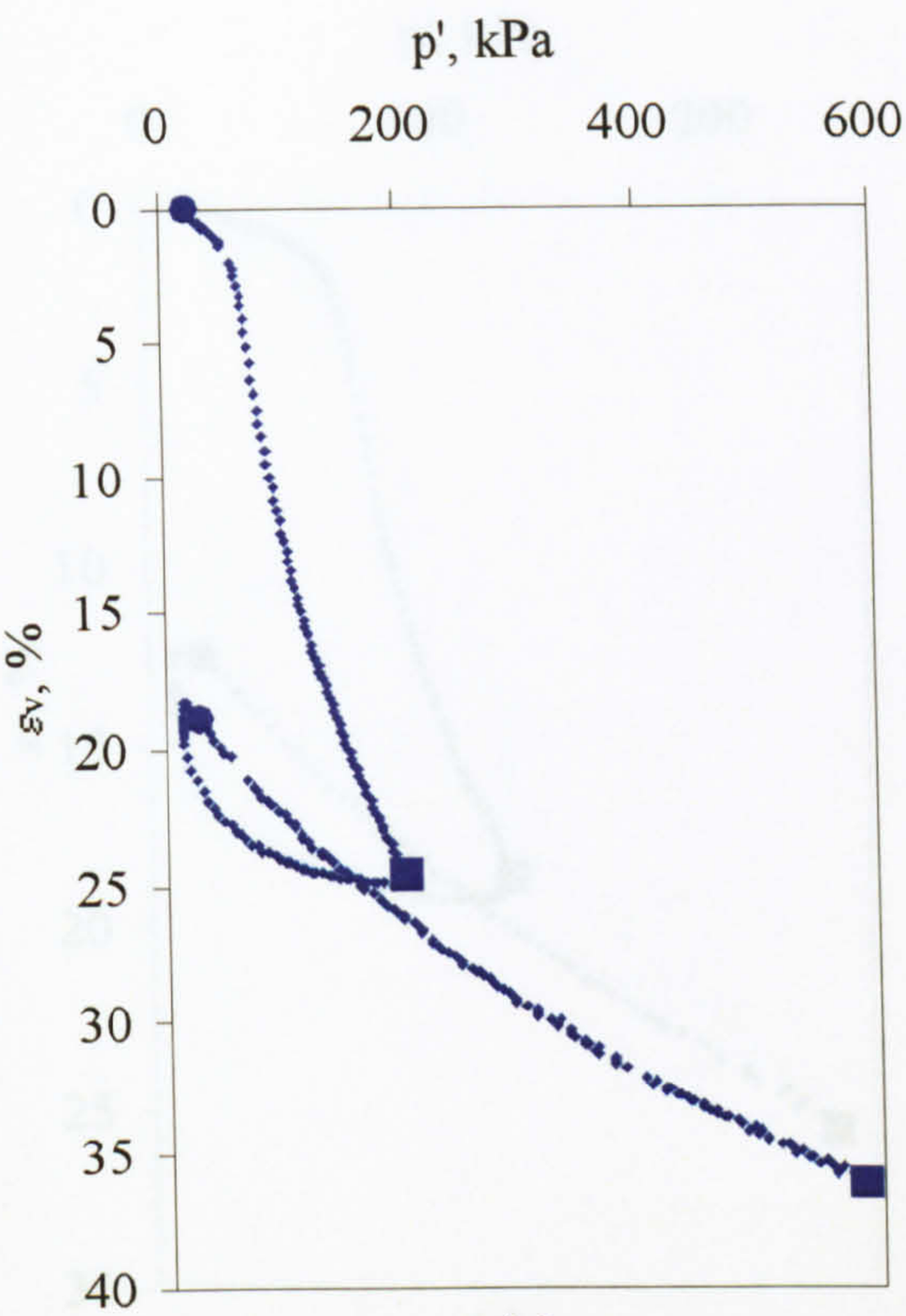

(a)

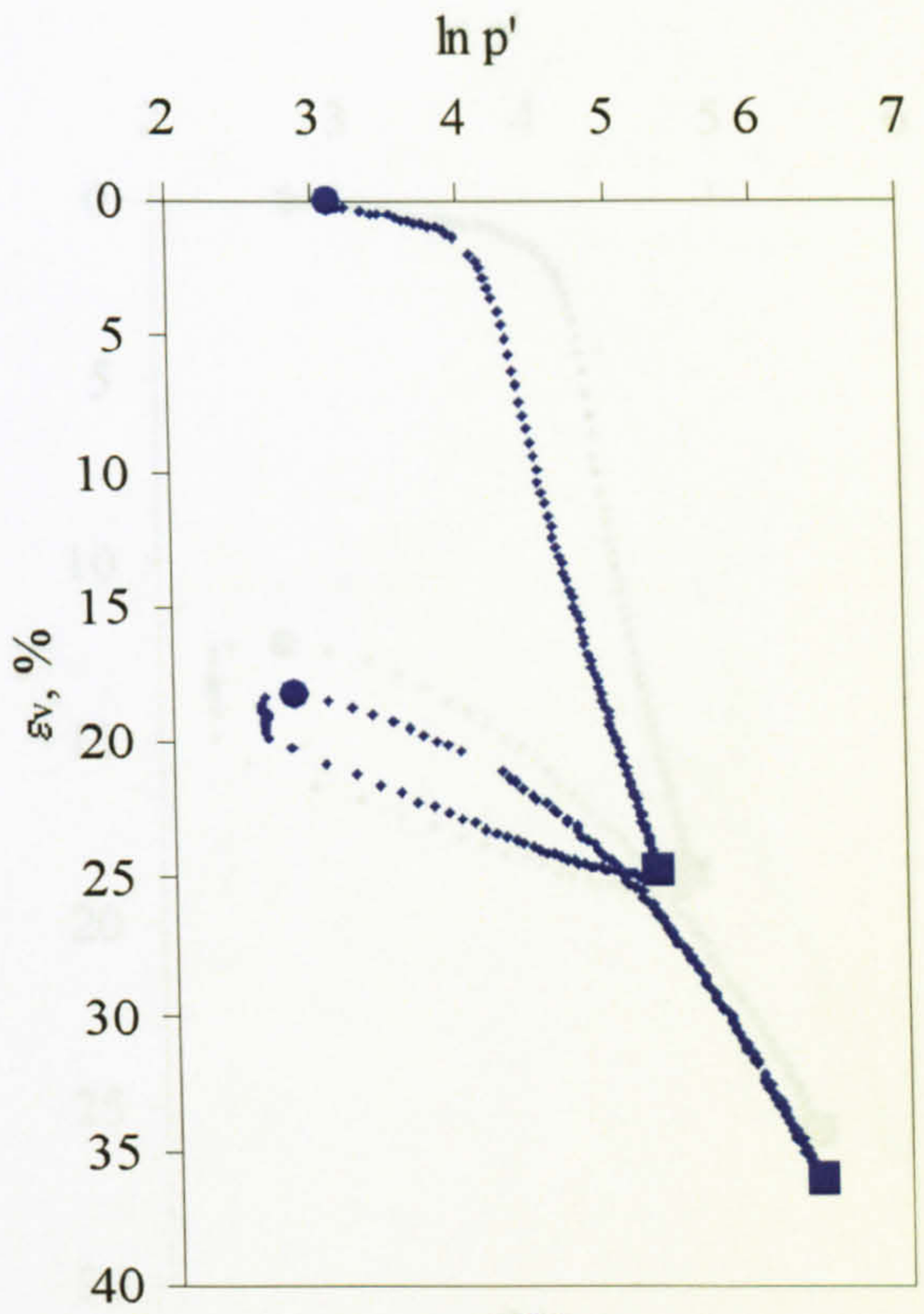

(b)

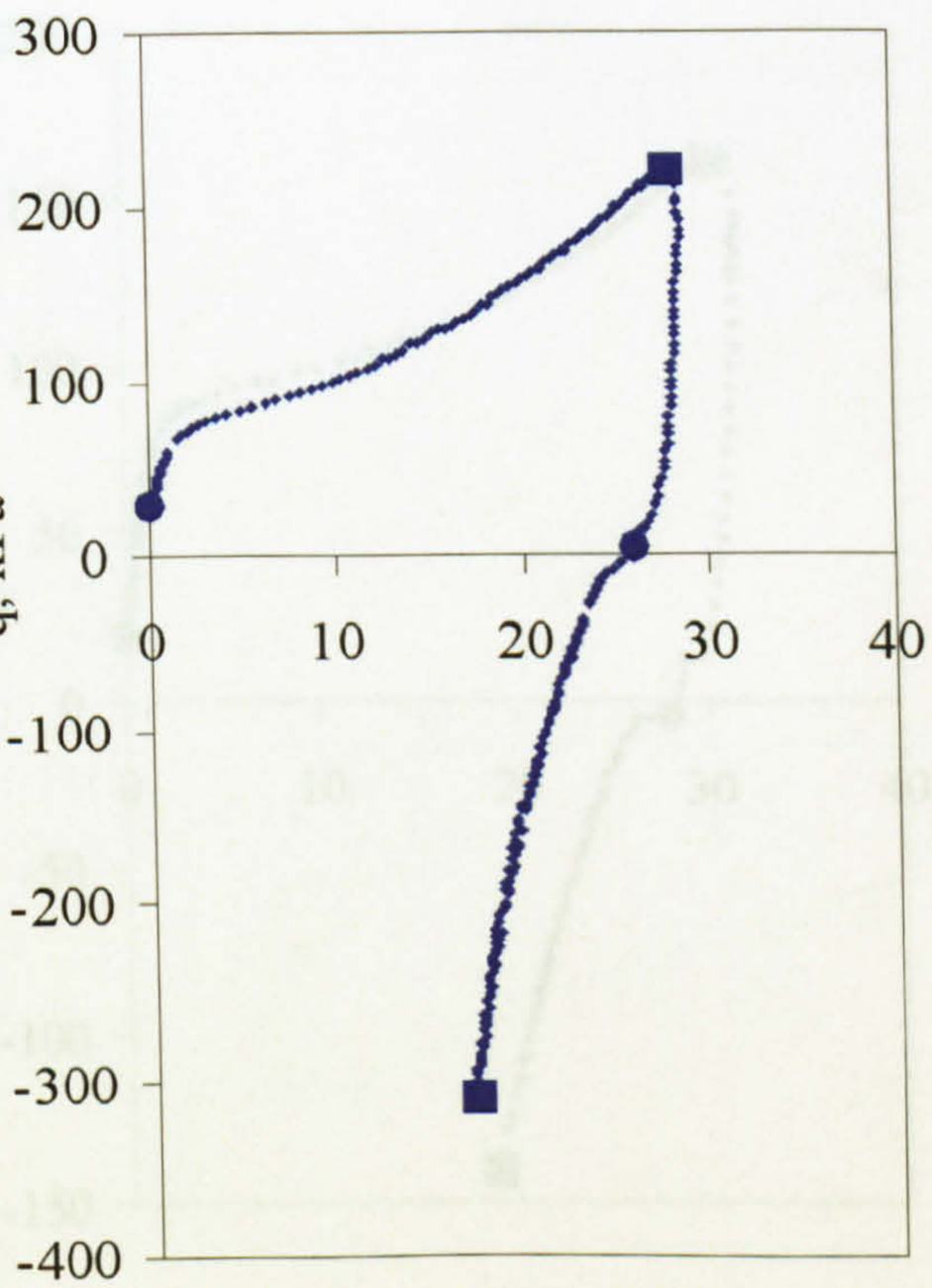

(c)

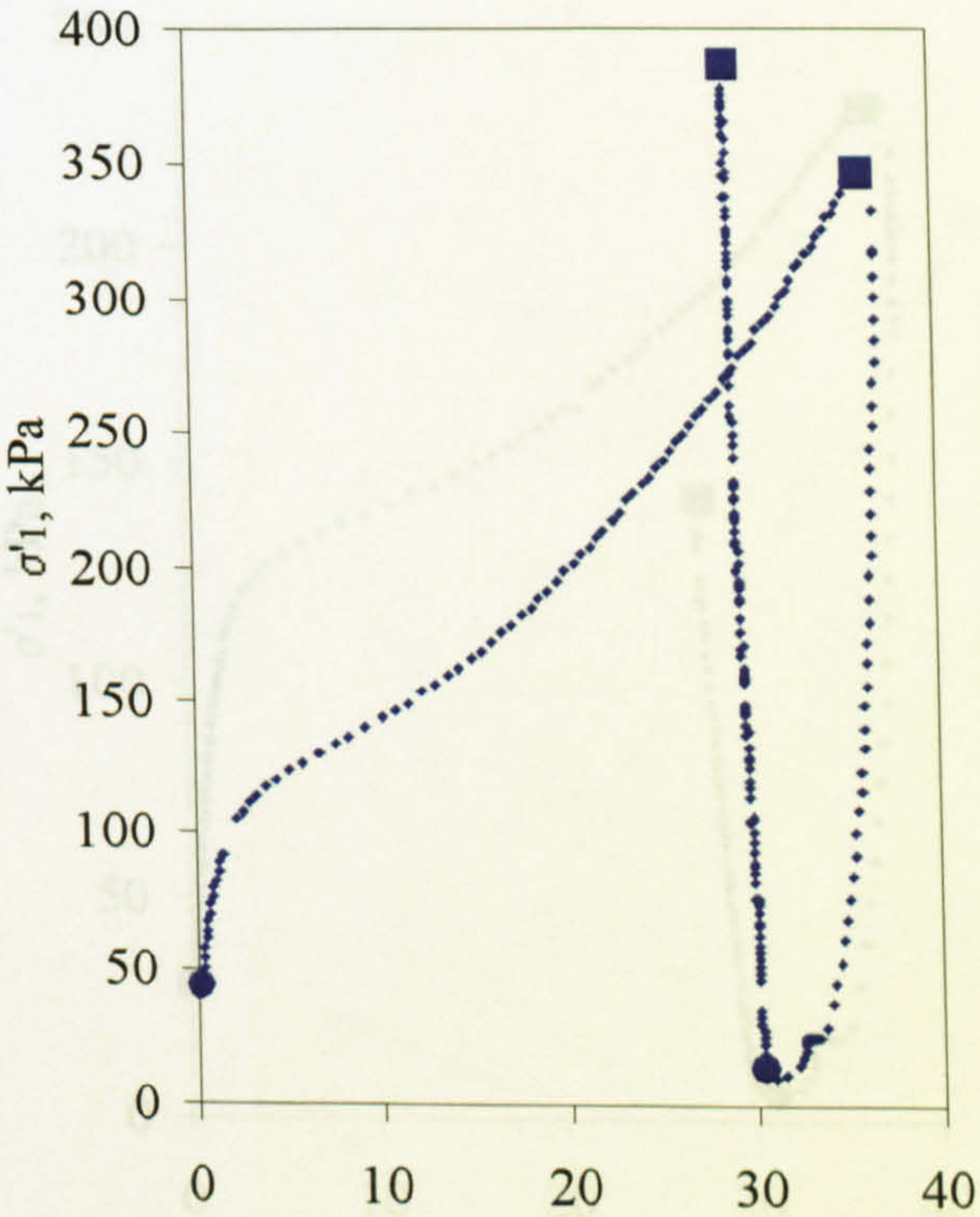

(d)

Figure 6.19. Stress-strain behaviour in Test C2 (η_1 = 1.10 and η_2 = -0.50): (a), (b) compression behaviour, (c) deviatoric behaviour and (d) axial behaviour.

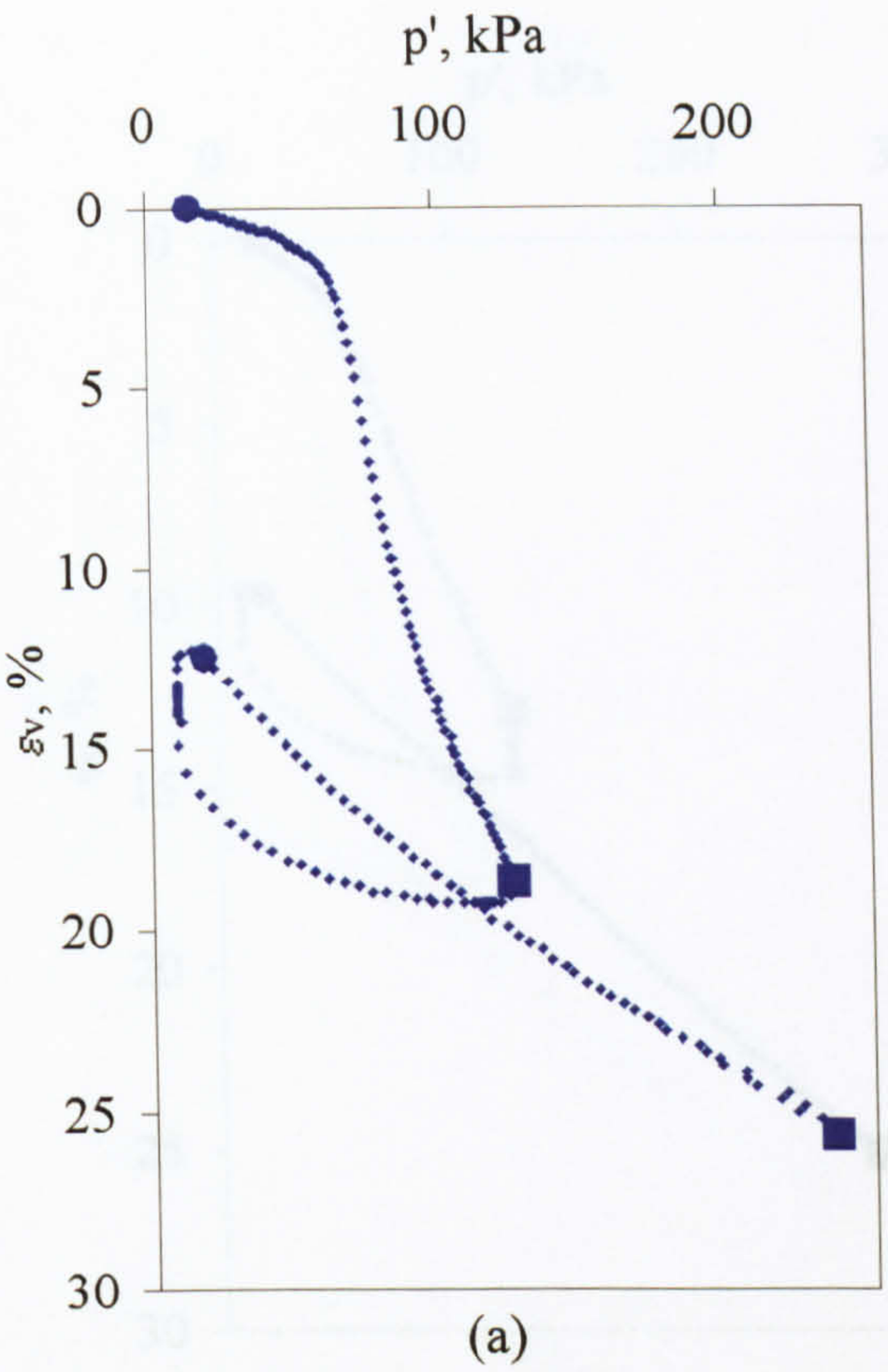

(a)

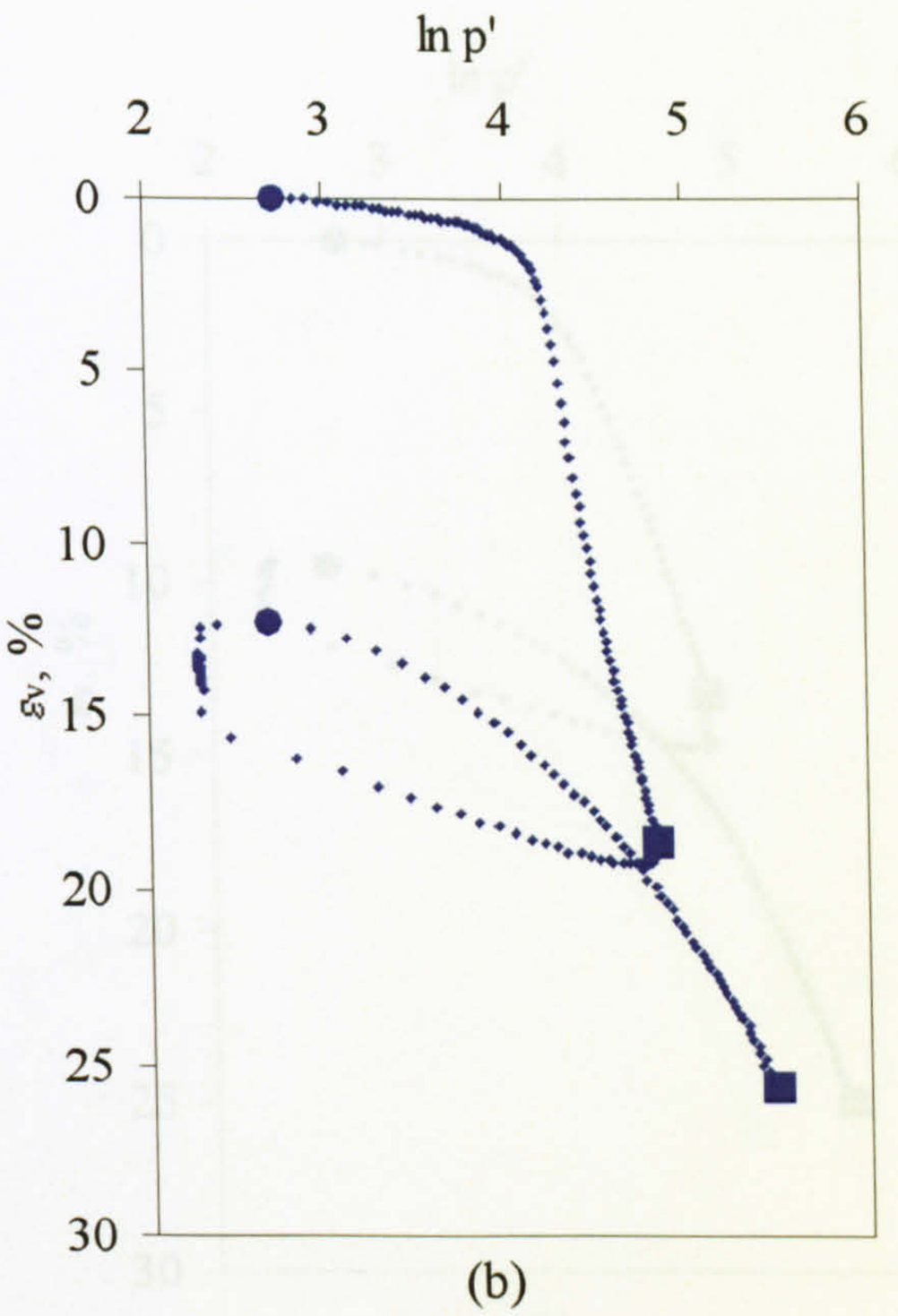

(b)

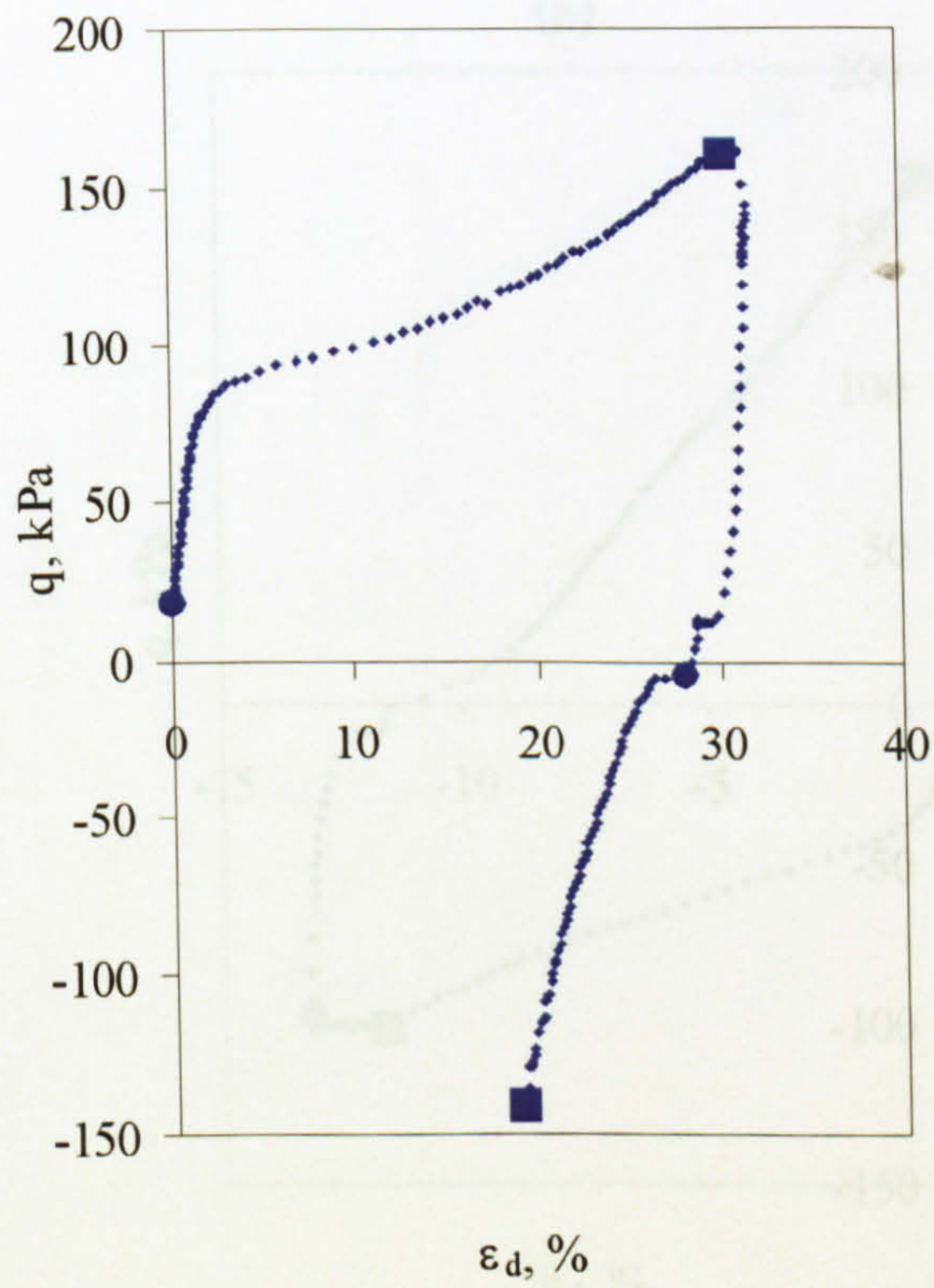

(c)

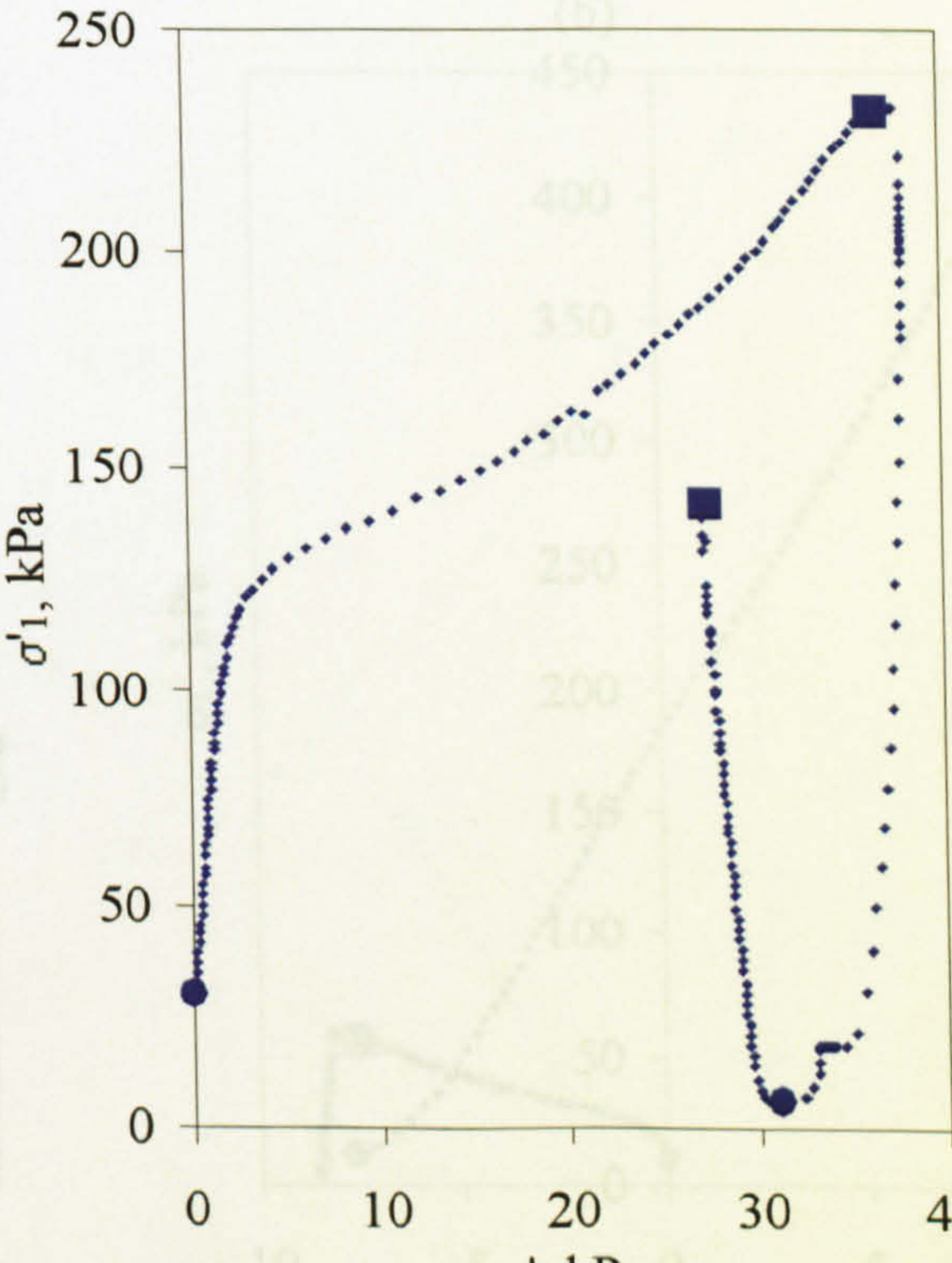

(d)

Figure 6.20. Stress-strain behaviour in Test C3 (η_1 = 1.30 and η_2 = -0.60): (a), (b) compression behaviour, (c) deviatoric behaviour and (d) axial behaviour.

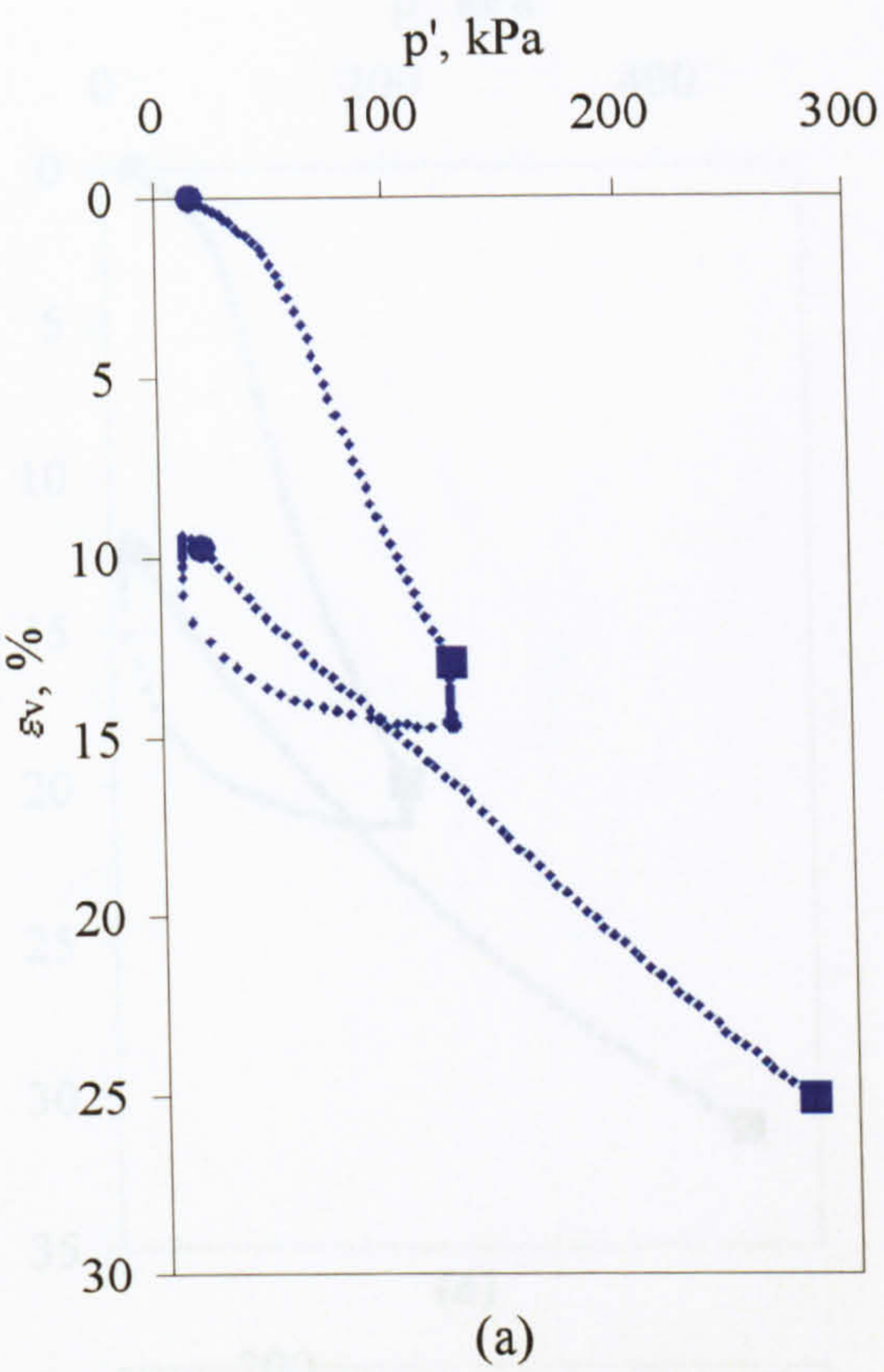

(a)

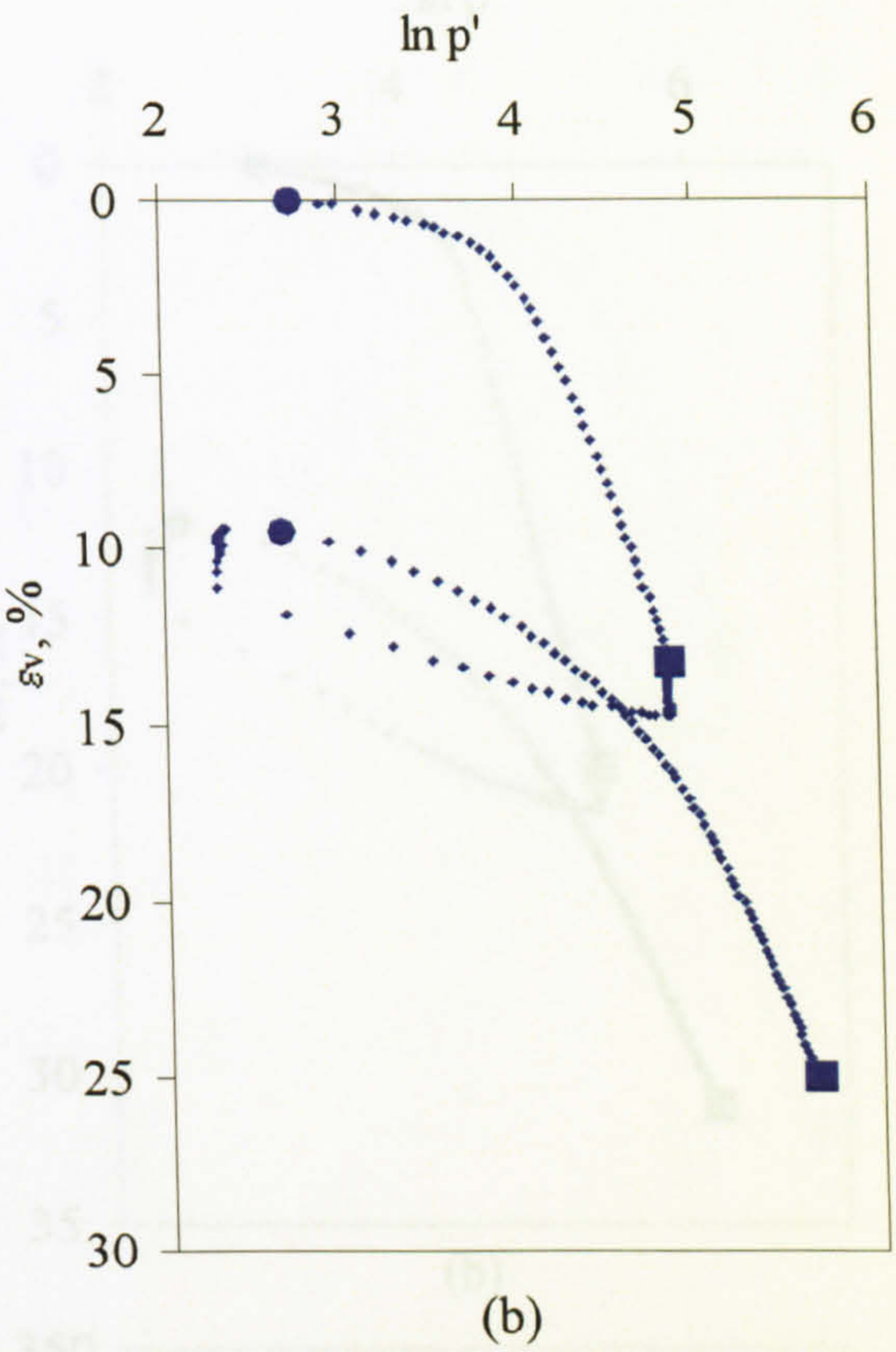

(b)

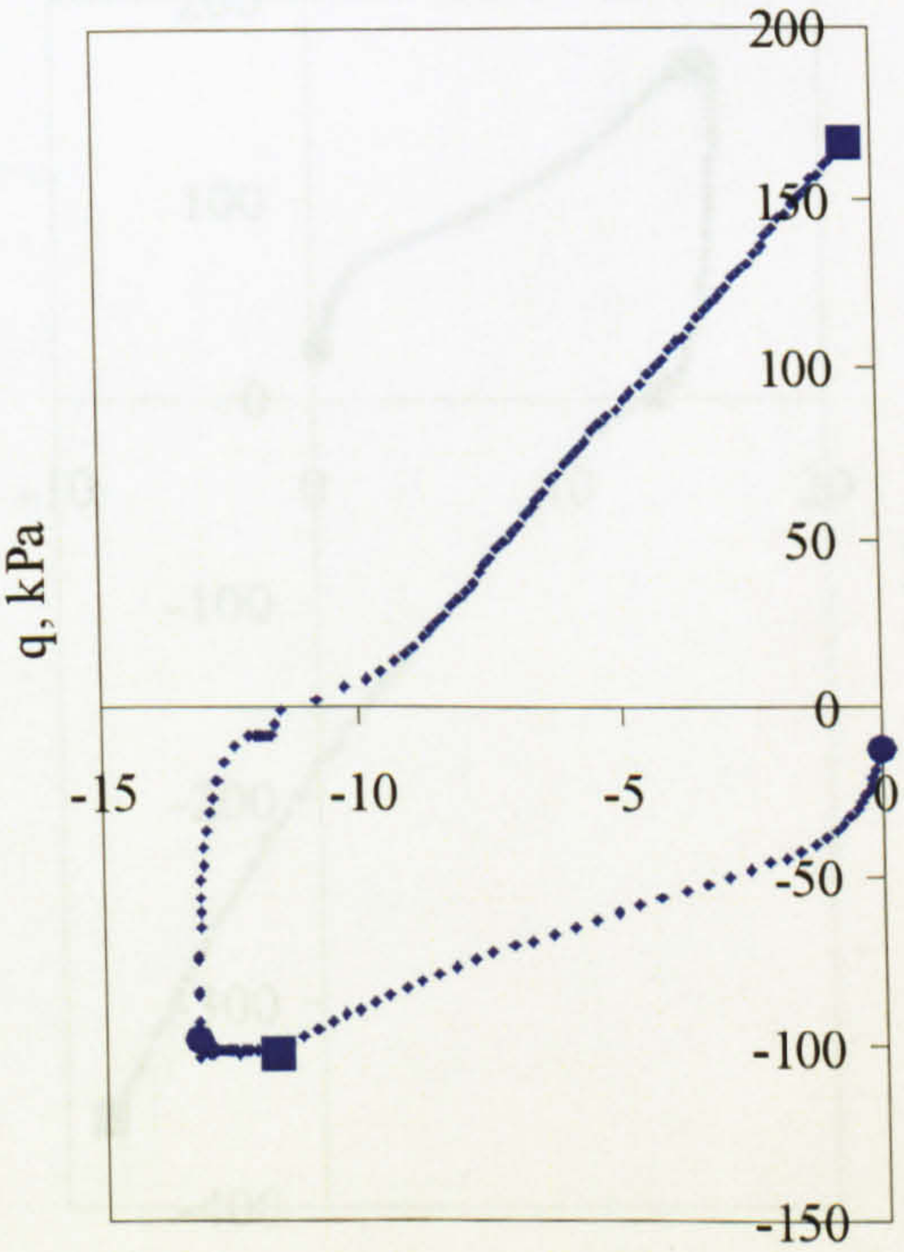

(c)

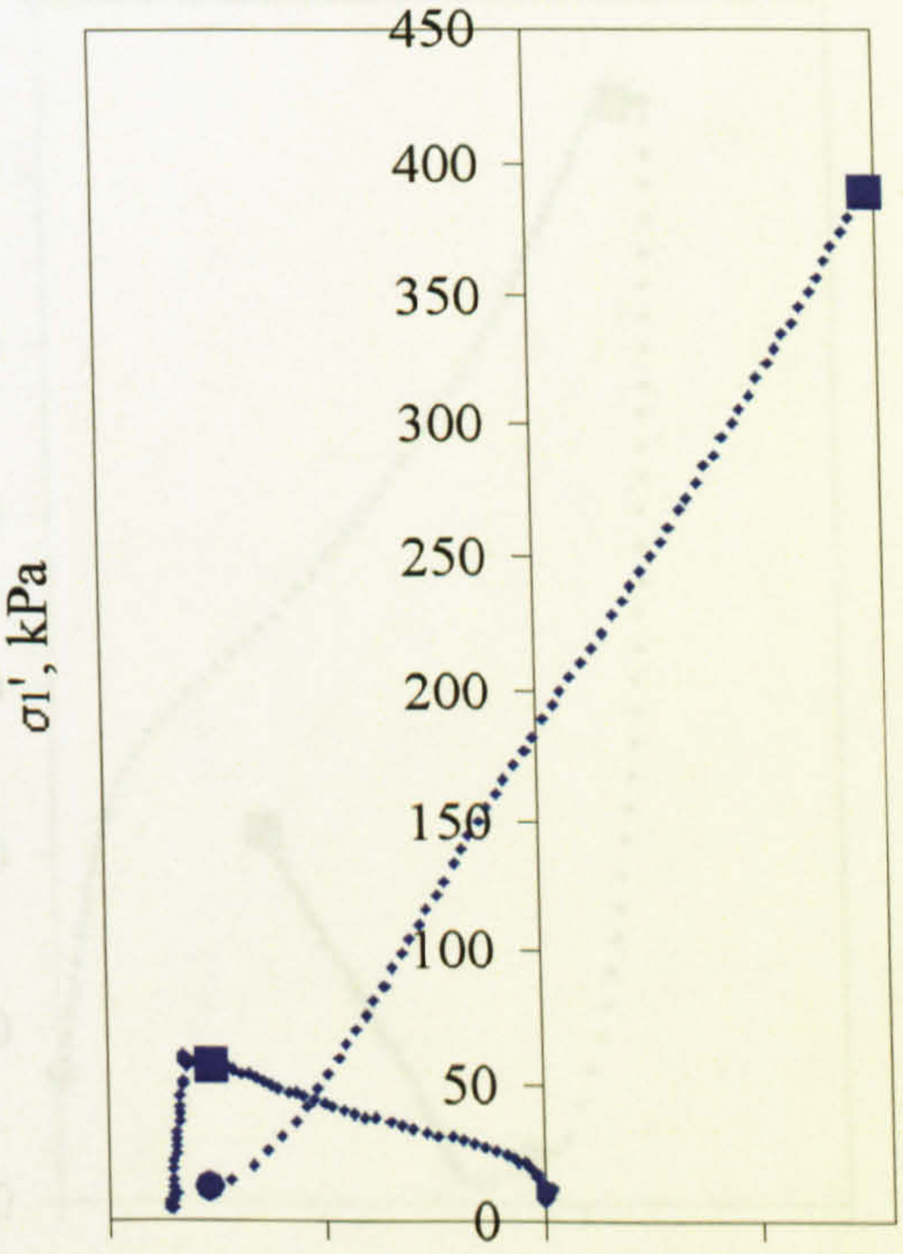

(d)

Figure 6.21. Stress-strain behaviour in Test C4 (η_1 = -0.80 and η_2 = 0.60): (a), (b) compression behaviour, (c) deviatoric behaviour and (d) axial behaviour.

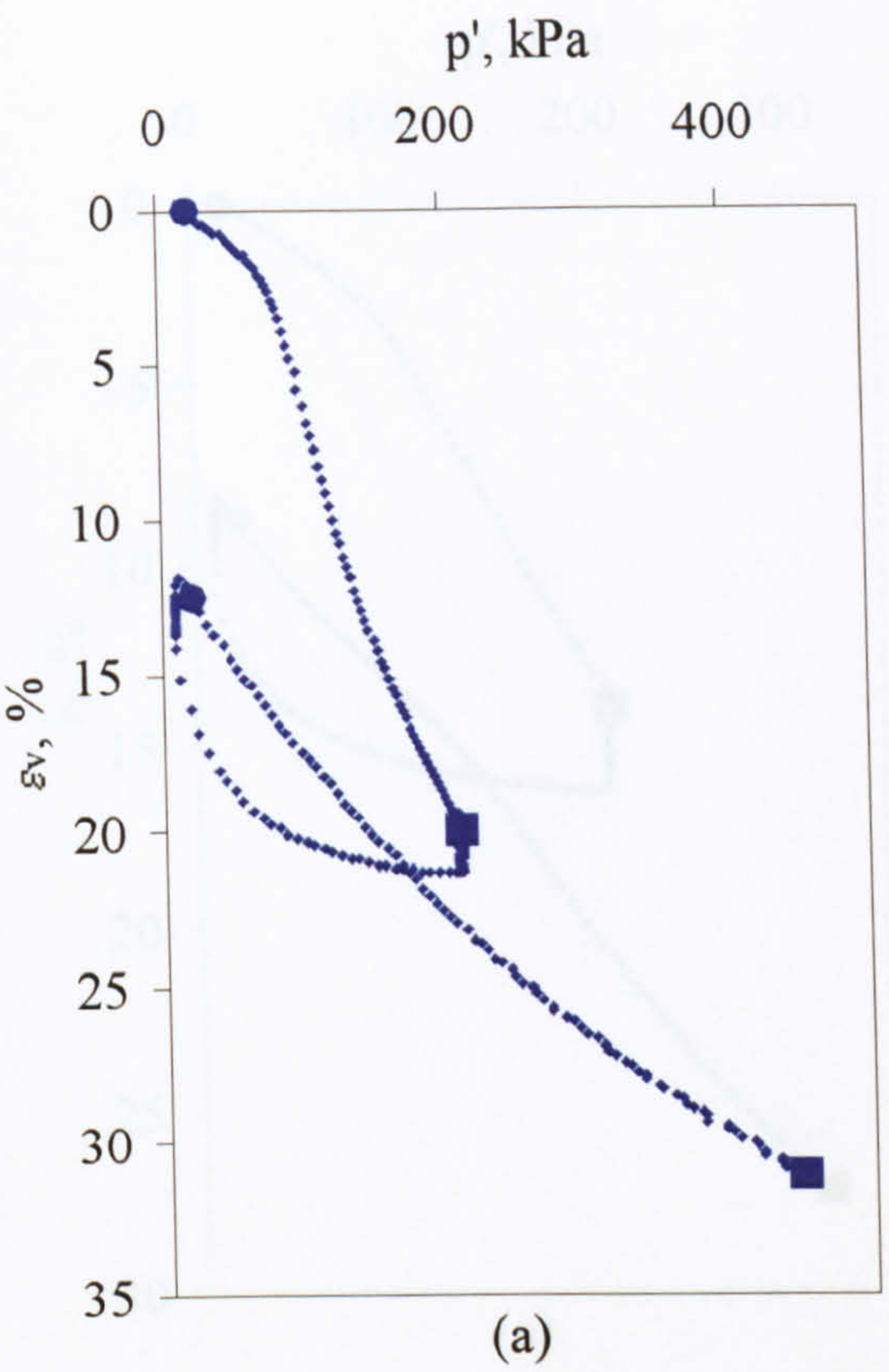

(a)

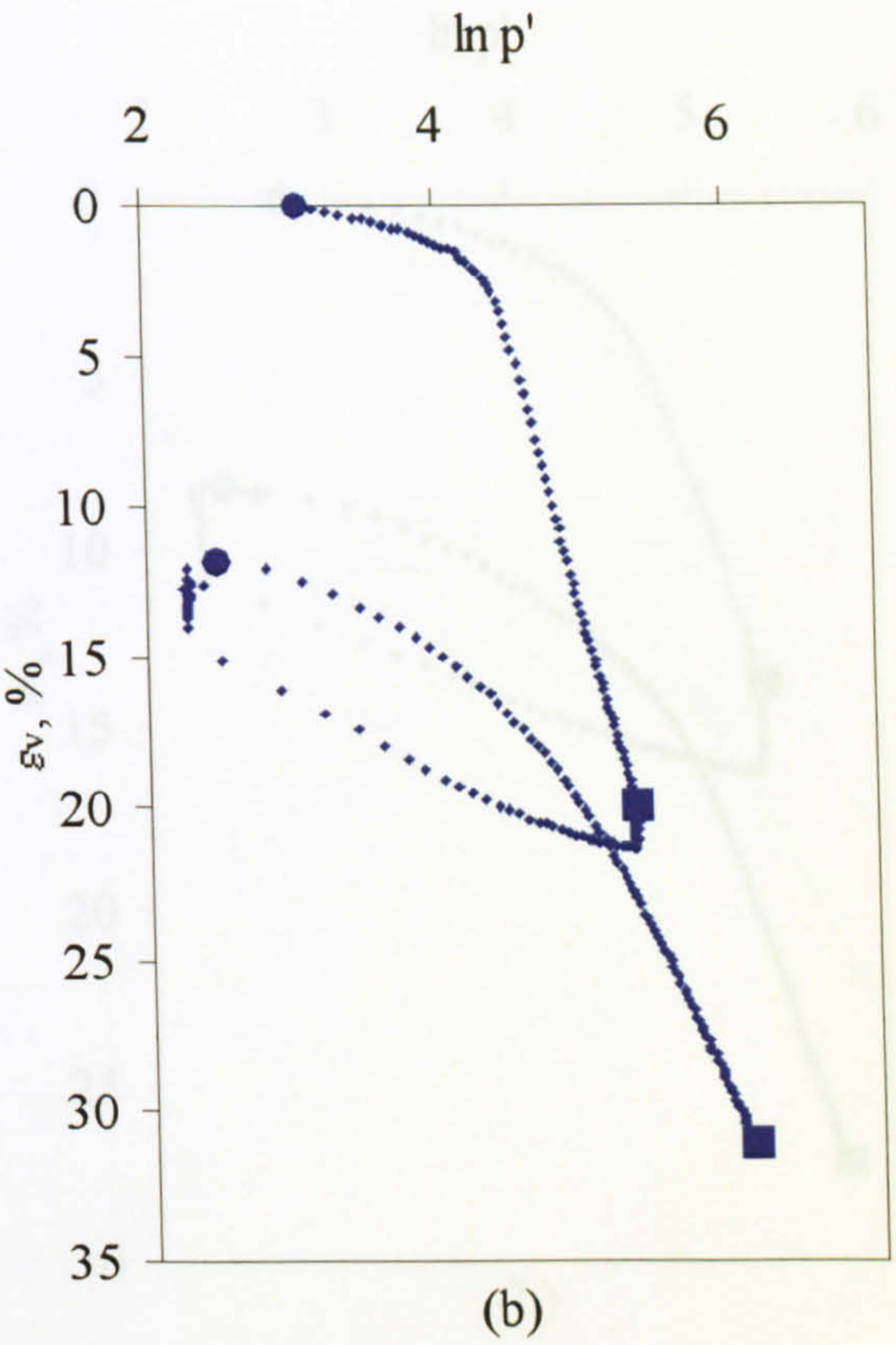

(b)

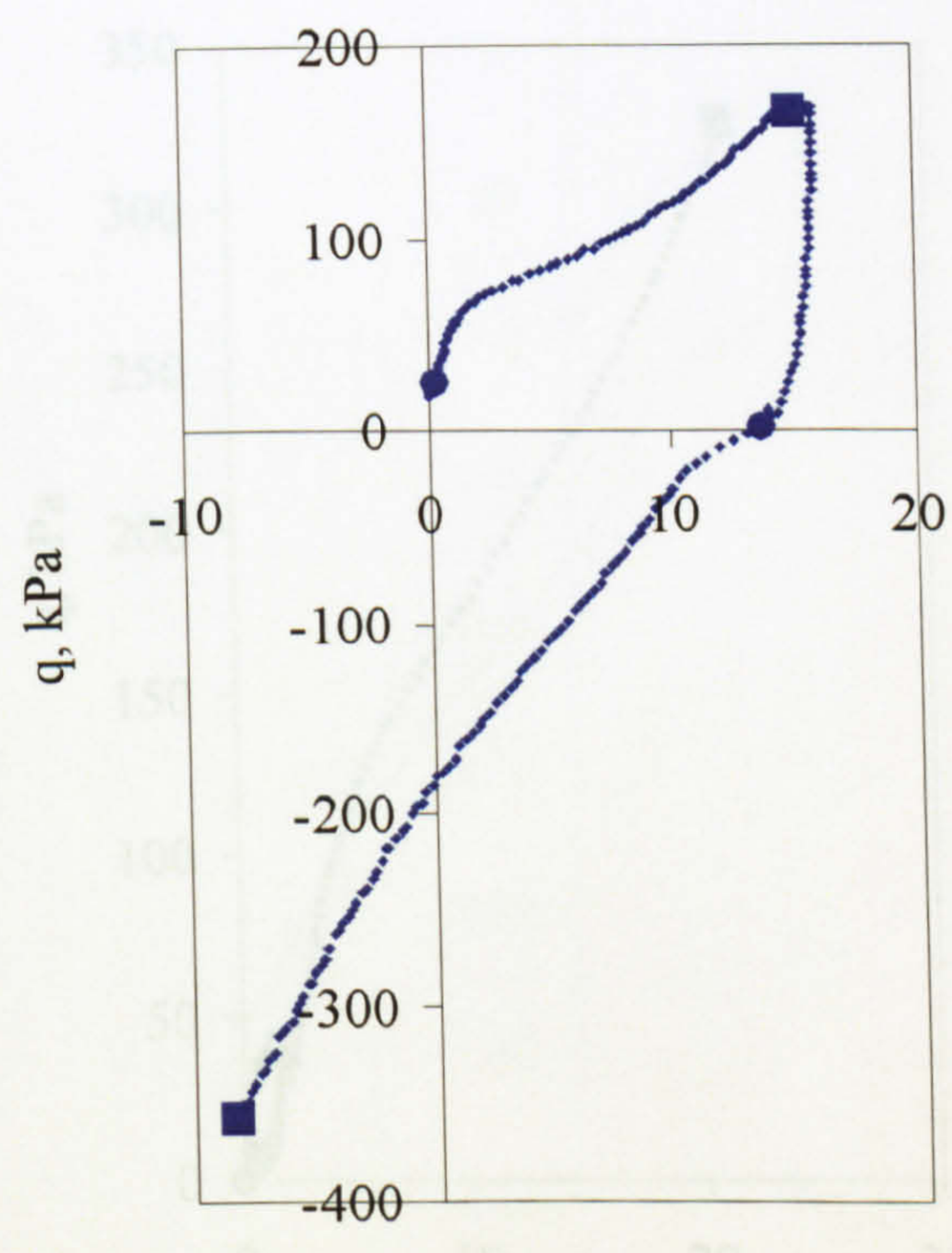

(c)

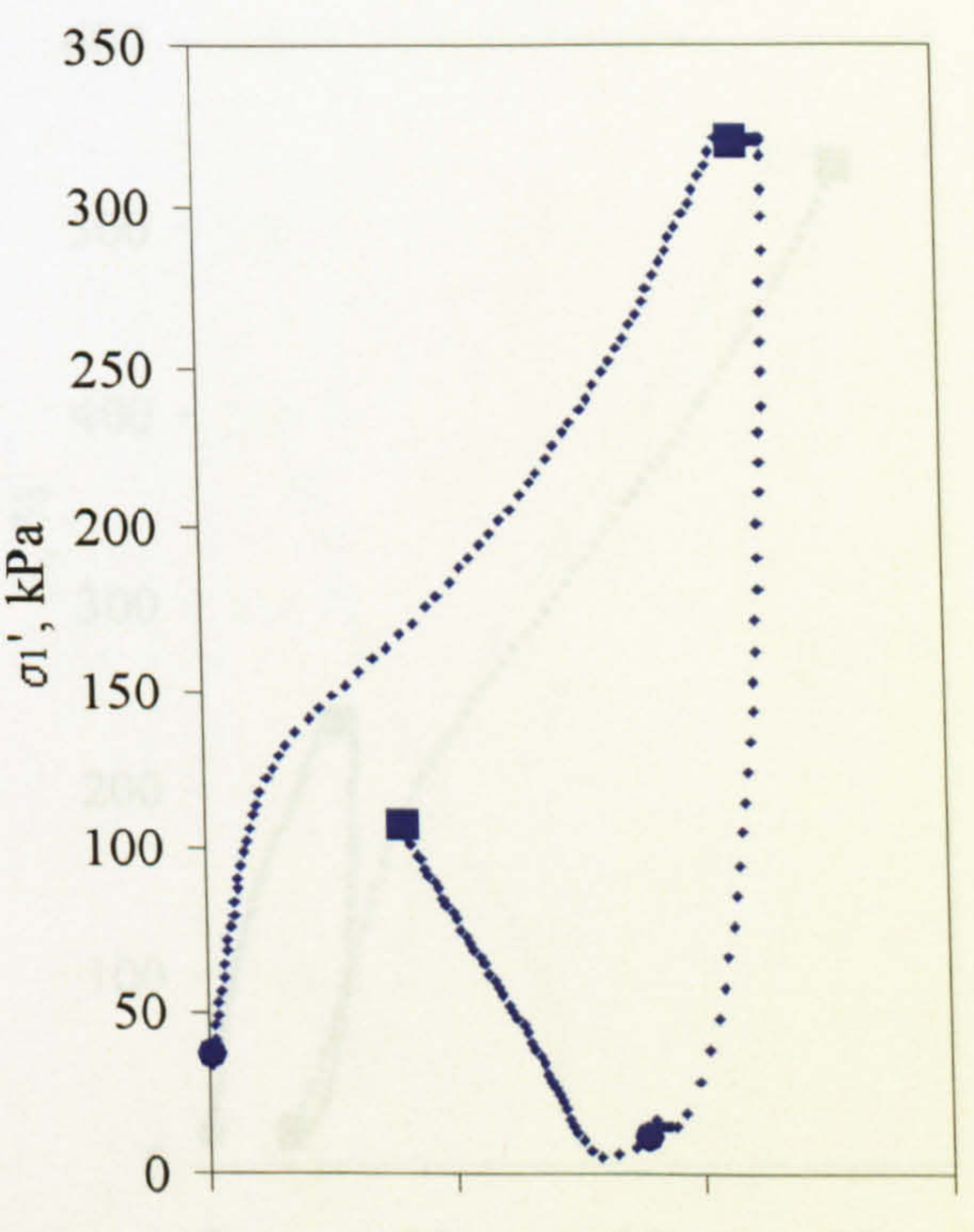

(d)

Figure 6.22. Stress-strain behaviour in Test C5, ($\eta_1 = 0.80$ and $\eta_2 = -0.80$): (a), (b) compression behaviour, (c) deviatoric behaviour and (d) axial behaviour.

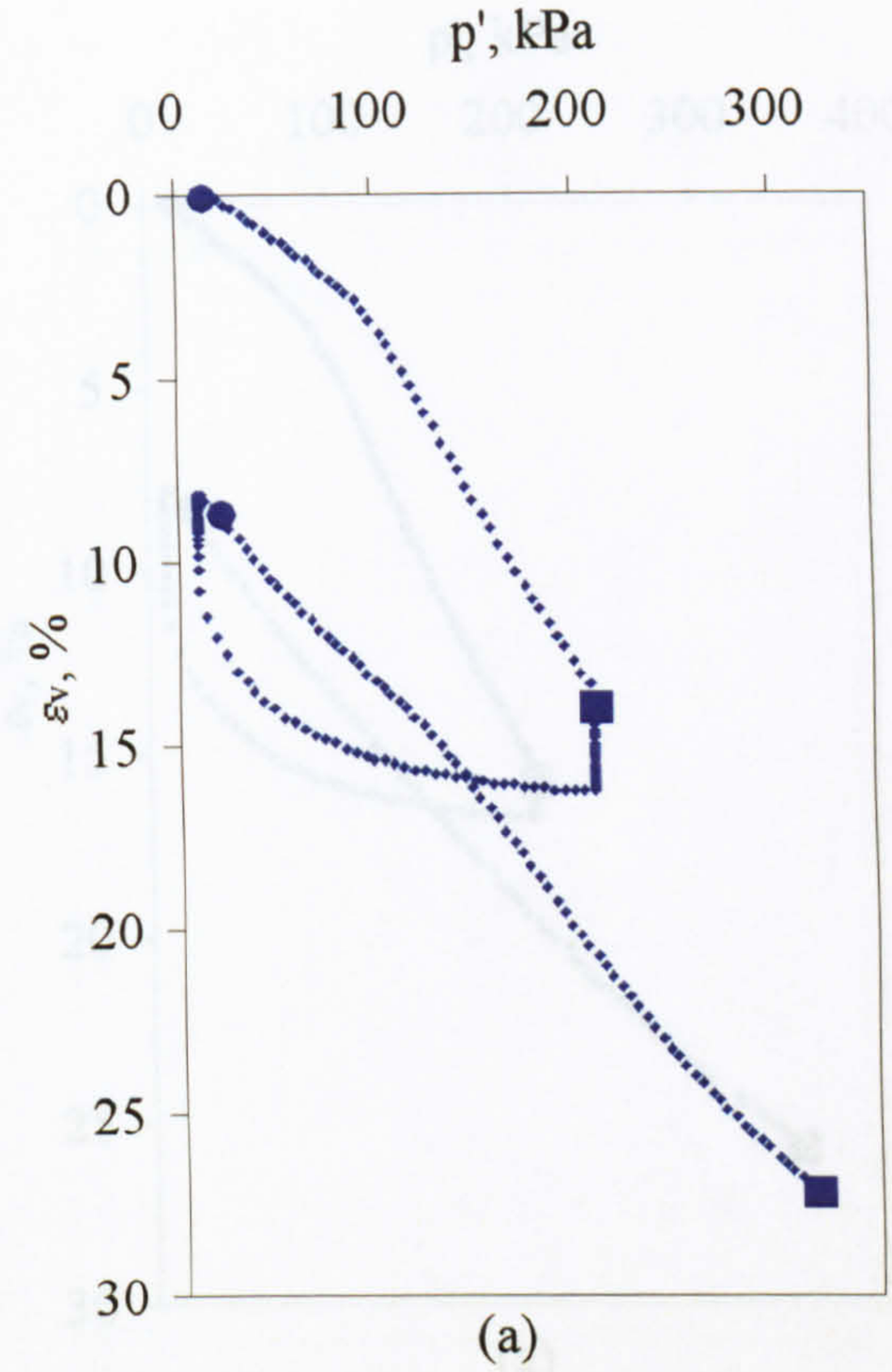

(a)

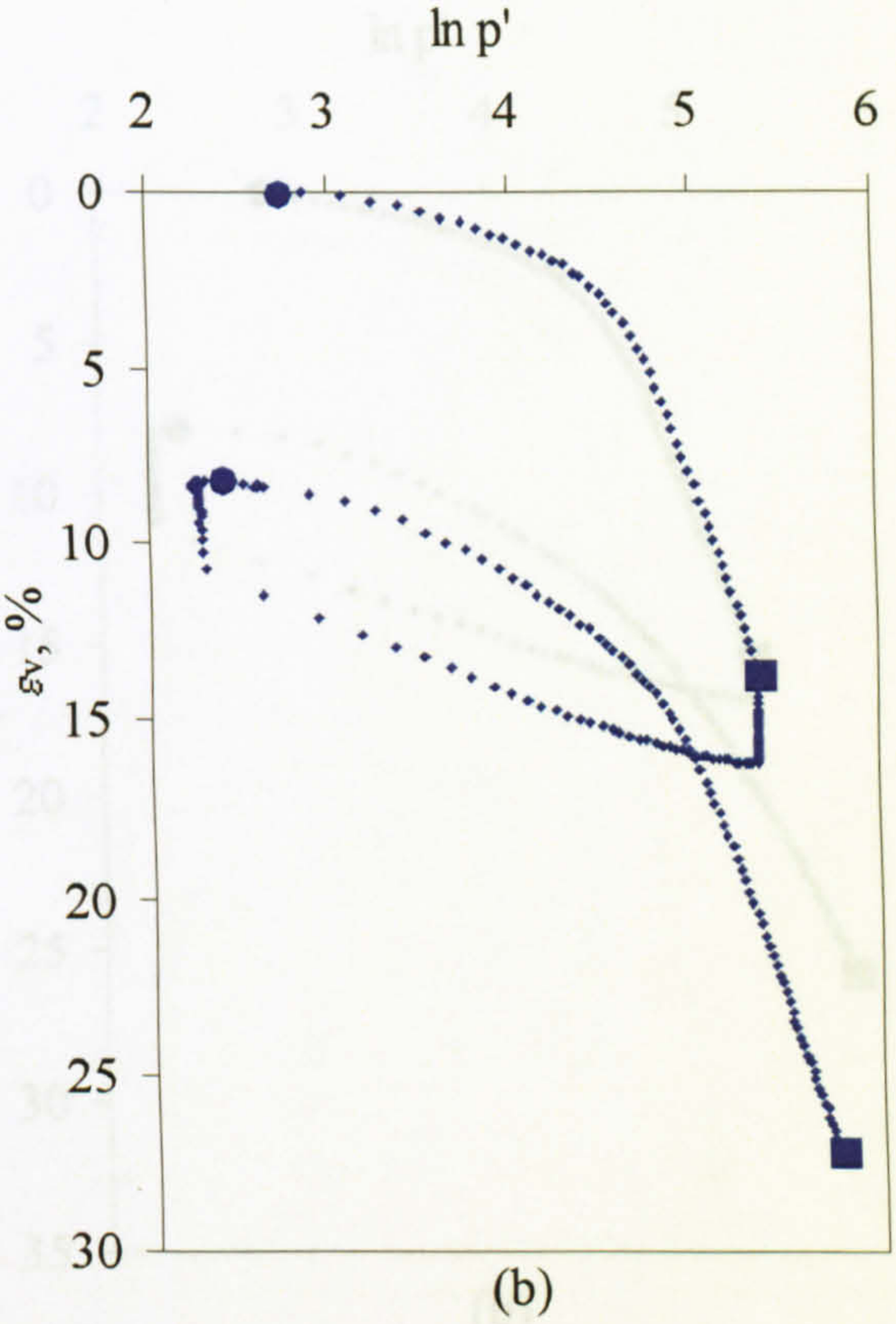

(b)

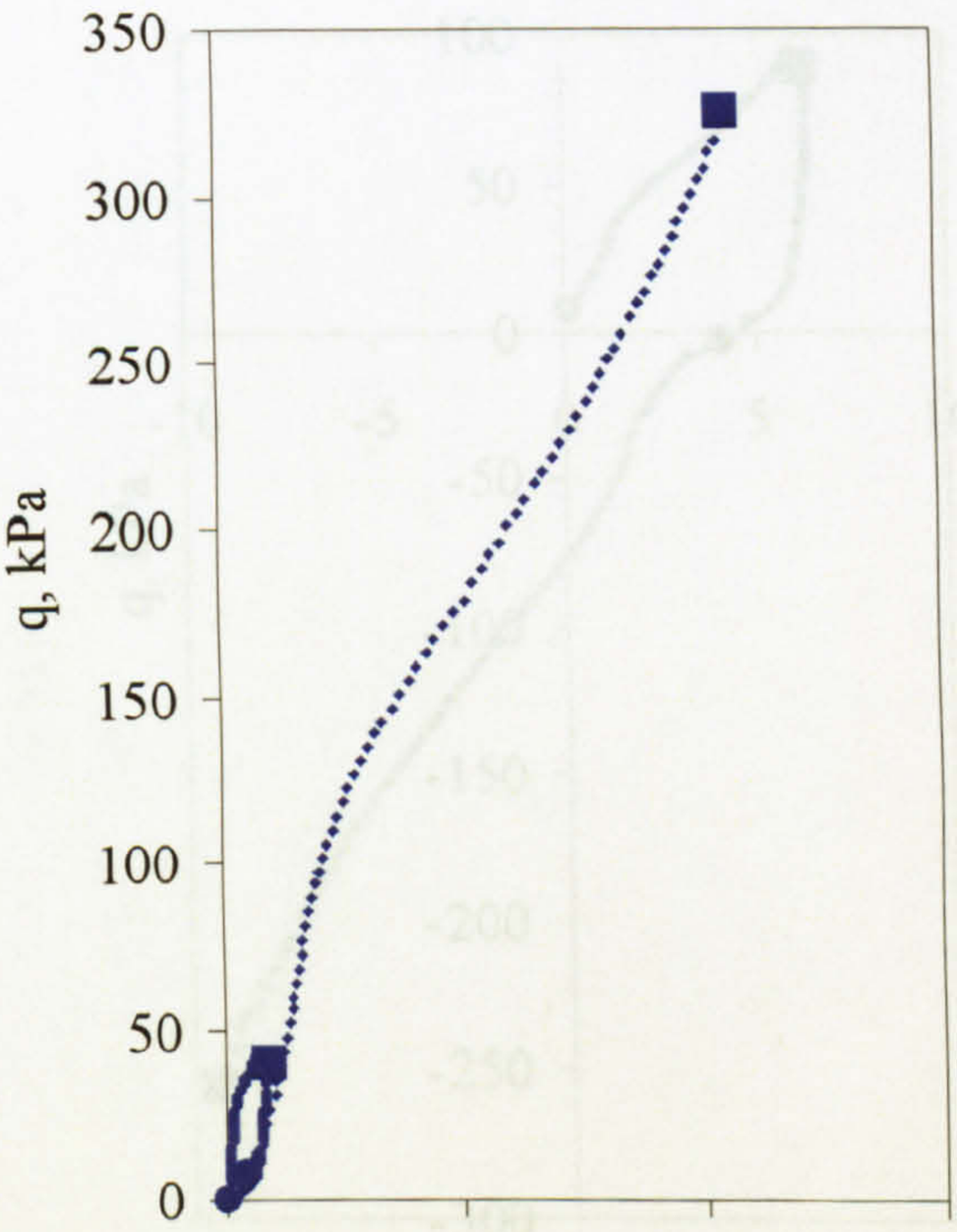

(c)

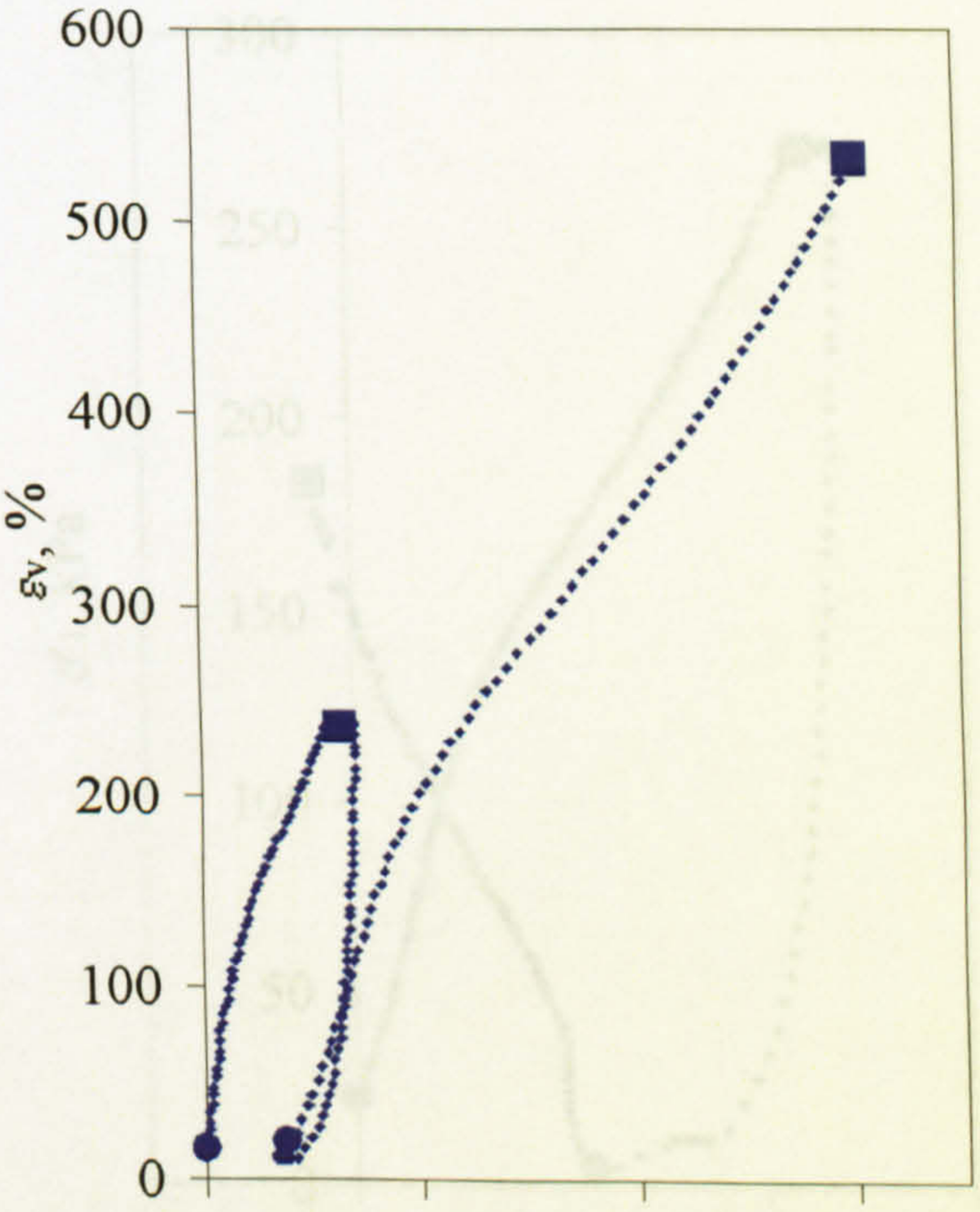

(d)

Figure 6.23. Stress-strain behaviour in Test C6 ($\eta_1 = 0.20$ and $\eta_2 = 1.03$) (a), (b) compression behaviour, (c) deviatoric behaviour and (d) axial behaviour.

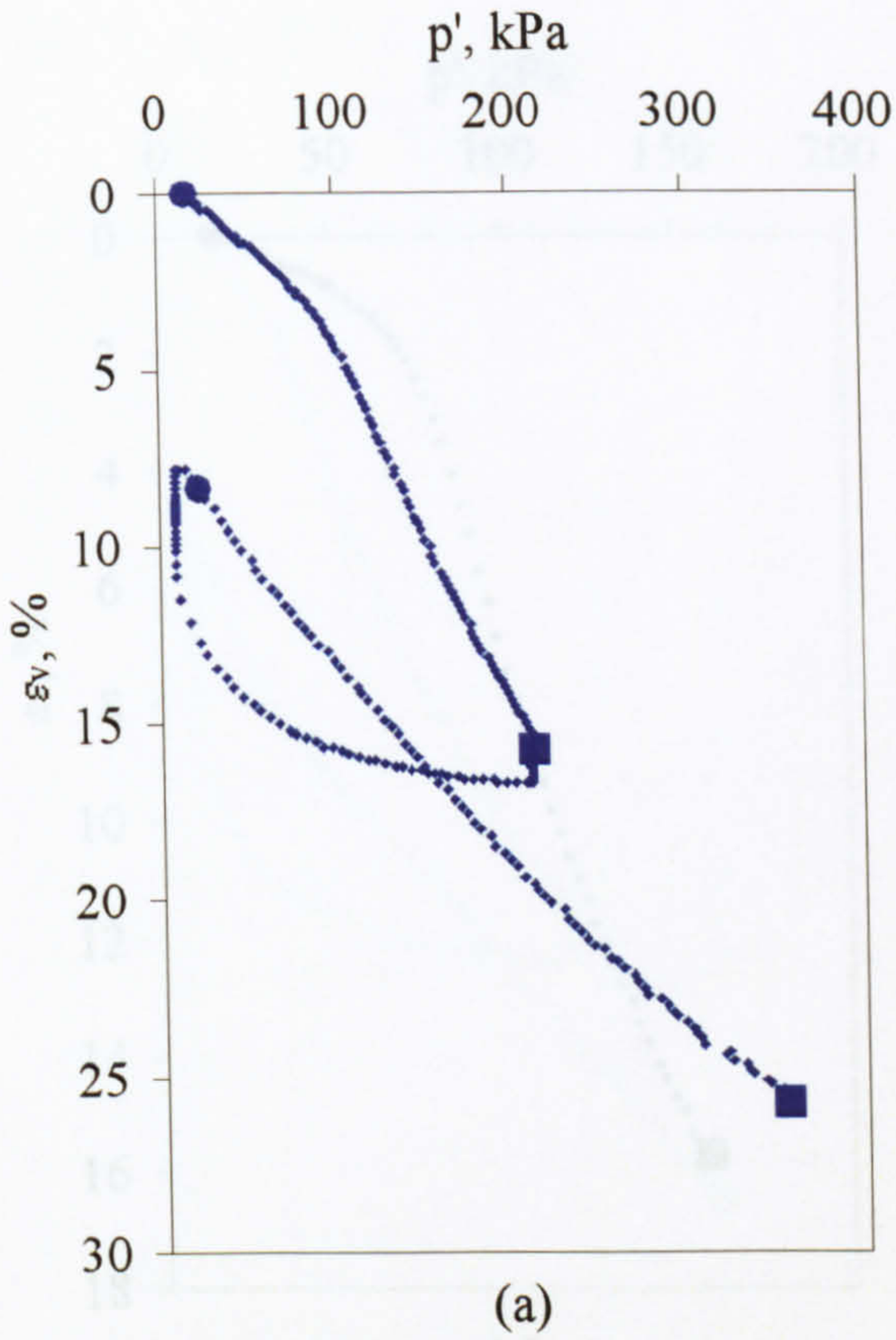

(a)

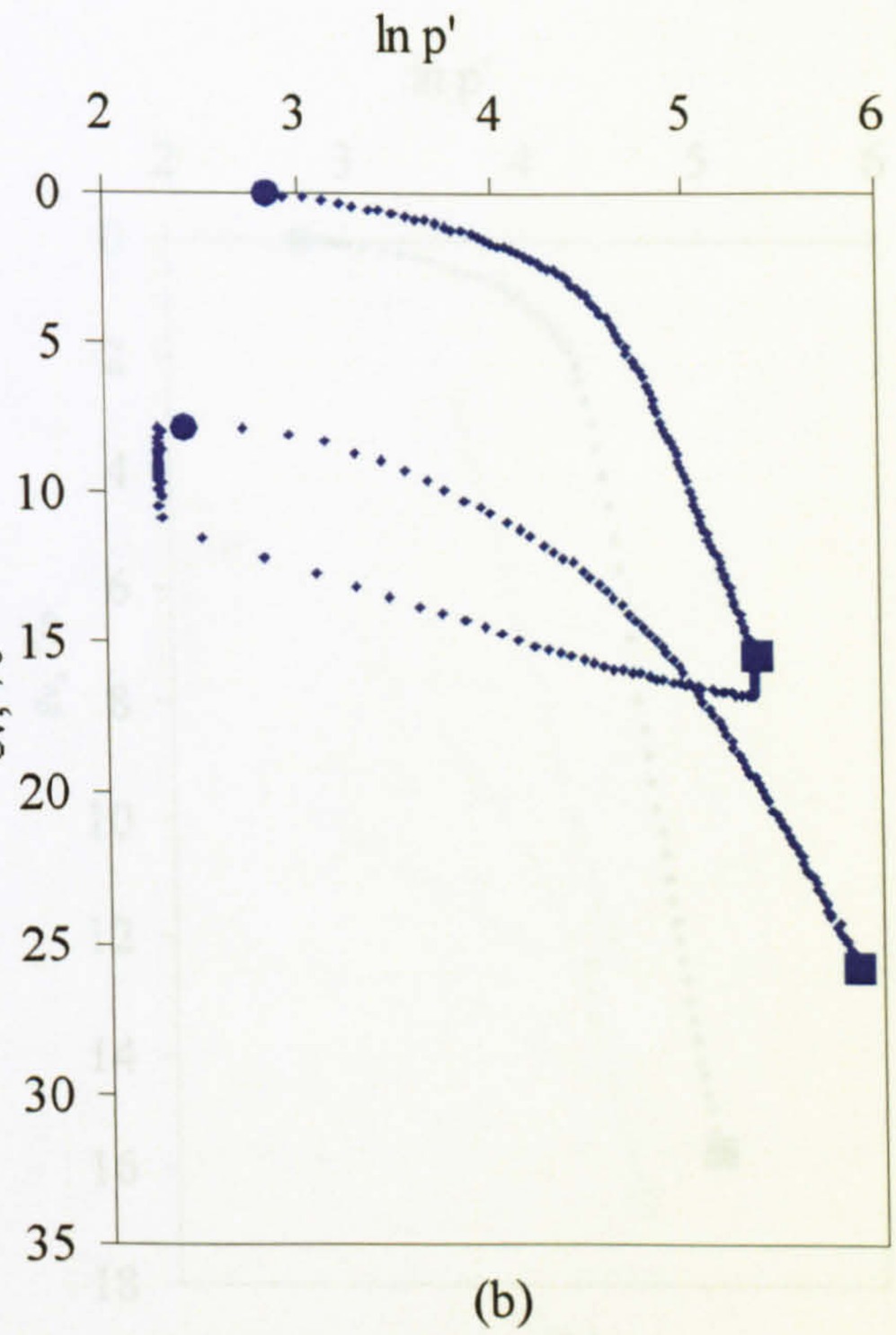

(b)

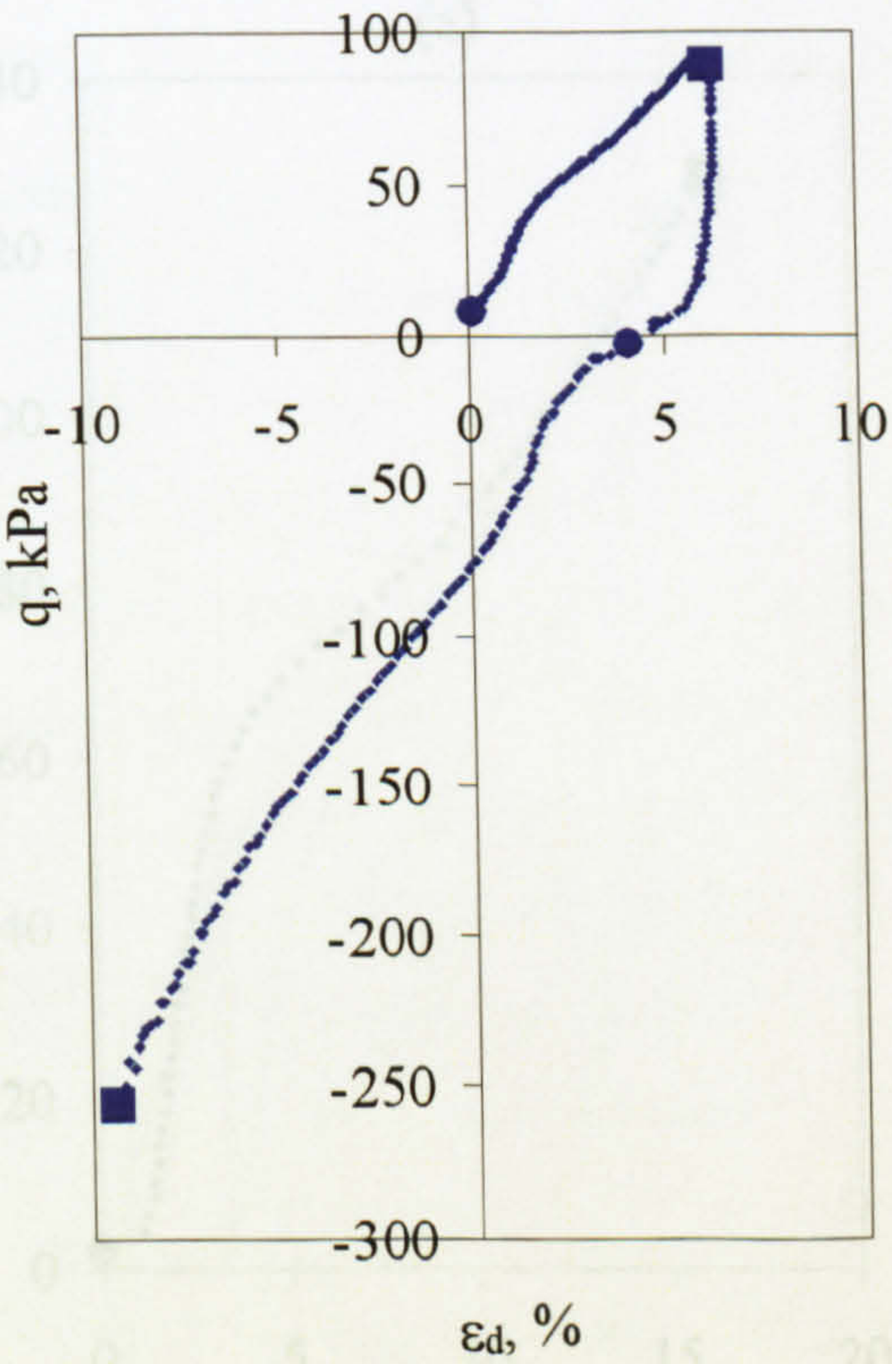

(c)

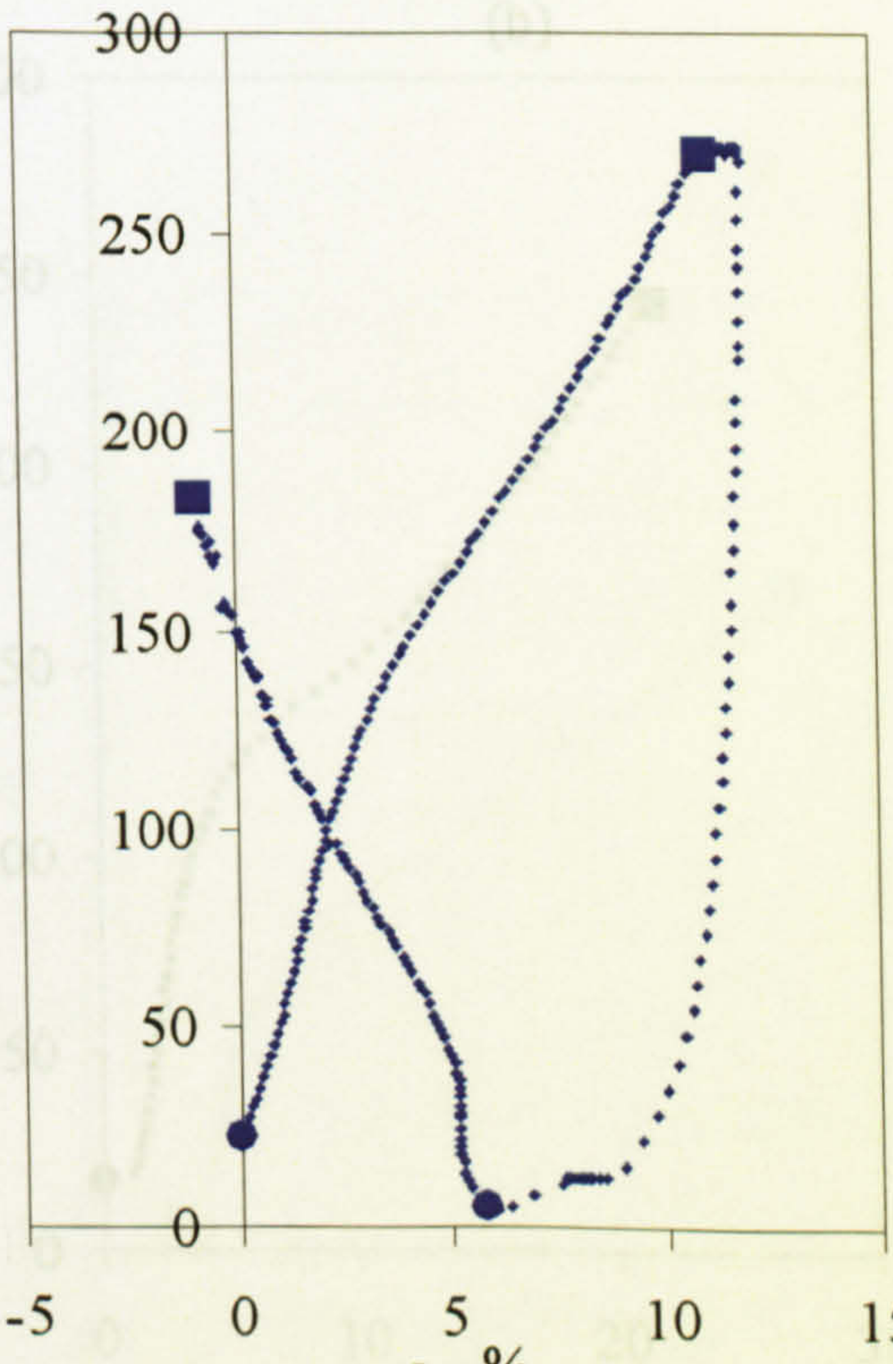

(d)

Figure 6.24. Stress-strain behaviour in Test C7 ($\eta_1 = 0.42$ and $\eta_2 = 0.72$): (a), (b) compression behaviour, (c) deviatoric behaviour and (d) axial behaviour.

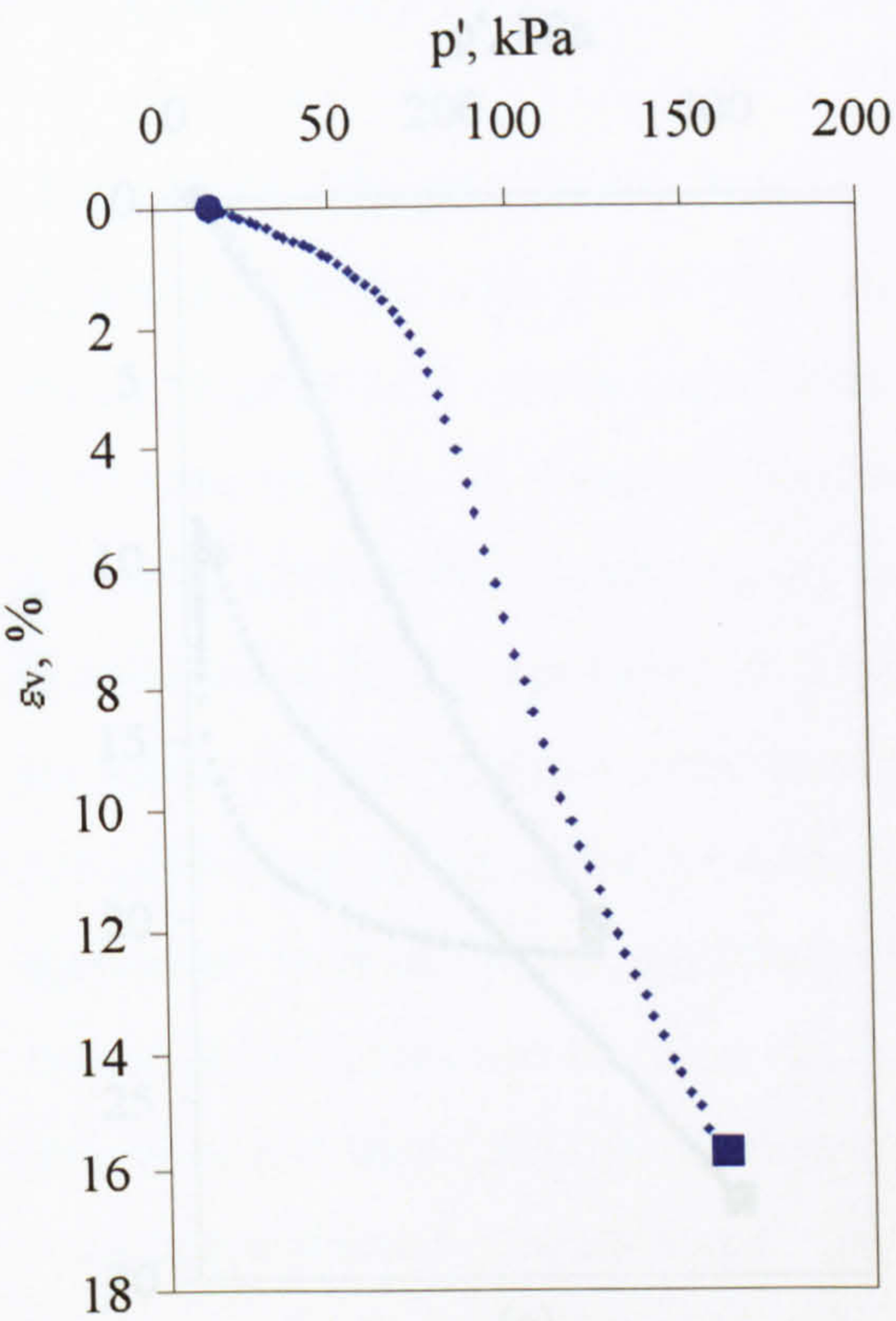

(a)

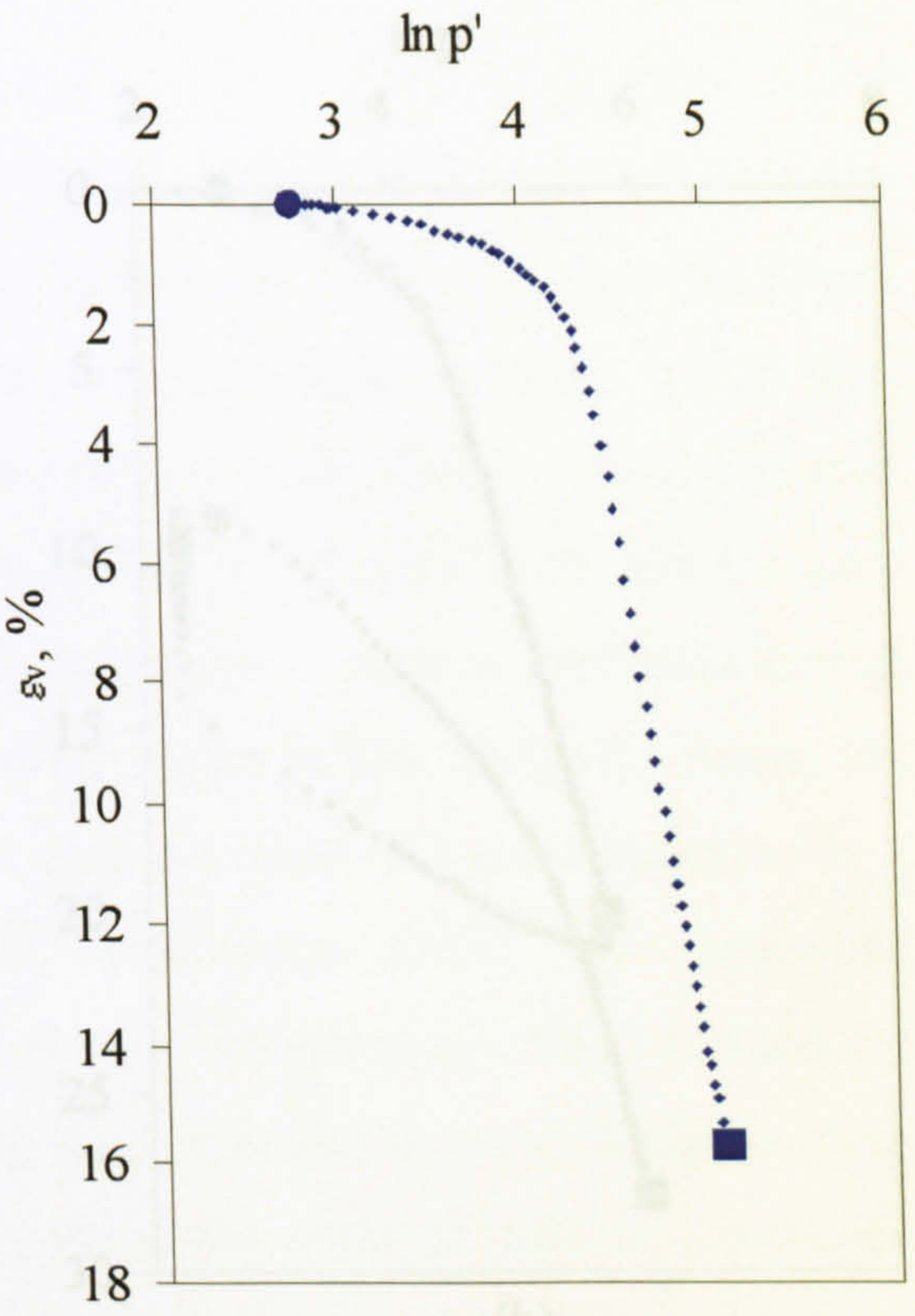

(b)

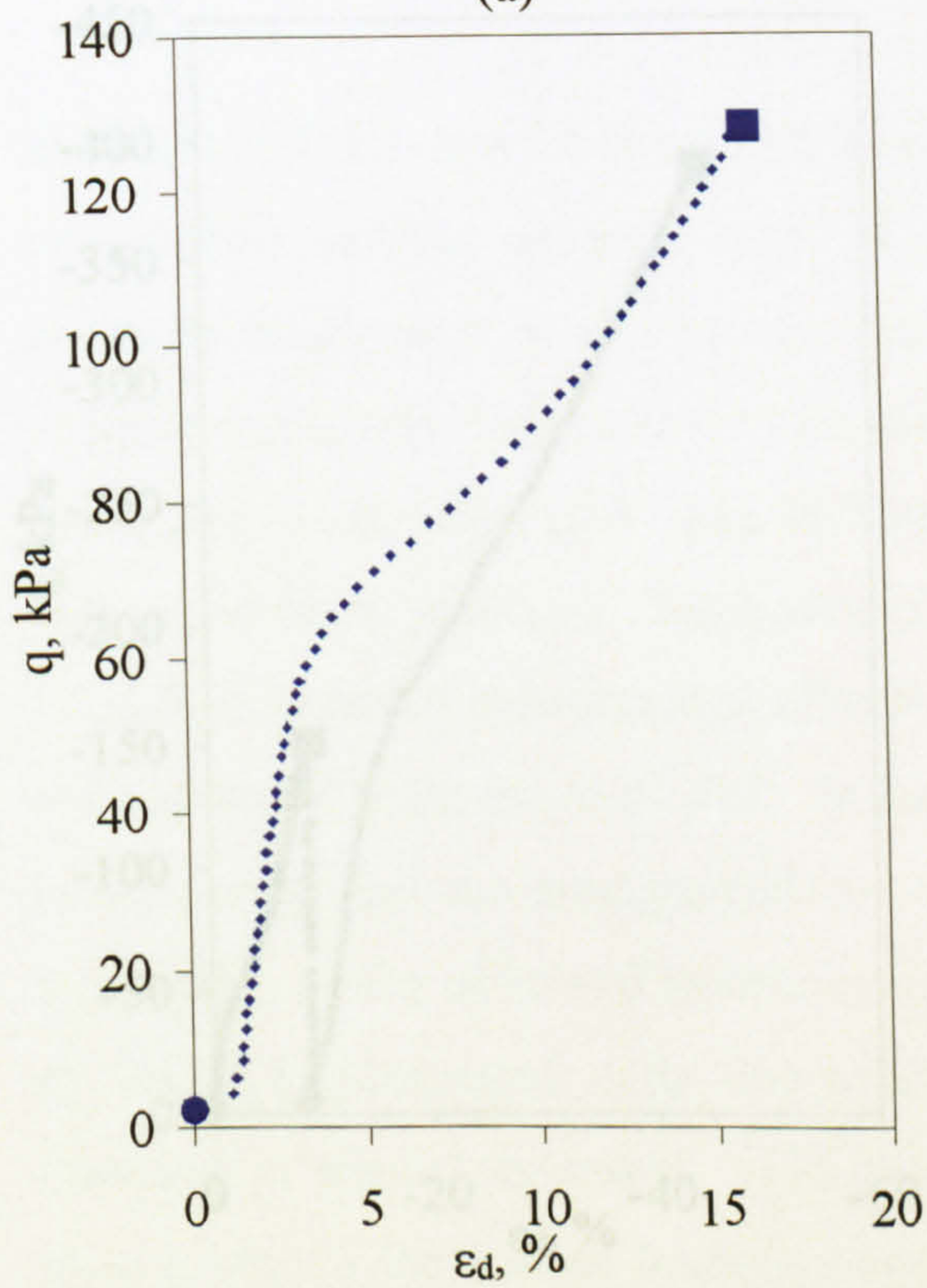

(c)

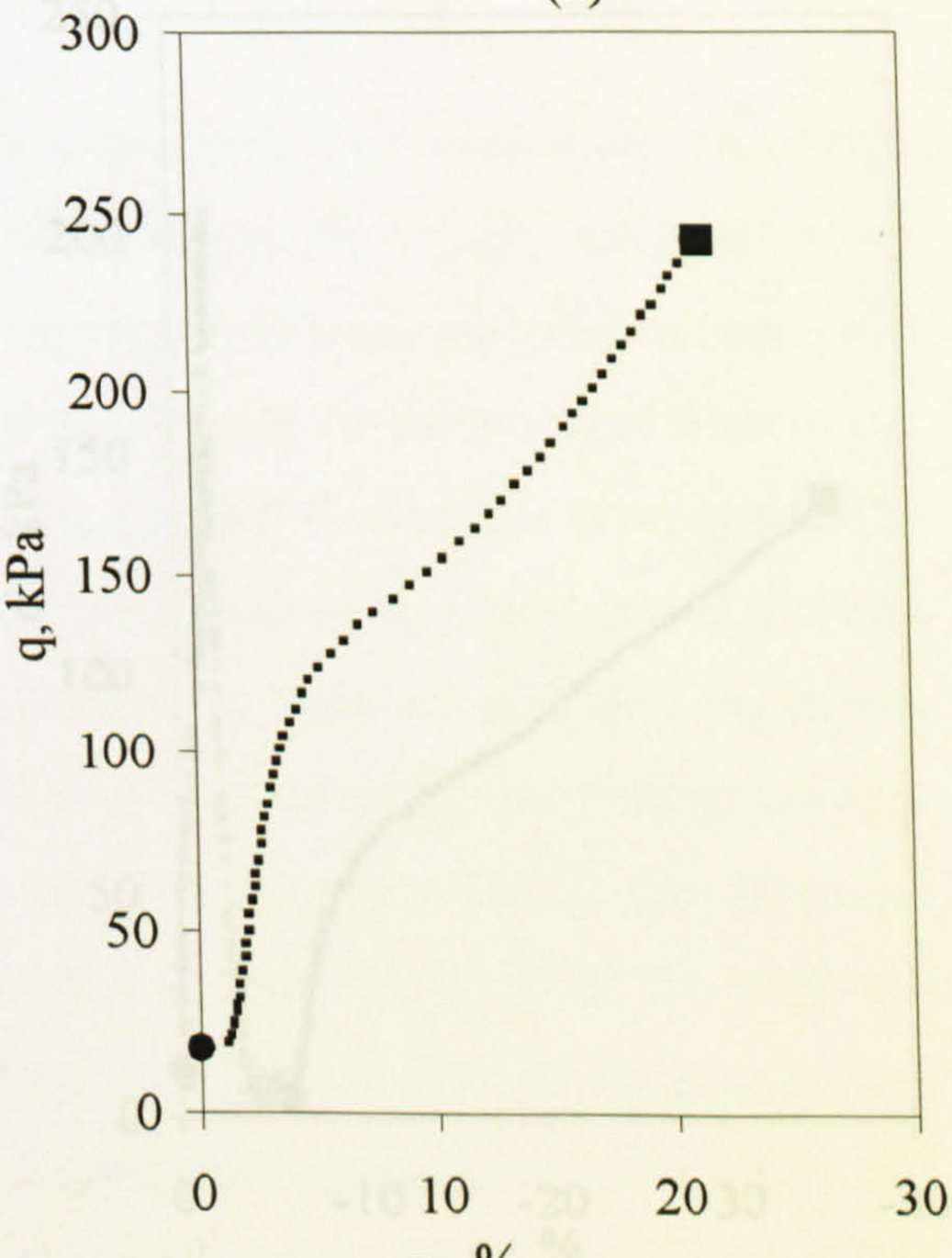

(d)

Figure 6.25. Stress-strain behaviour in Test C8 ($\eta_1 = 0.81$): (a), (b) compression behaviour, (c) deviatoric behaviour and (d) axial behaviour.

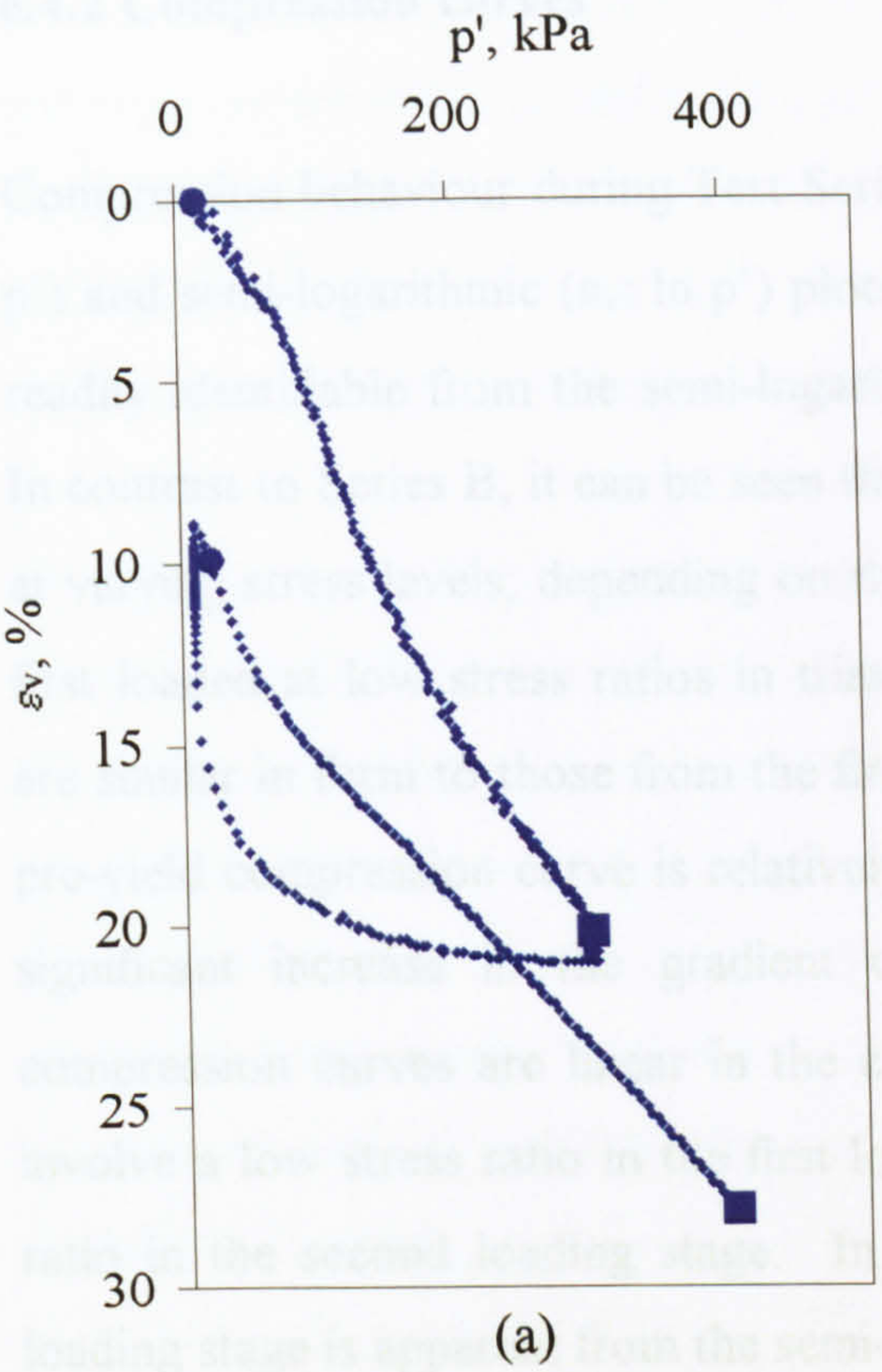

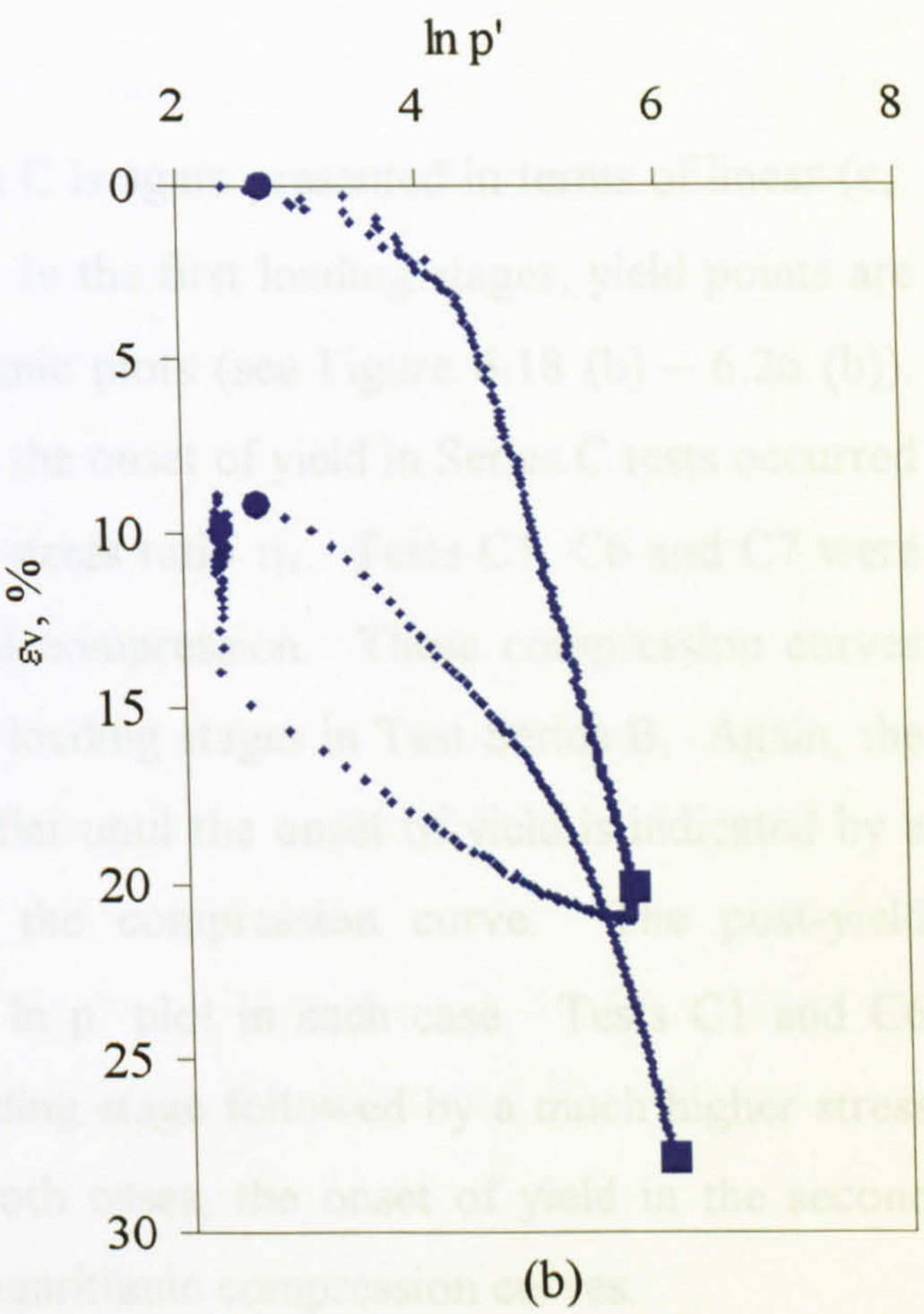

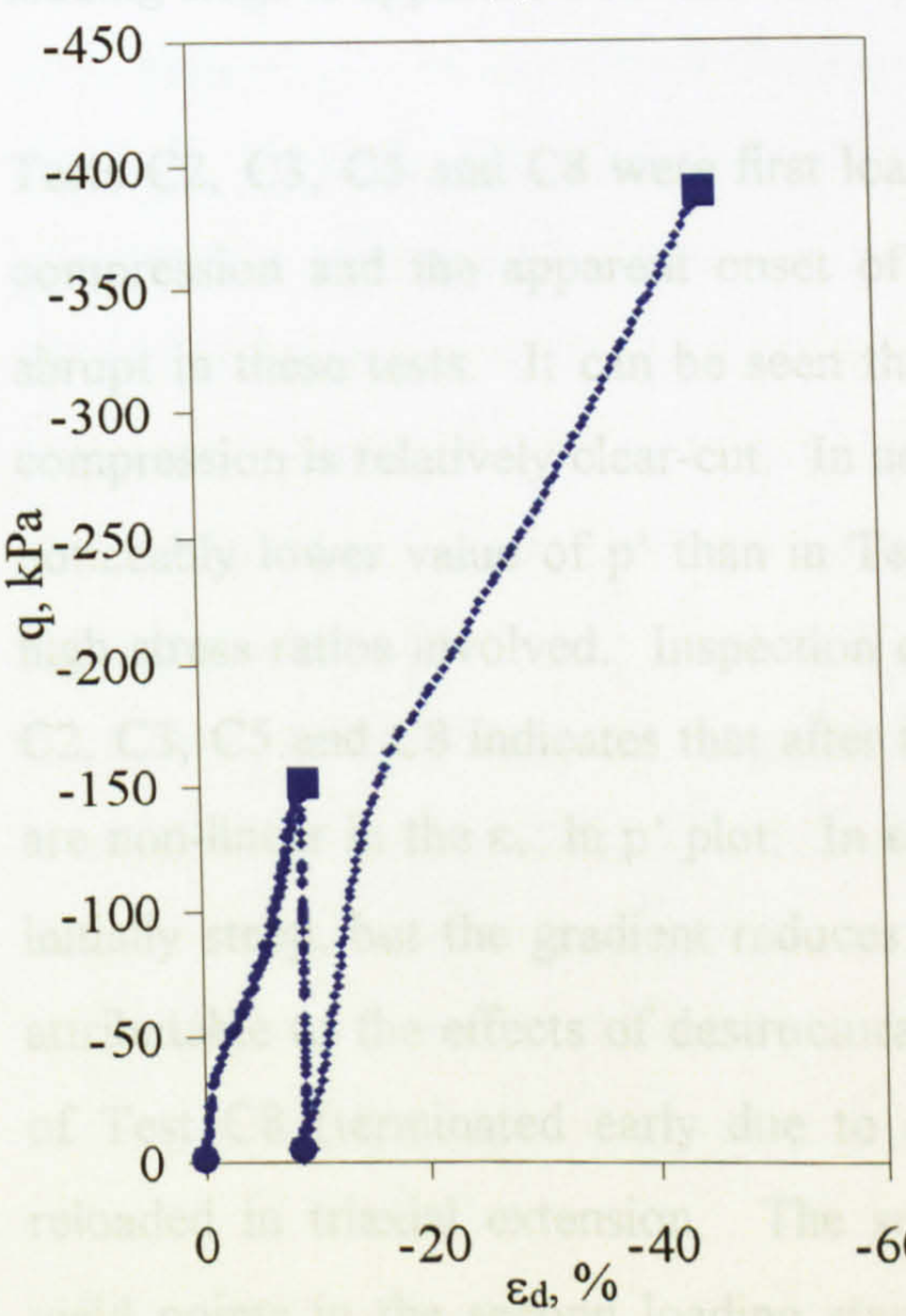

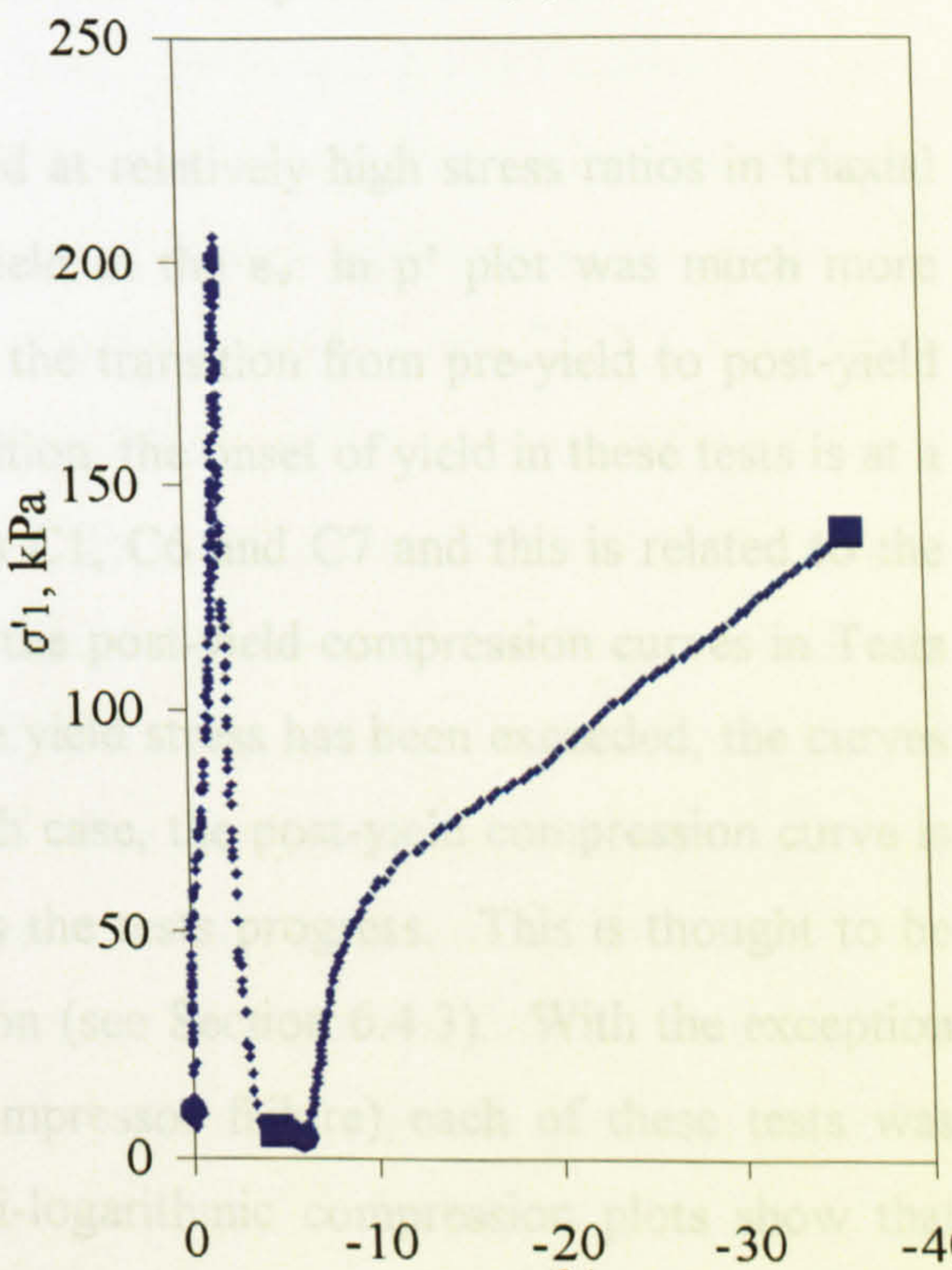

Figure 6.26. Stress-strain behaviour in Test C9 (η_1 = -0.50 and η_2 = -0.96): (a), (b) compression behaviour, (c) deviatoric behaviour and (d) axial behaviour.

6.4.2 Compression curves

Compression behaviour during Test Series C is again presented in terms of linear (ε_v: p') and semi-logarithmic (ε_v: ln p') plots. In the first loading stages, yield points are readily identifiable from the semi-logarithmic plots (see Figure 6.18 (b) – 6.26 (b)). In contrast to Series B, it can be seen that the onset of yield in Series C tests occurred at varying stress levels, depending on the stress ratio η_1. Tests C1, C6 and C7 were first loaded at low stress ratios in triaxial compression. These compression curves are similar in form to those from the first loading stages in Test Series B. Again, the pre-yield compression curve is relatively flat until the onset of yield is indicated by a significant increase in the gradient of the compression curve. The post-yield compression curves are linear in the ε_v: ln p' plot in each case. Tests C1 and C6 involve a low stress ratio in the first loading stage followed by a much higher stress ratio in the second loading stage. In both cases, the onset of yield in the second loading stage is apparent from the semi-logarithmic compression curves.

Tests C2, C3, C5 and C8 were first loaded at relatively high stress ratios in triaxial compression and the apparent onset of yield in the ε_v: ln p' plot was much more abrupt in these tests. It can be seen that the transition from pre-yield to post-yield compression is relatively clear-cut. In addition, the onset of yield in these tests is at a noticeably lower value of p' than in Tests C1, C6 and C7 and this is related to the high stress ratios involved. Inspection of the post-yield compression curves in Tests C2, C3, C5 and C8 indicates that after the yield stress has been exceeded, the curves are non-linear in the ε_v: ln p' plot. In each case, the post-yield compression curve is initially steep, but the gradient reduces as the tests progress. This is thought to be attributable to the effects of destructuration (see Section 6.4.3). With the exception of Test C8 (terminated early due to compressor failure) each of these tests was reloaded in triaxial extension. The semi-logarithmic compression plots show that yield points in the second loading stages are much more difficult to identify. The transition from pre-yield to post-yield straining is much more gradual. In the second stages of these tests, it is possible that the yield point is being obscured by the effects of evolving anisotropy, as the soil is being reloaded at a radically different stress ratio from the first loading stage. The plots suggest, however, that the yield point

occurs at a mean effective stress that is significantly lower than the previous maximum mean effective stress (p'_{max1}). In addition, it is clear that the gradient of the post-yield compression curve is much smaller than in the first loading stage, particularly in Tests C2 and C3. This is again thought to be a consequence of destructuration occurring during the first loading stage (see Section 6.4.3).

In contrast, the ε_v: ln p' compression curves during first loading in triaxial extension (Tests C4 and C9) indicate that yield is relatively gradual and the yield points are less distinct than in other first loading stages. In the second loading stages of these two tests, Test C9 was reloaded at a higher stress ratio in triaxial extension, whereas Test C4 was reloaded in triaxial compression. Both second stage compression curves are of similar form to those from the second stages of Tests C2, C3 and C5. Again, the compression curve gradient changes throughout the stage and the yield point is therefore obscured.

Compression curves are shown plotted on linear scales (ε_v: p') in Figures 6.18 (a) – 6.26 (a). In these plots, the pre-yield compression curves tend to be almost linear, whereas the post-yield compression curves are always significantly non-linear. In the first loading stages, the yield points are most obvious in Tests C2, C3, C5 and C8 in the ε_v: p' plots. Where samples are first loaded in triaxial extension (Tests C4 and C9), the yield points are less well defined in the ε_v: p' plots. In many of the second loading stages it is virtually impossible to detect the onset of yield from the linear ε_v: p' curves. In tests involving large differences in stress ratio between first and second loading (Tests C2, C3, C4, C5 and C7) the change in gradient in the ε_v: p' compression curve is very subtle. In tests involving less radical changes in stress ratio (such as Tests C1, C6 and C9) it is possible to detect the onset of yield from the ε_v: ln p' plots, although yielding is less apparent than in the semi-logarithmic plots.

6.4.3 λ and κ values

Semi-logarithmic plots of v against ln p' have been used to obtain values of λ in both the first loading stages (λ_1) and second loading stages (λ_2) in Test Series C. Each value of λ was measured from the steepest section of the post-yield compression

curve (see Figure 6.14). These values are listed in Table 6.5. In the first loading stages, the lowest value of λ_1 is 0.35 in Test C6 and this corresponds to the lowest value of η_1 in Test Series C. The highest value of λ_1 corresponds to Test C3, which involves the highest stress ratio. In Figure 6.27, the measured values of λ_1 for both test Series B and C are plotted against the corresponding values of stress ratio (η_1). The values of λ_1 range from 0.30 in Test B4 (where $\eta_1 = 0$) to 0.74 in Test C3 (where $\eta_1 = 1.30$). Generally, higher values of λ_1 were observed at higher stress ratios, particularly in triaxial compression. From the best-fit curve to the data in Figure 6.27, it can be seen that an apparent λ value of approximately 0.34 is appropriate for isotropic loading, whereas a value of about 0.48 is appropriate for K_0 loading (where $\eta_{K0} = 0.913$).

TEST	η_1	λ_1	κ_{unload}	η_2	λ_2
C1	0.42	0.37	0.035	1.04	0.29
C2	1.11	0.54	0.037	-0.50	0.18
C3	1.30	0.74	0.043	-0.60	0.18
C4	-0.80	0.36	0.035	0.60	0.25
C5	0.80	0.47	0.052	-0.80	0.21
C6	0.20	0.35	0.040	1.03	0.30
C7	0.42	0.38	0.043	-0.70	0.24
C8	0.80	0.43	-	-	-
C9	-0.50	0.36	0.046	-0.96	0.29

Table 6.5. λ and κ values observed in Test Series C.

In tests involving high stress ratios in triaxial compression, the post-yield compression curves were significantly non-linear (concave upwards) in the v: ln p' plots (see the ε_v: ln p' plots on Figures 6.19, 6.20, 6.22 and 6.25) i.e. the apparent value of λ_1 tended to decrease as plastic straining progressed. This phenomenon was particularly marked in Tests C2 ($\eta_1 = 1.10$) and Test C3 ($\eta_1 = 1.30$). It is likely that this is a consequence of destructuration. In these tests, it is apparent that the gradient of the post-yield compression is very high immediately after the yield point has been

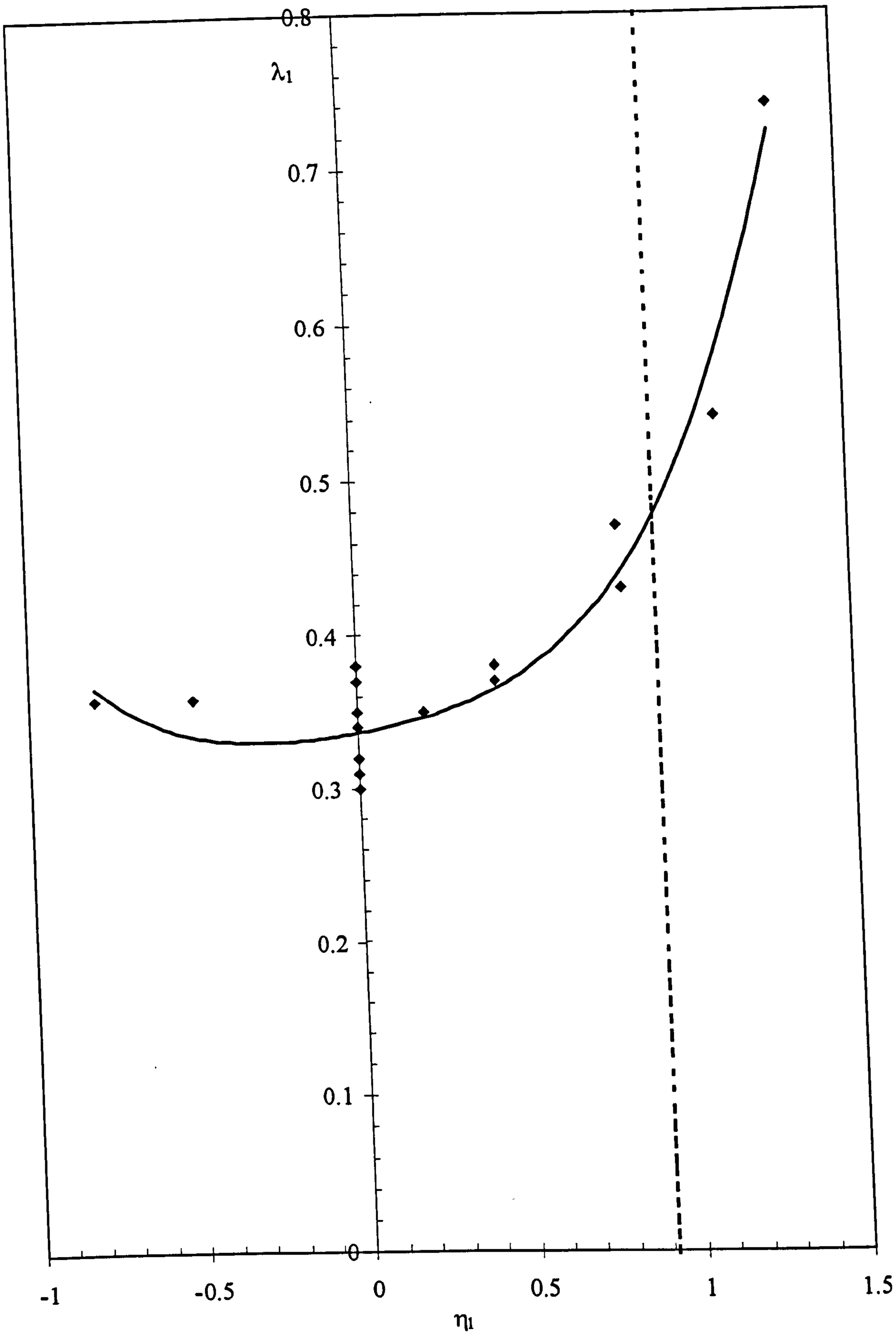

Figure 6.27. Post-yield compression slopes (λ_1) in first loading stages.

exceeded. This may be a result of powerful destruction of inter-particle bonds, assisted by the large shear strains occurring at these high values of η_1. As post-yield straining progresses, the bonding effect is progressively destroyed and the soil tends towards an intrinsic state, accompanied by a decrease in the rate of compression, as demonstrated in Figure 6.19 (b) and Figure 6.20 (b). Hence, the "apparent" value of λ_1 has reduced by the end of first loading. Tests involving low values of η_1 result in values of λ_1 that are much lower than those obtained for tests C2, C3 and C5, but the values of λ_1 remain essentially constant during first loading. This suggests that the rate of destructuration is highly dependent on the stress ratio. Presumably, the rate of destructuration is influenced by a combination of both plastic volumetric strains and plastic shear strains. The suggestion is that plastic volumetric strains cause destructuration at all values of η_1 (in addition to causing primary consolidation) and plastic shear strains produce an enhancement of destructuration that is greatest at high values of η_1 (where the plastic shear strains are very large).

Values of λ_2 from the second loading stages in Series C are presented in Table 6.5, and Figure 6.28 shows the measured values of λ_2 plotted against the corresponding stress ratio η_2 for all tests in Series B and C. The first point arising from Figure 6.28 is that the values of λ_2 measured in the second loading stages were significantly lower than the corresponding values of λ_1 measured in the first loading stages (see Figure 6.27). This is consistent with the explanation that destructuration occurring during the first loading stage meant that there was a reduced amount of bonding present at the start of the second loading stage, and therefore reduced potential for further destructuration in the second loading stage.

Another point emerging from Figure 6.28 is that, although there is a general suggestion of higher values of λ_2 at high positive values of η_2, there is considerably more scatter of the value of λ_2 in Figure 6.28 than for the corresponding values of λ_1 in Figure 6.27. This can be attributed to different amounts of destructuration occurring during the preceding first loading stages. For example, Tests C2, C3, B5 and B6 all involved similar values of η_2, but the measured values of λ_2 were significantly lower in Tests C2 and C3 than in Tests B5 and B6 (see Figure 6.28).

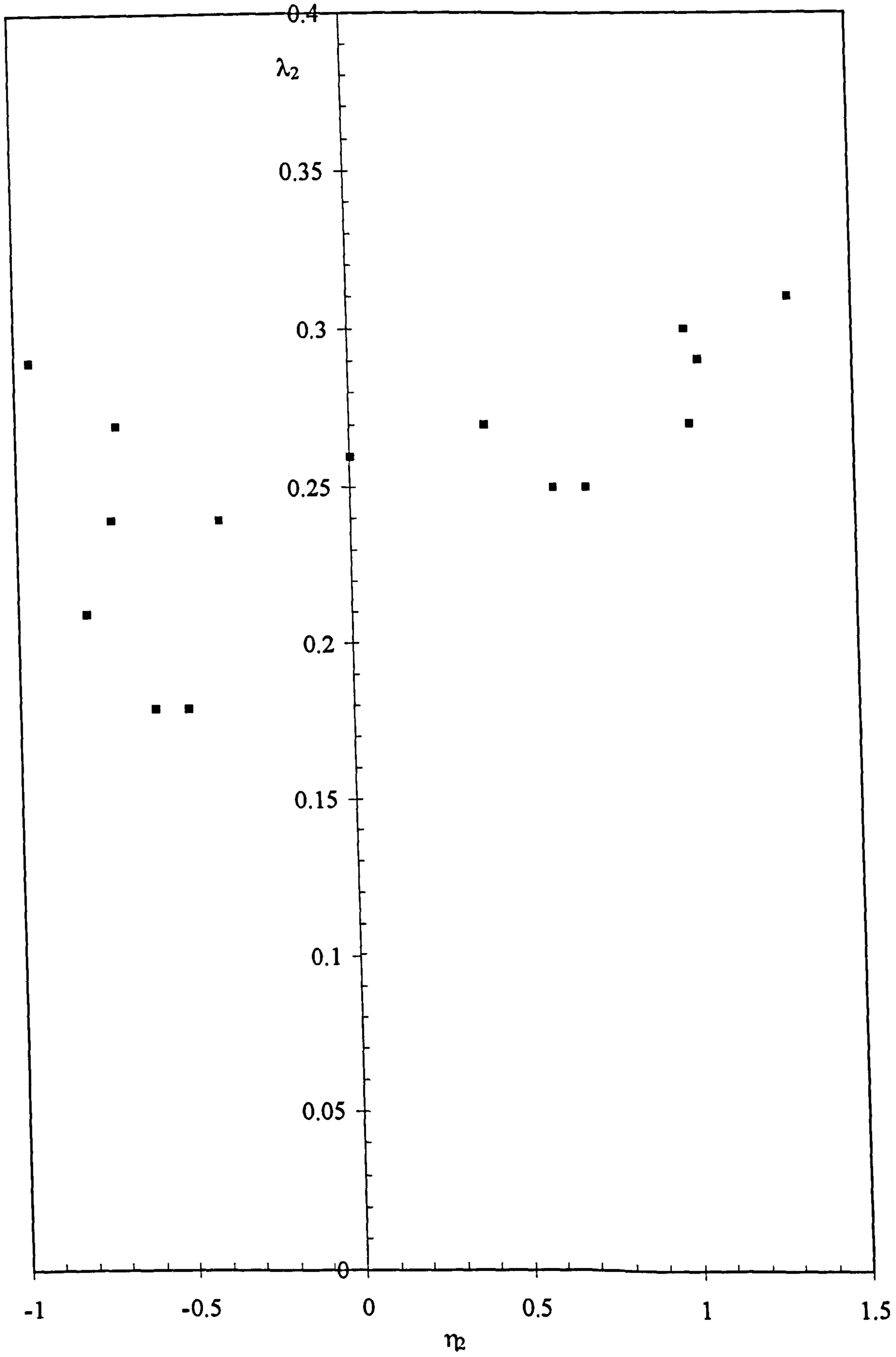

Figure 6.28. Post-yield compression slopes (λ_2) in second loading stages.

This is consistent with the suggestion that Tests C2 and C3 involved larger amounts of destructuration in the first loading stages (at $\eta_1 = 1.11$ or $\eta_1 = 1.30$), than occurred in Tests B5 and B6 (with $\eta_1 = 0$), and hence there was much less bonding left at the start of the second loading stages for Tests C2 and C3.

Another feature of the data in Figures 6.27 and 6.28 is that even the values of λ_2 measured in Series B tests at a given value of η_2 were significantly lower than corresponding values of λ_1 measured in Series B or Series C at the same stress ratio. This is significant, because it suggests that substantial destructuration has occurred even during the first loading stages of Series B tests ($\eta_1 = 0$). Shear strains remained very small during the first loading stages of Series B tests, and it therefore appears likely that the destructuration occurring during these stages must be largely attributable to plastic volumetric strains. The experimental results therefore strongly support the suggestion that both plastic shear strains and plastic volumetric strains contribute to destructuration, as assumed in the constitutive model S-CLAY1S (see Section 3.3.1). Clayton et al. (1992) examined the progressive destructuration of Bothkennar clay in a series of consolidated-undrained triaxial tests. They found that destructuration could be caused by undrained shear strains or by volumetric strains during consolidation. They suggested that volumetric strains were more effective in the destructuration process.

Figure 6.28 also shows that the two lowest values of λ_2 measured ($\lambda_2 = 0.18$ for Tests C2 and C3) coincide with the intrinsic value of λ measured during one-dimensional loading of reconstituted Bothkennar clay ($\lambda_i = 0.18$ by Koskinen (2001) using material retained from the samples tested in Series B and C). This suggests that for Tests C2 and C3 the large amounts of destructuration occurring during the first loading stages (at $\eta_1 = 1.10$ or $\eta_1 = 1.30$) may have been sufficient to effectively remove all bonding prior to the second loading stages. The results, however, should be viewed with caution, since there is the possibility that the compression curves during the second loading stages are also influenced by evolving anisotropy.

Overall, it may be concluded that it is probably necessary to incorporate the effects of destructuration within a constitutive model if the compression curves are to be

accurately predicted over a full range of η values and over both first and second loading stages of the tests in Series B and Series C. These issues are examined further using S-CLAY1 simulations in Chapter 8 and S-CLAY1S simulations in Chapter 9.

Values of κ cannot be estimated from first or second loading stages in Test Series C because the pre-yield behaviour during loading is highly non-linear in the v: ln p' plots, particularly during the second loading stages. However, as noted during Test Series B, the unloading stages were relatively linear in the v: ln p' plots. Values of κ_{unload} were therefore obtained from the unloading stages in each test (using the same methodology as in Test Series B) and are listed in Table 6.5. These give an average value of 0.041, very similar to the average value of 0.038 from Test Series B. Overall therefore, an average value of 0.04 for κ_{unload} is appropriate.

6.4.4 Volumetric strains occurring during rest periods

Inspection of both the semi-logarithmic (ε_v: ln p') and linear compression plots (ε_v: p') shows that a significant amount of positive volumetric compression occurred during the 24-hour rest period at the end of the first loading stage in each test (see Figures 6.5-6.13 and 6.18-6.26). The magnitude of this volumetric strain ranged from 1 % in Test B1 to 2.5 % in Test C6. In addition, negative volumetric strains occurred in each test during the 24-hour rest period following the unloading stage. One possible explanation for these additional volumetric strains was that they were the result of delayed primary consolidation or swelling, caused by loading or unloading that was conducted too rapidly. Another possibility is that the additional strains represent creep effects (otherwise known as secondary compression). Creep effects would be expected in a natural soft clay, particularly one with a significant organic content. Results from organic content tests (see Section 5.2) indicate that the organic content in the samples ranged from 3-4 % and is therefore considered to be significant. The fact that swelling occurs at the end of unloading causes the true κ value to be raised by the end of the rest period.

During the rest periods at the end of the first loading stages, the gradient of a plot of void ratio against the logarithm of time was used to determine an apparent value of creep index C_α. Values of C_α were found to range from 0.01 to 0.035. It is useful to compare these values of creep index with the corresponding values of compression index, C_c, which is linked to primary compression and can be retrieved from values of λ_1 via

$$C_c = 2.303\lambda_1 \qquad (6.7)$$

The ratio C_α/C_c was found to lie within the range 0.025 to 0.043. Mesri and Godlewski (1977) have shown that for a variety of soils, C_α/C_C ranges from 0.03 to 0.05. The values obtained from Test Series B and C are therefore consistent with the suggestion that volumetric strains occurring during the rest periods at the end of the first loading stages could be explained as predominantly due to creep effects. However, it is unlikely that the large swelling strains during the rest periods at the end of the unloading stages can be attributed to creep effects, as various researchers such as Graham et al. (1983) and Mesri and Godlewski (1977) have shown that creep strain rates are very low for overconsolidated samples. In addition, creep strains would be expected to be positive (compressive) under positive values of p', even though an unloading stage has just occurred.

6.4.5 Other stress-strain plots

The stress-strain behaviour observed in Series C tests is plotted in terms of deviatoric stresses and strains in Figures 6.18 (c) – 6.26 (c). Axial stress-strain behaviour is shown in Figures 6.18 (d) – 6.26 (d). During the first loading stages, pre-yield behaviour was generally reasonably linear in these plots and the yield points are well defined. The post-yield behaviour in the first loading stages was generally non-linear in these q: ε_d and σ'_1: ε_1 plots, as expected in any constant η test. In many of the second loading stages, yield points are much less apparent in the axial or deviatoric stress-strain plots. In the linear compression plots (ε_v: p'), yield points in tests involving second stages which were at radically different stress ratios to the first loading stages were difficult to identify. Correspondingly, plots of q: ε_d and σ'_1: ε_1

from Tests C2, C3, C4, and C5 show that there is very little change of gradient in the stress-strain curves and therefore the yield points are not apparent. Again, this is possibly due to the effects of evolving anisotropy. The onset of yield in the second loading stage is more apparent in plots involving Tests C1 and C6, where the first and second loading stages are in triaxial compression, and in Test C9, where the first and second loading stages both involve triaxial extension (i.e. there was not such a significant change of stress ratio between first and second loading stages). An exception to the trend is Test C7, where yielding is still fairly apparent in the second loading stage in triaxial extension, following on from a first loading stage in triaxial compression.

6.4.6 Strain paths

Strain paths plotted in terms of deviatoric and volumetric strains for each of the tests in Series C are shown in Figure 6.29. The yield points identified from v: ln p' are indicated on the plots (Y_1 and Y_2 for the first and second loading stages respectively). The strain path plots indicate that, as would be expected, both pre-yield and post-yield patterns of straining are strongly dependent on the stress ratio. In terms of the pre-yield behaviour, positive volumetric strains are accompanied by positive shear strains in Tests C1, C2, C3, C5, C6 and C7 (all involving triaxial compression), whereas positive volumetric strains are accompanied by negative shear strains in Tests C4 and C9 (both involving triaxial extension). In Section 6.3.5, evidence from the pre-yield sections of the first loading stages in Test Series B (at $\eta_1 = 0$) suggested that elastic behaviour was anisotropic. This can now be examined further by considering the elastic behaviour during unloading in Test Series B and C.

Figure 6.30 shows data obtained from the unloading stages in both Test Series B and C. Large increments of deviatoric and volumetric strains have been considered, taking a step increment from the start of unloading to the end of unloading (but not including any strain occurring during the 24-hours rest period at the end of unloading). The ratio of these strain increments ($\Delta\varepsilon_d/\Delta\varepsilon_v$) has been plotted against corresponding value of stress ratio η. It was considered that the unloading stages would represent the truest record of "elastic" behaviour. When considering loading

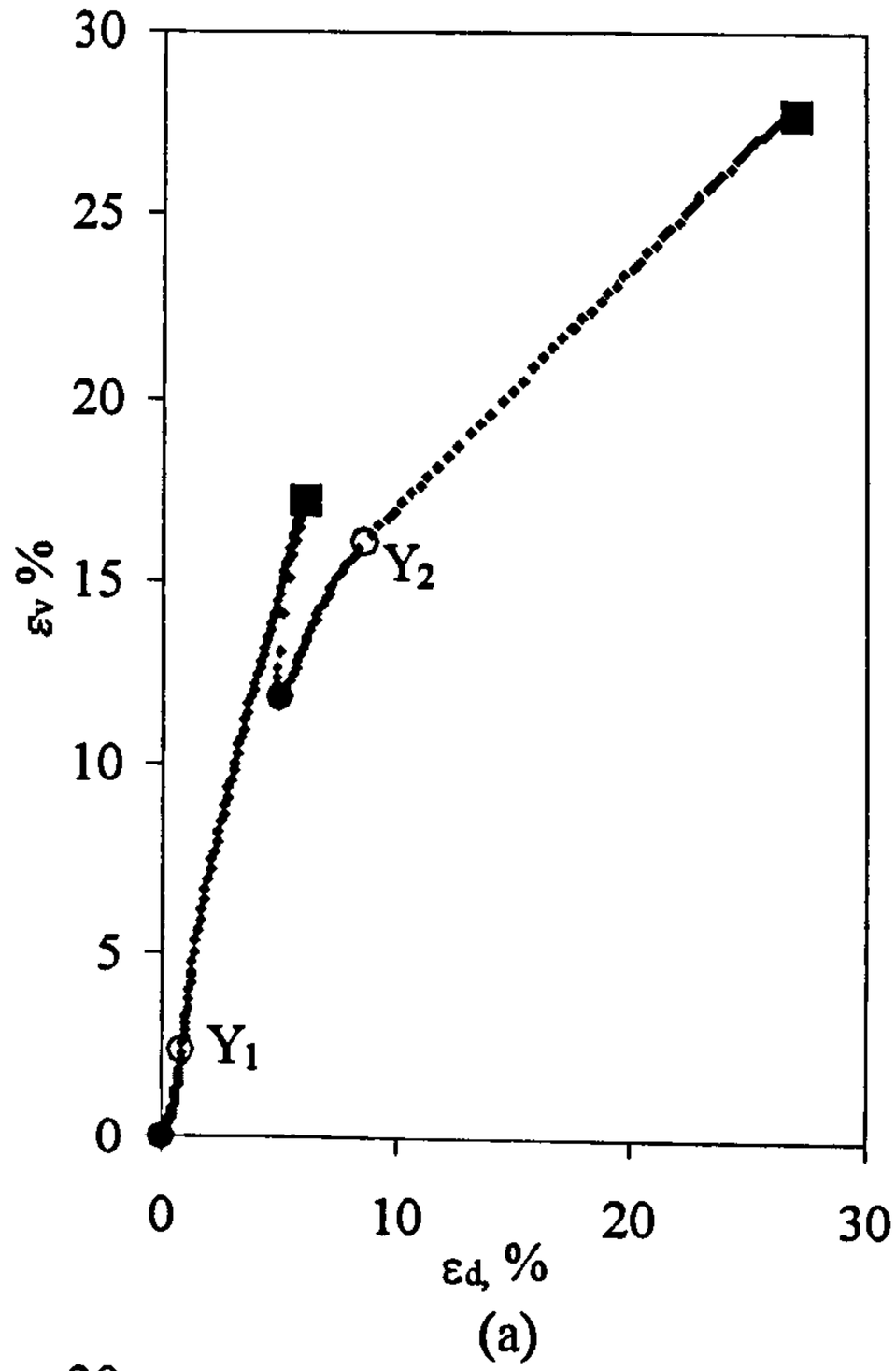

(a)

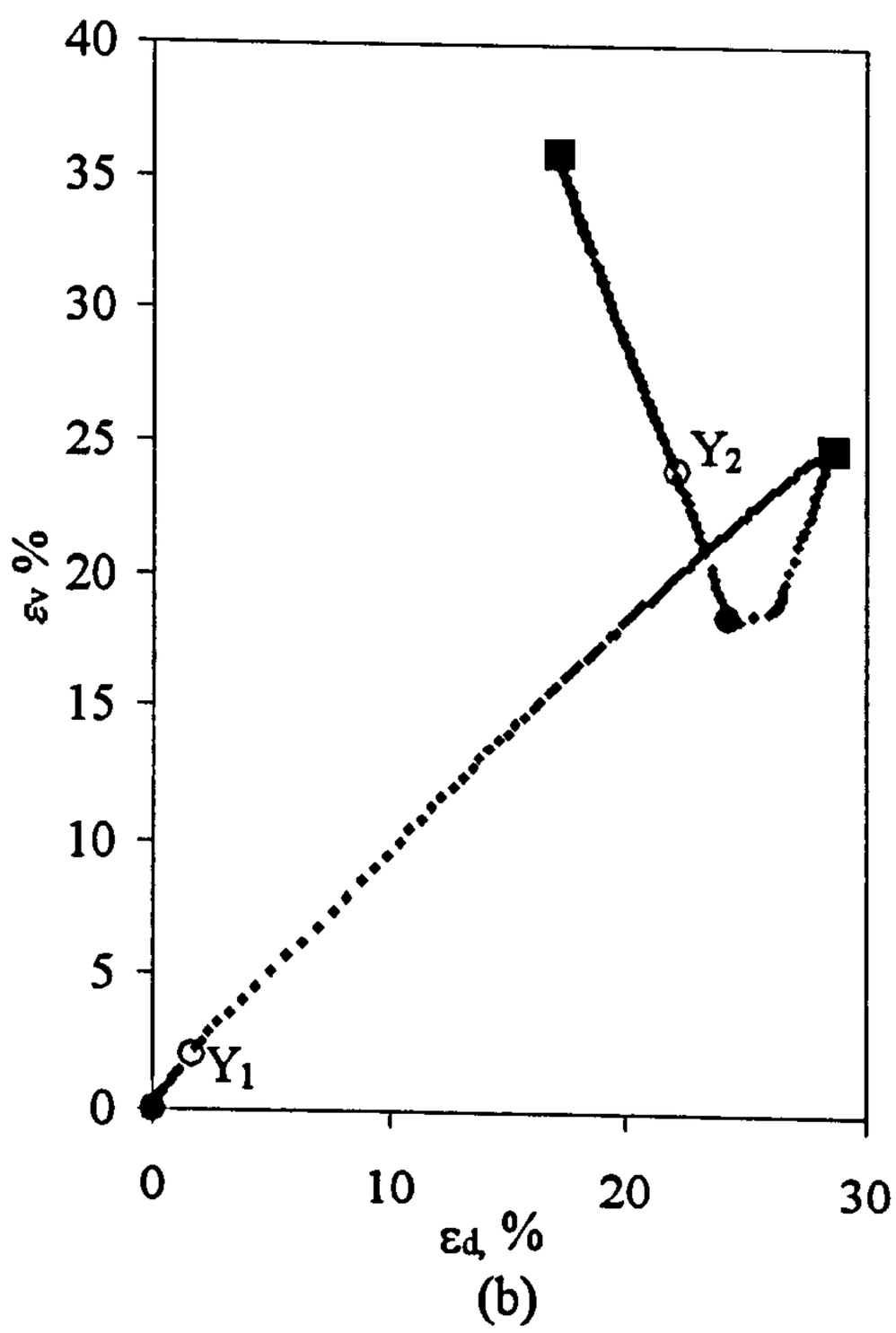

(b)

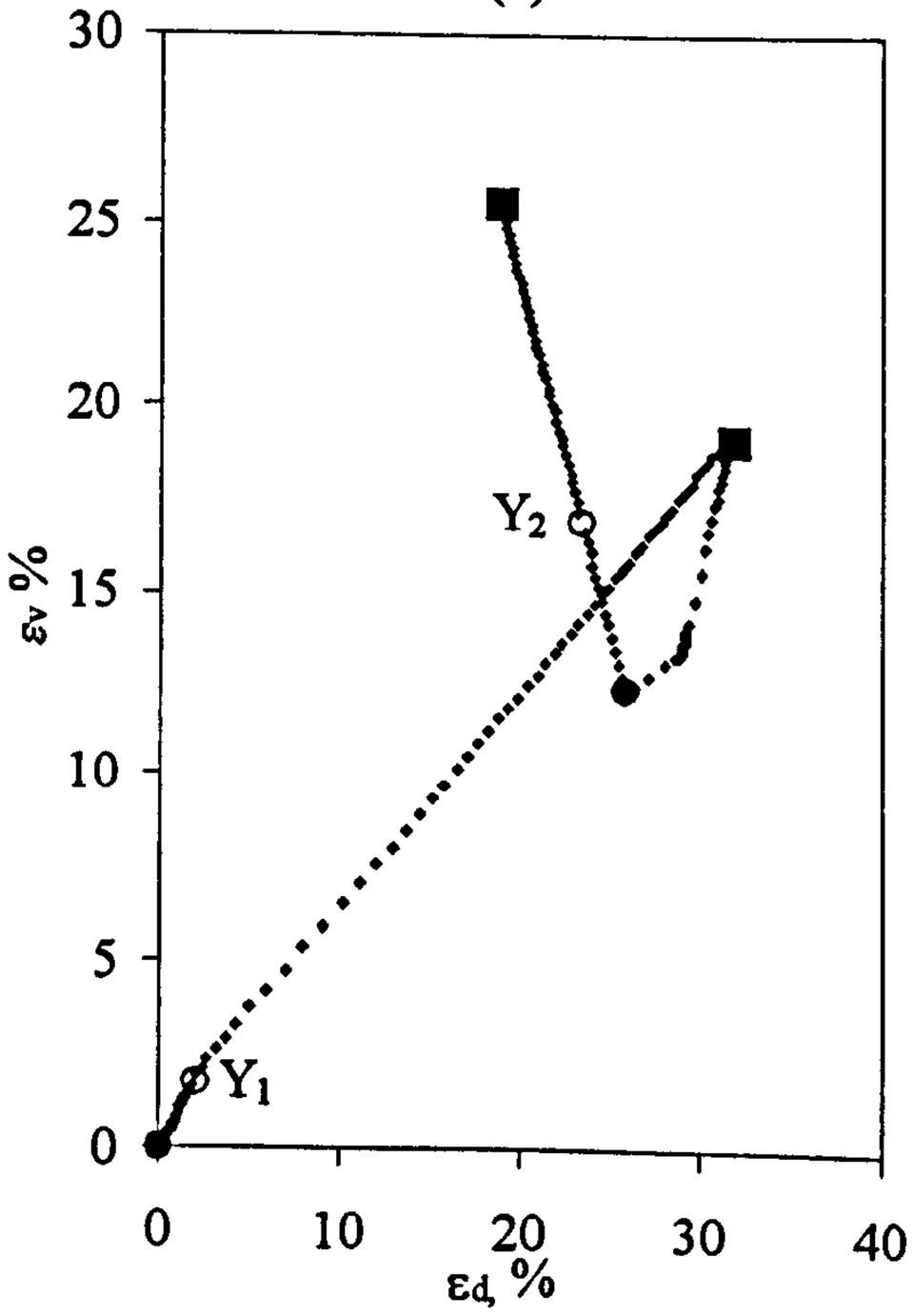

(c)

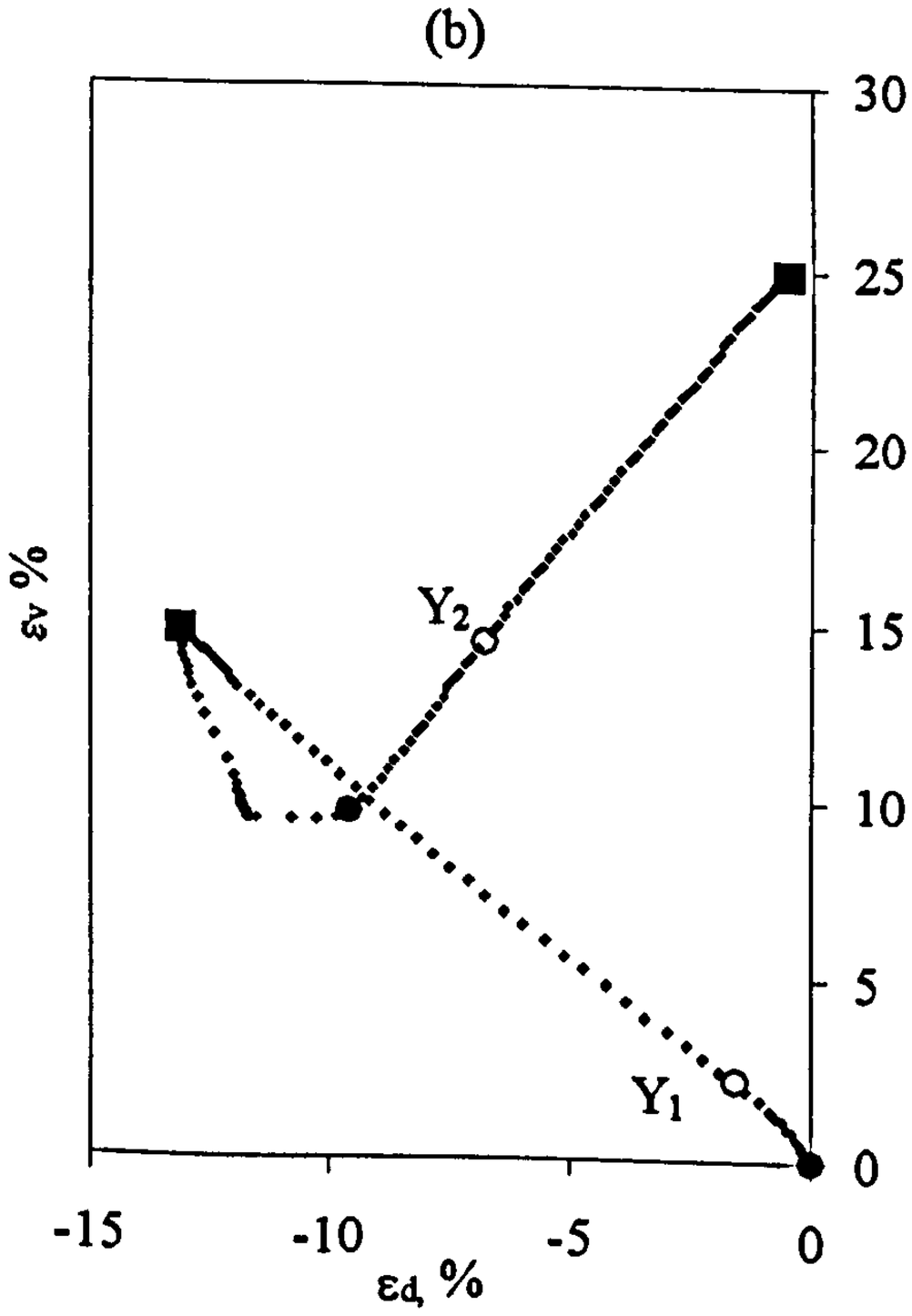

(d)

Figure 6.29. Strain paths in Test Series C; (a) Test C1, (b) Test C2, (c) Test C3 and (d) Test C4.

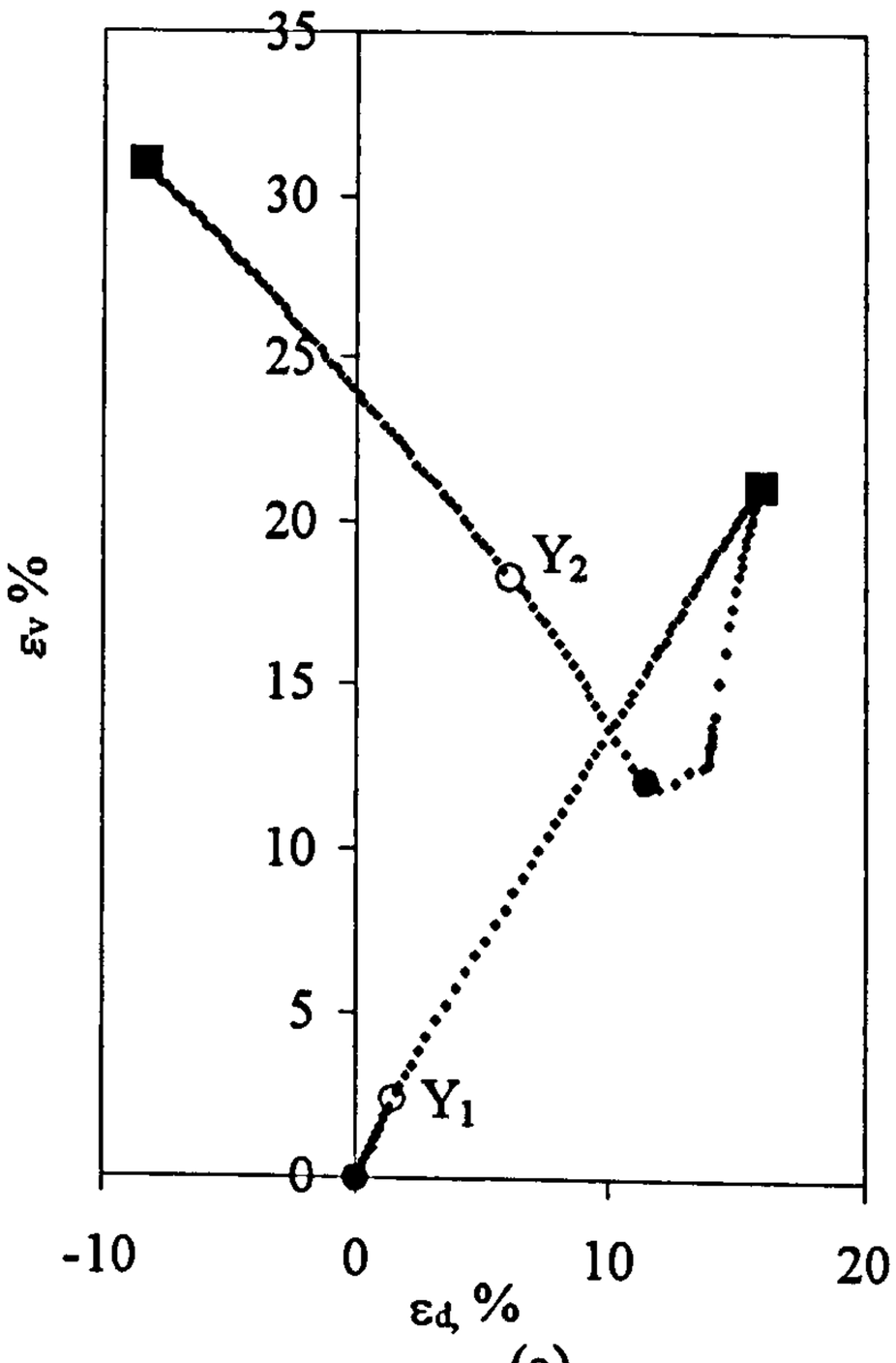

(a)

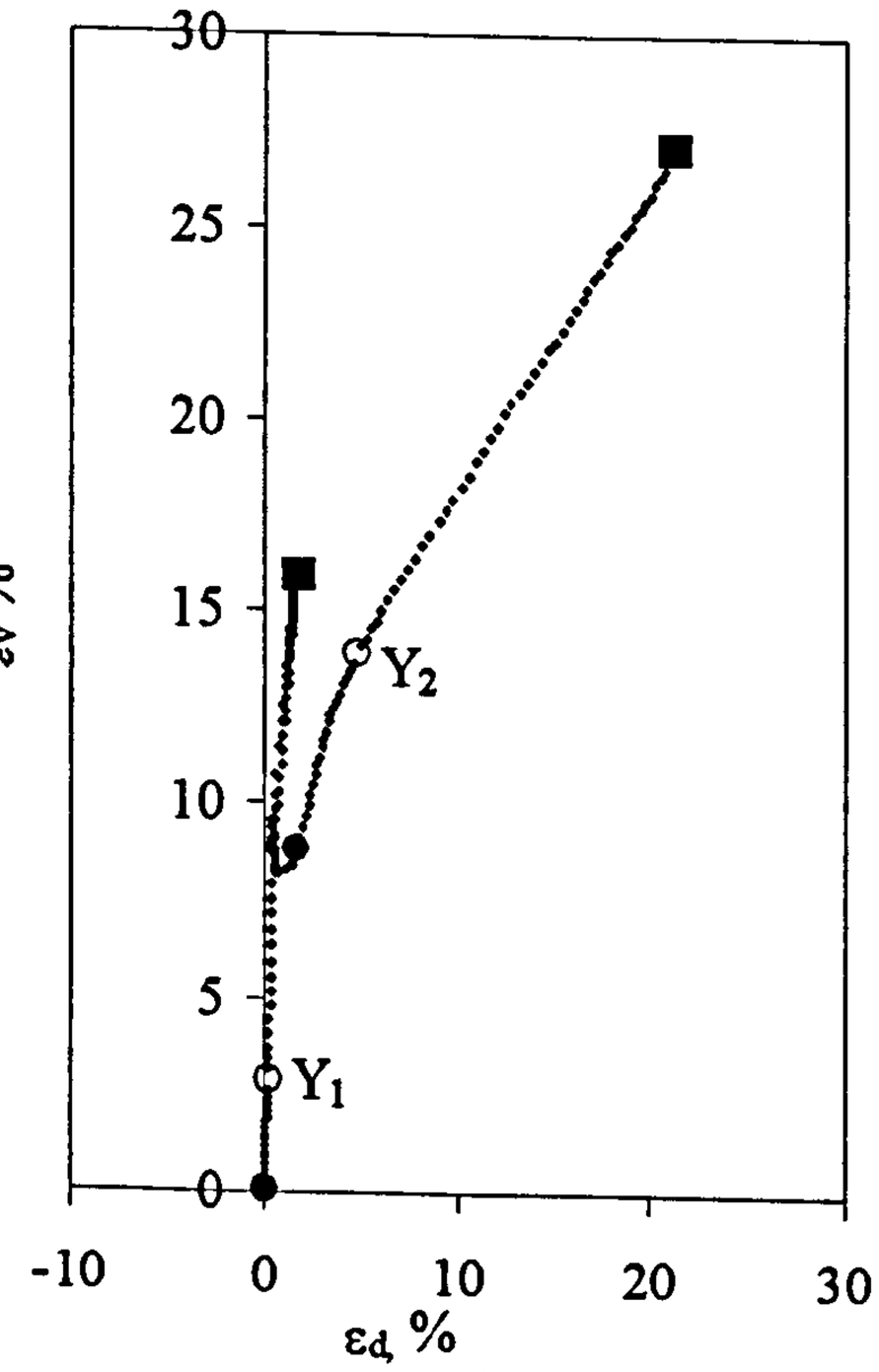

(b)

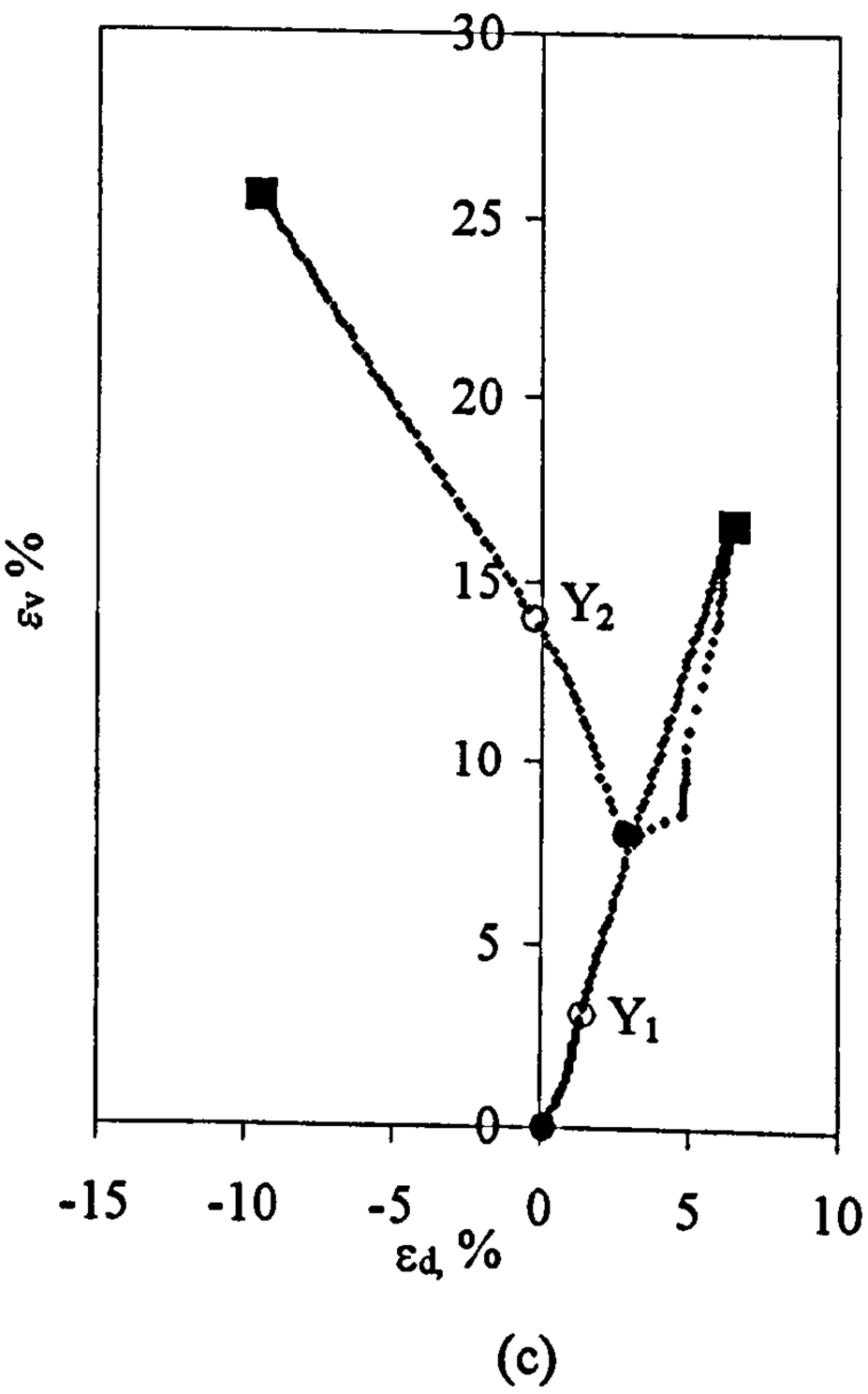

(c)

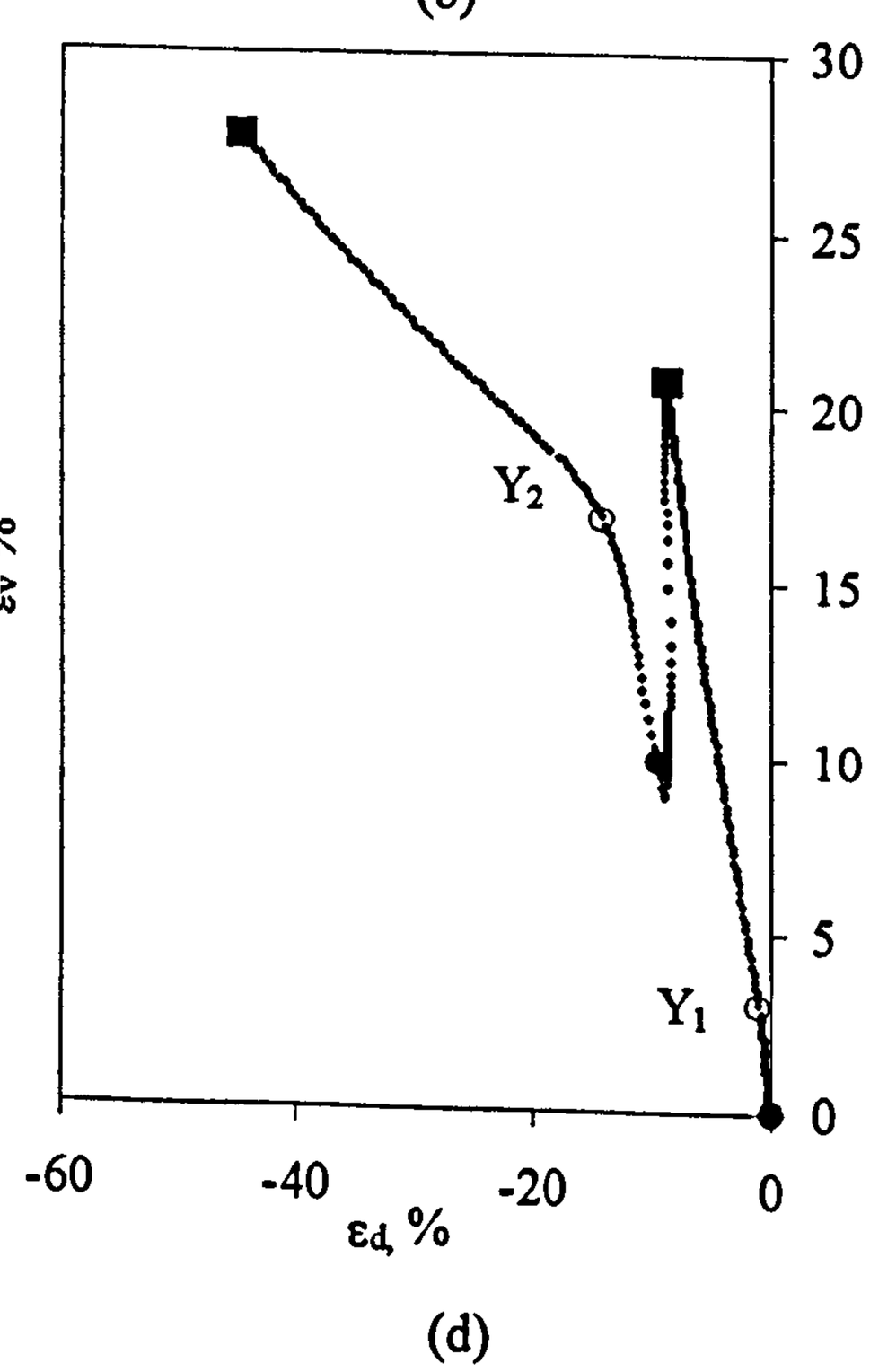

(d)

Figure 6.29. Strain paths in Test Series C; (e) Test C5, (f) Test C6, (g) Test C7 and (h) Test C9.

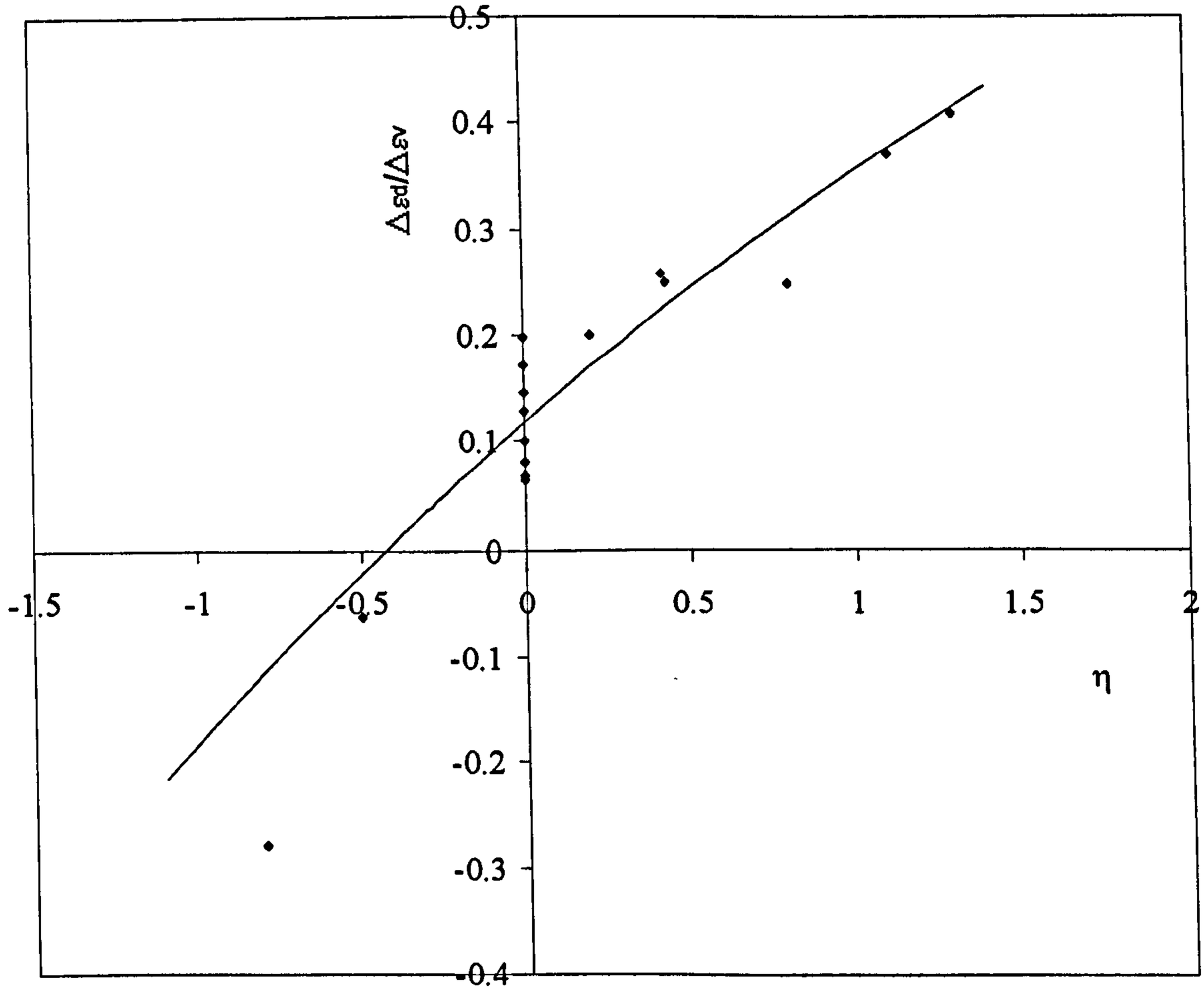

Figure 6.30. Strain increments from unloading stages in Test Series B and C.

stages, it is difficult to estimate (or guarantee) a true cut off point between pre-yield and post-yield behaviour.

As previously discussed, if the behaviour inside the yield surface was isotropic and elastic, then the unloading stages from Test Series B (with $\eta = 0$) would produce $\delta\varepsilon_d/\delta\varepsilon_v = 0$. Figure 6.30 shows that all of these data points from Series B lie significantly above the origin, suggesting that during isotropic unloading, the "elastic" behaviour was anisotropic. The corresponding data points from Series C indicate that, as expected, the ratio $\Delta\varepsilon_d/\Delta\varepsilon_v$ tends to increase as the stress ratio η was increased.

For a constant η test (where $\delta q/\delta p' = \eta$) the cross-anisotropic stress-strain relations of Graham and Houlsby (1983), given in Equation 6.6, can be re-written as a relationship between the strain ratio $\delta\varepsilon_d/\delta\varepsilon_v$ and the stress ratio η.

$$\frac{\delta\varepsilon_d}{\delta\varepsilon_v} = \frac{K^*\eta - J}{3G^* - J\eta} \tag{6.8}$$

and where $\eta = 0$,

$$\frac{\delta\varepsilon_d}{\delta\varepsilon_v} = -\frac{J}{3G^*} \tag{6.9}$$

A best-fit curve (of the form given by Equation 6.8) has been applied to the data points and suggests that at $\eta = 0$, with the optimum fit being given by $J/G^* = -0.35$ and $K^*/G^* = 0.83$. The data is qualitatively consistent with the findings of Graham et al. (1983) and subsequent authors, who found that for most natural clays the value of J is negative and smaller in magnitude than both K^* and G^*. Section 7.4 shows that the test results on horizontal samples provided additional information on the cross-anisotropic elastic properties of Bothkennar clay.

The constitutive models S-CLAY1 and S-CLAY1S ignore any anisotropy of elastic behaviour, in the interests of simplicity (see Section 3.2.1). The data in Figure 6.30 were used to establish the most appropriate values of Poisson's ratio ν to use with an assumption of isotropic elasticity. For isotropic elasticity ($J = 0$), Equation 6.8 simplifies to:

$$\frac{\delta\varepsilon_d}{\delta\varepsilon_v} = -\frac{K'}{3G'}\eta \tag{6.10}$$

i.e. a straight line relationship passing through the origin would be predicted between $\Delta\varepsilon_d/\Delta\varepsilon_v$ and η. Using the data presented in Figure 6.30 a best-fit straight line was forced through the origin to give $K/3G^* = 0.49$ and hence $\nu = 0.20$. This was therefore taken as the value of Poisson's ratio in the S-CLAY1 and S-CLAY1S model simulations presented in Chapters 8 and 9 respectively.

Inspection of Figure 6.29 indicates that yield points occurring during first and second loading stages (marked Y_1 and Y_2 respectively) are often accompanied by a distinct

change of strain path gradient. This would be expected, given that for a constant η stress path the ratio of plastic shear strains to plastic volumetric strains after yielding is not the same as the ratio of elastic shear strains to elastic volumetric strains. For a few specific values of η, elastic and plastic ratios of shear strain to volumetric strain happen to coincide, and for these cases there is no change of stress path gradient at the yield point.

Figure 6.29 shows that post-yield strain paths in both first and second loading stages are reasonably linear. In some stages there is curvature of the strain path immediately after the yield point, as would be expected if a change in anisotropy was occurring, caused by plastic straining at a new value of η (see S-CLAY1 and S-CLAY1S simulations in Chapters 8 and 9 respectively). However, the curvature observed in the post-yield strain paths is not particularly marked in the test data shown in Figure 6.29.

Figure 6.31 shows the final strain path gradients measured in first and second loading stages in Series B and Series C plotted against the stress ratio η. Each value of $\Delta\varepsilon_d/\Delta\varepsilon_v$ shown in Figure 6.31 has been taken from either Figure 6.17 or Figure 6.29 as the final gradient of the strain path achieved at the end of a loading stage. They should therefore be close to the final equilibrium value of $\Delta\varepsilon_d/\Delta\varepsilon_v$ corresponding to a given constant η strain path.

Also shown in Figure 6.31, for comparison with the experimental results, is a curve of final equilibrium values of plastic strain increment ratio $\Delta\varepsilon_d^p/\Delta\varepsilon_v^p$ predicted by S-CLAY1 for constant η stress paths (once all yield curve rotation has finished). A similar theoretical curve is shown for Modified Cam Clay (MCC). It should be noted that the theoretical curves are for ratios of plastic strain increments, whereas the experimental points give ratios of total strain increments. However, plastic strain increments are likely to be much larger than elastic strain increments, and therefore the comparison is fairly justified. The theoretical curve for S-CLAY1 shown in Figure 6.31 was derived by inserting equilibrium values of α from Equation 3.9 into the flow rule of Equation 3.5. Values of $M_C = 1.4$ and $M_E = 1.1$ were used in triaxial

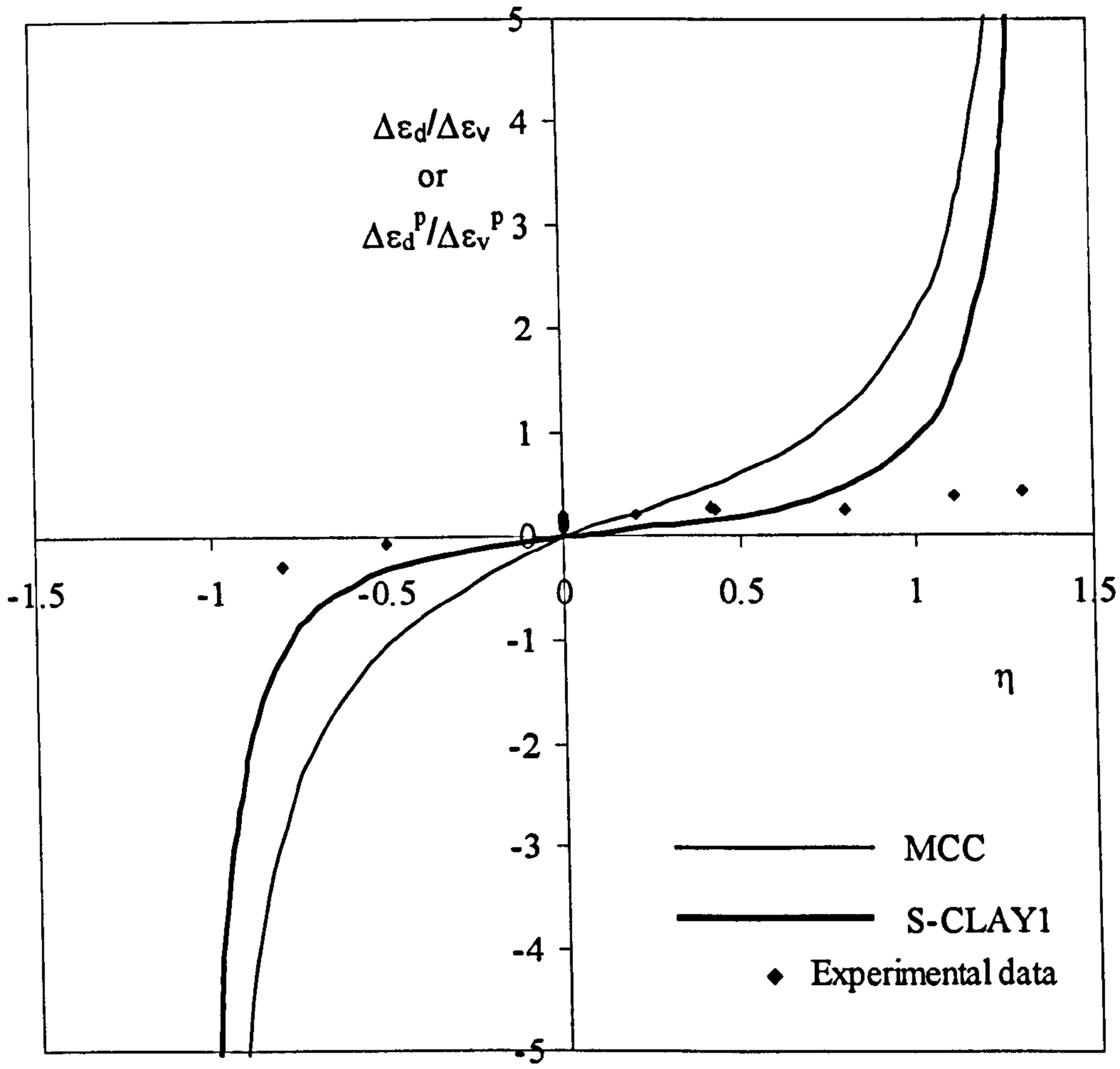

Figure 6.31. Experimental and theoretical equilibrium strain ratios.

compression ($\eta > 0$) and triaxial extension ($\eta < 0$) respectively (see Section 6.2.2) and $\beta = 0.94$ was assumed (see Section 8.2). The curve for MCC shown in Figure 6.31 was derived from the flow rule of Equation 3.5 with α set to zero.

Figure 6.31 shows that the assumed flow rules work well in both models at low positive and low negative values of η. At intermediate positive values of η (η ranging from about 0.4 to 0.8) and intermediate negative values of η (η ranging from about –0.5 to –0.8) S-CLAY1 matches the data better than MCC. However as η tends towards M_C in triaxial compression or M_E in triaxial extension, both models grossly overpredict the plastic strain ratio. One possible explanation is that the flow rule is not truly associated at extreme values of η. Another explanation might be that the assumed S-CLAY1 and MCC yield curve shapes are inaccurate.

6.5 Identification of yield points

6.5.1 Methodology

The various stress-strain plots presented in Figures 6.5-6.13 and 6.18-6.26 have indicated that the yielding of Bothkennar clay is often a rather gradual process and that yield points are often not particularly obvious. The yield point was particularly hard to locate precisely in cases where the stress ratio in the second loading stage was radically different to that in the first loading stage. It is therefore necessary to have a consistent method of identifying the yield stress for the entire set of tests, with a view to establishing the initial size and shape of the yield curve and subsequent changes to this yield curve. In order to do so, Test C4 and Test C5 were closely examined. Test C5 involved a first loading stage at $\eta_1 = 0.80$, slightly less than the stress ratio estimated for K_0 conditions where $\eta_{K0} = 0.91$. In this first loading stage the yield point was reasonably clear and was not obscured by the influence of evolving anisotropy (see Figure 6.22). The second loading was in triaxial extension and the yield point was much less clear in the stress-strain plots. In contrast, Test C4 (see Figure 6.21) involved first loading in triaxial extension ($\eta_1 = -0.80$) and the yield point was relatively ambiguous, as was the case in the second loading stage in triaxial compression ($\eta_2 = 0.60$). Two methods of attempting to locate a yield point are now considered.

Tangent Stiffness

If the onset of plastic straining is associated with a decrease in the stiffness of the clay, then it is useful to examine this reduction in tangent stiffness as the test progresses. Janbu (1985) indicated that the onset of large plastic strains may be observed by considering the tangent modulus to a stress-strain curve. The tangent value of apparent bulk modulus, K', can be defined by

$$K' = \frac{dp'}{d\varepsilon_v} \tag{6.11}$$

Note that in there is no suggestion that K' defined by Equation 6.11 is a true elastic bulk modulus; it is simply the tangent to a stress-strain curve.

Similarly, the tangent value of apparent shear modulus, G', is given by:

$$G' = \frac{dq}{3d\varepsilon_d} \tag{6.12}$$

and again G' is the tangent to a stress-strain curve, rather than a true elastic modulus.

Bi-linear interpretation

In this method, the pre-yield and post-yield sections of the compression curve plotted in terms of specific volume v against ln p' are both approximated by straight lines and the yield stress is determined from the intersection of these two straight lines. The construction of these lines is shown in Figures 6.32 (Test C5) and 6.33 (Test C4). The post-yield straight lines correspond to the appropriate λ values listed in Tables 6.2 and 6.3 and are therefore the steepest section of the post-yield compression curve. In Section 6.3.3 it was shown that it was not possible to establish a pre-yield κ line during the first and second loading stages due to non-linearity in the pre-yield compression curves. Values of κ could, however, be established by considering data from the unloading stages and the average value of κ_{unload} from Test Series B and C was found to be 0.04 (see Section 6.4.3). However, it was found that when attempting to impose a line of this gradient through the data in the first loading stages, the rate of pre-yield compression was inappropriately high and this caused the yield point to be overestimated. Therefore, for the purposes of yield point determination, a straight line of lower gradient had to be used for the pre-yield line. After inspection of all first loading stages in Series B and Series C it was decided that a line of gradient $\kappa = 0.02$ imposed through point O, the first point at the required stress ratio η_1, (see Figures 6.32 and 6.33) was appropriate for the first loading stages. The yield stress in the first loading stage (p'_{y1}) was taken as the intersection of this pre-yield line of gradient $\kappa = 0.02$ with the post-yield line of gradient λ_1.

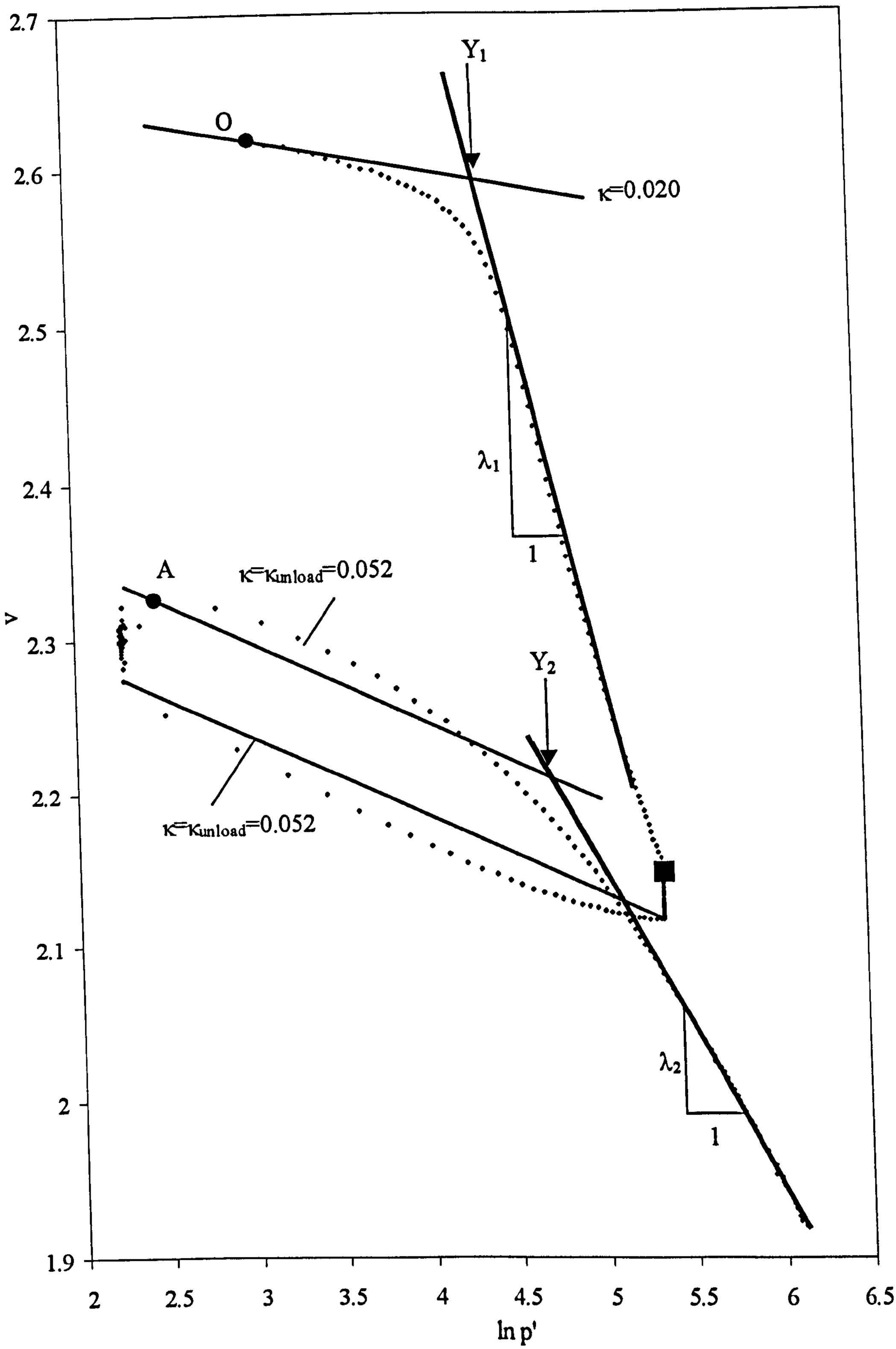

Figure 6.32. Bi-linear yield point interpretation for Test C5.

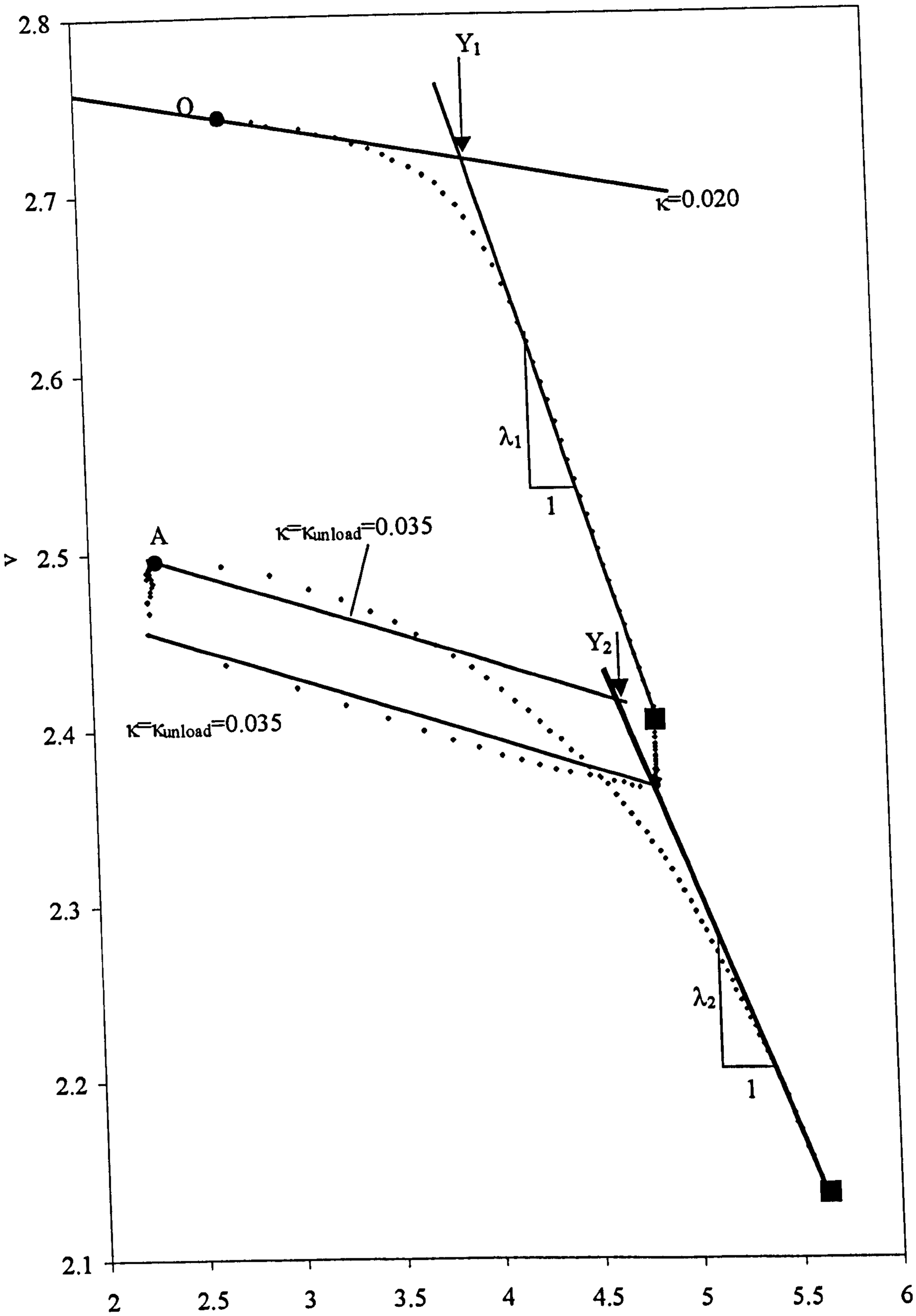

Figure 6.33. Bi-linear yield point interpretation for Test C4.

In the second loading stages, the shapes of the pre-yield compression curves were highly variable. It was found that a single value of κ was not sufficient to represent the pre-yield behaviour in all of the tests. A more consistent method appeared to be to draw a straight line with a gradient corresponding to a test-specific value of κ_{unload} through point A, the first point at the required stress ratio η_2 during the second loading stage, as shown in Figures 6.32 and 6.33. The yield stress in the second loading stages (p'_{y2}) was taken as the intersection of this line with the post-yield line of gradient λ_2.

It should be noted that this bi-linear method of interpretation is inherently inconsistent with the S-CLAY1 constitutive model. The solid line in Figure 6.34 shows a typical S-CLAY1 simulation for a stress path involving yield curve rotation. The model predicts a curved post-yield compression curve, as the yield curve rotates to a new orientation. In consequence, the bi-linear graphical construction, if fitted to the actual model predictions, would inevitably lead to an overestimation of the true model yield stress (see dashed lines in Figure 6.34). Clearly, it is very difficult to extract yield points from experimental data in a consistent fashion, in order to see whether experimental yield curves are consistent with a constitutive model. The only way to test properly how well a constitutive model is working is to compare full model simulations with experimental stress-strain data. This is explored in Chapter 8 and Chapter 9.

6.5.2 First loading stages

Tangent stiffness method

Plots of the variation of tangent stiffnesses for Tests C5 and C4 are shown in Figures 6.35 and 6.36, respectively. Figure 6.35 (a) shows the variation of the tangent bulk modulus, K', plotted against the mean effective stress for the first loading stage in Test C5. Figure 6.35 (b) shows the tangent shear modulus plotted against the deviatoric stress for the first stage in Test C5. In processing the data it was necessary to reduce the scatter observed between successive data points by using 5 successive

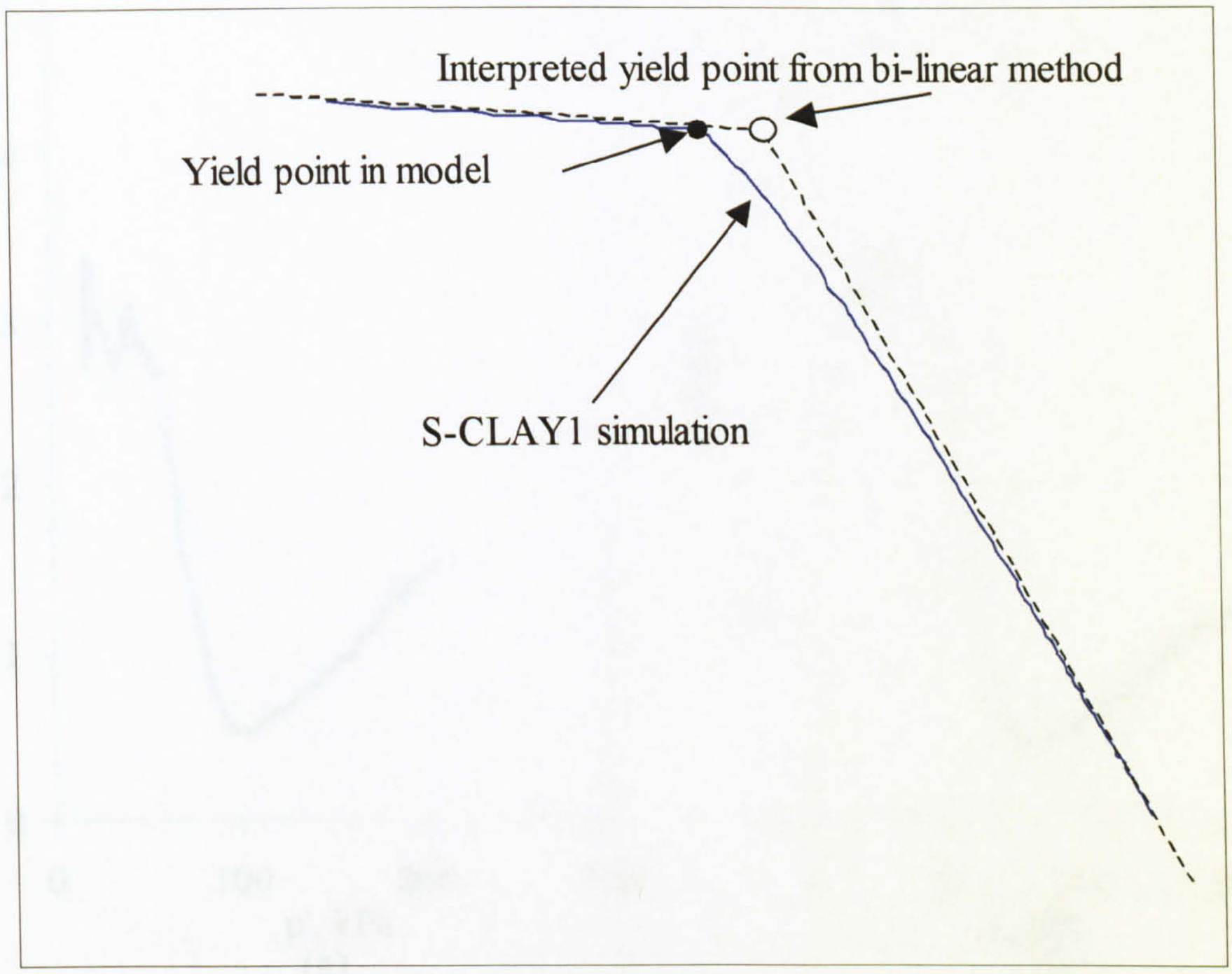

Figure 6.34. Comparison of predicted yield point from model involving yield curve rotation and interpreted yield point.

measurements of stress and strain (at intervals of dp' = 1kPa) in the determination of each tangent stiffness value shown in Figures 6.35 and 6.36.

In Figure 6.35 (a) a sharp reduction in K' can be seen starting at around p' = 59 kPa and continuing until a minimum value of K' is reached at approximately p' = 100 kPa. After this a steady increase in tangent bulk stiffness K' occurs as would be expected once plastic straining is fully developed (assuming non-linear elastic and plastic behaviour assumed, for example, in MCC or S-CLAY1, Equations 3.1, 3.2, 3.3 and 3.6). There is also a sharp decrease in G' shown in Figure 6.35 (b) commencing at about q = 40 kPa (corresponding to p' = 50 kPa) and continuing until a minimum value of G' is reached at about q = 79 kPa (p' = 100kPa). After this the value of tangent shear stiffness G' begins to steadily increase (as expected, given the form of non-linear plasticity usually assumed). It is therefore reasonable to assume that large plastic deformations begin to occur at a mean effective stress of about 50 - 60 kPa and when p' reaches 100 kPa, plastic straining is fully mobilized.

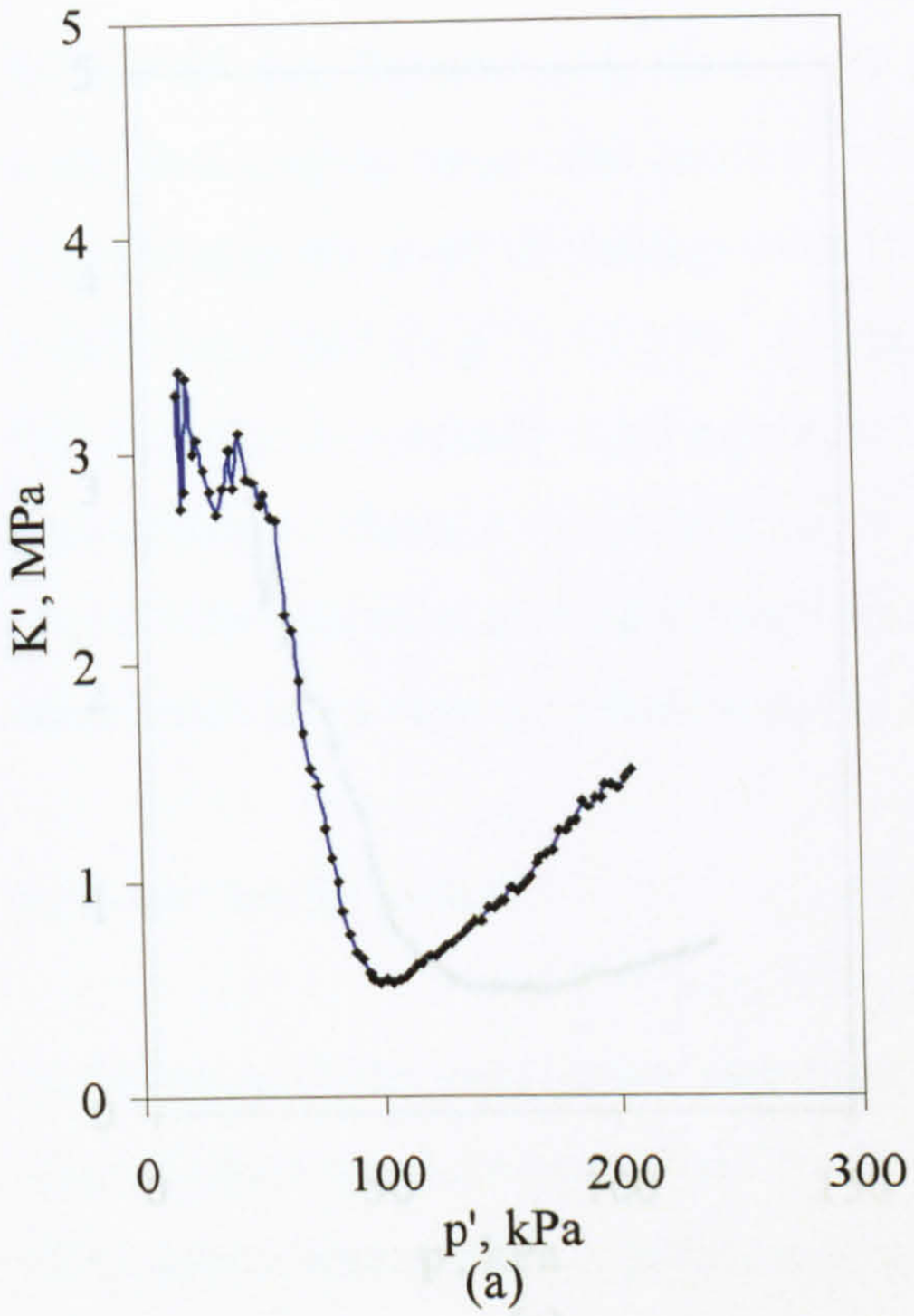

(a)

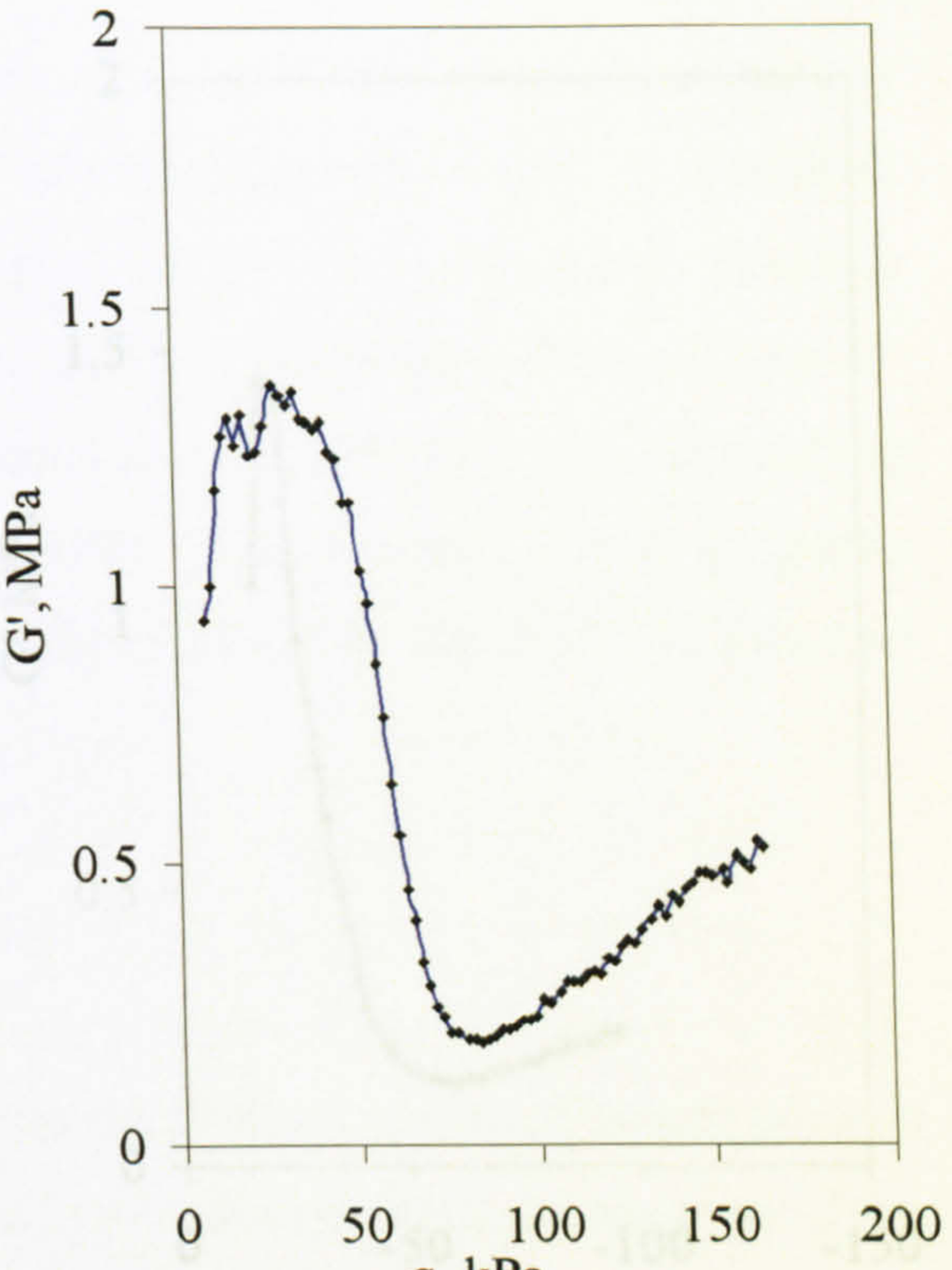

(b)

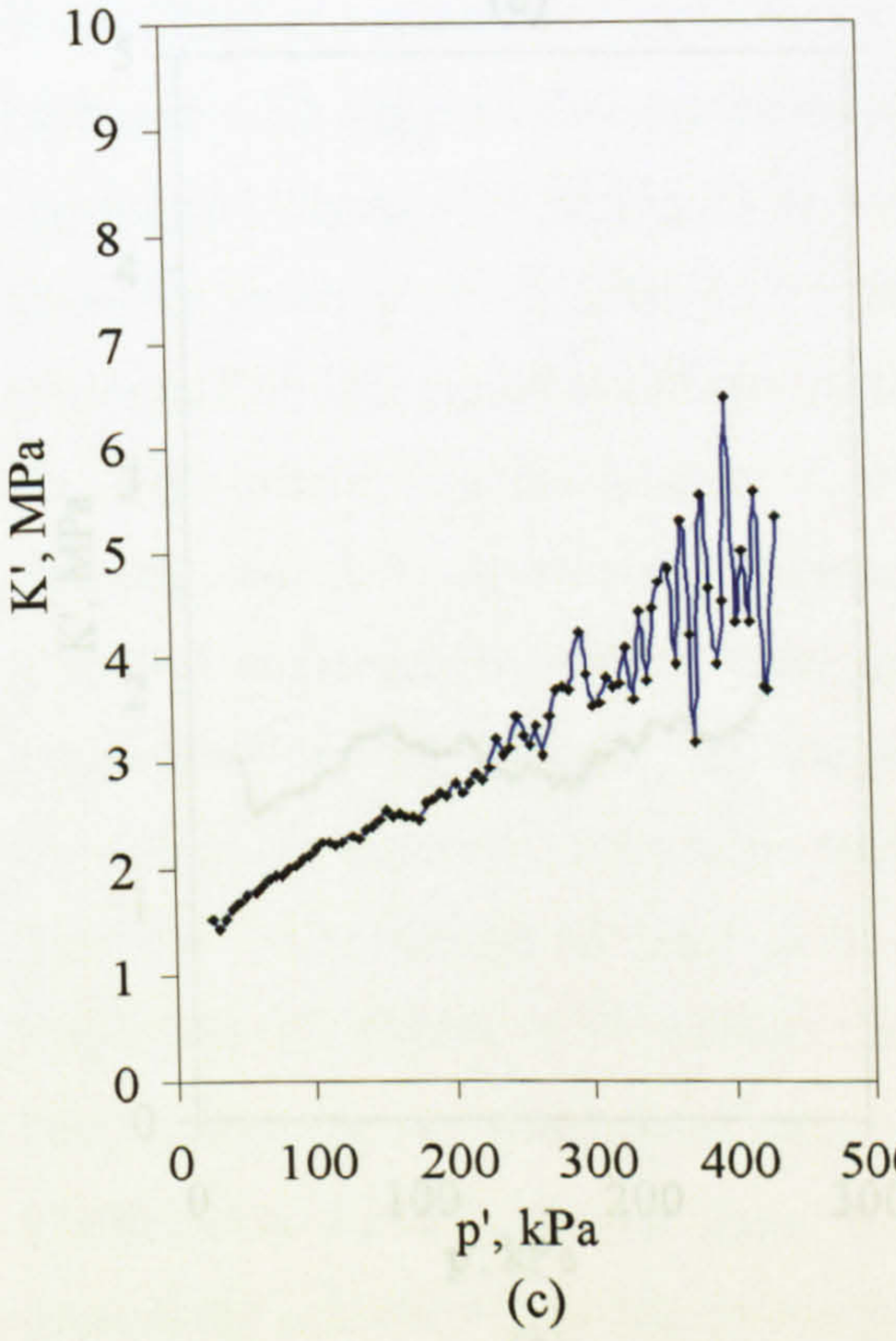

(c)

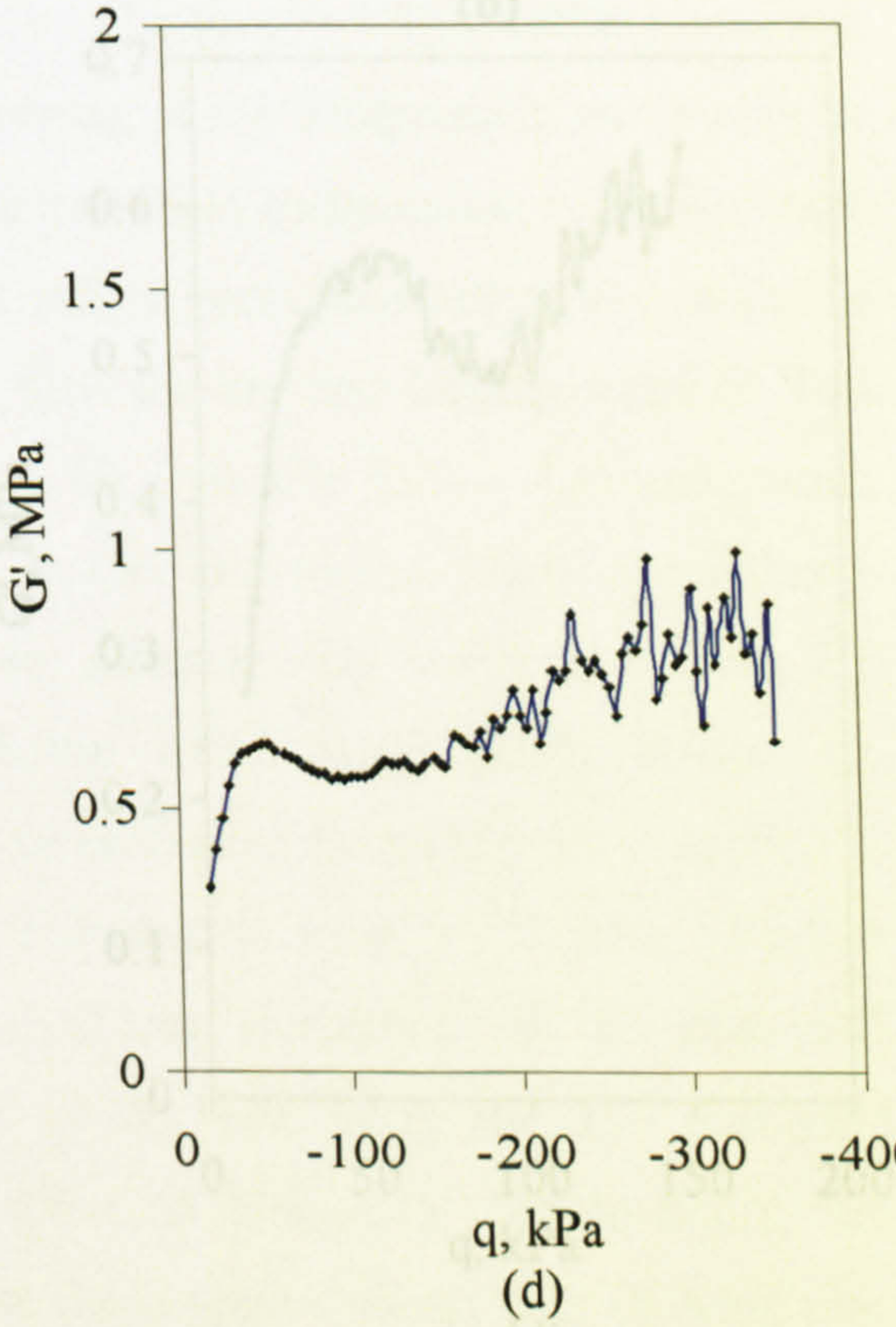

(d)

Figure 6.35. Variation of tangent stiffnesses in Test C5 ($\eta_1 = 0.80$, $\eta_2 = -0.80$); (a) tangent bulk stiffness in first loading stage, (b) tangent shear stiffness in first loading stage, (c) tangent bulk stiffness in second loading stage, (d) tangent shear stiffness in second loading stage.

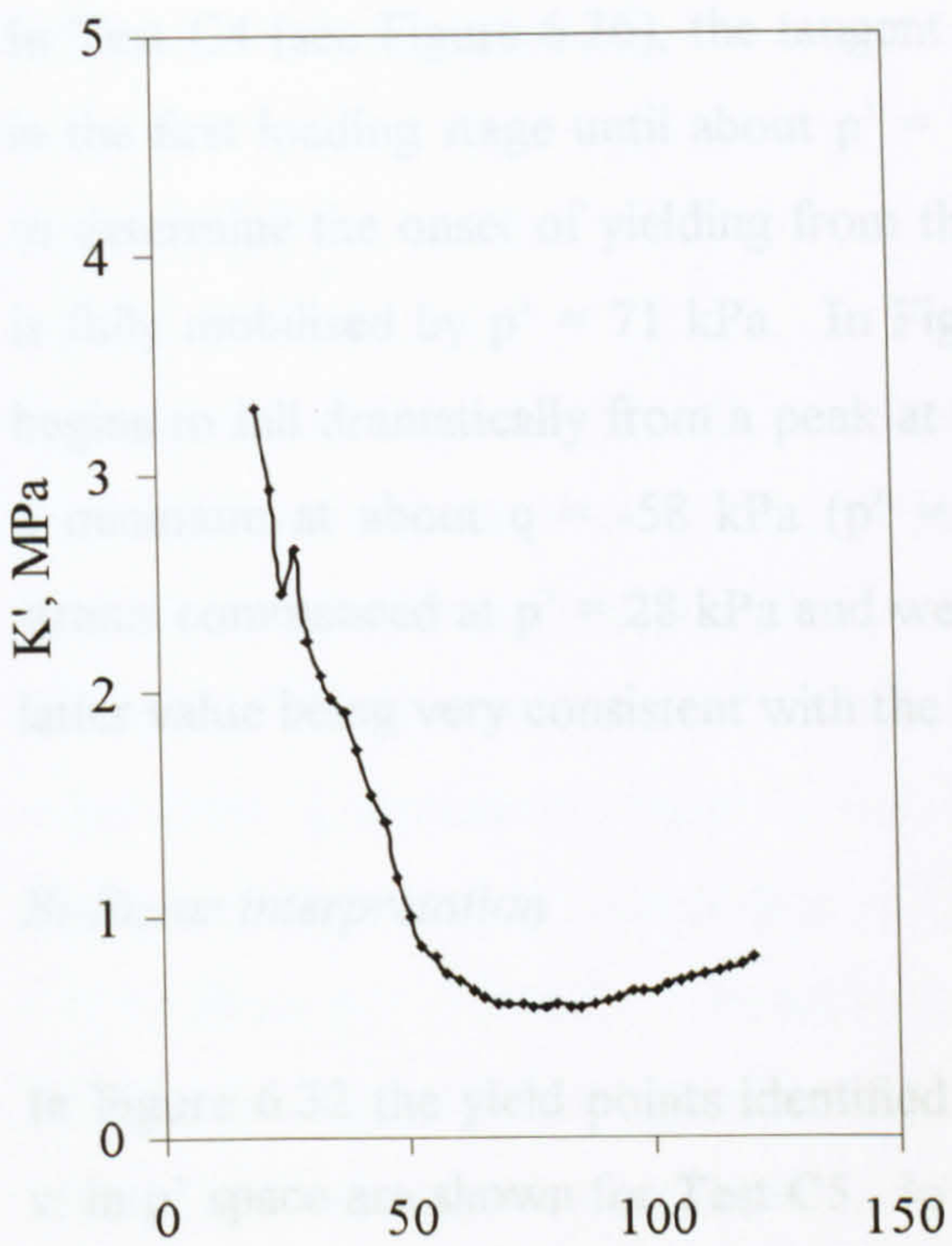

Figure 6.36. Variation of tangent stiffnesses in Test C4 (η_1 = -0.80, η_2 = 0.60); (a) tangent bulk stiffness in first loading stage, (b) tangent shear stiffness in first loading stage, (c) tangent bulk stiffness in second loading stage, (d) tangent shear stiffness in second loading stage.

In Test C4 (see Figure 6.36), the tangent bulk modulus K' falls almost continuously in the first loading stage until about p' = 71 kPa (see Figure 6.36 (a)). It is difficult to determine the onset of yielding from this plot, but it is likely that plastic straining is fully mobilised by p' = 71 kPa. In Figure 6.36 (b) the tangent shear stiffness G' begins to fall dramatically from a peak at around q = -22 kPa (p' = 28 kPa) reaching a minimum at about q = -58 kPa (p' = 72 kPa). This suggests that large plastic strains commenced at p' = 28 kPa and were fully mobilised by about p' = 72 kPa (the latter value being very consistent with the K' plot).

Bi-linear interpretation

In Figure 6.32 the yield points identified from the bi-linear graphical construction in v: ln p' space are shown for Test C5. In the first loading stage the intersection of the lines occurs where the compression curve is rapidly steepening. The yield point Y_1 is calculated at a mean effective stress of p' = 81 kPa (ln p'= 4.4). Further inspection of Figure 6.32 suggests that significant steepening of the compression curve may be starting as early as p' = 50 kPa (3.9) and the post-yield compression curve is almost linear by about p' = 90 kPa (4.5). These values agree reasonably well with the evidence from the tangent stiffness method that, for the first loading stage of Test C5, large plastic strains commenced at p' = 50 - 60 kPa (3.9 – 4.1) and plastic straining was fully developed by about p' = 100 kPa (4.6). Using the bi-linear graphical construction method, therefore, the selected yield stress of 80 kPa lies reasonably centrally within the range during which large plastic strains are increasing. In Figure 6.33 the same method of estimating the yield point is applied to Test C4. The calculated yield point Y_1 corresponds to p' = 52 kPa. Further inspection of Figure 6.33 shows that significant steepening of the post-yield compression curve commences around p' = 33 kPa (3.5) and the post-yield compression curve is almost linear from about 63 kPa (4.1). These figures are reasonably consistent with the evidence from the tangent stiffness data showing that, for the first loading stage of Test C4, large plastic strains commenced at abut p' = 28 kPa and were fully developed by about p' = 72 kPa. Again, therefore, the yield point of p' = 52 kPa calculated with the bi-linear graphical representation seems to lie fairly centrally within the range where plastic strains are increasing significantly.

6.5.3 Second loading stages

Tangent stiffness method

The variation of the tangent stiffnesses K' and G' for the second loading stages in Tests C5 and C4 are also shown in Figures 6.35 and 6.36. In Figure 6.35 (c) no marked drop of tangent bulk stiffness K' is apparent. Instead, there is a gradual increase of K' from the start of the loading stage. Towards the end of the loading stage there is increasing scatter in the data, but K' is still generally increasing. In Figure 6.35 (d) there is a small drop of tangent shear stiffness G' from about q = -54 kPa to about q = -100 kPa. The effect is, however, relatively modest, and the results presented in Figures 6.35 (c) and 6.36 (d) suggest that it would be difficult to use the tangent stiffness approach to determine the yield point from the second loading stage of Test C5 with any degree of confidence. Figures 6.36 (c) and 6.36 (d) show similar results for the second loading stages of Test C4. There are minor drops of tangent bulk stiffness K' from about p' = 90 kPa to about p' = 170 kPa and of tangent shear stiffness G' from about q = 66 kPa to q = 90 kPa (p' = 110 kPa to p' = 150 kPa), but the drop in stiffness is probably not sufficiently clear-cut to be used to locate a yield point with any degree of confidence.

Bi-linear interpretation

In the second loading stages of Tests C5 and C4 the pre-yield compression curves are highly non-linear (see Figures 6.32 and 6.33) and this makes use of the bi-linear method to determine a yield point more difficult than for the first loading stages. However, the imposed κ-line (based on a gradient of $\kappa = \kappa_{unload}$) appears a reasonable compromise for constructing a linear pre-yield line in both Tests C5 and C4. The post-yield compression curves eventually become linear and it is therefore reasonably straightforward to construct a straight line of gradient λ_2 through the steepest section of the post-yield compression curve. Inspection of Figures 6.32 and 6.33 shows that the second loading stage yield points Y_2 identified by applying the bi-linear construction in this way (at p' = 110 kPa in Test C5 and at p' = 93 kPa in Test C4) coincide roughly with the middle of the range over which significant steepening of the compression curve occurred.

6.5.4 Conclusion

In the first loading stages of Tests C5 and C4 the tangent stiffness approach clearly shows the onset of large plastic strains and the point at which plastic straining is fully mobilised. While this is informative, for comparison with model predictions it is useful to idealise this as a single point rather than a range over which plastic straining is mobilised. In the tangent stiffness plots, it could be argued that the steepest portion of the curve showing the drop of K' and G' represents a yield point. However, as seen in Figures 6.35 and 6.36, this portion of the plot may itself cover a large stress range. The bi-linear intersection method, in contrast, provides a single value of yield stress that can be determined with a reasonably repeatable procedure. This does not, however, guarantee that the method provides a fully meaningful definition of a yield point: yielding is, of course, a gradual process. There is therefore no guarantee that the method will not be subject to some consistent error. However, for cases where the tangent stiffness method clearly indicated a stress range over which large plastic strains were increasing significantly (such as the first loading stages of Tests C4 and C5), the bi-linear method provided values of yield stress that were close to the middle of this range.

For the purpose of yield point identification the bi-linear intersection method in v: ln p' space was therefore adopted. The values of yield stress determined using this method in the first and second loading stages of all tests in Series B and Series C are listed in Table 6.6. The graphical constructions used in the determination of these yield stress are given in Appendix B.

6.6 Initial shape and size of yield curve

Figure 6.37 (a) shows the experimental values of yield stresses from the first loading stages of the tests in Series B and Series C. These yield points define the initial shape and size of the yield curve in the q: p' plane, representing the in-situ state of the soil from the ground. The scatter among the initial yield points may be attributed to natural variation, or the fact that three Laval samples from slightly different depths were used. No attempt was made to normalize the yield stresses by dividing by the

in-situ stress, since it is not likely that the scatter would have been reduced greatly over such a small depth range.

Test	p'_{y1} (kPa)	q_{y1} (kPa)	p'_{y2} (kPa)	q'_{y2} (kPa)
B1	80	0	-	-
B2	75	0	134	94
B3	77	0	110	111
B4	79	0	98	127
B5	81	0	148	-59
B6	83	0	122	-85
B7	79	0	198	0
B8	80	0	151	60
B9	86	0	120	122
C1	78	33	132	137
C2	60	66	137	-69
C3	62	81	75	-45
C4	52	-42	93	56
C5	76	61	110	88
C6	90	18	110	113
C7	85	36	110	109
C8	66	53	-	-
C9	67	-34	134	-129

Table 6.6. Yield points from bi-linear approach for first and second loading stages in Test Series B and C.

Figure 6.37 (a) also shows the S-CLAY1 yield curve (Equation 3.4) fitted through the experimental data points assuming $M = M_C = 1.40$ for the full curve and a yield curve inclination α_{K0} determined by the procedure suggested by Wheeler et al. (1999, 2003), see Equation 3.14. This procedure for determining an initial value of α is meant to be appropriate for a soil with a history of one-dimensional straining to a normally consolidated or lightly overconsolidated state. Assuming $M_C = 1.40$ (See Section 6.2.2) and hence $\phi'_C = 34.6$ (Equation 6.3), $K_0 = 0.432$ (from Jaky's

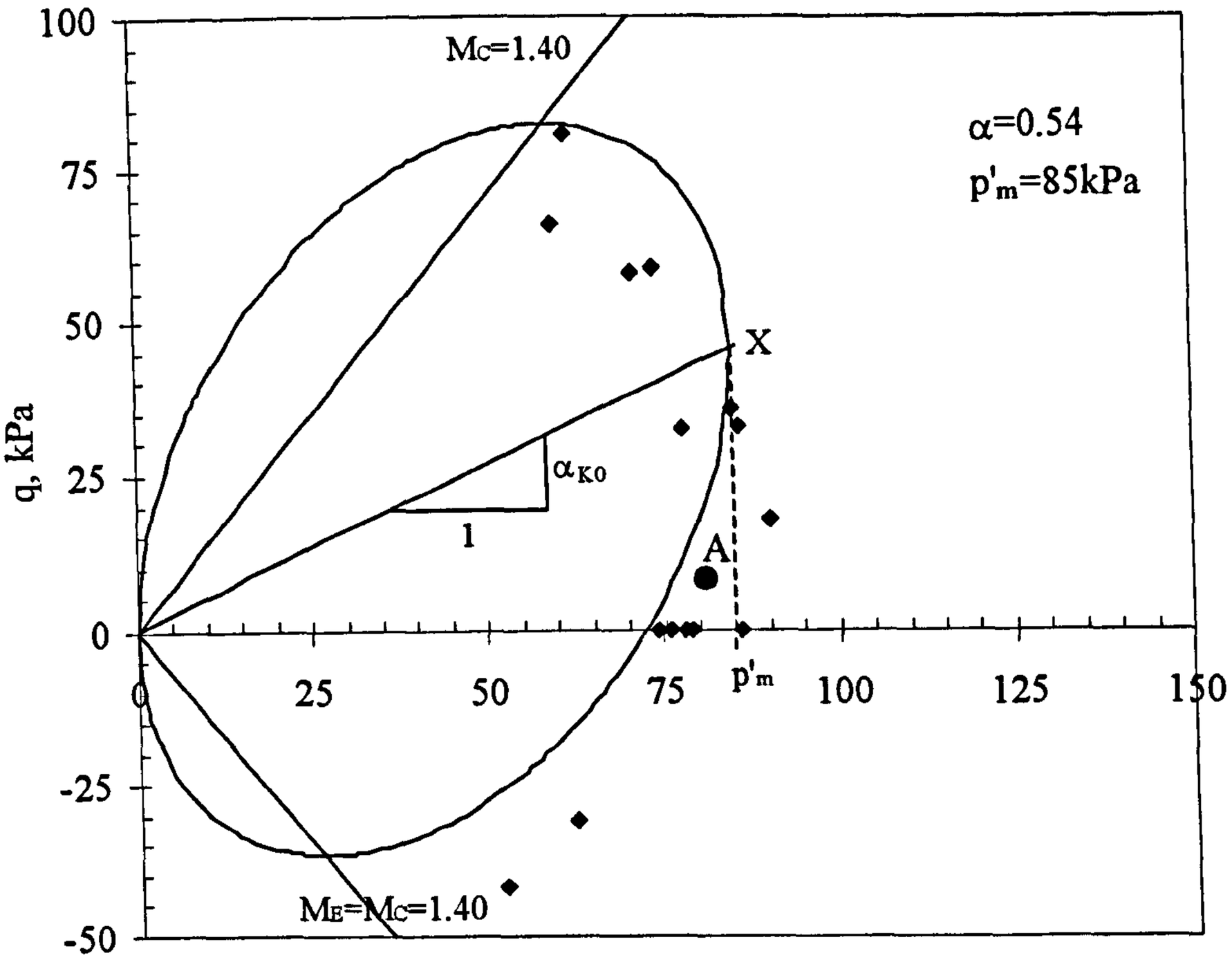

(a)

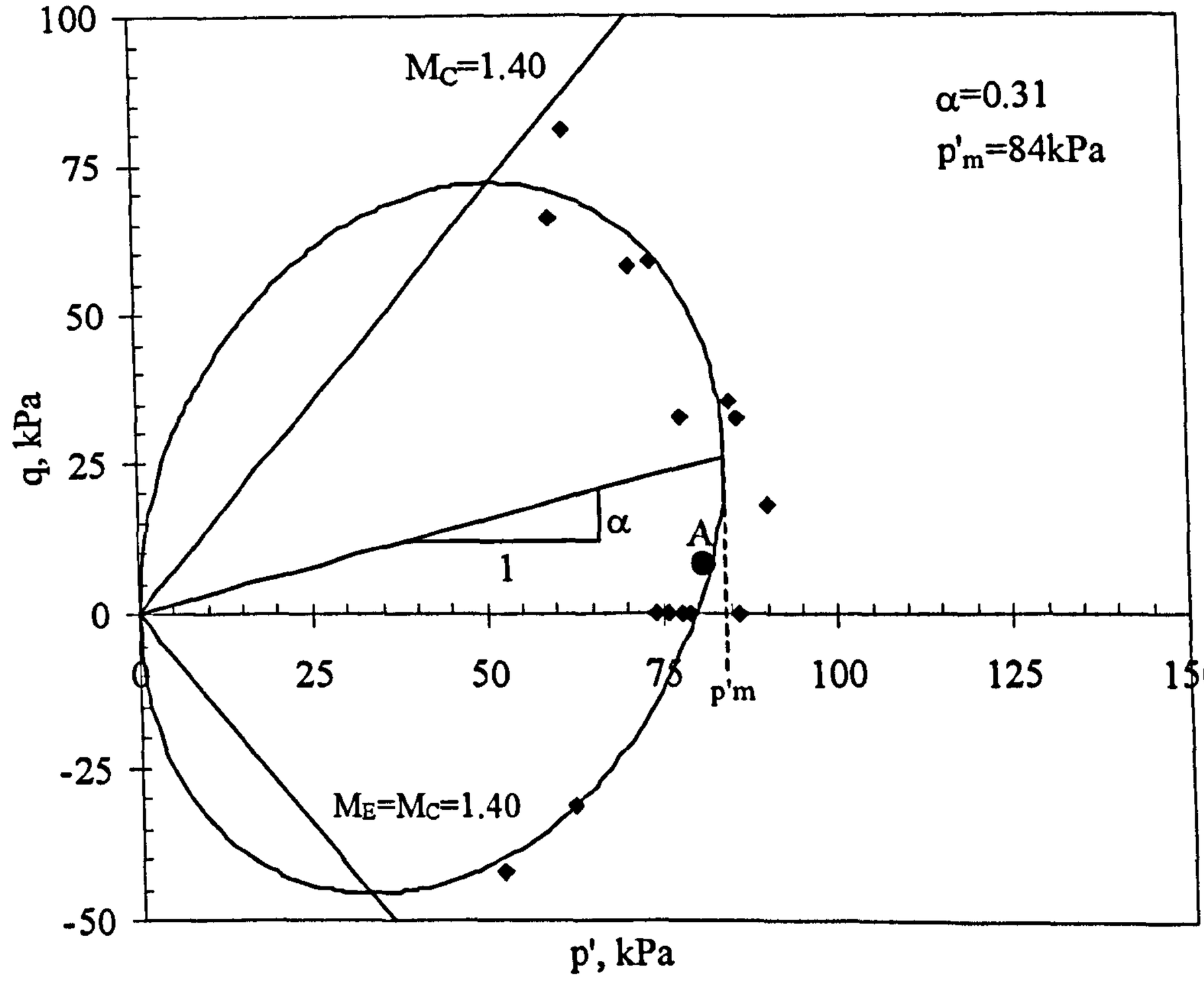

(b)

Figure 6.37. Yield points from first loading stages and initial S-CLAY1 yield curve (assuming $M_E = M_C$); (a) using $\alpha = \alpha_{K0}$, (b) using best-fit value of α.

simplified formula, Equation 3.11) and η_{K0} = 0.913 (Equation 6.5) gives, via Equation 3.14, a value of α_{K0} = 0.54. The size p'_m of the yield curve shown in Figure 6.37 (a) was then selected from to optimise the fit to the experimental yield points. In the first instance, the curve was fitted approximately to the data points by inspection, then the optimum size of the curve was determined using a least squares technique, considering the radial distances of each of the individual data points from the yield curve. Figure 6.37 (a) shows that the best fit was achieved with p'_m equal to 85kPa.

Inspection of Figure 6.37 (a) indicates that a lower value of α would give a significantly better match to the data (the data points above point X on the curve generally lie significantly inside the curve whereas the data points below point X generally lie outside the curve). A reduced value of α = 0.31 combined with a slightly reduced p'_m value of 84 kPa gave the best fit to the data and this is shown in Figure 6.37 (b). Again a value of $M=M_C=1.40$ was used in the S-CLAY1 yield curve expression of Equation 3.4 for plotting the entire curve shown in Figure 6.37 (b).

It is evident that the independent procedure of Wheeler et al. (1999, 2003) for estimating the initial orientation of the yield curve ($\alpha = \alpha_{K0}$) did not match the yield point data from Bothkennar clay well, and a much lower value of α was required to give the optimum fit. It should be noted, however, that Wheeler et al. (2003) and Näätänen and Lojander (2000) showed that for a number of other natural soft clays (including Bothkennar clay from 5 – 6m depth) the S-CLAY1 yield curve was a very good match to the experimental data when the in-situ value of α was calculated by the method suggested by Wheeler et al. (1999, 2003). The lower than expected value of α for the Bothkennar clay from 10 - 11m depth tested in the current study would be explainable if the yield curve had undergone some clockwise rotation in-situ from an earlier orientation α_{K0}. This would have occurred in-situ if the soil yielded during unloading to an overconsolidated state.

The possibility that clockwise rotation of the yield curve (reducing the value of α) occurred due to yielding of the soil during unloading of the soil in-situ to an overconsolidated state is supported by data on the in-situ stress state reported by

Nash et al. (1992), who tested material from around the same depths as was used in Series B and C. According to Nash et al. (1992), the in-situ stress state for this depth would plot almost exactly on the yield curve shown in Figure 6.37 (b) (see Point A in the Figure), consistent with the possibility of yielding during unloading in-situ. In contrast, when plotted in Figure 6.37 (a) the in-situ stress state actually plots slightly outside the yield curve constructed using $\alpha = \alpha_{K0} = 0.54$ (clearly impossible). Importantly, if the OCR is defined in terms of one-dimensional loading, the soil is overconsolidated in the in-situ state, despite the fact that the in-situ stress state lies on the yield curve. Whilst an isotropic stress increment from the in-situ stress state would cause immediate yielding of the soil, one-dimensional loading would follow a very steep stress path in the p': q plot that would initially progress inside the yield curve.

As described in Section 3.2.2, it may be necessary to adjust the shape of the yield curve if the critical state stress ratios in triaxial compression and triaxial extension are not equal. As shown in Section 6.2.2 for vertical samples of Bothkennar clay the critical state stress ratio in triaxial compression was $M_C = 1.40$ whereas the corresponding value in triaxial extension was $M_E = 1.10$, so that the values are significantly different. Using this lower value of M_E in the yield curve expression for the section of the yield curve below the α-line causes the yield curve below the α-line to be altered significantly, resulting in the majority of the yield points below the α line in Figure 6.37 (b) now lying outside the yield curve. It was found that by using $M = M_E = 1.10$ below the α line the value of p'_m had to be increased slightly to 85 kPa and the α-value had to be reduced still further to 0.28 in order to give the best fit. The fit of the S-CLAY1 curve to the experimental data points in Figure 6.38 (using $M = M_E$ below the α line) is not as good as in Figure 6.37 (b).

6.7 Expanded and rotated yield curves

6.7.1 Test Series B

In Test Series B, each of the nine tests involved a first loading stage at $\eta = 0$ to a maximum stress level of p' = 210 kPa. After unloading, each test had a second

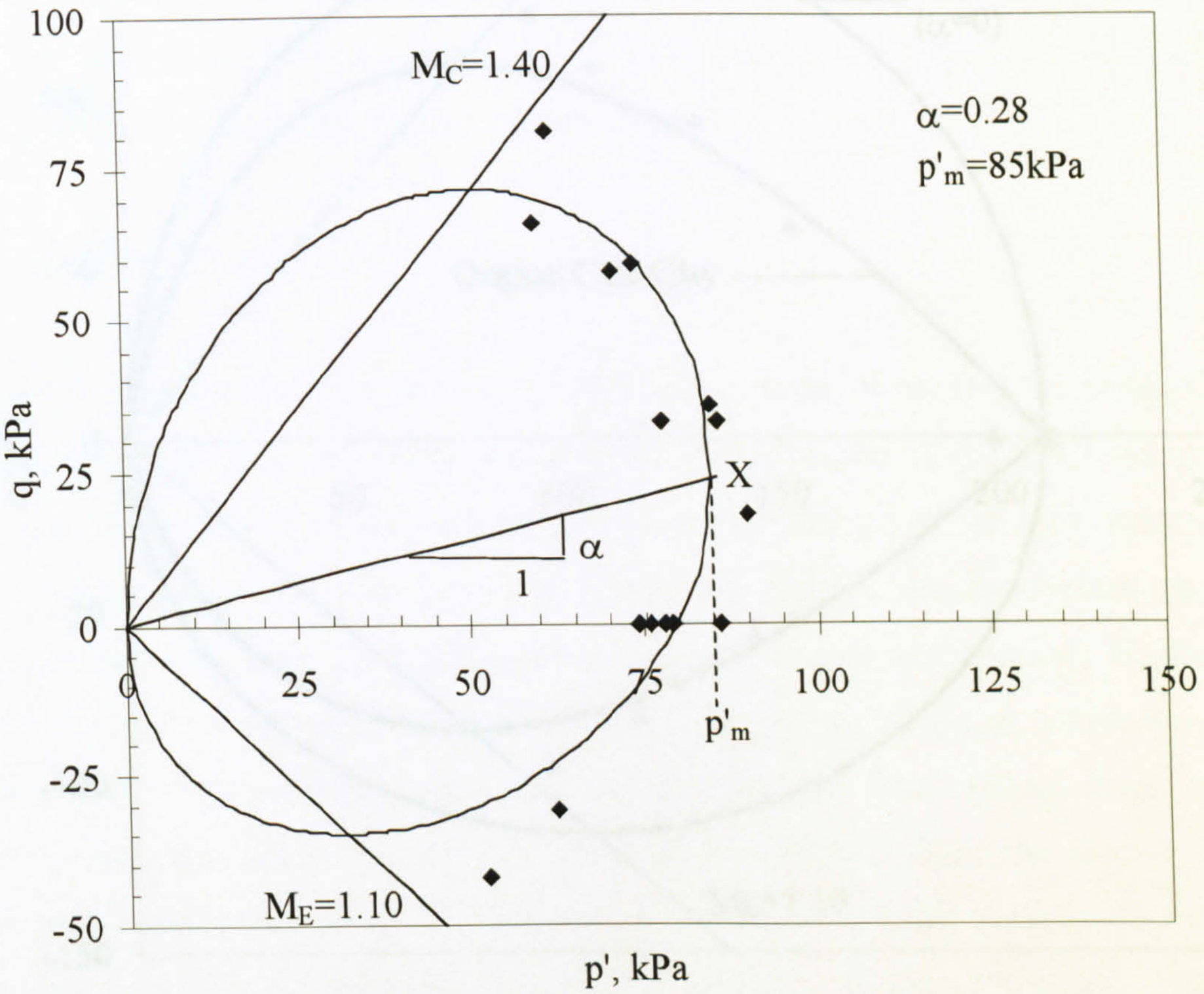

Figure 6.38. Best-fit S-CLAY1 yield curve adjusted so that $M = M_E$ below α-line.

loading stage at a different value of η (ranging from $\eta_2 = -1.00$ in Test B9 to $\eta_2 = 1.30$ in Test B4, see Table 6.2). Using the yield points identified in the 9 second loading stages, it was possible to examine the size and shape of the expanded and rotated yield curve produced by the isotropic first loading stage. The yield points from the second loading stages in Series B are shown in Figure 6.39. The single square data point indicates the maximum stress in the common first loading stage, while the triangular data points represent the yield points identified from the individual second loading stages. The yield points in Figure 6.39 are reasonably symmetric about the p'-axis, suggesting that, as expected, the isotropic loading in the first stage had rotated the yield curve clockwise to an isotropic orientation i.e. symmetrical about the p'-axis. However the yield curve expression for S-CLAY1 with $\alpha = 0$ and $p'_m = 210$ kPa (corresponding to the Modified Cam Clay yield curve expression) is a very poor match to the experimental data. Each data point is well inside this curve and reduction of the value of p'_m does not improve the match significantly, because the apparent shape of the yield curve corresponding to the data

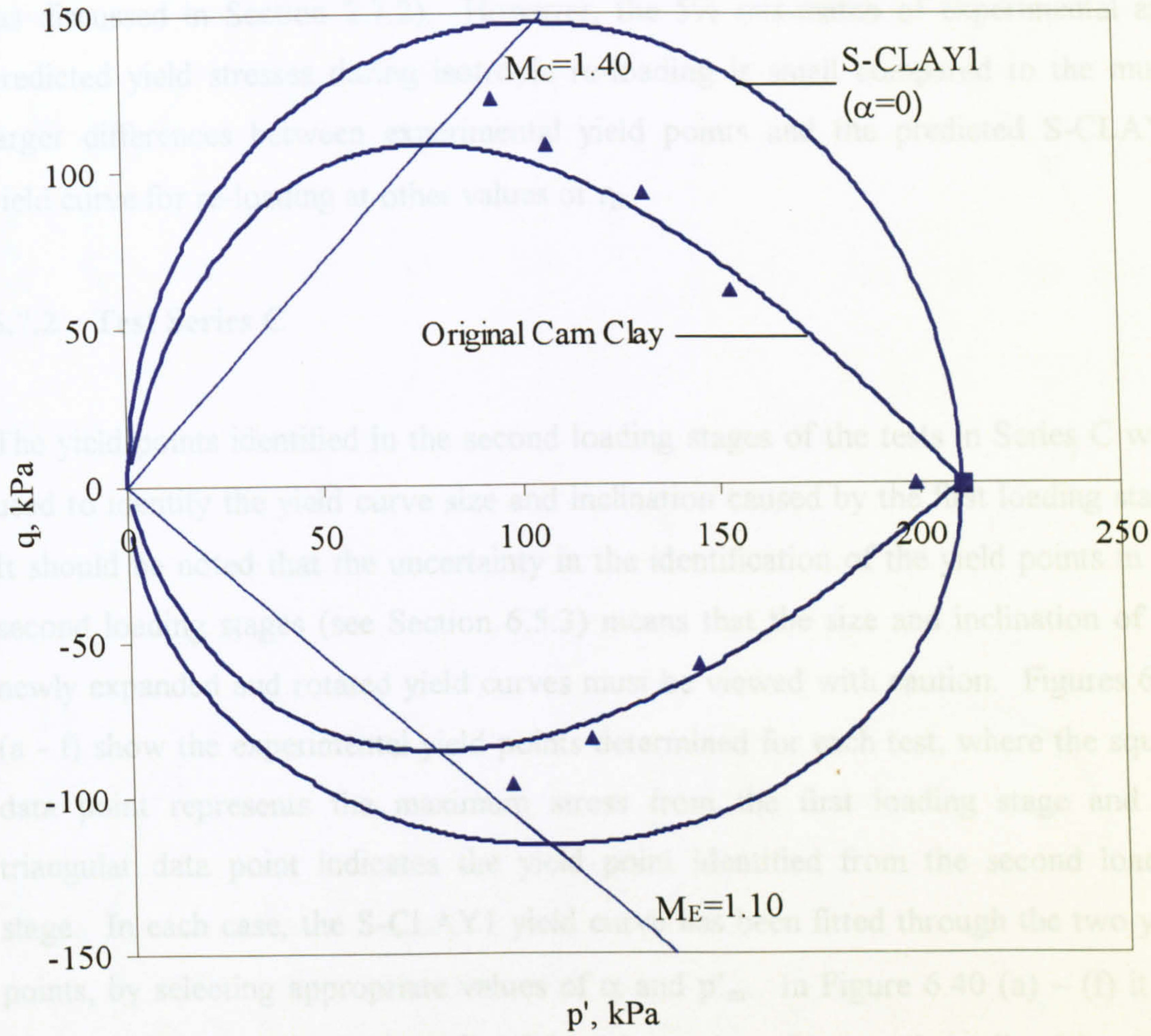

Figure 6.39. Expanded and rotated yield curve following isotropic loading stages in Test Series B.

points is quite different from that of S-CLAY1. It is interesting to note that the Cam Clay yield curve (Roscoe and Schofield, 1963), with tip stress p'_0 set to 210 kPa, gives a better match to the data (see Figure 6.39).

It is useful to note that Test B7, involving a second loading stage at $\eta = 0$ showed a yield point during second loading that was about 5% lower than the maximum stress previously applied in the first stage. This small discrepancy might be caused by uncertainty in the procedure used for identifying yield points from the experimental stress-strain curves (see Section 6.5.3). Alternatively it might indicate that the classical elasto-plastic framework of S-CLAY1 is not entirely correct and that on unloading-reloading large plastic strains re-commence at a slightly lower stress than the maximum stress previously applied. This type of behaviour would be predicted by some models incorporating multiple yield surfaces or bounding surface plasticity

(as discussed in Section 2.7.2). However, the 5% mis-match of experimental and predicted yield stresses during isotropic re-loading is small compared to the much larger differences between experimental yield points and the predicted S-CLAY1 yield curve for re-loading at other values of η_2.

6.7.2 Test Series C

The yield points identified in the second loading stages of the tests in Series C were used to identify the yield curve size and inclination caused by the first loading stage. It should be noted that the uncertainty in the identification of the yield points in the second loading stages (see Section 6.5.3) means that the size and inclination of the newly expanded and rotated yield curves must be viewed with caution. Figures 6.40 (a - f) show the experimental yield points determined for each test, where the square data point represents the maximum stress from the first loading stage and the triangular data point indicates the yield point identified from the second loading stage. In each case, the S-CLAY1 yield curve has been fitted through the two yield points, by selecting appropriate values of α and p'_m. In Figure 6.40 (a) – (f) it has been assumed that above the α-line $M = M_C = 1.4$ and below the α-line $M = M_E = 1.1$.

Test C4, shown in Figure 6.40 (a), involved first loading in triaxial extension ($\eta_1 = -0.80$) to $p' = 126$ kPa then a second loading stage in triaxial compression ($\eta_2=0.60$) to $p' = 300$ kPa. The figure suggests that the yield curve was rotated clockwise to a value of $\alpha = -0.36$ (with $p'_m = 140$ kPa) during the first loading stage. This agrees qualitatively with the expected behaviour, that a first loading stage in triaxial extension will cause the yield curve to be rotated to a negative value of α.

Test C6, shown in Figure 6.40 (b) involved a first loading stage at a low positive value of η ($\eta_1 = 0.20$) and a second loading stage at a much higher positive value of η ($\eta_2 = 1.03$). The yield curve fitted through the two data points suggests a large negative value of α ($\alpha = -0.47$, with $p'_m = 264$ kPa). This outcome is highly unlikely; qualitatively, it would not be expected that loading in triaxial compression during the first loading stage would cause the yield curve to rotate to a negative value

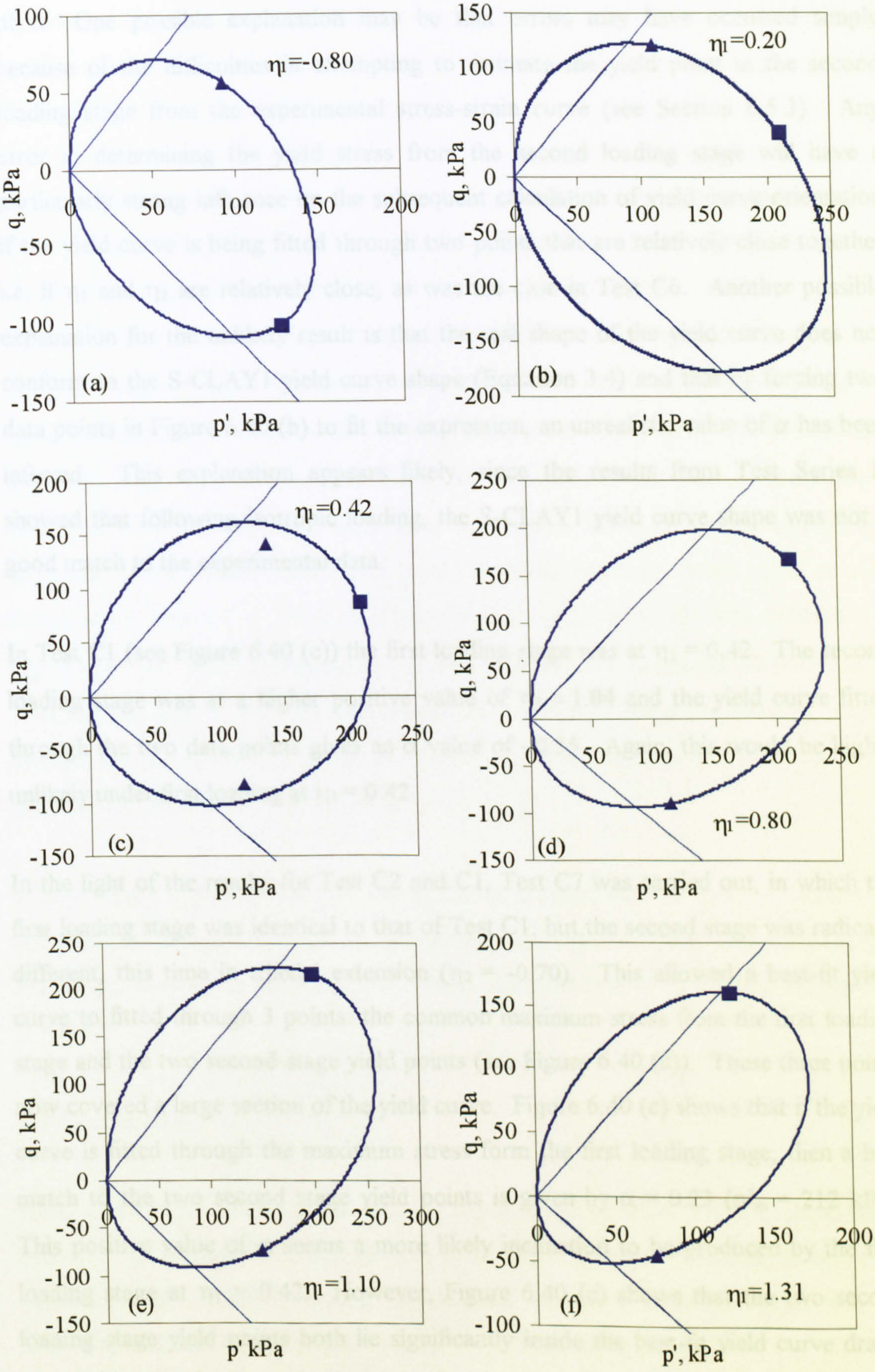

Figure 6.40. Expanded and rotated yield curves in Test Series C: (a) Test C4, (b) Test C6, (c) Tests C1 and C7, (d) Test C5, (e) Test C2, (f) Test C3.

of α. One possible explanation may be that errors may have occurred simply because of the difficulties in attempting to estimate the yield point in the second loading stage from the experimental stress-strain curve (see Section 6.5.3). Any error in determining the yield stress from the second loading stage will have a particularly strong influence on the subsequent calculation of yield curve orientation if the yield curve is being fitted through two points that are relatively close together i.e. if η_1 and η_2 are relatively close, as was the case in Test C6. Another possible explanation for the unlikely result is that the real shape of the yield curve does not conform to the S-CLAY1 yield curve shape (Equation 3.4) and that by forcing two data points in Figure 6.40 (b) to fit the expression, an unrealistic value of α has been inferred. This explanation appears likely, since the results from Test Series B showed that following isotropic loading, the S-CLAY1 yield curve shape was not a good match to the experimental data.

In Test C1 (see Figure 6.40 (c)) the first loading stage was at $\eta_1 = 0.42$. The second loading stage was at a higher positive value of $\eta_2 = 1.04$ and the yield curve fitted through the two data points gives an α value of -0.55. Again, this would be highly unlikely under first loading at $\eta_1 = 0.42$.

In the light of the results for Test C2 and C1, Test C7 was carried out, in which the first loading stage was identical to that of Test C1, but the second stage was radically different, this time in triaxial extension ($\eta_2 = -0.70$). This allowed a best-fit yield curve to fitted through 3 points: the common maximum stress from the first loading stage and the two second-stage yield points (see Figure 6.40 (c)). These three points now covered a large section of the yield curve. Figure 6.40 (c) shows that if the yield curve is fitted through the maximum stress form the first loading stage, then a best match to the two second stage yield points is given by $\alpha = 0.23$ ($p'_m = 212$ kPa). This positive value of α seems a more likely inclination to be produced by the first loading stage at $\eta_1 = 0.42$. However, Figure 6.40 (c) shows that the two second loading stage yield points both lie significantly inside the best-fit yield curve drawn through the maximum stress from the first loading stage. This may imply that the method of experimental yield point determination has consistently resulted in underestimation of yield points from the second loading stages or that the S-CLAY1

yield curve shape is not a good match to the observed yield behaviour following first loading at $\eta_1 = 0.42$. A similar conclusion was reached from tests in Series B (see Figure 6.39).

In the other tests the two data points were more widely separated around the yield curve. Test C5, shown in Figure 6.40 (d) involved first loading in triaxial compression at $\eta_1 = 0.80$ (slightly less than the stress ratio estimated for K_0 conditions, $\eta_{K0} = 0.91$) to a maximum stress of 210 kPa, followed by unloading and then reloading in triaxial extension at $\eta_2 = -0.80$. The resulting rotated yield curve, fitted through the two data points, gives a curve with inclination $\alpha = 0.49$ and size $p'_m = 222$ kPa. This increase in the value of α (from an initial value of $\alpha = 0.28$) is consistent with the fact that loading at this higher value of η will cause anti-clockwise rotation of the yield curve. Test C2 was loaded in the first stage at an even higher stress ratio ($\eta_1 = 1.10$) to a maximum stress of $p' = 198$ kPa as shown in Figure 6.40 (f). After unloading this sample was reloaded in triaxial extension at $\eta_2 = -0.50$. The best-fit yield curve corresponds to $\alpha = 0.51$ and $p'_m = 240$ kPa. Again this anti-clockwise rotation of the yield curve (from $\alpha = 0.28$ to $\alpha = 0.51$) conforms qualitatively with the S-CLAY1 model predictions.

Finally, Test C3 (Figure 6.40 (f) was loaded at a stress ratio of $\eta_1 = 1.31$ in triaxial compression, slightly less than the critical state ratio ($M_C = 1.40$). This first loading has, again, caused the yield curve to rotate significantly anti-clockwise, this time to $\alpha = 0.67$.

6.8 Conclusions

Data from Test Series A, B and C provided information on the stress-strain behaviour of vertically oriented samples of Bothkennar clay. A number of important issues relevant to the modelling of soft clay behaviour were addressed and the following conclusions can be drawn from these three suites of tests:

- Data from Test Series A indicates that suitable values for the critical state stress ratio in triaxial compression and extension are, respectively, $M_C = 1.40$

and M_E = 1.10. The S-CLAY1 and S-CLAY1S models must therefore incorporate Lode angle dependency if they are to reflect this difference.

- Yield points are identifiable from the various stress-strain plots presented. Yielding is generally reasonably clearly identified during first loading stages, but is less obvious during second loading stages. The fact that yield points are more obscured during second loading may be a consequence of the influence of evolving anisotropy, particularly where the stress ratio η_2 during second loading stages is significantly different from the stress ratio η_1 in the first loading stages.

- Pre-yield behaviour appears to be anisotropic. During unloading it appears that the soil behaviour can be represented by a cross-anisotropic elastic model. This elastic anisotropy remains unchanged during all loading and unloading stages. This anisotropy of elastic behaviour is currently ignored in the S-CLAY1 and S-CLAY1S constitutive models.

- The post-yield gradient λ (in plots of v: ln p') shows significant variation with the stress ratio η and is also influenced by the choice of η in a previous loading stage. This is probably caused by the effects of destructuration. In particular, plastic straining at high values of η (especially in triaxial compression) causes more rapid destructuration. As a result, the rate of destructuration during a second loading stage is reduced if large amounts of destructuration have occurred during the first loading stage.

- The yield points determined from the first loading stages in Test Series B and C were well matched by S-CLAY1. However, the value of yield curve orientation α for this initial location of the yield curve was lower than the yield curve orientation derived on a theoretical basis from a value of K_0. Wheeler et al. (2003) have shown, however, that the S-CLAY1 yield curve shape matches well with experimental data from a number of other clays. It is suggested that the discrepancy in this study can be attributed to an in-situ change in α caused by unloading to an overconsolidated state.

- In the second loading stages, the yield points obtained suggested that the S-CLAY1 yield curve shape (fitted through the maximum stress point from the first loading stage and the second loading yield point) is not a good match to the experimental data. This is in contrast with previous investigations on other soft clays including Wheeler et al. (2003) and Karstunen and Koskinen (2004).

- Tests results confirm that yield curve rotation is caused by loading at a stress ratio that differs from the previous stress history of the soil. There is some evidence that the form of yield curve rotation is qualitatively consistent with the form assumed in the S-CLAY1 model. However, the evidence is less compelling than has been shown for other soft clays, because of the apparently poor match of the S-CLAY1 yield curve shape to the experimental yield points observed in second loading stages.

- The S-CLAY1 flow rule appears to provide a closer match to experimental data than MCC. However, both models give poor predictions at high positive or negative values of η.

- It is necessary to rigorously test whether the S-CLAY1 and S-CLAY1S models are able to accurately model the stress-strain behaviour of Bothkennar clay by comparing the experimental data with model simulations. The simulations are presented in Chapters 8 and 9.

CHAPTER 7: TESTS ON HORIZONTAL SAMPLES

7.1 Introduction

In this chapter the experimental data from triaxial tests on horizontal samples are presented and discussed. Results from Test Series D, involving drained shearing tests to failure are discussed in Section 7.2 and compared to those of the vertical samples (see Section 6.2). The stress-strain responses from the multi-stage stress path tests in Test Series E are presented in Section 7.3, including locally measured radial strains. The issue of pre-yield behaviour is discussed in Section 7.4 and the cross-section of the yield surface observable from triaxial testing of horizontal samples is presented in Section 7.5. Finally, comparisons between tests on horizontal samples and analogous tests on vertical samples are given in Section 7.6. All data from Test Series D and E are presented in terms of natural strains, as described in Section 6.1.

7.2 Test Series D: shearing tests to failure

7.2.1 Stress-strain behaviour

Four conventional drained shearing tests to failure (two in triaxial compression and two in triaxial extension) were carried out in order to establish the critical state stress ratios M_C and M_E (in triaxial compression and triaxial extension respectively). These tests were carried out using the same apparatus and methods as employed in the equivalent tests on vertical samples in Test Series A (see Section 6.2.1). A summary of these drained shear tests is shown in Table 7.1, where the symbols have been previously defined in Section 6.2.1. Triaxial samples were selected from each of the Laval samples 20A, 20B and 21A so as to provide a representation of all the material tested in this study. As with Test Series A, these tests were taken to high levels of strain so that post-peak behaviour could be properly observed. The stress paths involved in each test are shown in Figure 7.1. The stress-strain behaviour in each test is shown in terms of deviator stress and deviator strain in Figure 7.2 (a) and in terms of volumetric strain against ln p' in Figure 7.2 (b). The open circles in Figure 7.2 indicate points corresponding to peak deviator stress.

Test	σ'_c (kPa)	q_{peak} (kPa)	η_{peak}	ε_{dpeak} (%)	ε_{vpeak} (%)	v_{peak}	Laval Sample
D1	100	232	1.31	32.91	14.81	2.22	20A
D2	175	421	1.33	30.30	18.05	1.92	20B
D3	100	-83	-1.14	0.11	2.12	2.50	20B
D4	65	-56	-1.25	-2.98	-3.67	2.77	21A

Table 7.1. Details of shearing tests to failure on horizontal samples.

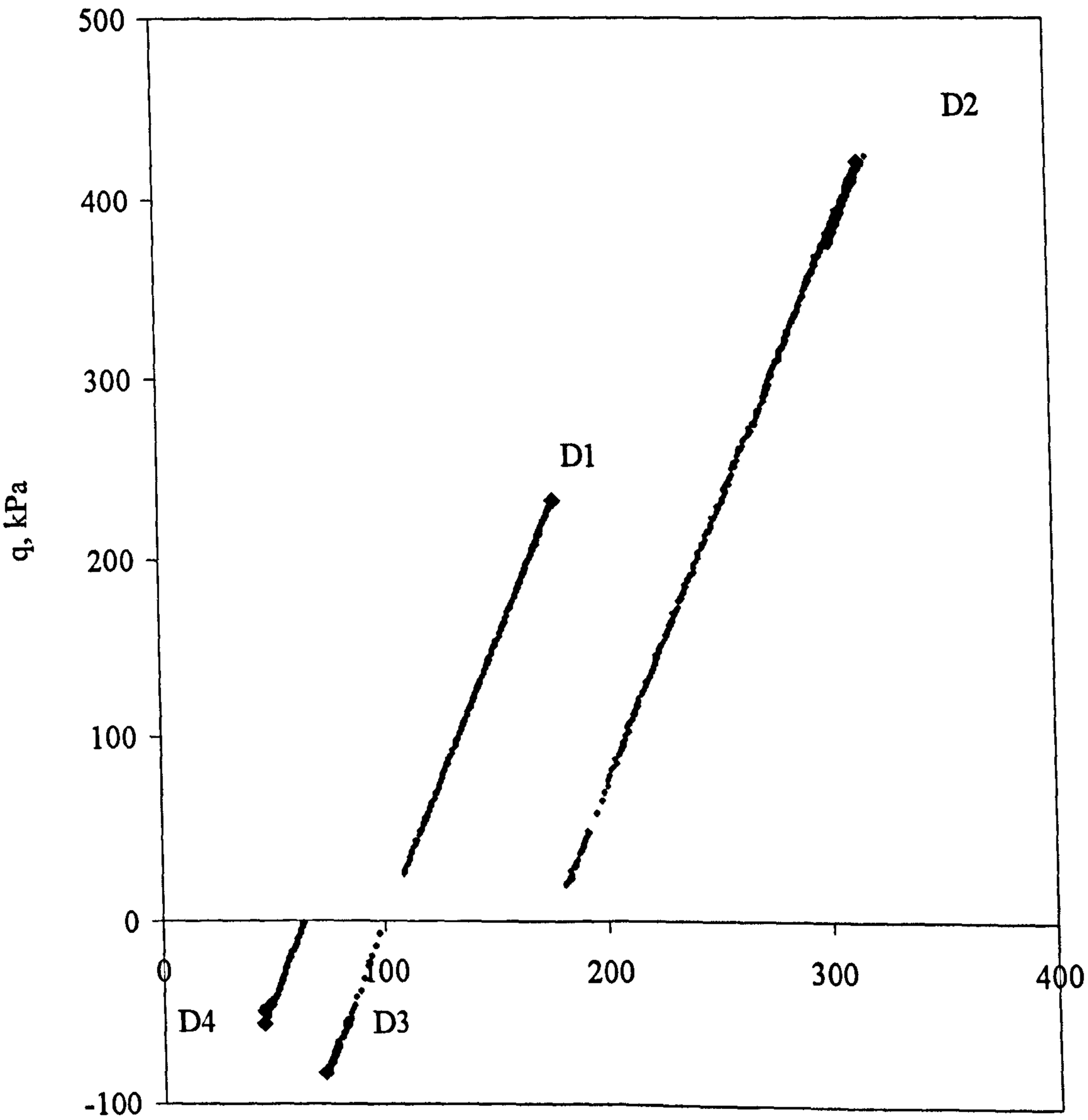

Figure 7.1. Stress paths for drained shearing tests to failure on horizontal samples.

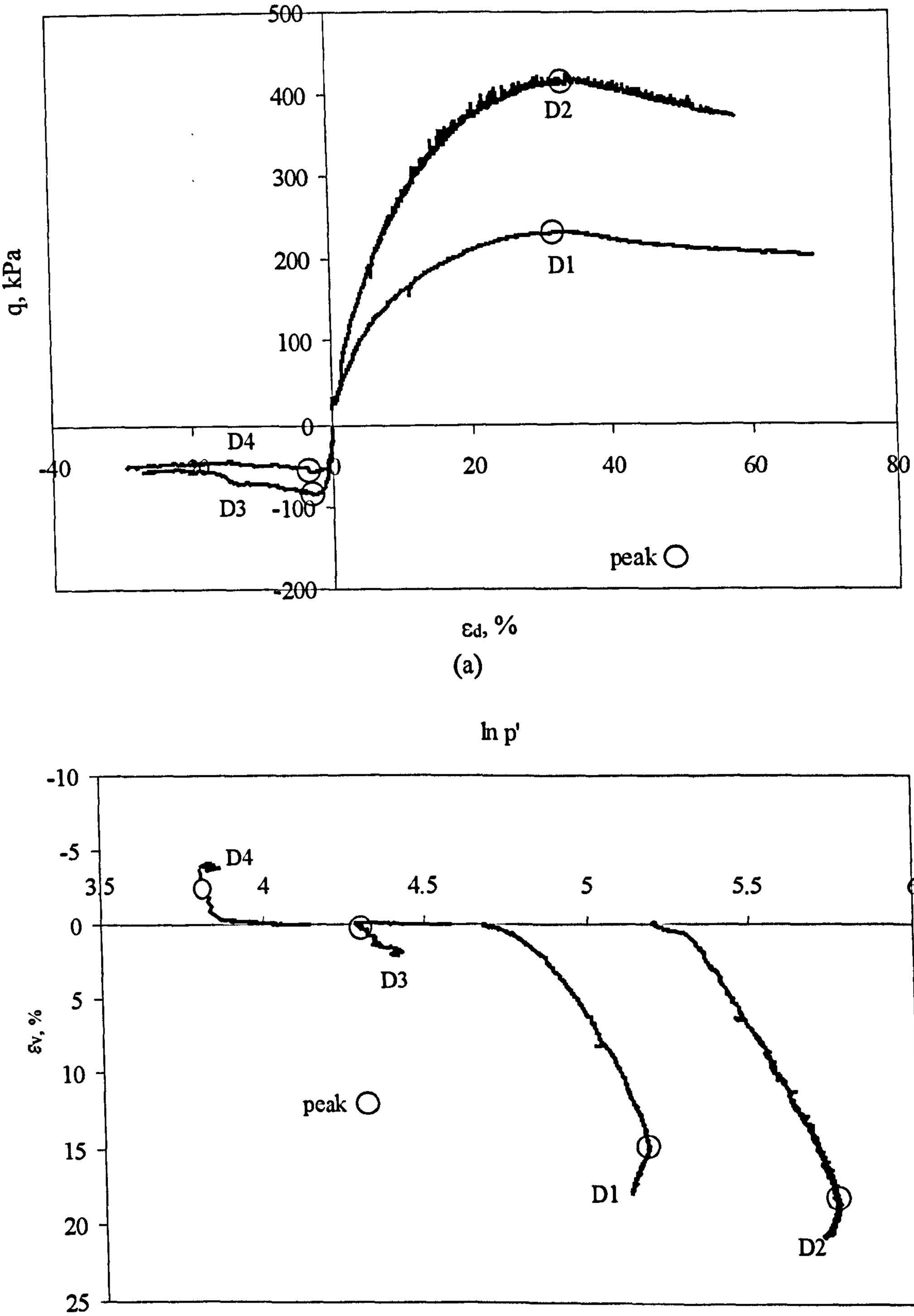

Figure 7.2. Stress-strain behaviour of drained shear tests on horizontal samples; (a) deviatoric behaviour, (b) compression behaviour.

Table 7.1 and Figure 7.2 indicate that the peak deviator stress occurred at high magnitudes of shear and volumetric strains in triaxial compression and lower levels of shear and volumetric strains in triaxial extension. In Figure 7.2 (a) the stress-strain behaviour observed in the compression tests (D1 and D2) is qualitatively similar to that of Tests A1, A2 and A3 on the vertical samples. The plots show that after the peak deviator stress was reached in Tests D1 and D2, there was a significant reduction in deviator stress. In both tests, no distinct failure plane could be identified upon inspection of the sample after testing had ceased. The corresponding peak stress ratios are shown in Table 7.1. In Figure 7.2 (b) the peak deviator stress is again indicated on the compression curves for each test. In Tests D1 and D2 the samples continued to compress beyond the peak deviator stress.

In triaxial extension, Figure 7.2 (a) shows that for both Tests D3 and D4, a peak in deviator stress was reached followed by a gradual reduction in deviator stress. Figures 7.2 (a) and 7.2 (b) indicate that during drained shearing in triaxial extension, Test D4 (σ'_c = 65 kPa) experienced a significant amount of swelling. The yield curve proposed for the horizontal samples, based on the stress path tests in Test Series E, (see Section 7.5) suggests that the sample in Test D4 yielded on the dry (supercritical) side of the yield curve and this is confirmed by the significant swelling noted in the later part of the stress path. The behaviour of Test D4 may be compared to that in Test D3 (σ'_c = 100 kPa), where the sample was isotropically consolidated to a higher stress than Test D4. The sample in Test D3 appears to have yielded on the wet side of the critical state, although the extremely low magnitude of volumetric straining at peak stress ratio (ε_{vpeak} = 0.1%) suggests that yielding has occurred very close to the critical state.

7.2.2 Critical state

The identification of the critical state stress ratio was discussed in Section 6.2.2. Each of the four tests in Test Series D showed similar patterns of stress-strain behaviour to their counterparts in Test Series A, in which a peak and subsequent fall in deviator stress occurred, accompanied by further changes in the volumetric state. Again, it is unclear whether the post-peak reduction of deviator stress is towards a

critical state or towards some lower post-rupture or residual strength. In the interests of consistency, the peak deviator stress is again nominated as the point at which critical state is achieved, as already explained for tests on vertical samples (see Section 6.2.2).

Figure 7.3 (a) shows strains paths for each of the four shearing tests in terms of volumetric and shear strains. These show that in each test in triaxial extension some initial swelling occurred prior to the peak deviator stress, but then post-peak volumetric compression occurs. In triaxial compression, post-peak shearing is accompanied by continuing volumetric compression. Figure 7.3 (c) shows the data points representing the peak conditions from each of the four tests in Series D in a q: p' plot. Also shown in Figure 7.3 (c) are the critical state lines that have been established in both triaxial compression and triaxial extension. The best-fit line in Figure 7.3 (c) suggests that the critical state stress ratios for horizontal samples in triaxial compression, M_{CH}, and triaxial extension, M_{EH}, are approximately 1.30 and 1.20 respectively. These values of M_{CH} and M_{EH} have been quoted to the nearest ±0.05, as this is the level of precision considered appropriate, given the variability between individual tests (see Table 7.1). The values of M_{CH} and M_{EH} suggested from Test Series D lend support to the widely reported suggestion that M_C is significantly greater than M_E, but the difference appears significantly less than for vertical samples. Figure 7.3 (b) shows test data plotted in the v: ln p' plane with the peak conditions marked. A best-fit line has been fitted through the data points corresponding to the peak deviator stress in each test. The position of the line is different to the equivalent line observed for the vertical samples (see Figure 6.3 (b)), and the gradient of the line (0.41) is much steeper than for the vertical sample (0.27). This may be due natural variability within the samples.

The fact that, for the horizontal specimens, the stress ratios at peak observed in triaxial compression and triaxial extension were notably different to those observed for the vertical samples (see Section 6.2) suggests that the stress ratio at peak may be influenced by the major principal stress direction. This must be due to the fact that the soil is anisotropic and that when shearing to failure in the triaxial test, the major principal stress is parallel to the axis of deposition for vertical samples, but is

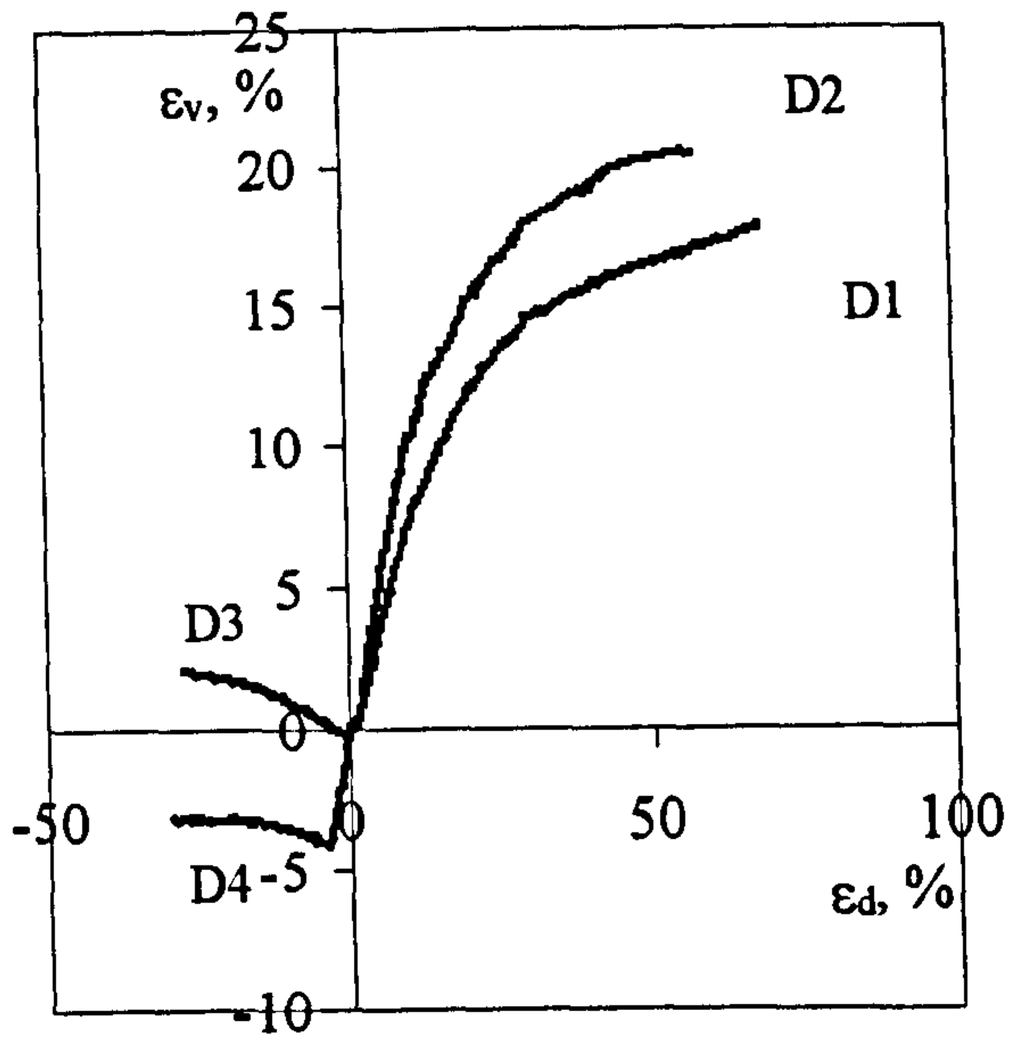

(a)

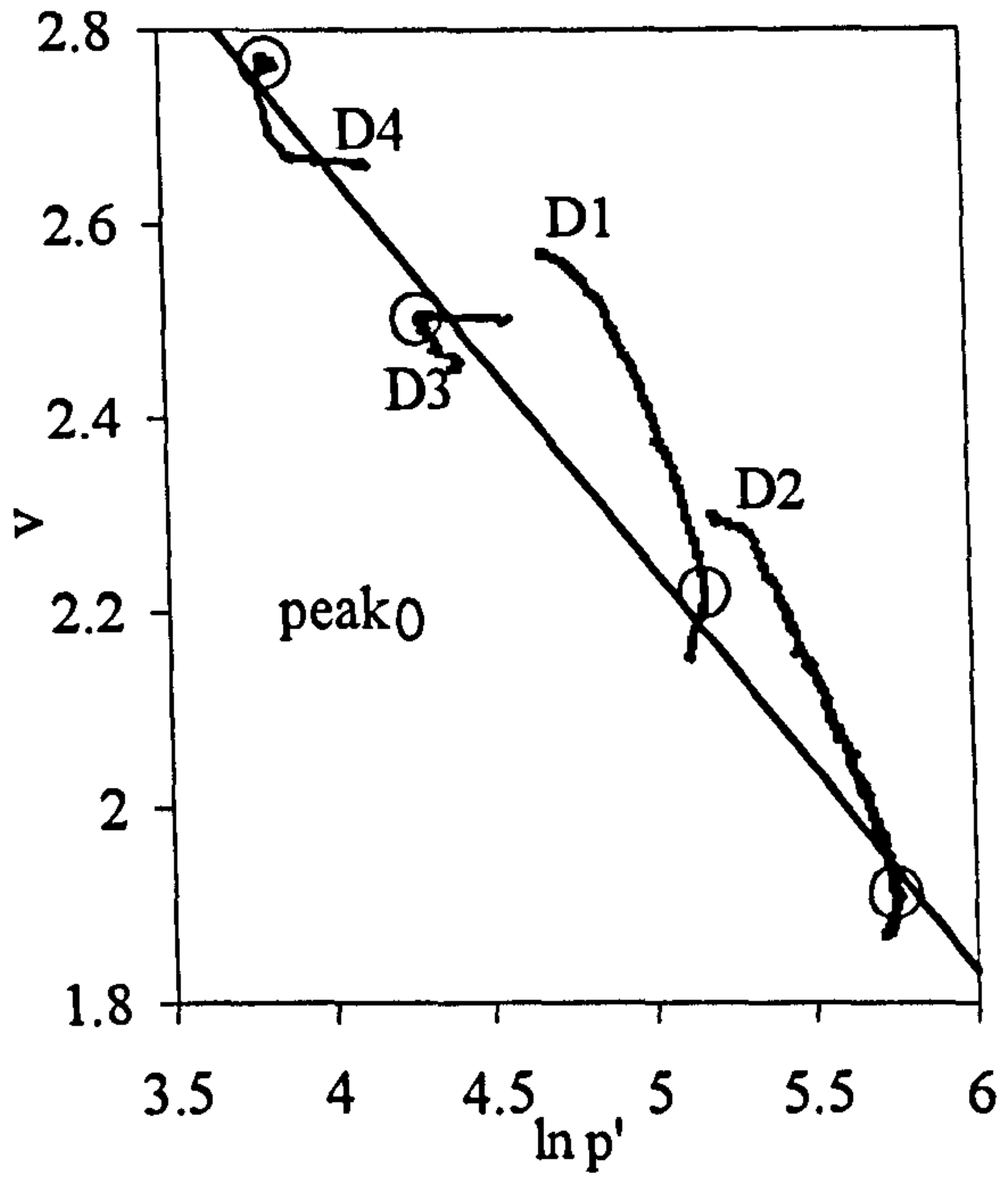

(b)

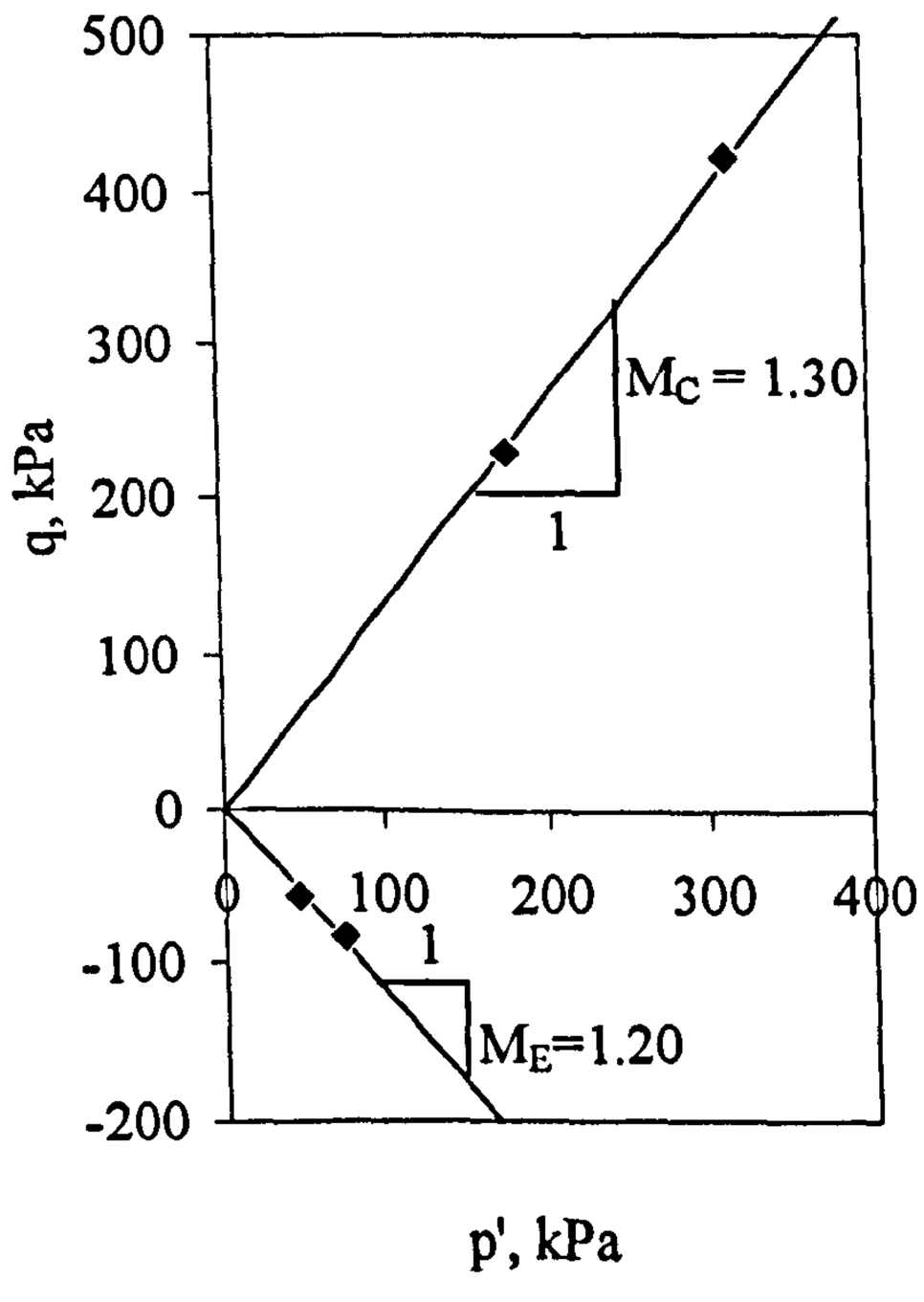

(c)

Figure 7.3. Shearing tests to failure of horizontal samples (a) strain paths, (b) compression plane and (c) critical state lines in q: p' space.

perpendicular to this axis for horizontal samples. This contravenes a fundamental assumption of S-CLAY1 that as a critical state is reached, the soil fabric is being continuously destroyed and re-created and that any previous memory of fabric arrangement has been lost. This could mean that, even at advanced stages of shearing, plastic straining has not been sufficient to totally erase initial anisotropy of fabric. A number of authors including Broms and Casbarian (1964), Shibata and Karube (1979), Adachi et al. (1979) and Kirkgard and Lade (1993) have reported similar findings (at peak deviatoric stresses). Tests by these authors have shown that the failure surface for natural clays is not defined by a single parameter such as the critical state stress ratio M, but that there is a dependency on the orientation of the principal stresses in relation to the fabric anisotropy of the sample.

7.3 Stress-strain behaviour during Test Series E

7.3.1 Summary of samples properties and stress paths

Preliminary tests on the horizontal samples (including oedometer tests) were conducted and the results of these tests are detailed in Chapter 5. The index properties for all samples in this study were given in Table 6.1. A summary of test conditions involved in Test Series E is given in Table 7.2.

TEST	e_0	η_1	p'_{max1} (kPa)	η_2	p'_{max2} (kPa)	Laval sample
E1	1.504	0.00	210	0.70	458	20A
E2	1.617	0.41	210	-0.79	441	20A
E3	1.681	0.80	102	-	-	21A
E4	1.654	0.41	210	0.99	293	21A
E5	1.708	1.10	130	-	-	20A
E6	1.627	-0.81	146	-	-	20B
E7	1.653	-0.4	207	-	-	20B

Table 7.2. Summary of test details for Test Series E.

7.3.2 Axes convention and strain measurement

It is necessary to specify the axis convention adopted for the tests presented. In the ground (Fig. 7.4 a), the vertical direction is referred to as the Y-axis, whereas the horizontal directions are labelled as X-and Z-axes. In discussion of test data, the y-axis is taken to coincide with the axial direction in the triaxial apparatus, with x and z-axes coinciding with the radial directions (Figs. 7.4 (b) and 7.4 (c)). Using these axes conventions, the axes in the ground can be linked to the axes of the sample as Y=y, X=x and Z=z for samples that have been cut vertically (Fig. 7.4 (b)), and Y=x, X=y and Z=z for samples that have been cut horizontally (Fig. 7.4 (c)) from the ground. In this study, these samples will be referred to as vertical and horizontal samples, respectively. Note that for the horizontal samples the x radial direction in the triaxial apparatus coincides with the vertical direction in the ground, whereas the z radial direction in the triaxial apparatus coincides with a horizontal direction in the ground.

Due to the process of one-dimensional deposition and subsequent one-dimensional consolidation and creep, the soil is initially cross-anisotropic, with the X-Z plane in the ground as the plane of initial isotropy (Fig. 7.4 (a)). Using the axes convention adopted, this means that the initial plane of isotropy is the x-z plane for a vertical sample (Fig. 7.4 (b)), but the y-z plane for horizontal samples.

7.3.3 Compression curves

The compression response of each of the tests is shown in Figures 7.5 - 7.11. The data have been plotted on a linear scale (ε_v: p') and on a semi-logarithmic scale (ε_v: ln p'). In each plot, the large circular data point indicates the start of a loading stage (when the stress ratio first reached the required value of η_1 or η_2) and the large square data point represents the end of a loading stage.

In the single-stage tests (Tests E3, E5, E6 and E7) and the first loading stages of the multi-stage tests (Tests E1, E2 and E4) yielding is apparent in the semi-logarithmic plots in Figures 7.5 (b) – 7.11 (b). The behaviour is qualitatively similar to that

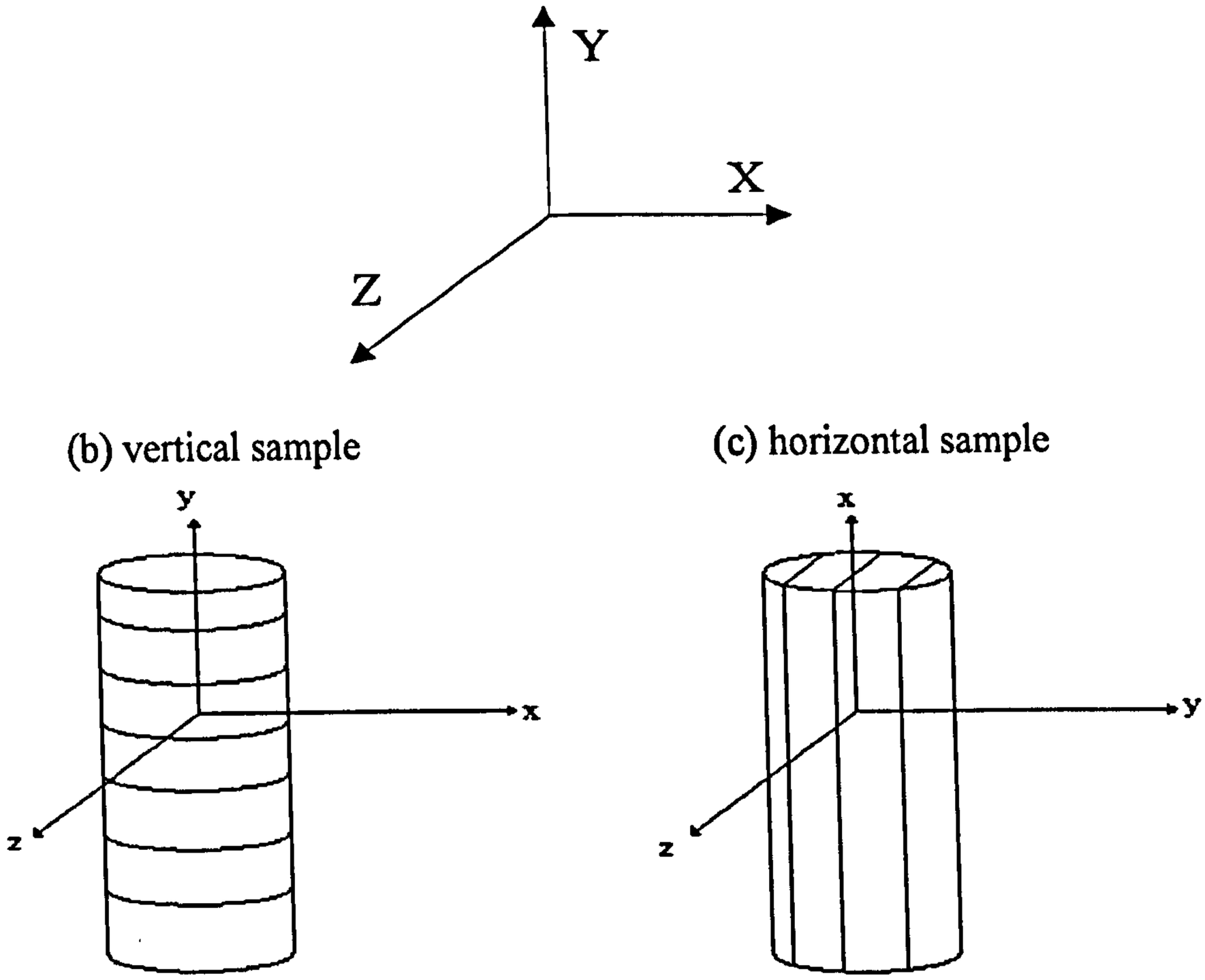

Figure 7.4. Axes convention for vertical and horizontal samples.

observed for the vertical samples. Prior to yield, the ε_v: ln p' curves are non-linear from the start of the loading stage but the gradient of the curve is relatively low. The onset of yield is marked by a distinct increase in gradient of the curves. The post-yield compressions curves are approximately linear. In the second loading stages, yielding is again apparent in the ε_v: ln p' plots.

The mean effective stress at which the yield is observed during the first loading stages can be compared to yielding of vertical samples at corresponding stress ratios. In tests involving stress ratios in triaxial compression, yield appears to occur at a lower mean effective stress in horizontal samples, particularly when comparing Test E5 with Test C2 where $\eta_1 = 1.10$. Where samples are loaded first in triaxial extension, the yield stress appears to be higher in the horizontal samples (compare Test E6 ($\eta_1 = -0.81$) with Test C4 ($\eta_1 = -0.80$)). This has implications for the shape of the yield curve and is examined fully in Section 7.5.

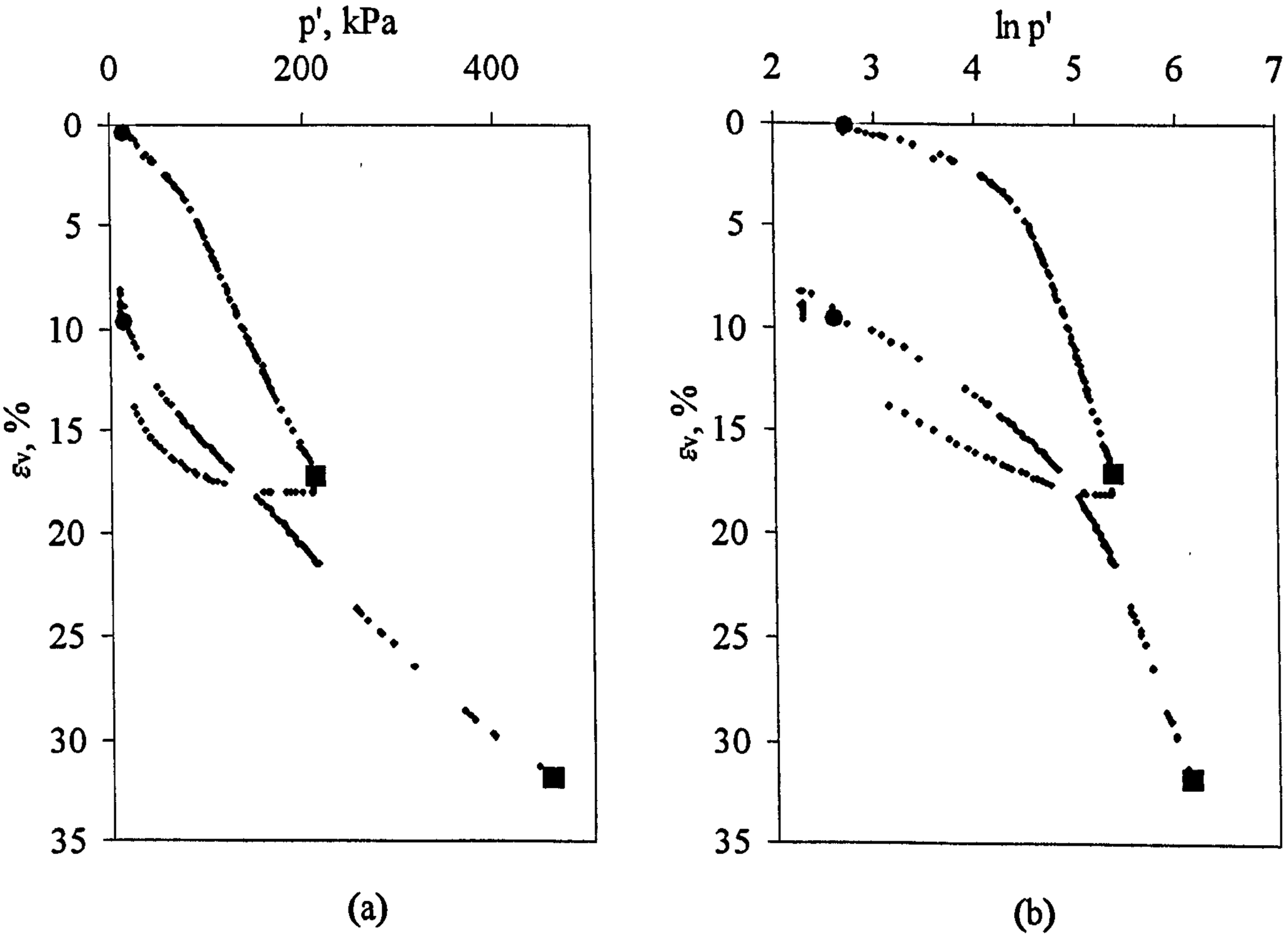

Figure 7.5. Compression behaviour for Test E1: (a) linear, (b) semi-logarithmic.

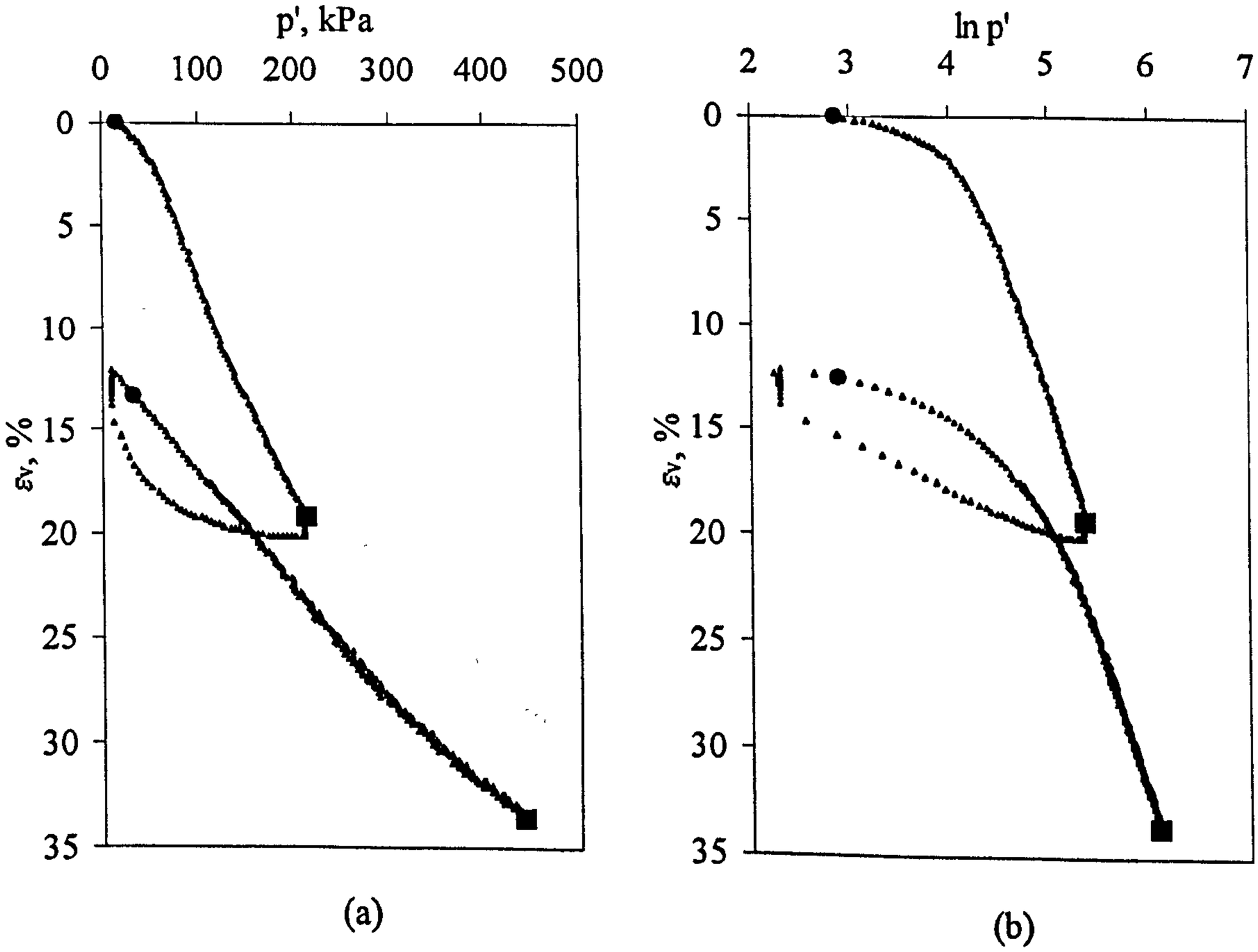

Figure 7.6. Compression behaviour for Test E2: (a) linear, (b) semi-logarithmic.

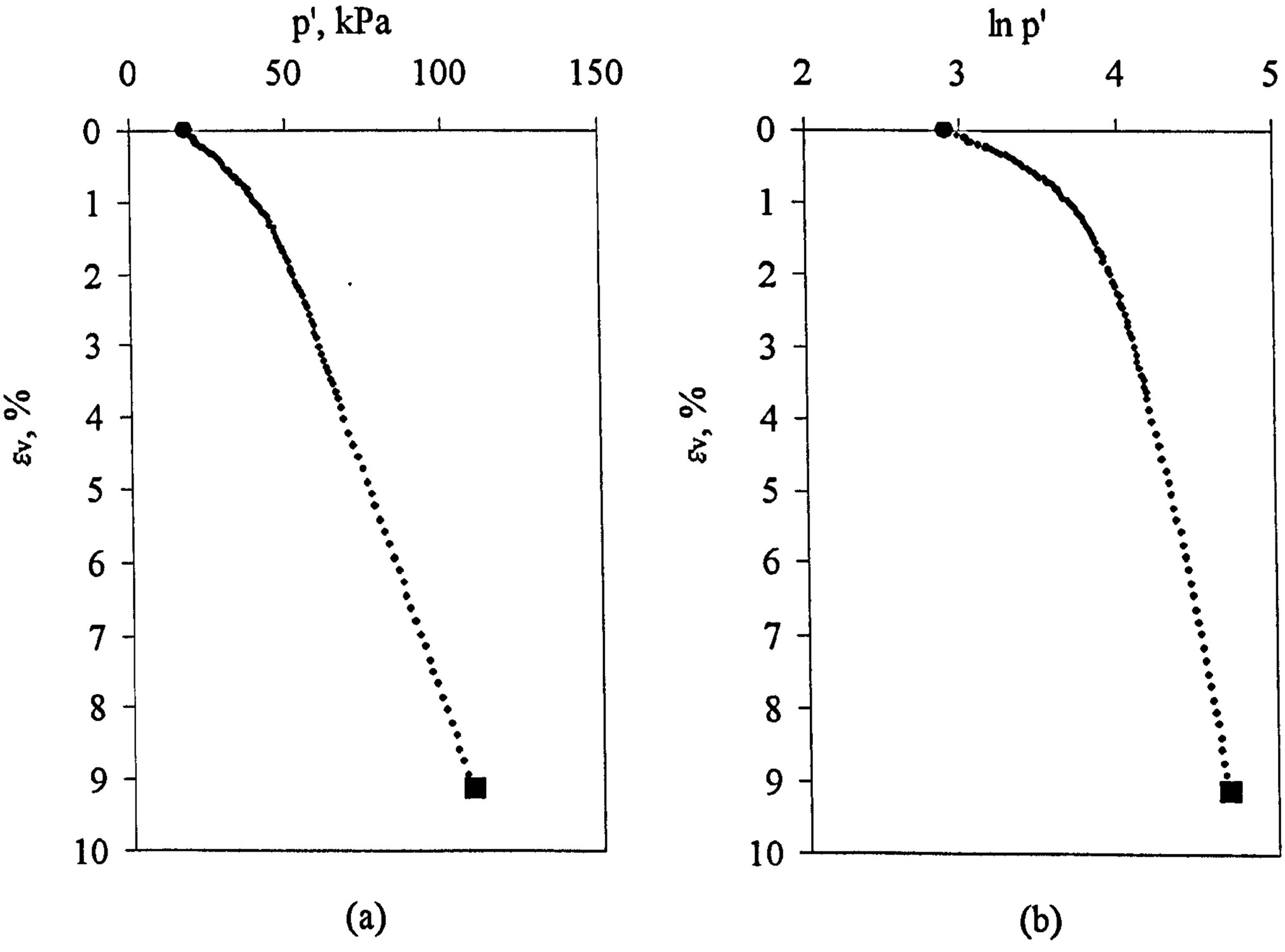

Figure 7.7. Compression behaviour for Test E3; (a) linear, (b) semi-logarithmic.

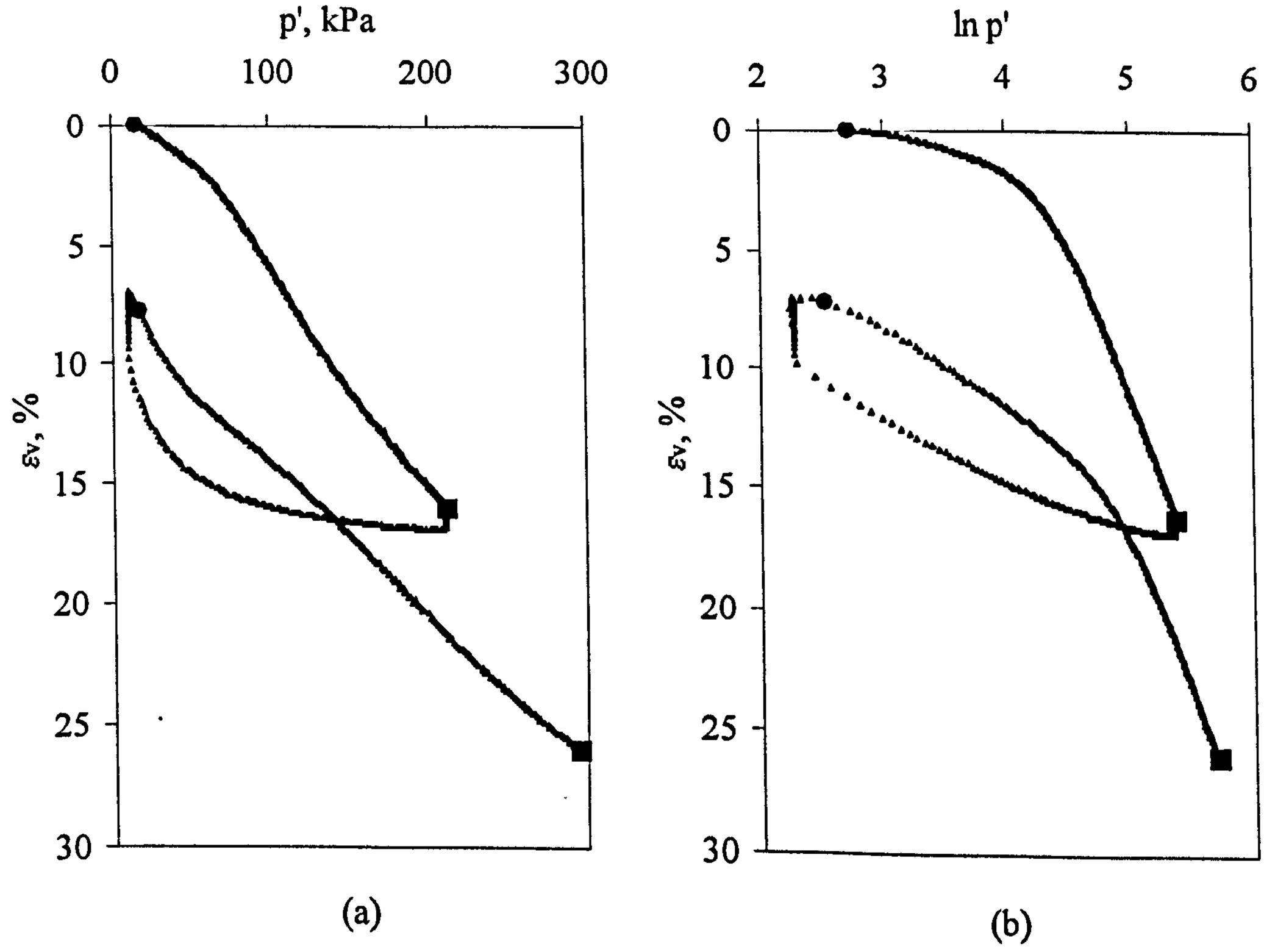

Figure 7.8. Compression behaviour for Test E4; (a) linear, (b) semi-logarithmic.

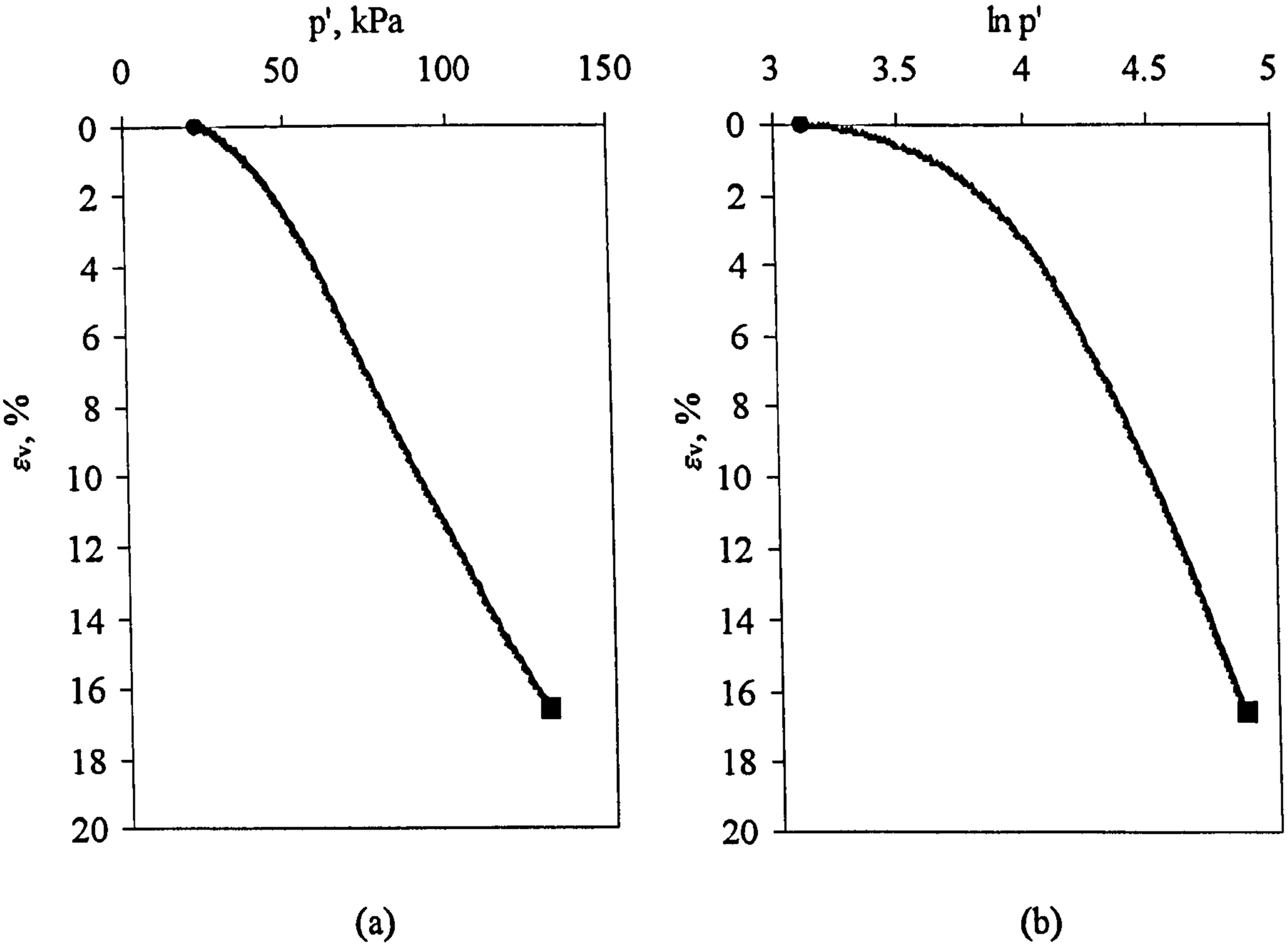

Figure 7.9. Compression behaviour for Test E5; (a) linear, (b) semi-logarithmic.

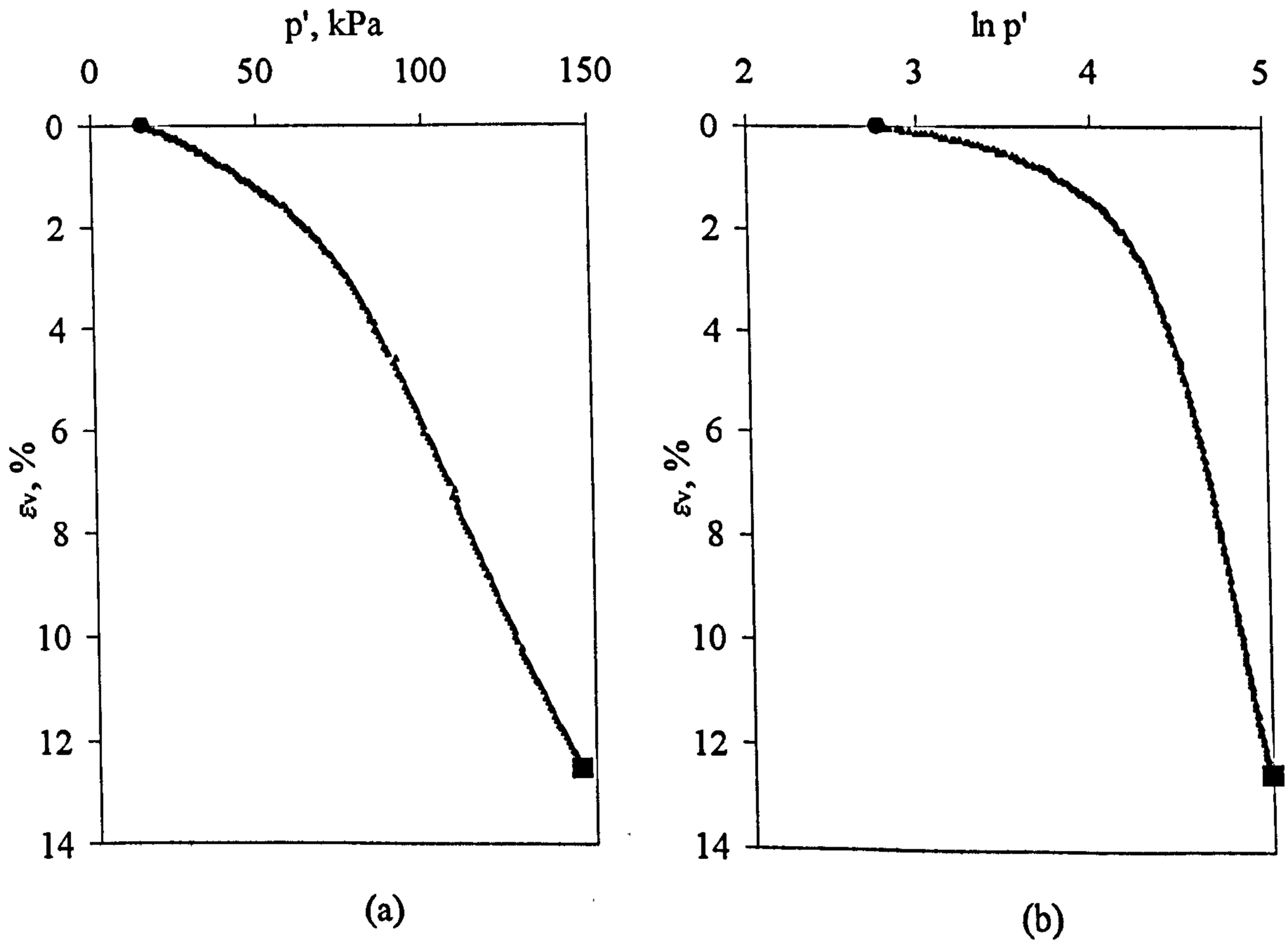

Figure 7.10. Compression behaviour for Test E6; (a) linear, (b) semi-logarithmic.

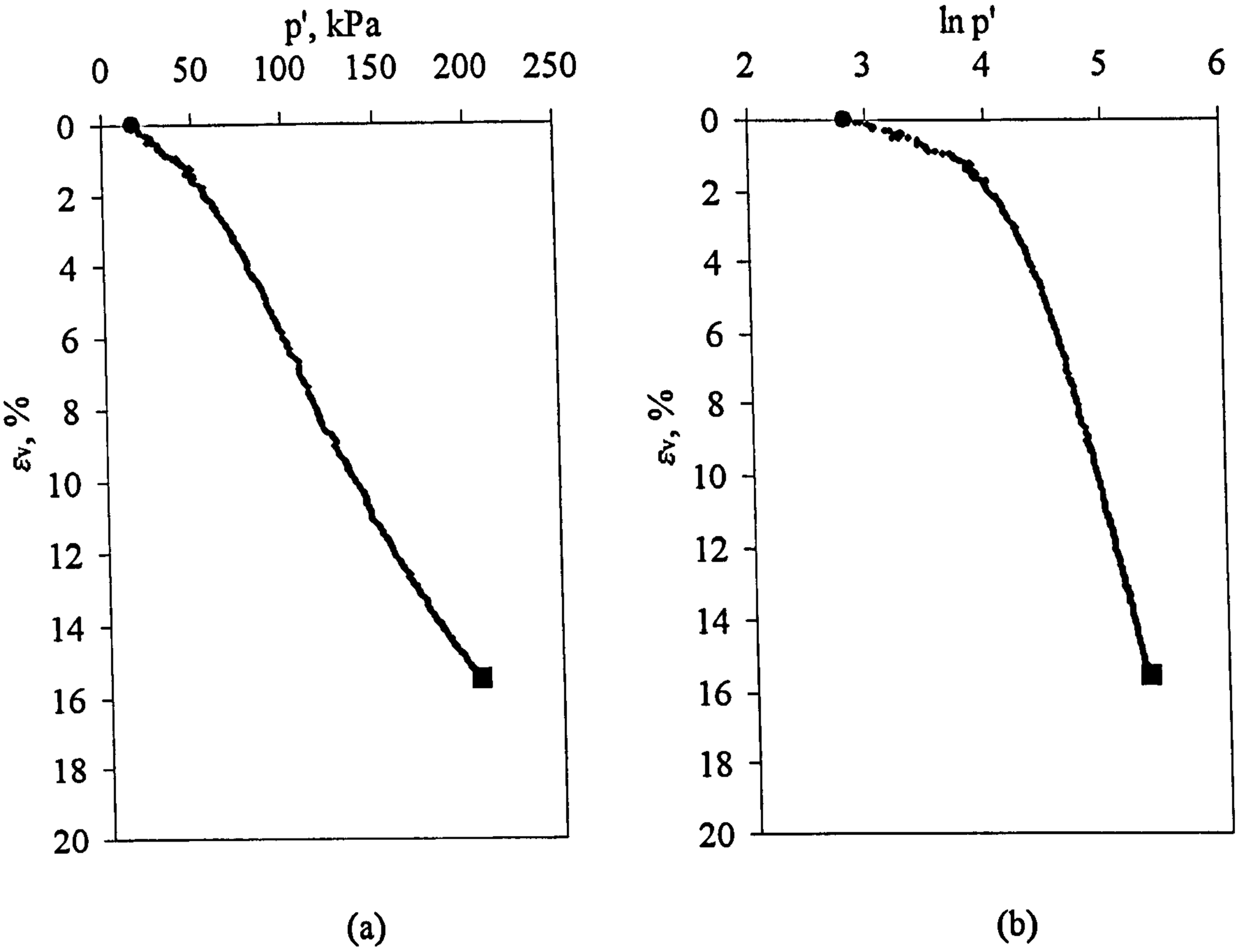

Figure 7.11. Compression behaviour for Test E7; (a) linear, (b) semi-logarithmic.

The linear ε_v: p' plots in Figures 7.5 (a) – 7.11 (a) show for the first loading stages that, although yield is indicated by a change in gradient in the curves, this change is often less clearly defined than in the semi-logarithmic ε_v: ln p' plots. During the second loading stages of Tests E1, E2 and E4, it is difficult or impossible to detect any yield points from the ε_v: p' curves. During these second loading stages, the apparent gradient of the post-yield compression curves in the ε_v: ln p' plots are lower than during the first loading stage, suggesting that destructuration has occurred during the first loading stages.

κ and λ value

Values of κ and λ have been measured for the loading and unloading stages in Test Series E in the same manner as for Test Series B and C (see Section 6.3.3). The v: ln p' plots from which these have been obtained are given in Appendix 7.1. The measured values for Test Series E are given in Table 7.3.

TEST	η_1	λ_1	κ_{unload}	η_2	λ_2
E1	0.00	0.35	0.061	0.70	0.26
E2	0.41	0.34	0.045	-0.79	0.28
E3	0.80	0.28	-	-	-
E4	0.41	0.32	0.035	0.99	0.29
E5	1.14	0.43	-	-	-
E6	-0.81	0.42	-	-	-
E7	-0.4	0.32	-	-	-

Table 7.3. Measured κ and λ values for Test Series E.

In Figure 7.12, values of λ_1 from horizontal samples have been plotted against the stress ratio η_1 alongside corresponding data from vertical samples from Test Series B and C. The value of λ_1 recorded in the isotropic first loading stage of Test E1 is almost identical to the mean value of λ_1 (0.34) obtained from the vertical samples. In triaxial compression, however, the values of λ_1 from the horizontal samples are significantly lower than those from the vertical samples. In Sections 6.3 and 6.4 it has been suggested the combination of large plastic shear strains combined with plastic volumetric strains, associated with high values of η, contribute to higher rates of destructuration than is observed under isotropic loading where volumetric strains are dominant. This in turn causes apparently higher values of λ, particularly during first loading. The fact in triaxial compression that λ_1 is lower for the horizontal samples suggests that the influence of plastic shear strains is less prevalent in horizontal samples than in vertical samples tested at the same stress ratio. In triaxial extension, there is the suggestion from Test E6 (η_1 = -0.81) that for higher values of η_1, the influence of destructuration is greater in horizontal samples than in vertical samples.

Figure 7.13 shows values of λ_2 from horizontal samples plotted against η_2 alongside corresponding data from vertical samples in Test Series B and C. For the three tests on horizontal samples presented, the apparent values of λ_2 are fairly similar to the equivalent values on vertical samples (allowing for the scatter amongst the data points discussed in Section 6.4.3).

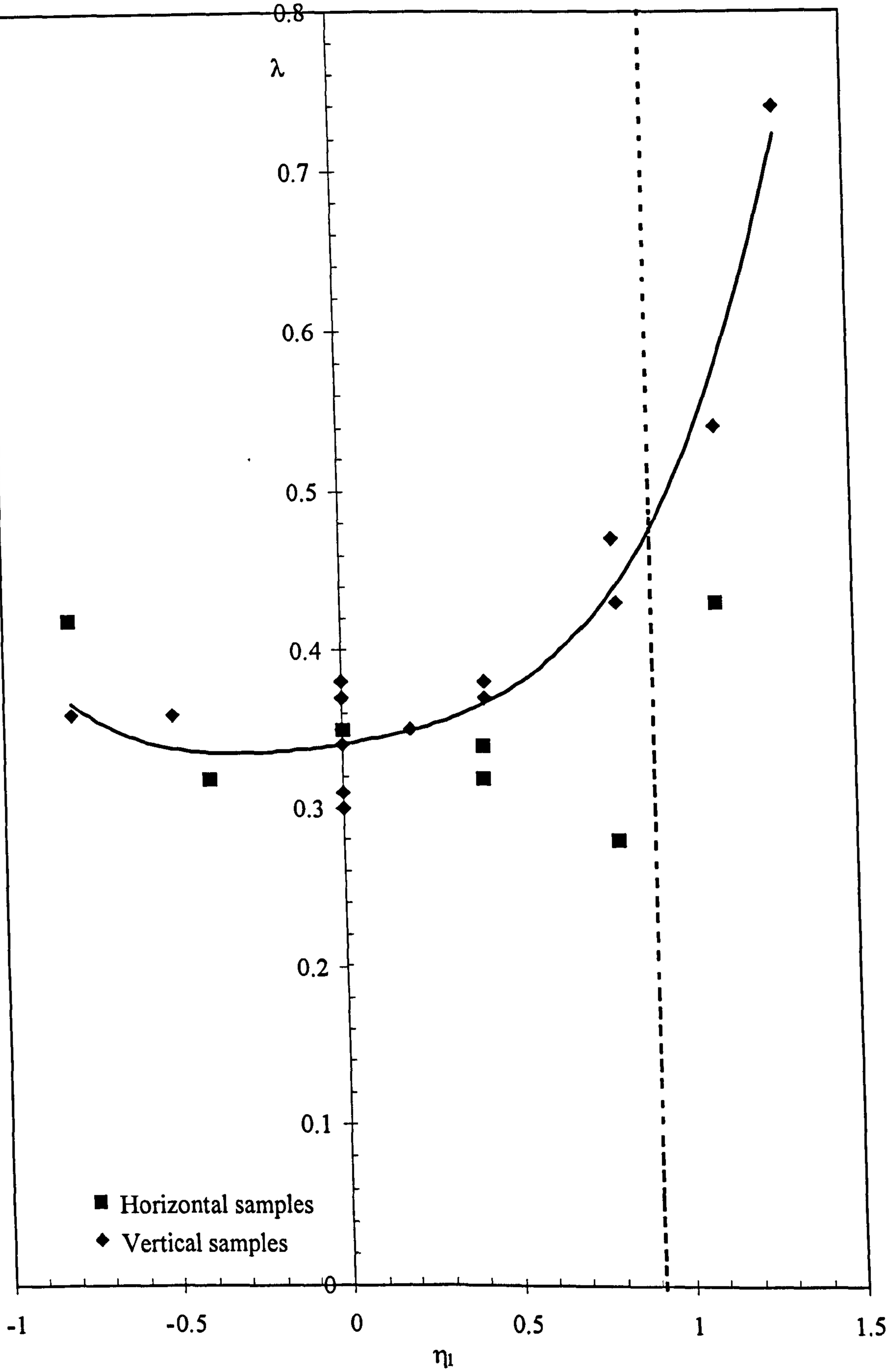

Figure 7.12. Post-yield compression gradients (λ_1) in first loading stages of horizontal and vertical samples.

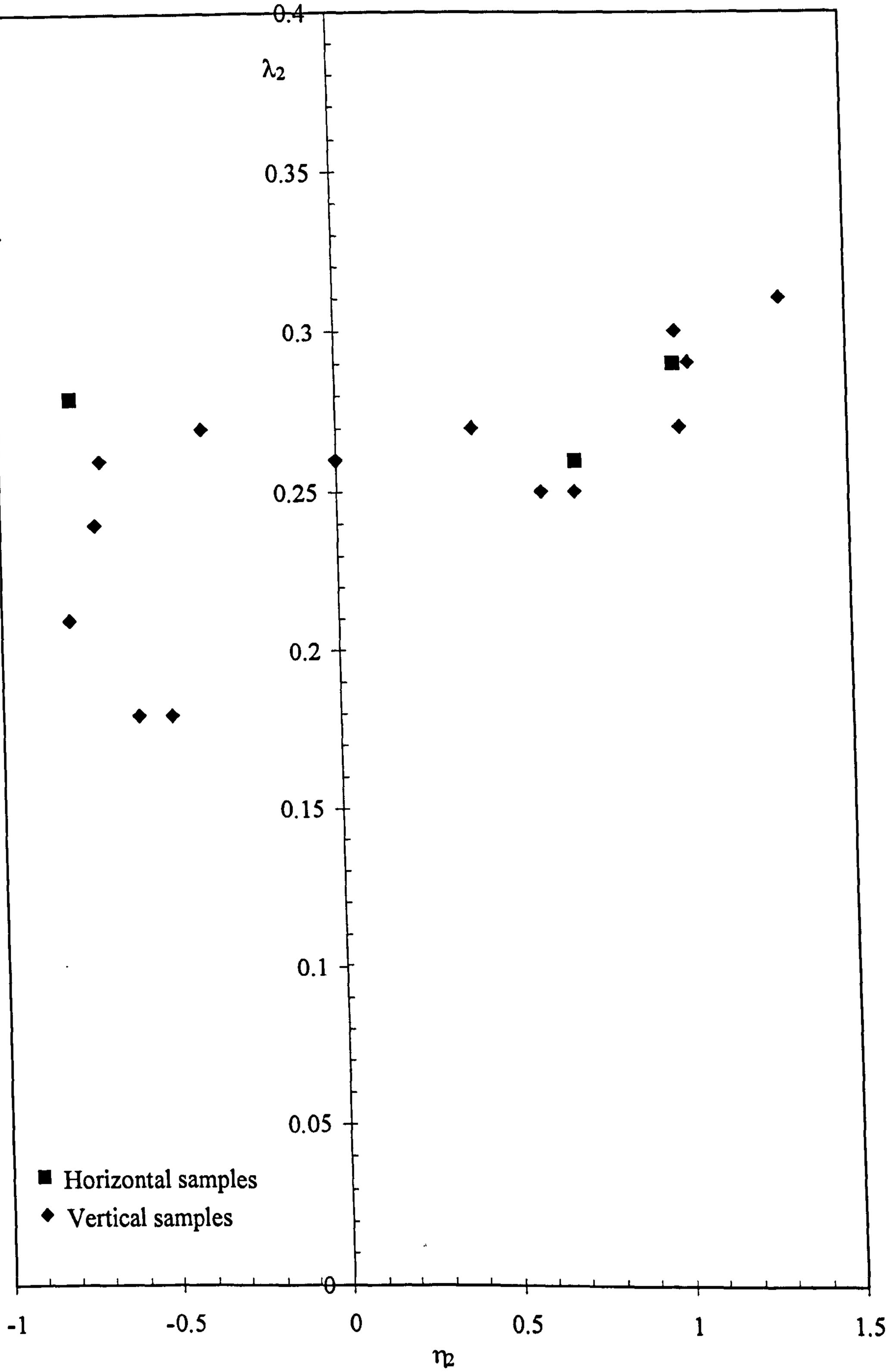

Figure 7.13. Post-yield compression gradients (λ_2) in second loading stages of horizontal and vertical samples.

7.3.4 Principal strain behaviour

Plots detailing the progress of the individual principal strain components for all tests in Series E are shown in Figures 7.14 – 7.20. In each of the tests on vertical samples in Series B and C, it was expected that, due to the one-dimensional stress history of the soil, the principal strain components in the two perpendicular radial directions would be identical (see Section 3.5.1). These samples were initially cross-anisotropic and remained so, due to the restrictions of the triaxial test. However, for the horizontally oriented samples it would be expected that each of the three principal strain increments would, in general, be unequal.

Test E1

The principal strain components for Test E1 ($\eta_1 = 0$, $\eta_2 = 0.75$) have been plotted against mean effective stress p' in Figure 7.14 and the yield points determined from the v: ln p' plot for the two loading stages are indicated. In the first loading stage the rate of straining in each of the three principal directions is different. In particular, the axial strain ε_y is significantly larger than both radial strains ε_x and ε_z. Differences in the strains corresponding to horizontal directions in the ground, ε_y and ε_z, would not be expected under isotropic loading because these strains correspond to the plane of isotropy within the soil. One possible explanation for this is that these strains have been measured quite differently - strain in the y-direction has been measured using the external axial strain gauge, whilst strain in the z-direction has been measured locally with the radial strain gauge. Another possibility is that the end restraints on the sample give rise to differences in measured strain.

Figure 7.14 also shows that during first loading stage of the test, there are differences in the radial strain responses of ε_x and ε_z. This would be expected due to the initially anisotropic fabric arrangement of the sample. Prior to the yield point in the first loading stage ($p'_{y1} = 76$ kPa) $\Delta\varepsilon_z$ is greater than $\Delta\varepsilon_x$ and this suggests that there is anisotropy of elastic behaviour. However, immediately after p'_{y1}, $\Delta\varepsilon_x$ is greater than $\Delta\varepsilon_z$ and by the end of the loading stage ε_x is greater than ε_z.

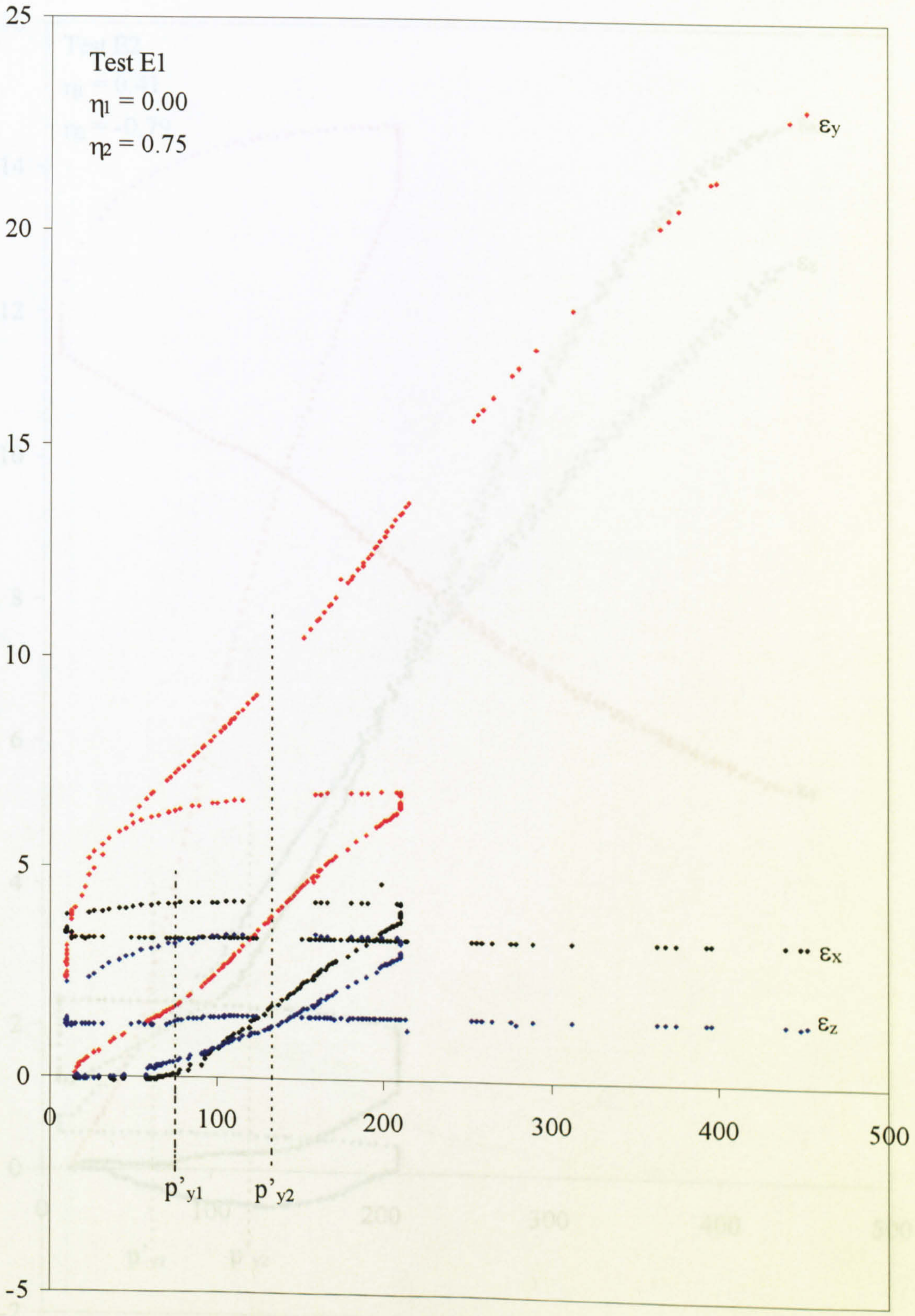

Figure 7.14. Principal strain behaviour in Test E1.

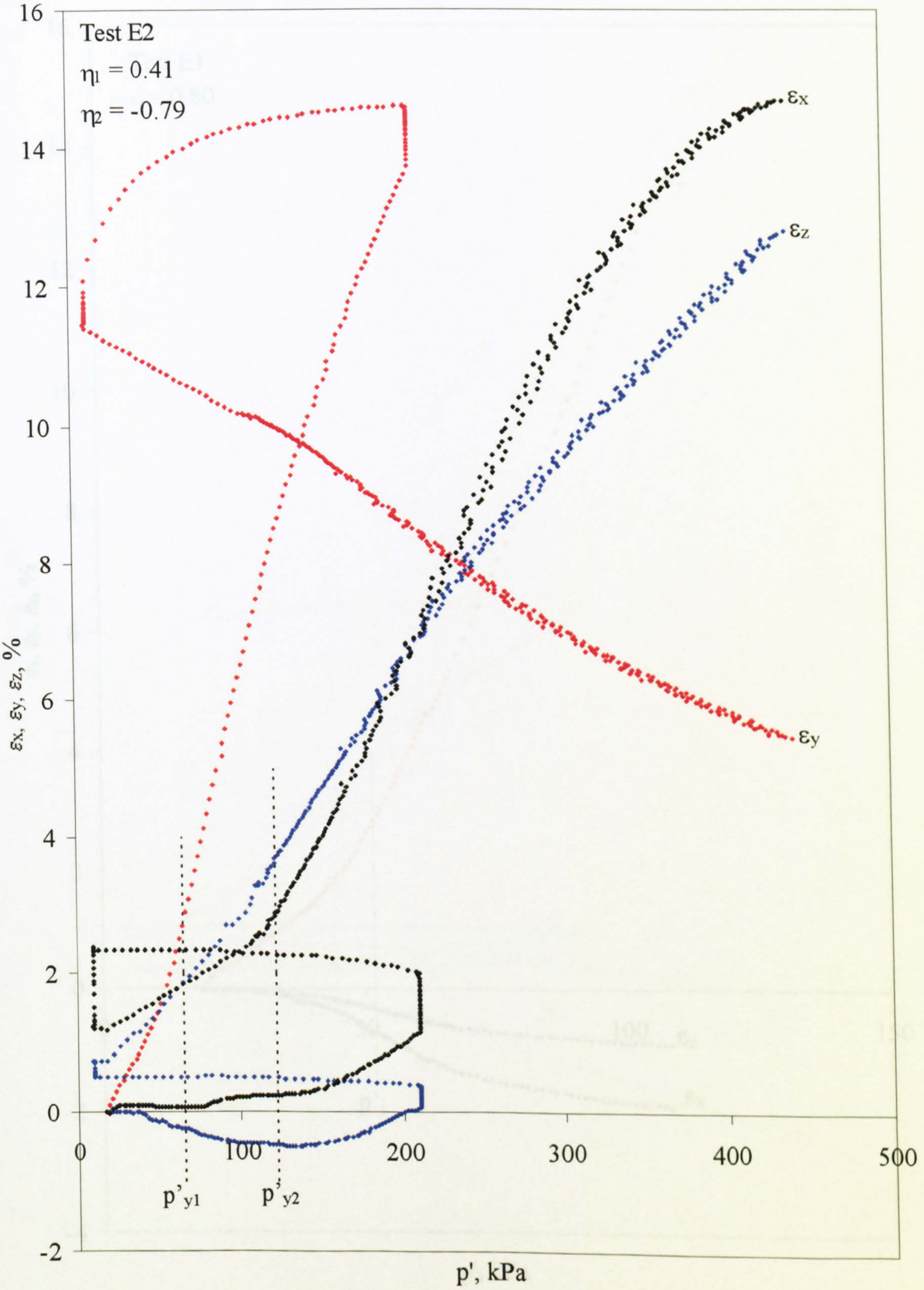

Figure 7.15. Principal strain behaviour in Test E2.

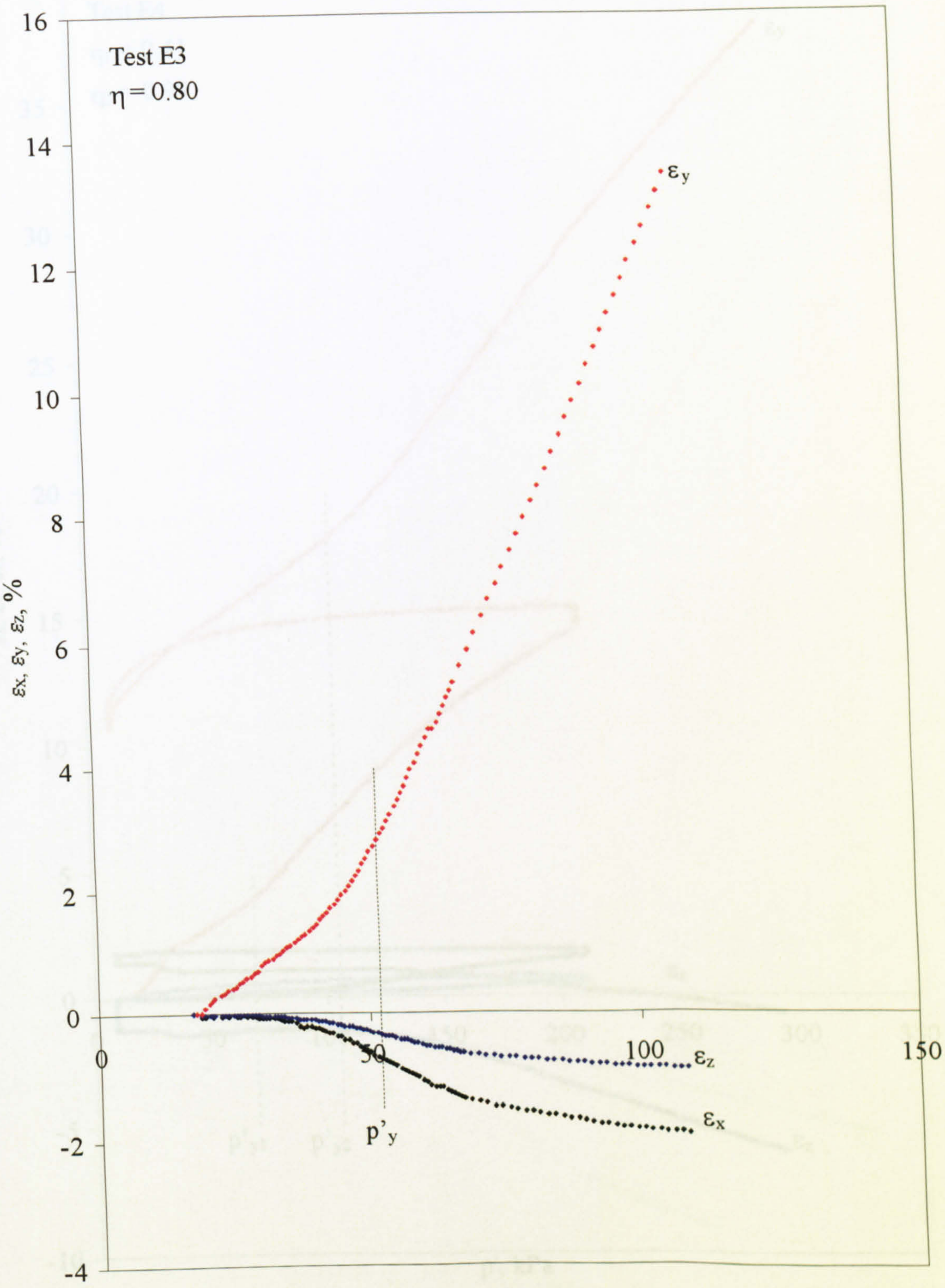

Figure 7.16. Principal strain behaviour in Test E3.

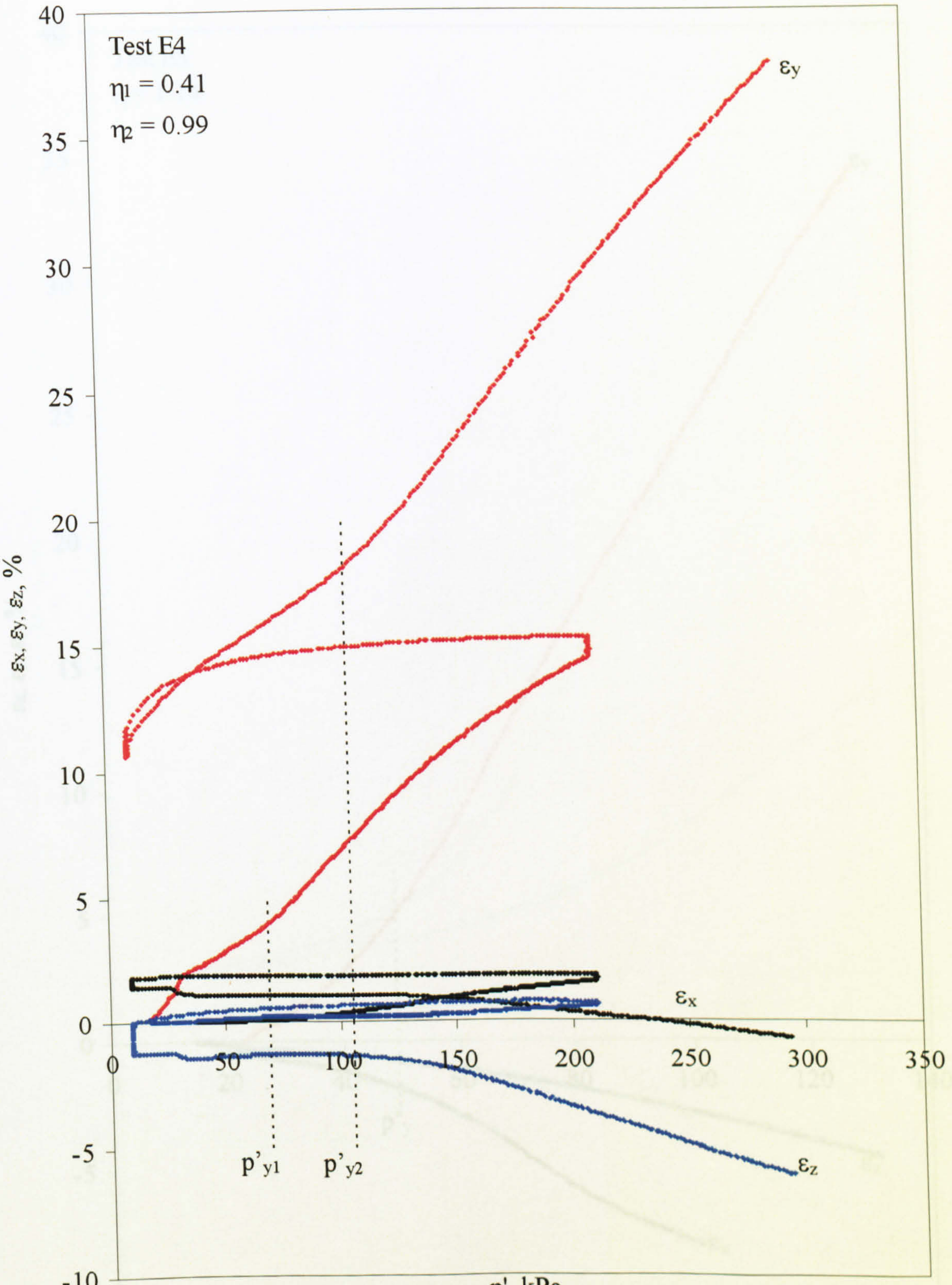

Figure 7.17. Principal strain behaviour in Test E4.

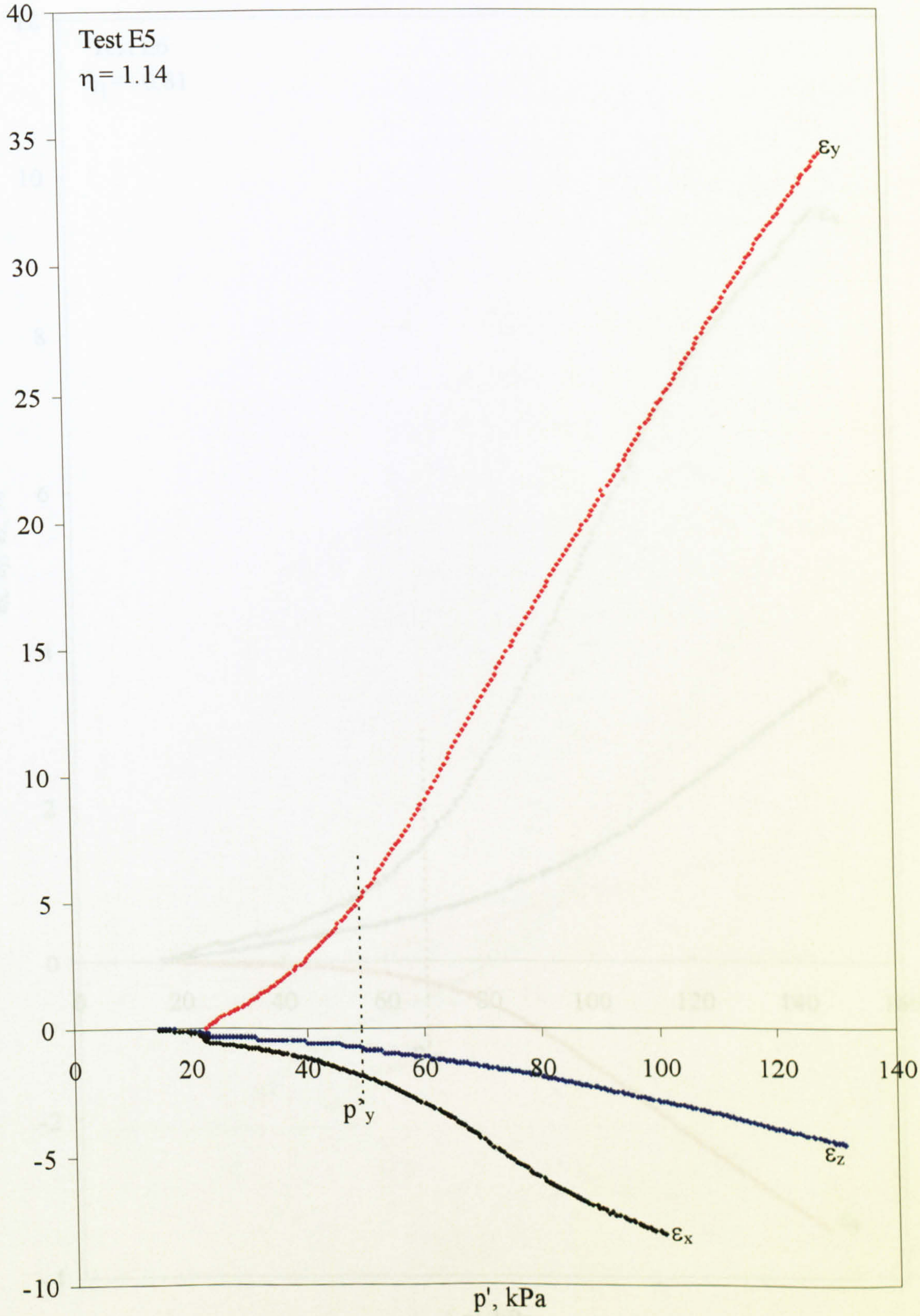

Figure 7.18. Principal strain behaviour in Test E5.

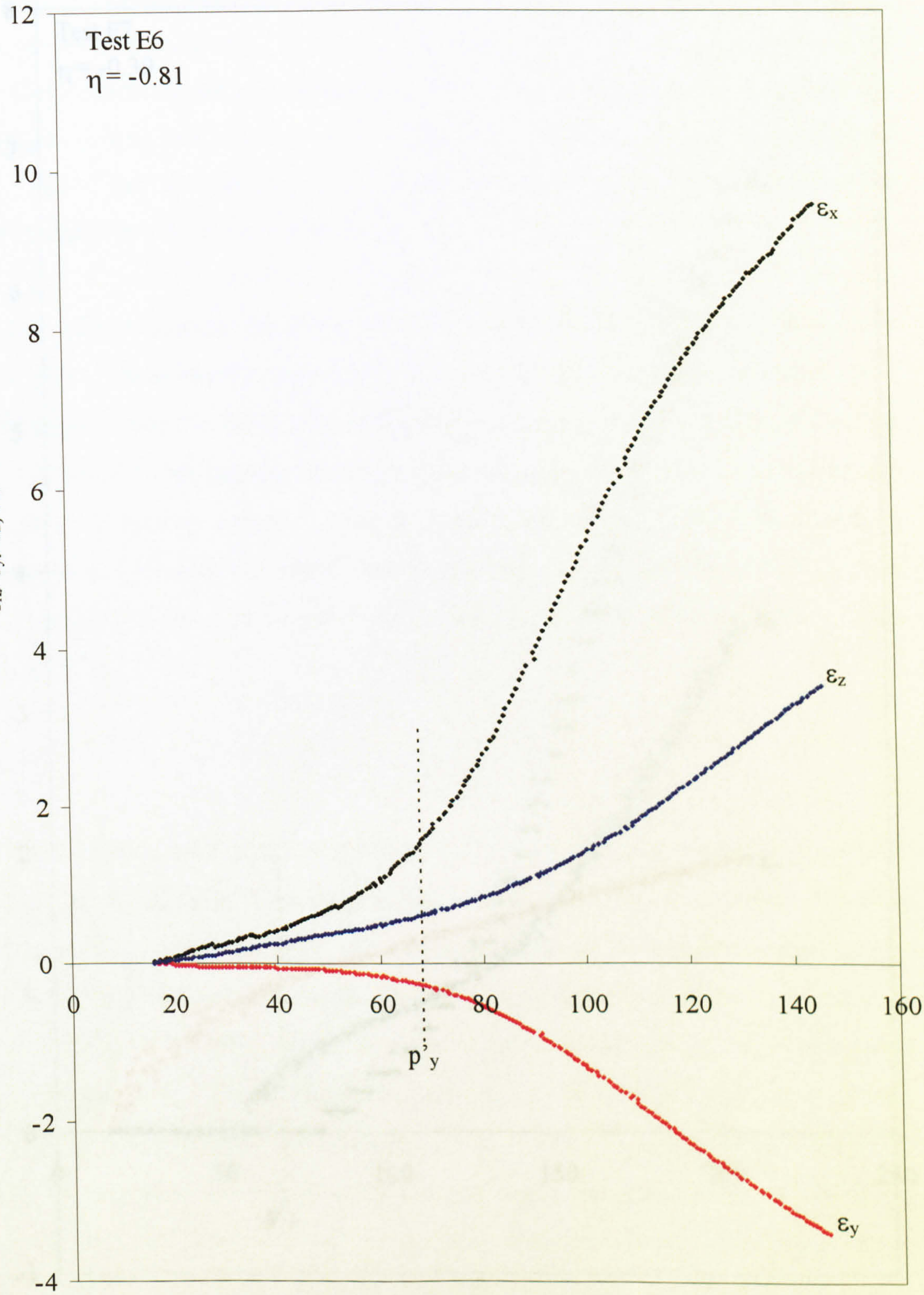

Figure 7.19. Principal strain behaviour in Test E6.

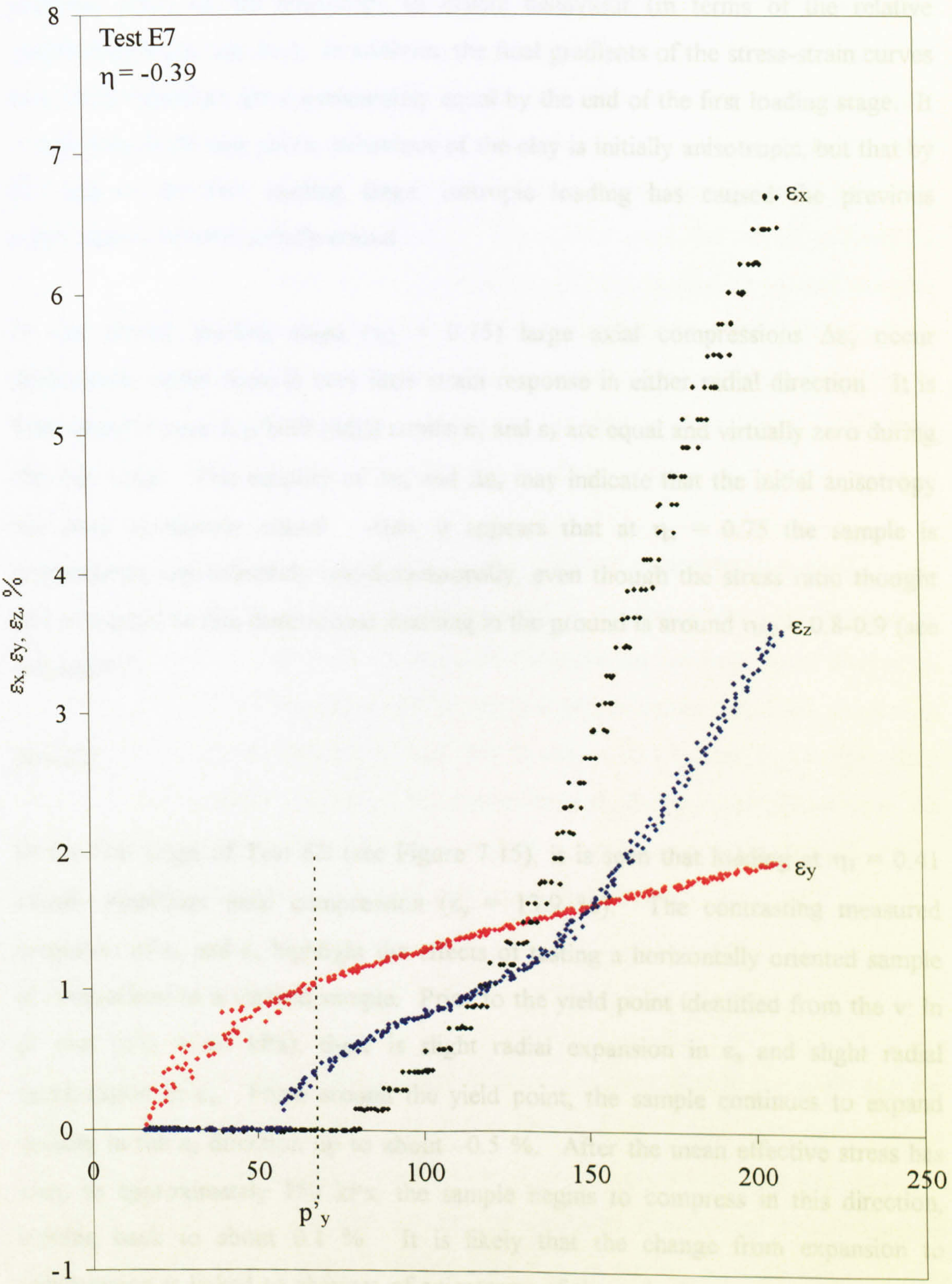

Figure 7.20. Principal strain behaviour in Test E7.

This suggests that, for this stress path, the anisotropy of plastic behaviour has the opposite effect to the anisotropy of elastic behaviour (in terms of the relative magnitudes of $\Delta\varepsilon_x$ and $\Delta\varepsilon_z$). In addition, the final gradients of the stress-strain curves in x and z directions are approximately equal by the end of the first loading stage. It is therefore likely that plastic behaviour of the clay is initially anisotropic, but that by the end of the first loading stage, isotropic loading has caused the previous anisotropy to be substantially erased.

In the second loading stage ($\eta_2 = 0.75$) large axial compressions $\Delta\varepsilon_y$ occur throughout, whilst there is very little strain response in either radial direction. It is interesting to note that both radial strains ε_x and ε_z are equal and virtually zero during this test stage. This equality of $\Delta\varepsilon_x$ and $\Delta\varepsilon_z$ may indicate that the initial anisotropy has been completely erased. Also, it appears that at $\eta_2 = 0.75$ the sample is compressing approximately one-dimensionally, even though the stress ratio thought to correspond to one-dimensional straining in the ground is around $\eta_{K0} = 0.8$-0.9 (see Section 6.2).

Test E2

In the first stage of Test E2 (see Figure 7.15), it is seen that loading at $\eta_1 = 0.41$ causes significant axial compression ($\varepsilon_y = 13.9$ %). The contrasting measured responses of ε_z and ε_x highlight the effects of testing a horizontally oriented sample in comparison to a vertical sample. Prior to the yield point identified from the v: ln p' plot ($p'_{y1} = 65$ kPa), there is slight radial expansion in ε_z and slight radial compression in ε_x. From around the yield point, the sample continues to expand radially in the ε_z direction up to about –0.5 %. After the mean effective stress has risen to approximately 150 kPa, the sample begins to compress in this direction, coming back to about 0.1 %. It is likely that the change from expansion to compression is linked to changes of anisotropy of the soil. In contrast, the strain ε_x indicates modest radial compression throughout this first loading stage and the rate at which this occurs increases noticeably from a mean effective stress of around 150 kPa. Furthermore, the rate of radial compression in both directions is similar by the end of the first loading stage, suggesting that the initial anisotropy between x and z

directions has been substantially erased. Due to the anisotropic stress state in this test stage, it would be expected that the sample would now be anisotropic, but with different properties in the y direction to the x and z directions. This is because the sample has been subjected to stress in the axial direction that was significantly different to those experienced in the two radial directions. It should also be noted that significant additional axial and radial strains occurred during the 24 hour rest period at the end of the first loading stage. This phenomenon also occurs in Tests E1 and E4, although to a lesser extent. As discussed in the context of vertical samples (see Section 6.4.4) it is possible that these additional strains are related to the effects of creep, although in the case of Test E2 the strains observed seem too large in comparison with the preceding strains during the first loading stage. This may, therefore, indicate that the rate of loading was too fast.

The second stage of Test E2 involved loading in triaxial extension at $\eta_2 = -0.79$. As would be expected for a highly negative value of η, this stress path resulted in significant extension in the axial direction and compression in both radial directions. The magnitudes of radial compression in the two perpendicular directions are similar in this stage: ε_z has risen from 0.7 % to 12.8 % ($\Delta\varepsilon_z$ = 12.1 %) and ε_x has risen from 1.2 % to 14.7 % ($\Delta\varepsilon_x$ = 13.5 %). The increasingly similarity in the behaviour in the two radial directions suggests that the sample is once again approximately cross-anisotropic, but now with the plane of isotropy in the x-z plane.

Test E3

Test E3 involved a single loading stage in triaxial compression at $\eta = 0.80$ and the principal stress-strain behaviour is shown in Figure 7.16. Large axial deformations occurred, while radial expansion took place. The yield point identified from the v: ln p' plot is marked at p' = 52 kPa, but the measurement of individual principal strains suggest that the yield is slightly earlier than this, at around p' = 35 kPa. At this point, the radial strain components progress at different rates with a greater rate of expansion in ε_x than in ε_z. This again emphasises the fact that the soil behaviour is different in these two directions. In contrast, in Tests E1 and E2, initial anisotropy was such that plastic straining immediately after yield in the x direction is more

positive than in the z direction. However, the opposite of this response was observed in Test E3, which involved a much higher positive stress ratio than in E1 or E2.

Test E4

The first stage in Test E4 was identical to that of Test E2 and the stress-strain behaviour is shown in Figure 7.17. Again, a large amount of axial compression was observed during this stage (14.9 %). There appeared to be no radial straining, ε_x, until around p' = 58 kPa, whereupon there was an apparently sudden jump to ε_x = 0.15 % (not visible in Figure 7.17, due to the scale employed). It is likely that there has been a measurement error here involving a stick and slip response in the device. The yield point was observed at p' = 69 kPa in the v: ln p' plot and the sample undergoes radial compression in the x direction from around this point until the end of the loading stage. As the mean effective stress is increased beyond yield, further moderate radial compression in the x direction is observed, the final magnitude being 1.6 %. The radial strain ε_z shows modest radial compression (0.7 %) and is comparable to the first stage in Test E2. Axial deformations in the first loading stage are consistent with the findings in Test E2 where the rate of straining is highest just after the yield point but is gradually slowing towards the end of the stage.

The second stage in Test E4 involved loading at a relatively high value of η in triaxial compression (η_2 = 0.99) under which one would expect large axial compression and expansion in both radial directions. Prior to yielding at p' = 105 kPa, the sample compressed in the axial direction and showed very little straining in both radial directions. However, after this yield point the sample began to expand in both radial directions. Figure 7.17 shows that the axial strain has increased to 37.9 % by the end of second loading. The radial strain ε_z indicates expansion of the sample to -6.1 %, but ε_x expands only to -0.7 %.

Test E5

Test E5 involved a single loading stage at η = 1.14 and the principal strain behaviour is shown in Figure 7.18. The extent of this stress probe was restricted by the large

axial strains occurring at this high stress ratio (see also Tests C2 and C3). Prior to the yield stress identified in the v: ln p' plot (p'_y = 49 kPa), the sample underwent slight expansion in both radial directions. After yield, this radial expansion increased, but at different rates in both directions. Radial strain ε_x increases more rapidly than ε_z until around a mean effective stress of 100 kPa where the magnitude of strain has reached around 8 %. Thereafter, the strain gauge had passed its limit of travel and the readings have become meaningless (and are therefore excluded from Figure 7.18). The progress of radial strain ε_z in Figure 7.18 represents slower radial expansion, but the rate of straining appears to be increasing up to and beyond p' = 110 kPa. This may suggest that the rate of straining in both radial directions was becoming equal and that the plane of isotropy was now coincident with the x-z plane. It is interesting to note that in Test E5, where the stress ratio was highest in this series, it was only possible to carry the test through to p' = 130 kPa. This was because the axial strain had reached 35% (approaching the limit of axial travel in the Bishop-Wesley cell) and the test had to be aborted. In Test C2 (first loading stage η_1 = 1.10) it was possible to load as far as p' = 198 kPa. The maximum stress reached in Test E5 is similar to that reached in Test C3 (η_1 = 1.30, see Table 6.3). If the critical state stress ratio M_{CH} for horizontal samples is lower than M_C = 1.40 for vertical samples, as suggested in Section 7.2, then a stress ratio of 1.12 will involve loading relatively closer to the critical state for horizontal samples than for a vertical sample. If so, the S-CLAY1 model would predict that the rate of post-yield axial straining during a stress-controlled test on a horizontal sample at η_1 = 1.12 would be greater than a corresponding test on a vertical sample. Test E5 therefore supports the suggestion that M_C is less than 1.40 when testing horizontal samples.

Test E6

This test comprised a single loading stage in triaxial extension at η = -0.81. As expected, the sample underwent significant axial extension and compression in both radial directions (see Figure 7.19). As was the case in Test E5, it is interesting to note the differences in straining in the two radial directions. The rate of compression in ε_z is relatively low up to the yield point identified in the v: ln p' plot (p'_y = 72 kPa), but noticeably increases as the stress path progresses further. In the other

radial direction, ε_x exhibits more rapid compression than ε_z both pre-yield and immediately post-yield, but as the loading continues the rate of compression decreases. This is again indicative of changing anisotropy, but the progress of ε_x and ε_z towards the end of the stress path shows that the two radial strain rates had not yet converged. This suggests that much higher stresses would be required to produce cross-anisotropy, again with the plane of isotropy in the x-z direction.

Test E7

In Test E7 (η = -0.39, see Figure 7.20), the sample compressed in all three principal directions throughout the test. In Figure 7.20, the data points are highly abnormal and this is thought be due to a fault in the equipment during this test. At the start of loading there was virtually no strain response in the x and z directions. Given the data in preceding tests, this is unlikely to be a true reflection of the soil behaviour. Corresponding data in the y direction shows radial compression, but the data points appear to be highly erratic. Therefore, the data in Figures 7.20 and 7.11 should be viewed with caution. Yield was observed in the v: ln p' plot at p' = 68 kPa and after yielding the rate of straining in ε_x was initially much more rapid than in ε_z. As the test progressed, the rate of ε_z increased as the rate of ε_x slightly decreased. The rate of axial straining was relatively low throughout the test and tended to decrease around the onset of yield. The principal strain behaviour in this test was qualitatively consistent with the first stage from Test E1. As expected, the axial compression in Test E7 is lower than in Test E1, but the radial compression (in both directions) is significantly higher than in E4.

7.3.5 Comparison of two methods of calculating volumetric strain

In each of the plots shown in Figures 7.5 - 7.11, volumetric strain has been calculated using data from the volume change unit. It is also possible to calculate volume changes using the individual strain components measured axially and radially. With the volume change unit, the natural volumetric strain ε_v is calculated from the nominal volumetric strain ε_{vn} as follows:

$$\varepsilon_v = -\ln(1-\varepsilon_{vn}) \qquad (7.1)(6.1\text{bis})$$

With the individual principal strain components, the increment of volumetric strain $\delta\varepsilon_{vpr}$ is calculated from

$$\delta\varepsilon_{vpr} = \delta\varepsilon_x + \delta\varepsilon_y + \delta\varepsilon_z \qquad (7.2)$$

where $\delta\varepsilon_x$, $\delta\varepsilon_y$, and $\delta\varepsilon_z$ are the increments of natural principal strains.

For each of the loading stages in Test Series E, the amount of volumetric strain calculated using both Equations 7.1 and 7.2 has been recorded. In Figure 7.21 this data had been expressed as a ratio plotted against the stress ratio η. Therefore for values of $\Delta\varepsilon_{vpr}/\Delta\varepsilon_v$ greater than unity, the volumetric strain calculated using Equation 7.2 is greater than the strain calculated in Equation 7.1. Figure 7.21 indicates that the volumetric strains derived in the two different ways are approximately equal, but there is a suggestion that $\Delta\varepsilon_{vpr}/\Delta\varepsilon_v$ is slightly greater than 1 at high positive values of η and slightly less than 1 for all other values of η. The fact that the radial strain is measured at the mid-height of the sample means that during radial expansion, the strain gauges tend to overestimate the amount of expansion because the sample is restrained at the top and bottom. Since expansive radial strains are negative, it would be expected that this would result in Equation 7.2 giving a lower estimate of volumetric strain than is actually occurring. For the same reason, where a sample compresses radially (negative or low positive values of η), the radial gauges will overestimate the amount of compressive straining in the radial direction. This would result in overestimation of the volumetric strain from Equation 7.2. However, the given the scatter in the data points, differences in the two methods of recording volumetric strain may not be statistically significant.

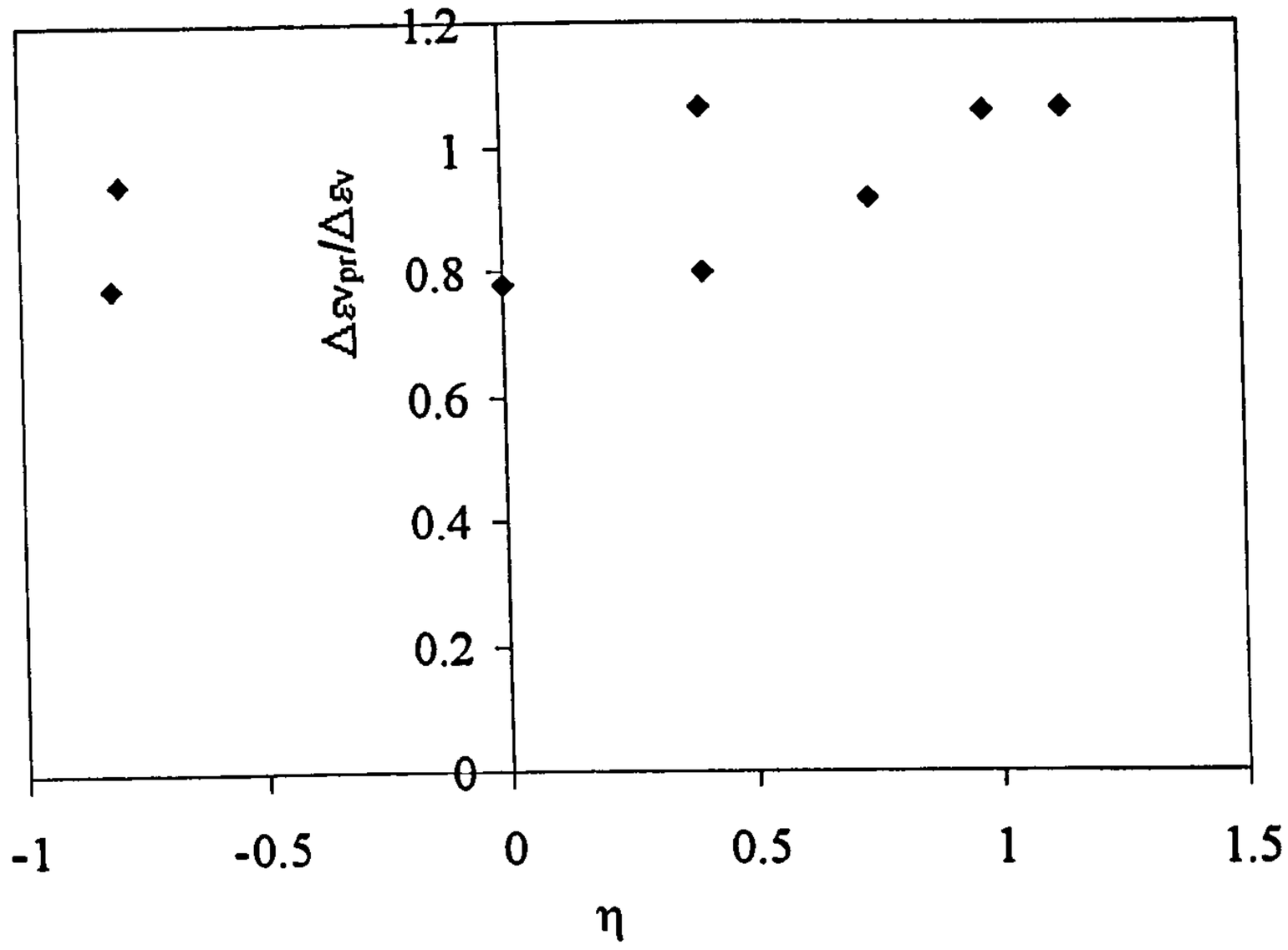

Figure 7.21. Comparison of volumetric strains measured locally ($\Delta\varepsilon_{vpr}$) and by volume change unit ($\Delta\varepsilon_v$).

7.4 Pre-yield behaviour

Muir Wood (1990) has shown general stress-strain equations for a cross-anisotropic elastic material, involving 5 independent elastic constants (E'_h, E'_v, ν'_{vh}, ν'_{hh} and G'_{vh}). For the particular case of a stress-state where one of the principal stresses is perpendicular to the plane of isotropy, such as a triaxial test on a vertical or horizontal sample, the elastic constant G'_{vh} is not involved. For a triaxial test on a horizontal sample the stress-strain relations are:

$$\begin{bmatrix} \delta\varepsilon_x \\ \delta\varepsilon_y \\ \delta\varepsilon_z \end{bmatrix} = \begin{bmatrix} \frac{1}{E'_v} & -\frac{\nu'_{vh}}{E'_v} & -\frac{\nu'_{vh}}{E'_v} \\ -\frac{\nu'_{vh}}{E'_v} & \frac{1}{E'_h} & -\frac{\nu'_{hh}}{E'_h} \\ -\frac{\nu'_{vh}}{E'_v} & -\frac{\nu'_{hh}}{E'_h} & \frac{1}{E'_h} \end{bmatrix} \begin{bmatrix} \delta\sigma'_x \\ \delta\sigma'_y \\ \delta\sigma'_z \end{bmatrix} \qquad (7.3)$$

in which E'_v and E'_h are equivalent values of Young's Modulus in the vertical and horizontal directions in the ground respectively and ν'_{vh} and ν'_{hh} are modified values of Poisson's ratio, for the particular case of a cross-anisotropic material. It should be

noted that in Equation 7.3 the x direction corresponds to the vertical direction in the ground, which in this case is a radial direction in the triaxial test (so that $\delta\sigma'_x = \delta\sigma'_z$). Further inspection of Equation 7.3 shows that in general

$$\delta\varepsilon_x \neq \delta\varepsilon_z \tag{7.4}$$

and in principle all 4 elastic constants can be obtained if tests following different stress paths are applied and the three principal strains are measured. If we note that

$$\delta\sigma'_y = \delta p' + \frac{2}{3}\delta q \tag{7.5}$$

and

$$\delta\sigma'_x = \delta\sigma'_z = \delta p' - \frac{\delta q}{3} \tag{7.6}$$

then inserting Equations 7.5 and 7.6 into Equation 7.3 the following can be obtained for constant η stress path tests (where $\delta q/\delta p' = \eta$)

$$\frac{\delta\varepsilon_x}{\delta p'} = \frac{1-2\nu'_{vh}}{E'_v} - \frac{1}{3}\frac{(1+\nu'_{vh})}{E'_v}\eta \tag{7.7}$$

$$\frac{\delta\varepsilon_z}{\delta p'} = \left(-\frac{\nu'_{vh}}{E'_v} + \frac{1-\nu'_{hh}}{E'_h}\right) - \frac{1}{3}\left(-\frac{\nu'_{vh}}{E'_v} + \frac{(1+2\nu'_{hh})}{E'_h}\right)\eta \tag{7.8}$$

A similar equation could be derived for $\delta\varepsilon_y/\delta p'$, but only 2 equations are necessary to recover the 4 elastic constants providing at least two different stress paths have been followed. In Equations 7.7 and 7.8 it is preferable to use $\delta\varepsilon_x$ and $\delta\varepsilon_z$ as these are both measured in the same manner (using radial strain devices), whereas $\delta\varepsilon_y$ is measured in a different fashion.

Figure 7.22 shows data points relating to the pre-yield sections of the first loading stages in Test Series E. Each data point in Figure 7.22 is taken from the average gradient of the appropriate stress-strain curve in Figures 7.14-7.19 (either ε_x: p' or ε_z: p') from the start of the first loading stage up to yield point identified from the v: ln

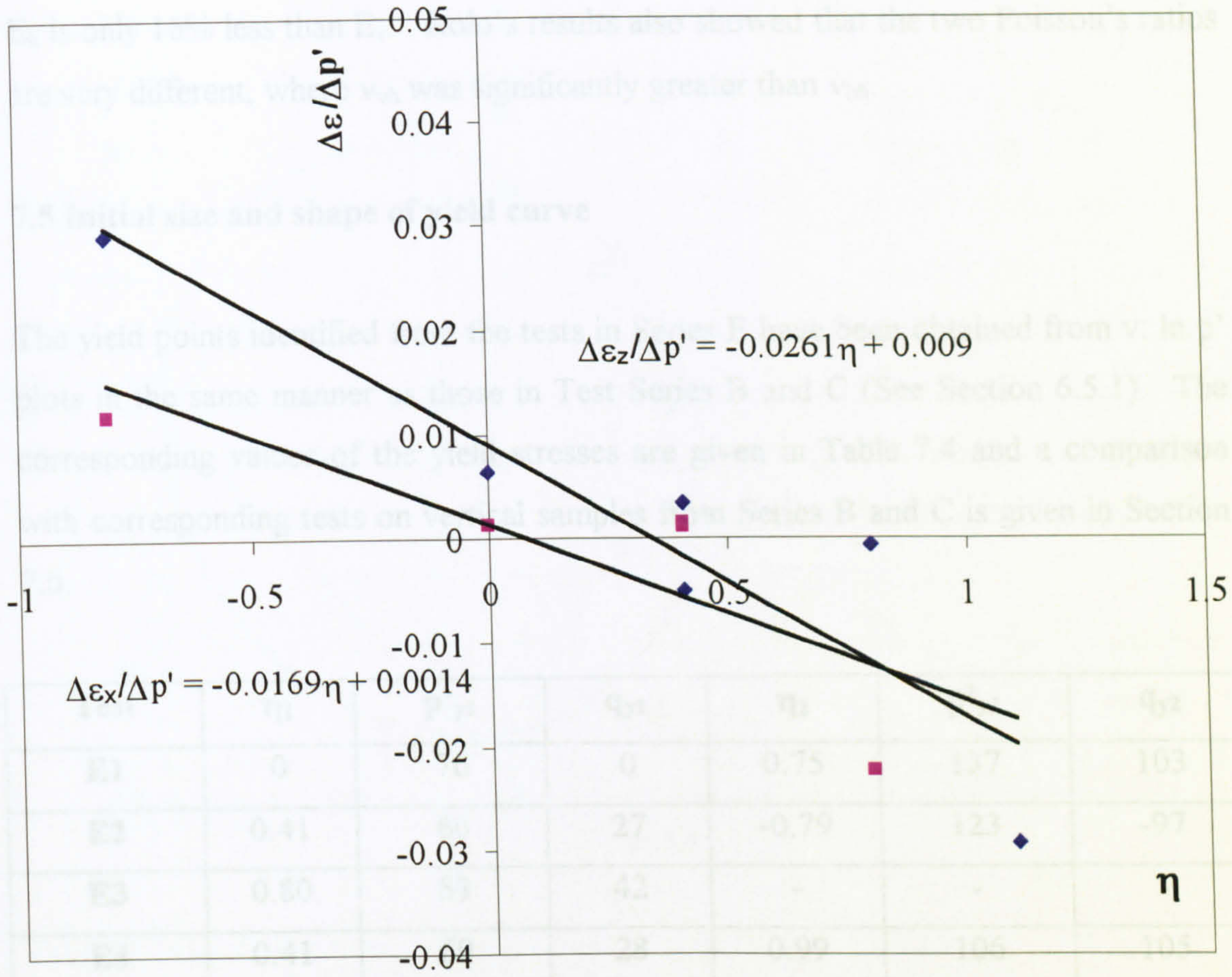

Figure 7.22. Pre-yield elastic radial straining in Test Series E.

p' plot. Note that Test E7 has been omitted due to uncertainty over the validity of the pre-yield data (see Figure 7.20). As expected, increasingly positive values of η result in greater amounts of radial expansion. For each of the two radial directions, a best-fit line has been applied. From the gradients and vertical-axis intercepts of these lines, the four elastic constants can be deduced using Equations 7.7 and 7.8. Results suggest that E_v = 2.9 MPa and E_h = 1.4 MPa. Thus the stiffness in the vertical direction is approximately twice the stiffness in the horizontal direction. The value of E_v is comparable with results from Tests Series B and C where E_v was estimated from measurements of axial stress-strain. The values of E_v measured on the vertical samples were typically around 3MPa. The resulting Poisson's ratios are ν_{vh} = 0.48 and ν_{hh} = 0.15. These results confirm that the elastic behaviour of Bothkennar clay is highly anisotropic. Rolo (2003) conducted triaxial tests on Bothkennar clay (at a depth of 6m) using bender elements to measure soil stiffnesses. His results suggested that the vertical stiffness was greater than the horizontal stiffness, although

E_h is only 16% less than E_v. Rolo's results also showed that the two Poisson's ratios are very different, where ν_{vh} was significantly greater than ν_{hh}.

7.5 Initial size and shape of yield curve

The yield points identified from the tests in Series E have been obtained from v: ln p' plots in the same manner as those in Test Series B and C (See Section 6.5.1). The corresponding values of the yield stresses are given in Table 7.4 and a comparison with corresponding tests on vertical samples from Series B and C is given in Section 7.6.

Test	η_1	p'_{y1}	q_{y1}	η_2	p'_{y2}	q_{y2}
E1	0	76	0	0.75	137	103
E2	0.41	66	27	-0.79	123	-97
E3	0.80	53	42	-	-	-
E4	0.41	69	28	0.99	106	105
E5	1.14	52	59	-	-	-
E6	-0.81	73	-59	-	-	-
E7	-0.39	67	26	-	-	-

Table 7.4. Yield stresses from v: ln p' plots for horizontal samples.

It was shown in Section 3.5 that the section of the S-CLAY1 yield surface that can be examined during testing of a cross-anisotropic horizontal sample is defined as

$$f=\left(q+\frac{\alpha p'}{2}\right)^2-\left(M^2-\frac{\alpha^2}{4}\right)\left(\frac{\left(M^2-\alpha^2\right)}{\left(M^2-\frac{\alpha^2}{4}\right)}p'_m-p'\right)p'=0 \qquad (7.9)$$

Equation 7.9 represents a section of the same yield surface that was already examined (in a different section) in the tests on vertical samples (see Section 6.5). The size p'_m and inclination parameter α are therefore defined by the best-fit

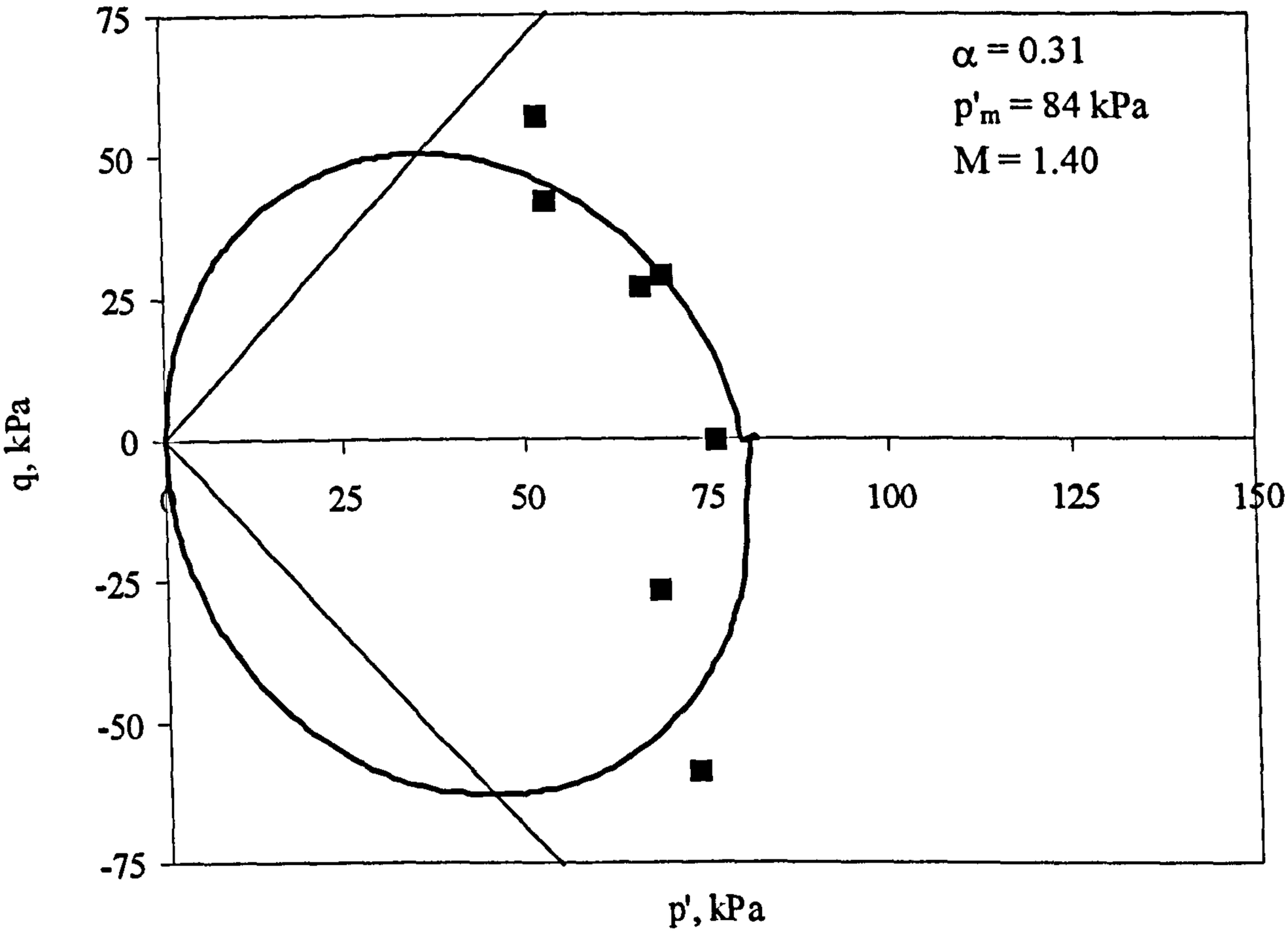

(a)

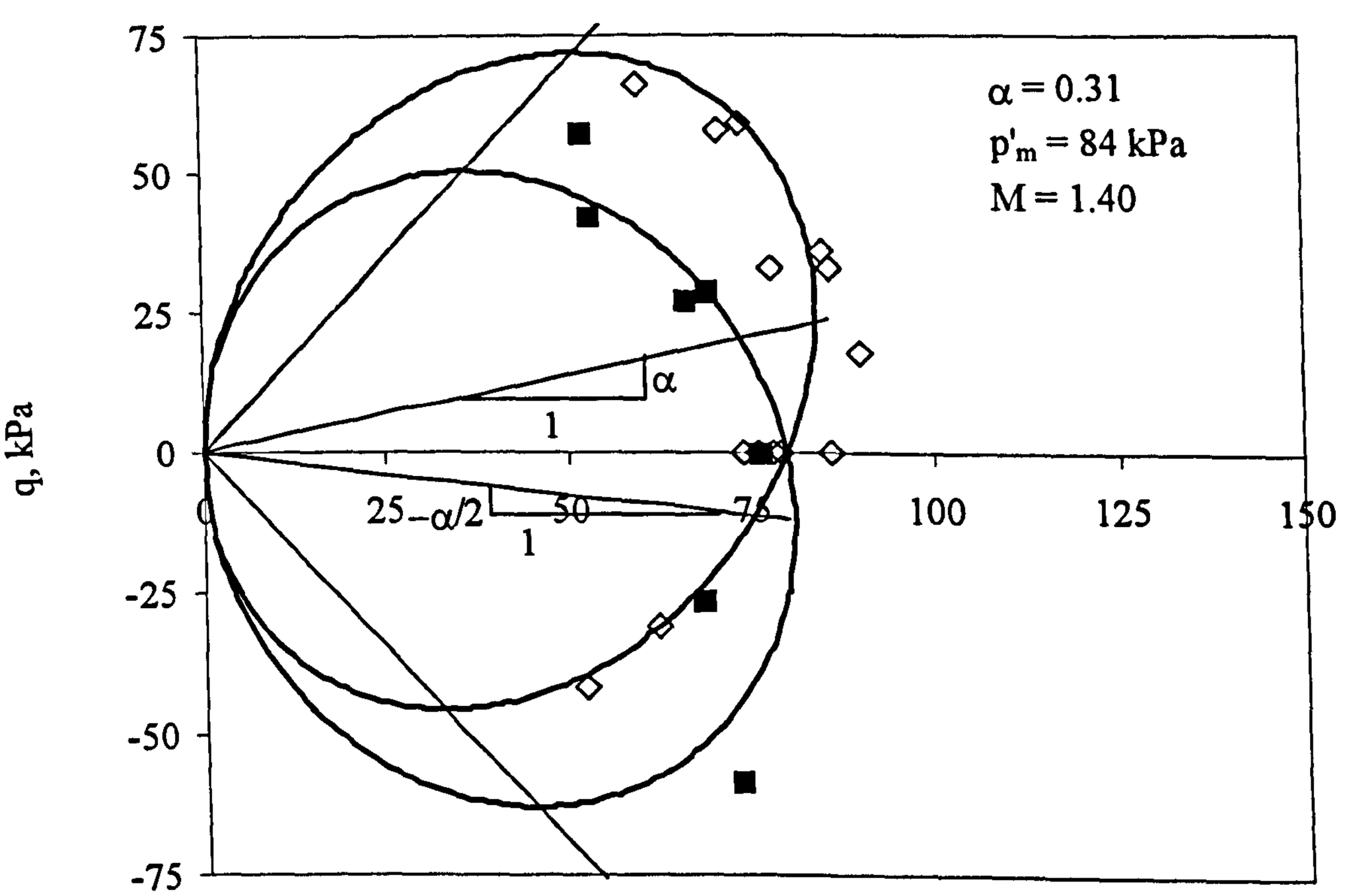

(b)

Figure 7.23. S-CLAY1 yield curves; (a) horizontal samples, (b) horizontal and vertical samples.

parameters obtained in Section 6.5. Thus the values $\alpha = 0.31$ and $p'_m = 85$ kPa are retained (where M = 1.40 for the entire yield curve).

The experimental yield points along with the S-CLAY1 yield curve predicted by Equation 7.9 are shown in q: p' space in Figure 7.23 (a). In this instance, a value M= 1.40 has been applied to the entire curve. From Equation 7.9, the curve shown in Figure 7.23 (a) has an orientation of $-\alpha/2$ (= -0.155). It is apparent that the proposed section of the yield surface is a reasonable match to the data, although the majority of the points lie slightly inside the curve. For comparison, the S-CLAY1 yield surface sections for both horizontal and vertical samples have been plotted in Figure 7.23 (b), along with the identified yield points. The yield points for horizontal samples are shown as square data points and the yield points for vertical samples as diamonds. Both yield curves are shown with M= 1.40 for the entire yield curve. Figure 7.23 (b) emphasises the fact that in triaxial compression, the yield stresses are significantly lower for the horizontal samples than for the vertical samples, but in triaxial extension the yield stresses are higher for the horizontal samples.

7.6 Comparison of vertical and horizontal samples

7.6.1 Axial and volumetric stress-strain behaviour

Figures 7.24 – 7.29 show volumetric strain plotted against the log of mean effective stress and axial strain plotted against the mean effective stress for each of the tests on horizontal samples in Test Series E. In each plot, data from the corresponding test on a vertical sample Series B or C is also shown for comparison. Data from the horizontal samples is shown in red and data from the vertical samples is shown in black.

It has been established that the samples tested in Series B, C and E have an initial anisotropy, both in terms of elastic and plastic behaviour. It would therefore be expected that when comparing horizontal and vertical samples tested at the same stress ratios, a number of important features would be observed. If elastic behaviour is anisotropic, then the measured pre-yield axial strain should be different between

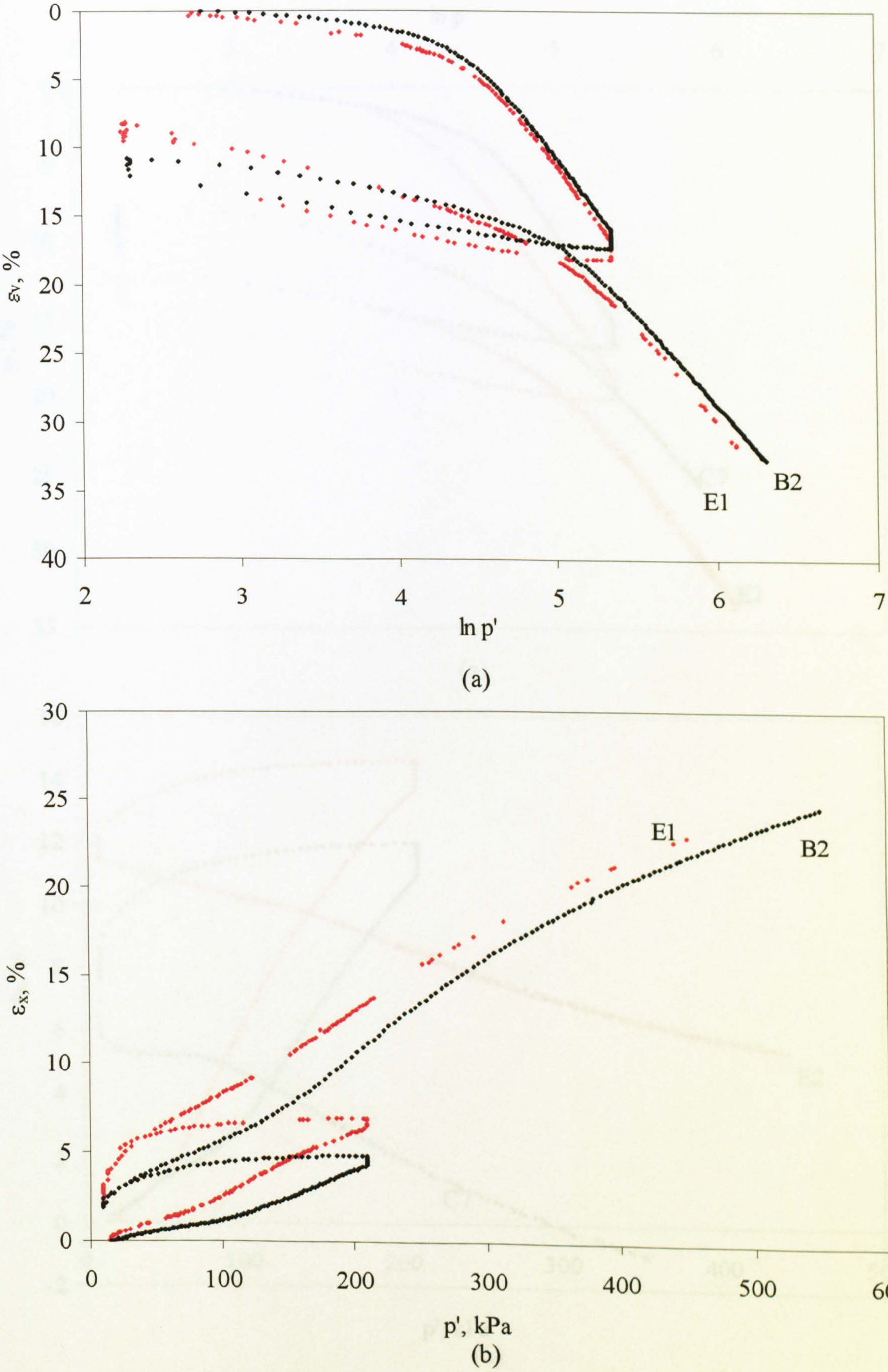

Figure 7.24. Tests E1 ($\eta_1 = 0$, $\eta_2 = 0.70$) and B2 ($\eta_1 = 0$, $\eta_2 = 0.75$); (a) compression behaviour, (b) axial behaviour.

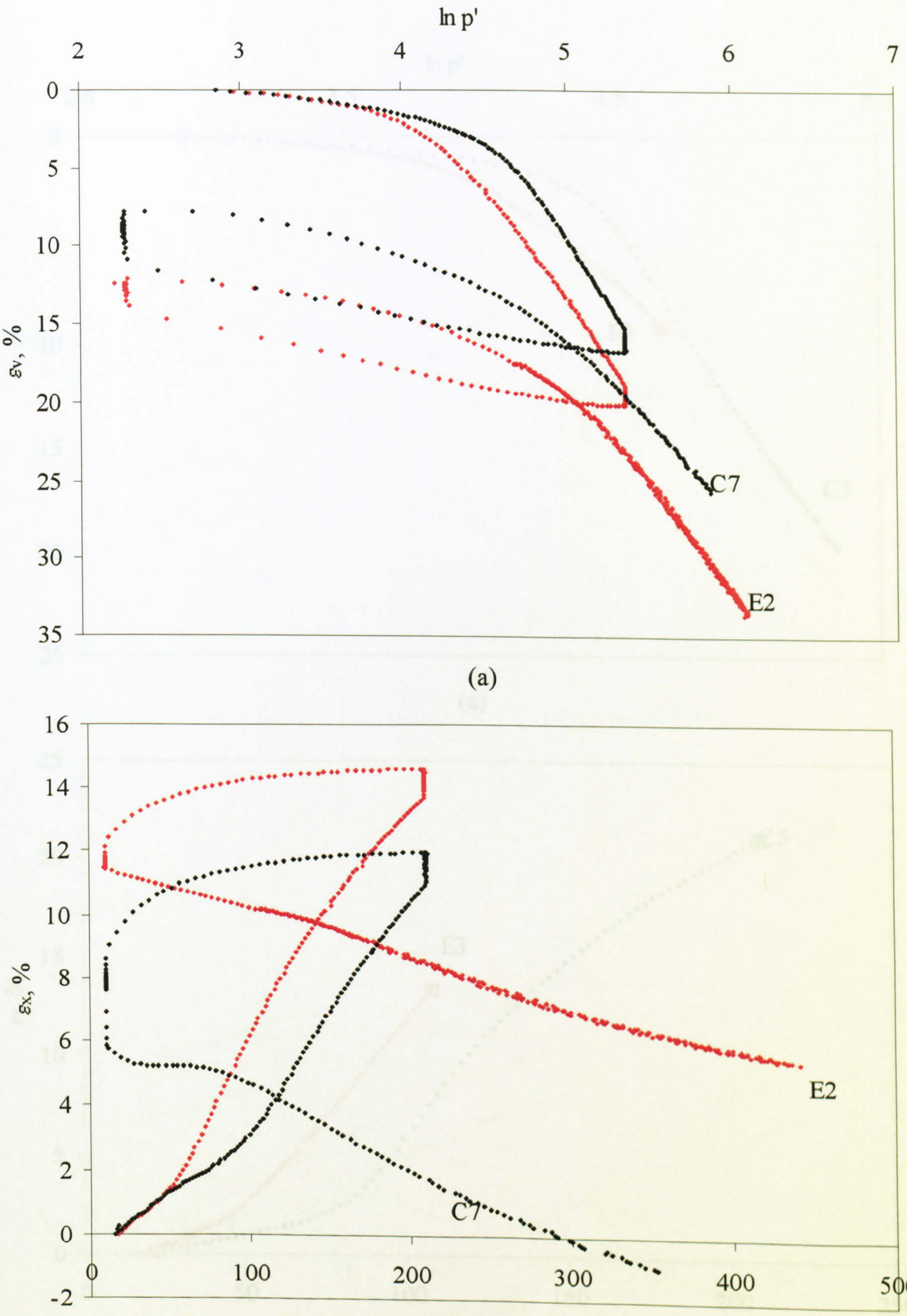

Figure 7.25. Tests E2 ($\eta_1 = 0.42$, $\eta_2 = -0.79$) and C7 ($\eta_1 = 0.41$, $\eta_2 = -0.79$); (a) compression behaviour, (b) axial behaviour.

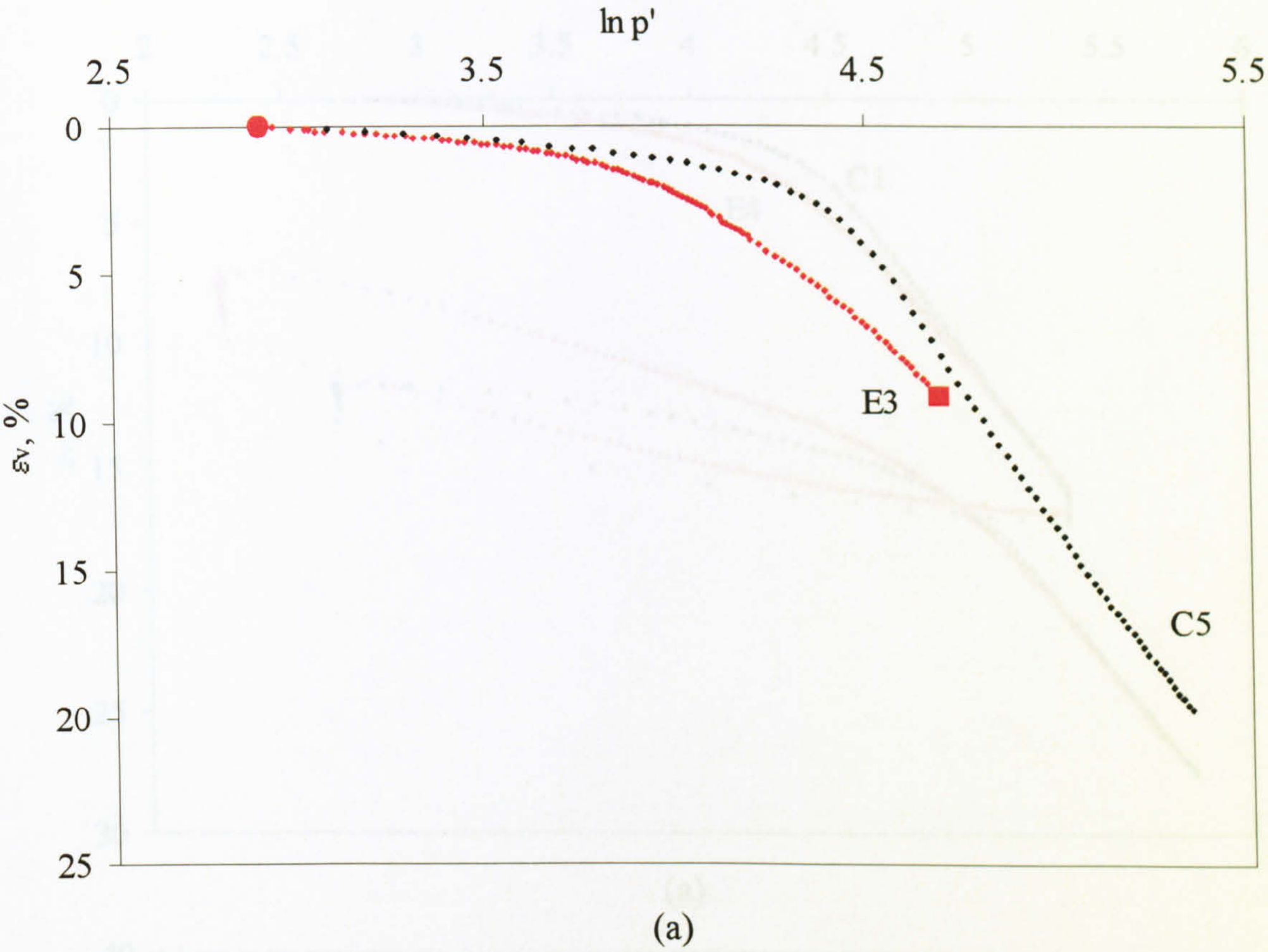

Figure 7.26. Tests E3 ($\eta_1 = 0.42$) and C5 ($\eta_1 = 0.80$); (a) compression behaviour, (b) axial behaviour.

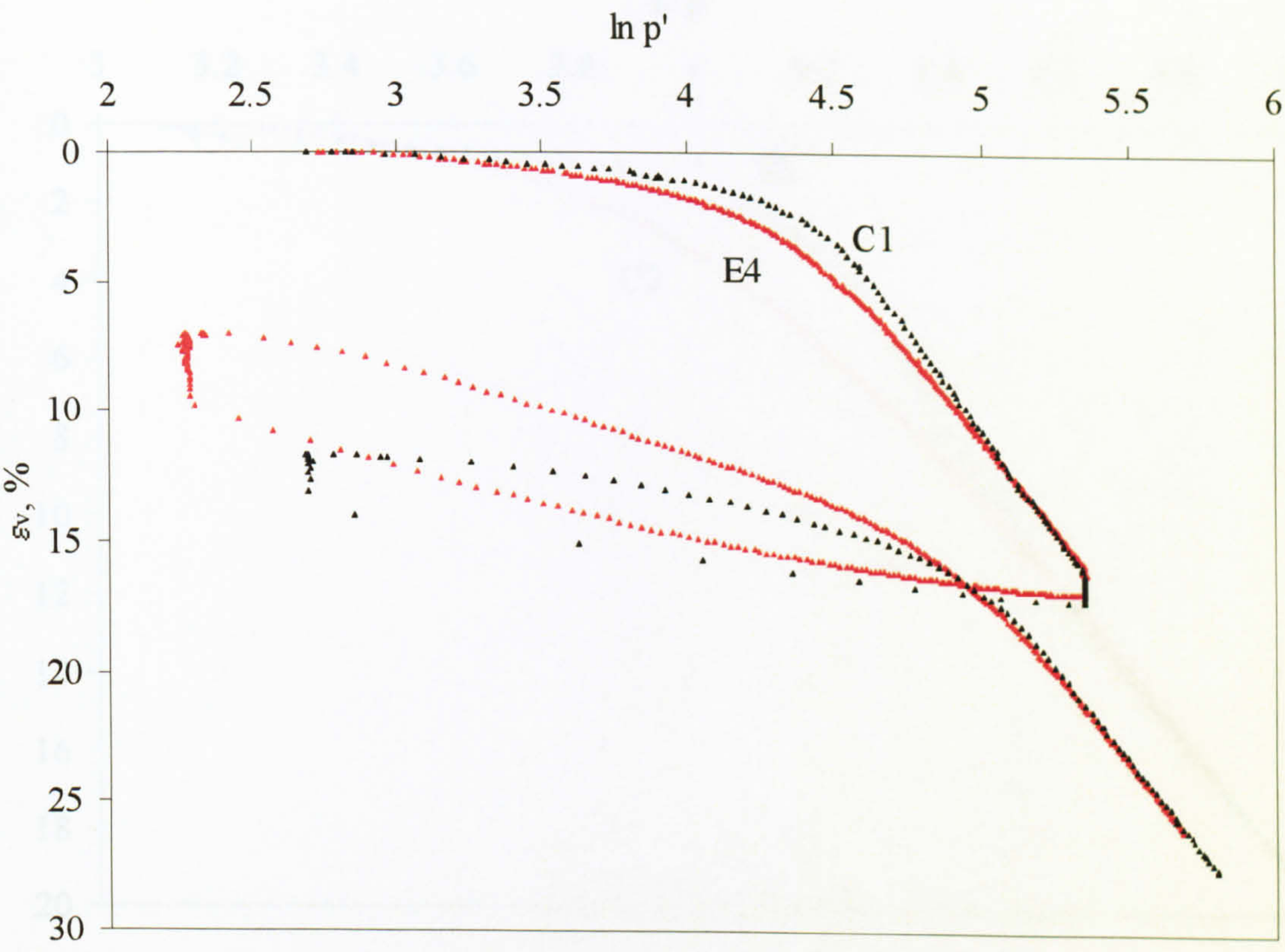

(a)

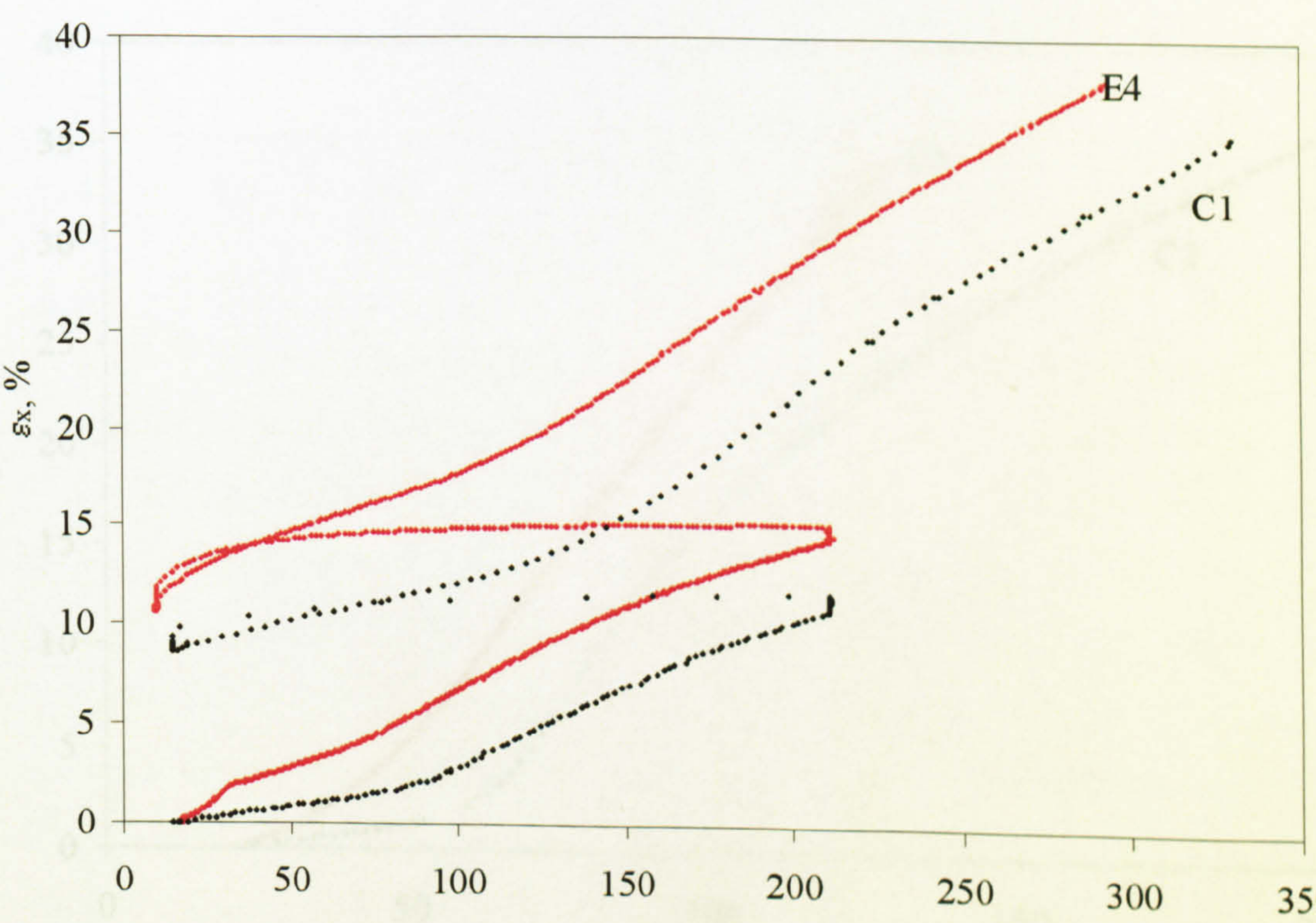

(b)

Figure 7.27. Tests E4 ($\eta_1 = 0.41$, $\eta_2 = 1.00$) and C1 ($\eta_1 = 0.42$, $\eta_2 = 1.03$); (a) compression behaviour, (b) axial behaviour.

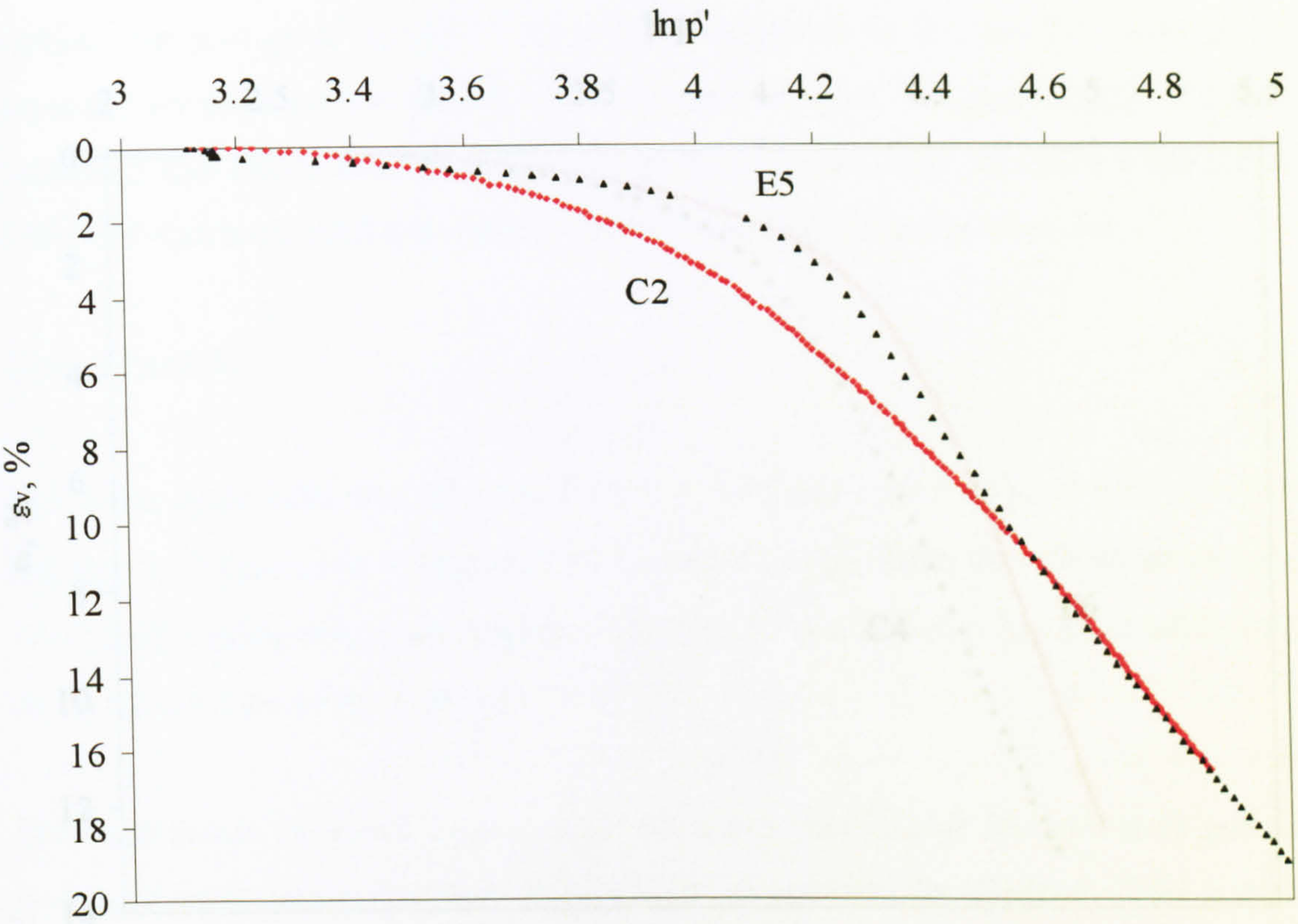

(a)

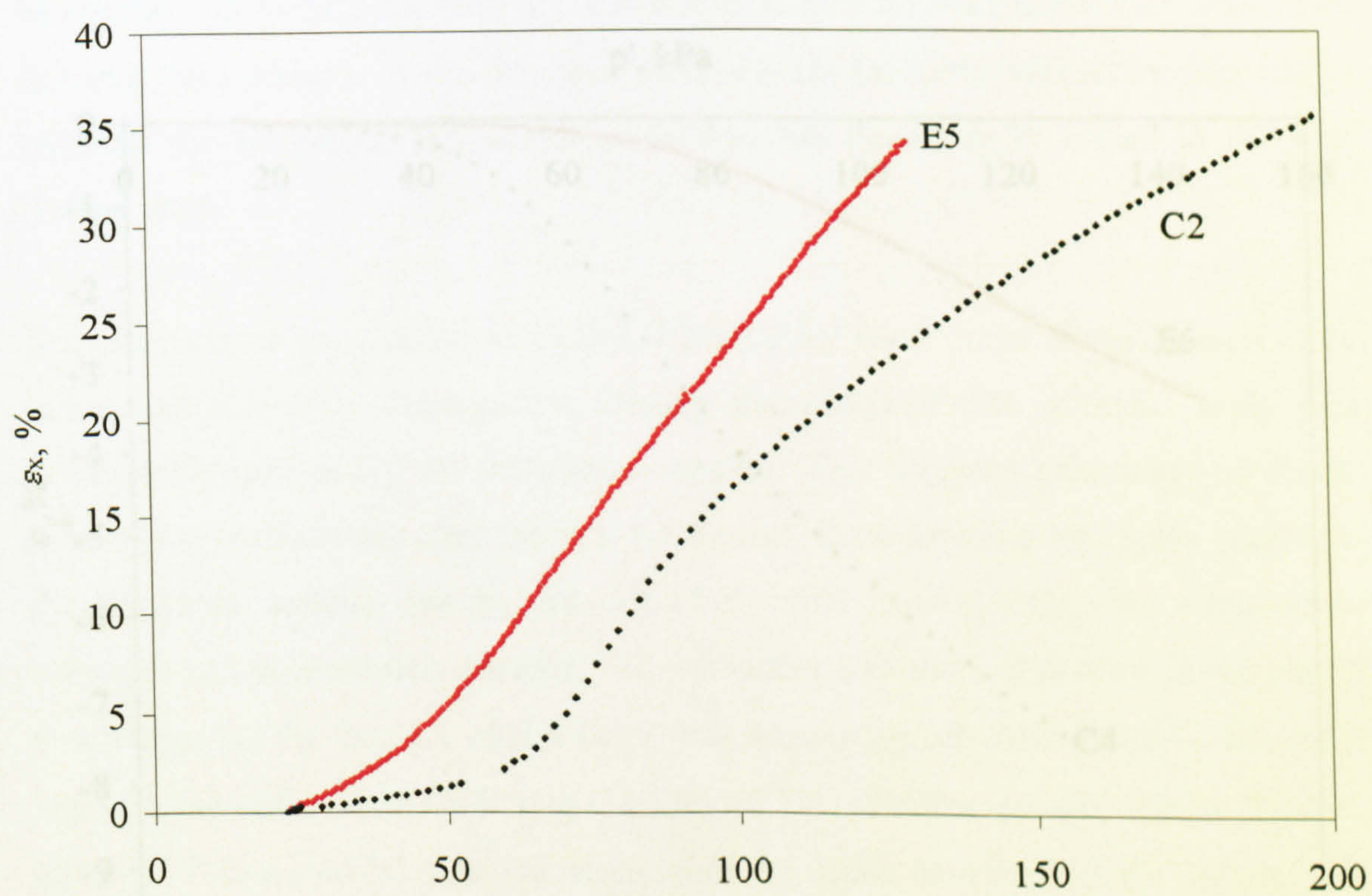

(b)

Figure 7.28. Tests E5 ($\eta = 1.14$) and C2 ($\eta = 1.10$); (a) compression behaviour, (b) axial behaviour.

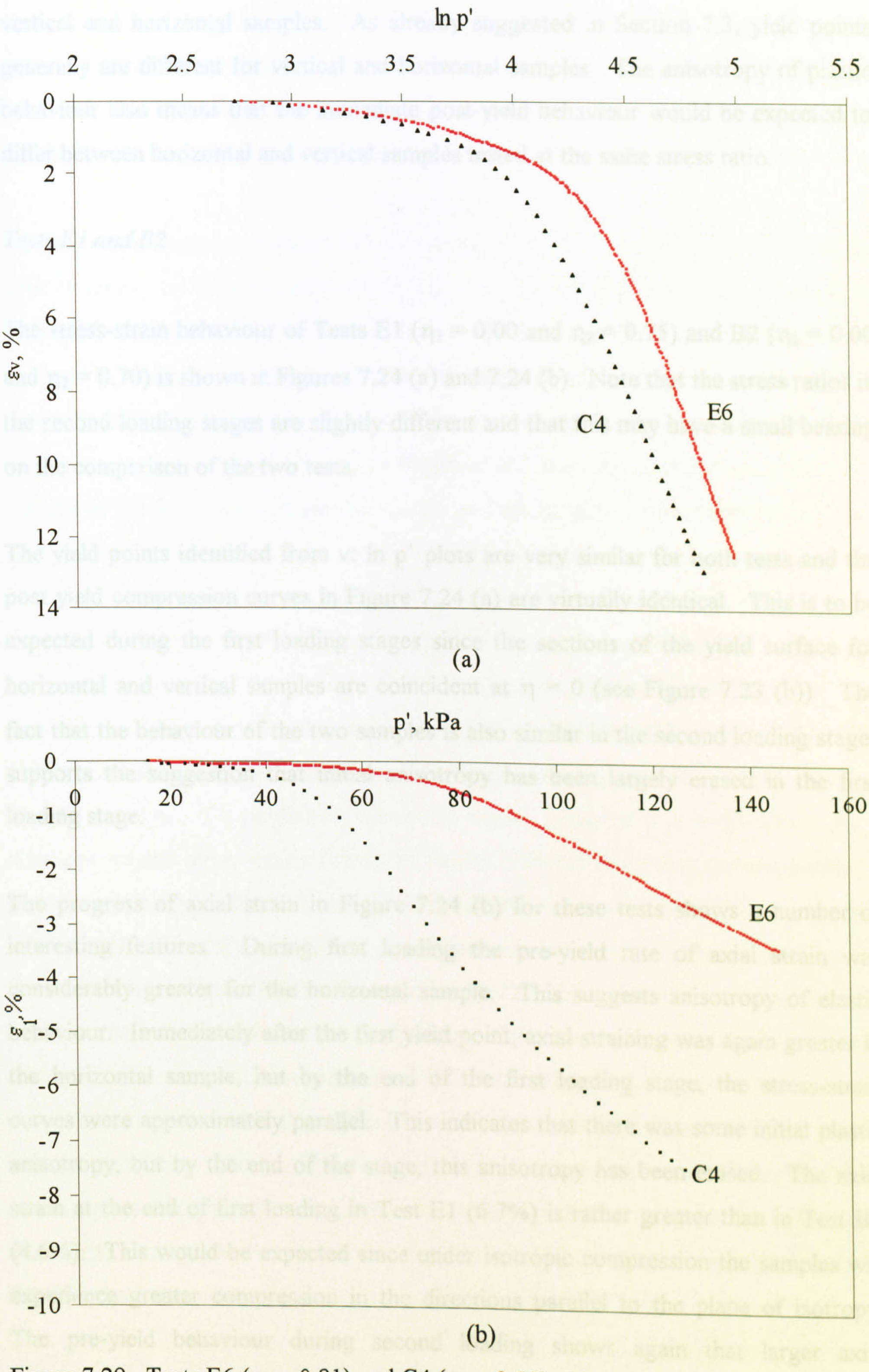

Figure 7.29. Tests E6 ($\eta = -0.81$) and C4 ($\eta = -0.80$); (a) compression behaviour, (b) axial behaviour.

vertical and horizontal samples. As already suggested in Section 7.3, yield points generally are different for vertical and horizontal samples. The anisotropy of plastic behaviour also means that the immediate post-yield behaviour would be expected to differ between horizontal and vertical samples tested at the same stress ratio.

Tests E1 and B2

The stress-strain behaviour of Tests E1 ($\eta_1 = 0.00$ and $\eta_2 = 0.75$) and B2 ($\eta_1 = 0.00$ and $\eta_2 = 0.70$) is shown in Figures 7.24 (a) and 7.24 (b). Note that the stress ratios in the second loading stages are slightly different and that this may have a small bearing on the comparison of the two tests.

The yield points identified from v: ln p' plots are very similar for both tests and the post yield compression curves in Figure 7.24 (a) are virtually identical. This is to be expected during the first loading stages since the sections of the yield surface for horizontal and vertical samples are coincident at $\eta = 0$ (see Figure 7.23 (b)). The fact that the behaviour of the two samples is also similar in the second loading stages supports the suggestion that initial anisotropy has been largely erased in the first loading stage.

The progress of axial strain in Figure 7.24 (b) for these tests shows a number of interesting features. During first loading the pre-yield rate of axial strain was considerably greater for the horizontal sample. This suggests anisotropy of elastic behaviour. Immediately after the first yield point, axial straining was again greater in the horizontal sample, but by the end of the first loading stage, the stress-strain curves were approximately parallel. This indicates that there was some initial plastic anisotropy, but by the end of the stage, this anisotropy has been erased. The axial strain at the end of first loading in Test E1 (6.7%) is rather greater than in Test B2 (4.6%). This would be expected since under isotropic compression the samples will experience greater compression in the directions parallel to the plane of isotropy. The pre-yield behaviour during second loading shows again that larger axial compressive strains were generated in the horizontal sample. It appears that the elastic anisotropy noted in the first loading stage still exists. The rate of post-yield

axial straining in Test B2 is initially slightly greater than in Test E1, suggesting that some influence of the initial plastic anisotropy remains. By the end of the second loading stage, however, the stress-strain curves are once again approximately parallel.

It is also interesting to compare the measured radial strain ε_x from Test E1 and the axial strain in Test B2 (both corresponding to the vertical direction in the ground). In each case, the strain being measured is that which is perpendicular to the plane of isotropy in the soil. It would therefore be expected that stress-strain behaviour is identical. Comparing Figure 7.14 with Figure 7.24 (b), it can be seen that the shape of the stress-strain curves are almost identical and the final magnitudes of strain at the end of the first loading stage (ε_x = 4.2% in Test E1 and ε_y = 4.5% in Test B2) are very similar.

Tests E2 and C7

Test E2 involved a first loading stage at η_1 = 0.41 and Test C7 at η_1 = 0.42. The yield points identified from the v: ln p' plots indicate that Test E2 yielded at p'_{y1} = 66 kPa but Test C7 yielded at the much higher stress of p'_{y1} = 85 kPa. As a consequence the compression curves in Figure 7.25 (a) show that the magnitude of post-yield straining is much greater in Test E2. However, the post-yield compression curve in Test C7 is slightly steeper and appears to be converging with the curve for Test E2. Plots of axial strain shown in Figure 7.25 (b) indicate that, during the first loading stage, the initial pre-yield behaviour of these samples was almost identical. The post-yield stress-strain curves show that the horizontal sample underwent greater axial strain than the vertical sample, but as loading continued the stress-strain curves became parallel. This is again consistent with the suggestion of initial plastic anisotropy producing differences in behaviour of the two samples, but this initial anisotropy was gradually erased and replaced with a new anisotropy that was the same for both samples.

In the second loading stages, where both samples were reloaded in triaxial extension at η_2 = -0.79, the yield points identified from the v: ln p' plots were p'_{y2} = 123 kPa in

Test E2 and p'_{y2} = 110 kPa in Test C7. In Figure 7.25 (a) the mismatch in the compression curves is almost entirely caused by the difference of volumetric strain at the end of the first loading stage. The post-yield compression curves are almost identical and suggest that the influence of initial anisotropy has been substantially erased. However, the post-yield axial strain behaviour in Figure 7.25 (b) indicates some differences between the two samples (the sample in Test C7 expanded more rapidly than in Test E2), suggesting that there was still some remaining influence of initial anisotropy.

Tests E3 and C5

Test E3 involved a single loading stage in triaxial compression at $\eta = 0.80$, and was equivalent to the first loading stage of Test C5. The yield points identified from the v: ln p' plots were very different for these two samples. In the horizontal sample, the yield point obtained was p'_{y1} = 53 kPa, while in the vertical sample yield was recorded at p'_{y1} = 76 kPa. The compression curves in Figure 7.26 (a) show that although the yield points were different, the post-yield compression curve was initially much steeper in Test C5 so that by the time the sample in Test E3 had reached p' = 100 kPa (almost double the yield stress), the compression curves have almost converged (consistent with the influence of initial anisotropy being gradually erased and replaced with a new anisotropy that was the same for both samples). The first loading stage of Test C5 ($\eta_1 = 0.80$) was close to the stress ratio corresponding to one-dimensional consolidation ($\eta_{K0} = 0.93$). Therefore the effects of evolving anisotropy are minimal. On the horizontal sample, however, significant changes in anisotropy would be expected as the direction of major principal stress was changed from the x-direction in the ground to the y-direction in the first loading stage of the triaxial test. The post-yield compression curve is rounded, which appears to confirm the influence of changing plastic anisotropy.

Figure 7.26 (b) shows yet again that prior to yield, the rate of axial straining was greater in the horizontal sample than in the vertical sample. The stress-strain curves also confirm that yielding occurred much earlier in the horizontal sample. Immediately after yield, the axial stress-strain curves are similar for the two tests.

Tests E4 and C1

Test E4 was first loaded in triaxial compression at $\eta_1 = 0.41$ and Test C1 was first loaded at $\eta_1 = 0.42$. In this loading stage, the yields point from the v: ln p' plots were $p'_{y1} = 69$ kPa for the horizontal samples and $p'_{y1} = 78$ kPa for the vertical sample. As was seen in the comparison of Tests E2 and C7, the compression curves in Figure 7.27 (a) converged as post-yield straining progressed. In this instance, the curves were virtually coincident by the end of first loading. The compression curves converged more rapidly in this case, perhaps due to the fact that the yield points are more similar in Tests E4 and C1 than in Tests E2 and C7. The axial stress-strain plots in Figure 7.27 (b) indicate that once more, elastic anisotropy exists and that the horizontal sample underwent greater axial straining prior to yield in the first loading stage. Immediately after yield, slightly larger axial strains occurred in the horizontal sample, but thereafter the stress-strain curves are approximately parallel. In this respect, Figure 7.27 (b) is very consistent with Figure 7.26 (b). The overall suggestion is that only a small amount of post-yield straining was necessary to erase the differences in anisotropy between the horizontal and vertical samples at this stress ratio.

Both samples were reloaded at a much higher stress ratio in triaxial compression, where $\eta_2 = 1.00$ in Test E4 and $\eta_2 = 1.03$ in Test C1. The slight difference in stress ratio is not thought to be significant in the following discussion. For Test E4, yield was obtained from the v: ln p' plot at $p'_{y2} = 106$ kPa and for Test C1 at $p'_{y2} = 132$ kPa. The difference in yield stress between the two samples is considerable and raises the possibility that the influence of initial anisotropy was not completely erased during the first loading stage. However, Figure 7.27 (a) shows that the compression curves rapidly converged. The axial strain curves in Figure 7.27 (b) show that the influence of initial anisotropy on elastic strains still remained since larger axial strains occurred prior to yield in the horizontal sample than in the vertical sample. Despite the apparent difference in yield stress in the second loading stage, the post-yield development of axial strain was almost identical for the two samples.

Tests E5 and C2

Test E5 involved a single loading stage almost identical to the first loading stage in Test C2 ($\eta_1 = 1.10$ and $\eta_1 = 1.12$ respectively). The yield points observed from v: ln p' curves are $p'_{y1} = 52$ kPa for the horizontal sample and $p'_{y2} = 60$ kPa for the vertical sample. Yielding was much more sudden in Test C2 than in Test E5, as shown in Figure 7.28 (a). In addition, the initial gradient of the post-yield compression curve was much greater in Test C2. Given this information and the fact that Test C2 was tested at a stress ratio only slightly higher than η_{K0}, it is to be expected that the effects of evolving plastic anisotropy will be much more prevalent in the horizontal sample. Figure 7.28 (a) shows that the initial post-yield behaviour is very different with the vertical sample undergoing more rapid compression. However, the compression curves rapidly converged, suggesting that initial differences due to anisotropy may have been erased. The post-yield stress-strain curves in Figure 7.28 (b) show that post-yield behaviour was initially similar but the rate of axial straining reduces in the vertical sample. This reduction in straining is related to the fact that a large amount of destructuration occurred immediately after yield. This does not appear to be the case for Test E5 where the gradient of the stress-strain curve remains approximately constant and is eventually higher than that of the vertical sample.

Test E6 and C4

Test E6 involved a single loading stage in triaxial compression at $\eta = -0.81$ and is comparable to the first loading stage in Test C4, carried out at $\eta = -0.80$. The yield stress for Test E6 was $p'_{y1} = 73$ kPa and for Test C4 was $p'_{y1} = 52$ kPa. Figure 7.29 (a) shows that although the yield stresses are very different, the post-yield compression curves are similar. As testing progressed, the compression curve from test E6 gradually converged with the curve from Test C4. The stress-strain curves in Figure 7.29 (b) indicate that prior to yield, greater axial strains were experienced by the vertical sample. This is in contrast to the pairs of horizontal and vertical tests first loaded either isotropically or in triaxial compression. Figure 7.29 (b) also shows that post-yield behaviour of these samples was very contrasting. This is the only

instance in which the axial strain progressed more rapidly in the vertical sample. The contrast in stress-stress behaviour appeared to decrease as the test progressed, although it is difficult to tell whether the curves are becoming parallel or not.

7.6.2 Conclusion on comparison of horizontal and vertical samples

Comparisons of horizontal and vertical samples tested in the triaxial cell at the same stress ratios show that the two sets of samples respond quite differently. In terms of yielding, ε_v: ln p' plots confirmed that in triaxial extension, the onset of yield occurs at higher stresses for the horizontal samples than for the vertical samples. In contrast, the horizontal samples tested in triaxial compression have lower yield stresses than their vertical counterparts. Differences in the magnitude of volumetric straining are generally attributed to the fact that the onset of yield is significantly different between the horizontal and vertical samples. Comparison of the axial straining shows that, in general, the rate of straining differs between horizontal and vertical samples, particularly around the onset of yield. In both axial and volumetric stress-strain curves, it is apparent in many cases that the rate of straining of the samples becomes increasingly similar as the tests progress, especially in the tests which involved unloading and a second loading stage.

7.7 Conclusions

The results from Test Series D and E have provided information on the stress-strain behaviour of horizontally oriented samples of Bothkennar clay. A number of important issues relevant to understanding soft clay behaviour have been discussed and the following conclusions can be drawn from these three suites of tests:

- Drained shear tests to failure in Test Series D indicate that a more general form of failure criterion needs to be encapsulated in the modelling of natural clays. The data suggest that suitable values for the critical state stress ratio in triaxial compression and extension for these horizontal samples are, respectively, $M_{CH} = 1.30$ and $M_{EH} = 1.20$.

- The stress-strain response of the samples in Test Series E indicates a number of important aspects of soil behaviour. The influence of evolving anisotropy is prevalent and is particularly apparent in the compression curves (see Figures 7.5 – 7.11). Examination of the principal stress-strain behaviour has shown that the soil behaviour is significantly anisotropic. Data from several tests suggested that the initial cross-anisotropy of plastic behaviour can be removed and, under continued triaxial loading, a new form of cross-anisotropy can be produced. The data also strongly suggests that (elastic) pre-yield behaviour is significantly anisotropic. This anisotropy of elastic behaviour appears to be more resistant to subsequent change than the anisotropy of plastic behaviour.

- For the particular section of the yield surface relating to horizontal samples, the observed yield points are well matched by the S-CLAY1 yield surface, where the parameters have been retained from the best-fit curve for the vertical samples (see Figure 7.23).

- Comparison of results from horizontal and vertical samples indicate that, for the horizontal samples, the onset of yield is generally at a higher mean effective stress than for vertical samples in triaxial extension, but is at a slightly lower mean effective stress than for vertical samples in triaxial compression.

In the light of the above observations, S-CLAY1 models simulations using the parameters obtained are required in order to assess how well the various features of the soil behaviour can be modelled. These simulations are presented in Sections 8.3 and 8.4.

CHAPTER 8: S-CLAY1 MODEL SIMULATIONS

8.1 Introduction

This chapter describes S-CLAY1 model simulations of triaxial tests on vertical and horizontal samples of Bothkennar clay. The purpose of these simulations is to assess the applicability of the S-CLAY1 model in predicting soft clay behaviour, in particular the evolution of anisotropy during plastic straining. Values of model parameters have been obtained from the experimental results (discussed in Chapters 6 and 7) and are summarised in Section 8.2. Section 8.3 contains simulations involving only vertically oriented samples first loaded isotropically (Test Series B). Section 8.4 discusses model simulations of vertical samples first loaded anisotropically (Test Series C). Section 8.5 includes simulations on horizontal samples (Test Series E) and therefore involves the fully generalized model. In each set of simulations, a corresponding model simulation for the widely-used Modified Cam Clay (MCC) model is included. This inclusion of MCC simulations provides a benchmark in order to assess whether the S-CLAY1 model represents a more accurate constitutive model than is currently being used in engineering practice.

In many of the tests in Series B, C and E, the values of stress ratio η in the first and second loading stages were radically different. The data from these tests provide the opportunity for rigorous assessment of the ability of the S-CLAY1 model to predict the stress-strain behaviour when substantial changes of anisotropy and yield curve orientation are occurring. In other tests, the changes in the yield surface orientation are expected to be less radical and these tests allow further investigation of the model.

8.2 Parameter selection for vertical samples

The stress-strain relationship for S-CLAY1 presented in Chapter 3 was implemented into a single stress-point simulation program written in Fortran. The simulations are based on the assumption that the triaxial sample is a single homogenous element deforming as a right-cylinder (i.e. end-effects due to sample restraint are ignored). For this specific case of triaxial loading, the plastic strains are generated using a simplified version of Equation 3.60 (where y is the vertical direction in the ground):

$$\begin{Bmatrix} d\varepsilon_x \\ d\varepsilon_y \\ d\varepsilon_z \end{Bmatrix} = \frac{1}{H} \begin{bmatrix} \frac{\partial f}{\partial \sigma'_x}\frac{\partial f}{\partial \sigma'_x} & \frac{\partial f}{\partial \sigma'_x}\frac{\partial f}{\partial \sigma'_y} & \frac{\partial f}{\partial \sigma'_x}\frac{\partial f}{\partial \sigma'_z} \\ \frac{\partial f}{\partial \sigma'_y}\frac{\partial f}{\partial \sigma'_x} & \frac{\partial f}{\partial \sigma'_y}\frac{\partial f}{\partial \sigma'_y} & \frac{\partial f}{\partial \sigma'_y}\frac{\partial f}{\partial \sigma'_z} \\ \frac{\partial f}{\partial \sigma'_z}\frac{\partial f}{\partial \sigma'_x} & \frac{\partial f}{\partial \sigma'_z}\frac{\partial f}{\partial \sigma'_y} & \frac{\partial f}{\partial \sigma'_z}\frac{\partial f}{\partial \sigma'_z} \end{bmatrix} \begin{Bmatrix} d\sigma'_x \\ d\sigma'_y \\ d\sigma'_z \end{Bmatrix} \quad (8.1)$$

The program was also used to generate Modified Cam Clay simulations by setting the values of the parameters α, β and μ involved in S-CLAY1 to zero. As discussed in Section 6.1, all simulation output data are presented in terms of true strains (see Equation 6.1). Stress increments were chosen to be sufficiently small so that there was no influence of stress increment size. The chosen increment size, in terms of mean effective stress, was $\Delta p' = 0.1$ kPa. It was found that simulations with smaller increments did not significantly affect the results. The data presented in this chapter shows only simulation data points at mean effective stress intervals of 1 kPa, in order to save file space. The deviator stress increment is related to the mean effective stress increment by the specified stress ratio.

Table 8.1 summarises the S-CLAY1 model parameters based on the experimental results discussed in Chapter 6.

Model	λ	κ	ν'	M_C	M_E	μ	β	α_0	p'_{m0}
MCC	0.48	0.02	0.20	1.4	1.1	(0)	(0)	(0)	86 kPa
S-CLAY1	0.48	0.02	0.20	1.4	1.1	10, 30, 50	0.94	0.28	85 kPa

Table 8.1. Model parameter values for simulations of vertical samples.

The value of λ was assumed to be equal to 0.48, the value measured in a first loading stage at $\eta = \eta_{K0}$ (see Figure 6.27). As discussed in Sections 6.3.3 and 6.4.3, a κ value of 0.02 was selected. An appropriate value of Poisson's ratio, ν', was obtained in Section 6.4.6 and was found to be 0.2. In all simulations it was assumed that the critical state stress ratio for stress paths above the α-line was given by $M_C = 1.40$ and below this line $M_E = -1.10$ was assumed. As already discussed in Section 6.5, the choice of M_C and M_E has significant implications for the shape of the yield curve and the chosen values are discussed in Sections 8.3 and 8.4.

A range of values were examined for the rotational hardening parameter μ. Zentar et al. (2002b) suggested that the value of μ will typically lie within a range given by

$$\frac{10}{\lambda} < \mu < \frac{15}{\lambda} \tag{8.2}$$

Assuming $\lambda = 0.48$, this suggests that $\mu = 21$ to 31. In the first simulations, values of $\mu = 10$, 30 and 50 were therefore adopted in order to calibrate this parameter and to assess the sensitivity of predicted stress-strain behaviour to the value of μ under a number of diverse loading conditions. The value of β was derived using the procedure suggested by Wheeler et al (2003), which was described in Section 3.2.6.

The initial size and orientation of the S-CLAY1 yield curve has been discussed in Section 6.5, with $p'_{m0} = 85$ kPa and $\alpha_0 = 0.28$ considered the most appropriate combination (see Figures 6.15 and 8.1). The initial size of the yield curve p'_0 for the MCC model was chosen as the best-fit to the yield points and this results in a value of $p'_0 = 86$ kPa (see Figure 8.1). Also shown in Figure 8.1 are the experimental yield points from Test Series B and C. Figure 8.1 illustrates the fact that all but one of the yield points above the p'-axis lie outside the MCC locus and the points on or below the p'-axis lie inside the curve i.e. the MCC yield curve fits the experimental yield points less well than S-CLAY1.

8.3 Simulations of Test Series B

Simulations using S-CLAY1 and MCC models are compared with the experimental data for eight tests in Series B in Figures 8.2 – 8.9. In each figure the stress-strain behaviour is presented in terms of volumetric strain (ε_v) plotted against the logarithm of mean effective stress (ln p'), deviatoric stress (q) plotted against deviatoric strain (ε_d) and axial stress (σ'_1) plotted against axial strain (ε_1). The semi-logarithmic compression plots demonstrate not only the progress of volumetric straining, but highlight any differences between the experimental yield stress and the predicted yield stress. Plots of axial stress-strain have been included as well as the volumetric

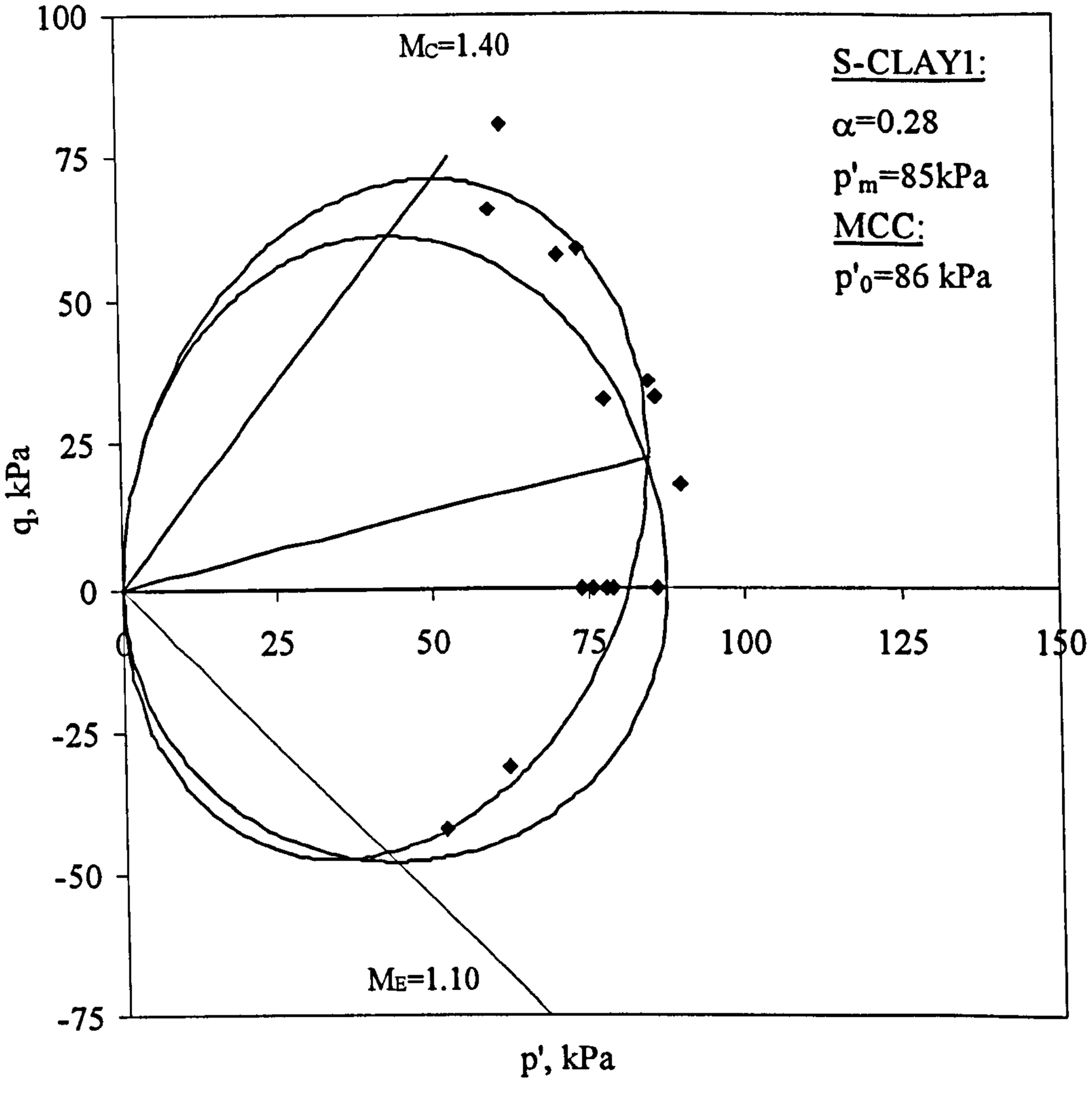

Figure 8.1. Relationship of MCC yield curve and S-CLAY1 yield curves for vertical samples.

and deviatoric stress-strain plots, because axial strain ε_1 was measured directly, whereas deviatoric strain ε_d was calculated from measurements of axial and volumetric strain. Also included in each figure are strain paths plotted in terms of deviatoric and volumetric strains. These provide information on the both the elastic behaviour and on the flow rule during plastic straining.

8.3.1 First loading stages: isotropic compression

Under isotropic compression, the S-CLAY1 model predicts yield at around p' = 79 kPa and is generally a good match to the experimental yield points (see Figures 8.2 (a) to 8.9 (a)). The MCC model predicts yield at a slightly higher mean effective stress (p' = 86 kPa), which generally provides a slightly poorer match to the

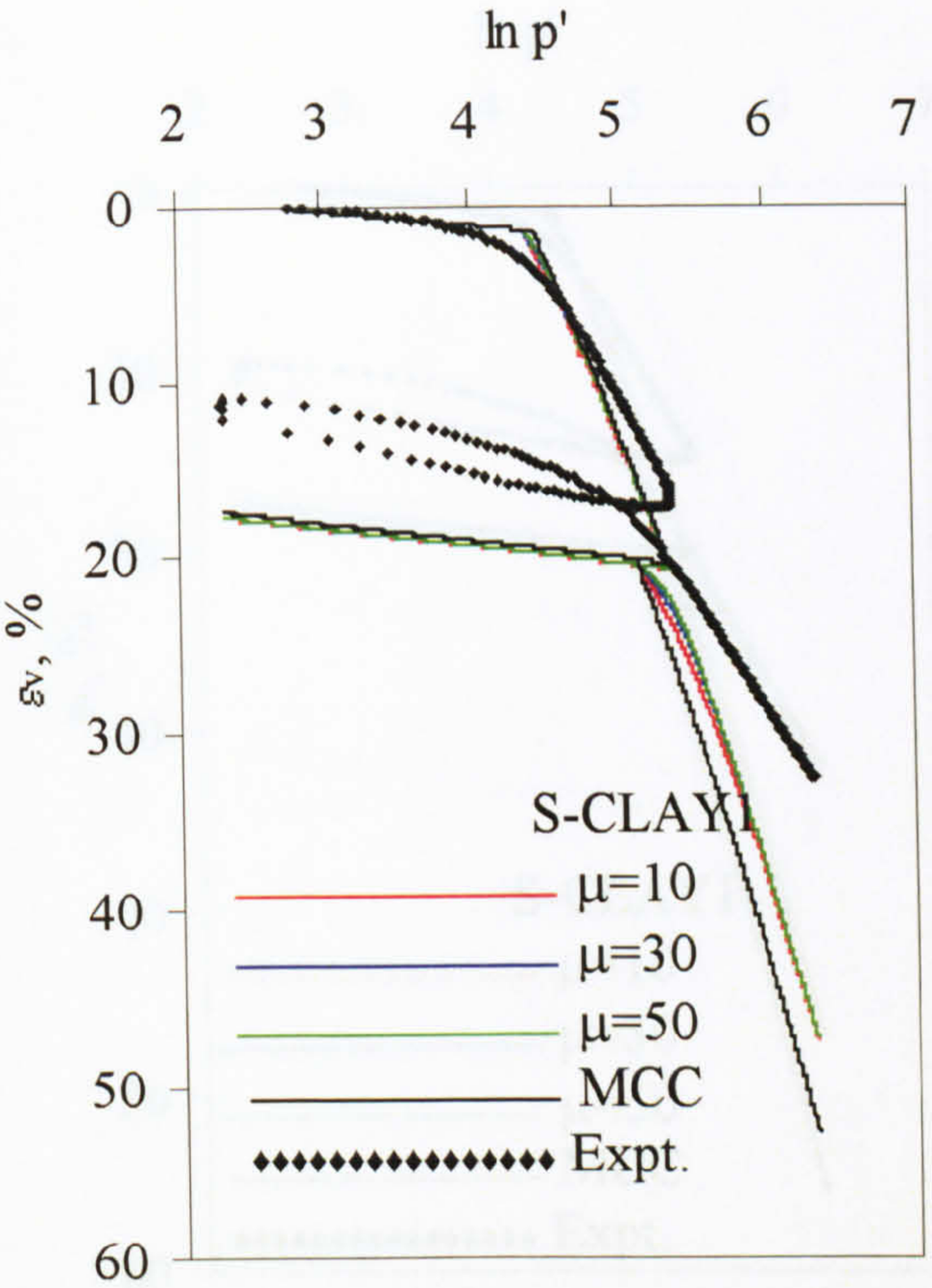

(a)

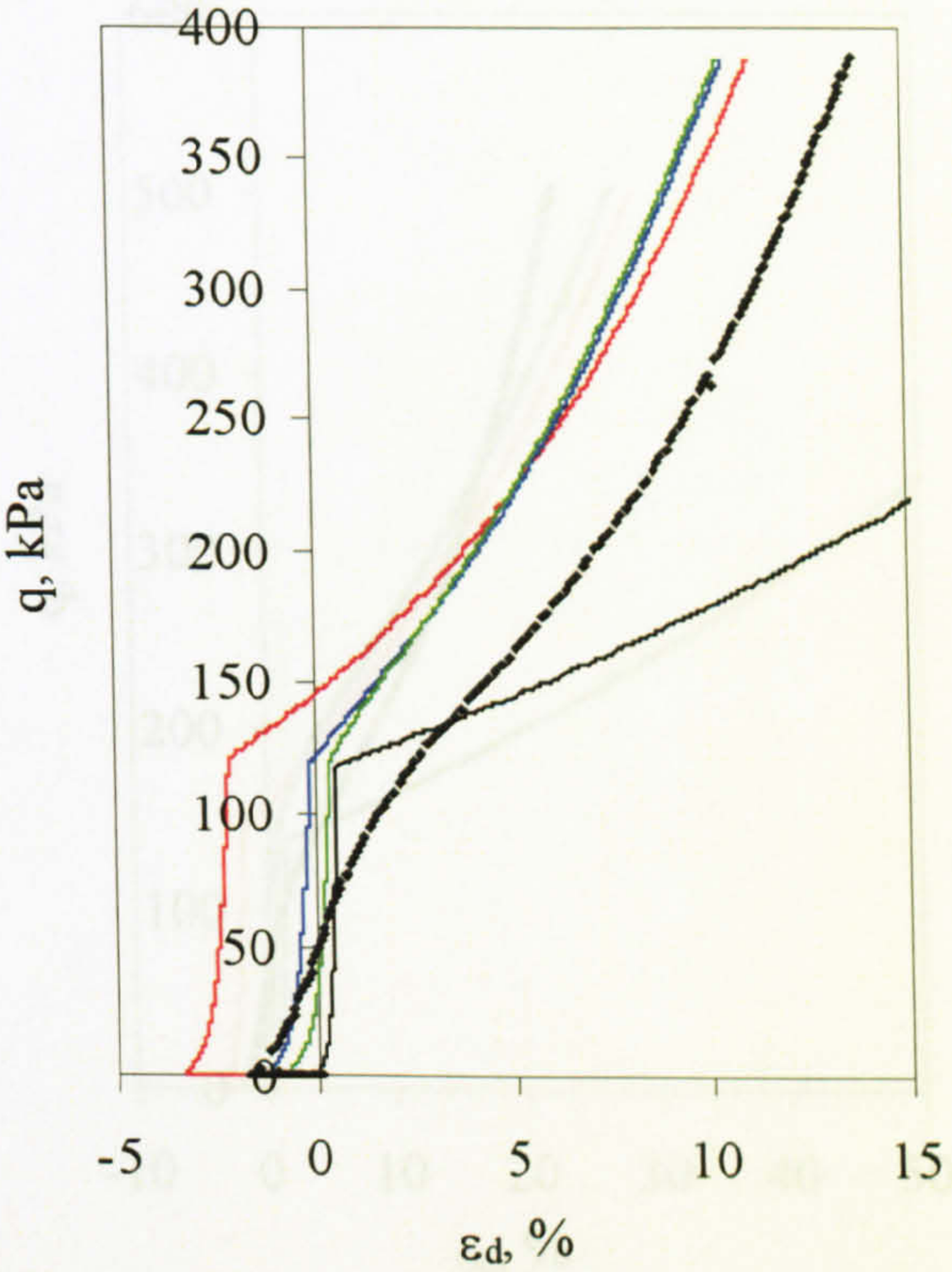

(b)

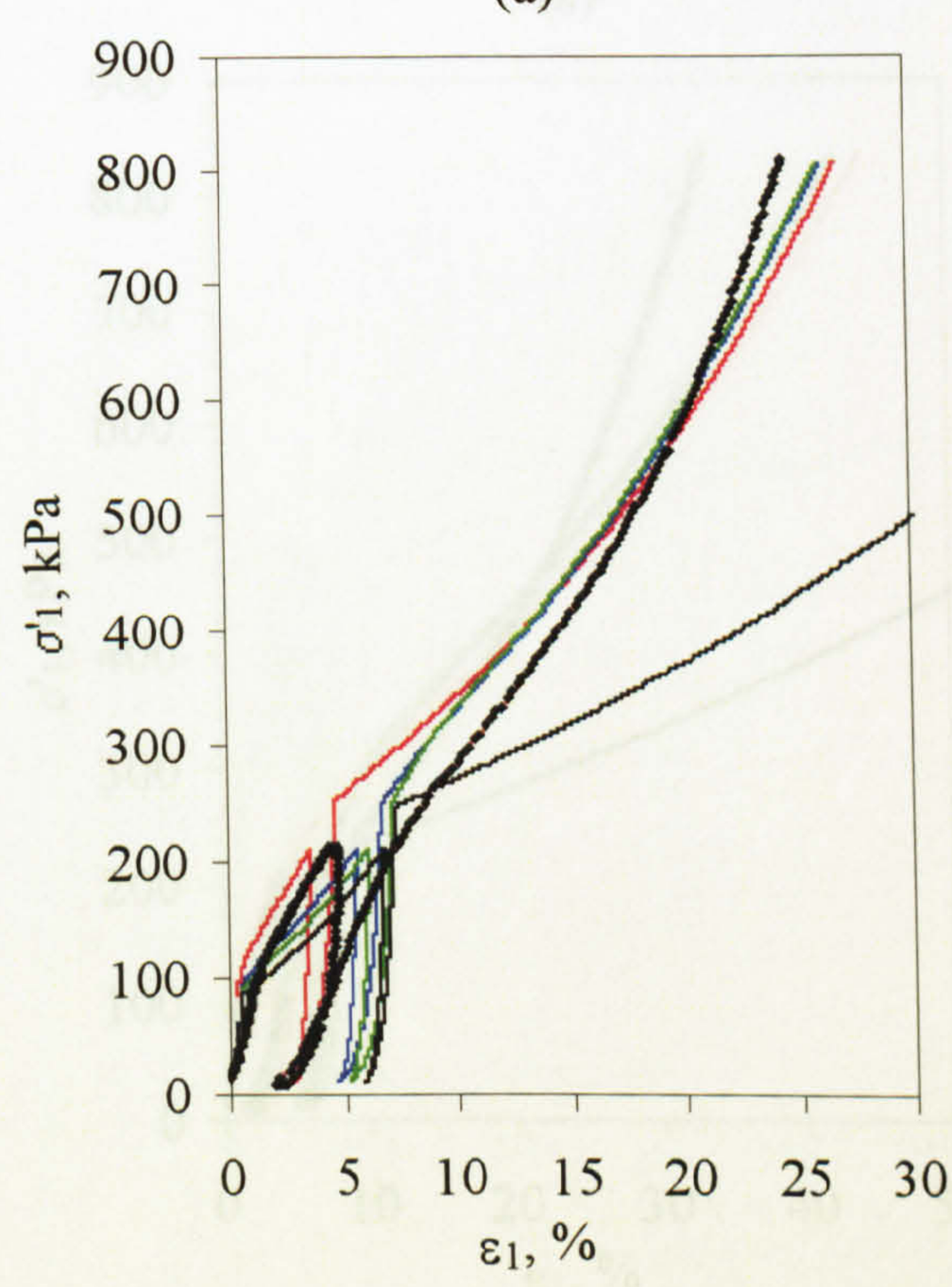

(c)

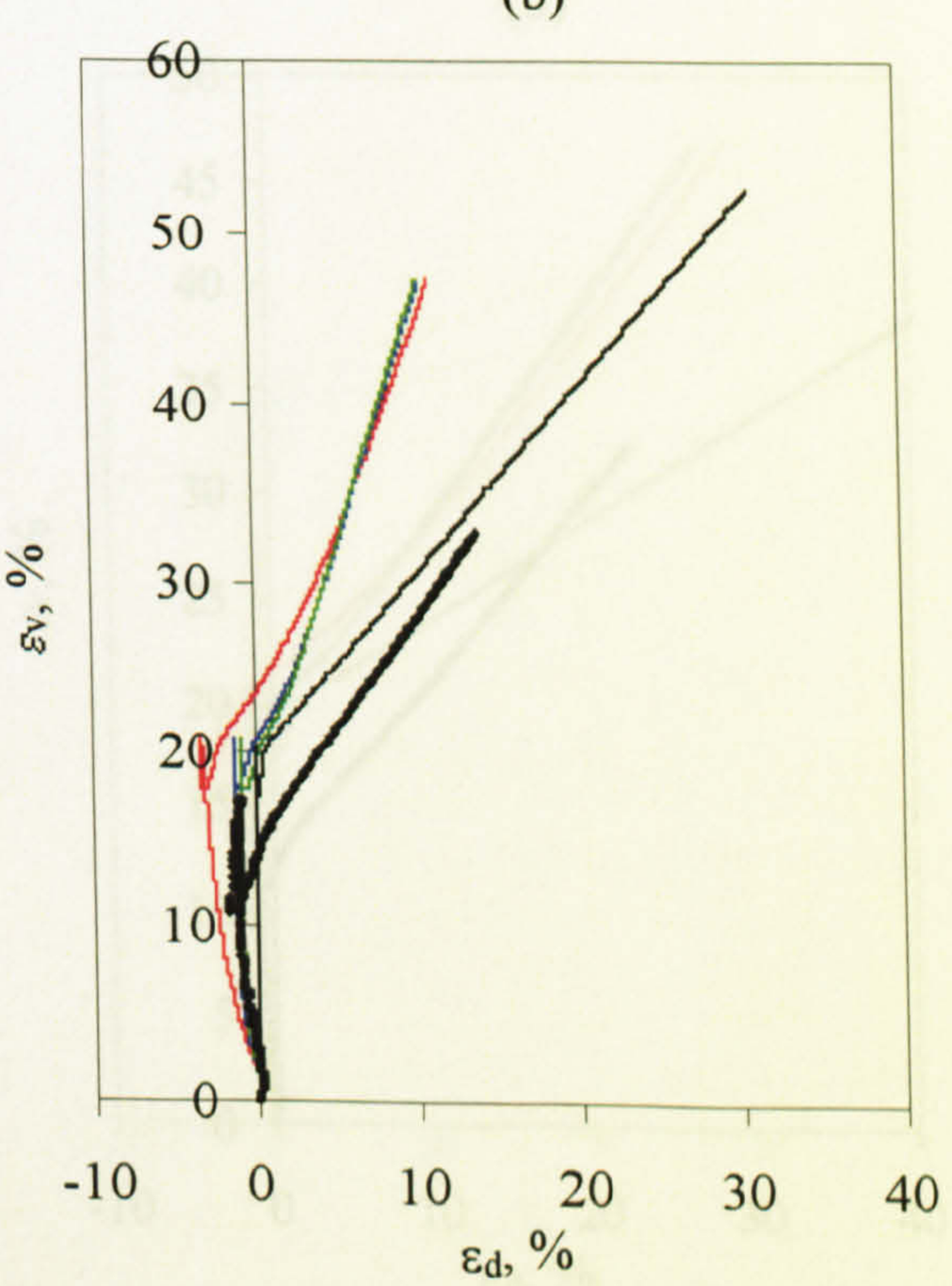

(d)

Figure 8.2. S-CLAY1 and MCC simulations of Test B2, where $\eta_1 = 0$ and $\eta_2 = 0.70$; (a) compression behaviour, (b) deviatoric stress-strain behaviour, (c) axial stress-strain behaviour, (d) strain paths.

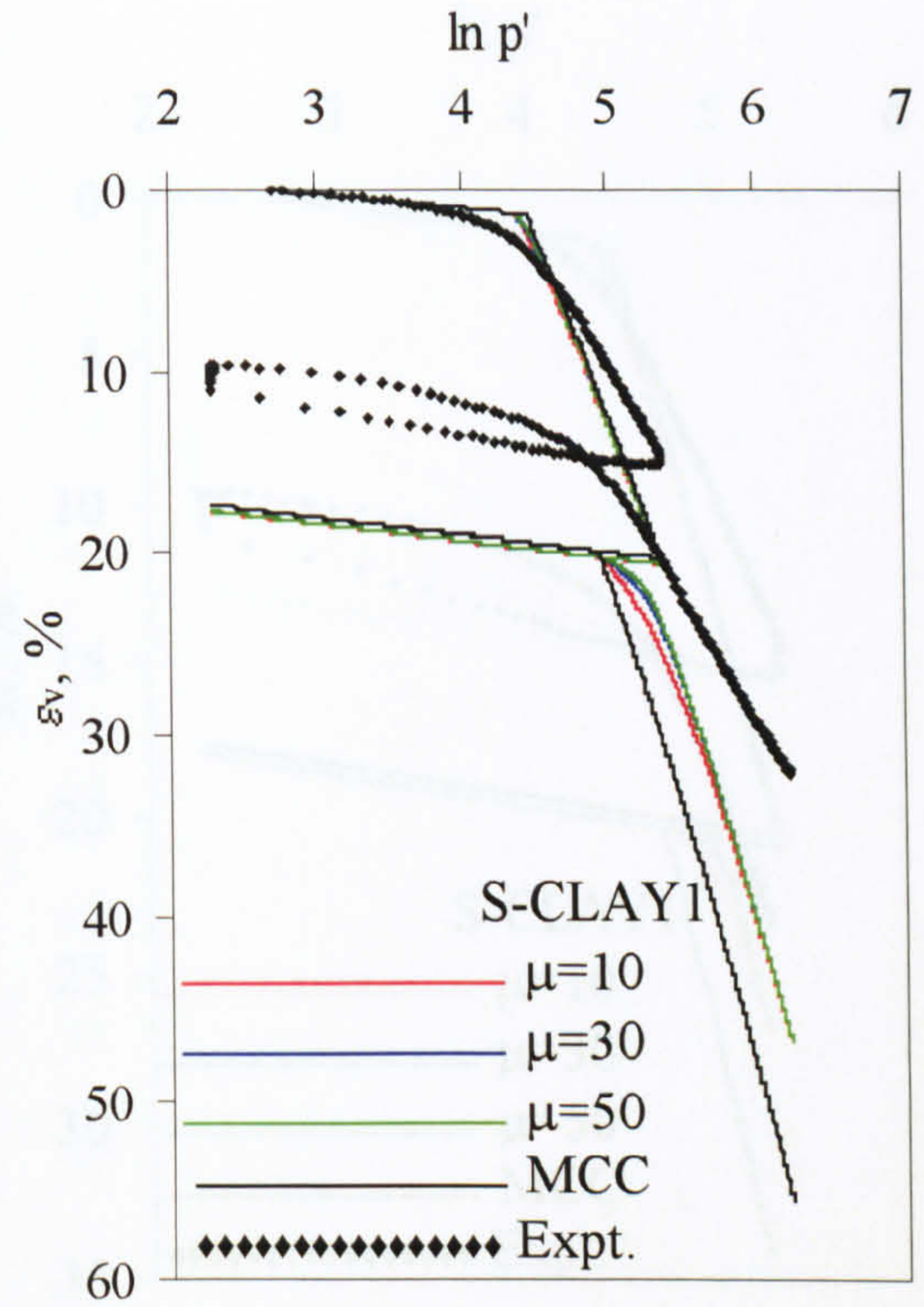

(a)

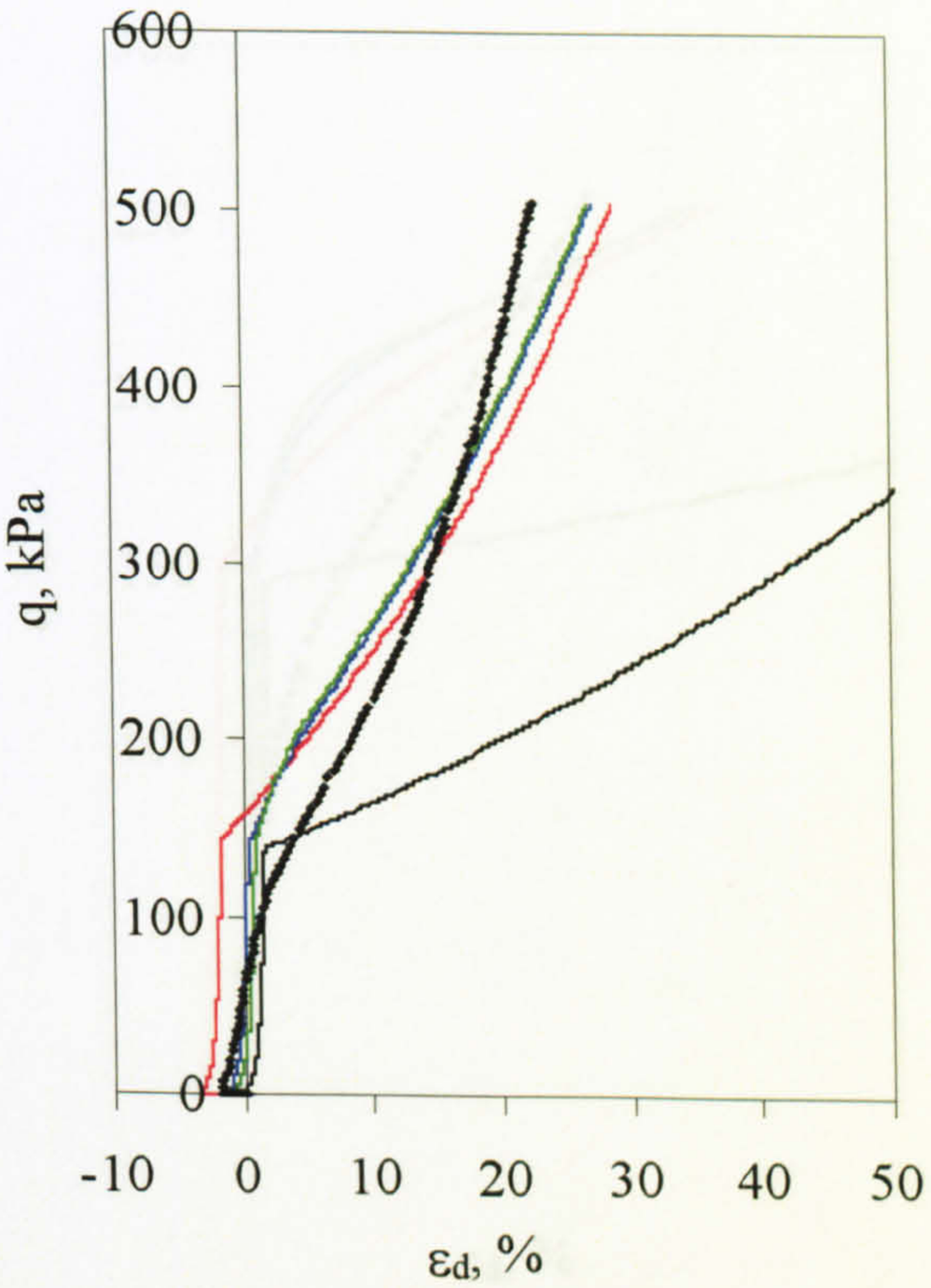

(b)

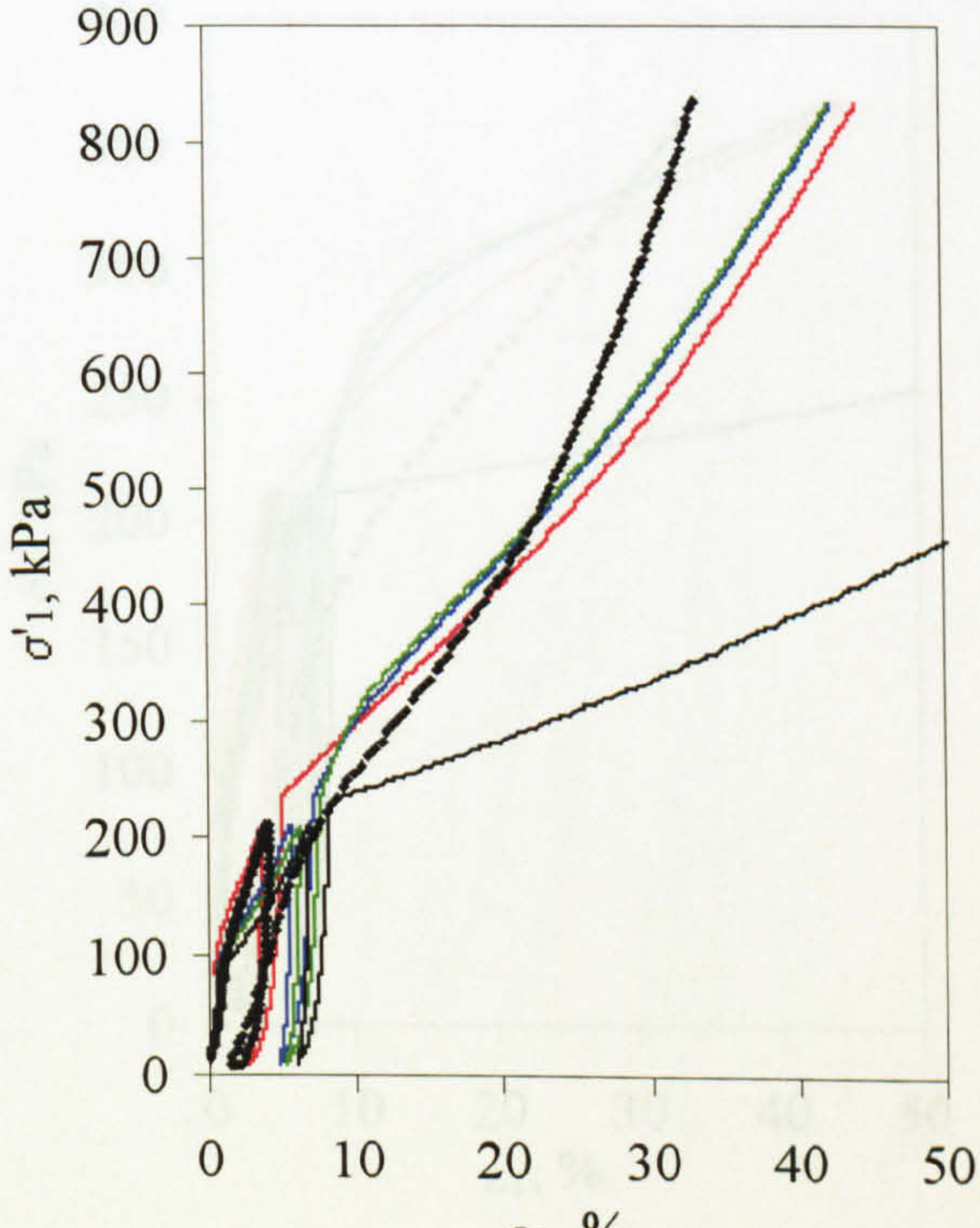

(c)

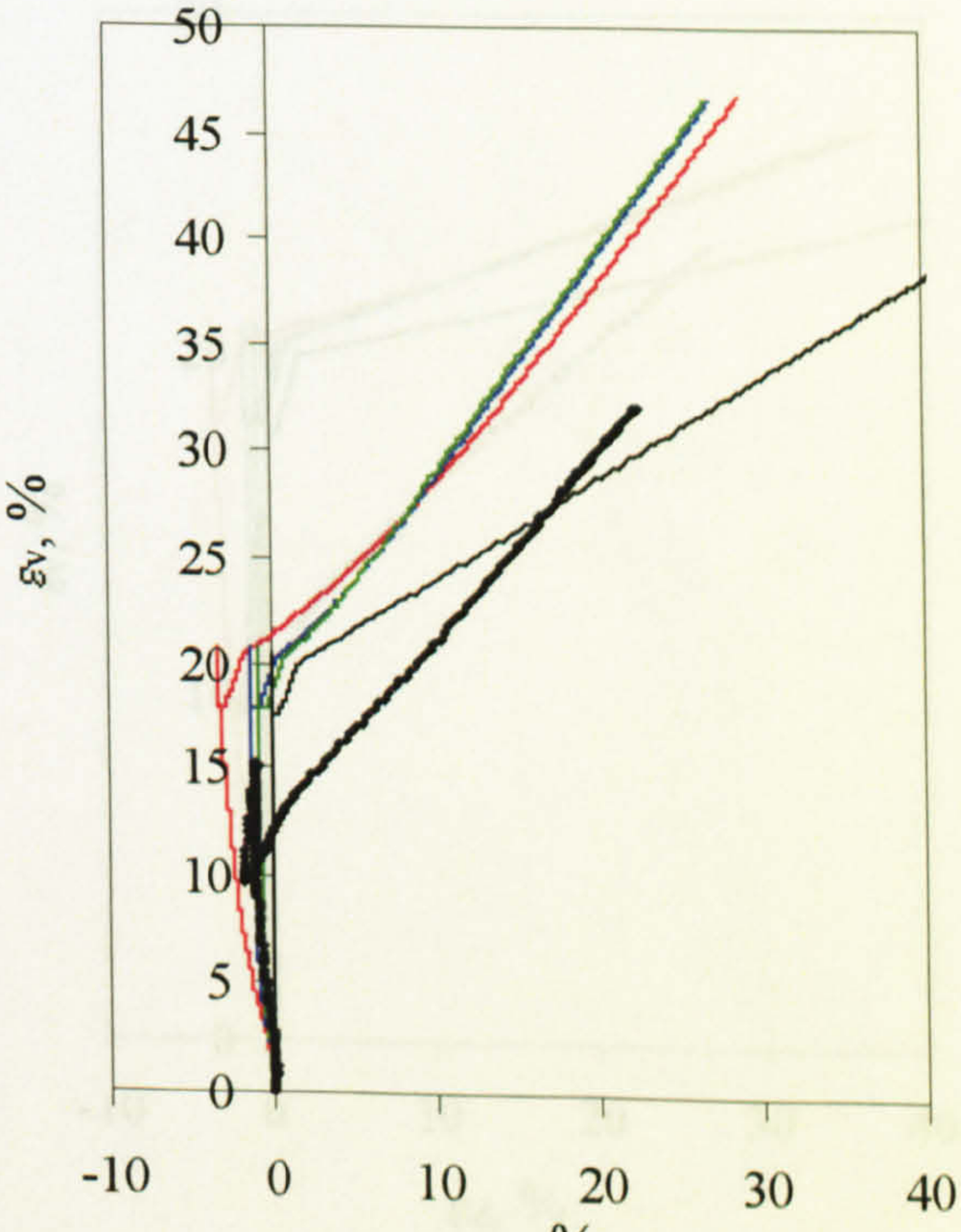

(d)

Figure 8.3. S-CLAY1 and MCC simulations of Test B3, where $\eta_1 = 0$ and $\eta_2 = 1.01$; (a) compression behaviour, (b) deviatoric stress-strain behaviour, (c) axial stress-strain behaviour, (d) strain paths.

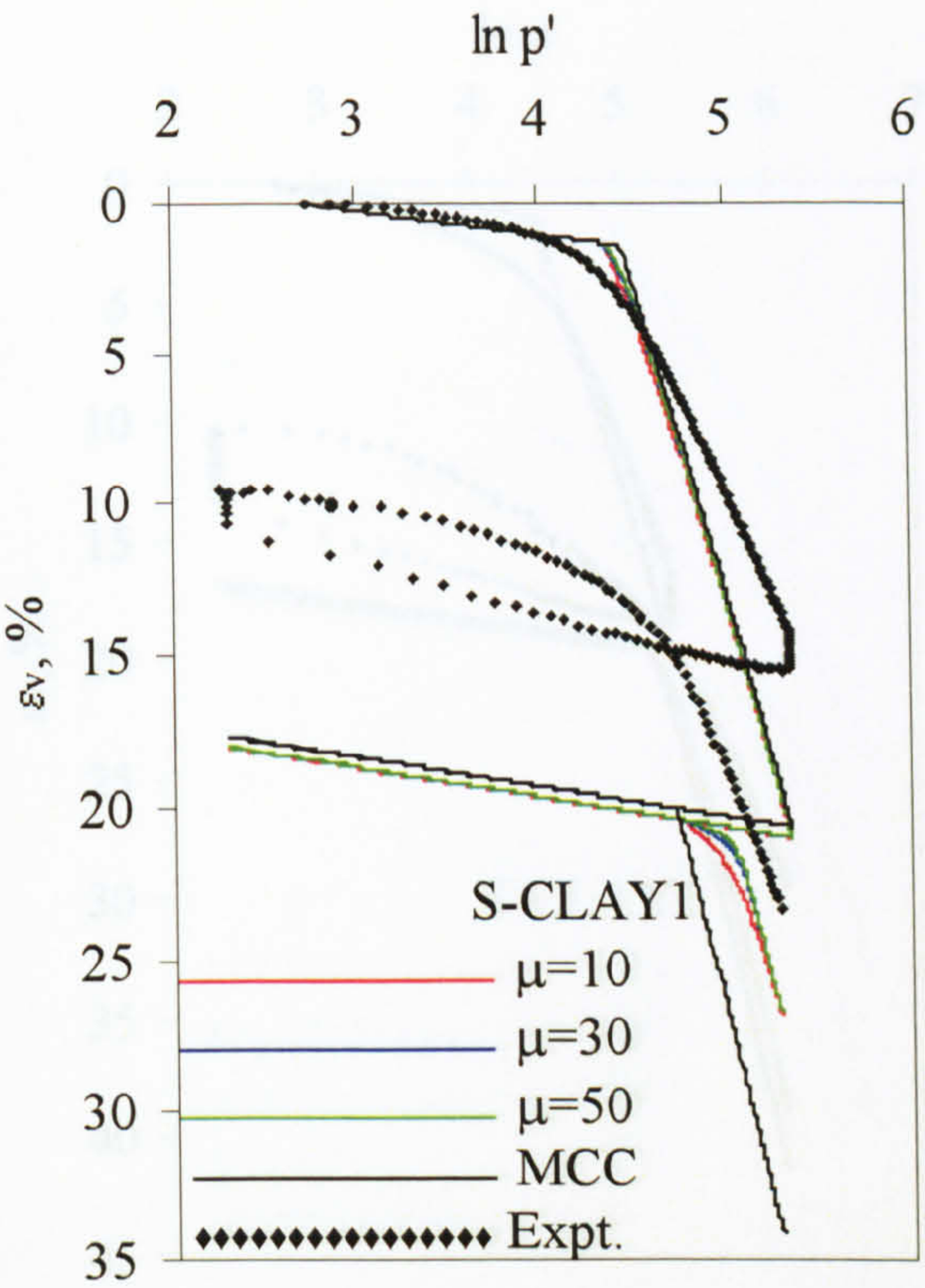

(a)

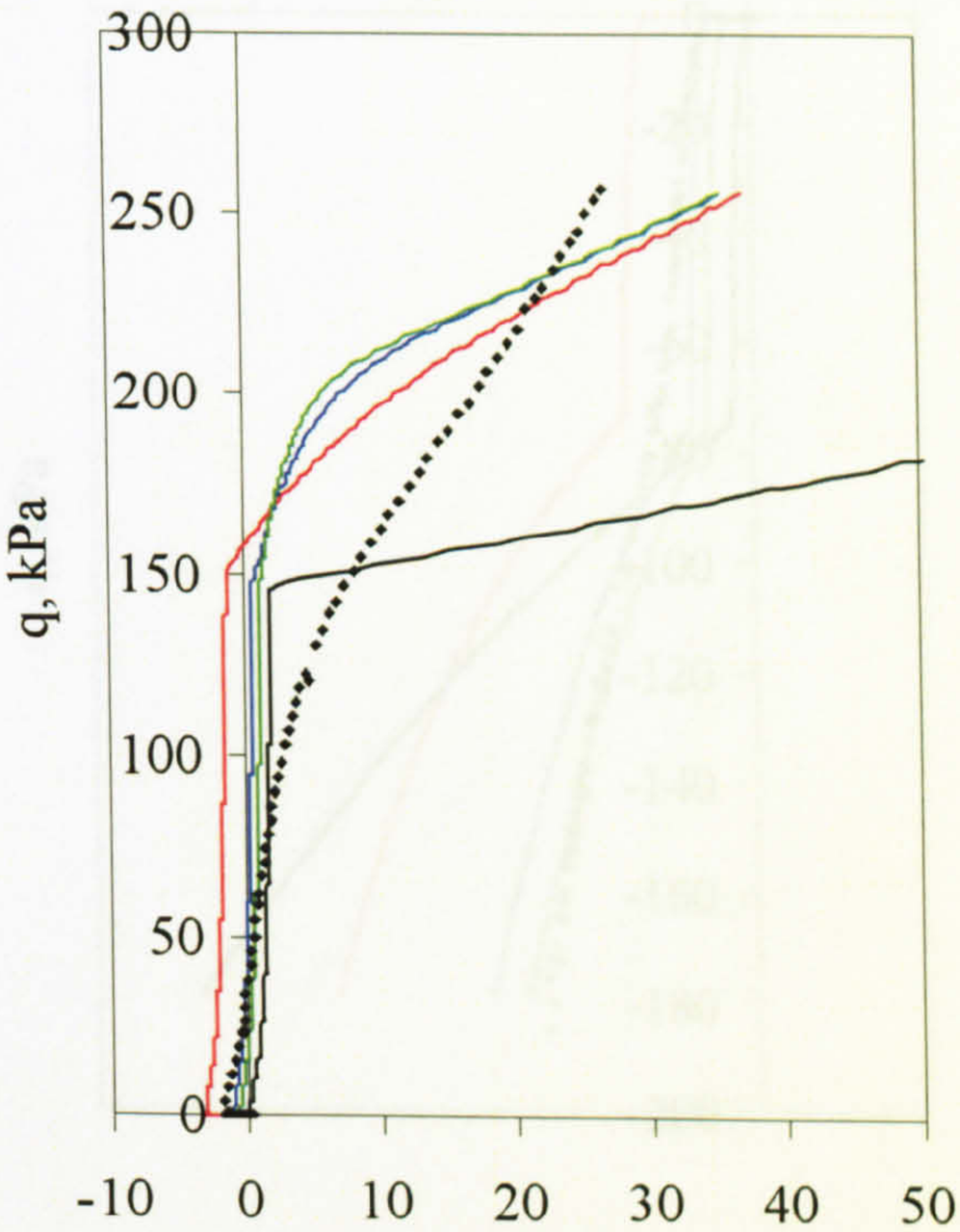

(b)

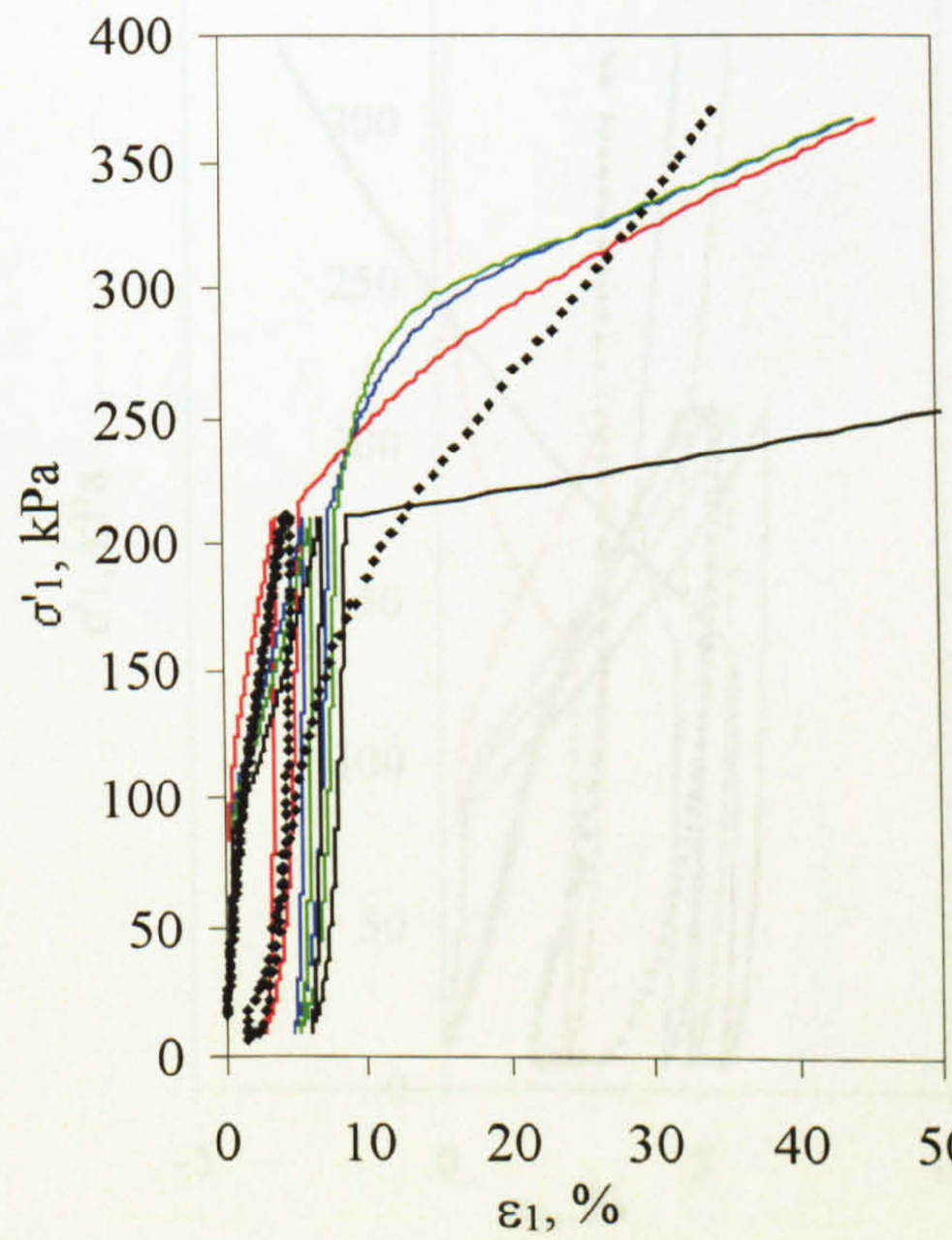

(c)

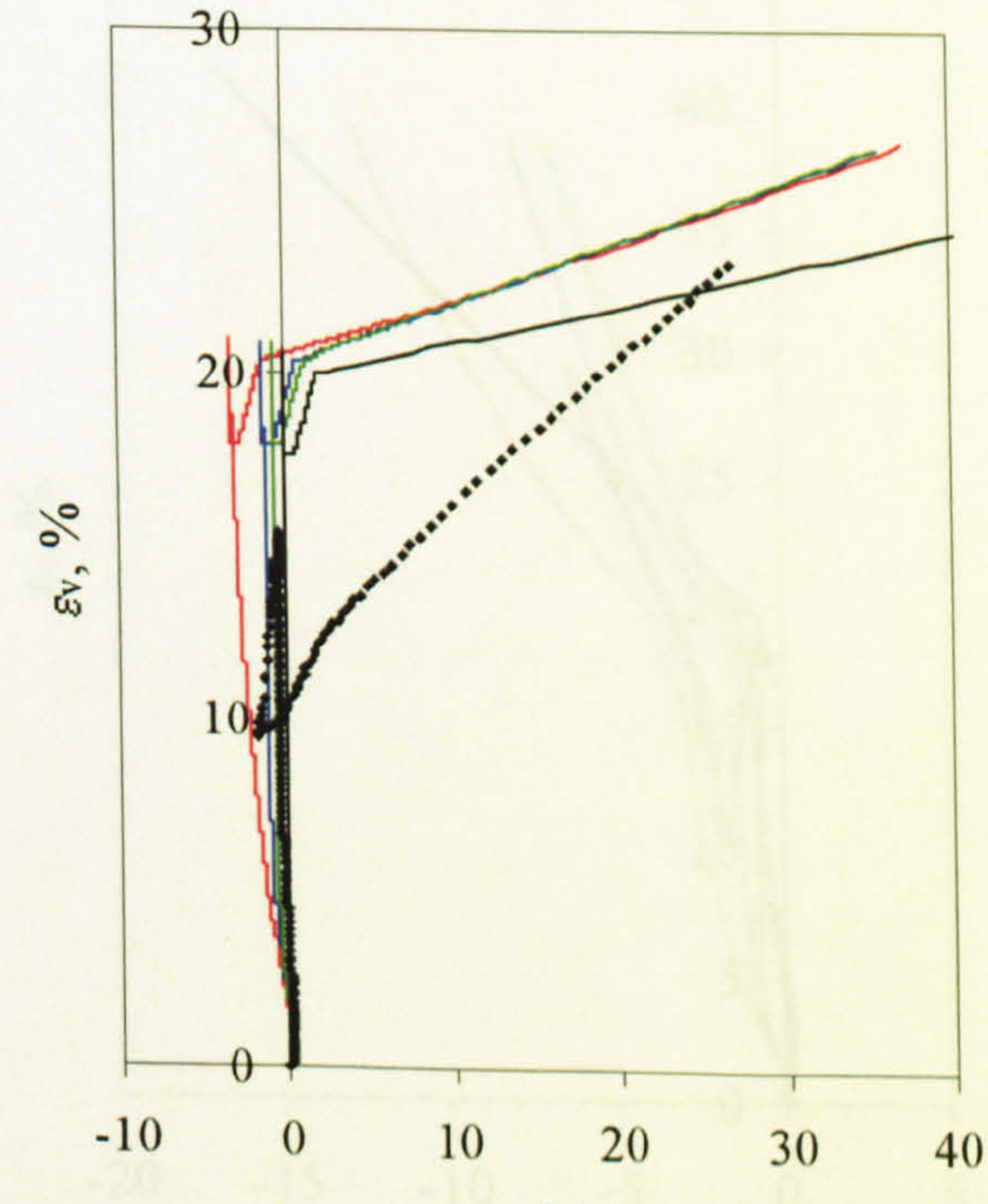

(d)

Figure 8.4. S-CLAY1 and MCC simulations of Test B4, where $\eta_1 = 0$ and $\eta_2 = 1.30$; (a) compression behaviour, (b) deviatoric stress-strain behaviour, (c) axial stress-strain behaviour, (d) strain paths.

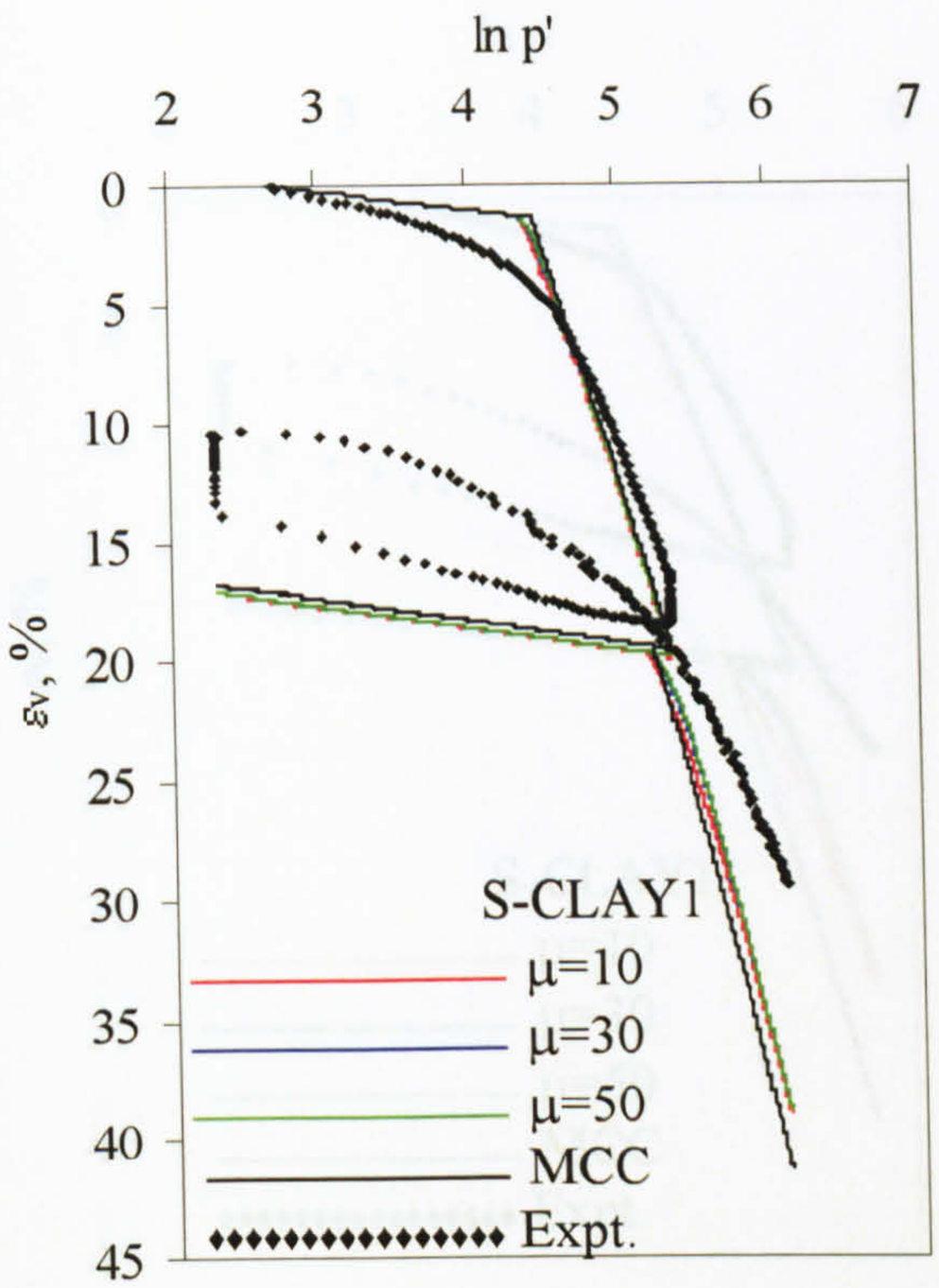

(a)

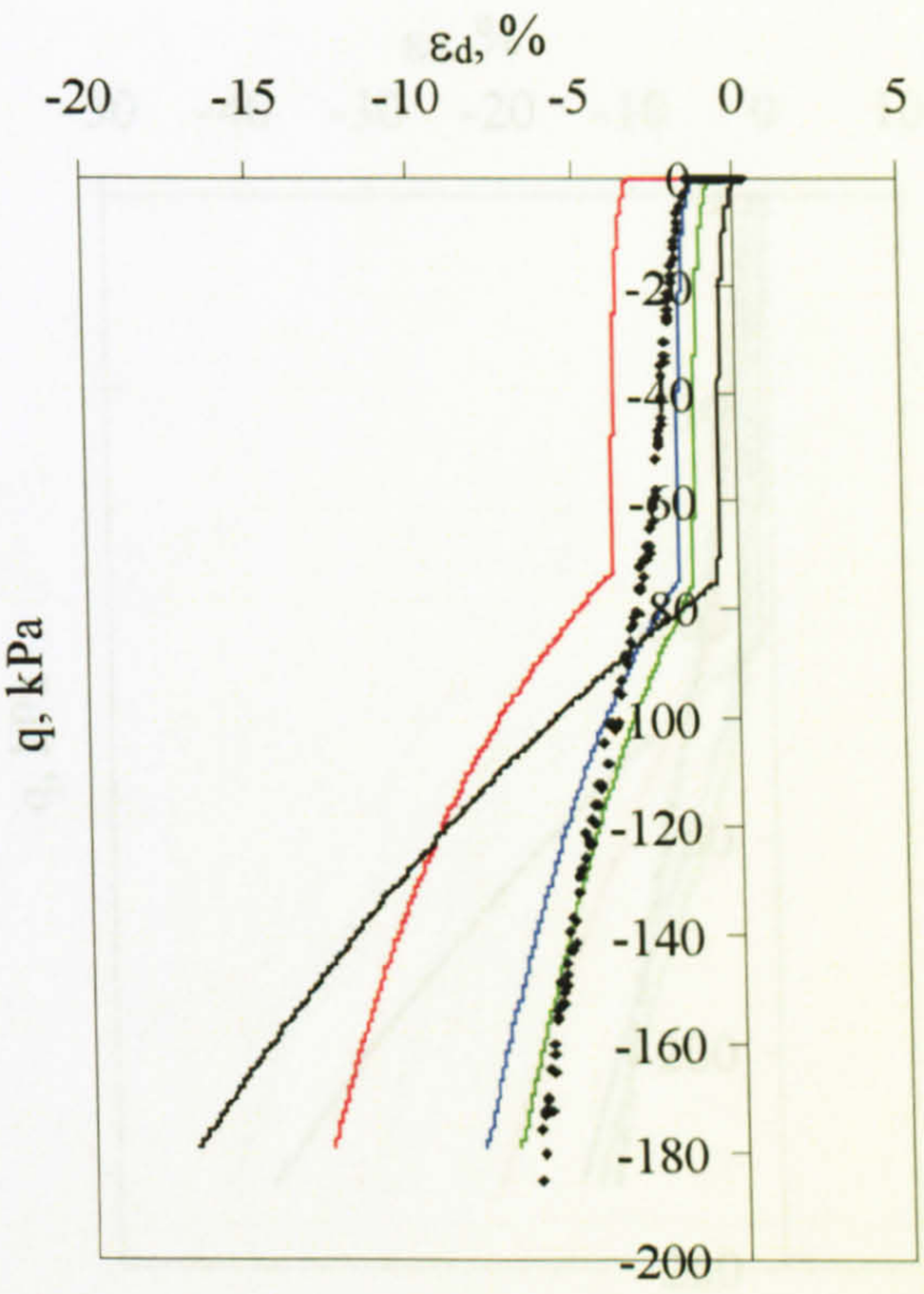

(b)

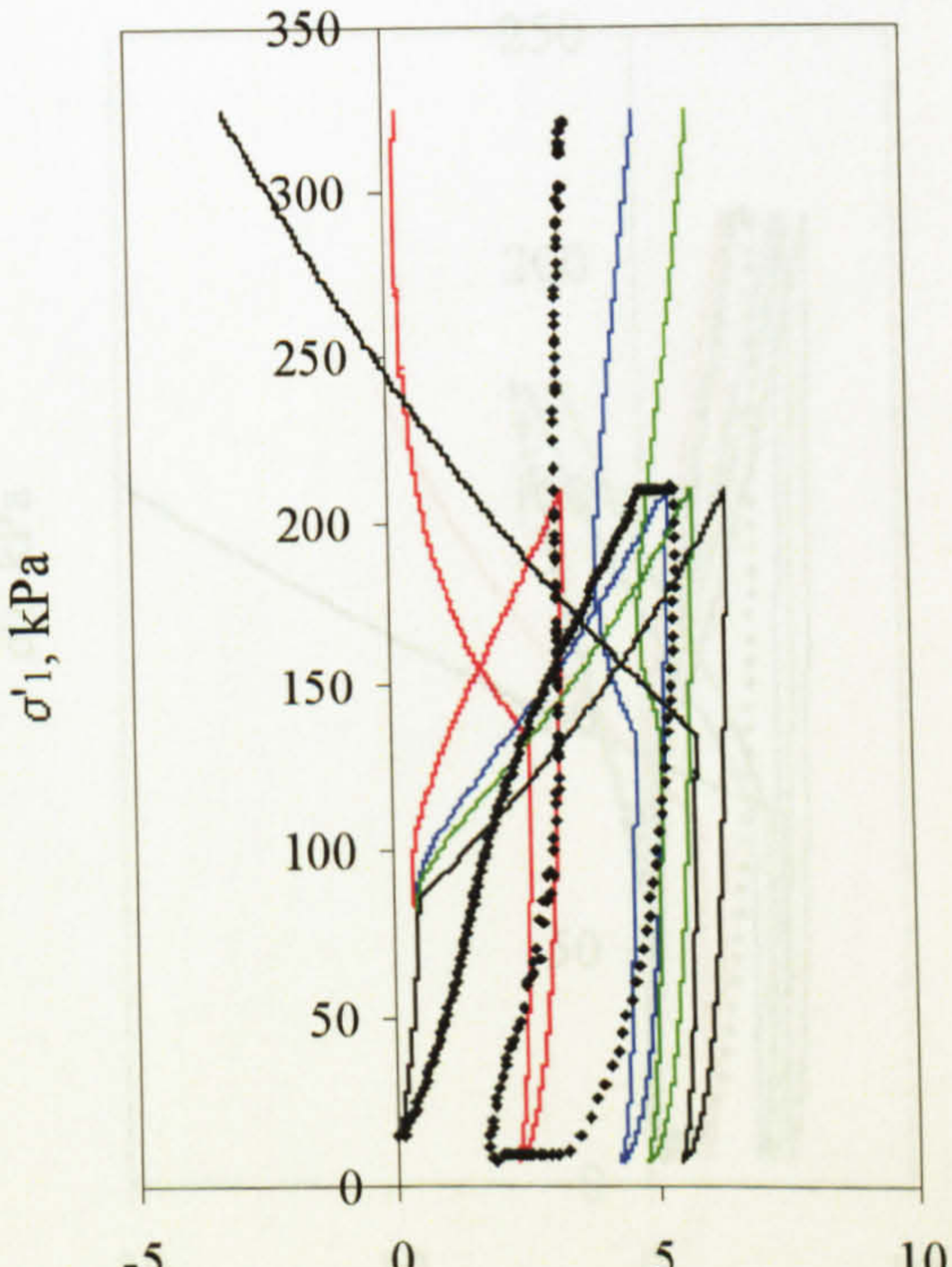

(c)

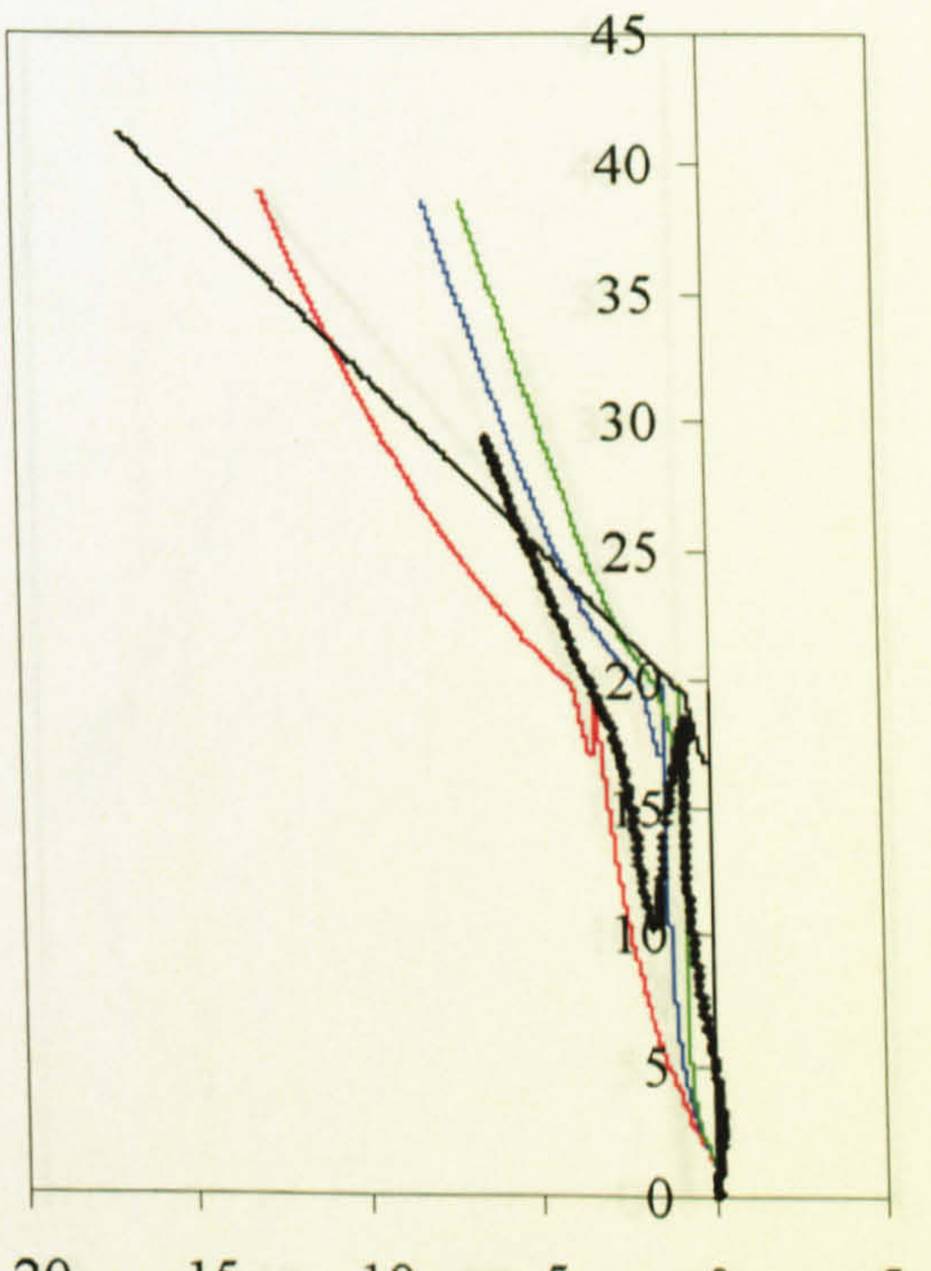

(d)

Figure 8.5. S-CLAY1 and MCC simulations of Test B5, where $\eta_1 = 0$ and $\eta_2 = -0.40$; (a) compression behaviour, (b) deviatoric stress-strain behaviour, (c) axial stress-strain behaviour, (d) strain paths.

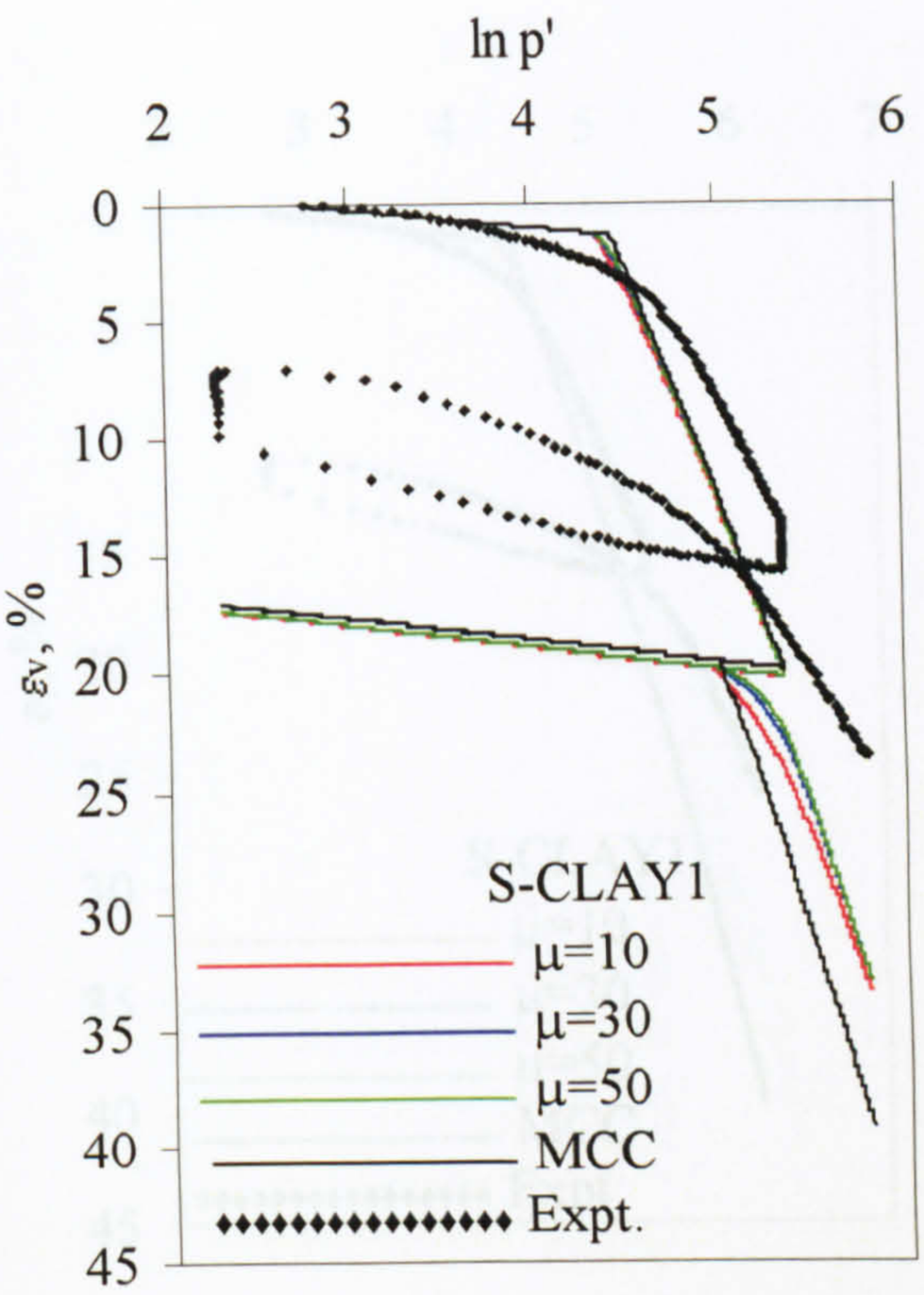

(a)

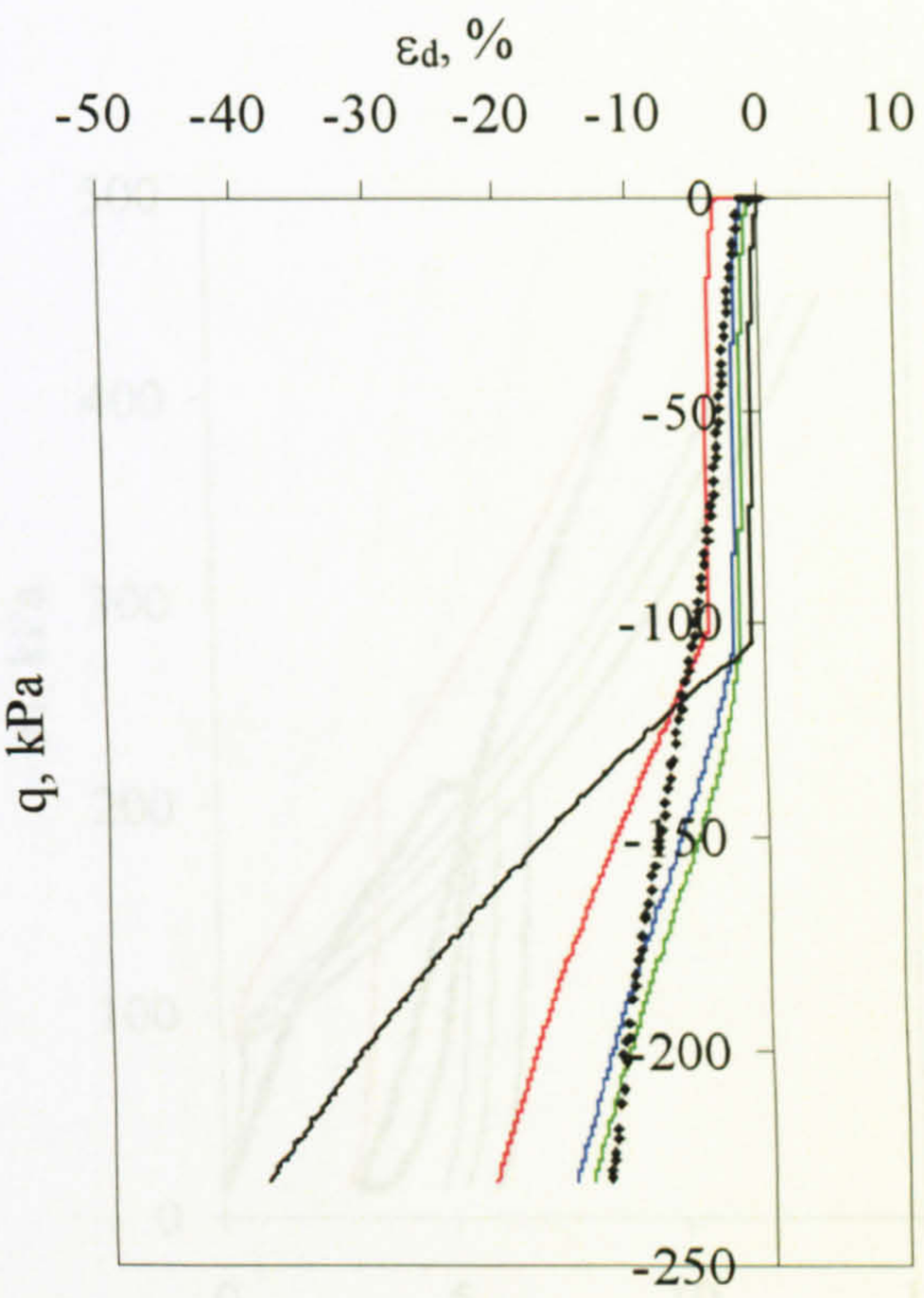

(b)

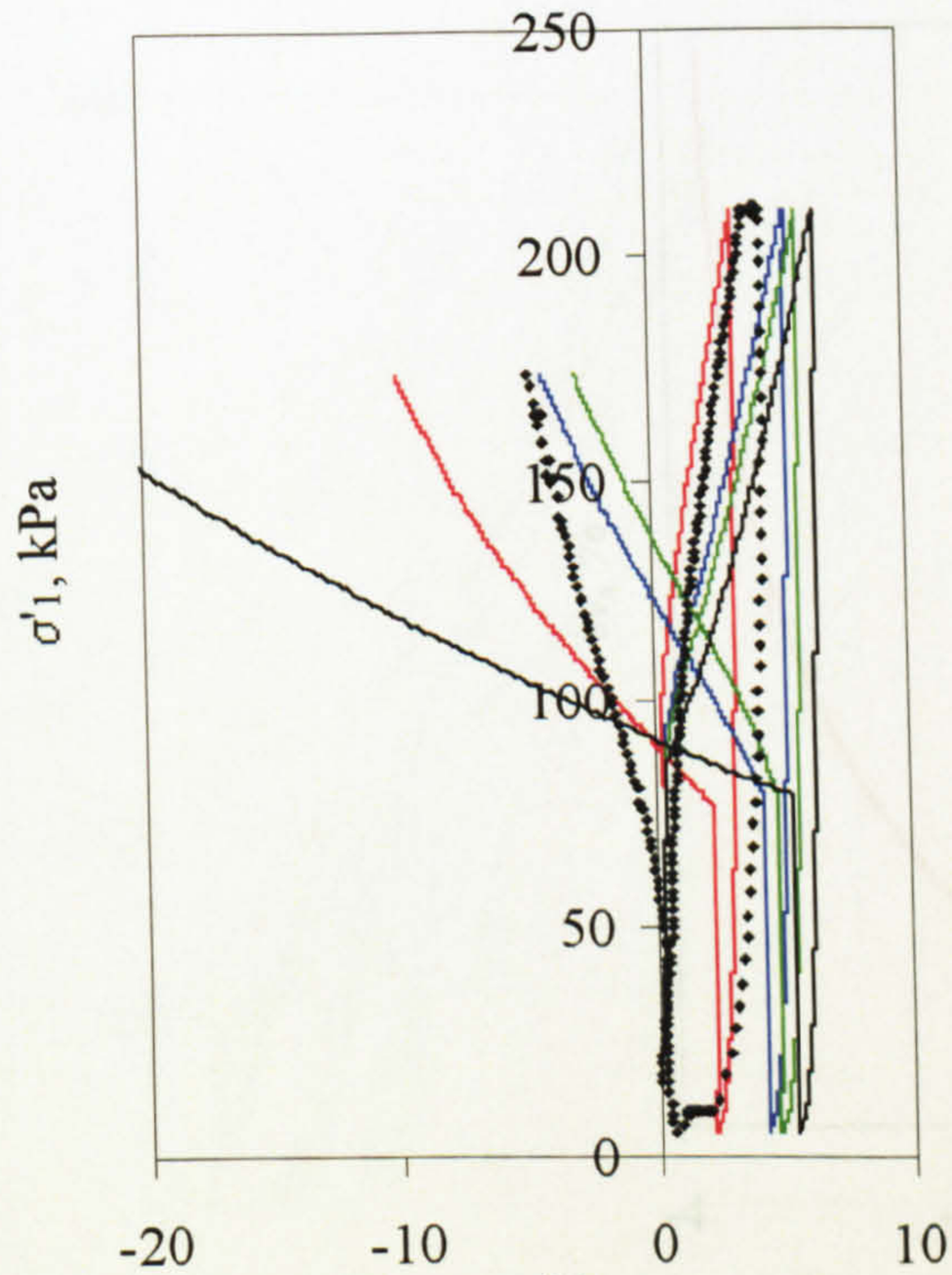

(c)

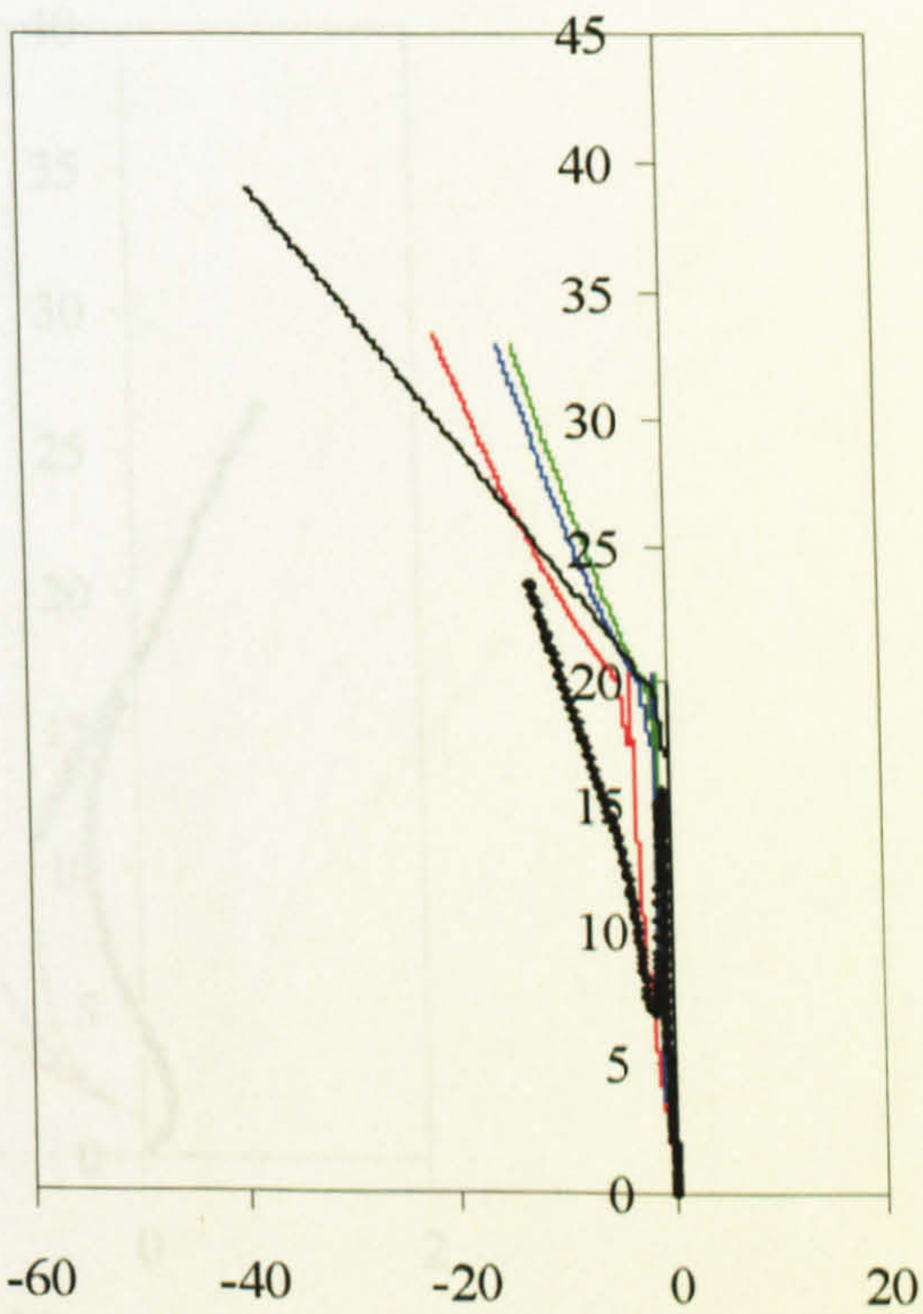

(d)

Figure 8.6. S-CLAY1 and MCC simulations of Test B6, where $\eta_1 = 0$ and $\eta_2 = -0.70$; (a) compression behaviour, (b) deviatoric stress-strain behaviour, (c) axial stress-strain behaviour, (d) strain paths.

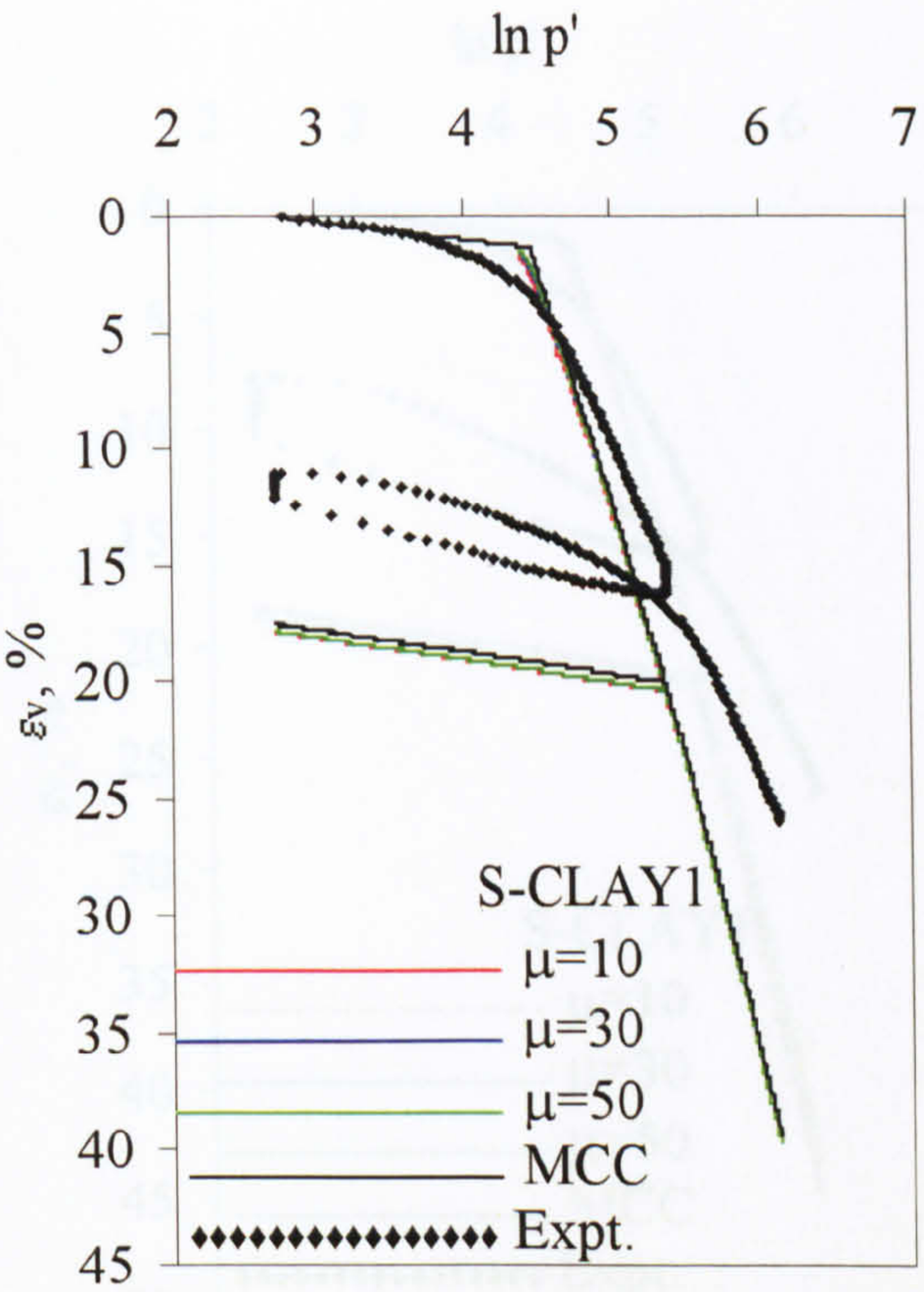

(a)

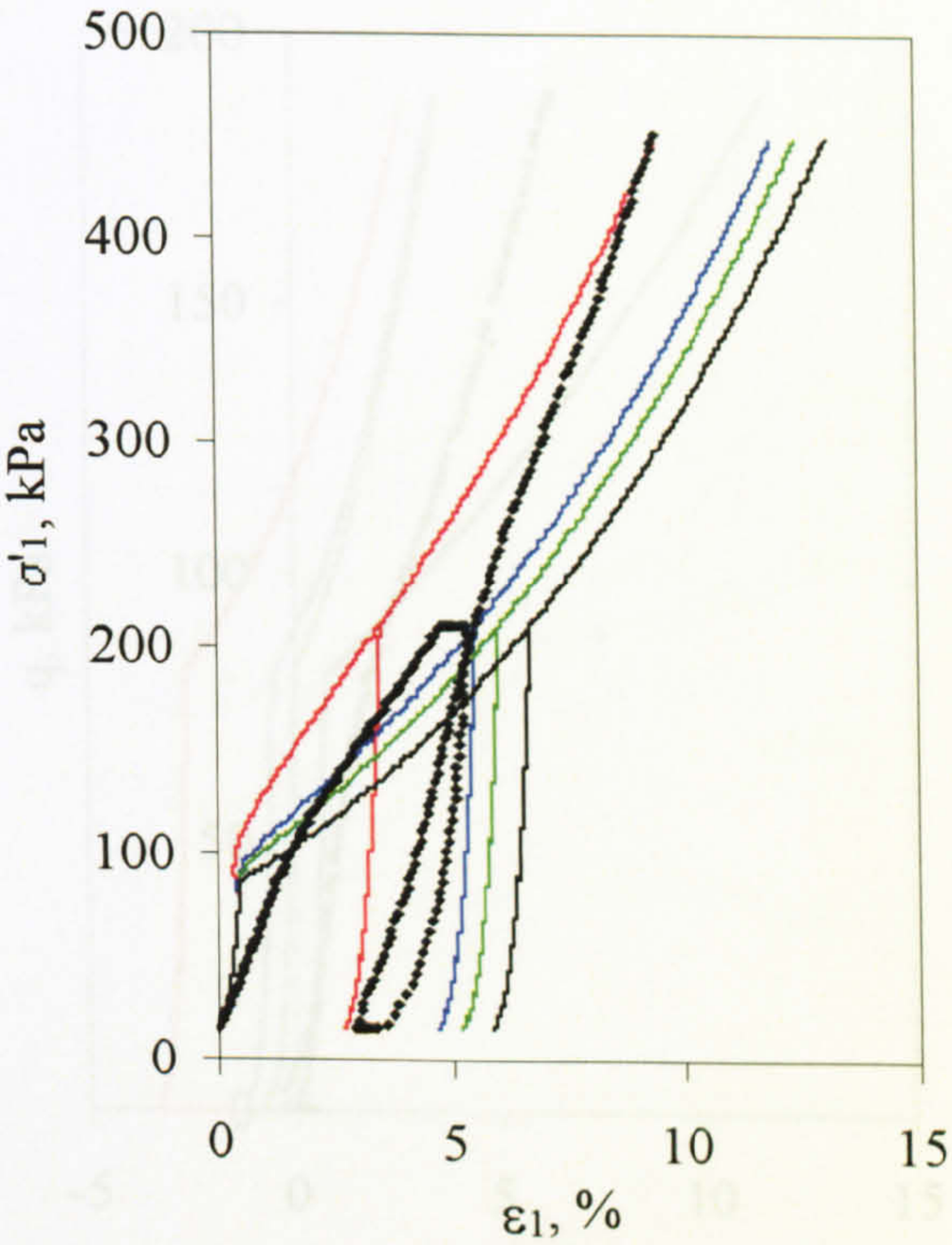

(b)

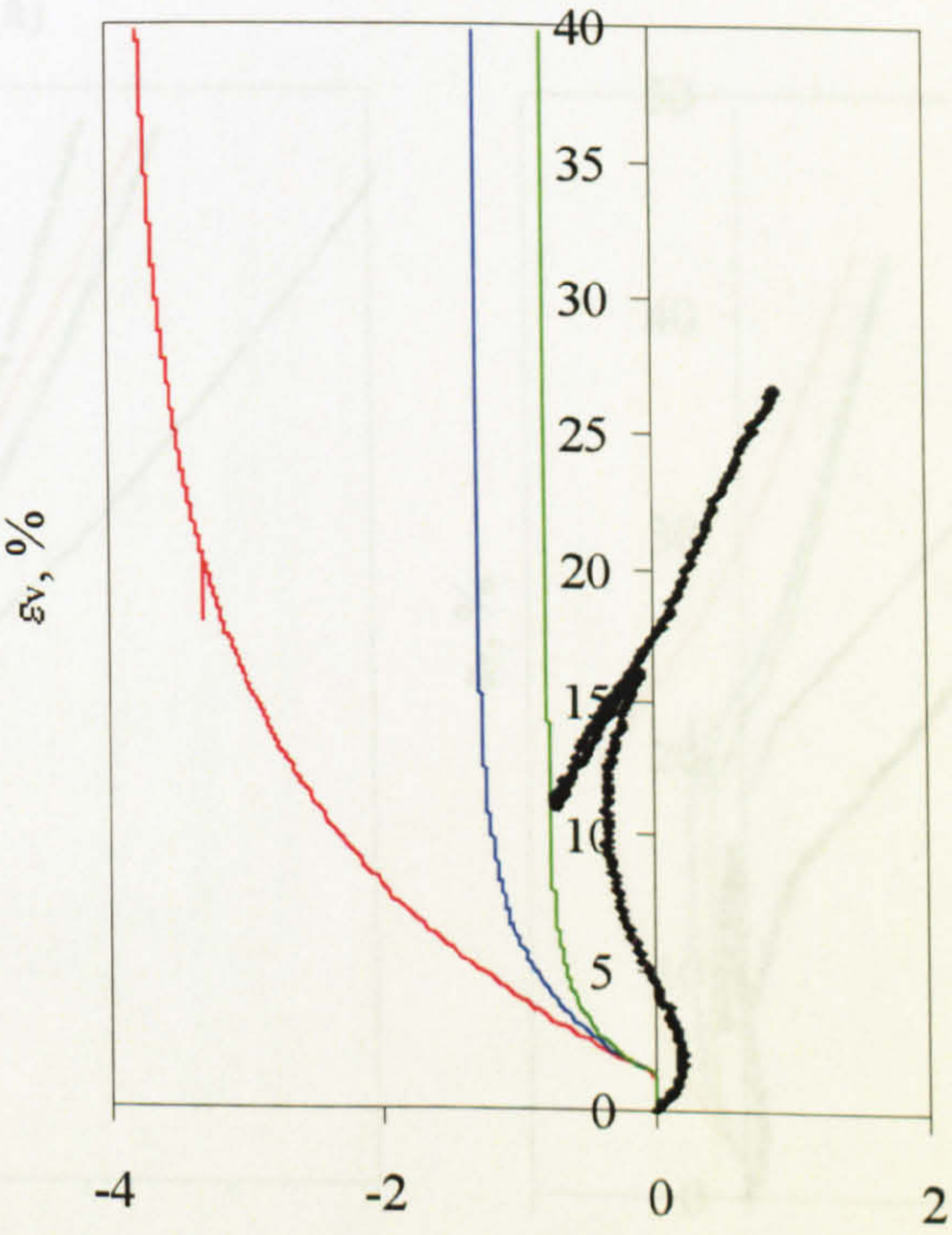

(c)

Figure 8.7. S-CLAY1 and MCC simulations of Test B7, where $\eta_1 = 0$ and $\eta_2 = 0$; (a) compression behaviour, (b) axial stress-strain behaviour, (c) strain paths.

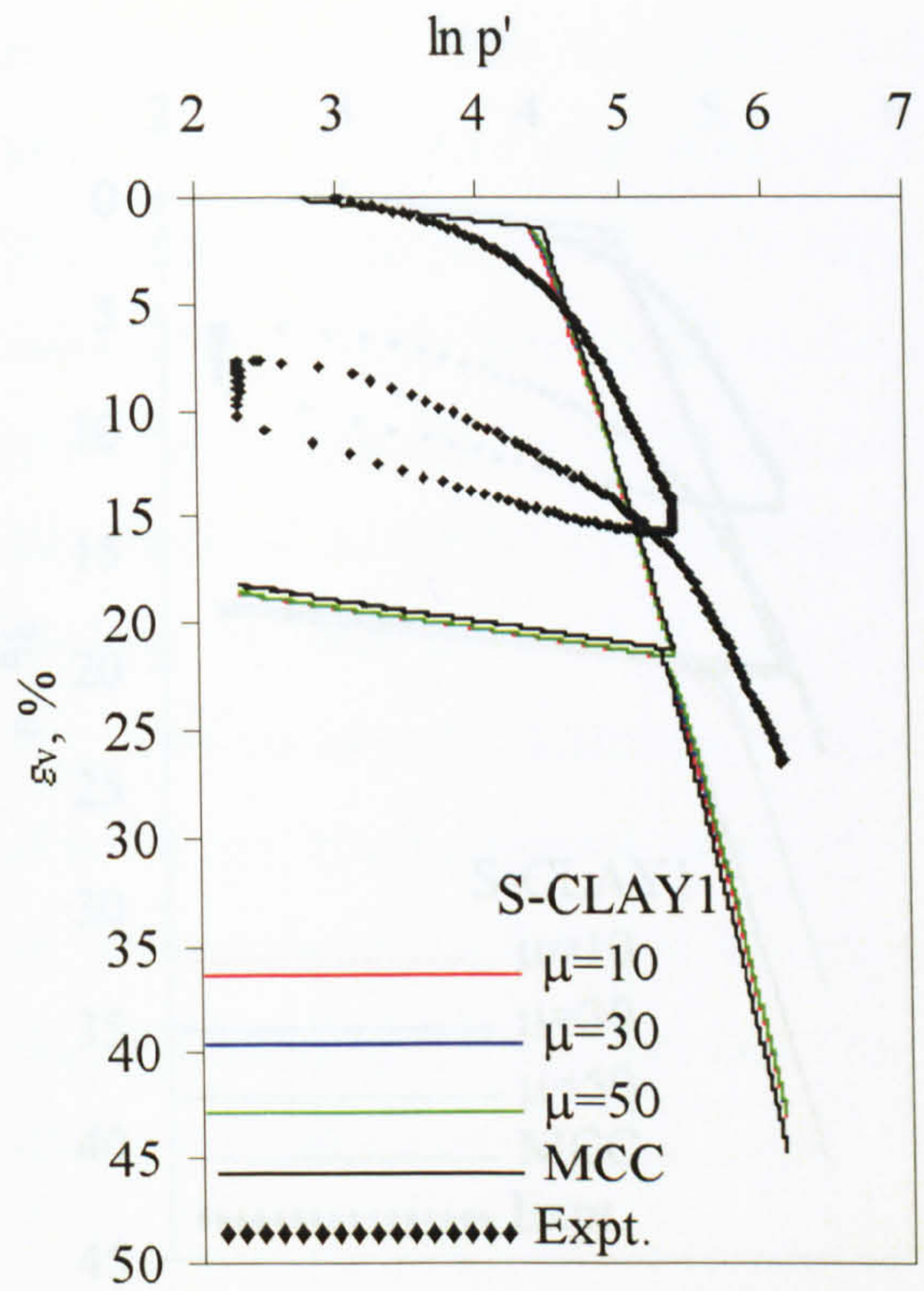

(a)

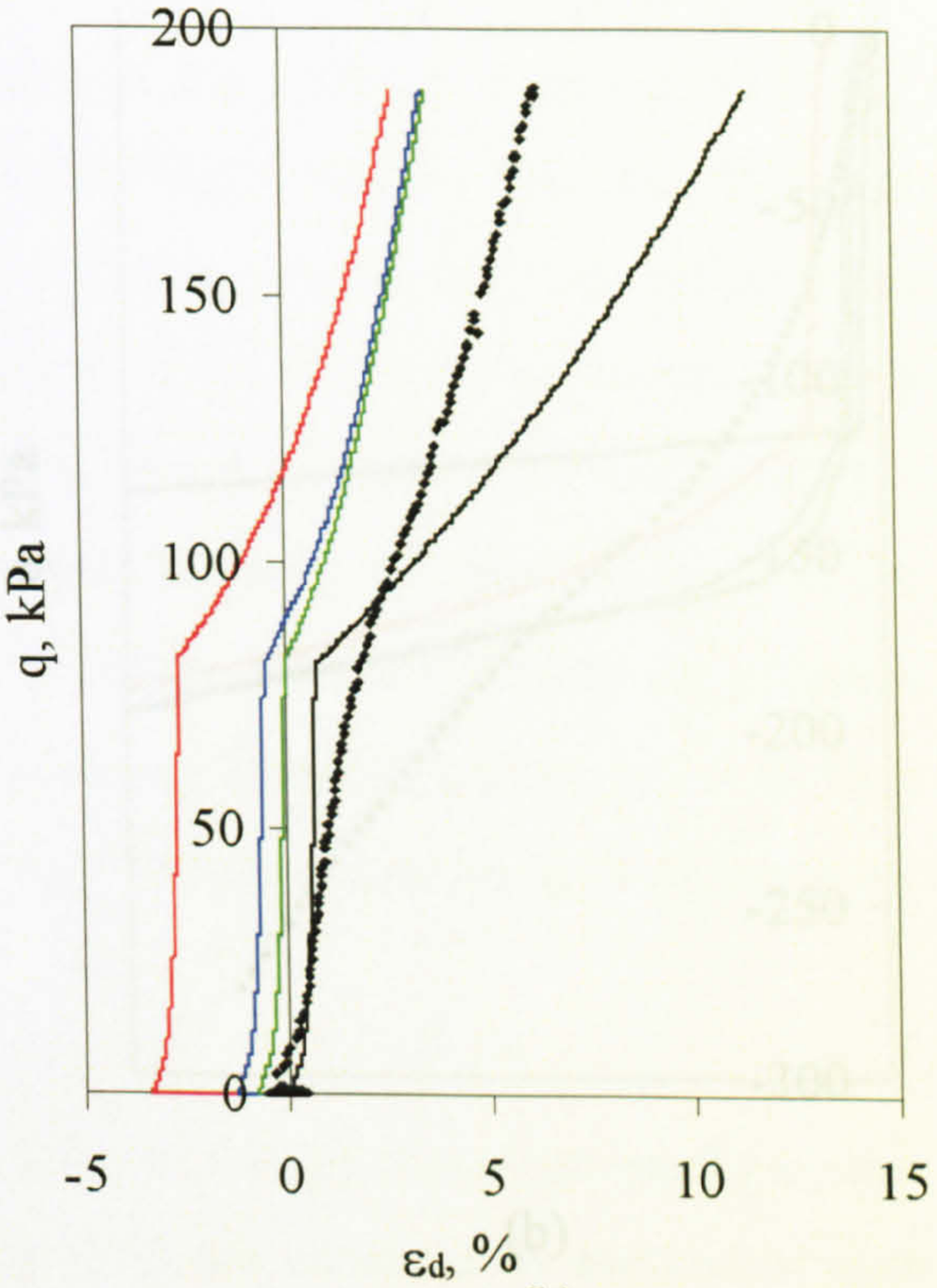

(b)

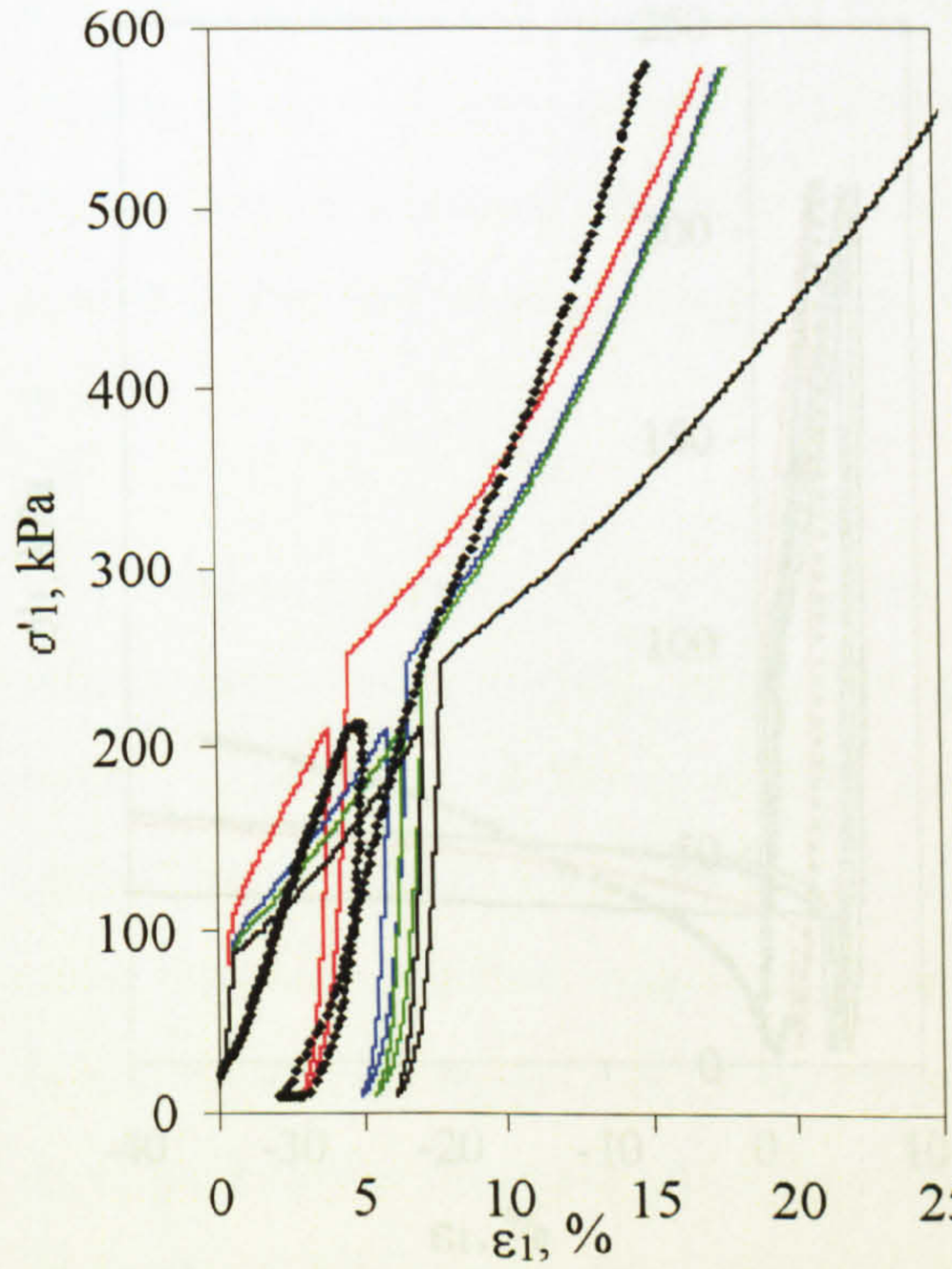

(c)

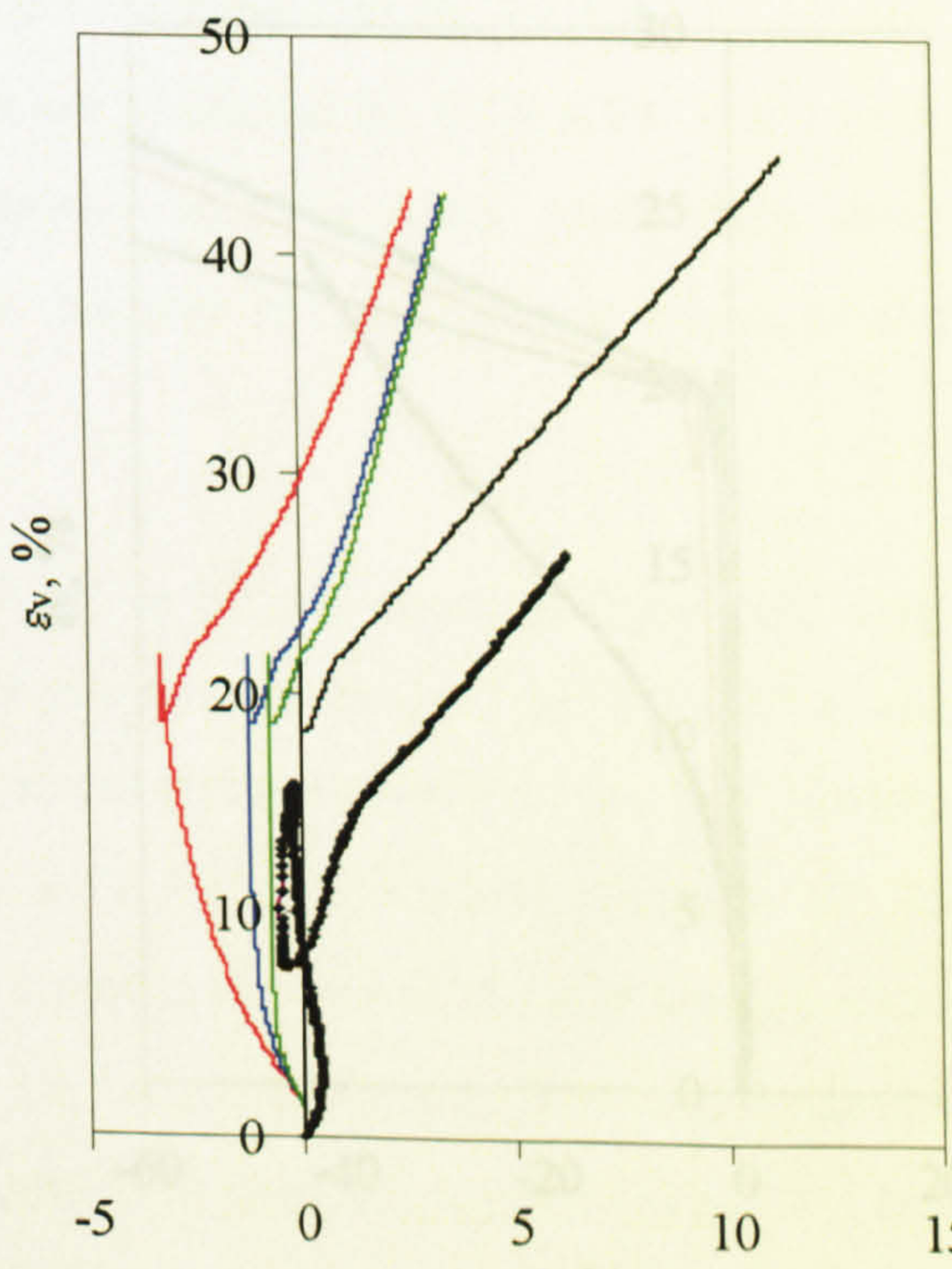

(d)

Figure 8.8. S-CLAY1 and MCC simulations of Test B8, where $\eta_1 = 0$ and $\eta_2 = 0.40$; (a) compression behaviour, (b) deviatoric stress-strain behaviour, (c) axial stress-strain behaviour, (d) strain paths.

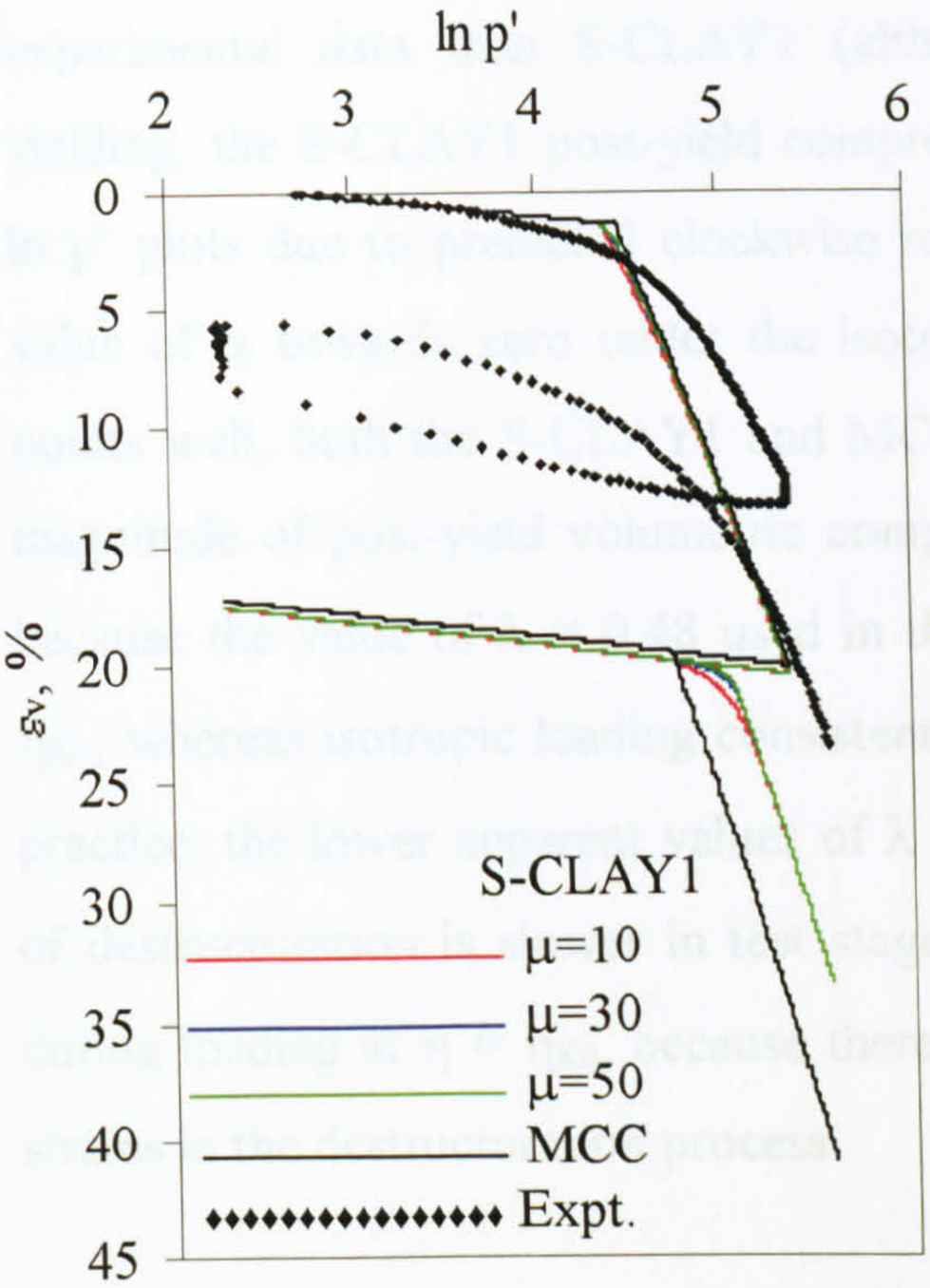

(a)

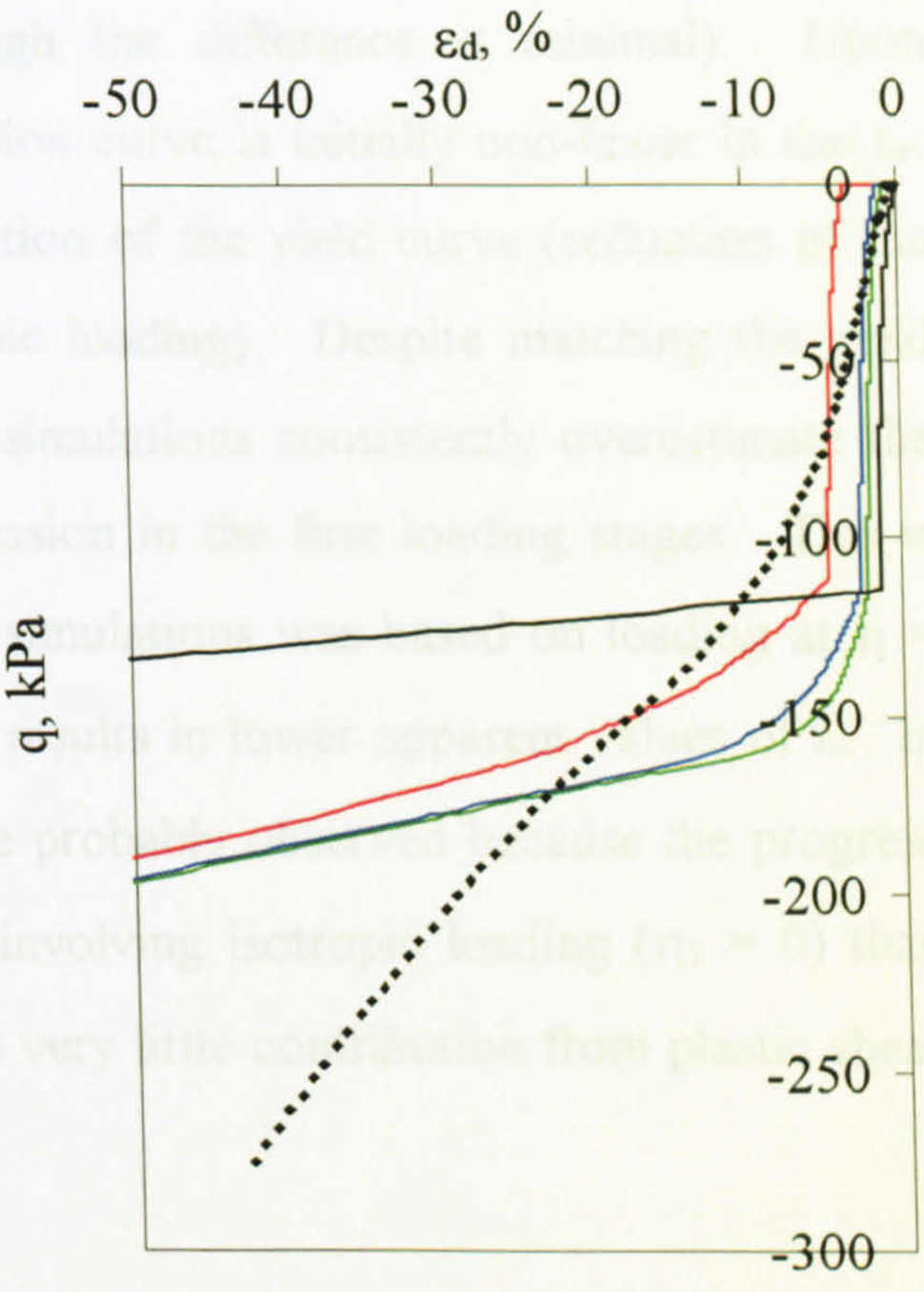

(b)

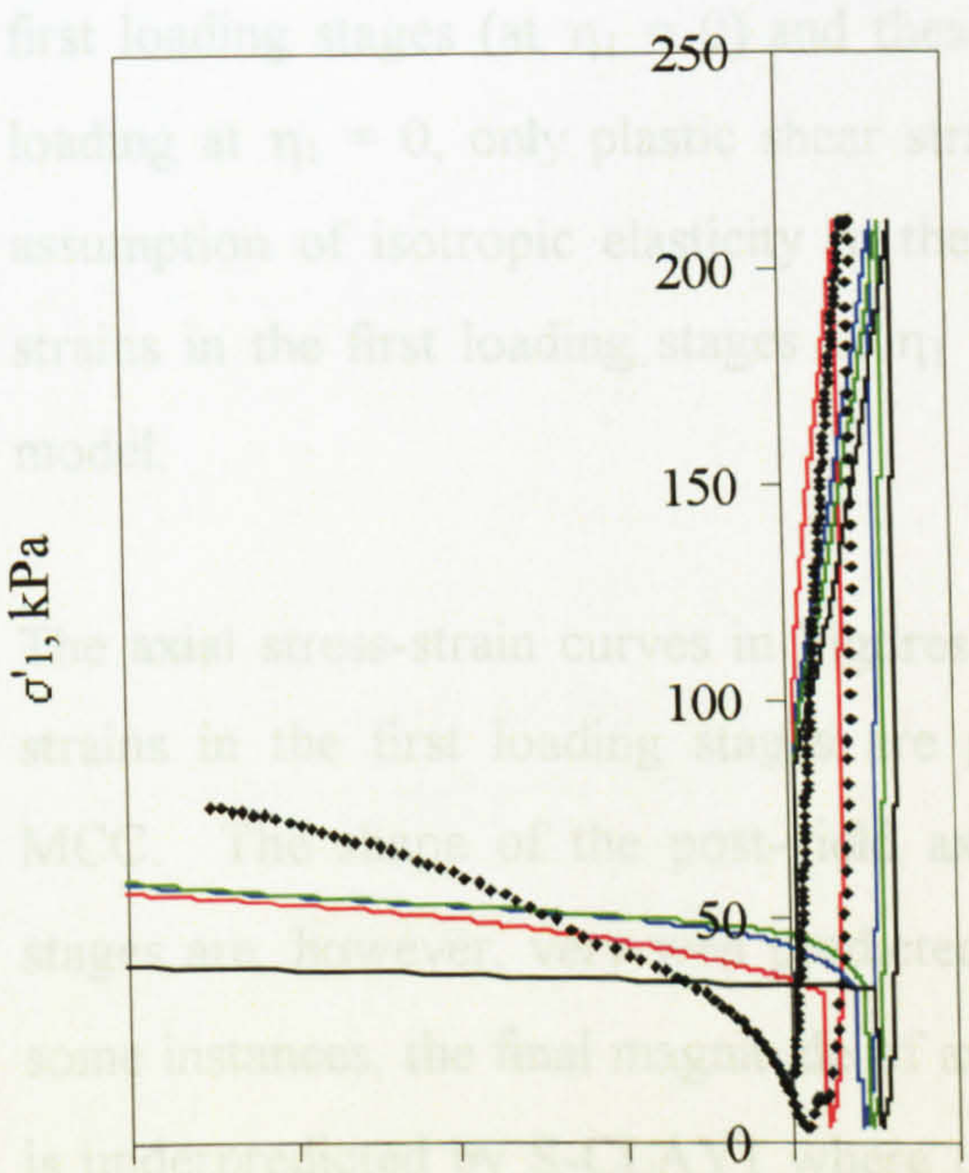

(c)

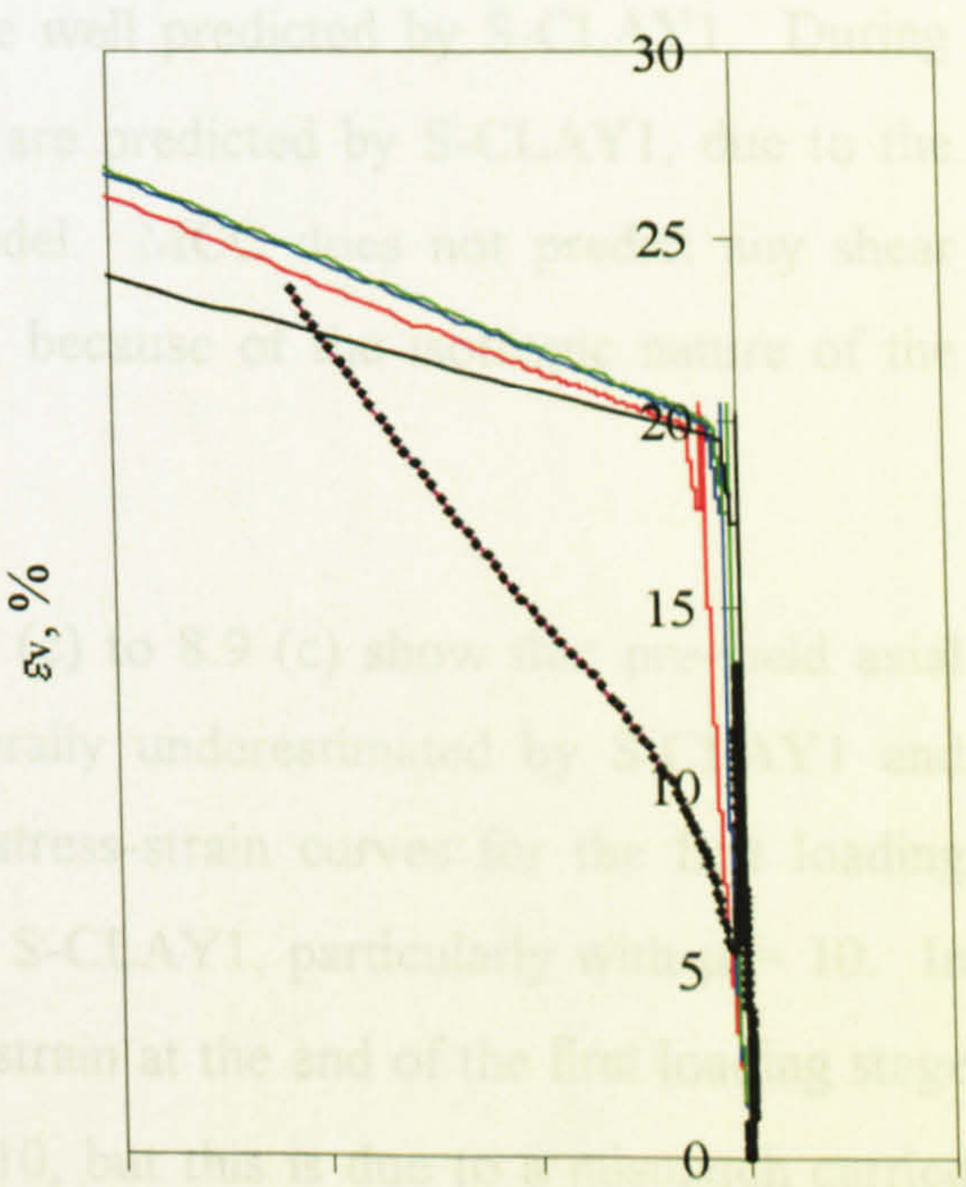

(d)

Figure 8.9. S-CLAY1 simulations of Test B9, where $\eta_1 = 0$ and $\eta_2 = -1.02$; (a) compression behaviour, (b) deviatoric stress-strain behaviour, (c) axial stress-strain behaviour, (d) predicted progress of anisotropy.

experimental data than S-CLAY1 (although the difference is minimal). Upon yielding, the S-CLAY1 post-yield compression curve is initially non-linear in the ε_v: ln p' plots due to predicted clockwise rotation of the yield curve (reduction of the value of α towards zero under the isotropic loading). Despite matching the yield points well, both the S-CLAY1 and MCC simulations consistently overestimate the magnitude of post-yield volumetric compression in the first loading stages. This is because the value of $\lambda = 0.48$ used in the simulations was based on loading at $\eta = \eta_{K0}$, whereas isotropic loading consistently results in lower apparent values of λ. In practice, the lower apparent values of λ are probably observed because the progress of destructuration is slower in test stages involving isotropic loading ($\eta_1 = 0$) than during loading at $\eta = \eta_{K0}$, because there is very little contribution from plastic shear strains in the destructuration process.

Plots of deviatoric stress-strain in Figures 8.2 (b) to 8.9 (b) show that small amounts of negative shear strain (typically about $\varepsilon_d = -1\%$) are observed by the end of each first loading stages (at $\eta_1 = 0$) and these are well predicted by S-CLAY1. During loading at $\eta_1 = 0$, only plastic shear strains are predicted by S-CLAY1, due to the assumption of isotropic elasticity in the model. MCC does not predict any shear strains in the first loading stages at $\eta_1 = 0$, because of the isotropic nature of the model.

The axial stress-strain curves in Figures 8.2 (c) to 8.9 (c) show that pre-yield axial strains in the first loading stages are generally underestimated by S-CLAY1 and MCC. The shape of the post-yield axial stress-strain curves for the first loading stages are, however, very well predicted by S-CLAY1, particularly with $\mu = 10$. In some instances, the final magnitude of axial strain at the end of the first loading stage is underpredicted by S-CLAY1 where $\mu = 10$, but this is due to a mismatch carried through from the pre-yield phase (see for example Figures 8.2 (c), 8.5 (c) and 8.7 (c). In terms of axial strains the S-CLAY1 predictions match the data more closely than MCC, even when higher values of μ are used in S-CLAY1.

During unloading after each of the first loading stages, negative shear strains developed and this response is consistent with the positive shear strains developed in

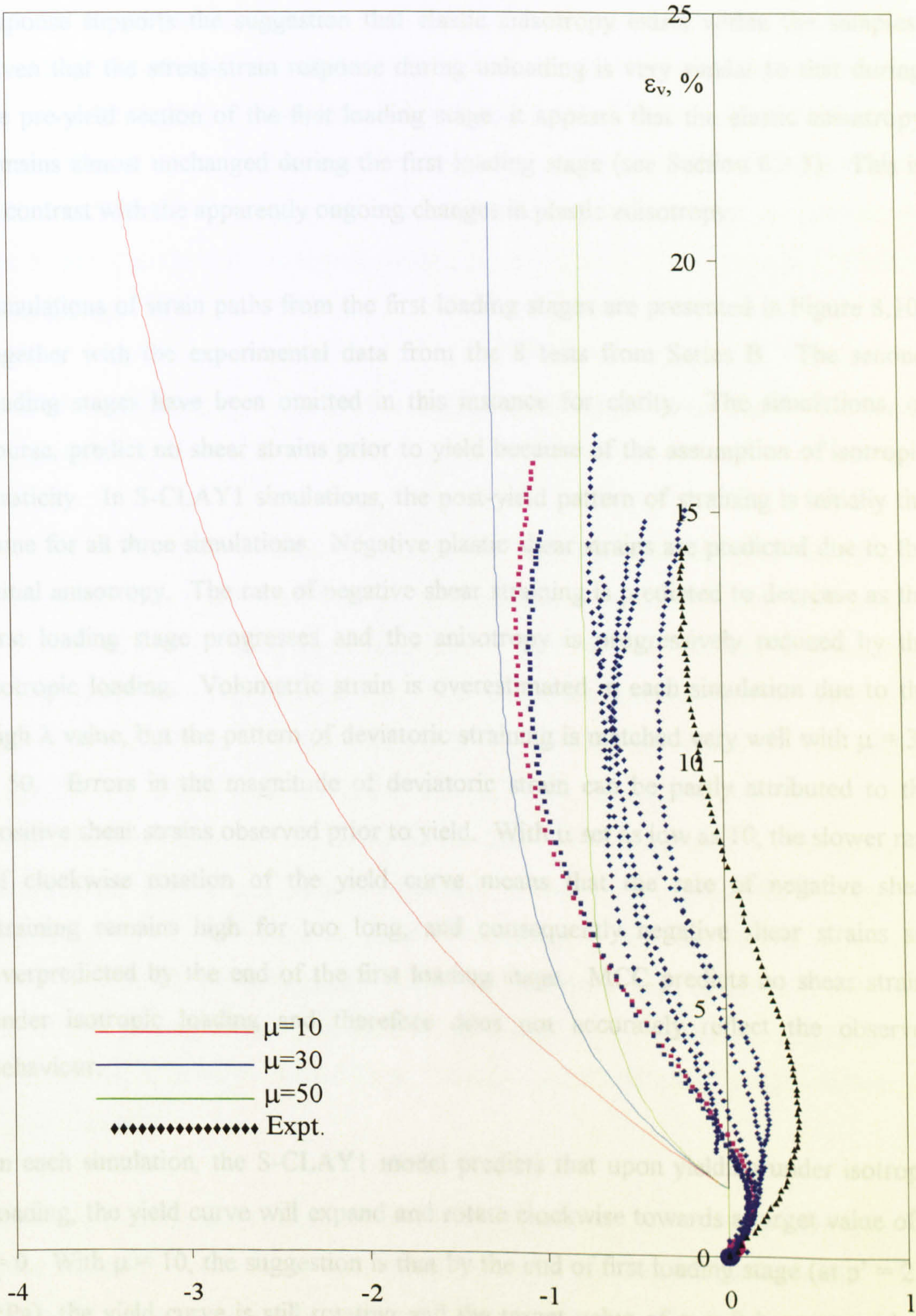

Figure 8.10. S-CLAY1 strain path simulations for first loading stages in Test Series B.

the elastic part of the first loading stages (see Section 6.3.5). This unloading response supports the suggestion that elastic anisotropy exists within the samples. Given that the stress-strain response during unloading is very similar to that during the pre-yield section of the first loading stage, it appears that the elastic anisotropy remains almost unchanged during the first loading stage (see Section 6.3.5). This is in contrast with the apparently ongoing changes in plastic anisotropy.

Simulations of strain paths from the first loading stages are presented in Figure 8.10, together with the experimental data from the 8 tests from Series B. The second loading stages have been omitted in this instance for clarity. The simulations, of course, predict no shear strains prior to yield because of the assumption of isotropic elasticity. In S-CLAY1 simulations, the post-yield pattern of straining is initially the same for all three simulations. Negative plastic shear strains are predicted due to the initial anisotropy. The rate of negative shear straining is predicted to decrease as the first loading stage progresses and the anisotropy is progressively reduced by the isotropic loading. Volumetric strain is overestimated in each simulation due to the high λ value, but the pattern of deviatoric straining is matched very well with $\mu = 30$ - 50. Errors in the magnitude of deviatoric strain can be partly attributed to the positive shear strains observed prior to yield. With μ set as low as 10, the slower rate of clockwise rotation of the yield curve means that the rate of negative shear straining remains high for too long, and consequently negative shear strains are overpredicted by the end of the first loading stage. MCC predicts no shear strains under isotropic loading and therefore does not accurately reflect the observed behaviour.

In each simulation, the S-CLAY1 model predicts that upon yielding under isotropic loading, the yield curve will expand and rotate clockwise towards a target value of $\alpha = 0$. With $\mu = 10$, the suggestion is that by the end of first loading stage (at $p' = 210$ kPa), the yield curve is still rotating and the target value of $\alpha = 0$ has not yet been reached. Increasing μ to 30 means that yield curve rotation is complete by around $p' = 170$ kPa. With μ set to 50, the model predicts that rotation is complete as early as $p' = 140$ kPa. The experimental data can be used to estimate the orientation of the yield curve at certain stages of loading. In the following discussion it is assumed that

the use of an associated flow rule is valid. With reference to Figure 8.10, it would be expected that clockwise rotation would be complete where the negative shear strains cease to develop. In each test, this phenomenon occurs at around a range of 10 - 13 % volumetric strain. From cross-referencing of the individual test data, this corresponds to a mean effective stress range of p' = 150 – 170 kPa. Therefore, it is likely that the rate of changing anisotropy is best represented with μ set between 30 and 50 and that the yield curve has rotated clockwise to $\alpha = 0$ by the end of the first loading stage.

8.3.2 Second loading stages: tests reloaded at high stress ratio in triaxial compression

Tests B2, B3 and B4 involved second loading stages at high values of η_2 in triaxial compression (see Figures 8.2 – 8.4). As discussed in Section 6.6, the yield stresses predicted by S-CLAY1 are significantly higher than the yield stresses identified from v: ln p' plots of the experimental data. This is on the assumption that the yield curve has rotated clockwise to a new orientation of $\alpha = 0$ by the end of the first loading stage. Compression plots in Figures 8.2 (a) – 8.4 (a) indicate that the S-CLAY1 simulations are relatively insensitive to the choice of parameter μ. The post-yield compression curves are initially rounded, reflecting the predicted changes in anisotropy. This curvature is most pronounced in test B4 where changes in anisotropy are initially very rapid. Despite the overprediction of the yield stresses in the second loading stages, post-yield compressions in the second loading stages are greatly overpredicted by S-CLAY1 in Tests B2 and B3, although the predictions are better than MCC.

Plots of deviatoric stress-strain behaviour in Figures 8.2 (b) – 8.4 (b) show that pre-yield deviatoric strains in the second loading stages are underestimated by S-CLAY1 and MCC. Post-yield deviatoric stress-strain behaviour in the second loading stage is predicted better by S-CLAY1 than by MCC for all three tests. Differences between experimental and predicted yield points may be due to uncertainty in the identification of yield points from the test data. In Tests B2 and B3 the post-yield deviatoric stiffness is predicted to gradually increase as the second loading stage

progresses and this compares well with the test data. In contrast, in Test B4, the S-CLAY1 predictions show the post-yield deviatoric stiffness initially decreasing (Figure 8.4 (b)). Although the S-CLAY1S predictions do not accurately match the test data in Figure 8.4 (b), the prediction is qualitatively correct. MCC massively overpredicts the final deviatoric strains in Tests B2, B3 and B4 (the MCC simulation shown in Figures 8.2 (b) – 8.4 (c) have been truncated well before the end of the test, in order to use a reasonable scale for ε_d in the graphs).

Plots of axial stress-strain in Figures 8.2 (c) – 8.4 (c) show similar predictions to the deviatoric stress-strain plots. Again, MCC massively overestimates the amount of post-yield axial straining in each of Tests B2, B3 and B4.

Strain paths for Tests B2, B3 and B4 are shown in Figures 8.2 (d), 8.3 (d) and 8.4 (d) respectively. In each test the initial pre-yield response is well matched by both models during the second loading stages. In the second loading stages of Tests B2 and B3, S-CLAY1 predicts post-yield strain paths that agree well with the test data, while MCC tends to overpredict the amount of post-yield shear strains. In Test B4, however, both models significantly overestimate the amount of post-yield plastic shear strains, although S-CLAY1 performs better than MCC. One possible explanation for this disagreement is that the assumption of an associated flow rule is not accurate. Alternatively, it may be that the estimated value of the critical state stress ratio in triaxial compression, M_C, is inaccurate. If M_C has been estimated incorrectly, even in the order of ± 0.05, this would significantly alter the predicted strain path at high stress ratios.

8.3.3 Tests reloaded at low stress ratios in triaxial compression

Two tests in Series B involved second loading stages at low values of η. Test B7 was reloaded at $\eta_2 = 0$ (see Figure 8.7) and Test B8 was reloaded at $\eta_2 = 0.40$ (see Figure 8.8). The yield stress obtained from the v: ln p' plot from the experimental data from both Tests B7 and B8 are well matched by S-CLAY1. Figures 8.7 (a) and 8.8 (a) shows that the volumetric strains predicted in the S-CLAY1 simulations are very insensitive to changes in parameter μ, due to the fact that very little rotational

hardening is predicted in either test, the yield curve having rotated clockwise towards $\alpha = 0$ during the first loading stage. As a consequence, the S-CLAY1 simulations are very similar to MCC predictions. However, the predicted post-yield gradient of the compression curve in both tests is much higher than in the experimental data. This causes the post-yield compression to be greatly overpredicted.

Figure 8.8 (b) shows that S-CLAY1 matches the post-yield deviatoric stress-strain behaviour very well, while MCC overestimates the post-yield deviatoric strains. Plots of axial strain in Figures 8.7 (b) and 8.8 (c) show that both S-CLAY1 and MCC model predictions match the experimental data reasonably well, although tend to overestimate the post-yield axial strains (MCC more so than S-CLAY1).

Strain paths for Tests B7 and B8 are shown in Figures 8.7 (c) and 8.8 (d) respectively. In the first and second loading stages of Test B7, MCC predicts no shear strains. Once rotational hardening is complete and the yield curve has rotated to $\alpha = 0$, S-CLAY1 also predicts no further development of shear strains. As previously discussed in Section 6.3, the positive shear strains recorded in the test data may be due to anisotropy of elastic behaviour, or measurement errors. In the case of Test B8, MCC predicts the post-yield strain path very well during second loading, whilst S-CLAY1 predicts a strain path gradient that is too high, particularly with μ set to 30 or 50.

8.3.4 Tests reloaded in triaxial extension

Three tests in Series B involved a second loading stage in triaxial extension. These were Test B5 ($\eta_2 = -0.40$, see Figure 8.5), Test B6 ($\eta_2 = -0.70$, see Figure 8.6) and Test B9 ($\eta_2 = -1.02$, see Figure 8.9). Yield points taken from v: ln p' plots for these second loading stages are reasonably well matched by both the S-CLAY1 and MCC simulations. The S-CLAY1 model predicts clockwise rotation of the yield curve, to a negative value of α in each case. Figures 8.5, 8.6 and 8.9 show that the deviatoric and axial stress-strain behaviour predicted by S-CLAY1 is very sensitive to changes in parameter μ. Compression plots in Figures 8.5 (a), 8.6 (a) and 8.9 (a) show that the predicted gradients of the post-yield compression curve for both S-CLAY1 and

MCC are generally higher than observed in the test data. However, S-CLAY1 shows considerable improvement over MCC in the prediction of post-yield volumetric strains during the second loading stages, particularly at higher negative values of η_2, in Tests B6 and B9.

Plots of deviatoric stress-strain behaviour in Figures 8.5 (b) and 8.6 (b) show that both pre-yield and post-yield responses are well matched by S-CLAY1. This is also the case for predictions of axial strain in Figures 8.5 (c) and 8.6 (c). The deviatoric behaviour is particularly well matched by the S-CLAY1 simulation in Figure 8.5 (b) where μ = 30 - 50, but MCC overpredicts the magnitude of negative shear strains. This can be investigated further by examining the axial stress-strain behaviour in Figure 8.5 (c). At the onset of yield, the experimental data shows slight axial extension followed by very slight axial compression during the remainder of the test. Qualitatively, this response is matched very well by S-CLAY1. However, MCC predicts considerable axial extension throughout the remainder of the test and is therefore highly inaccurate. The good matches in Figure 8.5 (b) and 8.5 (c) suggest that the ability of S-CLAY1 to model both the initial shape of the yield curve and subsequent changes in yield curve orientation has resulted in improved predictions of the axial and deviatoric behaviour over MCC.

Plots showing the strain paths are shown for Test B5 (Figure 8.5 (d), Test B6, (Figure 8.6 (d)) and Test B9 (Figure 8.9 (d)). In the second loading stages of Tests B5 and B6, the strain path directions are very well matched by S-CLAY1, while MCC tends to overpredict the negative plastic shear strains. Test B9 involved a second loading stage at a very high negative stress ratio. In this instance, Figure 8.9 (d) shows that both models grossly misrepresent the strain path direction. As can be seen in Figures 8.9 (b) and (c), both models grossly overestimate the amount of deviatoric and axial strains. As with the second loading stage of Test B4, this suggests that the assumption of an associated flow rule may be inaccurate at very high stress ratios. Alternatively, it is possible that the model predictions are extremely sensitive to the choice of the critical state stress ratio M_E and may therefore be subject to error.

8.3.5 Conclusion

During the isotropic first loading stages in Test Series B experimentally observed yield points are well matched by S-CLAY1, but are generally slightly overpredicted by MCC. In terms of volumetric compression during this isotropic loading, both S-CLAY1 and MCC significantly overpredict the post-yield rate and overall magnitude of volumetric straining. This is due to the fact that the adopted value of λ is based on loading at η_{K0} and is much greater than the apparent λ value observed during isotropic compression. It is likely that this can be attributed to the influence of destructuration. Calibration of the parameter μ is impossible when using the compression simulations, since the model is insensitive to changes in μ under isotropic compression in the first loading stage. Simulations of axial and deviatoric strains are slightly sensitive to changes in μ and it was shown that the best simulations are achieved with $\mu = 30 - 50$. Strain paths in terms of deviatoric and volumetric strains have yielded important information. It is suggested that elastic anisotropy may exist and that this cannot be modelled by either S-CLAY1 or MCC. In addition, the post-yield changes in strain path direction suggest that by the end of the first loading, the yield curve has rotated to $\alpha = 0$. Plots of the predicted variation of α suggest that this is possible with $\mu = 30 - 50$, while setting $\mu = 10$ suggests that rotation of the yield curve is incomplete by the end of loading.

In the second loading stages, yield stresses are generally less well matched than in the first loading stages. Discrepancies might be partly attributed to uncertainty in the procedure used for identifying yield points from the experimental stress-strain curves (see Section 6.5).

At values of η_2 ranging from –0.7 in triaxial extension to 1.01 in triaxial compression, S-CLAY1 predictions of volumetric, axial and shear straining are generally accurate and show considerable improvements over the predictions of MCC. In this range of stress ratios, the model is most successful where the rate parameter μ is set to 30. Test B4 (η_2 =1.30) and Test B9 (η_2 = -1.02) involved the highest stress ratios in triaxial compression and extension respectively. In both cases, axial and deviatoric strains are massively overpredicted by MCC. S-CLAY1

provides improved predictions of axial and deviatoric strains, but they are still substantially overpredicted, regardless of the assumed value of μ. This implies that the flow rule may not be associated at these extreme stress ratios or that the values of M_C and M_E have been underestimated.

8.4 Simulations of Test Series C

Simulations using S-CLAY1 and MCC models are compared with the experimental data for eight tests in Series C in Figures 8.11 – 8.18.

8.4.1 Tests first loaded at low stress ratio in triaxial compression

Three tests in Series C involved first loading at a low stress ratio in triaxial compression. These were Test C6 ($\eta_1 = 0.20$, Figure 8.11), Test C1 ($\eta_1 = 0.42$, Figure 8.12) and Test C7 ($\eta_1 = 0.42$, Figure 8.13). In each case, the S-CLAY1 model predicts slight clockwise rotation of the yield curve (reduction of the value of α) in the first loading stages. The target yield curve orientations predicted by S-CLAY1 are $\alpha = 0.15$ in Test C6 and $\alpha = 0.27$ in Tests C1 and C7. In each of the plots in Figures 8.11 – 8.13, it is clear that the stress-strain behaviour predicted in the first loading stages by S-CLAY1 is relatively insensitive to changes in μ, due to the fact that very little rotation of the yield curve is predicted. Yield points in the first loading stages are well matched by both models (Figures 8.11 (a), 8.12 (a) and 8.13 (a)), but the post-yield compression is overestimated in all three tests by both models. The mismatch is similar in magnitude to the first loading stages in Test Series B. This is again because the value of $\lambda = 0.48$ used in the simulations was based on loading at $\eta = \eta_{K0}$, whereas loading in triaxial compression at stress ratios lower than η_{K0} results in lower apparent values of λ.

Plots of deviatoric stress-strain (see Figures 8.11 (b), 8.12 (b) and 8.13 (b)) show that during the first loading stages, the elastic response is well matched by both models in Test C6, but the amount of pre-yield deviatoric straining is slightly underestimated in Tests C1 and C7. Post-yield deviatoric strains in the first loading stage are well predicted by both models in Test C6. In the first loading stages of Tests C1 and C7

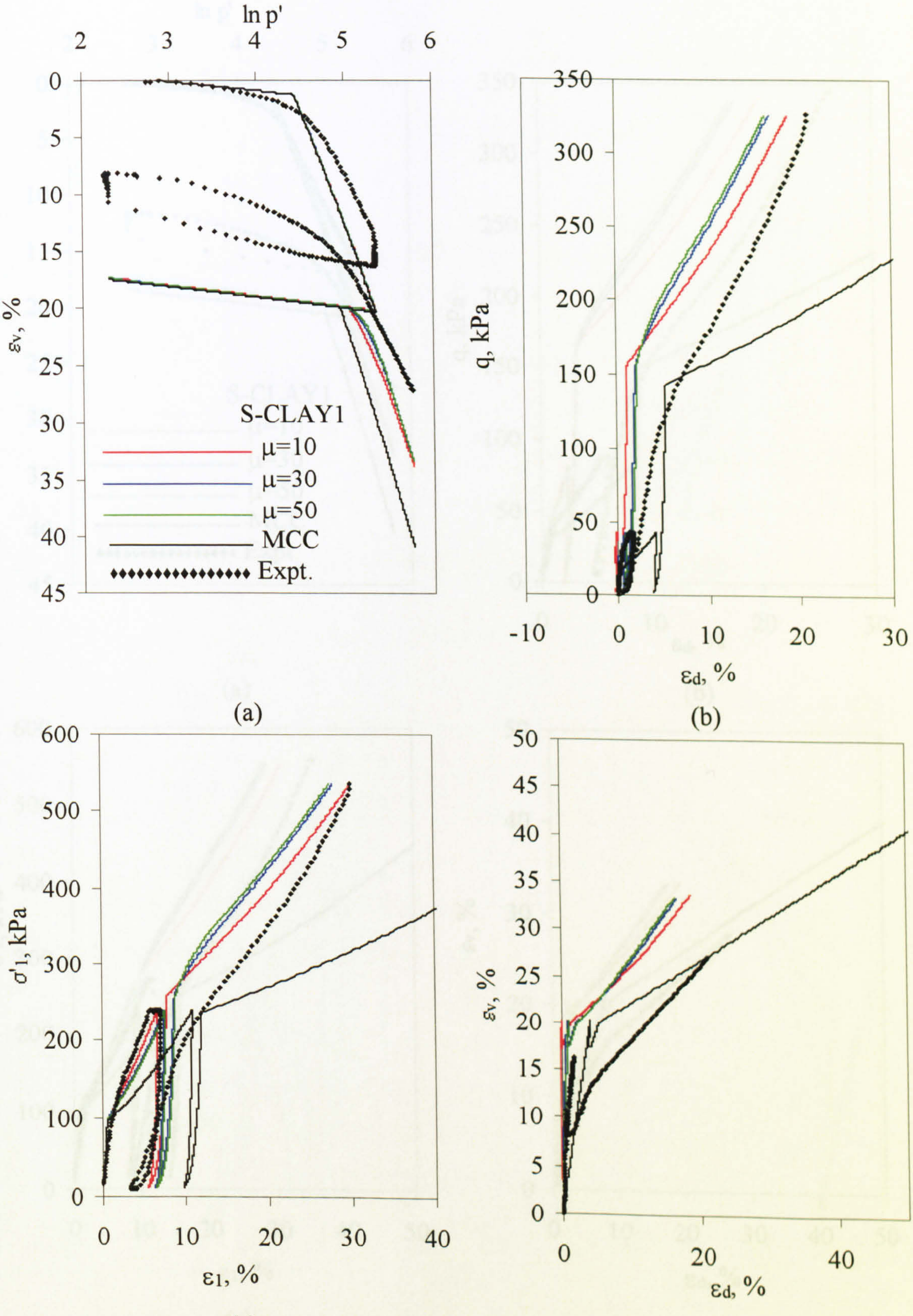

Figure 8.11. S-CLAY1 and MCC simulations of Test C6, where $\eta_1 = 0.20$ and $\eta_2 = 1.04$; (a) compression behaviour, (b) deviatoric stress-strain behaviour, (c) axial stress-strain behaviour, (d) strain paths.

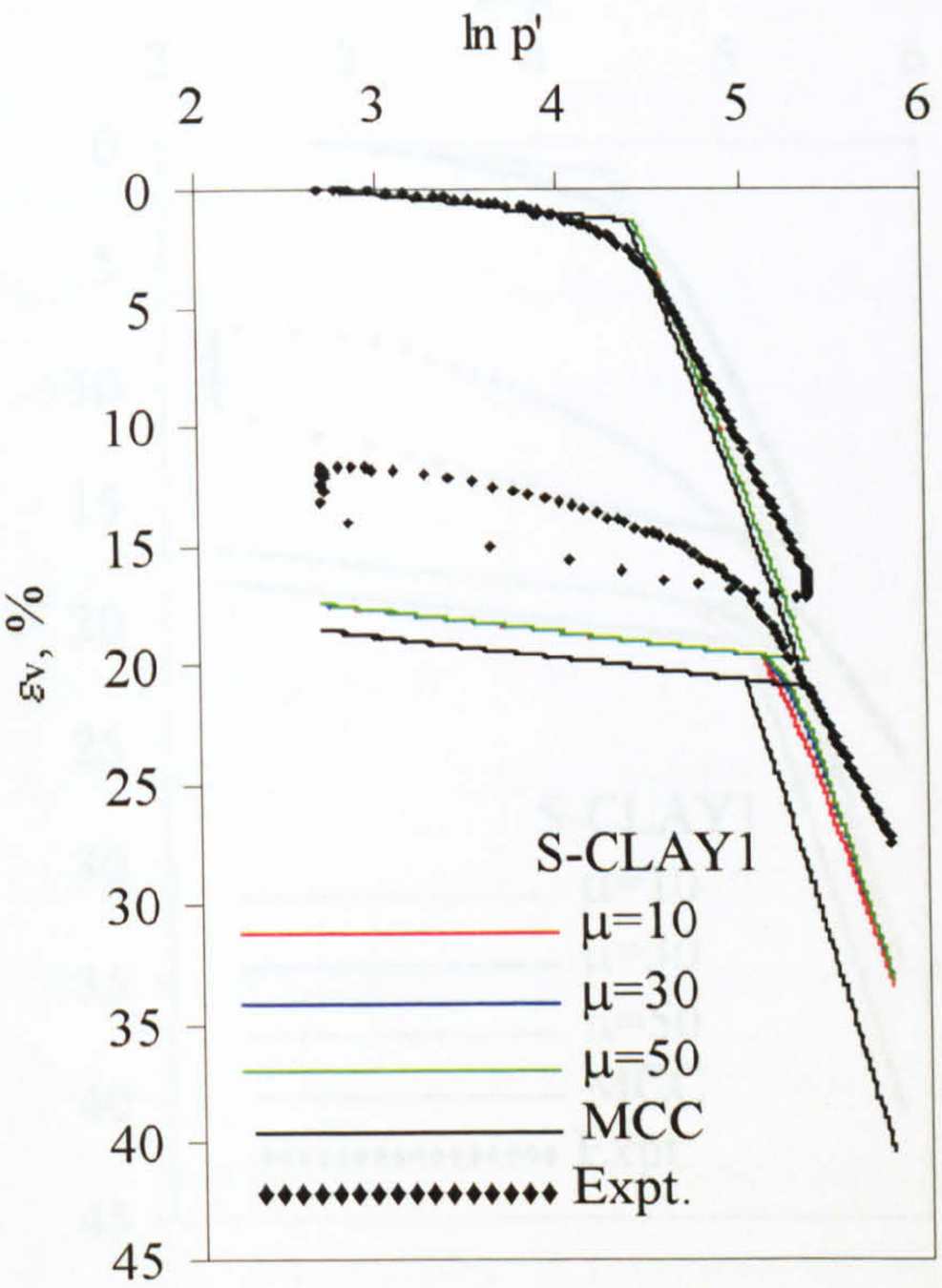

(a)

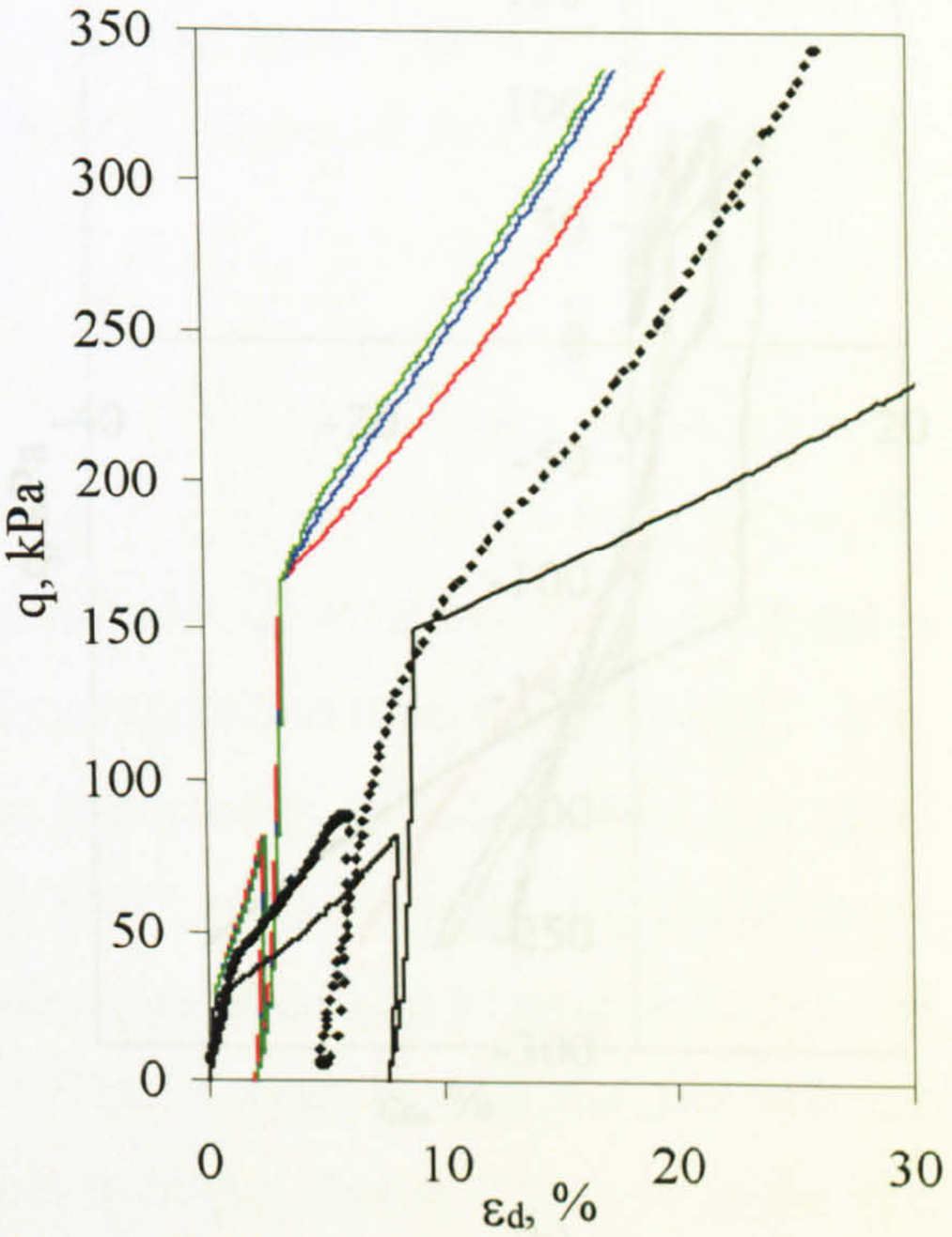

(b)

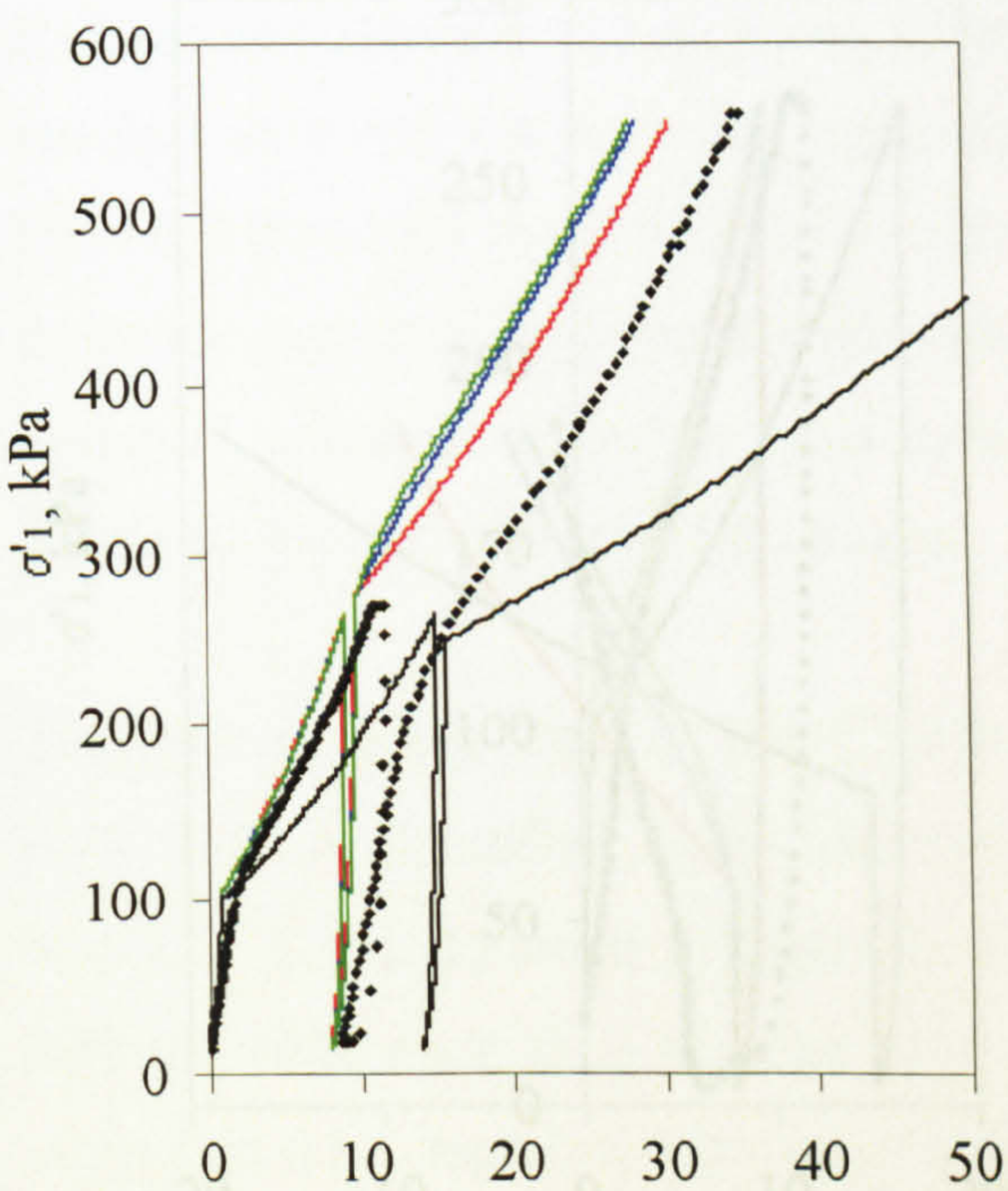

(c)

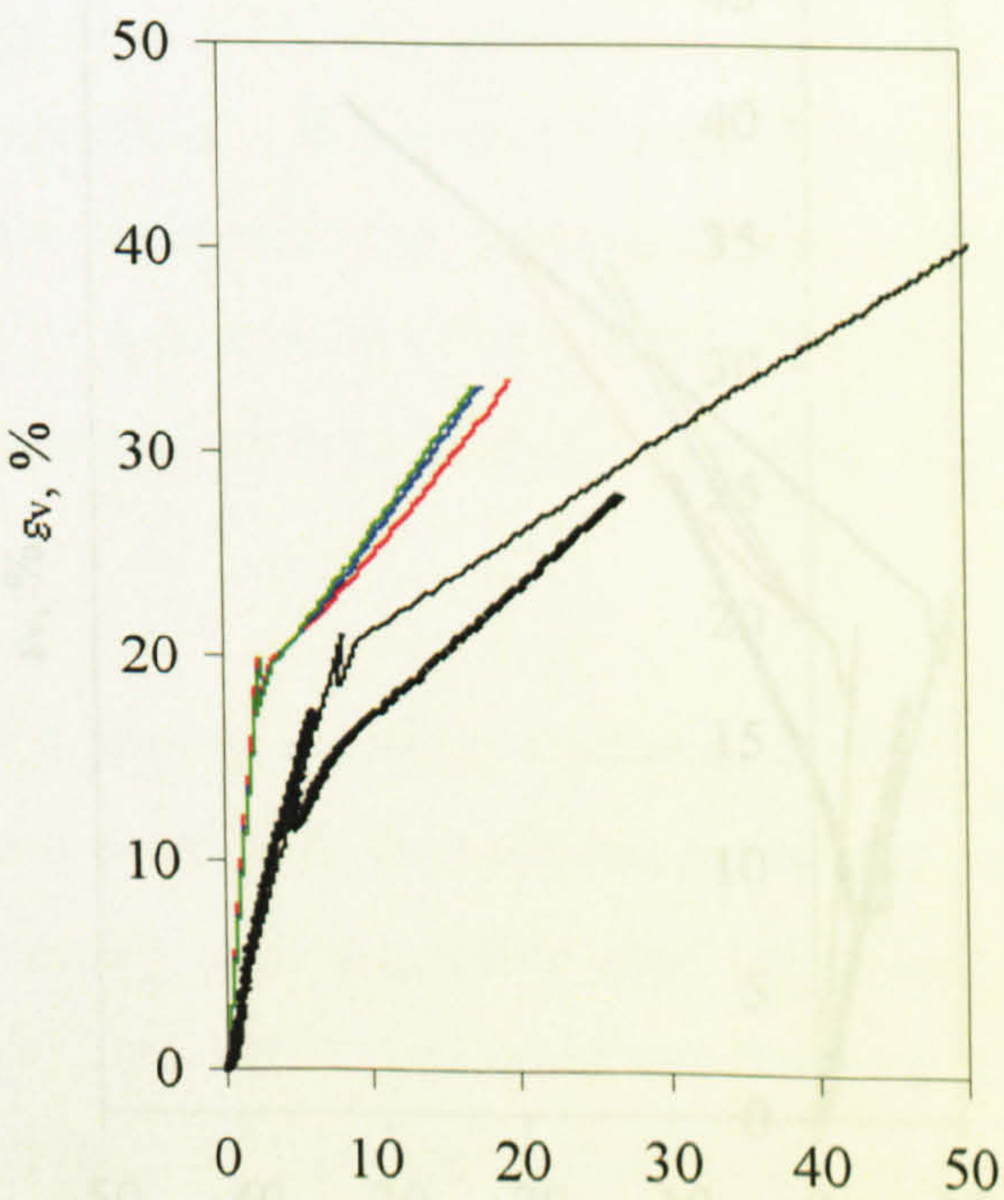

(d)

Figure 8.12. S-CLAY1 and MCC simulations of Test C1, where $\eta_1 = 0.42$ and $\eta_2 = 1.04$; (a) compression behaviour, (b) deviatoric stress-strain behaviour, (c) axial stress-strain behaviour, (d) strain paths.

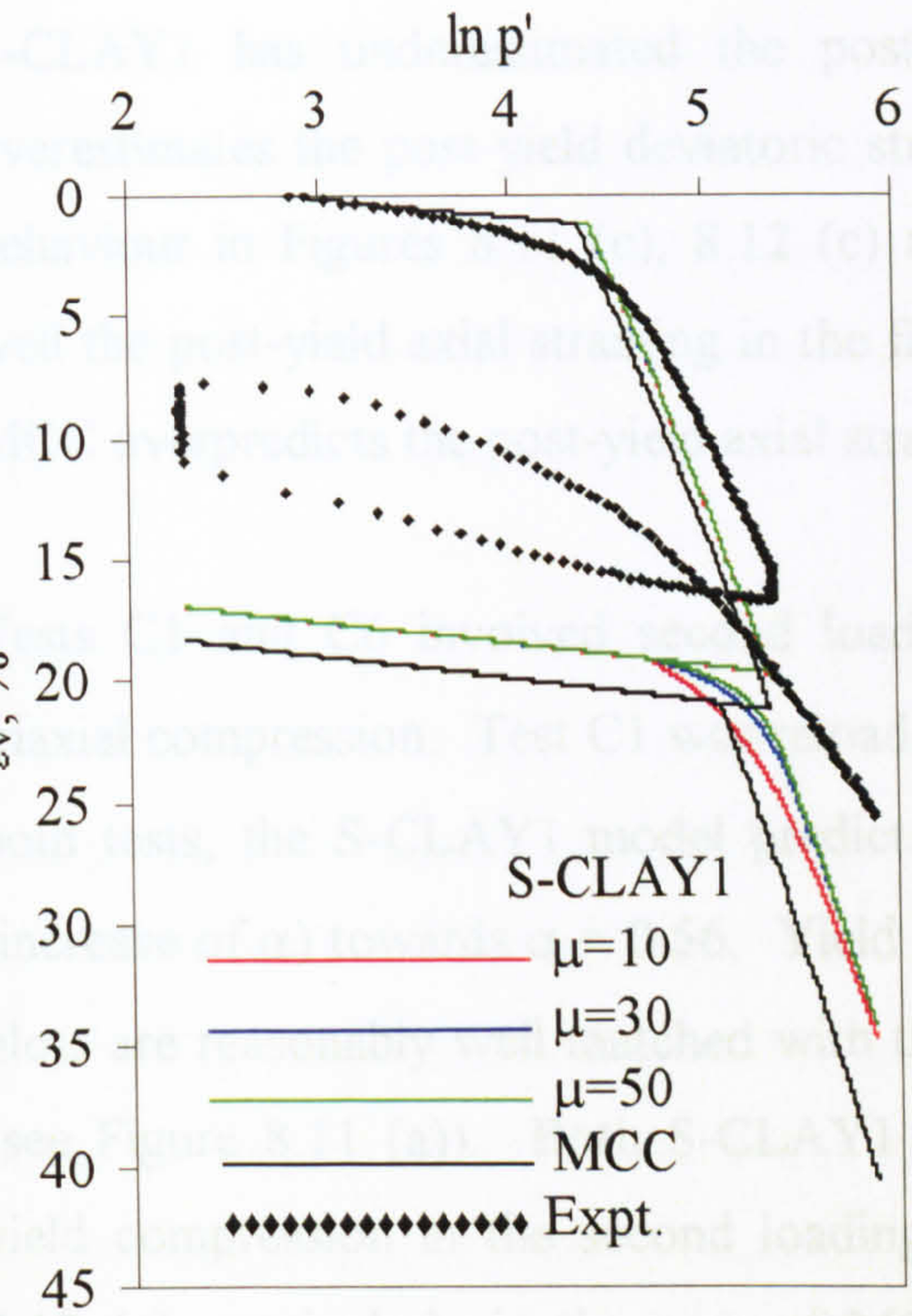

(a)

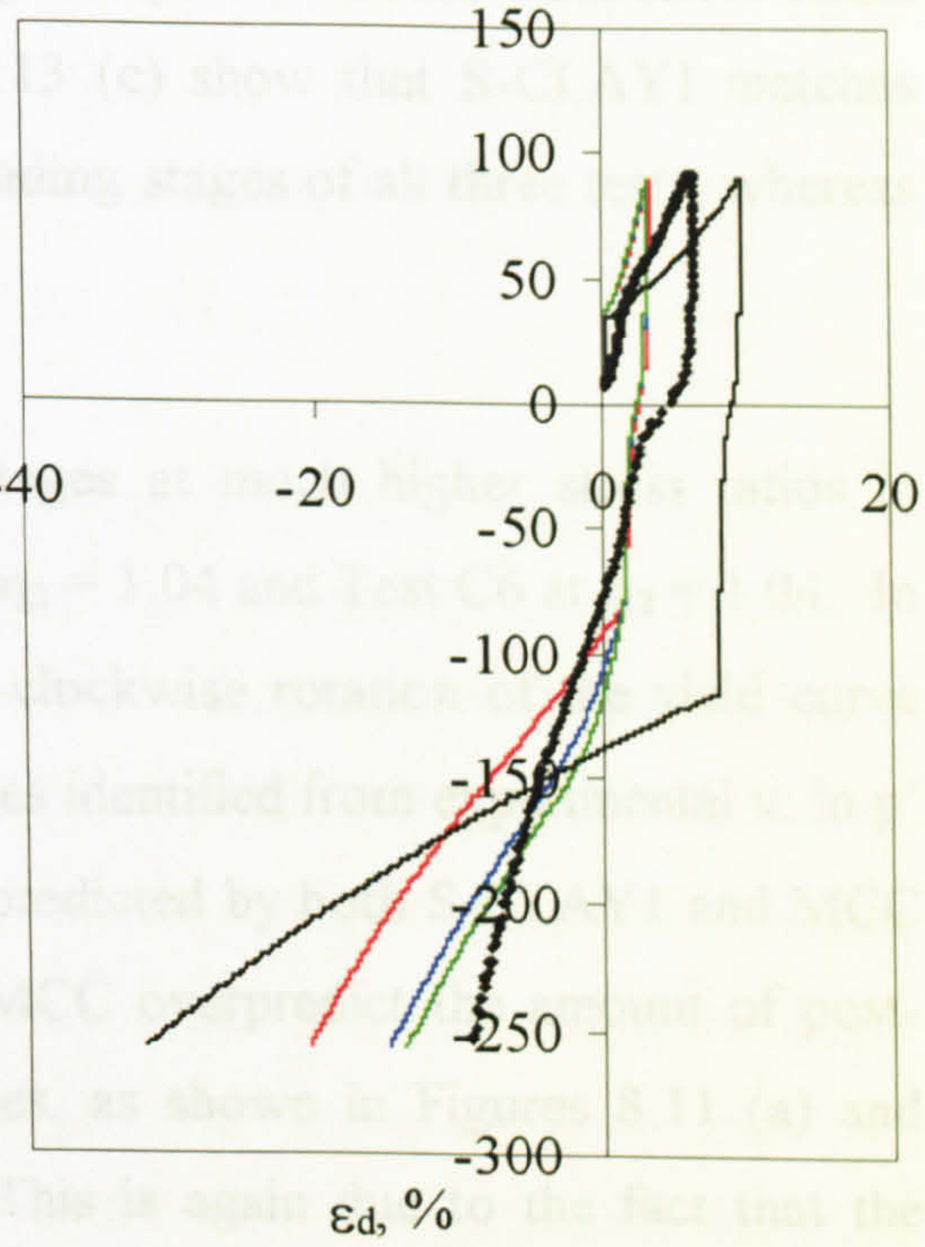

(b)

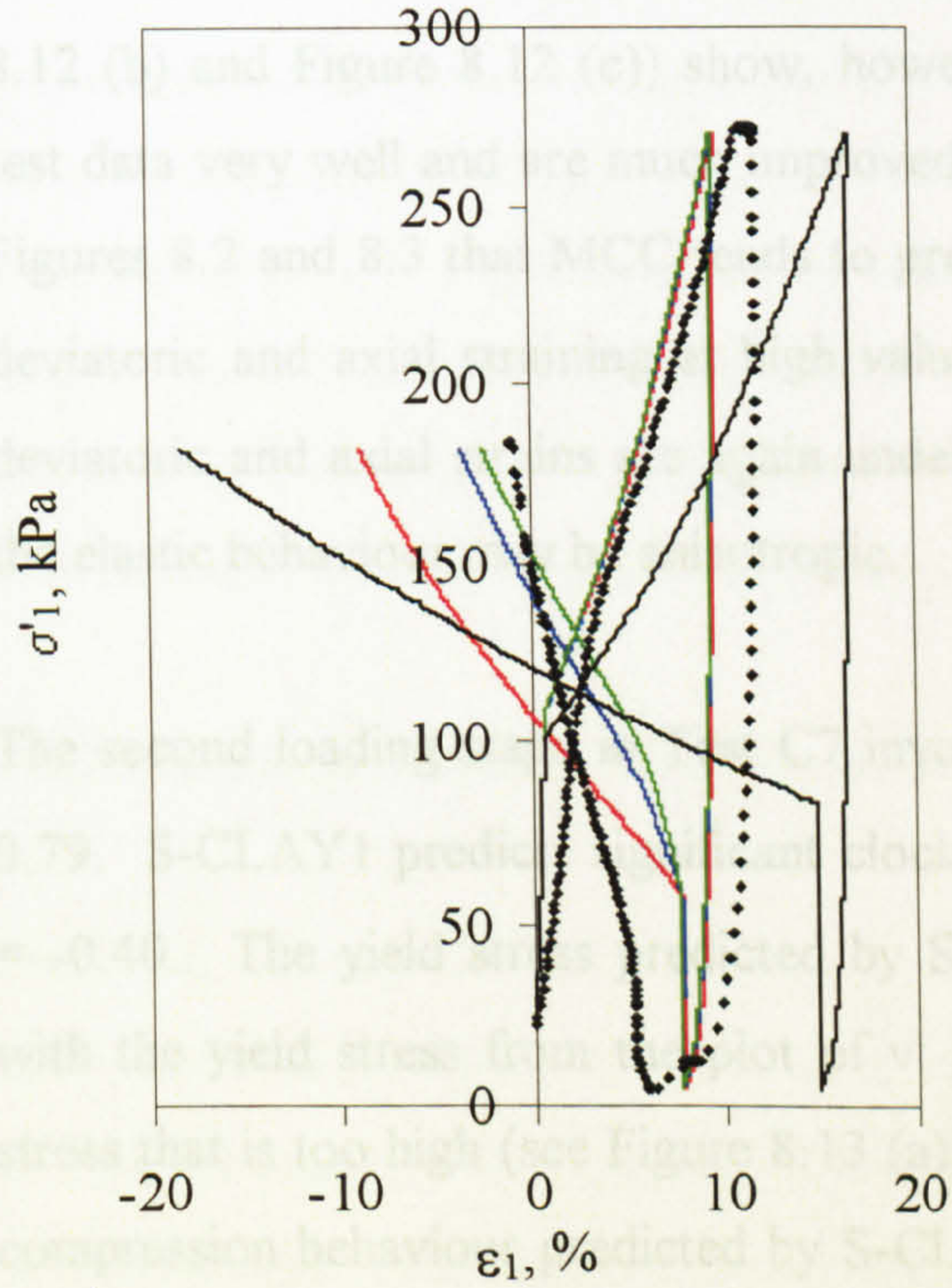

(c)

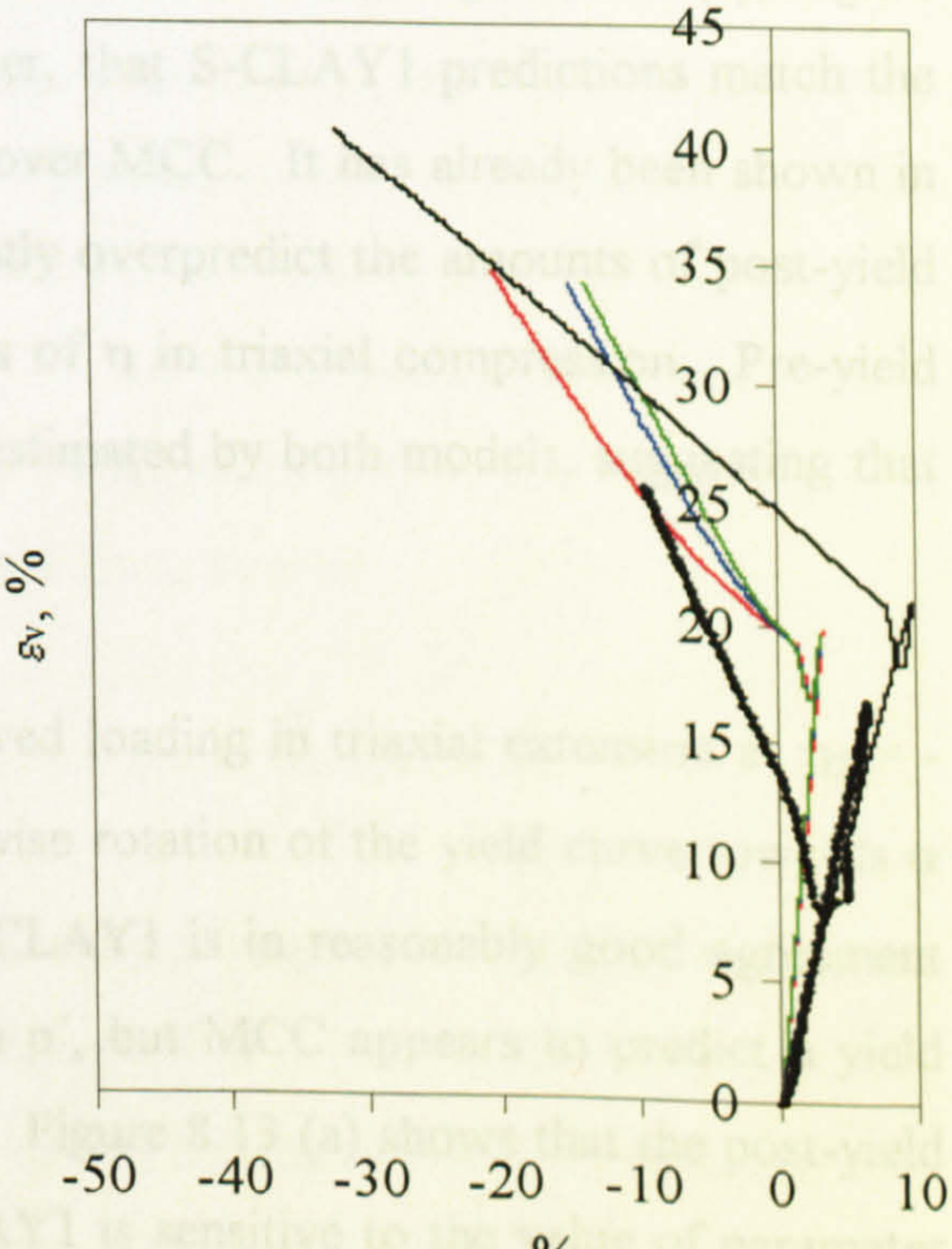

(d)

Figure 8.13. S-CLAY1 and MCC simulations of Test C7, where $\eta_1 = 0.42$ and $\eta_2 = -0.79$; (a) compression behaviour, (b) deviatoric stress-strain behaviour, (c) axial stress-strain behaviour, (d) strain paths.

S-CLAY1 has underestimated the post-yield deviatoric straining whereas MCC overestimates the post-yield deviatoric straining. Inspection of the axial stress-strain behaviour in Figures 8.11 (c), 8.12 (c) and 8.13 (c) show that S-CLAY1 matches well the post-yield axial straining in the first loading stages of all three tests, whereas MCC overpredicts the post-yield axial strains.

Tests C1 and C6 involved second loading stages at much higher stress ratios in triaxial compression. Test C1 was reloaded at $\eta_2 = 1.04$ and Test C6 at $\eta_2 = 1.04$. In both tests, the S-CLAY1 model predicts anti-clockwise rotation of the yield curve (increase of α) towards $\alpha = 0.56$. Yield stresses identified from experimental v: ln p' plots are reasonably well matched with those predicted by both S-CLAY1 and MCC (see Figure 8.11 (a)). Both S-CLAY1 and MCC overpredict the amount of post-yield compression in the second loading stages, as shown in Figures 8.11 (a) and 8.12 (a), particularly in the case of MCC. This is again due to the fact that the models continue to assume a value of λ that is higher than is observed in the test data. Plots of deviatoric and axial strain (see Figure 8.11 (b), Figure 8.11 (c), Figure 8.12 (b) and Figure 8.12 (c)) show, however, that S-CLAY1 predictions match the test data very well and are much improved over MCC. It has already been shown in Figures 8.2 and 8.3 that MCC tends to greatly overpredict the amounts of post-yield deviatoric and axial straining at high values of η in triaxial compression. Pre-yield deviatoric and axial strains are again underestimated by both models, suggesting that the elastic behaviour may be anisotropic.

The second loading stage in Test C7 involved loading in triaxial extension at $\eta_2 = -0.79$. S-CLAY1 predicts significant clockwise rotation of the yield curve towards $\alpha = -0.40$. The yield stress predicted by S-CLAY1 is in reasonably good agreement with the yield stress from the plot of v: ln p', but MCC appears to predict a yield stress that is too high (see Figure 8.13 (a)). Figure 8.13 (a) shows that the post-yield compression behaviour predicted by S-CLAY1 is sensitive to the value of parameter μ, due to substantial rotation of the yield curve. S-CLAY1 again overestimates the compression, but the prediction of volumetric strains during the second loading stage is better than MCC. MCC has significantly overpredicted the yield stress and predicts a rate of post-yield compression that is too great throughout.

In contrast to MCC predictions, post-yield deviatoric and axial strains in the second loading stage of Test C7 are well matched by S-CLAY1, particularly where $\mu = 30 - 50$ (figure 8.13 (b)). Negative post-yield deviatoric and axial strains are slightly overestimated by S-CLAY1, although this can be minimised by increasing the value of μ. MCC greatly overestimates the negative post-yield deviatoric and axial strains.

Strain paths are shown for Test C6 (Figure 8.11 (d)), Test C1 (Figure 8.12 (d)) and Test C7 (Figure 8.13 (d)). During the first loading stages, loading at low stress ratios means that both models predict that the post-yield behaviour is dominated by plastic volumetric strains. In each test S-CLAY1 predicts a strain path gradient during the first loading stages that is a little too high. The choice of parameter μ has very little effect on strain path direction. MCC predicts the strain path very accurately in the first loading stages of Tests C1 and C7, but the predicted gradient is too low in Test C6. In the second loading stages of Tests C1 and C6 the models predict that post-yield volumetric compression will be accompanied by large plastic shear strains, due to the fact that high values of η in triaxial compression were chosen. S-CLAY1 predictions correspond well with the test data in both tests, but the gradient of the MCC strain path is too low. Test C7 was reloaded in triaxial extension and post-yield compression is accompanied by negative plastic shear strains. The S-CLAY1 simulations are sensitive to the choice of μ, but the experimental strain path is matched well with μ set to 30 or 50. The MCC strain path is less accurate, as it overestimates the magnitude of negative plastic shear strains.

8.4.2 Tests first loaded at high stress ratio in triaxial compression

Tests C5, C2 and C3 each involved a first loading stage at a relatively high stress ratio in triaxial compression. The stress ratios were $\eta_1 = 0.80$ in Test C5, $\eta_1 = 1.10$ in Test C2 and $\eta_1 = 1.30$ in Test C3. The model simulations and experimental data associated with these tests are shown in Figures 8.14 – 8.16.

Inspection of the compression curves in the first loading stages of these tests indicate that yielding is reasonably well predicted by S-CLAY1, but MCC underestimates the yield stresses, particularly in Test C3 (see Figure 8.16 (a)). Figure 8.1 shows that

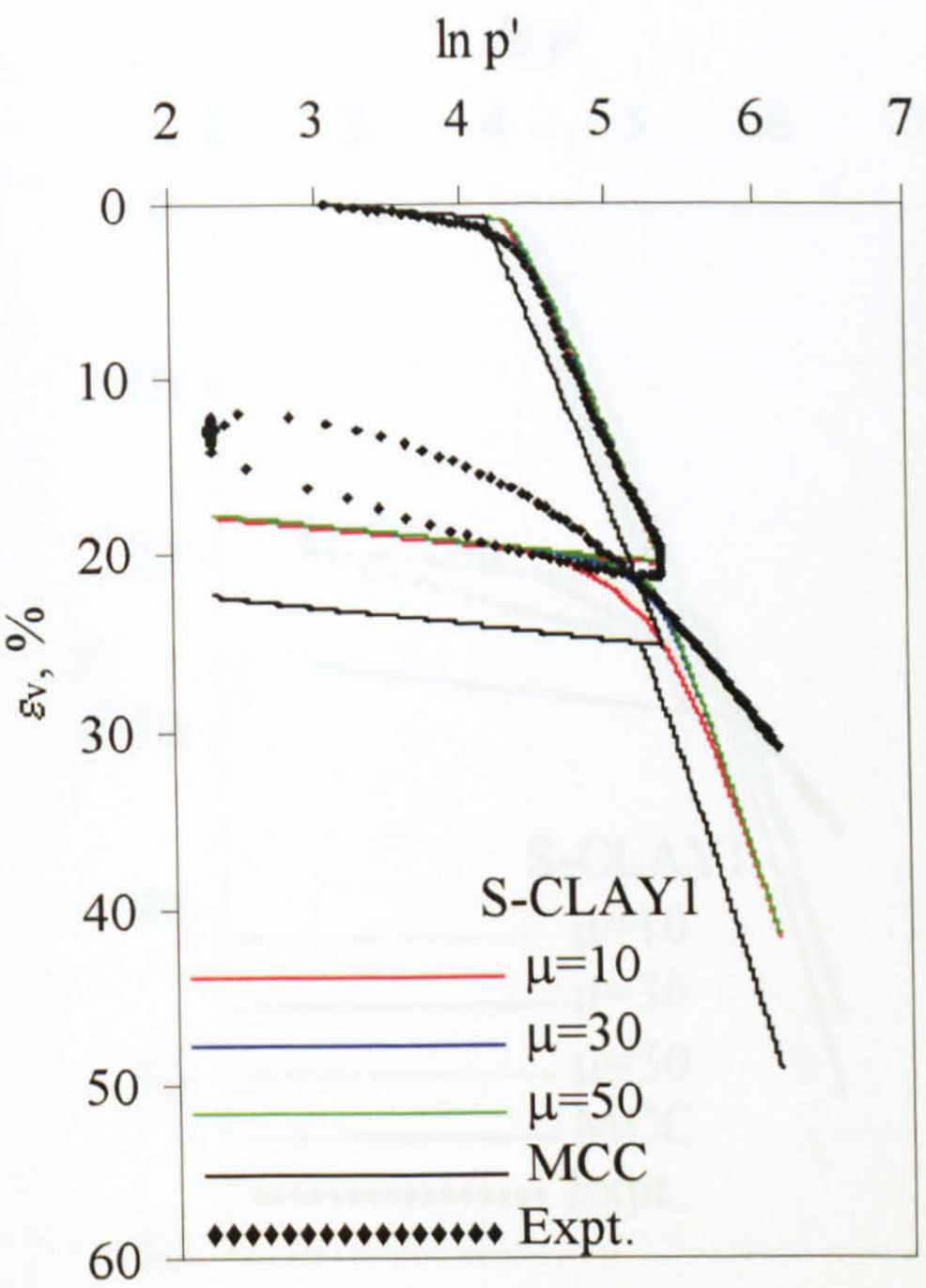

(a)

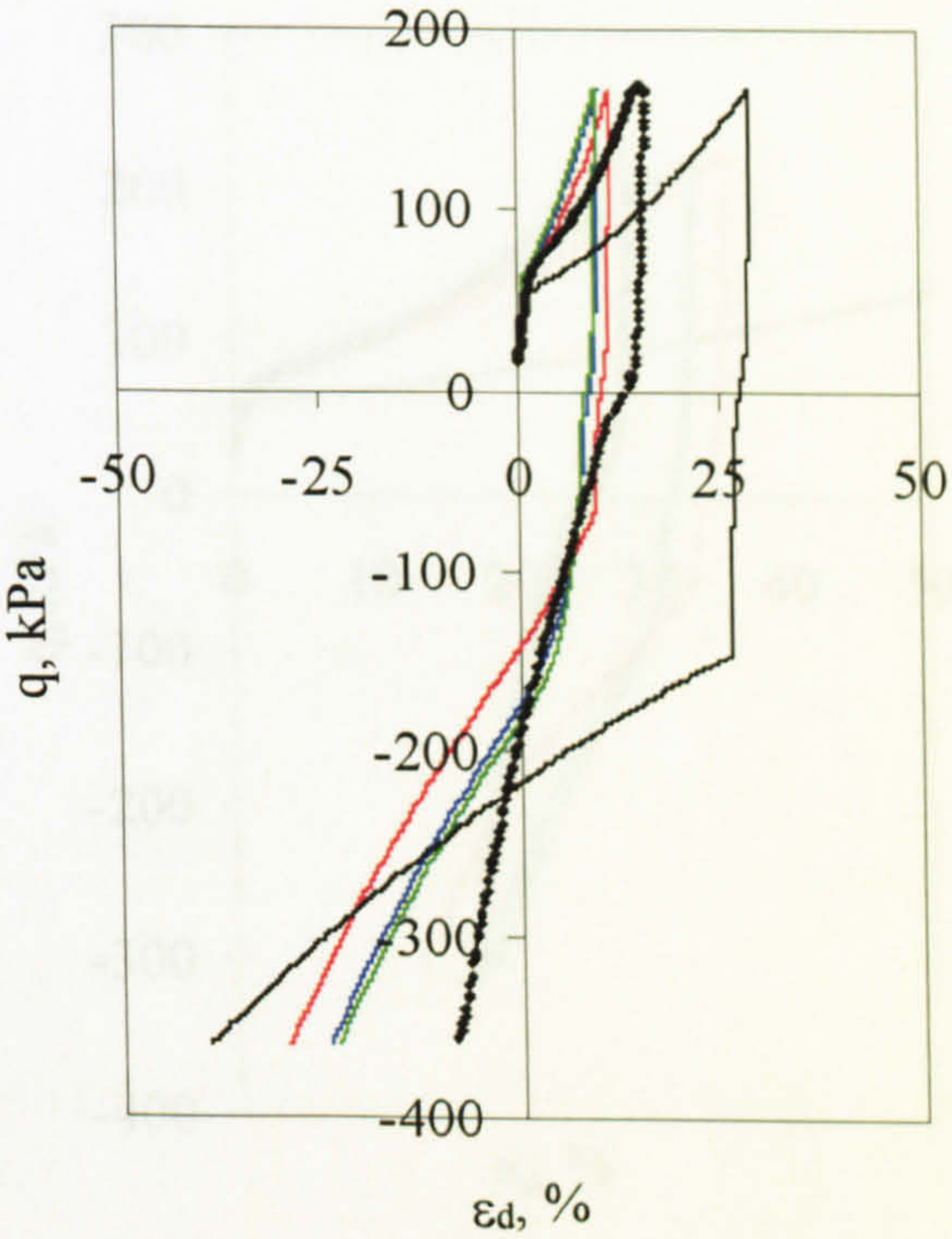

(b)

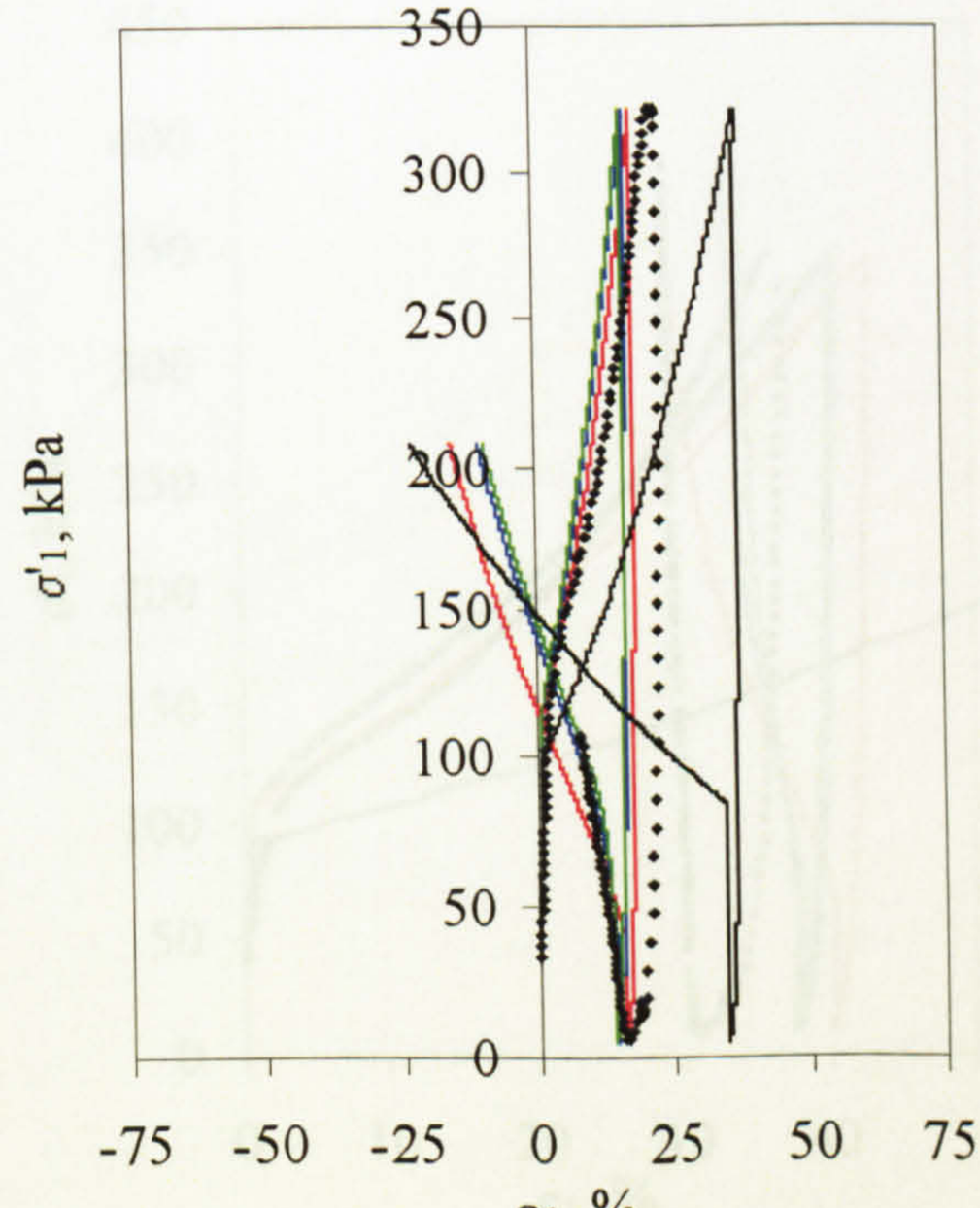

(c)

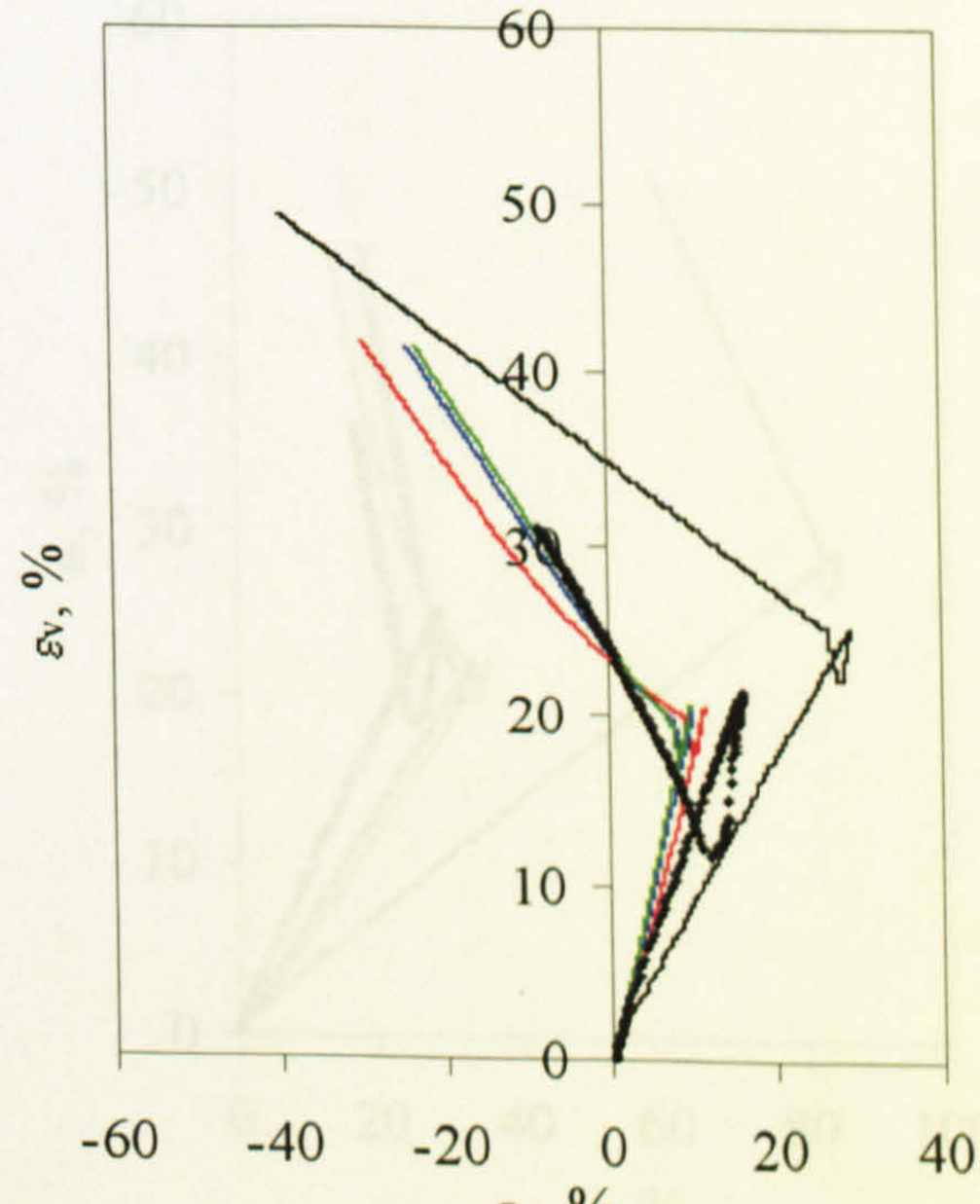

(d)

Figure 8.14. S-CLAY1 and MCC simulations of Test C5, where $\eta_1 = 0.80$ and $\eta_2 = -0.80$; (a) compression behaviour, (b) deviatoric stress-strain behaviour, (c) axial stress-strain behaviour, (d) strain paths.

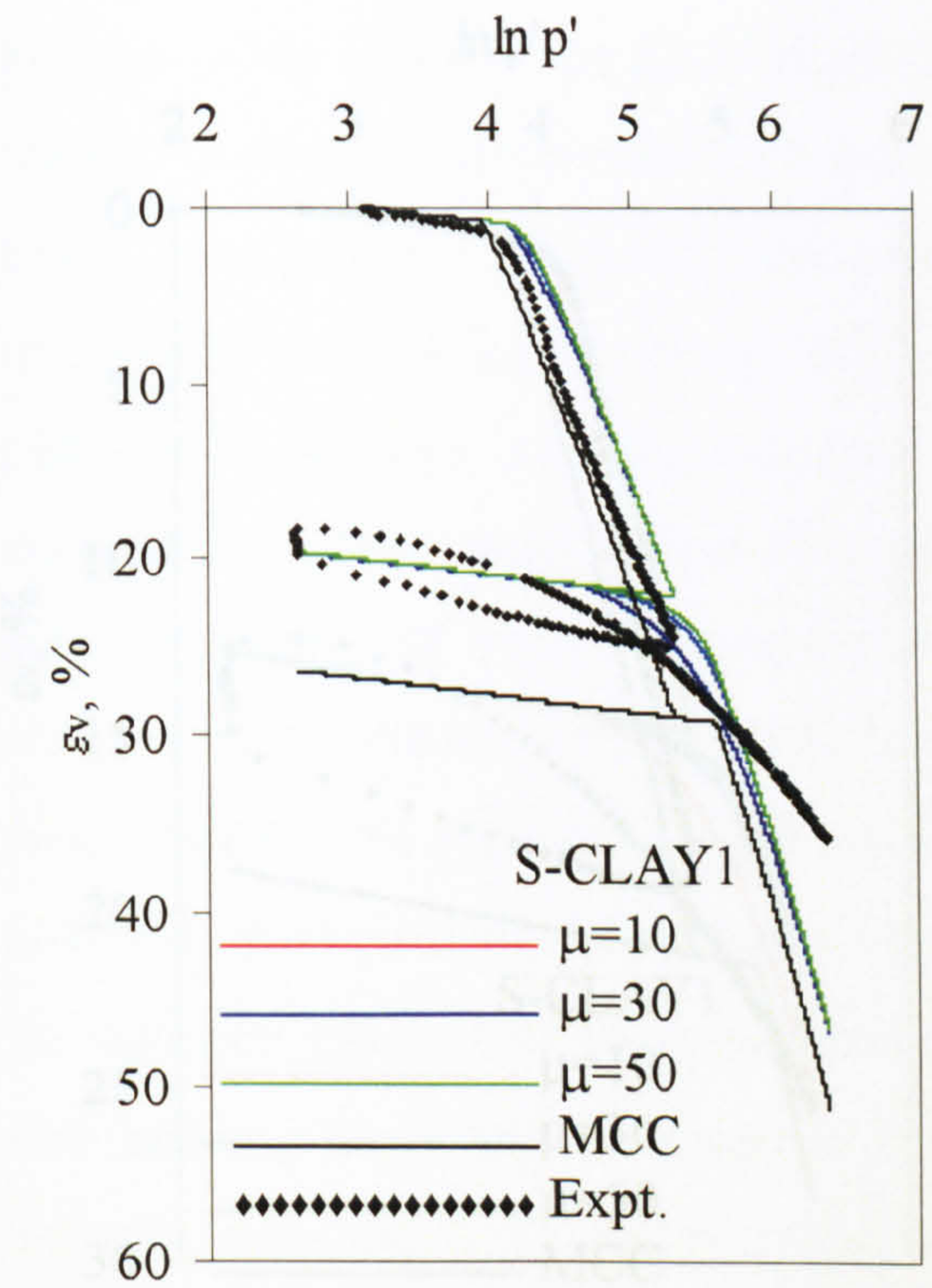

(a)

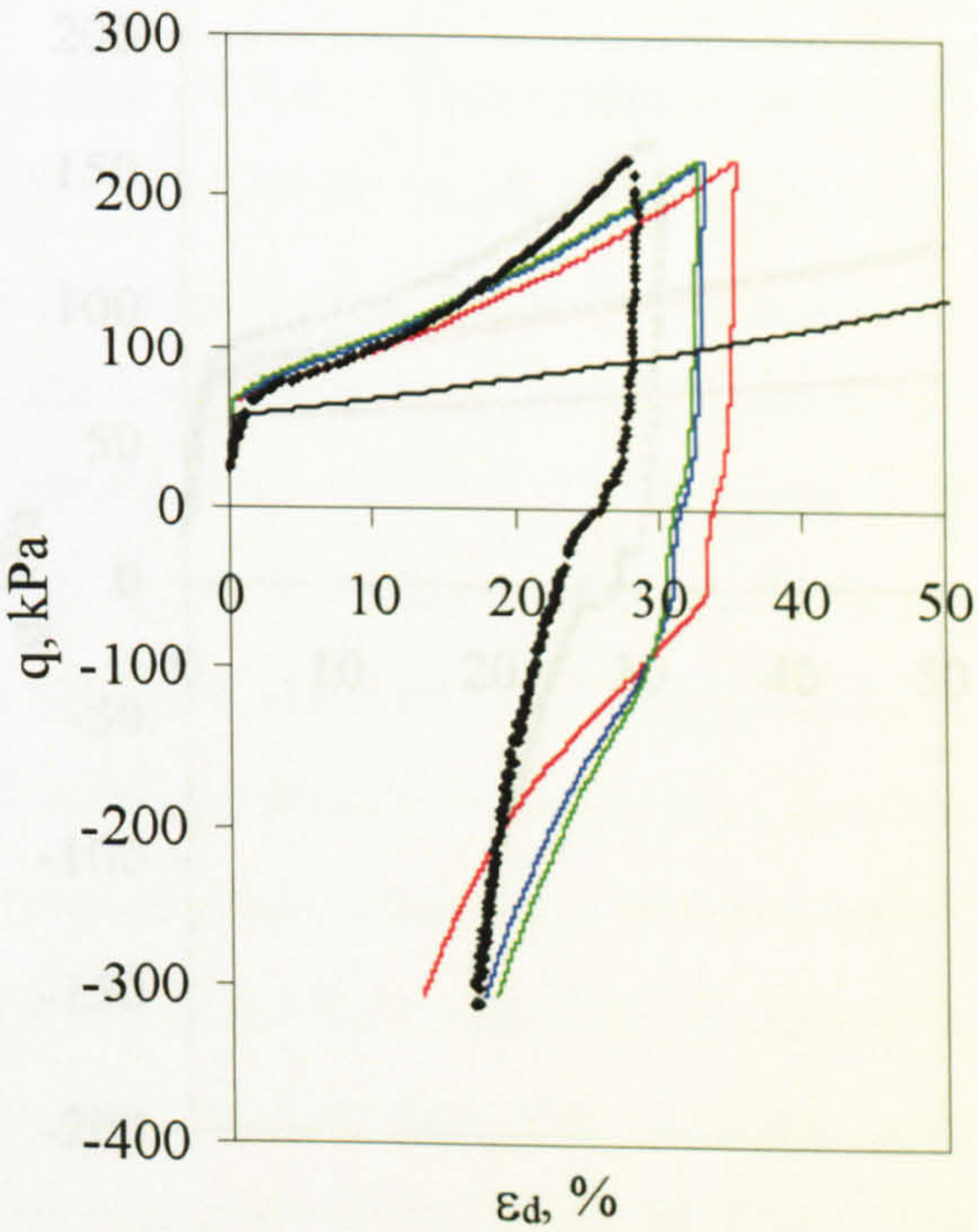

(b)

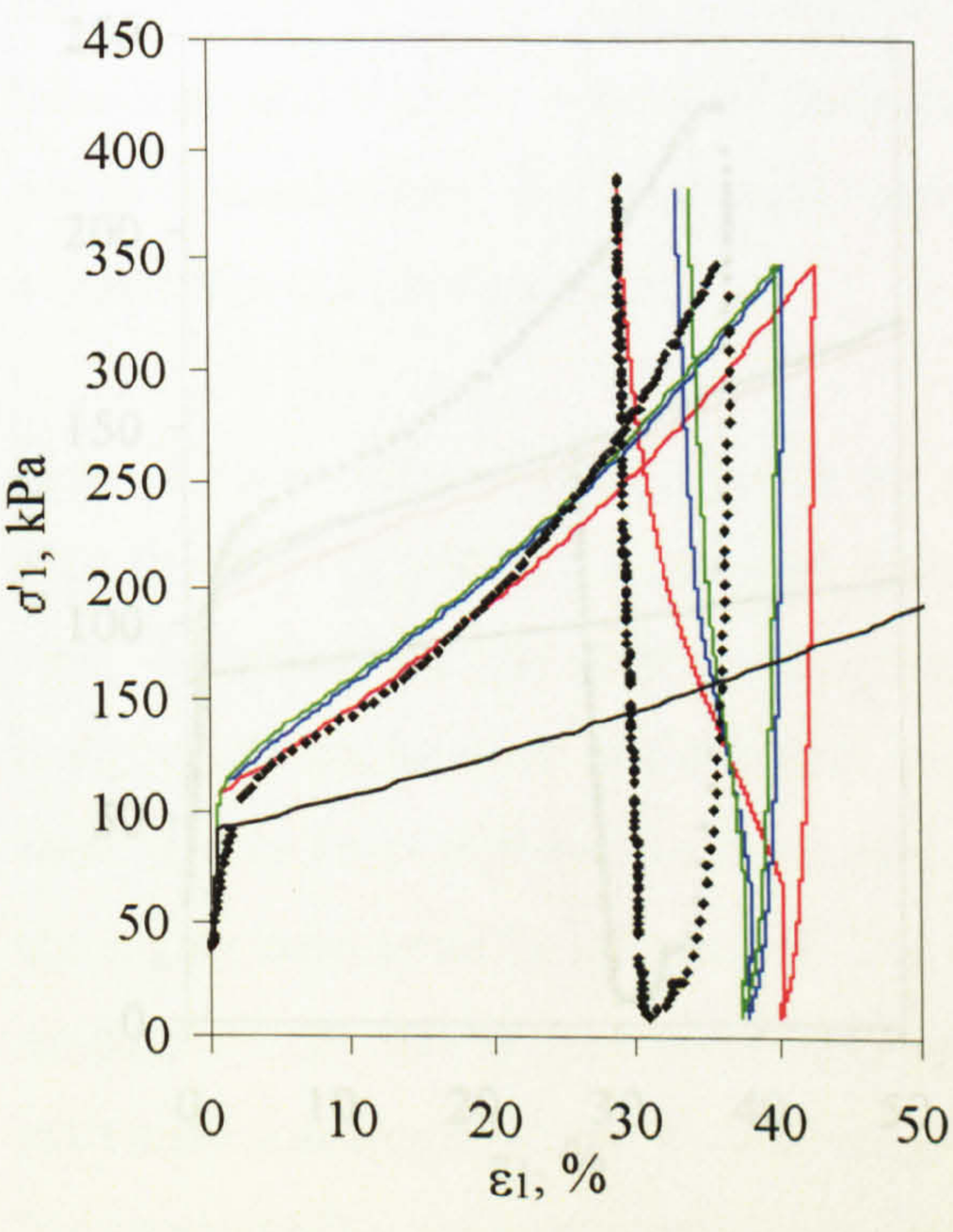

(c)

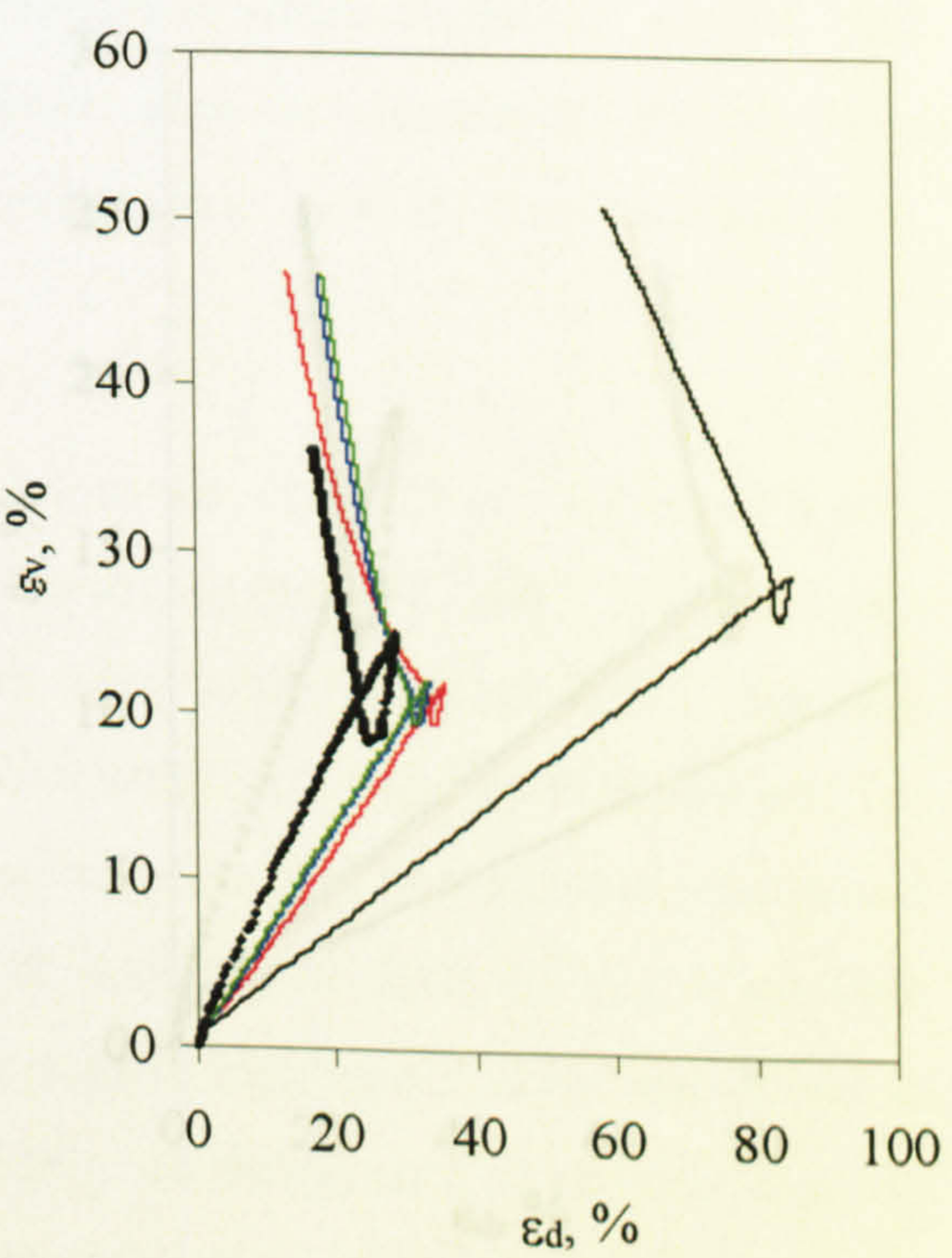

(d)

Figure 8.15. S-CLAY1 and MCC simulations of Test C2, where $\eta_1 = 1.10$ and $\eta_2 = -0.50$; (a) compression behaviour, (b) deviatoric stress-strain behaviour, (c) axial stress-strain behaviour, (d) strain paths.

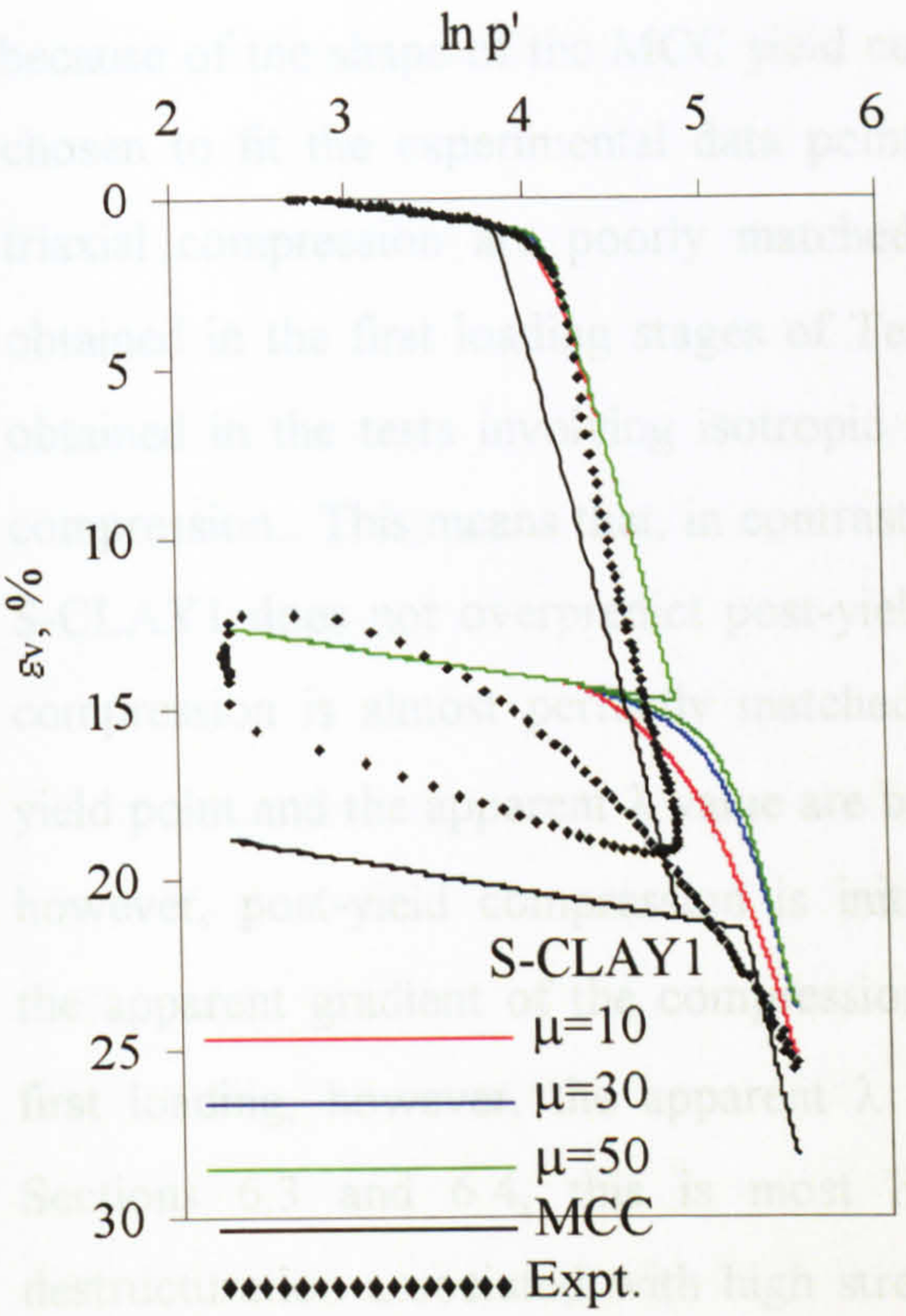

(a)

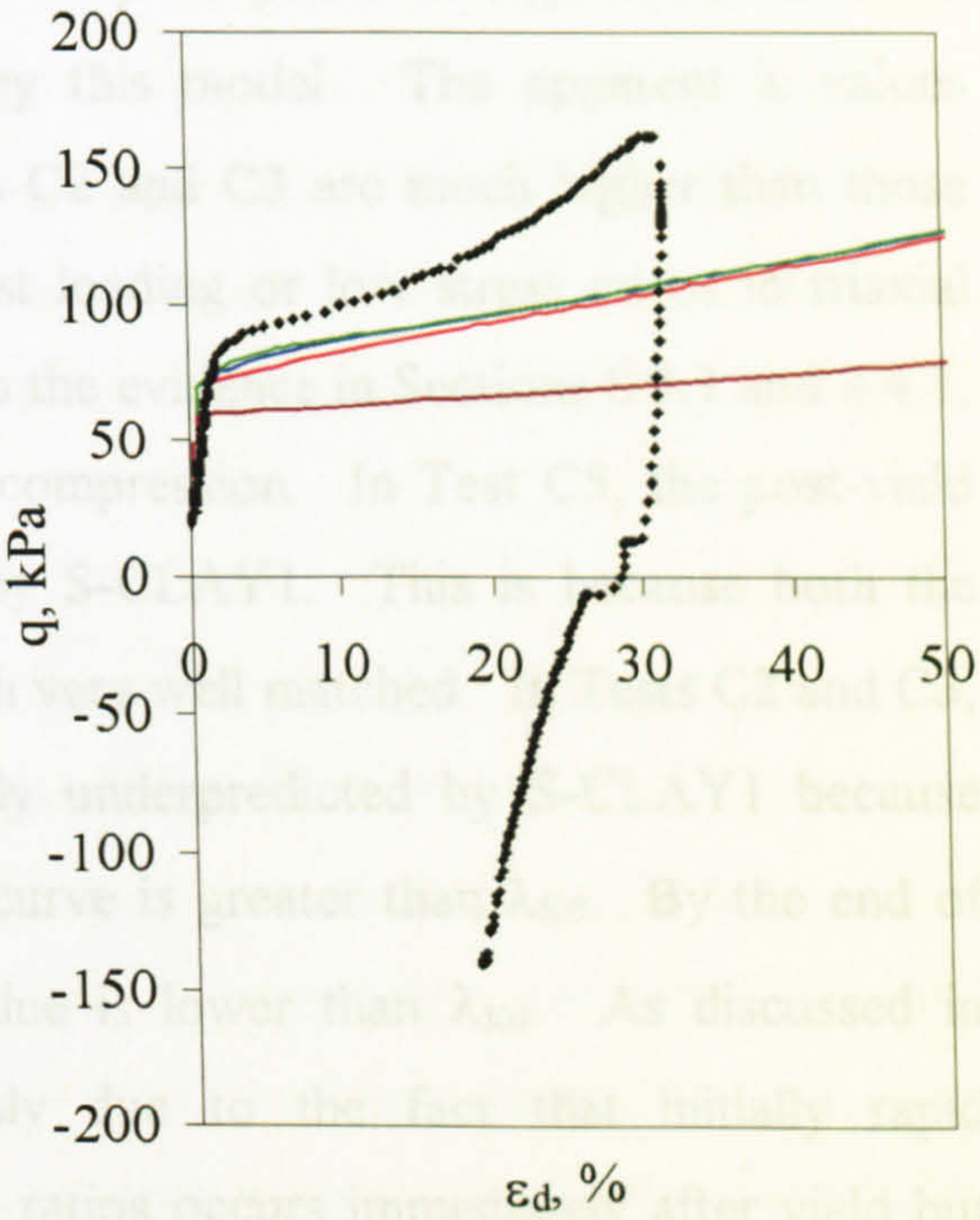

(b)

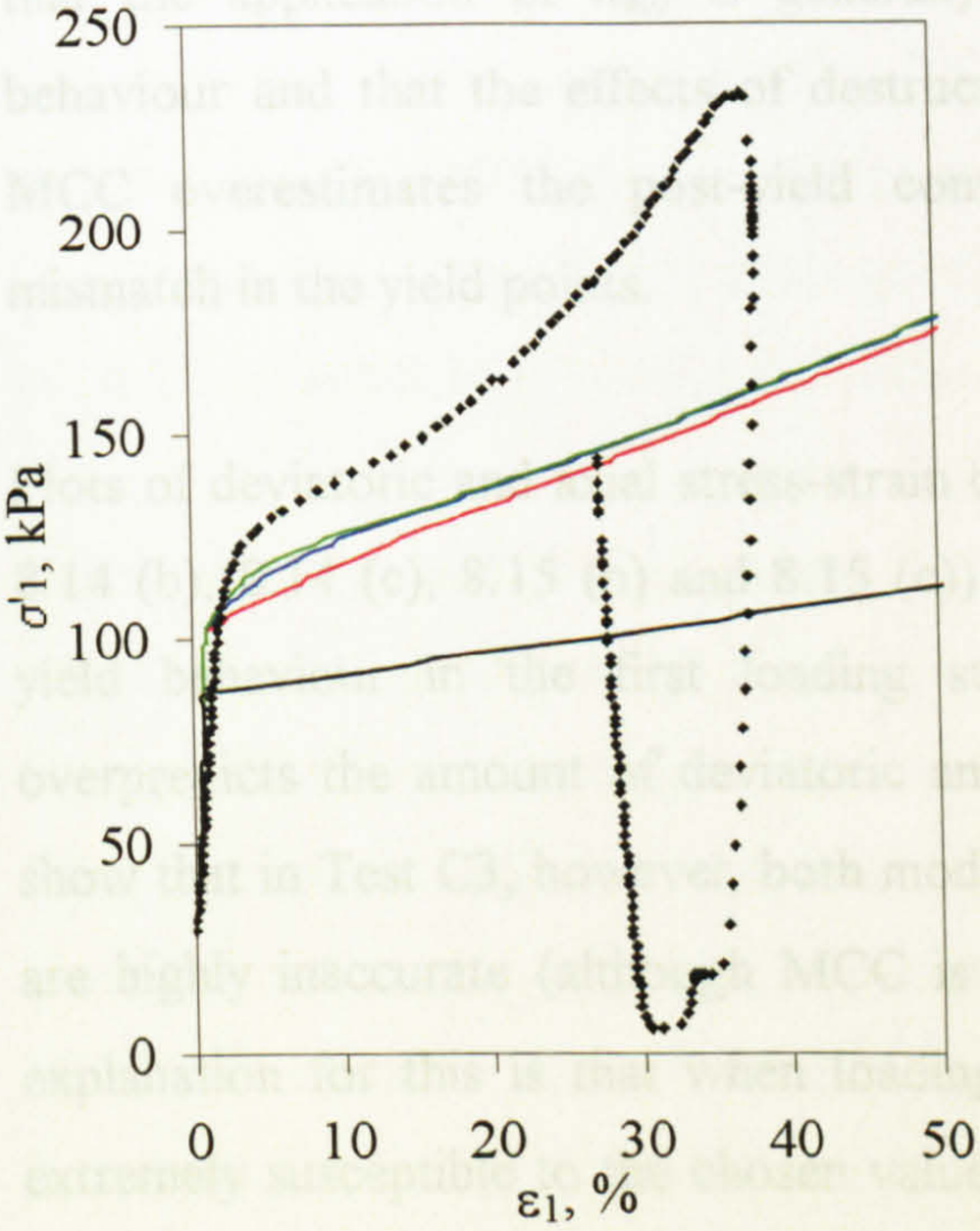

(c)

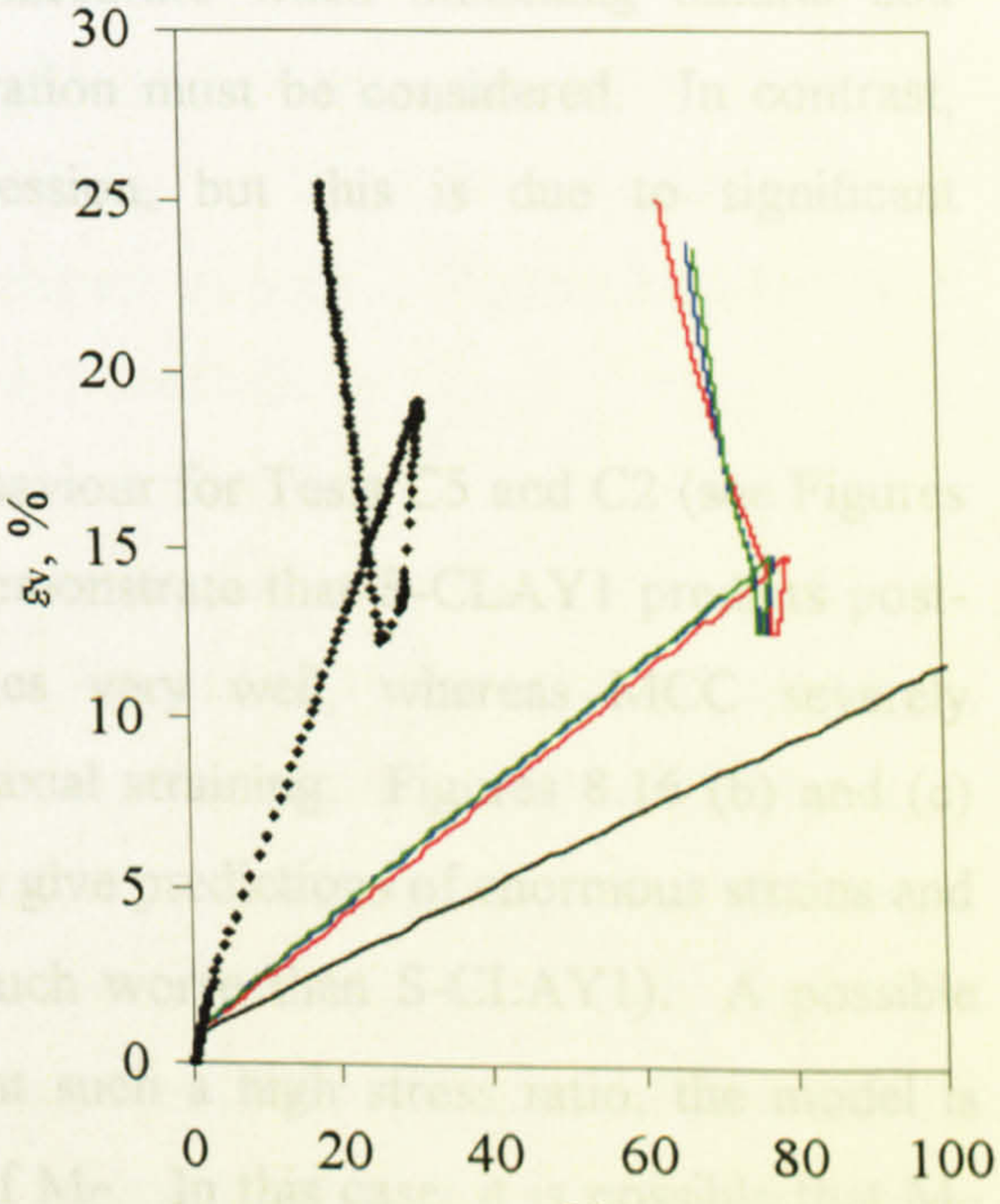

(d)

Figure 8.16. S-CLAY1 and MCC simulations of Test C3, where $\eta_1 = 1.30$ and $\eta_2 = -0.60$; (a) compression behaviour, (b) deviatoric stress-strain behaviour, (c) axial stress-strain behaviour, (d) strain paths.

because of the shape of the MCC yield curve and the fact that its size (p'_0) has been chosen to fit the experimental data points, the yield points at high stress ratios in triaxial compression are poorly matched by this model. The apparent λ values obtained in the first loading stages of Tests C2 and C3 are much higher than those obtained in the tests involving isotropic first loading or low stress ratios in triaxial compression. This means that, in contrast to the evidence in Sections 8.3.1 and 8.4.1, S-CLAY1 does not overpredict post-yield compression. In Test C5, the post-yield compression is almost perfectly matched by S-CLAY1. This is because both the yield point and the apparent λ value are both very well matched. In Tests C2 and C3, however, post-yield compression is initially underpredicted by S-CLAY1 because the apparent gradient of the compression curve is greater than λ_{K0}. By the end of first loading, however, the apparent λ value is lower than λ_{K0}. As discussed in Sections 6.3 and 6.4, this is most likely due to the fact that initially rapid destructuration associated with high stress ratios occurs immediately after yield but slows down as the test progresses and bonding is destroyed. This emphasises the fact that the application of λ_{K0} is generally inaccurate when modelling natural soil behaviour and that the effects of destructuration must be considered. In contrast, MCC overestimates the post-yield compression, but this is due to significant mismatch in the yield points.

Plots of deviatoric and axial stress-strain behaviour for Tests C5 and C2 (see Figures 8.14 (b), 8.14 (c), 8.15 (b) and 8.15 (c)) demonstrate that S-CLAY1 predicts post-yield behaviour in the first loading stages very well, whereas MCC severely overpredicts the amount of deviatoric and axial straining. Figures 8.16 (b) and (c) show that in Test C3, however, both models give predictions of enormous strains and are highly inaccurate (although MCC is much worse than S-CLAY1). A possible explanation for this is that when loading at such a high stress ratio, the model is extremely susceptible to the chosen value of M_c. In this case, it is possible that M_c has been slightly underestimated, resulting in prediction of massive deviatoric and axial strains. Alternatively, it may be that the assumption of an associated flow rule is inaccurate at this high stress ratio. Again this could cause the predicted rate of shear straining to be highly inaccurate.

Each of the tests was unloaded and then reloaded in triaxial extension. The stress ratios involved were η_2 = -0.80 in Test C5, η_2 = -0.50 in Test C2 and η_2 = -0.60 in Test C3. Reloading in triaxial extension means that S-CLAY1 predicts clockwise rotation of the yield curve towards a negative value of α. Figures 8.14 (a), 8.15 (a) and 8.16 (a) indicate that it is almost impossible to tell how well either model has predicted the yield stress since there is considerable uncertainty in identifying the yield stress in the test data.

The experimental compression curves from Tests C5, C2 and C3 (see Figures 8.14 (a), 8.15 (a) and 8.16 (a)) show that yield is indistinct and that the post-yield compression curves each have a relatively low gradient. As discussed in Section 6.4, yielding is less apparent due to the effects of anisotropy and the post-yield compression curve is of lower gradient due to the effects of preceding destructuration. Although the S-CLAY1 post-yield compression curves are initially rounded, the overall prediction is a poor match due to the continued deployment of λ_{K0}. Plots of axial and deviatoric stress-strain behaviour (see Figures 8.14 (b), 8.14 (c)) show that during second loading S-CLAY1 predictions are in better agreement with the data than MCC predictions, particularly for μ = 30 or 50. The same pattern emerged in Tests C2 and C3, although this cannot be seen in Figures 8.15 (b), 8.15 (c), 8.16 (b) and 8.16 (c) due to the scale used in the plots.

Figures 8.14 (d) and 8.15 (d) show that the strain paths for Tests C5 and C2 are reasonably well predicted by S-CLAY1 and less satisfactorily predicted by MCC. Figure 8.16 (d) shows that the strain path in the first loading stage of C3 (at η_1 = 1.30) is poorly predicted by both models because plastic deviatoric strains are grossly overpredicted at this very high stress ratio (the problem is particularly severe for MCC). Strain paths during the second loading stage of Test C3 are well predicted by both models (the MCC predictions for the second loading stage are not visible in Figure 8.16 (d) because the deviatoric strains predicted for the first loading stage are so large). In Figures 8.14 (d), 8.15 (d) and 8.16 (d), S-CLAY1 predictions of strain paths are generally best with μ = 30 - 50.

8.4.3 Tests first loaded in triaxial extension

Two tests in Series C involved a first a loading stage in triaxial extension. These were Test C9 (η_1 = -0.50) and Test C4 (η_1 = -0.80). Figure 8.17 (a) shows that the yield stress in the first loading stage is well matched by S-CLAY1 and MCC, but MCC overpredicts the yield stress in Figure 8.18 (a). S-CLAY1 predicts clockwise rotation of the yield curve (to a negative value of α) in each of these first loading stages. The compression curves from the tests in Figures 8.17 (a) and 8.18 (a) suggests that the first loading stage is significantly influenced by changes in anisotropy resulting in a relatively slow rate of compression throughout. The S-CLAY1 simulations reflect this, but still tend to overpredict the amount of compression. Due to large changes in anisotropy, rates of negative axial and deviatoric straining predicted by S-CLAY1 are highly sensitive to changes in μ (see Figures 8.17 (b), 8.17 (c), 8.18 (b) and 8.18 (c)). In each case the best S-CLAY1 prediction of deviatoric and axial straining in the first loading stage is achieved with μ = 50, while MCC overestimates the amount of negative deviatoric and axial straining during the first loading stage.

The second loading stage in Test C9 is at an even higher stress ratio in triaxial extension (η_2 = -0.98). As a consequence, S-CLAY1 predicts further clockwise rotation of the yield curve (to a larger negative value of α). The predicted stress-strain behaviour in Figure 8.17 is relatively insensitive to changes in parameter μ during the second loading stage. Figures 8.17 (b) and (c) show that all simulations overestimate the rate of negative axial and deviatoric straining, but S-CLAY1 shows a slight improvement over MCC. This is consistent with the tests at high stress ratios in triaxial compression, where the models also massively overpredict the quantity of plastic strains. It is again possible that the discrepancy could be caused by an underestimation of the value of the critical state stress ratio in triaxial extension, M_E. Alternatively, it could mean (again) that the flow rule is non-associated at very high stress ratios.

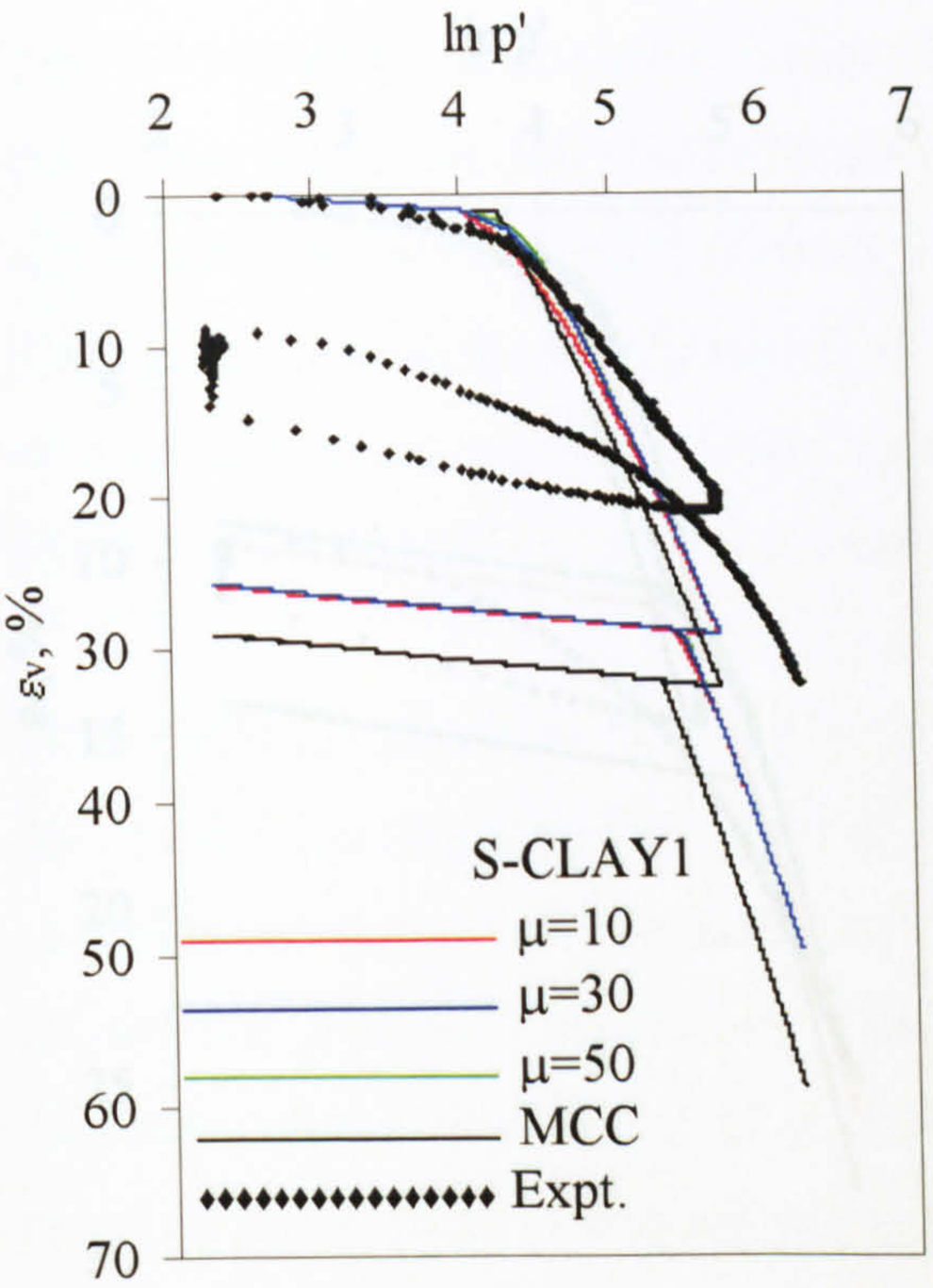

(a)

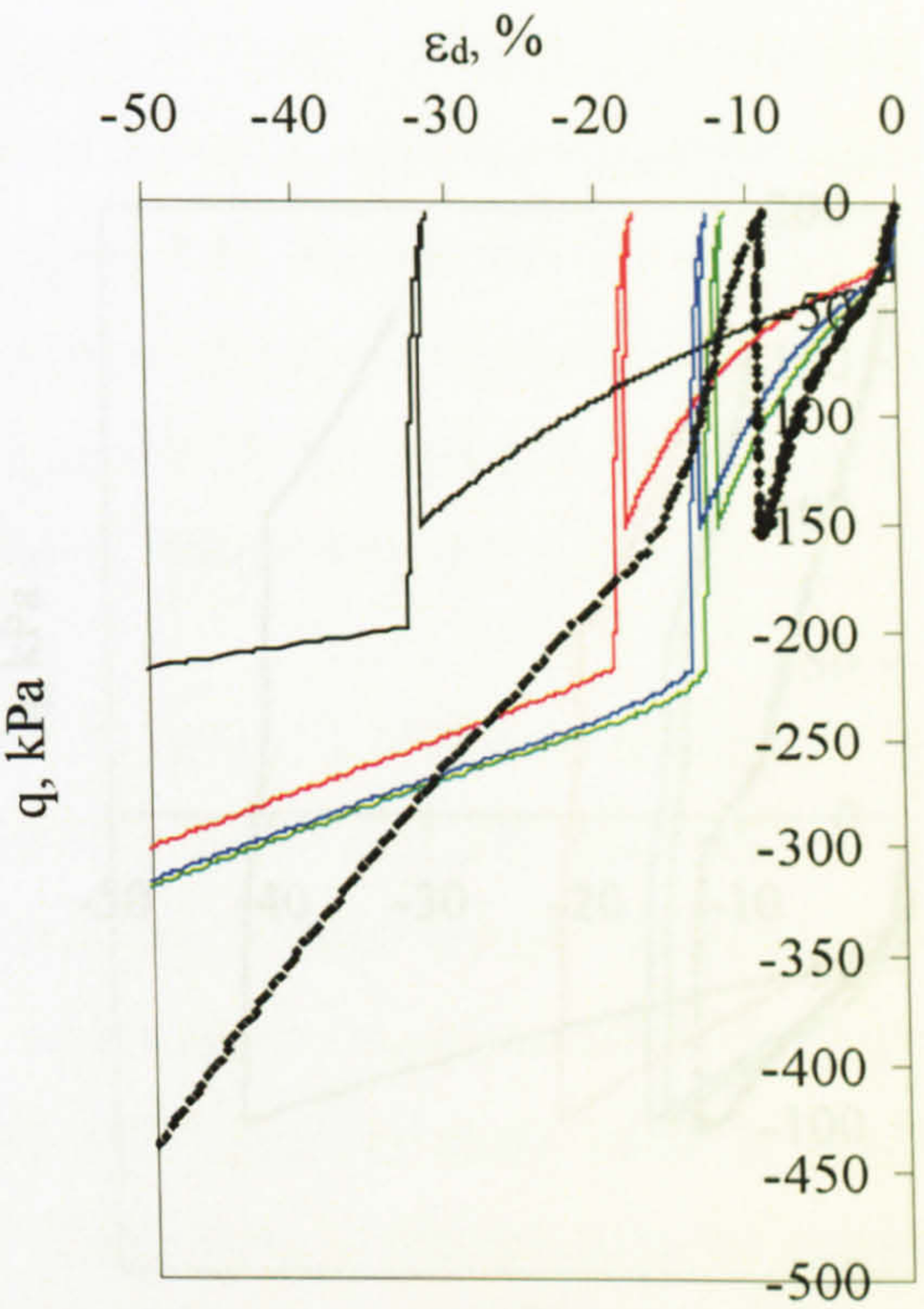

(b)

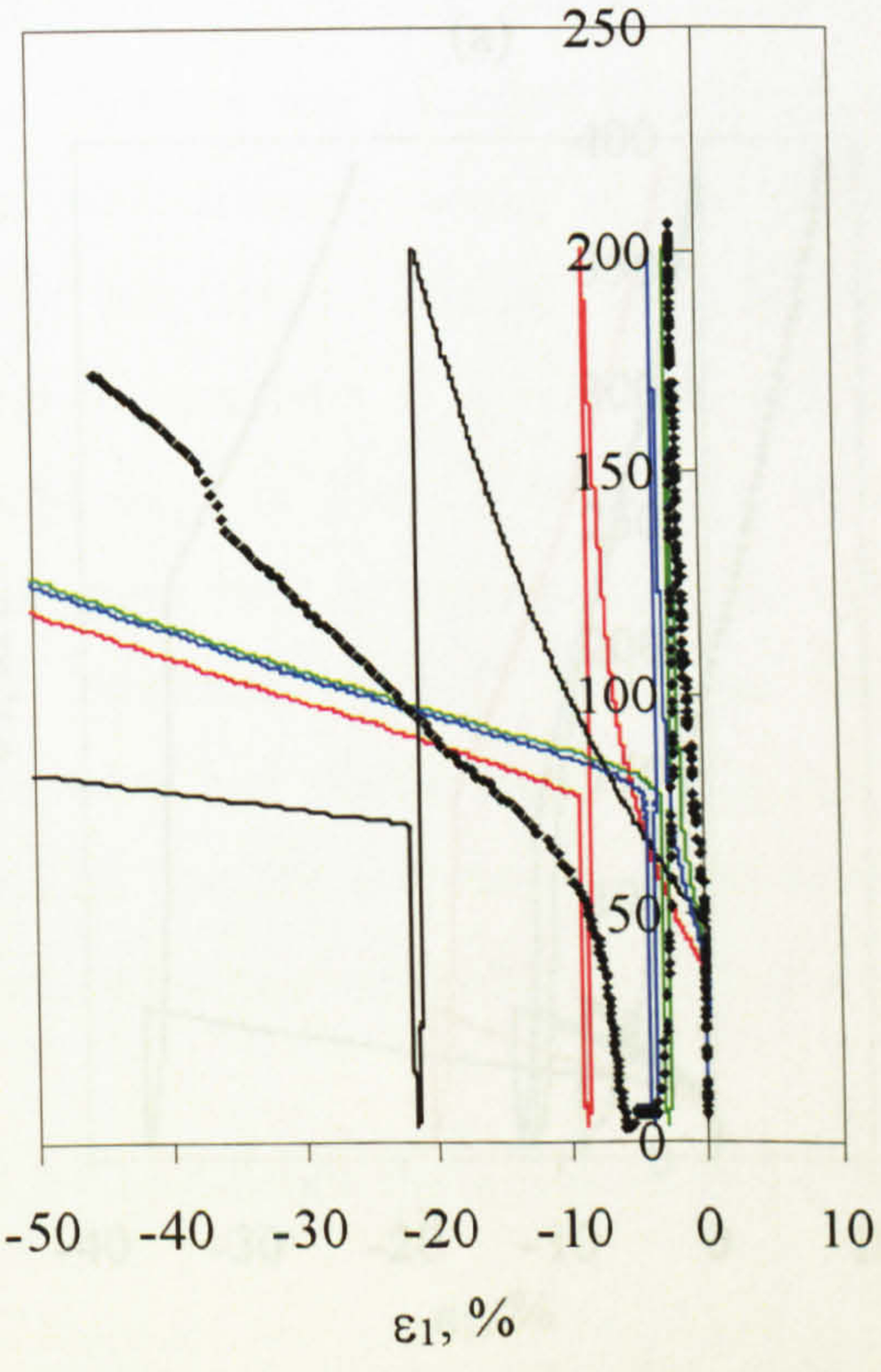

(c)

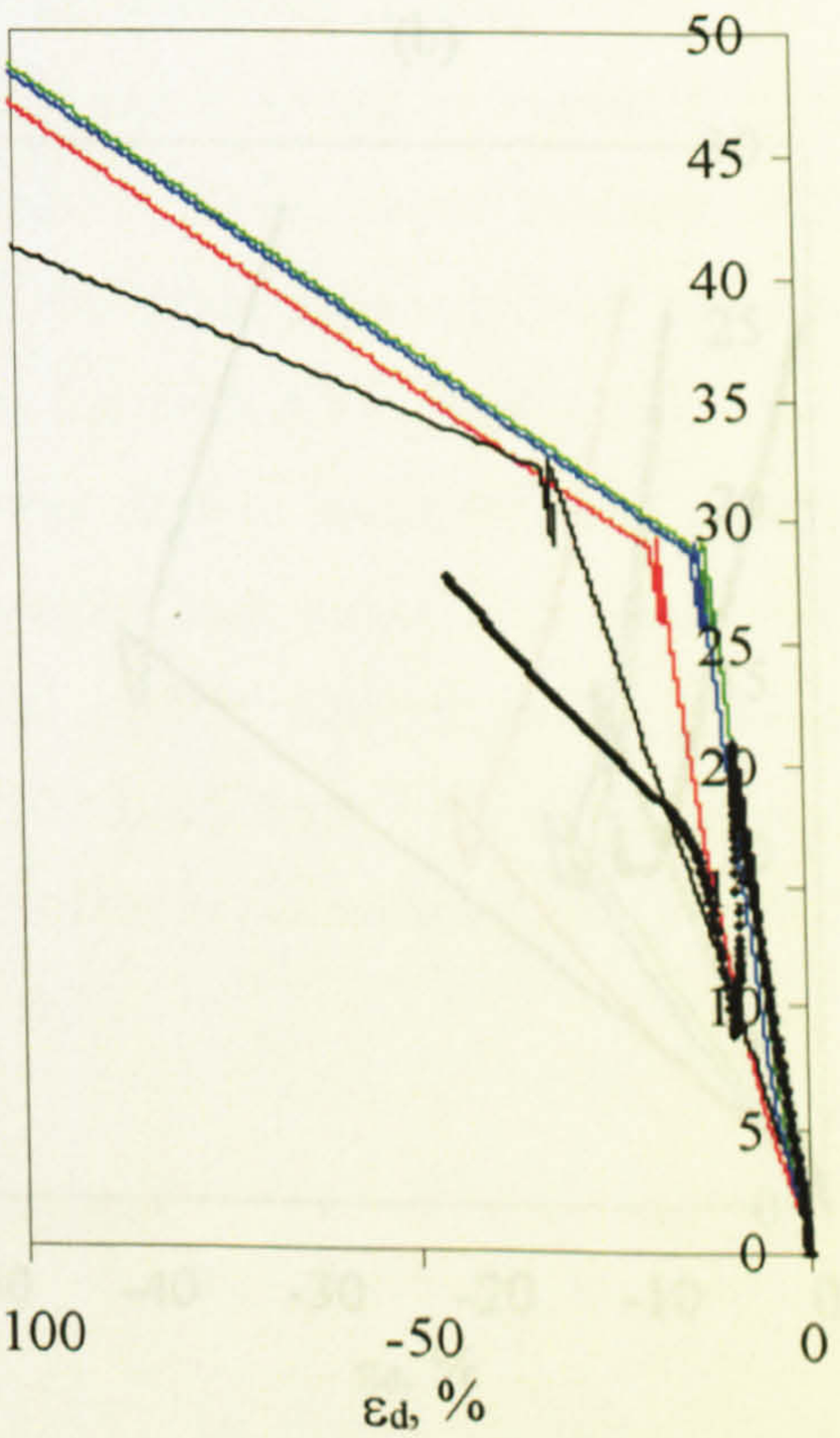

(d)

Figure 8.17. S-CLAY1 and MCC simulations of Test C9, where $\eta_1 = -0.50$ and $\eta_2 = -0.98$; (a) compression behaviour, (b) deviatoric stress-strain behaviour, (c) axial stress-strain behaviour, (d) strain paths.

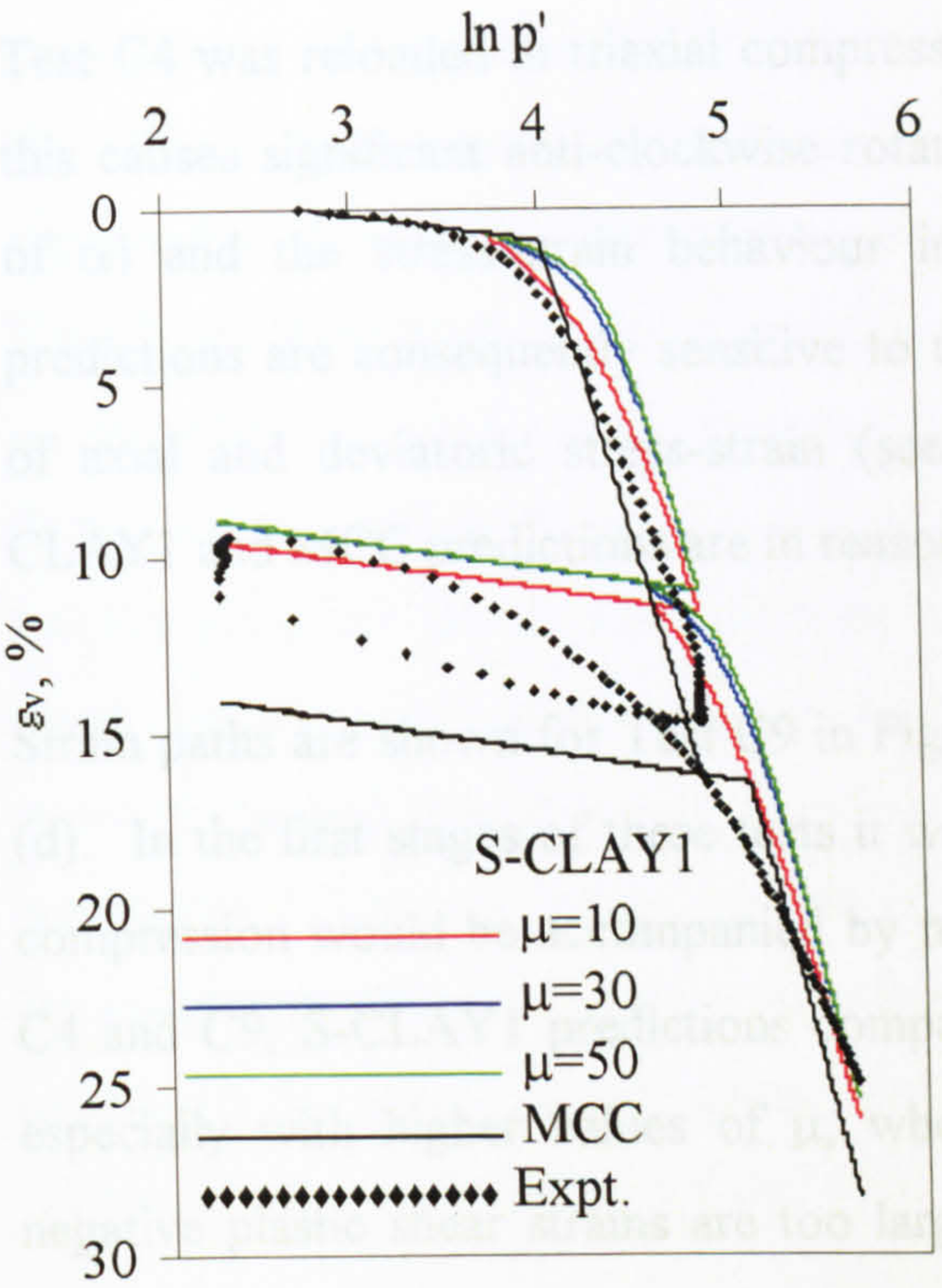

(a)

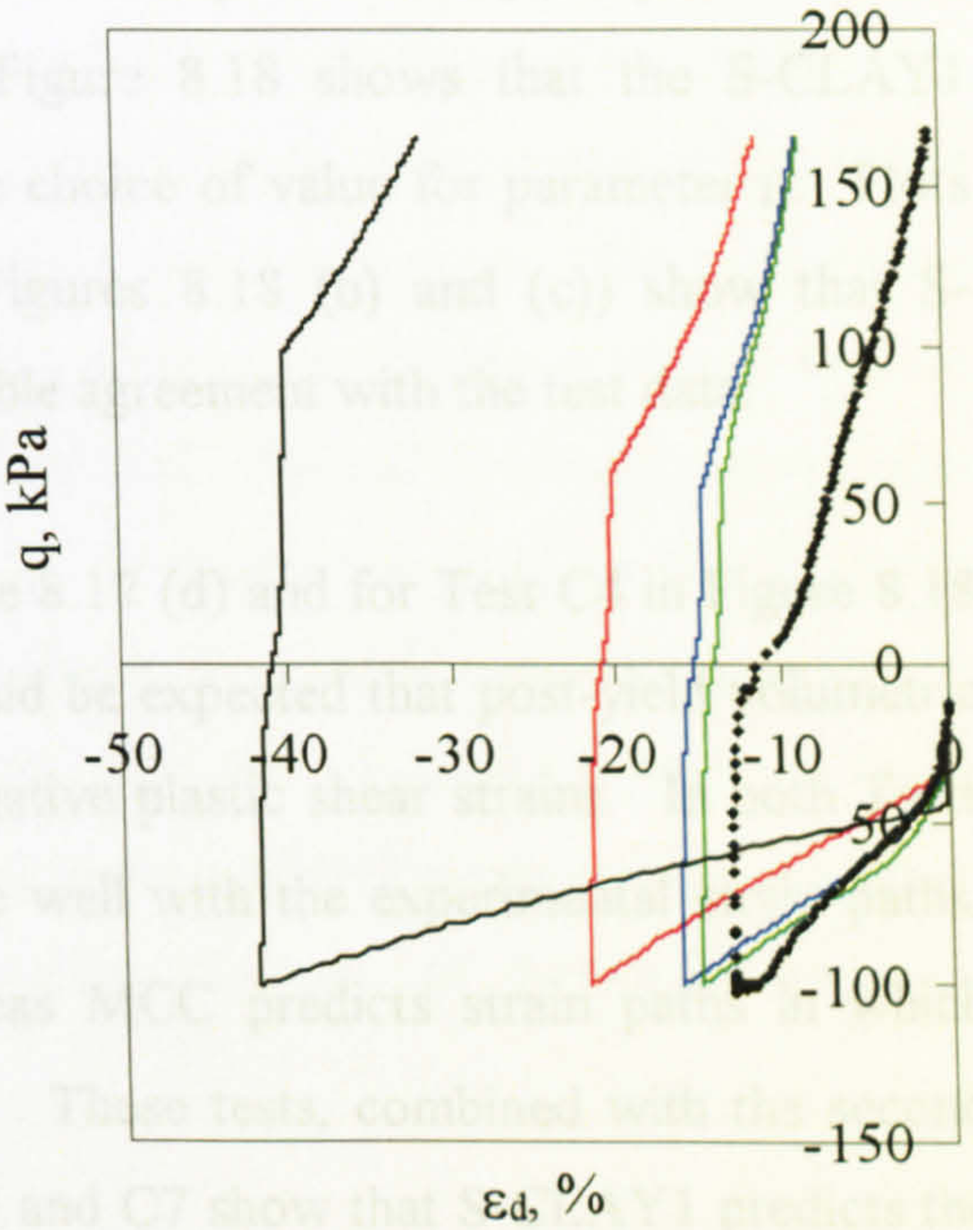

(b)

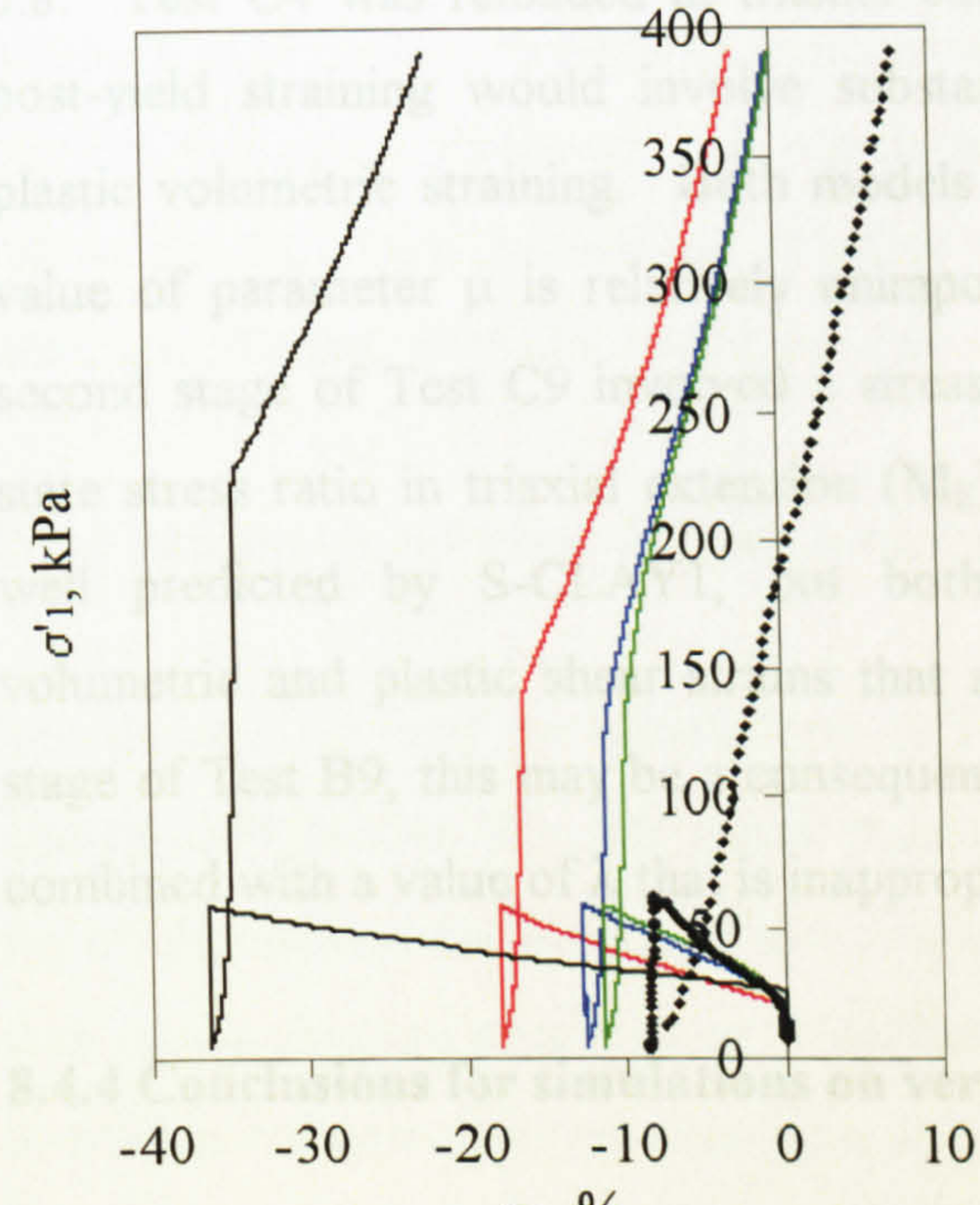

(c)

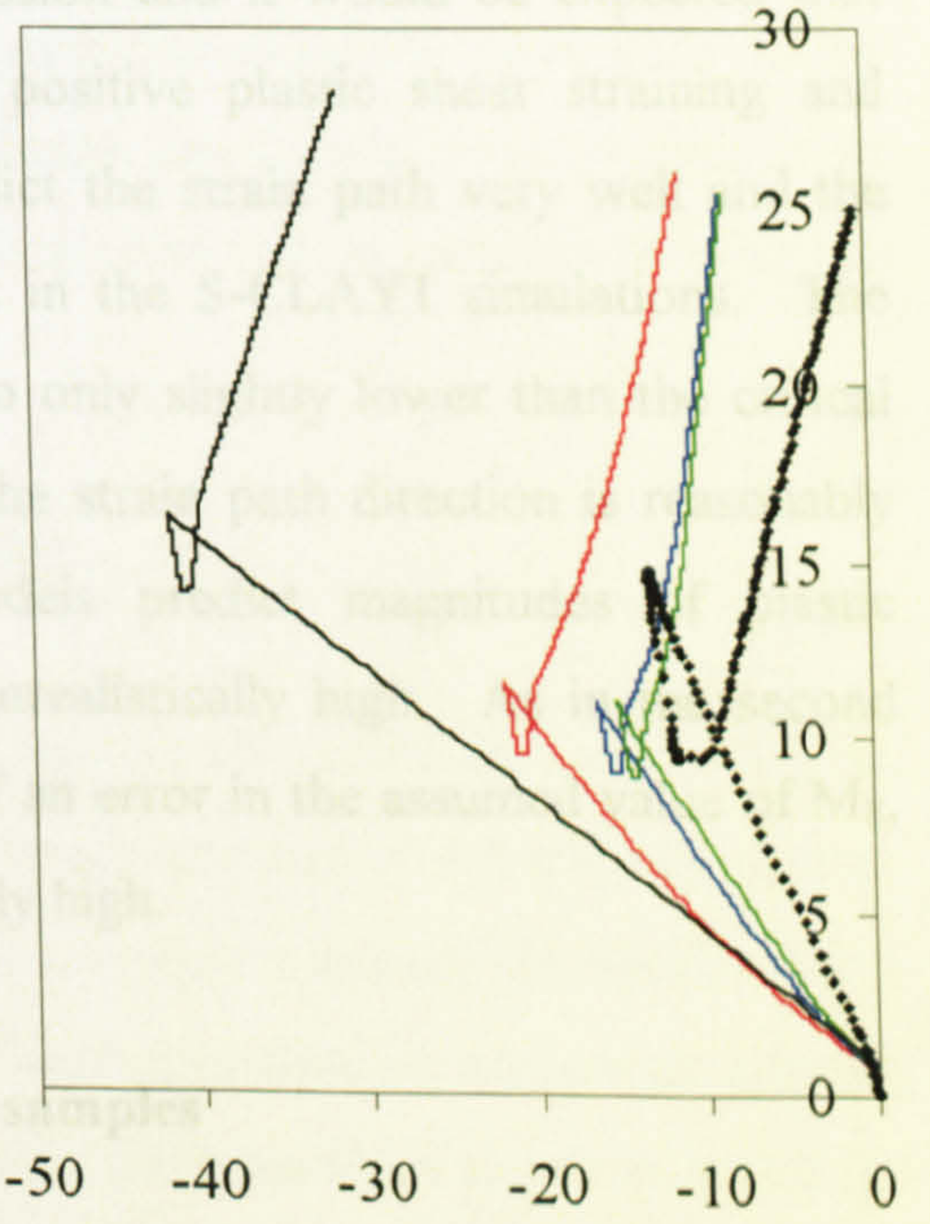

(d)

Figure 8.18. S-CLAY1 and MCC simulations of Test C4, where $\eta_1 = -0.80$ and $\eta_2 = 0.60$; (a) compression behaviour, (b) deviatoric stress-strain behaviour, (c) axial stress-strain behaviour, (d) strain paths.

Test C4 was reloaded in triaxial compression at $\eta_2 = 0.60$. S-CLAY1 predicts that this causes significant anti-clockwise rotation of the yield curve (to a positive value of α) and the stress-strain behaviour in Figure 8.18 shows that the S-CLAY1 predictions are consequently sensitive to the choice of value for parameter μ. Plots of axial and deviatoric stress-strain (see Figures 8.18 (b) and (c)) show that S-CLAY1 and MCC predictions are in reasonable agreement with the test data.

Strain paths are shown for Test C9 in Figure 8.17 (d) and for Test C4 in Figure 8.18 (d). In the first stages of these tests it would be expected that post-yield volumetric compression would be accompanied by negative plastic shear strains. In both Tests C4 and C9, S-CLAY1 predictions compare well with the experimental strain paths, especially with higher values of μ, whereas MCC predicts strain paths in which negative plastic shear strains are too large. These tests, combined with the second loading stages of Tests B5, B6, C2, C3, C5 and C7 show that S-CLAY1 predicts the pattern of straining very well for values of η in triaxial extension ranging from 0 to –0.8. Test C4 was reloaded in triaxial compression and it would be expected that post-yield straining would involve substantial positive plastic shear straining and plastic volumetric straining. Both models predict the strain path very well and the value of parameter μ is relatively unimportant in the S-CLAY1 simulations. The second stage of Test C9 involved a stress ratio only slightly lower than the critical state stress ratio in triaxial extension (M_E). The strain path direction is reasonably well predicted by S-CLAY1, but both models predict magnitudes of plastic volumetric and plastic shear strains that are unrealistically high. As in the second stage of Test B9, this may be a consequence of an error in the assumed value of M_E, combined with a value of λ that is inappropriately high.

8.4.4 Conclusions for simulations on vertical samples

In general, it is clear that the ability of S-CLAY1 to model changing plastic anisotropy means that it predicts stress-strain behaviour more accurately than MCC in nearly all of the loading conditions in Test Series C. This is due to the fact that the initial shape of the yield curve has been accurately matched to the test yield data points and that the model can match subsequent changes in anisotropy. However,

some aspects of modelling still require to be improved. There is strong evidence that the effects of destructuration must be accounted for. The gradients of the experimental post-yield compression curves are highly dependent on the stress ratio. The effects of destructuration appear to contribute to rapid compression at high stress ratios, while at lower stress ratios compression is more modest. Destructuration during a first loading stage also means that compression during a second loading stage is often less than would otherwise be expected. Pre-yield behaviour shows that elastic behaviour is significantly anisotropic. The magnitude of these elastic strains is not trivial and therefore incorporation of elastic anisotropic parameters should be considered. The use of an associated flow rule with S-CLAY1 appears to be generally applicable, but at very high stress ratios (in triaxial compression or triaxial extension) S-CLAY1 significantly overpredicts the rate of deviatoric straining (although not as severely as MCC).

8.5 Simulations of Test Series E

Model simulations on horizontal samples were generated using the same code as for vertical samples. However, the plastic compliance matrix was slightly altered to reflect the fact that the vertical direction in the ground is now coincident with the direction of radial stress in the triaxial cell.

8.5.1 Parameter selection for horizontal samples

The parameters used for simulations of Test Series E are shown in Table 8.2. As discussed in Section 7.3, the critical state parameters λ, κ and ν' are still appropriate for all simulations on horizontal samples and are therefore retained. In Section 7.2 it was shown that the critical state stress ratios observed in tests on horizontal samples in triaxial compression and extension were notably different from those recorded for the vertical samples. It is implicit in S-CLAY1 that M_C and M_E should be independent of sample orientation. Furthermore, if it is assumed that M_C and M_E are not equal, then in the generalized version of the model it would be appropriate to assume that the value of M is a function of the Lode angle of the tensor $\underline{\sigma}_d - p'\underline{\alpha}_d$. For tests on vertical samples, this simplifies to $M = M_C$ when $q - \alpha p'$ is positive ($\eta >$

α) and $M = M_E$ when $q-\alpha p'$ is negative ($\eta < \alpha$), and this is what was assumed in the simulations of tests on vertical samples presented in Sections 8.3 and 8.4. However, for tests on horizontal samples, the full expression for M as a function of the Lode angle of $\underline{\sigma}_d - p'\underline{\alpha}_d$ would be required and intermediate values of M (between M_C and M_E) would apply when the principal directions of $\underline{\sigma}_d$ and $\underline{\alpha}_d$ did not coincide (i.e. for most simulations). At present, there is insufficient evidence available to propose a suitable function for M. Therefore, in the interests of simplicity, a global value of M = 1.40 (the triaxial compression value for tests on vertical samples) has been adopted for all simulations of tests on horizontal samples.

Model	λ	κ	ν'	M	μ	β	α_0	p'_{m0}
MCC	0.48	0.02	0.20	1.4	(0)	(0)	(0)	86 kPa
S-CLAY1	0.48	0.02	0.20	1.4	10, 30, 50	0.94	0.28	85 kPa

Table 8.2. Model parameter values for simulations of horizontal samples.

The fact that $\alpha_0 = 0.28$ results in the following initial values for the fabric tensor components, as given by Equations 3.38 and 3.39; $\alpha_{y0} = 0.9$, $\alpha_{x0} = 1.2$ and $\alpha_{z0} = 0.9$ where the y direction corresponds to the axial direction in the triaxial test and the x radial direction corresponds to the vertical direction in the ground. The remaining "off-diagonal" terms of the fabric tensor components are equal to zero and remain so, hence; $\alpha_{xy} = \alpha_{yz} = \alpha_{zx} = 0$.

As an example Figure 8.19 shows the progress of the individual fabric tensor components for Test E1. During the first loading stage ($\eta_1 = 0$), each of the tensor components tends toward unity, corresponding to a scalar value of $\alpha = 0$ (isotropy). Each of the tensor components then remains unchanged during unloading. In the second loading stage ($\eta_2 = 0.75$) α_x and α_z (both radial directions in the triaxial test) tend towards a value of 0.84, while α_y (the axial direction), tends towards a value of 1.32. In Figure 8.19, S-CLAY1 predicts that during the second loading stage the plane of isotropy will develop in the x-z plane due to the equal radial stresses in the triaxial test. The application of a deviator stress has caused the value of α_y to be different from α_x and α_z.

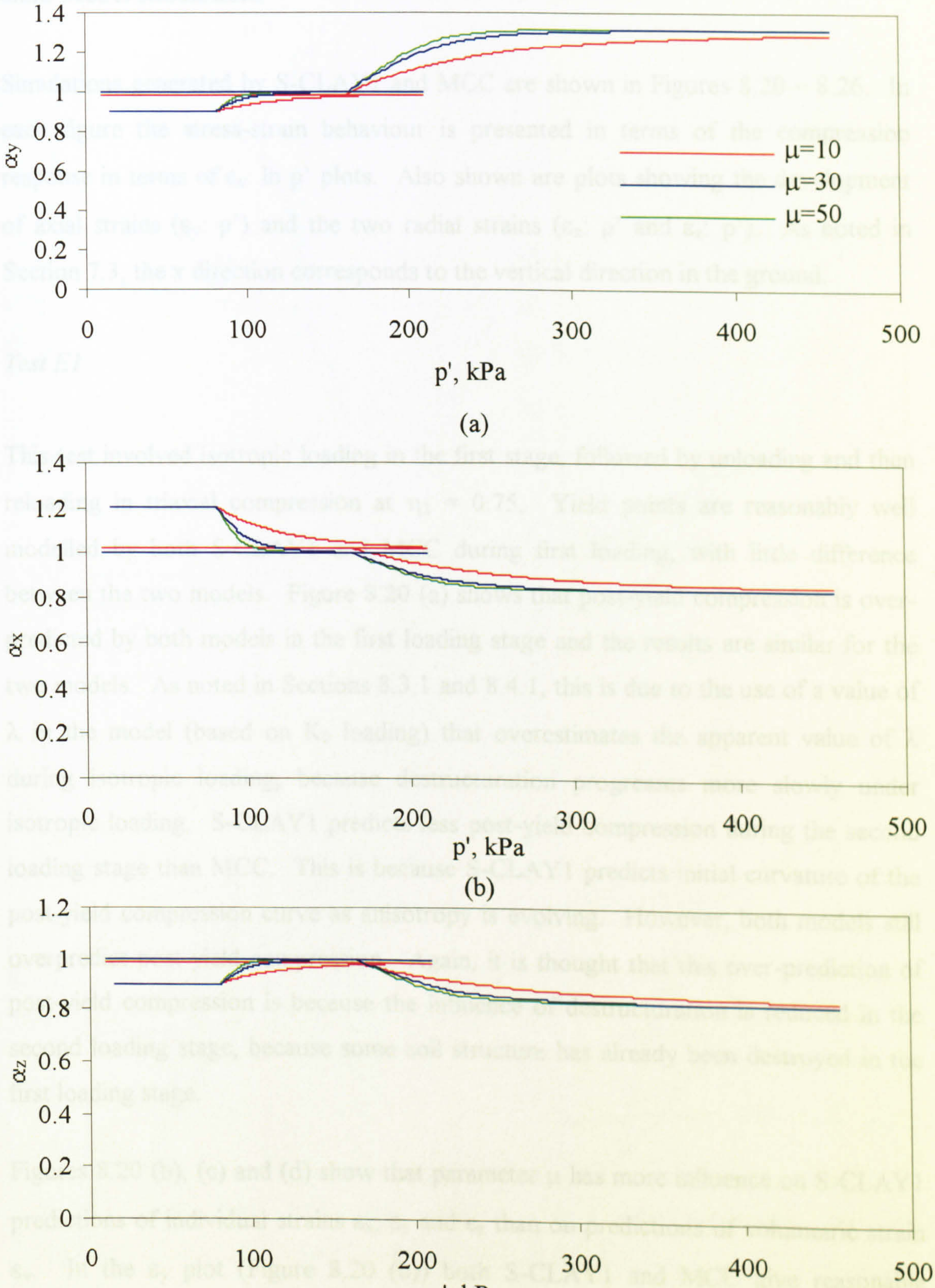

Figure 8.19. S-CLAY1 simulations of Test E1, where $\eta_1 = 0$ and $\eta_2 = 0.75$; (a) α_y, (b) α_x, (c) α_z.

8.5.2 Model simulations

Simulations generated by S-CLAY1 and MCC are shown in Figures 8.20 – 8.26. In each figure the stress-strain behaviour is presented in terms of the compression response in terms of ε_v: ln p' plots. Also shown are plots showing the development of axial strains (ε_y: p') and the two radial strains (ε_x: p' and ε_z: p'). As noted in Section 7.3, the x direction corresponds to the vertical direction in the ground.

Test E1

This test involved isotropic loading in the first stage, followed by unloading and then reloading in triaxial compression at $\eta_2 = 0.75$. Yield points are reasonably well modelled by both S-CLAY1 and MCC during first loading, with little difference between the two models. Figure 8.20 (a) shows that post-yield compression is over-predicted by both models in the first loading stage and the results are similar for the two models. As noted in Sections 8.3.1 and 8.4.1, this is due to the use of a value of λ in the model (based on K_0 loading) that overestimates the apparent value of λ during isotropic loading, because destructuration progresses more slowly under isotropic loading. S-CLAY1 predicts less post-yield compression during the second loading stage than MCC. This is because S-CLAY1 predicts initial curvature of the post-yield compression curve as anisotropy is evolving. However, both models still overpredict post-yield compression. Again, it is thought that this over-prediction of post-yield compression is because the influence of destructuration is reduced in the second loading stage, because some soil structure has already been destroyed in the first loading stage.

Figures 8.20 (b), (c) and (d) show that parameter μ has more influence on S-CLAY1 predictions of individual strains ε_x, ε_y and ε_z than on predictions of volumetric strain ε_v. In the ε_y plot (Figure 8.20 (b)) both S-CLAY1 and MCC give reasonable predictions of axial strains during the first loading stage. During second loading, however, S-CLAY1 gives much better predictions that MCC, which substantially overpredicts ε_y. For S-CLAY1, the best predictions of axial strain ε_y of are given by $\mu = 30$ or 50 rather than $\mu = 10$.

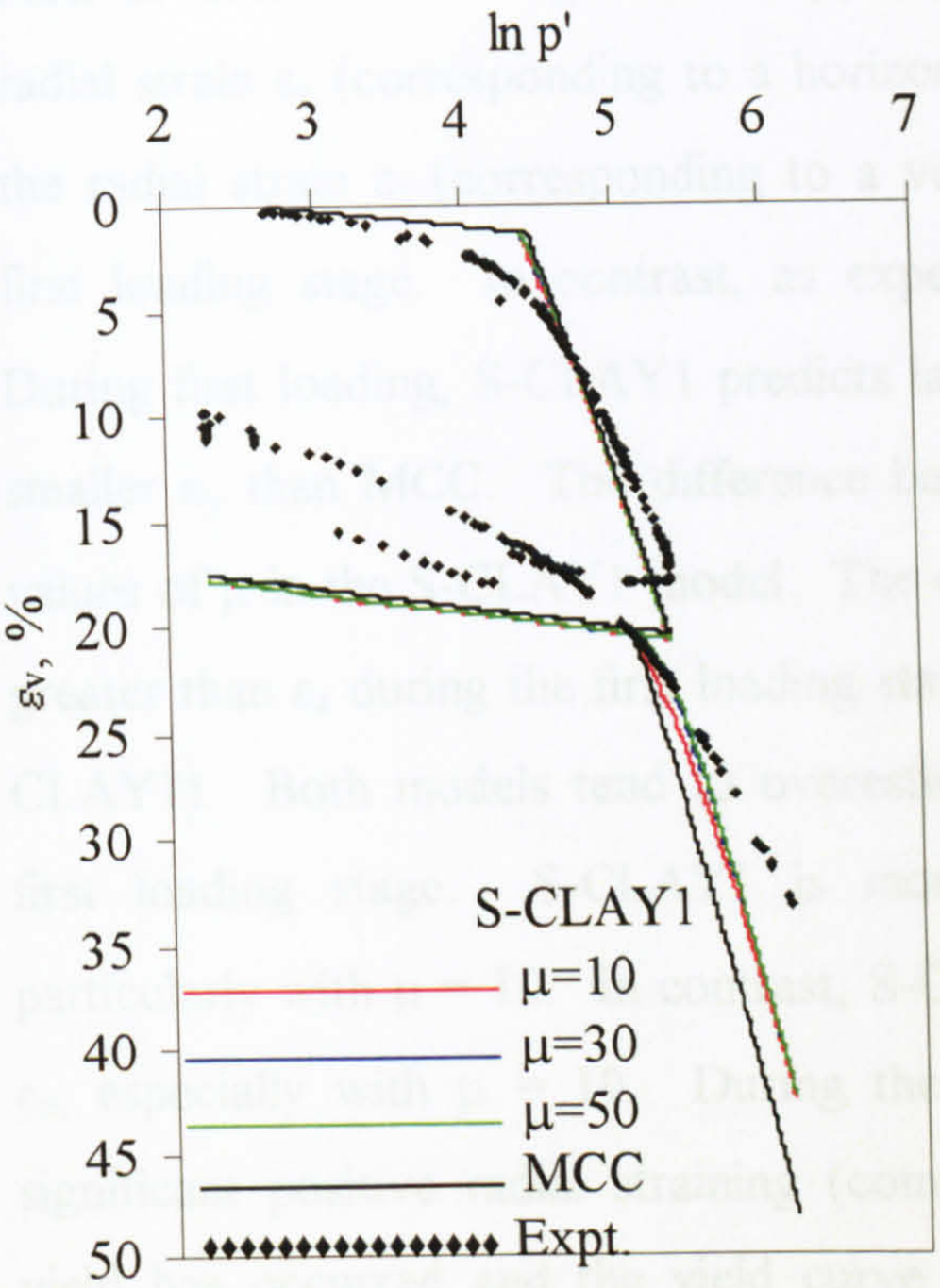

(a)

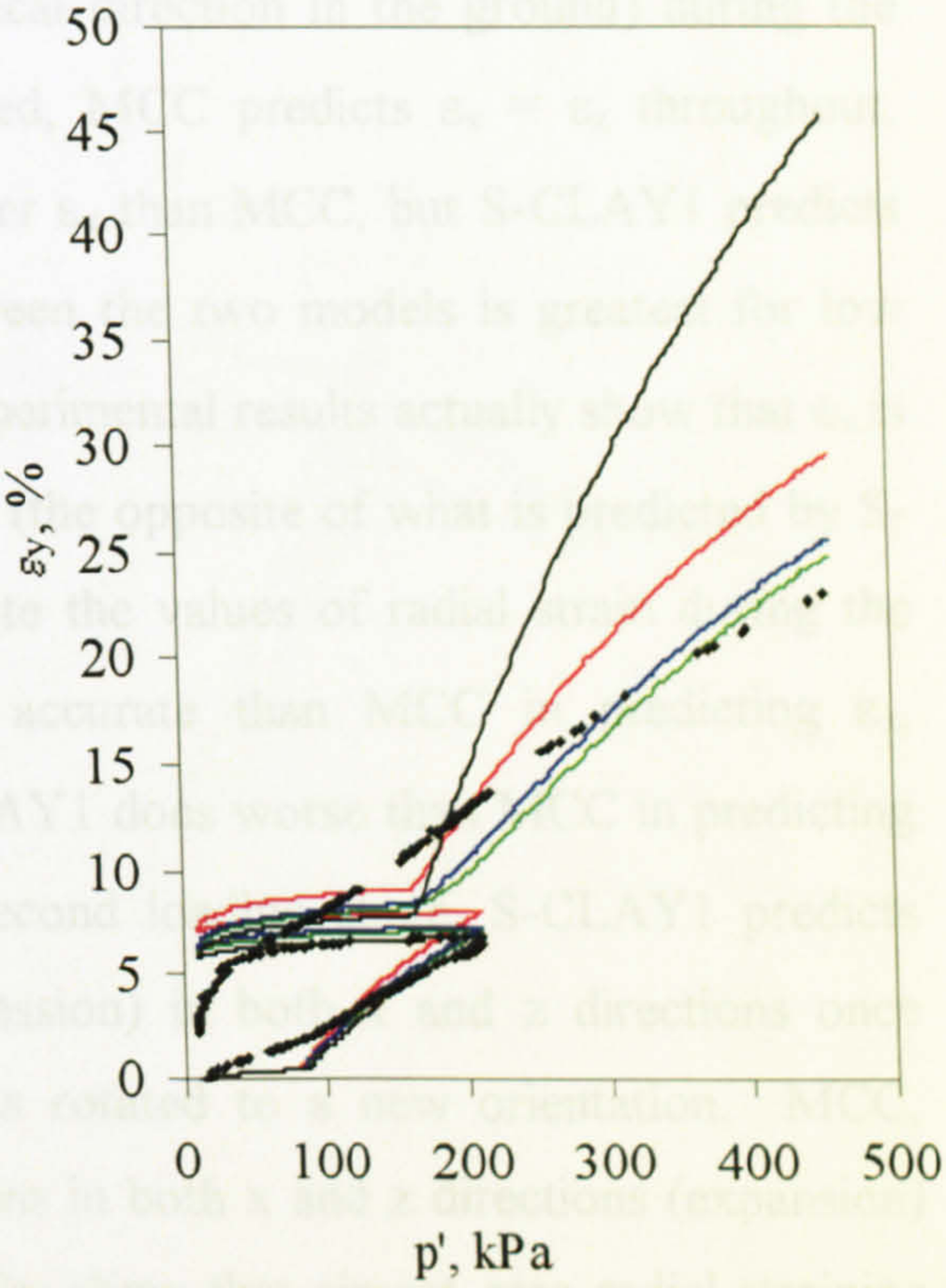

(b)

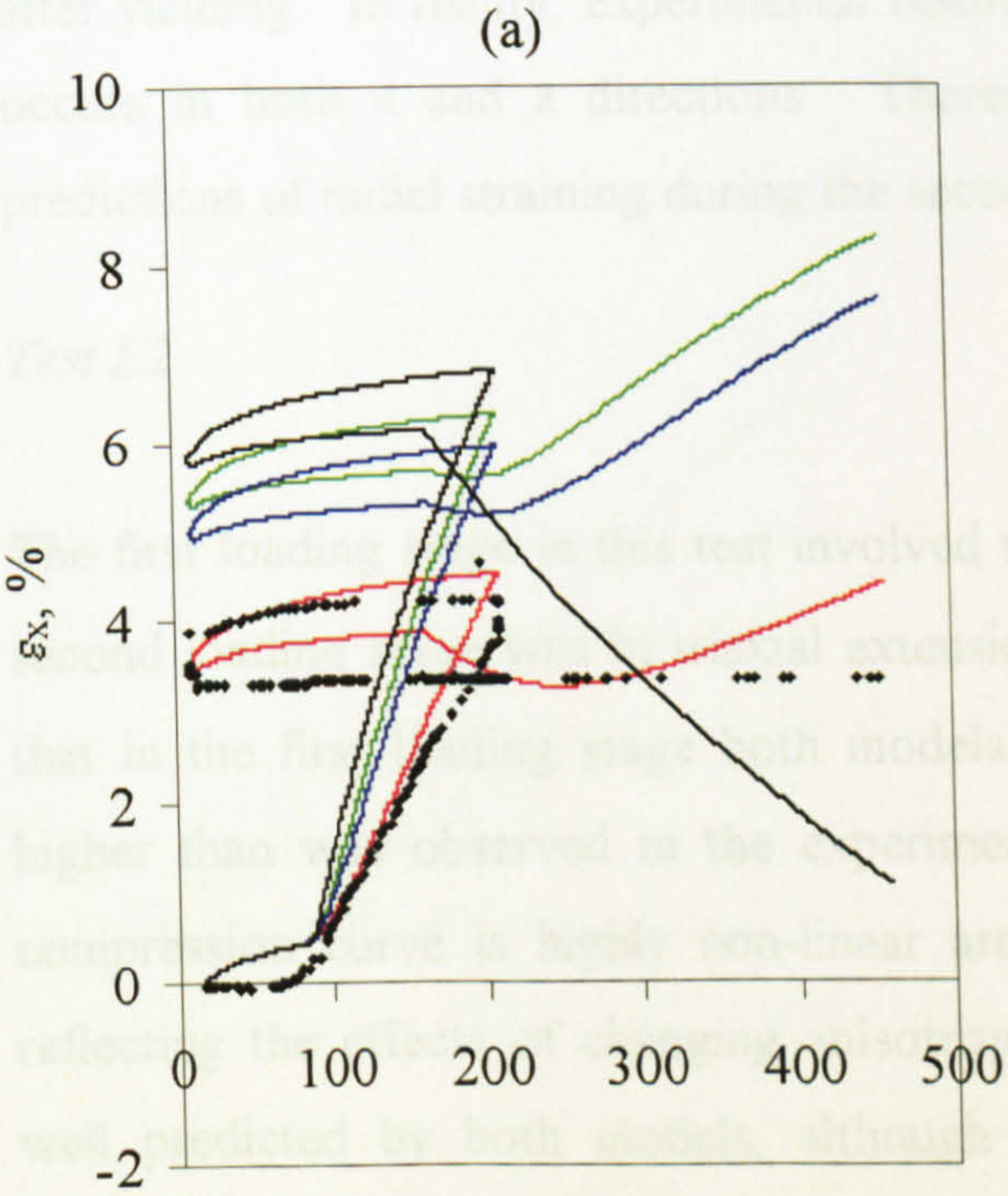

(c)

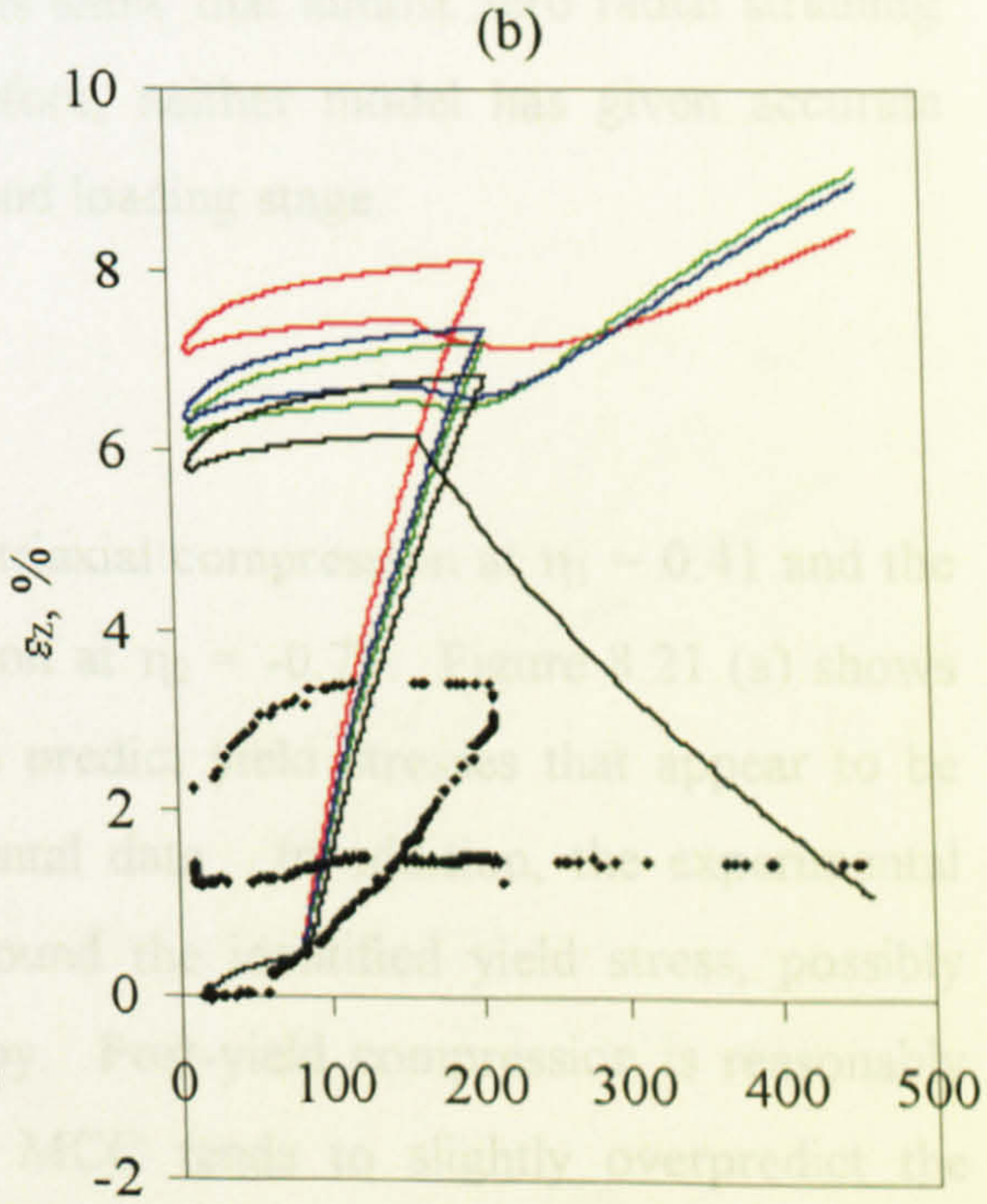

(d)

Figure 8.20. S-CLAY1 and MCC simulations of Test E1, where $\eta_1 = 0$ and $\eta_2 = 0.75$; (a) compression behaviour, (b) axial strain ε_y, (c) radial strain ε_x, (d) radial strain ε_z.

Plots of radial strain in Figures 8.20 (c) and (d) show that S-CLAY1 predicts that the radial strain ε_z (corresponding to a horizontal direction in the ground) is larger than the radial strain ε_x (corresponding to a vertical direction in the ground) during the first loading stage. In contrast, as expected, MCC predicts $\varepsilon_x = \varepsilon_z$ throughout. During first loading, S-CLAY1 predicts larger ε_x than MCC, but S-CLAY1 predicts smaller ε_y than MCC. The difference between the two models is greatest for low values of μ in the S-CLAY1 model. The experimental results actually show that ε_x is greater than ε_z during the first loading stage (the opposite of what is predicted by S-CLAY1). Both models tend to overestimate the values of radial strain during the first loading stage. S-CLAY1 is more accurate than MCC in predicting ε_x, particularly with $\mu = 10$. In contrast, S-CLAY1 does worse than MCC in predicting ε_z, especially with $\mu = 10$. During the second loading stage, S-CLAY1 predicts significant positive radial straining (compression) in both x and z directions once yield has occurred and the yield curve has rotated to a new orientation. MCC, however, predicts large negative radial strains in both x and z directions (expansion) after yielding. In reality, experimental results show that almost zero radial straining occurs in both x and z directions. Therefore, neither model has given accurate predictions of radial straining during the second loading stage.

Test E2

The first loading stage in this test involved triaxial compression at $\eta_1 = 0.41$ and the second loading stage was in triaxial extension at $\eta_2 = -0.79$. Figure 8.21 (a) shows that in the first loading stage both models predict yield stresses that appear to be higher than was observed in the experimental data. In addition, the experimental compression curve is highly non-linear around the identified yield stress, possibly reflecting the effects of changing anisotropy. Post-yield compression is reasonably well predicted by both models, although MCC tends to slightly overpredict the amount of compression (see Figure 8.21 (a)). The initial post-yield rate of compression is also apparently slower than in the corresponding first stages of Tests C1 and C7 (tests on vertical samples with $\eta_1 = 0.42$), emphasising the heightened influence of anisotropy in this test. During second loading, the experimental data in Figure 8.21 (a) shows that the compression curve is again highly non-linear and the

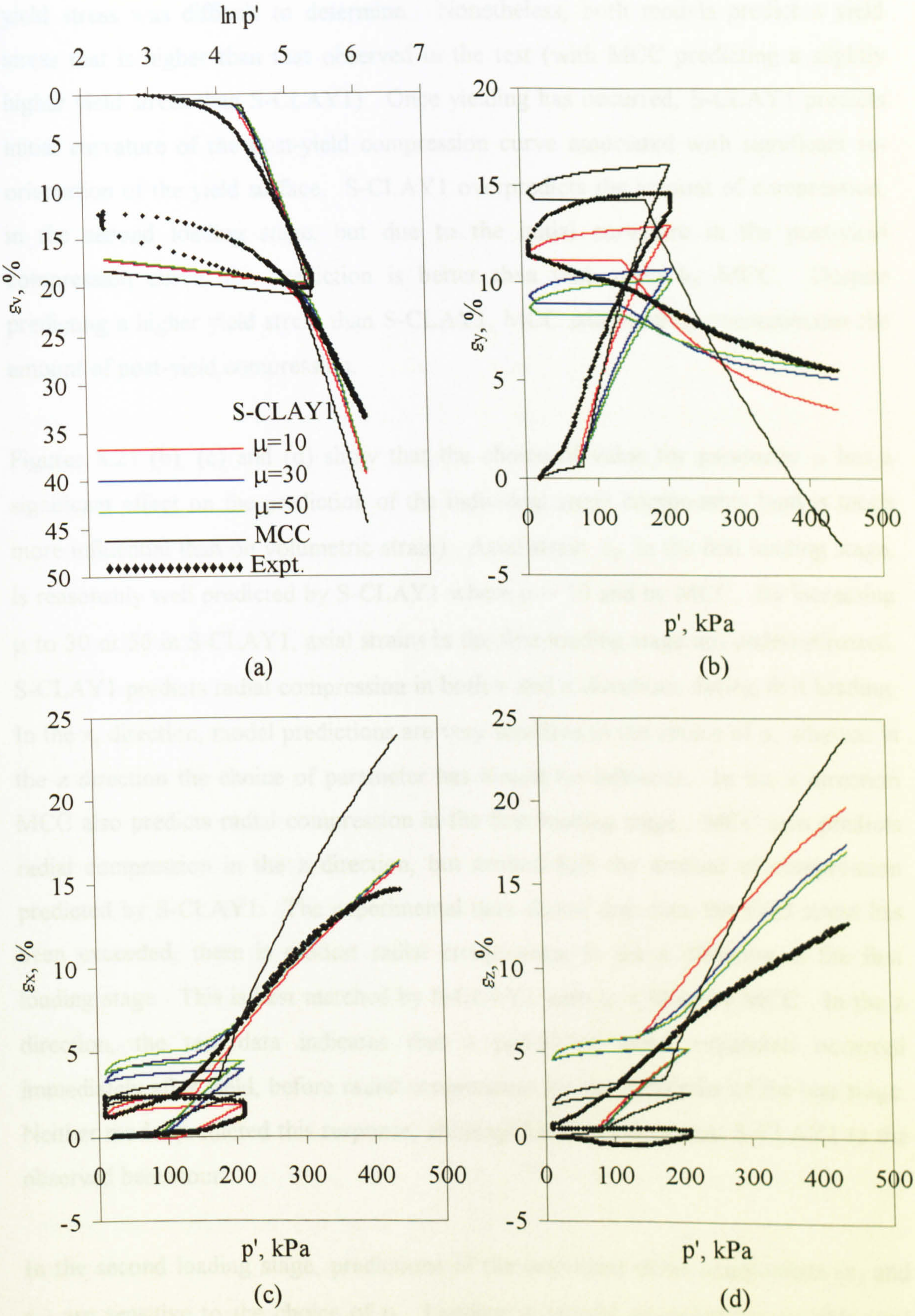

Figure 8.21. S-CLAY1 and MCC simulations of Test E2, where $\eta_1 = 0.41$ and $\eta_2 = -0.79$; (a) compression behaviour, (b) axial strain ε_y, (c) radial strain ε_x, (d) radial strain ε_z.

yield stress was difficult to determine. Nonetheless, both models predict a yield stress that is higher than that observed in the test (with MCC predicting a slightly higher yield stress than S-CLAY1). Once yielding has occurred, S-CLAY1 predicts initial curvature of the post-yield compression curve associated with significant re-orientation of the yield surface. S-CLAY1 overpredicts the amount of compression, in the second loading stage, but due to the initial curvature in the post-yield compression curve, the prediction is better than that given by MCC. Despite predicting a higher yield stress than S-CLAY1, MCC still severely overestimates the amount of post-yield compression.

Figures 8.21 (b), (c) and (d) show that the choice of value for parameter μ has a significant effect on the prediction of the individual strain components (and is much more influential than on volumetric strain). Axial strain, ε_y, in the first loading stage, is reasonably well predicted by S-CLAY1 where $\mu = 10$ and by MCC. By increasing μ to 30 or 50 in S-CLAY1, axial strains in the first loading stage are underestimated. S-CLAY1 predicts radial compression in both x and z directions during first loading. In the x, direction, model predictions are very sensitive to the choice of μ, whereas in the z direction the choice of parameter has almost no influence. In the x direction MCC also predicts radial compression in the first loading stage. MCC also predicts radial compression in the z direction, but around half the amount of compression predicted by S-CLAY1. The experimental data shows that once the yield stress has been exceeded, there is modest radial compression in the x direction in the first loading stage. This is best matched by S-CLAY1 with $\mu = 10$ or by MCC. In the z direction, the test data indicates that a period of radial expansion occurred immediately after yield, before radial compression for the remainder of the test stage. Neither model predicted this response, although MCC is closer than S-CLAY1 to the observed behaviour.

In the second loading stage, predictions of the individual strain components (ε_y and ε_z) are sensitive to the choice of μ. Loading in triaxial extension means that axial extension is predicted by both models (see Figure 8.21 (b)). The experimental data is in good agreement with S-CLAY1. MCC severely overestimates the amount of axial extension in the second loading stages. In both radial directions, S-CLAY1 is in

good agreement with the test data in the second loading stage. MCC significantly overpredicts the amount of radial compression in both directions.

Test E3

Test E3 involved a single loading stage in triaxial compression at $\eta = 0.80$. Figure 8.22 (a) shows that the yield stress is indistinct in the experimental data, although both models appear to overestimate this stress. In contrast to the vertical samples loaded at the same stress ratio (Test C5, see Figure 8.22 (a)) the post-yield compression curves predicted by S-CLAY1 in Test E3 are initially rounded and are sensitive to the choice of μ, due to influence of anisotropy (see Figure 8.22 (a)). S-CLAY1 matches the test data very well (particularly with $\mu = 10$), while MCC significantly overpredicts the amount of compression.

In the axial direction (see Figure 8.22 (b)) large compression is predicted by both S-CLAY1 and MCC. Despite overpredicting the yield stress, MCC significantly overpredicts the amount of post-yield axial compression. S-CLAY1 is in good agreement with the post-yield test data, particularly where $\mu = 10$. In the radial directions, both models predict slight radial compression as the pre-yield response. This is in contrast to the observed experimental data, which shows very slight radial expansion in both the x and z directions in the first part of the test. Post-yield S-CLAY1 predictions are sensitive to the choice of μ in both radial directions. In the x direction, each S-CLAY1 simulation initially predicts post-yield radial expansion. With μ set to 30 or 50, the model eventually predicts radial compression. MCC predicts post-yield radial expansion throughout the test. The test data shows post-yield radial expansion throughout, although the amount of expansion reduces as the test progresses. S-CLAY1 would probably match this behaviour reasonably well with an intermediate value of μ between 10 and 30. In the z direction S-CLAY1 predicts slight post-yield compression with μ set to 30 or 50 and very slight radial expansion with $\mu = 10$, whereas MCC predicts radial expansion throughout. The test data shows radial expansion in the z direction, although the shape of the stress-strain curve is not well matched by MCC (the observed response is intermediate between S-CLAY1 and MCC predictions).

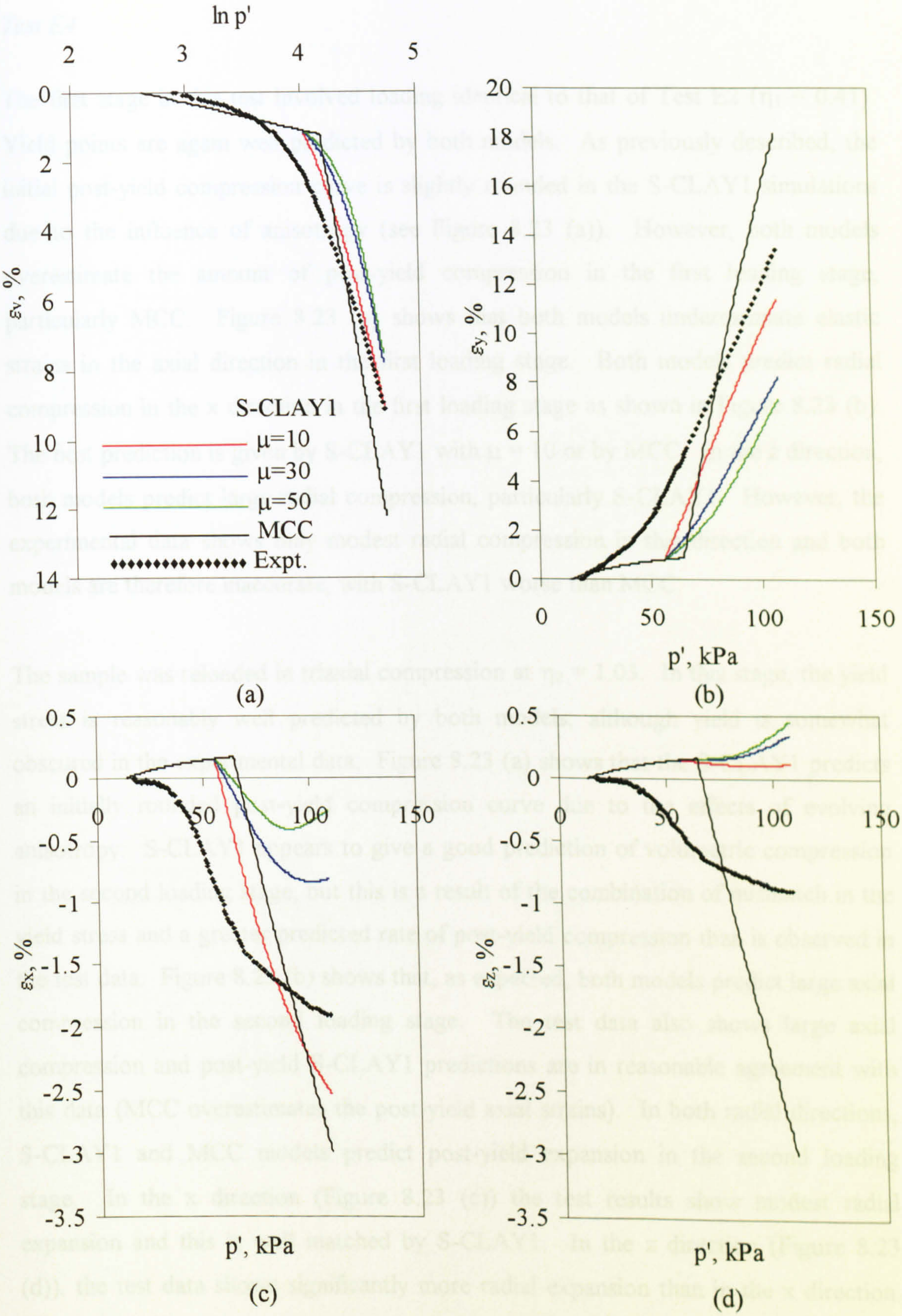

Figure 8.22. S-CLAY1 and MCC simulations of Test E3, where $\eta = 0.80$; (a) compression behaviour, (b) axial strain ε_y, (c) radial strain ε_x, (d) radial strain ε_z.

Test E4

The first stage in this test involved loading identical to that of Test E2 ($\eta_1 = 0.41$). Yield points are again well predicted by both models. As previously described, the initial post-yield compression curve is slightly rounded in the S-CLAY1 simulations due to the influence of anisotropy (see Figure 8.23 (a)). However, both models overestimate the amount of post-yield compression in the first loading stage, particularly MCC. Figure 8.23 (b) shows that both models underestimate elastic strains in the axial direction in the first loading stage. Both models predict radial compression in the x direction in the first loading stage as shown in Figure 8.23 (b). The best prediction is given by S-CLAY1 with $\mu = 10$ or by MCC. In the z direction, both models predict large radial compression, particularly S-CLAY1. However, the experimental data shows only modest radial compression in this direction and both models are therefore inaccurate, with S-CLAY1 worse than MCC.

The sample was reloaded in triaxial compression at $\eta_2 = 1.03$. In this stage, the yield stress is reasonably well predicted by both models, although yield is somewhat obscured in the experimental data. Figure 8.23 (a) shows that the S-CLAY1 predicts an initially rounded post-yield compression curve due to the effects of evolving anisotropy. S-CLAY1 appears to give a good prediction of volumetric compression in the second loading stage, but this is a result of the combination of mismatch in the yield stress and a greater predicted rate of post-yield compression than is observed in the test data. Figure 8.23 (b) shows that, as expected, both models predict large axial compression in the second loading stage. The test data also shows large axial compression and post-yield S-CLAY1 predictions are in reasonable agreement with this data (MCC overestimates the post-yield axial strains). In both radial directions, S-CLAY1 and MCC models predict post-yield expansion in the second loading stage. In the x direction (Figure 8.23 (c)) the test results show modest radial expansion and this is well matched by S-CLAY1. In the z direction (Figure 8.23 (d)), the test data shows significantly more radial expansion than in the x direction. The radial expansion in the z direction predicted by S-CLAY1 is less than occurred during the test. MCC greatly overpredicts the amount of radial expansion in both directions.

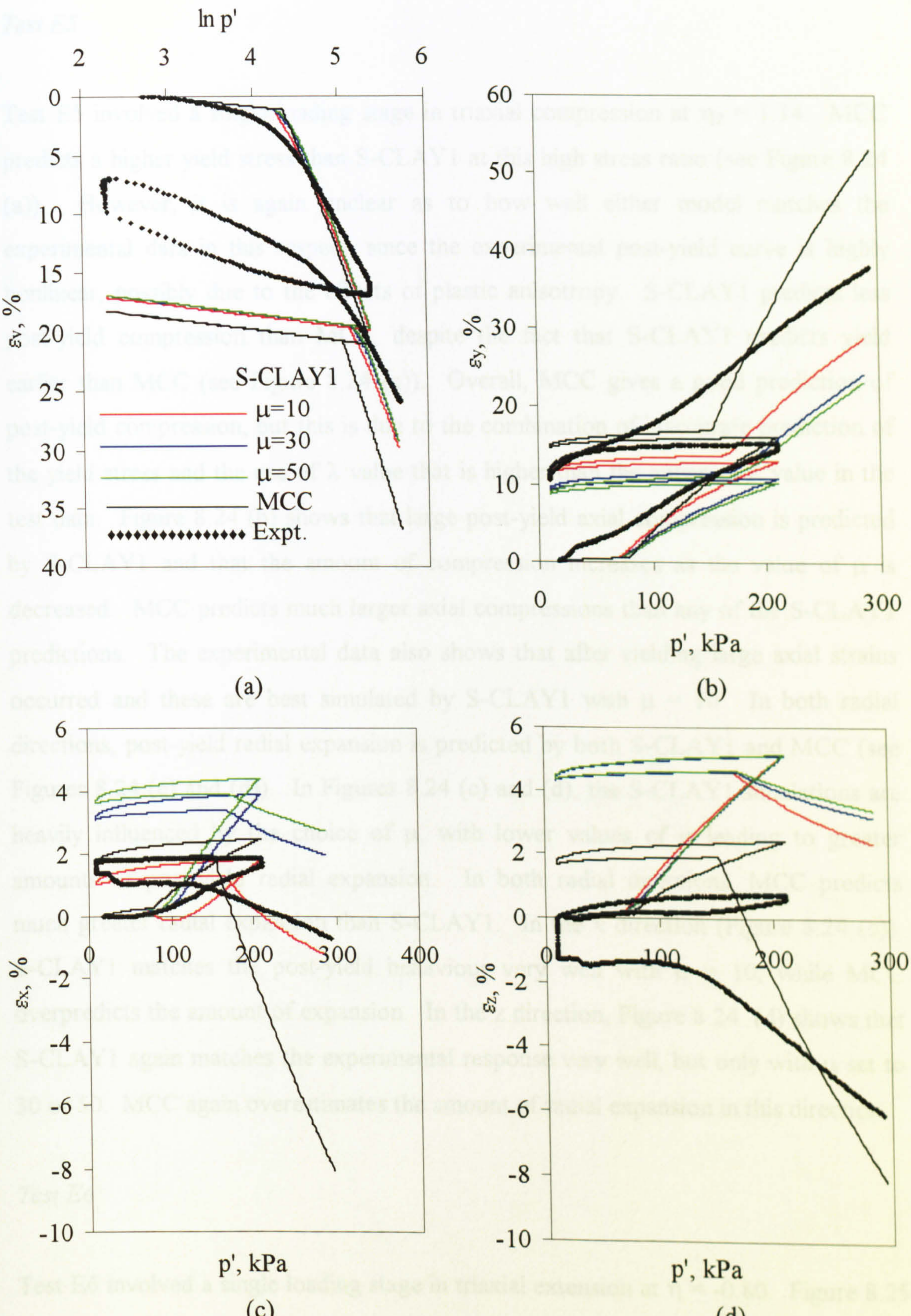

Figure 8.23. S-CLAY1 and MCC simulations of Test E4, where $\eta_1 = 0.41$ and $\eta_2 = 1.03$; (a) compression behaviour, (b) axial strain ε_y, (c) radial strain ε_x, (d) radial strain ε_z.

Test E5

Test E5 involved a single loading stage in triaxial compression at $\eta_2 = 1.14$. MCC predicts a higher yield stress than S-CLAY1 at this high stress ratio (see Figure 8.24 (a)). However, it is again unclear as to how well either model matches the experimental data in this respect, since the experimental post-yield curve is highly nonlinear, possibly due to the effects of plastic anisotropy. S-CLAY1 predicts less post-yield compression than MCC, despite the fact that S-CLAY1 predicts yield earlier than MCC (see Figure 8.24 (a)). Overall, MCC gives a good prediction of post-yield compression, but this is due to the combination of inaccurate prediction of the yield stress and the use of λ value that is higher than the apparent λ value in the test data. Figure 8.24 (b) shows that large post-yield axial compression is predicted by S-CLAY1 and that the amount of compression increases as the value of μ is decreased. MCC predicts much larger axial compressions than any of the S-CLAY1 predictions. The experimental data also shows that after yielding large axial strains occurred and these are best simulated by S-CLAY1 with $\mu = 10$. In both radial directions, post-yield radial expansion is predicted by both S-CLAY1 and MCC (see Figures 8.24 (c) and (d)). In Figures 8.24 (c) and (d), the S-CLAY1 simulations are heavily influenced by the choice of μ, with lower values of μ leading to greater amounts of post-yield radial expansion. In both radial directions, MCC predicts much greater radial expansion than S-CLAY1. In the x direction (Figure 8.24 (c)), S-CLAY1 matches the post-yield behaviour very well with $\mu = 10$, while MCC overpredicts the amount of expansion. In the z direction, Figure 8.24 (d) shows that S-CLAY1 again matches the experimental response very well, but only with μ set to 30 or 50. MCC again overestimates the amount of radial expansion in this direction.

Test E6

Test E6 involved a single loading stage in triaxial extension at $\eta = -0.80$. Figure 8.25 (a) shows that in this test, both MCC and S-CLAY1 predict approximately the same yield stress. Qualitatively, these predictions of yielding are in reasonable agreement with the experimental data, but again the compression curve from the test shows a rounded highly non-linear transition from pre-yield to post-yield behaviour. Figure

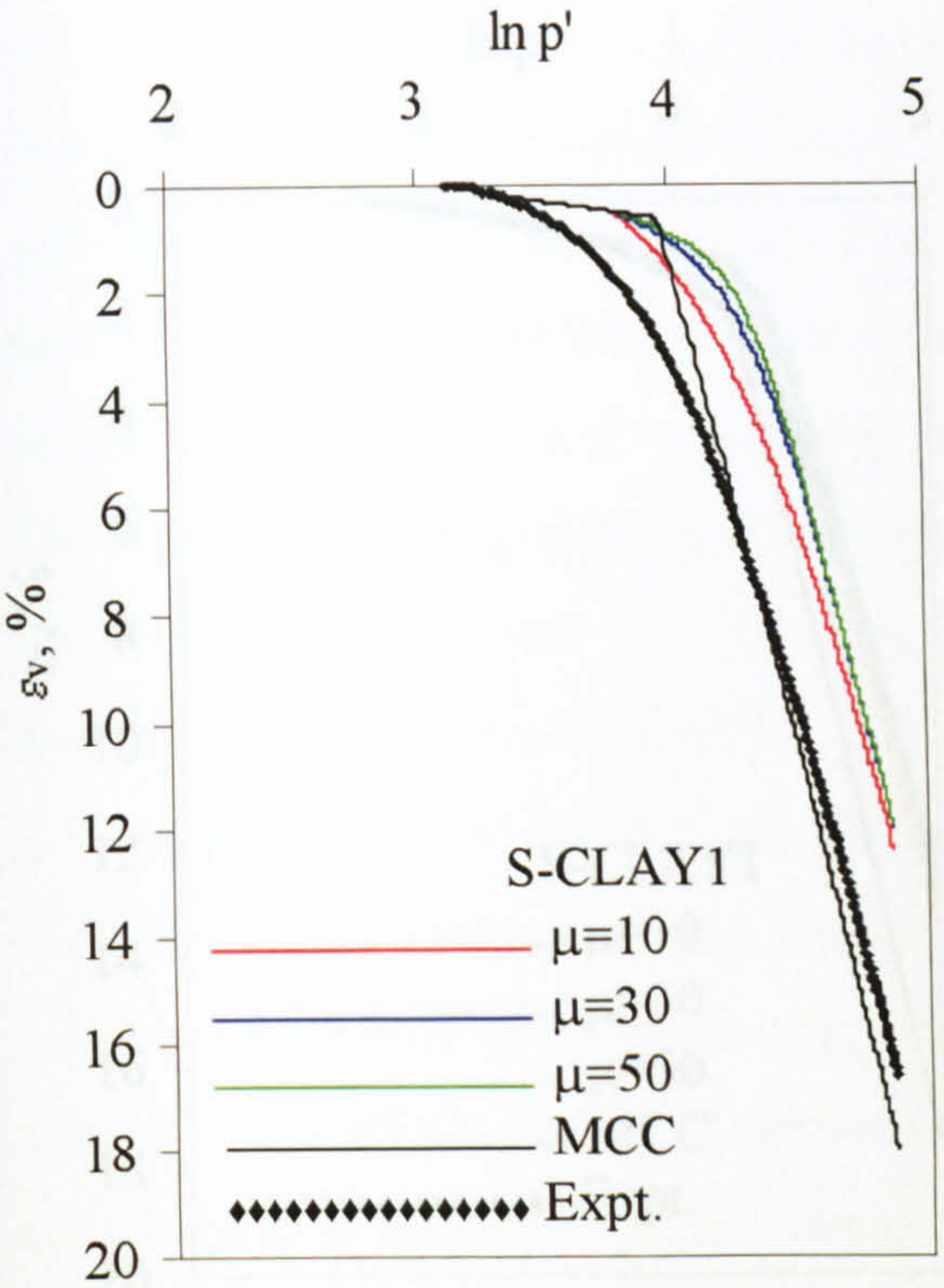

(a)

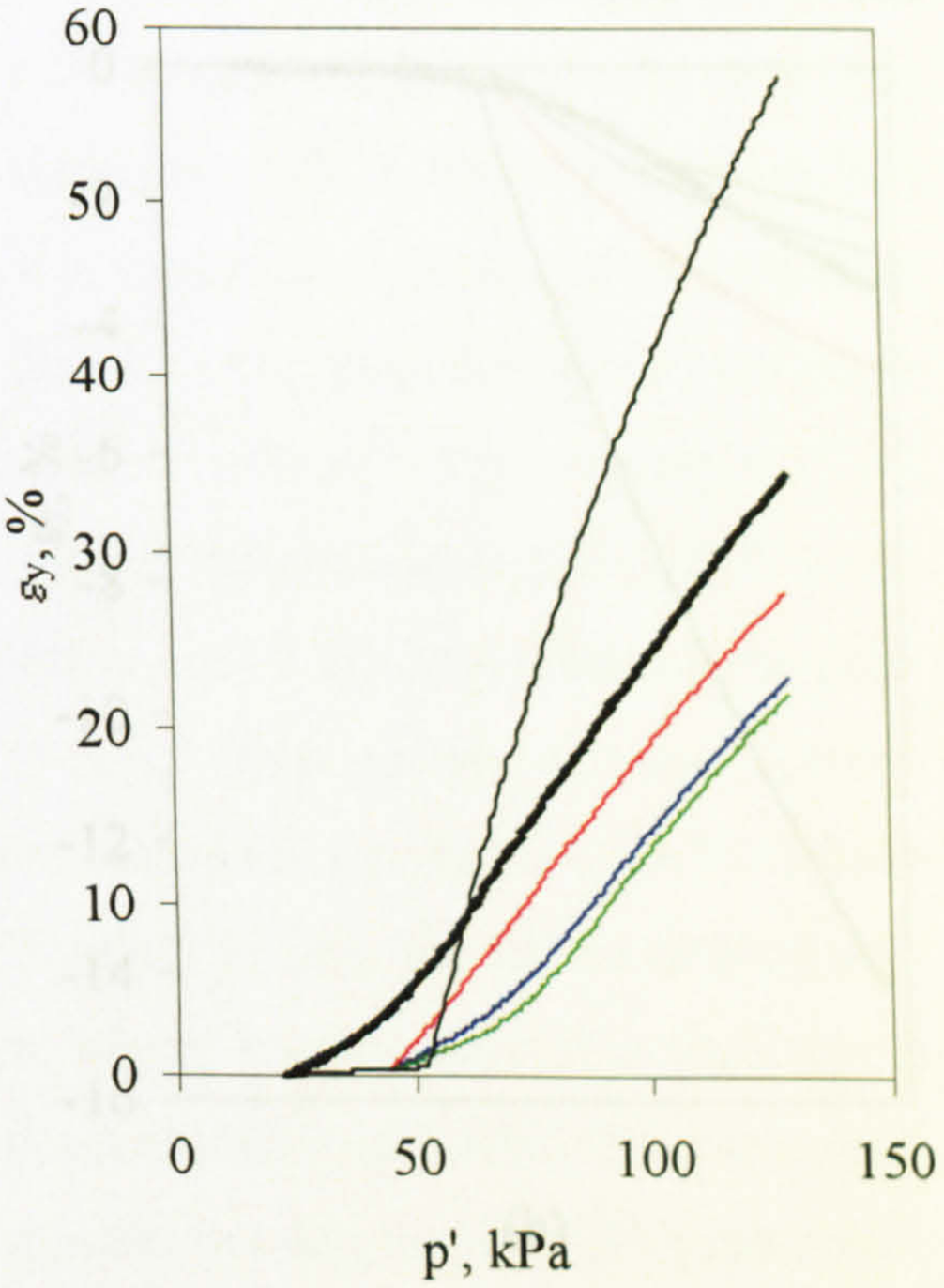

(b)

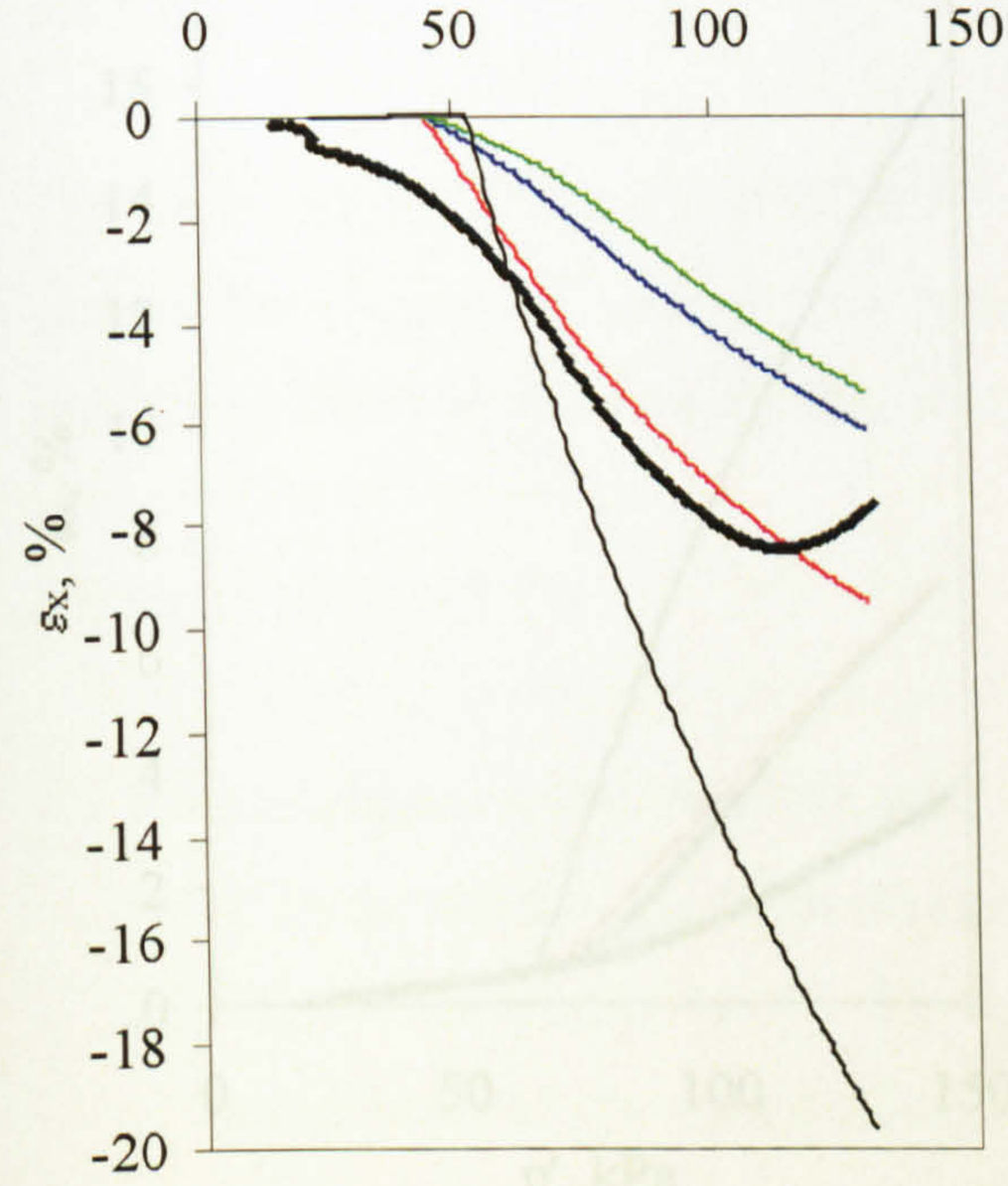

(c)

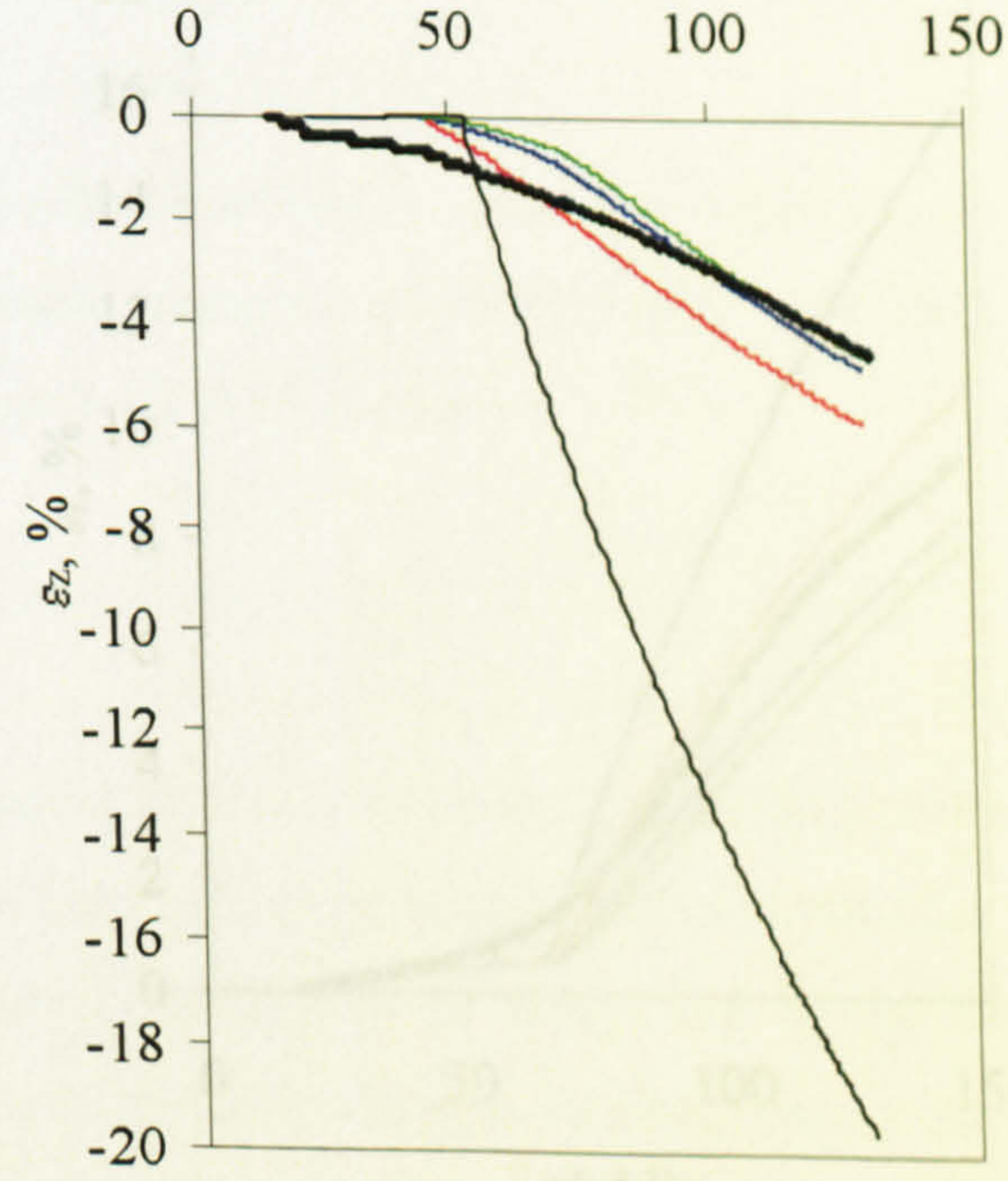

(d)

Figure 8.24. S-CLAY1 and MCC simulations of Test E5, where $\eta = 1.14$; (a) compression behaviour, (b) axial strain behaviour ε_y, (c) radial strain ε_x, (d) radial strain ε_z.

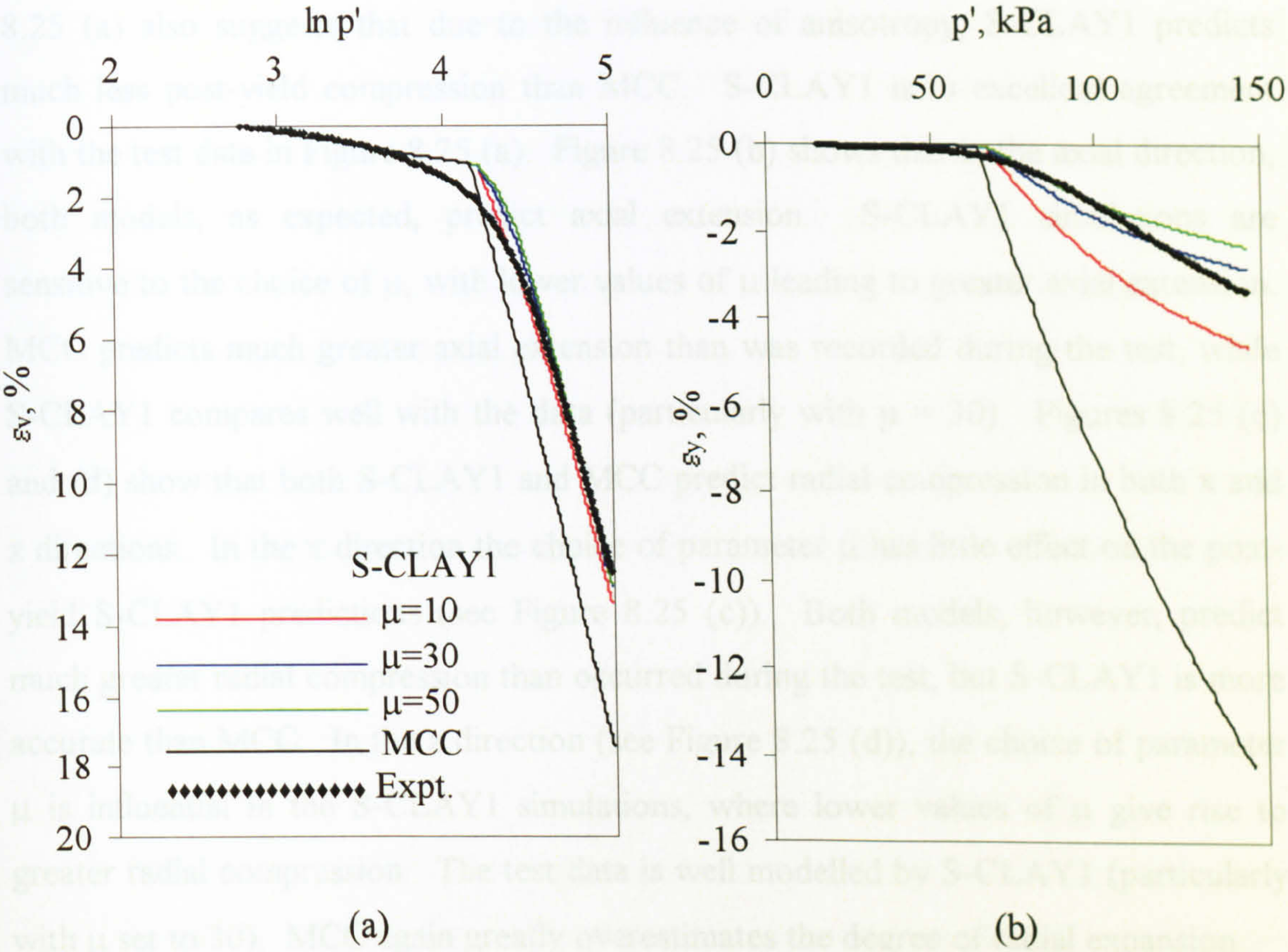

Figure 8.25. S-CLAY1 and MCC simulations of Test E6, where η = -0.80; (a) compression behaviour, (b) axial strain ε_y, (c) radial strain ε_x, (d) radial strain ε_z.

8.25 (a) also suggests that due to the influence of anisotropy, S-CLAY1 predicts much less post-yield compression than MCC. S-CLAY1 is in excellent agreement with the test data in Figure 8.25 (a). Figure 8.25 (b) shows that in the axial direction, both models, as expected, predict axial extension. S-CLAY1 simulations are sensitive to the choice of μ, with lower values of μ leading to greater axial extension. MCC predicts much greater axial extension than was recorded during the test, while S-CLAY1 compares well with the data (particularly with $\mu = 30$). Figures 8.25 (c) and (d) show that both S-CLAY1 and MCC predict radial compression in both x and z directions. In the x direction the choice of parameter μ has little effect on the post-yield S-CLAY1 predictions (see Figure 8.25 (c)). Both models, however, predict much greater radial compression than occurred during the test, but S-CLAY1 is more accurate than MCC. In the z direction (see Figure 8.25 (d)), the choice of parameter μ is influential in the S-CLAY1 simulations, where lower values of μ give rise to greater radial compression. The test data is well modelled by S-CLAY1 (particularly with μ set to 30). MCC again greatly overestimates the degree of radial expansion.

8.6 Conclusions

Comparisons of S-CLAY1 and MCC model simulations with the experimental results from tests on vertical and horizontal samples of Bothkennar clay have indicated various successes and failures of the S-CLAY1 model.

All tests

- Simulations using the S-CLAY1 model generally produce significantly more accurate predictions of Bothkennar clay behaviour than Modified Cam Clay. This is essentially due to the ability of S-CLAY1 to accurately model the initial form of the yield surface and subsequent changes in yield surface size and orientation associated with plastic straining and development of anisotropy.

- The effects of destructuration are significant in each test and cannot be accounted for by S-CLAY1. Both volumetric strains and shear strains appear

to be influential in the process of destructuration. Inaccurate model predictions are generally associated with the choice of λ_{K0}, which is inappropriate for first stages involving low stress ratios, where the apparent λ_1 value is less than λ_{K0} and for second loading stages where λ_2 is lower than λ_{K0} regardless of the stress ratio, due to the effects of destructuration in the preceding first loading stage.

- In many instances, pre-yield behaviour is not well matched by S-CLAY1. This is attributable to anisotropic and inelastic behaviour inside the yield S-CLAY1 yield surface.

Tests on vertical samples

- The use of an associated flow rule in simulations of vertical samples is generally justified for S-CLAY1. However, the magnitude of deviatoric strains tends to be overestimated at very high stress ratios in triaxial compression and triaxial extension. This may indicate either that the flow rule is non-associated at very high stress ratios or that the values of M_C and M_E have been underestimated.

Tests on horizontal samples

- The cross-section of the initial S-CLAY1 yield surface relating to horizontal samples, derived from knowledge of the yield surface cross-section for vertical samples, matches the yield points obtained for the horizontal samples very well.
- Experimental test data presented in Section 7.6 had shown that horizontal samples behave differently to corresponding vertical samples, due to the effects of initial anisotropy. The stress-strain behaviour is generally better matched by S-CLAY1 than by MCC, although S-CLAY1 predictions still sometimes show significant inaccuracies (possibly due to errors arising from incorrect yield surface shape). In addition to the factors already stated (the role of destructuration and the occurrence of anisotropic and inelastic

behaviour inside the S-CLAY1 yield surface), a contributory factor to these inaccuracies in the S-CLAY1 simulations for horizontal samples could be the assumption of a single value for the critical state stress ratio M. In future, it would be desirable to include dependency of M on the Lode angle of the tensor $\underline{\sigma}_d - p'\underline{\alpha}_d$ in the generalized version of S-CLAY1.

In the light of preceding evidence, it is necessary to further improve constitutive modelling of natural clay. The next step involves extending S-CLAY1 to incorporate soil bonding and destructuration and this is explored in Chapter 9 with the use of S-CLAY1S model simulations.

CHAPTER 9: S-CLAY1S MODEL SIMULATIONS

9.1 Introduction

Model simulations of the stress-strain behaviour of Bothkennar clay have shown that S-CLAY1 offers significantly improved predictions over Modified Cam Clay (see Chapter 8). However, there was also a clear suggestion that the accuracy could be improved further by incorporating the effects of destructuration. To investigate the role of destructuration, simulations using the S-CLAY1S model are now presented.

A single stress-point program (in Fortran) was written and used to generate S-CLAY1 simulations and has been extended to incorporate the additional features of S-CLAY1S. This program allows for an initial degree of bonding and destructuration associated with plastic straining. The S-CLAY1S simulations involve only vertical samples since simulations on horizontal samples would have required development of a generalized version of the code, which has not, at present, been written. However, it is considered that simulations on vertical samples will be sufficient to test whether S-CLAY1S shows an improvement over S-CLAY1.

9.2 S-CLAY1S parameter selection

The parameters used in the S-CLAY1 model simulations were retained with the exception of the λ-value (see Section 9.2.2 below). Therefore the soil constants were $\kappa = 0.02$, $M_C = 1.4$, $M_E = 1.1$, $\mu = 30$, $\beta = 0.94$ and $\nu' = 0.2$. Additional soil constants required for the S-CLAY1S model were destructuration parameters a and b (see Section 9.2.3 below). The initial state was given by $\alpha_0 = 0.28$, $p'_{m0} = 85$ kPa. The initial value of x_0 (degree of bonding) must be specified (Section 9.2.1).

9.2.1 Initial degree of bonding (x_0)

Since the degree of bonding may be estimated from the soil sensitivity, S_t, this can be used as a source of information in choosing the value of x_0 for Bothkennar clay. Koskinen et al. (2002b) suggested that bonding and sensitivity could be related by

$$x_0 = S_t - 1 \tag{9.1}$$

This estimation is likely to be conservative, given that, in measuring the sensitivity, some degree of bonding will have been lost during shearing to measure the "undisturbed" undrained shear strength of the soil. In tests on natural POKO clay, Koskinen (2002b) found that with S_t in the range 10 - 20 a value of $x_0 = 15$ was appropriate. For Bothkennar clay Nash et al. (1992a) reported values of sensitivity in the range 5-6 for a depth 10-11m below ground level. Hight et al. (1992) suggested $S_t = 5$ - 8, although more often the values were reported at around 5. Based on this information it is likely that $x_0 = 4 - 7$, with the possibility that a higher value of x_0 may be necessary if significant destructuration occurred during the process of shear testing to assess the sensitivity of the soil. In the first instance (see Section 9.3.1), a value of $x_0 = 5$ was used (and subsequently compared with higher values of x_0).

It should be noted that, as discussed in Chapter 2, Clayton et al. (1992) showed that even when samples are carefully extruded from the ground using high quality Laval samplers, the soil will suffer some loss of structure. It is therefore reasonable to suggest that the initial value of bonding x_0 of a clay in the field will be greater than would be deduced from laboratory tests. Clayton et al. (1992) demonstrated clearly that the effects of sampling would cause a shrinking of the soil's yield surface. Therefore, it is possible that estimation of the in-situ value of the initial bonding from laboratory tests may be slightly conservative.

9.2.2 Intrinsic λ-value (λ_i)

The S-CLAY1S model requires a value for λ_i, the gradient of the intrinsic compression line (for a reconstituted soil). As previously described in Section 6.4.3, it is thought that the slope of the intrinsic post-yield compression curve is described by $\lambda_i = 0.18$ and this value is therefore applied during S-CLAY1S simulations. S-CLAY1 simulations are again presented in this chapter for comparison and these retain a post-yield gradient $\lambda_{K0} = 0.48$.

9.2.3 Destructuration parameters a and b

To obtain the destructuration parameters a and b from laboratory test results, model simulations must be compared with the test results. Simulations involving high values of η will be influenced by both parameters a and b. At low values of η, the choice of parameter b has very little effect on the model predictions. Parameter a should therefore be examined under isotropic loading. Parameter b governs the relative influence of plastic shear strains in the destructuration process and should therefore be assessed with tests involving high values of η in triaxial compression or triaxial extension. Zentar et al. (2002a) suggested values of a = 8, b = 0.3 for Bothkennar clay, and Koskinen et al. (2002b) suggested a = 9, b = 0.2 for POKO clay. This information was useful in establishing starting values for a and b in the process of optimising the final values for Bothkennar clay.

9.3 S-CLAY1S Model simulations

9.3.1 Determination of value of parameter a

The simplest method of determining the value of the destructuration parameter a is by examining tests in which the first loading path involved a low stress ratio or isotropic loading. In these cases, the influence of plastic shear strains and therefore the parameter b on destructuration is relatively small. Each of the tests in Series B involved isotropic loading during the first stage to a mean effective stress of p' = 210 kPa. In the S-CLAY1S model predictions the initial value of the bonding parameter x_0 was 5. Three different S-CLAY1S simulations are shown in Figure 9.1, with values of 8, 10 and 12. In all cases a value of 0.2 was used for b. The value of parameter b has been selected on the basis that b = 0.2 is typical for other soft clays as reported by Koskinen et al.(2002b). Moreover, the actual value of b is unimportant in these simulations where plastic shear strains are very small. The predicted and observed stress-strain behaviour during these test stages is shown in Figure 9.1 (a) in

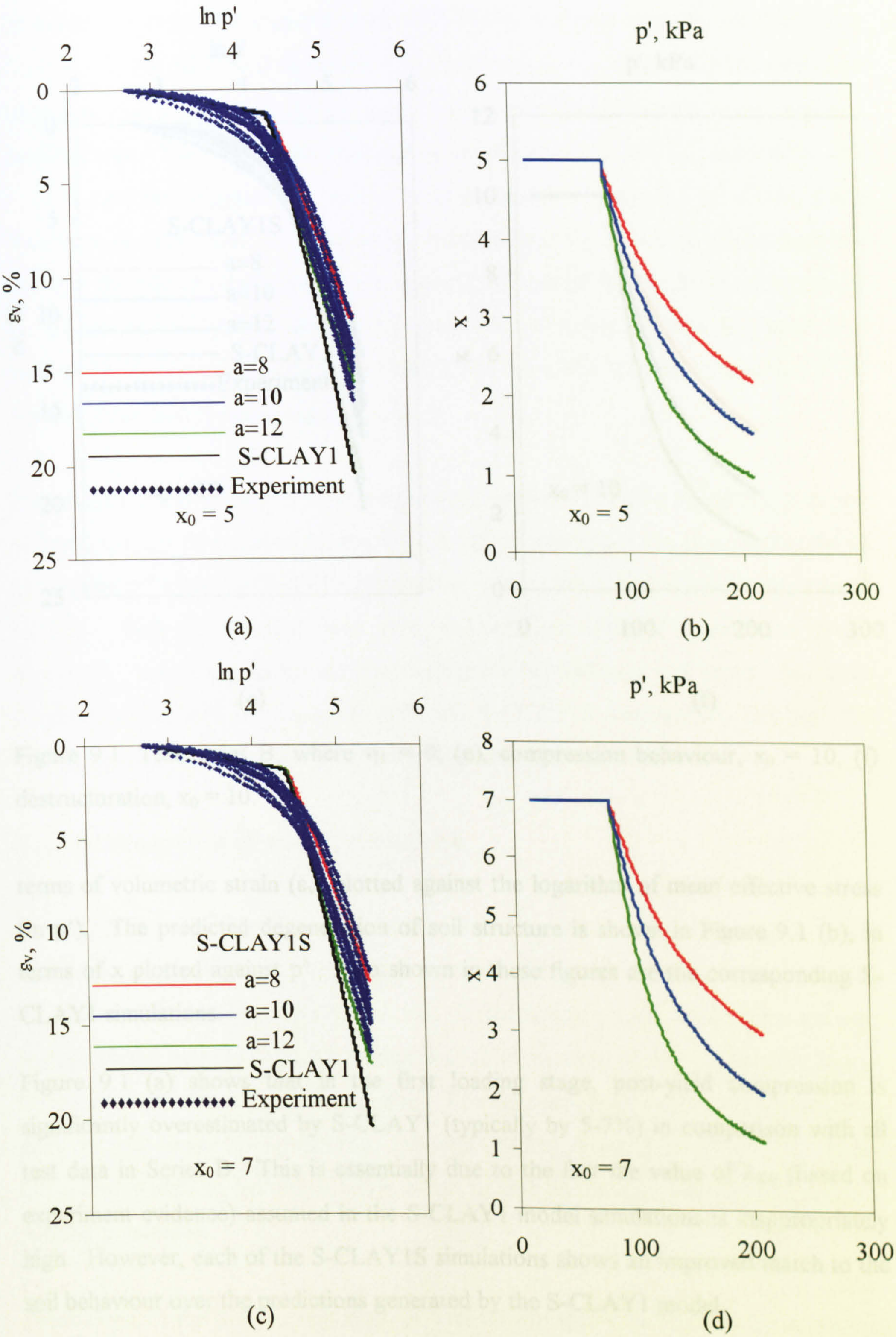

Figure 9.1. Predicted and observed behaviour during first loading stages in Test Series B, where η_1=0; (a), compression behaviour, x_0=5, (b) destructuration progress, x_0 = 5, (c) compression behaviour x_0 = 7, (d) destructuration progress, x_0 = 7.

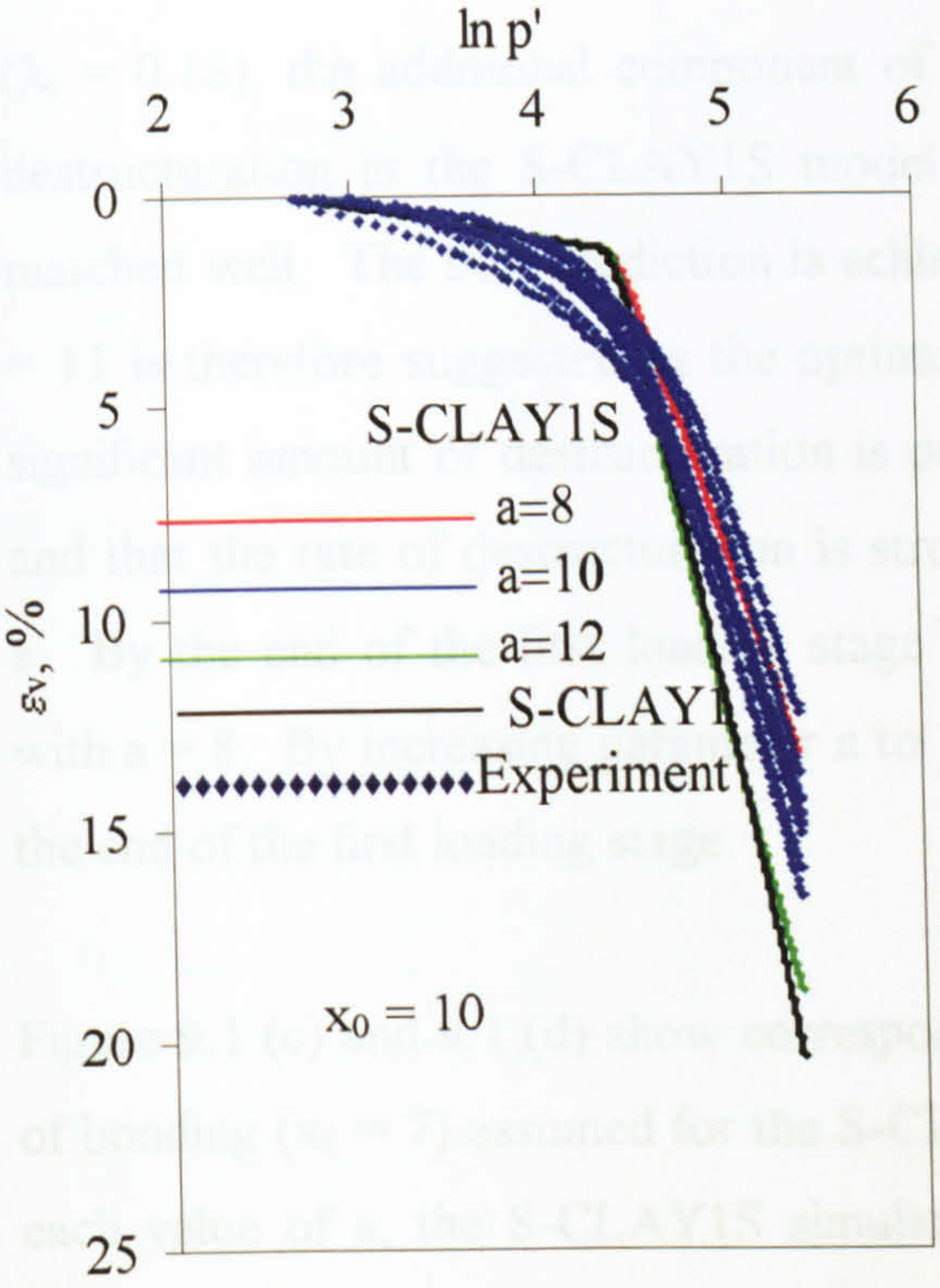

(e)

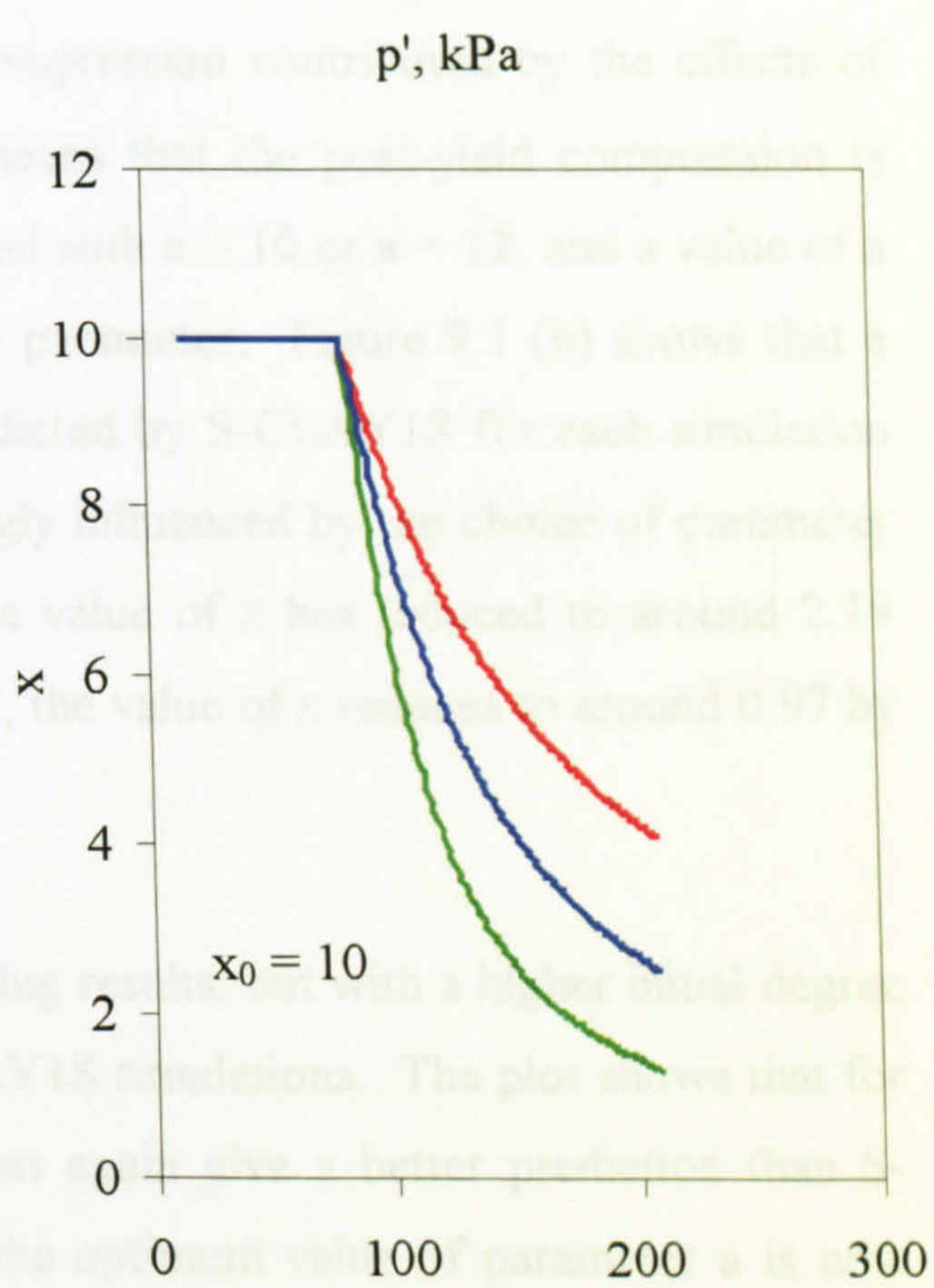

(f)

Figure 9.1. Test series B, where $\eta_1 = 0$; (e), compression behaviour, $x_0 = 10$, (f) destructuration, $x_0 = 10$.

terms of volumetric strain (ε_v) plotted against the logarithm of mean effective stress (ln p'). The predicted degeneration of soil structure is shown in Figure 9.1 (b), in terms of x plotted against p'. Also shown in these figures are the corresponding S-CLAY1 simulations.

Figure 9.1 (a) shows that in the first loading stage, post-yield compression is significantly overestimated by S-CLAY1 (typically by 5-7%) in comparison with all test data in Series B. This is essentially due to the fact the value of λ_{K0} (based on experiment evidence) assumed in the S-CLAY1 model simulations is inappropriately high. However, each of the S-CLAY1S simulations shows an improved match to the soil behaviour over the predictions generated by the S-CLAY1 model.

Although the measured apparent value of λ (0.33) is higher than the intrinsic value (λ_i = 0.18), the additional component of compression contributed by the effects of destructuration in the S-CLAY1S model means that the post-yield compression is matched well. The best prediction is achieved with a = 10 or a = 12, and a value of a = 11 is therefore suggested as the optimum parameter. Figure 9.1 (b) shows that a significant amount of destructuration is predicted by S-CLAY1S for each simulation and that the rate of destructuration is strongly influenced by the choice of parameter a. By the end of the first loading stage the value of x has reduced to around 2.19 with a = 8. By increasing parameter a to 12, the value of x reduces to around 0.97 by the end of the first loading stage.

Figure 9.1 (c) and 9.1 (d) show corresponding results, but with a higher initial degree of bonding (x_0 = 7) assumed for the S-CLAY1S simulations. The plot shows that for each value of a, the S-CLAY1S simulations again give a better prediction than S-CLAY1. With this elevated value of x_0, the optimum value of parameter a is now about 10. Increasing x_0 further to 10 (Figures 9.1 (e) and (f)) means that good predictions can still be achieved with the S-CLAY1S simulations, although the optimum match is now achieved by reducing parameter a to about 9.

9.3.2 Determination of model parameter b

In determining the value for parameter b, it is necessary to consider tests in which significant plastic shear strains were generated. Two tests have been selected: Test C2 (η_1 = 1.10) and Test C3 (η_1 = 1.30). In these simulations, yield points are very well predicted by both S-CLAY1S and S-CLAY1 models, so any mismatches cannot be attributed to this aspect of modelling. For the purpose of calibrating parameter b, only the first stages are considered, although full test simulations of Test C2, C4 and C5 are presented in Section 9.3.3 in order to test the model under a wide range of loading conditions.

Simulations of the first loading stage of Test C2 are shown in Figure 9.2. A value of x_0 = 5 has been selected for S-CLAY1S simulations and correspondingly parameter a = 11 (derived in Section 9.3.1). For S-CLAY1S simulations three values of

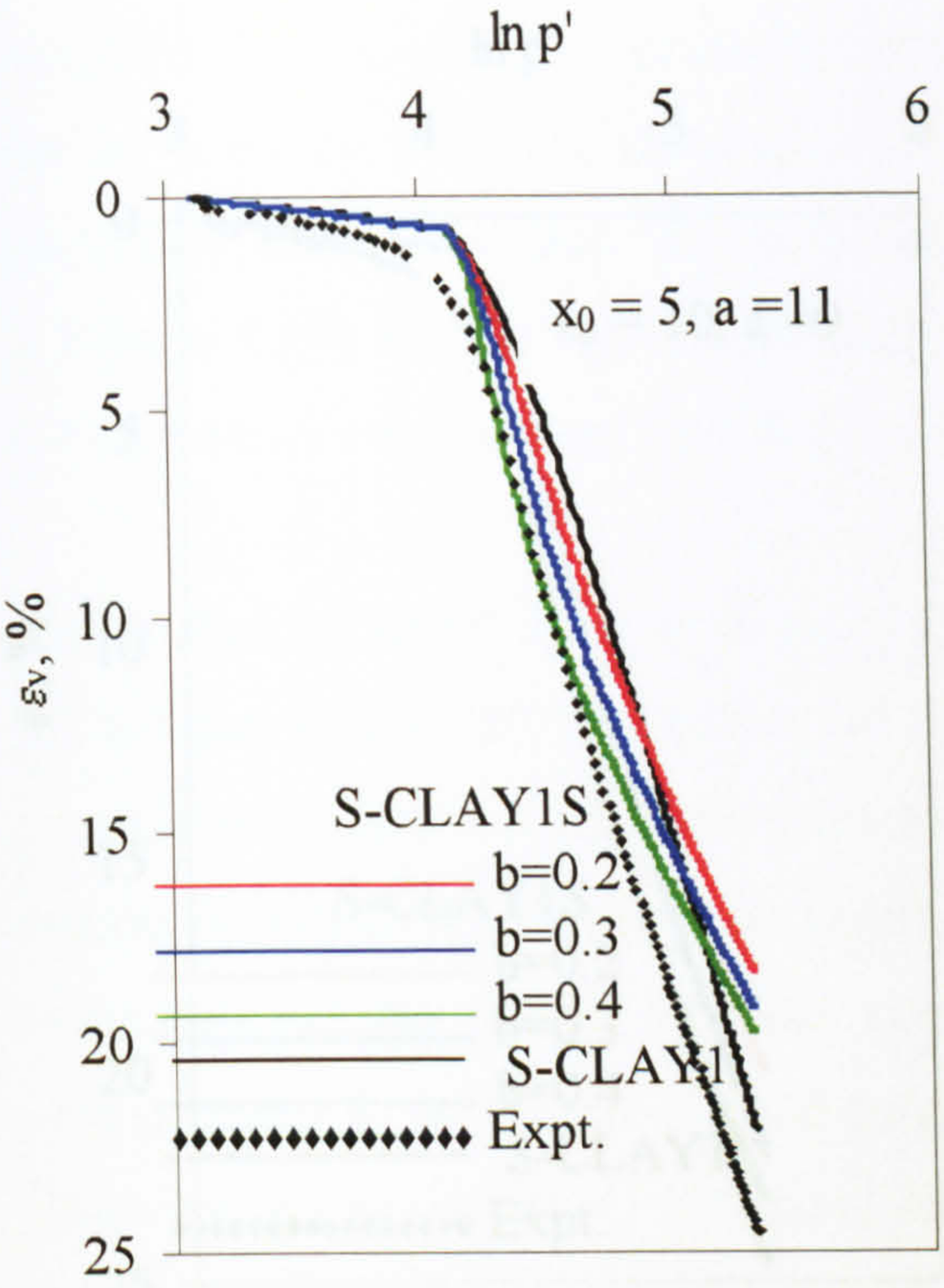

(a)

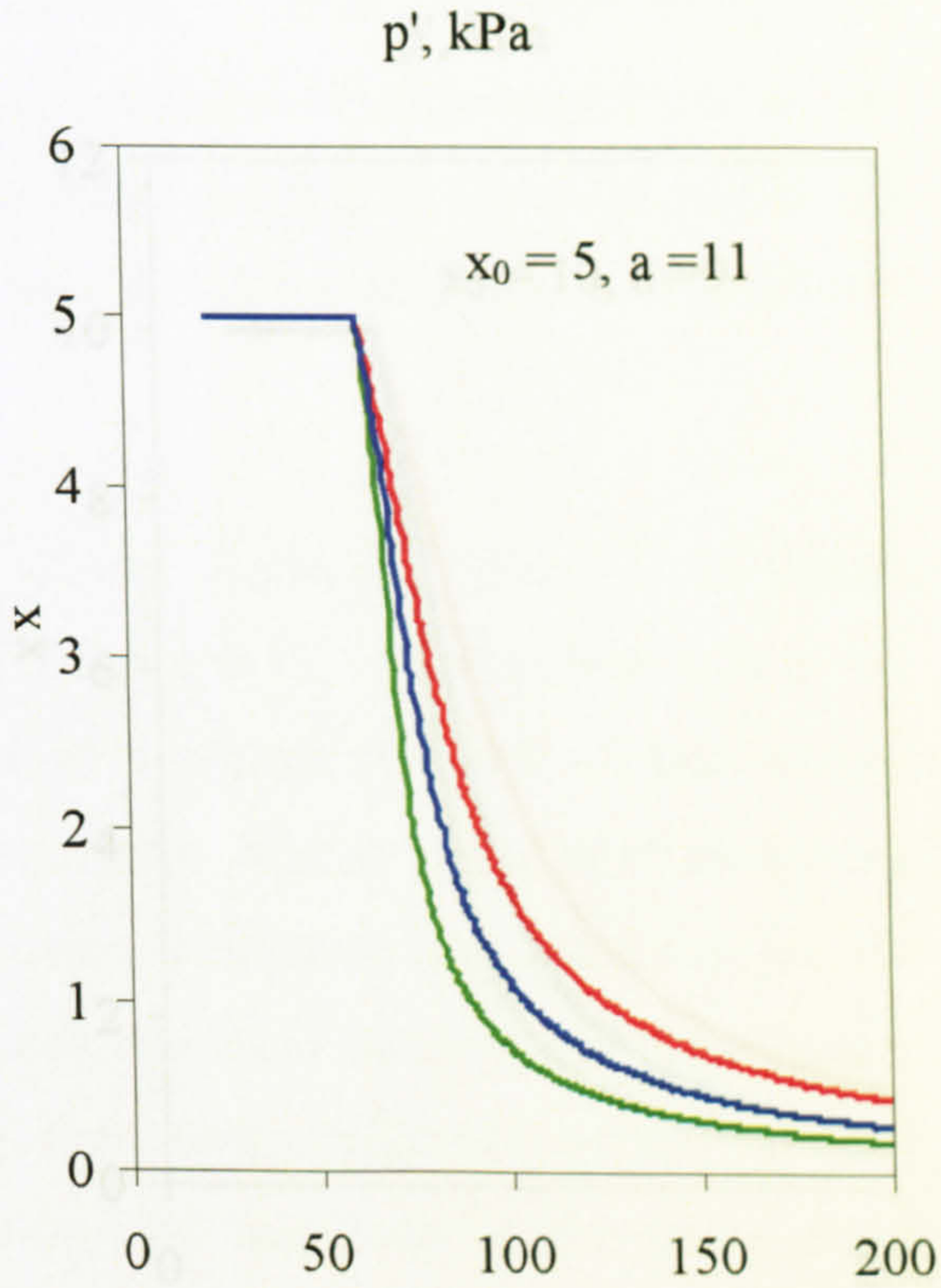

(b)

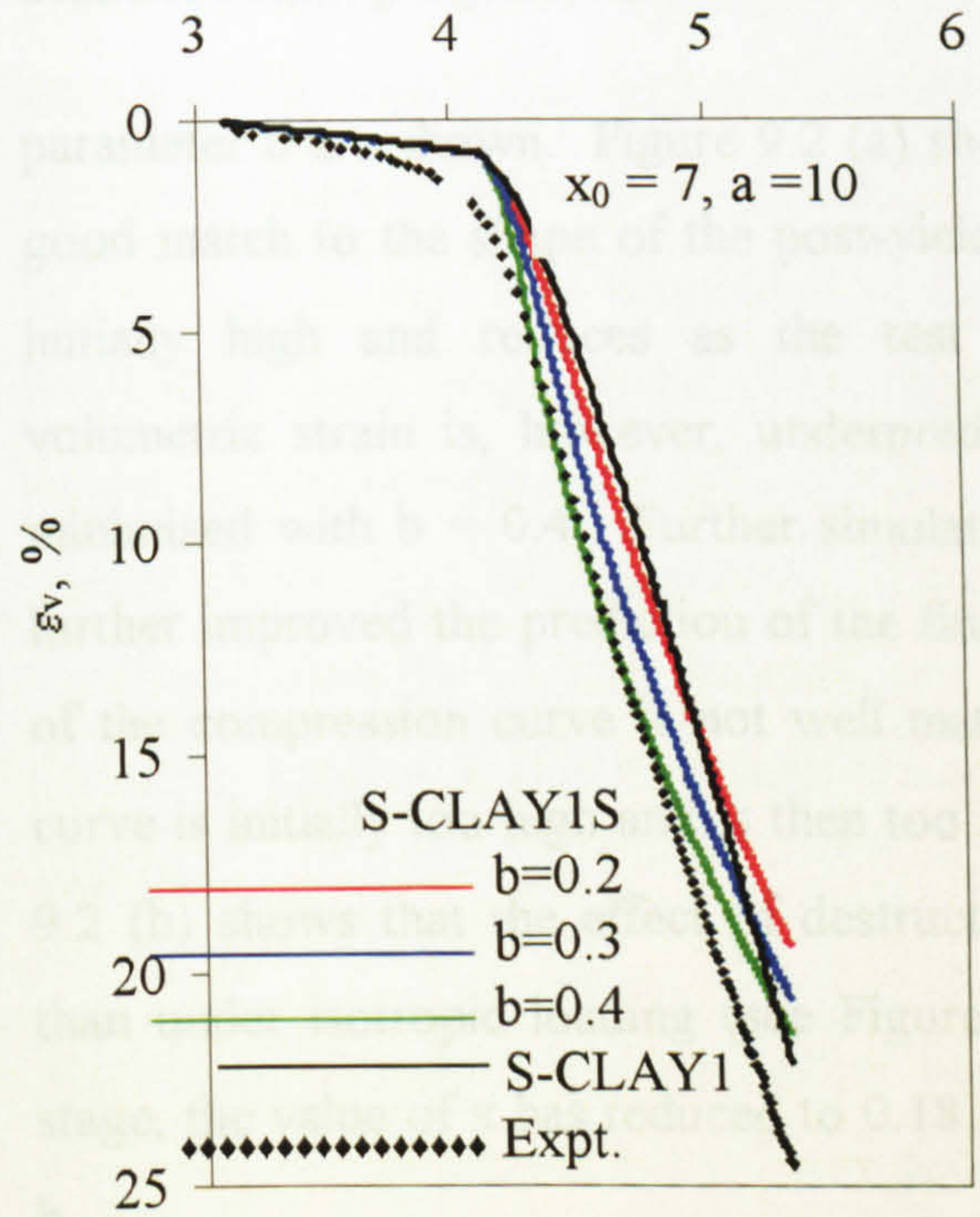

(c)

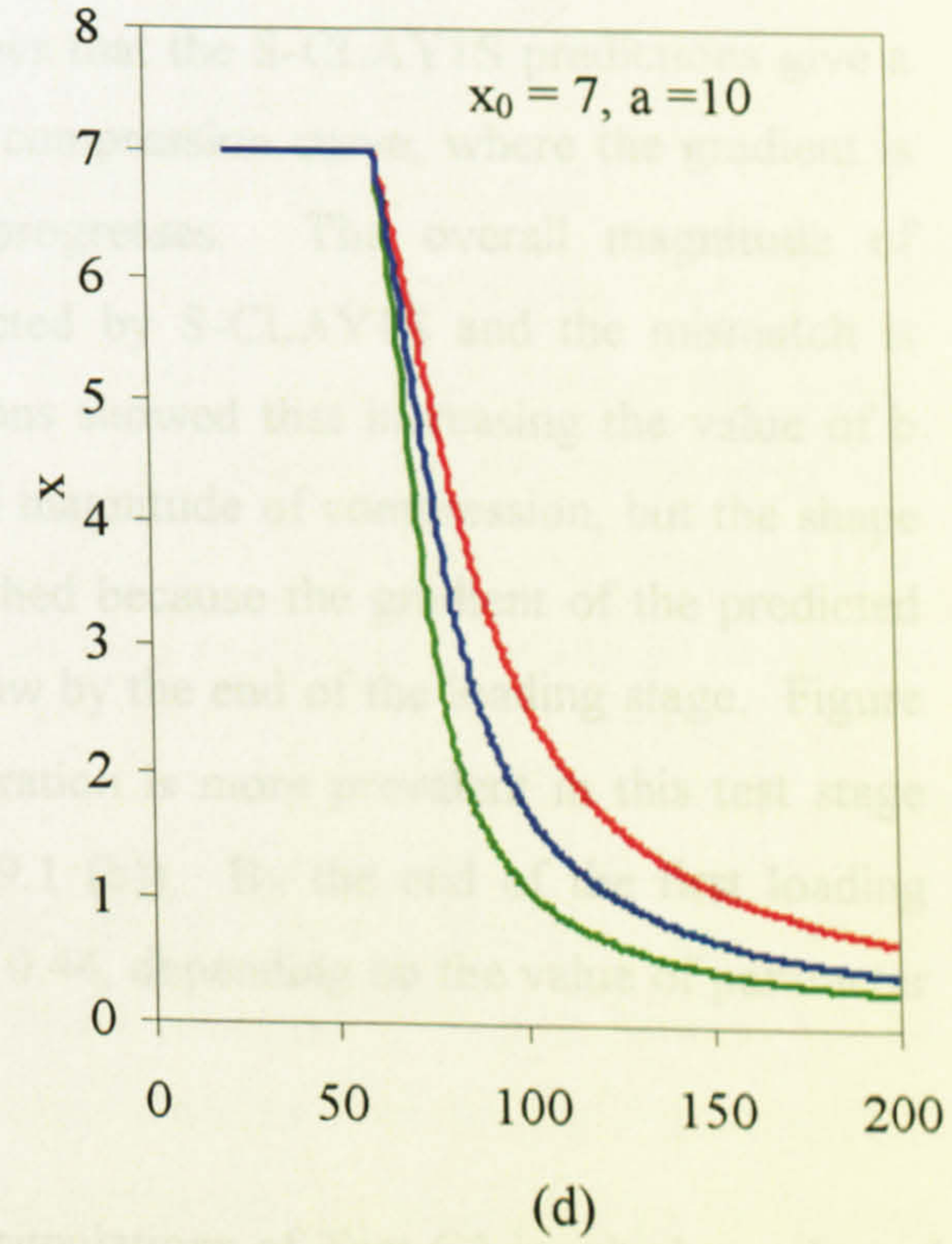

(d)

Figure 9.2. Test C2, where η_1 = 1.10; (a), compression behaviour, x_0 = 5, (b) destructuration progress, x_0 = 5, (c) compression behaviour x_0 = 7, (d) destructuration progress, x_0 = 7.

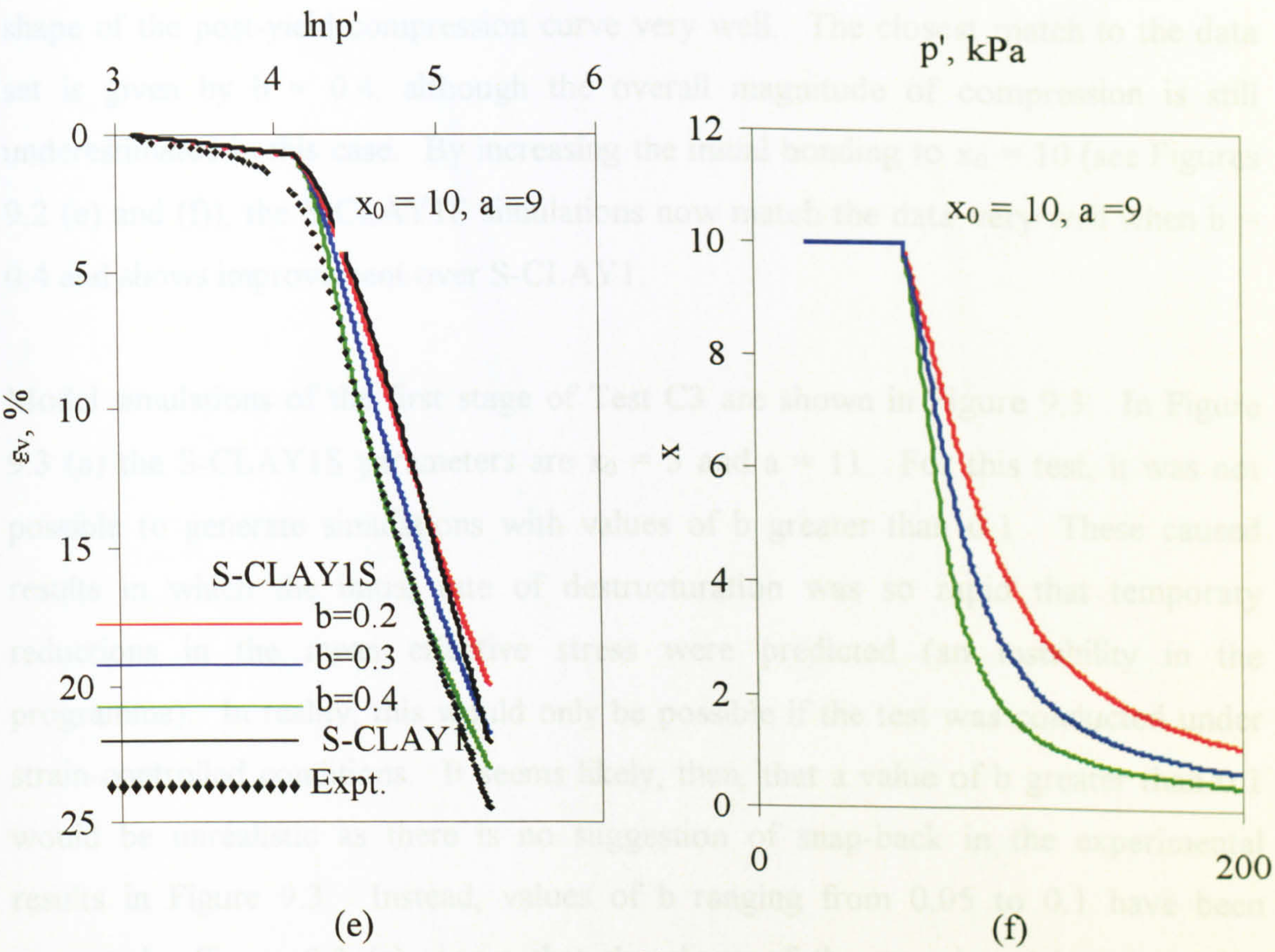

(e) (f)

Figure 9.2. Test C2, where $\eta_1 = 1.10$; (e), compression behaviour, $x_0 = 10$, (f) destructuration progress, $x_0 = 10$.

parameter b are shown. Figure 9.2 (a) shows that the S-CLAY1S predictions give a good match to the shape of the post-yield compression curve, where the gradient is initially high and reduces as the test progresses. The overall magnitude of volumetric strain is, however, underpredicted by S-CLAY1S and the mismatch is minimised with b = 0.4. Further simulations showed that increasing the value of b further improved the prediction of the final magnitude of compression, but the shape of the compression curve is not well matched because the gradient of the predicted curve is initially too high and is then too low by the end of the loading stage. Figure 9.2 (b) shows that the effect of destructuration is more prevalent in this test stage than under isotropic loading (see Figure 9.1 (b)). By the end of the first loading stage, the value of x has reduced to 0.18 – 0.44, depending on the value of parameter b.

Figures 9.2 (c) and (d) show S-CLAY1S simulations of Test C2 in which a value of $x_0 = 7$ and a corresponding value of a = 10 have been selected. Three trial values of parameter b have again been selected. The S-CLAY1S simulations again match the

shape of the post-yield compression curve very well. The closest match to the data set is given by b = 0.4, although the overall magnitude of compression is still underestimated in this case. By increasing the initial bonding to $x_0 = 10$ (see Figures 9.2 (e) and (f)), the S-CLAY1S simulations now match the data very well when b = 0.4 and shows improvement over S-CLAY1.

Model simulations of the first stage of Test C3 are shown in Figure 9.3. In Figure 9.3 (a) the S-CLAY1S parameters are $x_0 = 5$ and a = 11. For this test, it was not possible to generate simulations with values of b greater than 0.1. These caused results in which the initial rate of destructuration was so rapid that temporary reductions in the mean effective stress were predicted (an instability in the programme). In reality, this would only be possible if the test was conducted under strain-controlled conditions. It seems likely, then, that a value of b greater than 0.1 would be unrealistic as there is no suggestion of snap-back in the experimental results in Figure 9.3. Instead, values of b ranging from 0.05 to 0.1 have been presented. Figure 9.3 (a) shows that the shape of the experimental compression curve is concave upwards, similar to Test C2. This is well represented by S-CLAY1S, in which the initial post-yield compression is rapid, but has noticeably slowed by the end of the loading stage. S-CLAY1 does not reflect these features and in this instance the final magnitude of compression is underpredicted by S-CLAY1. S-CLAY1S also underpredicts the final magnitude of compression, although the mismatch can be minimised with b = 0.1. The overall suggestion here is that higher values of x_0 must be considered. Figure 9.3 (b) shows the degeneration of the bonding parameter x. Despite only being loaded to a mean effective stress of p' = 124 kPa, loading at this very high stress ratio has caused the bonding to be greatly reduced.

Figures 9.3 (c) and (d) show further simulations of Test C3, this time with $x_0 = 7$. The value of parameter a has been accordingly reduced to 10 (see Section 9.3.1). The S-CLAY1S simulations show further improvements over those in Figure 9.3 (a), particularly where b = 0.1. Figure 9.3 (e) shows that by increasing x_0 to 10 (and decreasing parameter a to 9) the compression curve is also matched very well for values of b = 0.075 - 0.1, although the improvement gained in increasing x_0 to 10 is less marked than increasing x_0 from 5 to 7.

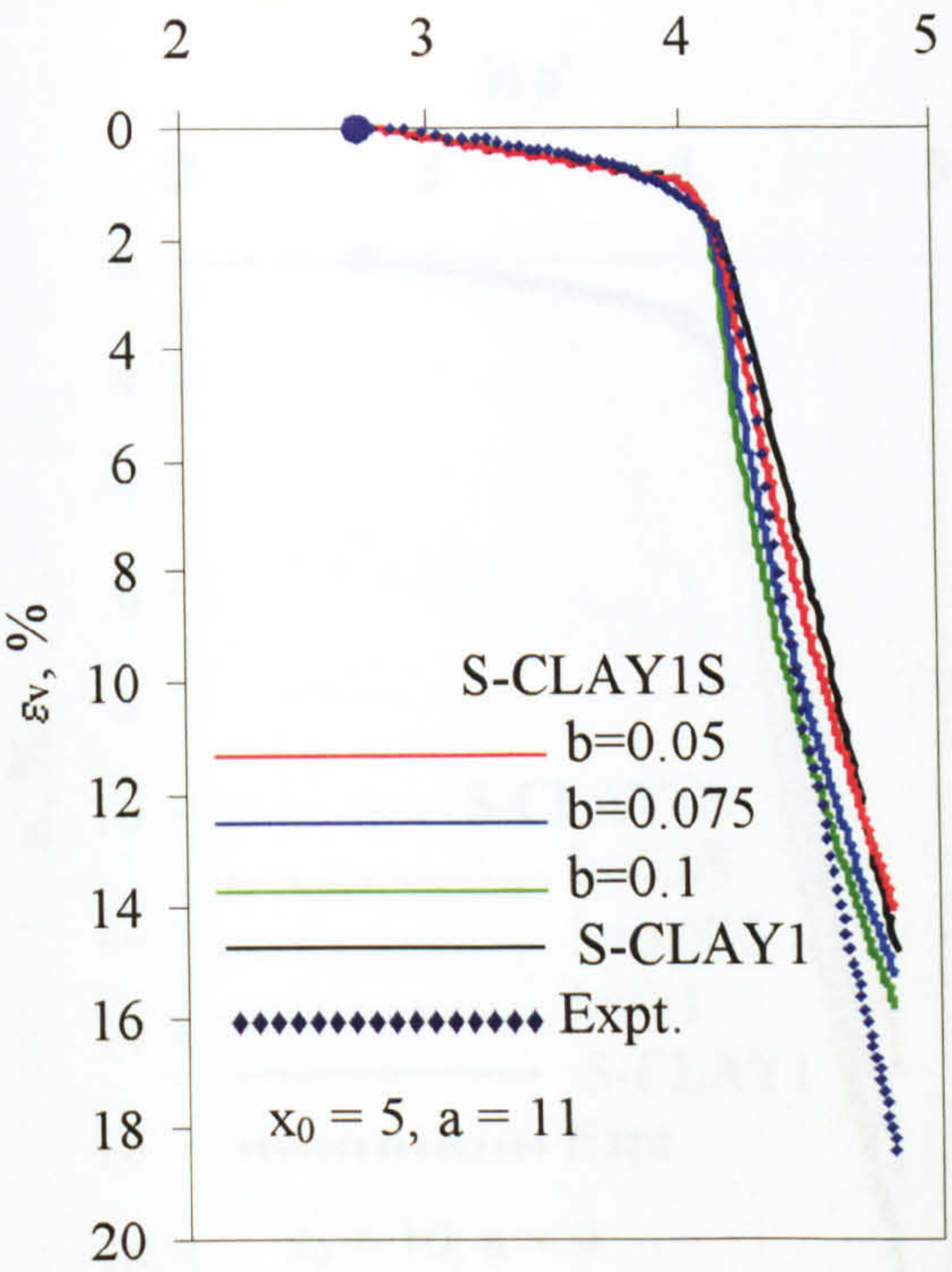

(a)

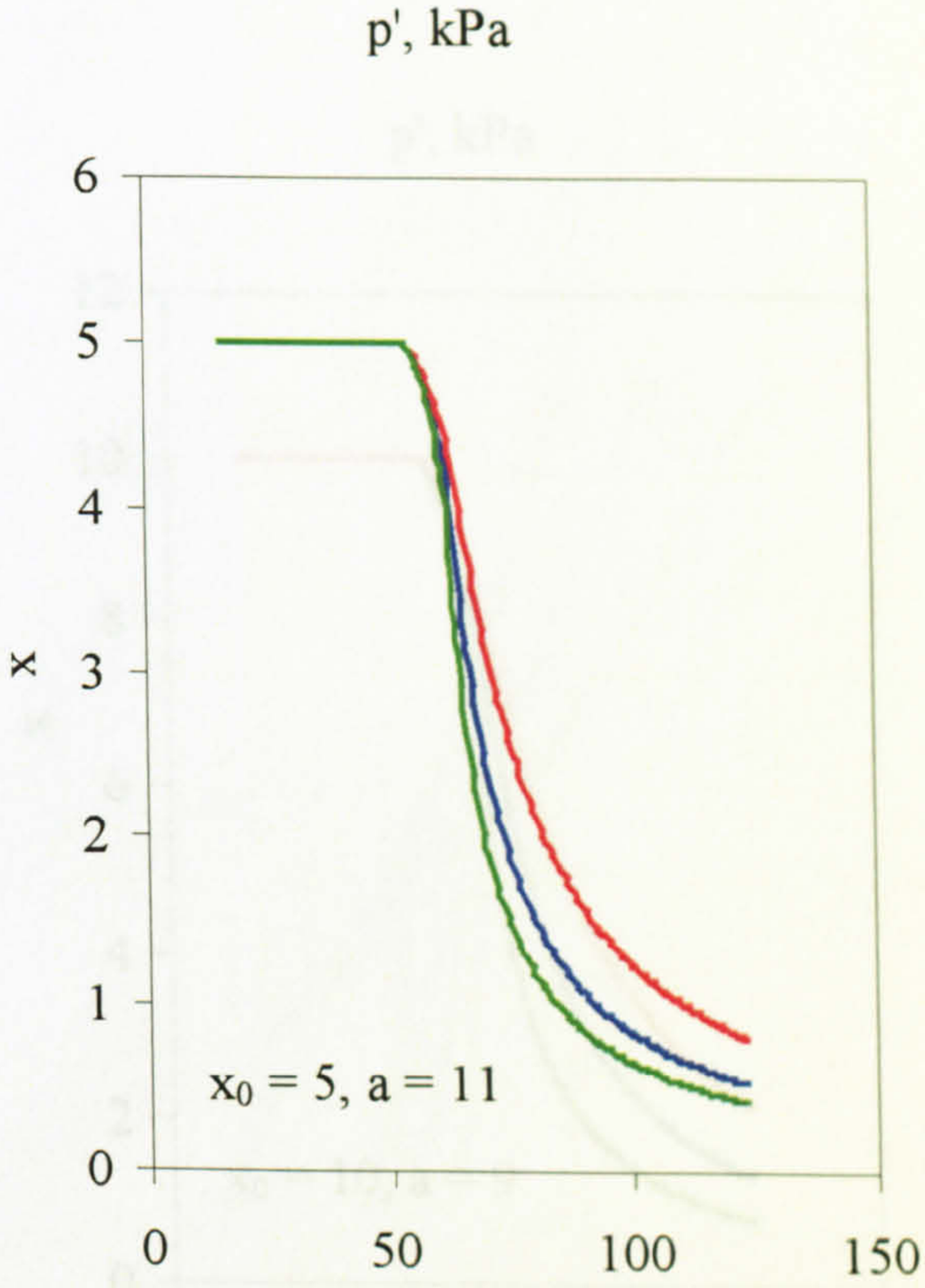

(b)

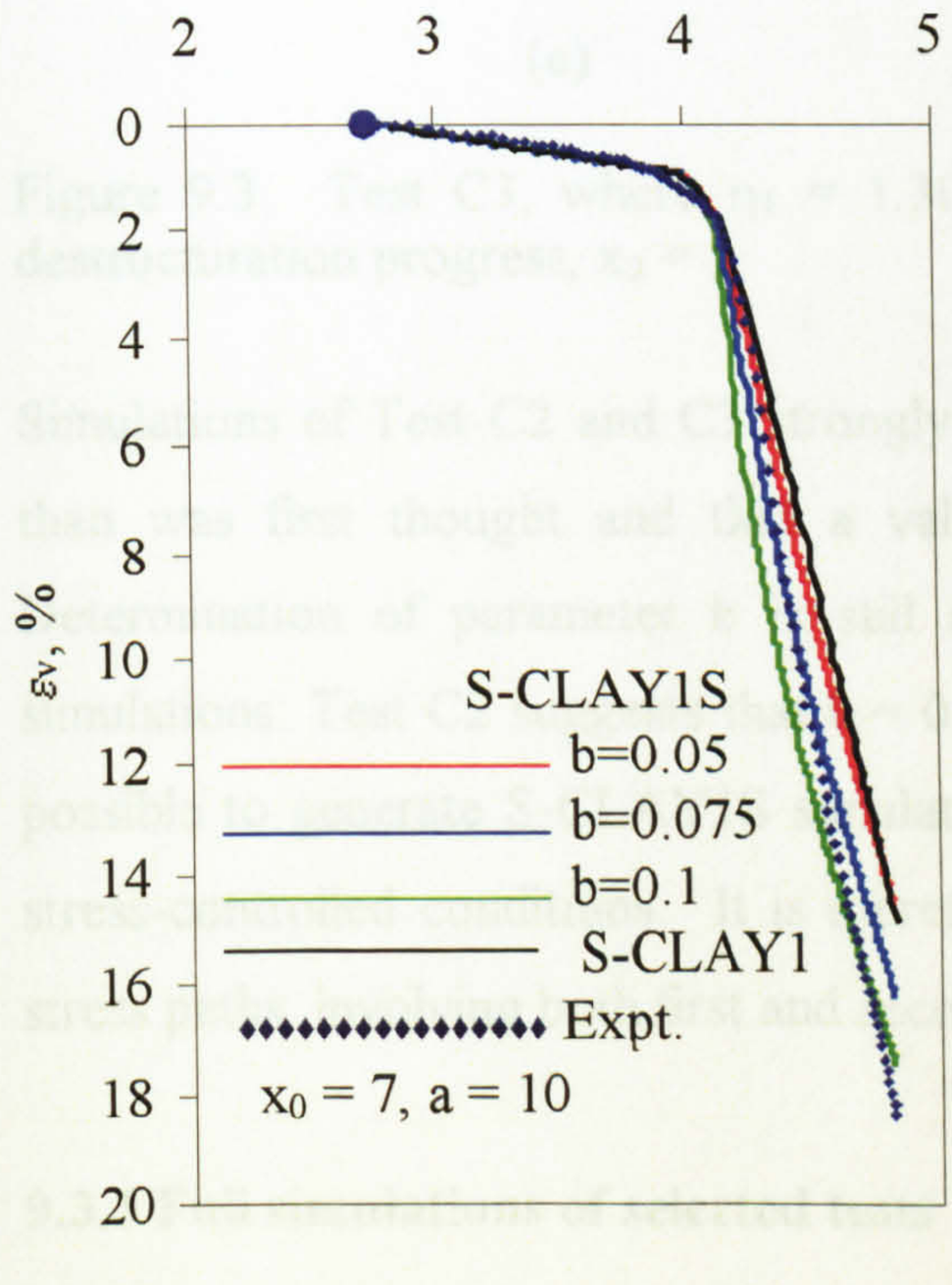

(c)

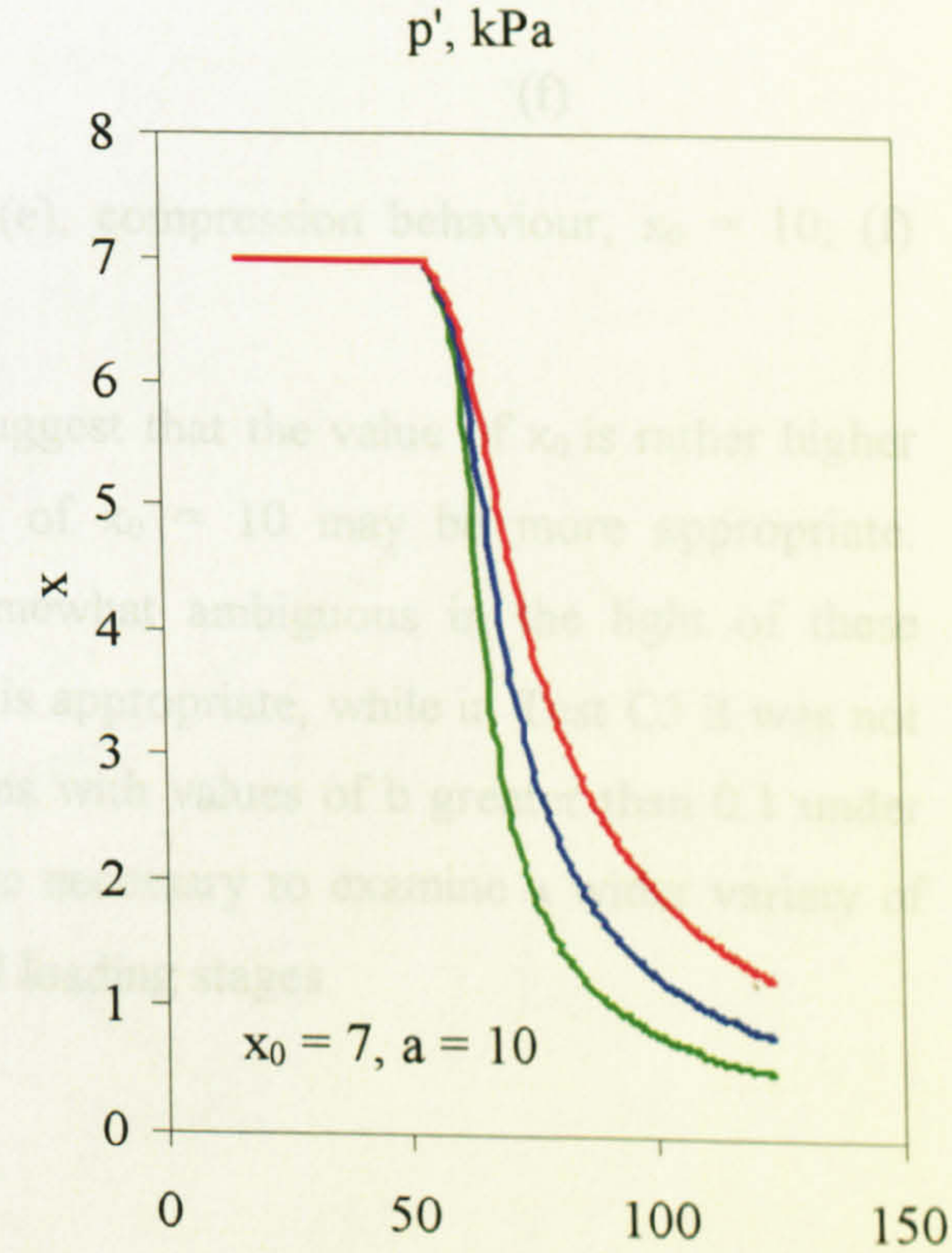

(d)

Figure 9.3 Test C3, where $\eta_1 = 1.30$; (a), compression behaviour, $x_0 = 5$, (b) destructuration progress, $x_0 = 5$, (c) compression behaviour $x_0 = 7$, (d) destructuration progress, $x_0 = 7$.

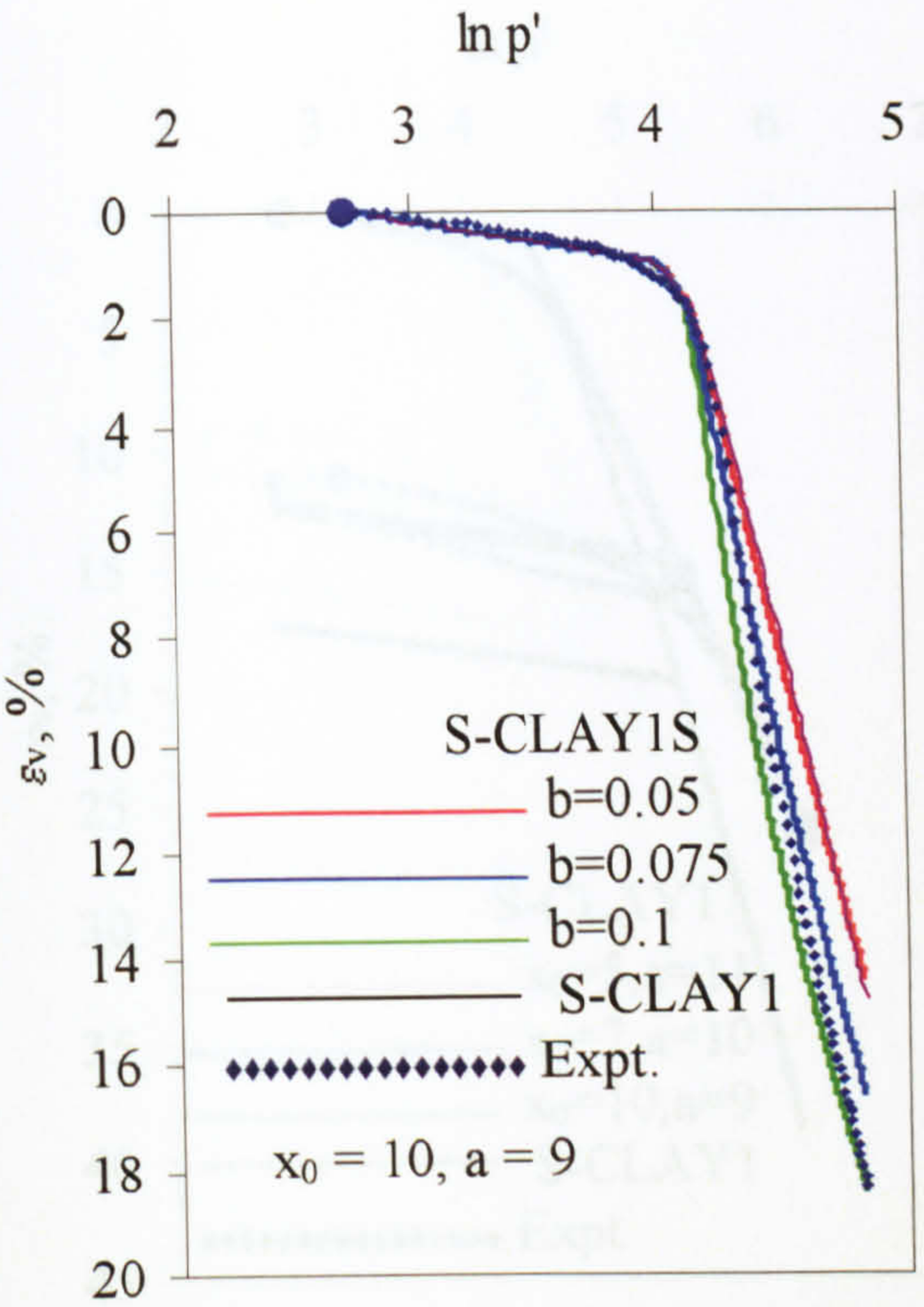

(e)

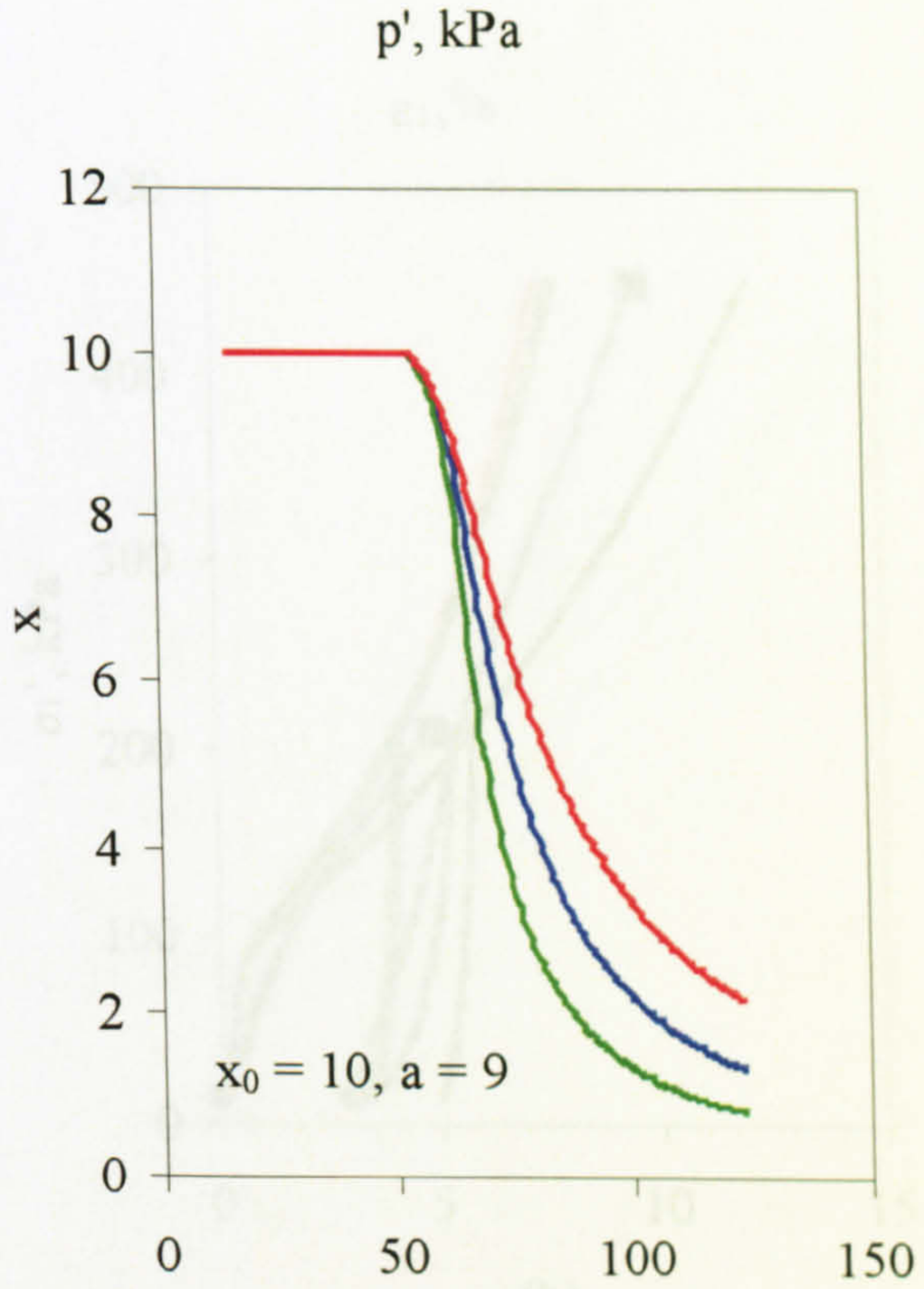

(f)

Figure 9.3. Test C3, where $\eta_1 = 1.30$; (e), compression behaviour, $x_0 = 10$, (f) destructuration progress, $x_0 = 5$.

Simulations of Test C2 and C3 strongly suggest that the value of x_0 is rather higher than was first thought and that a value of $x_0 = 10$ may be more appropriate. Determination of parameter b is still somewhat ambiguous in the light of these simulations: Test C2 suggests that b = 0.4 is appropriate, while in Test C3 it was not possible to generate S-CLAY1S simulations with values of b greater than 0.1 under stress-controlled conditions. It is therefore necessary to examine a wider variety of stress paths, involving both first and second loading stages.

9.3.3 Full simulations of selected tests

Six multi-stage stress path tests have been selected for comparison of model simulations with experimental results, as shown in Figures 9.4 – 9.9. These tests have been selected as they include loading paths that would be expected to involve both the effects of anisotropy and destructuration. In each case the stress-strain behaviour is assessed in terms of volumetric strain (ε_v) plotted against log of mean

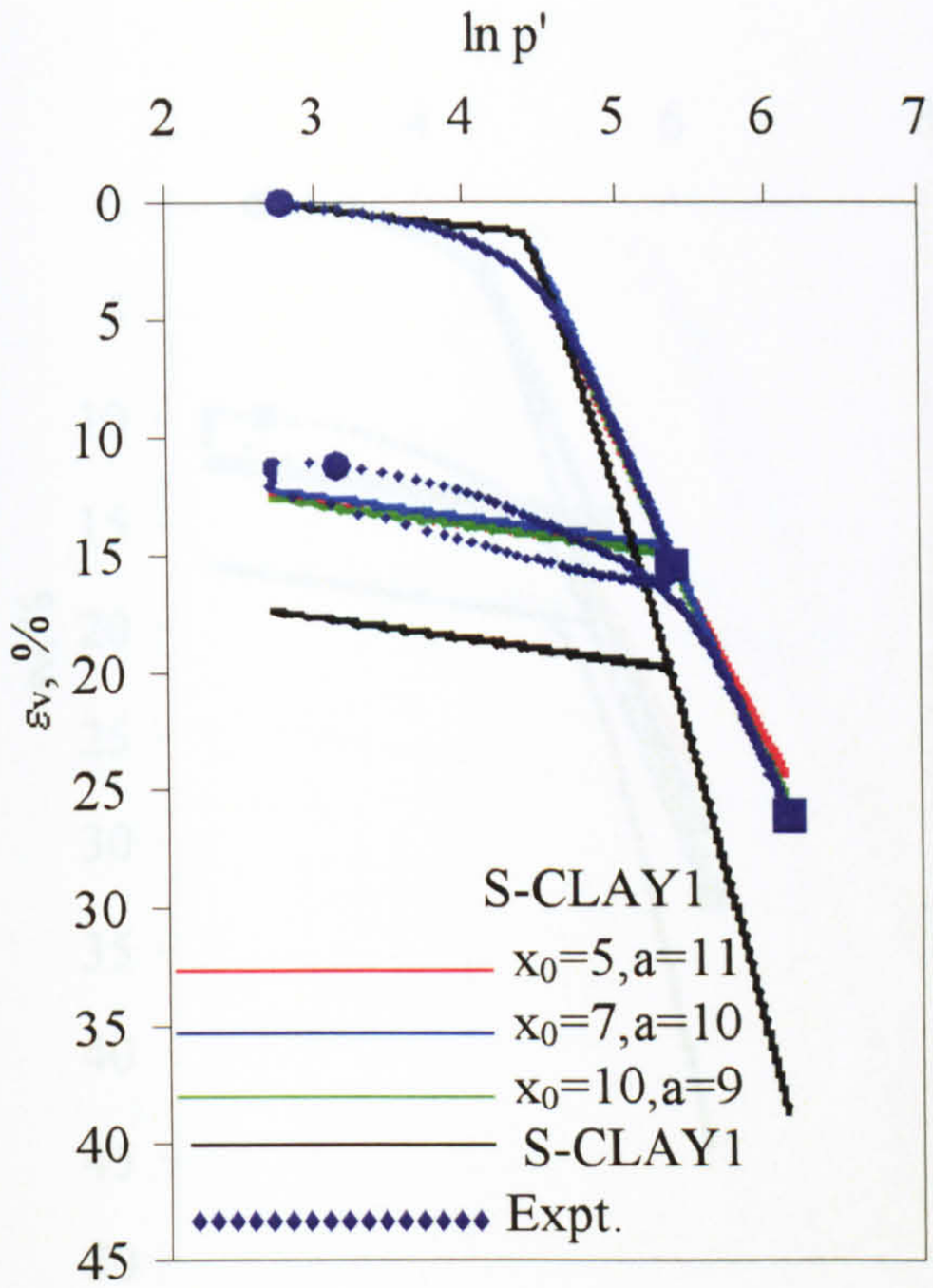

(a)

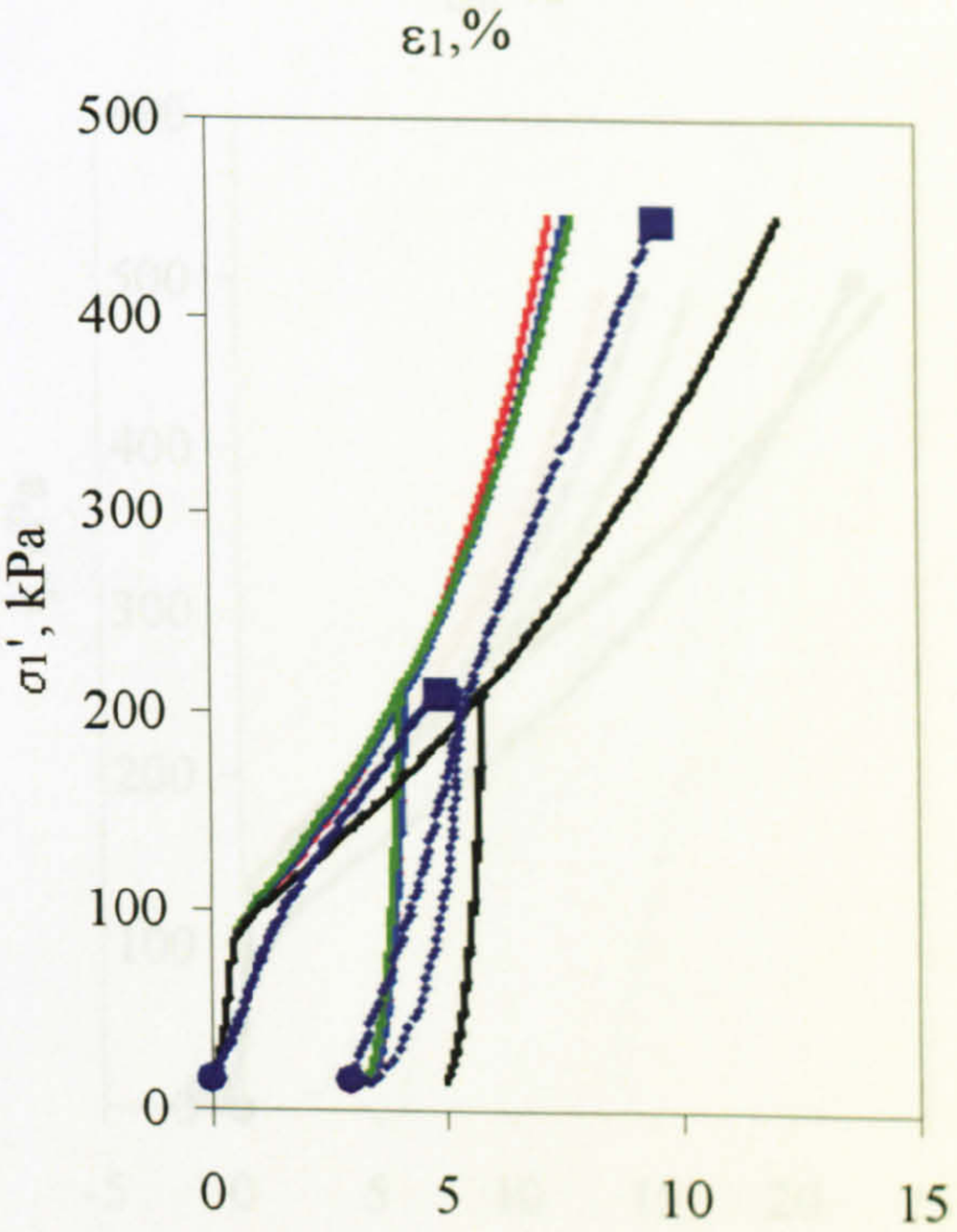

(b)

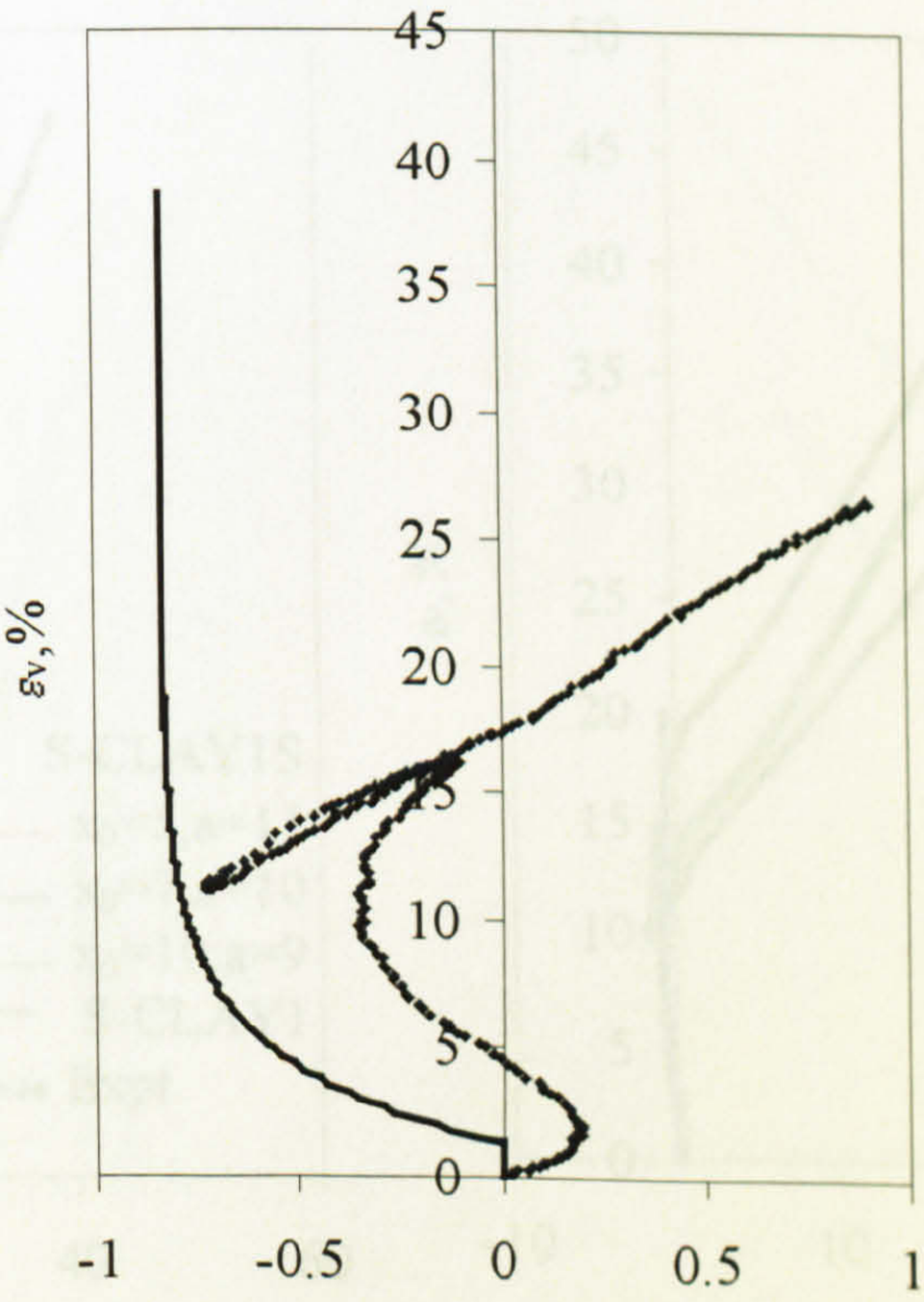

(c)

Figure 9.4. Simulations of Test B7 ($\eta_1 = \eta_2 = 0$); (a) compression behaviour, (b) axial stress-strain behaviour, (c) strain path

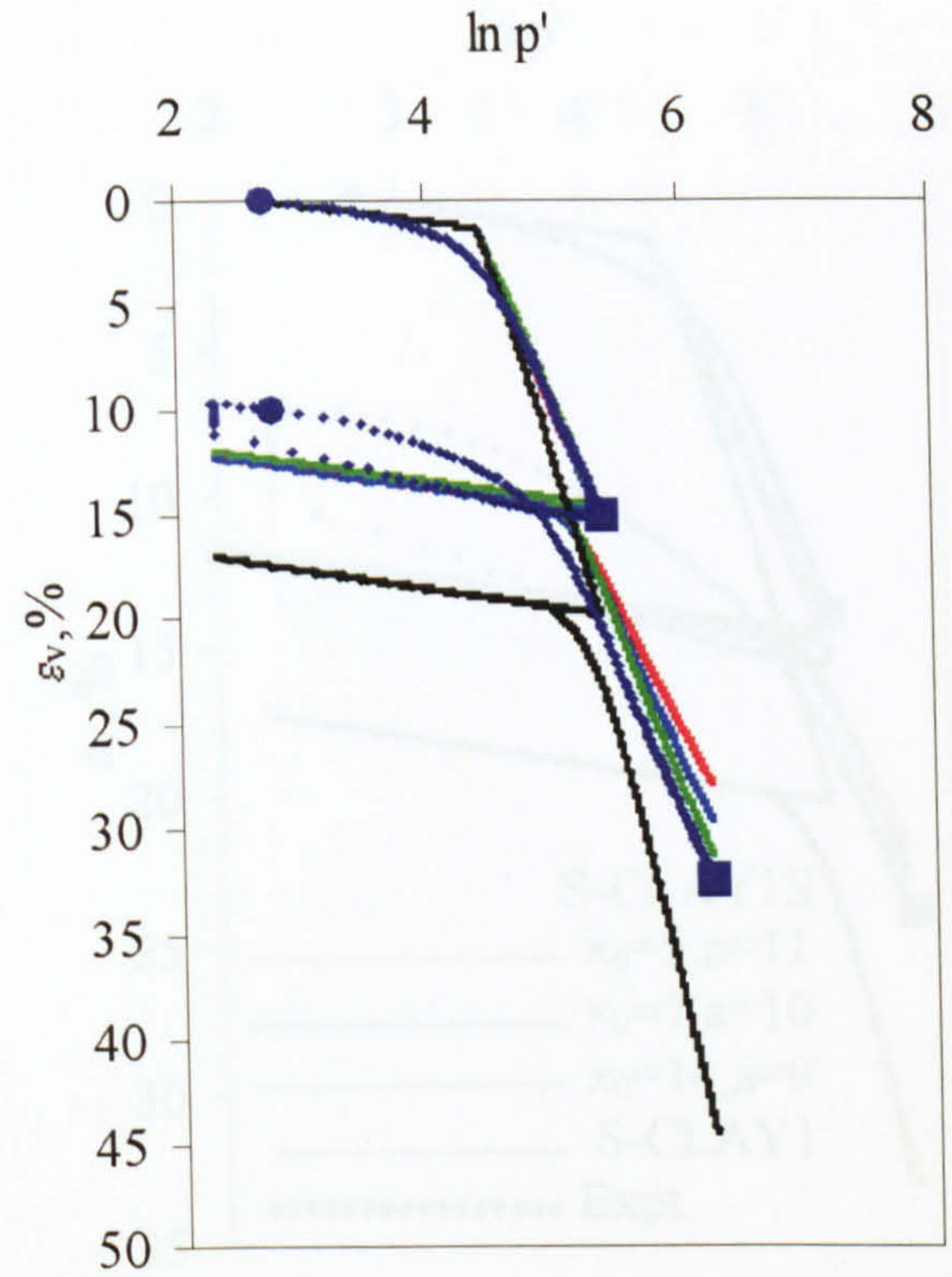

(a)

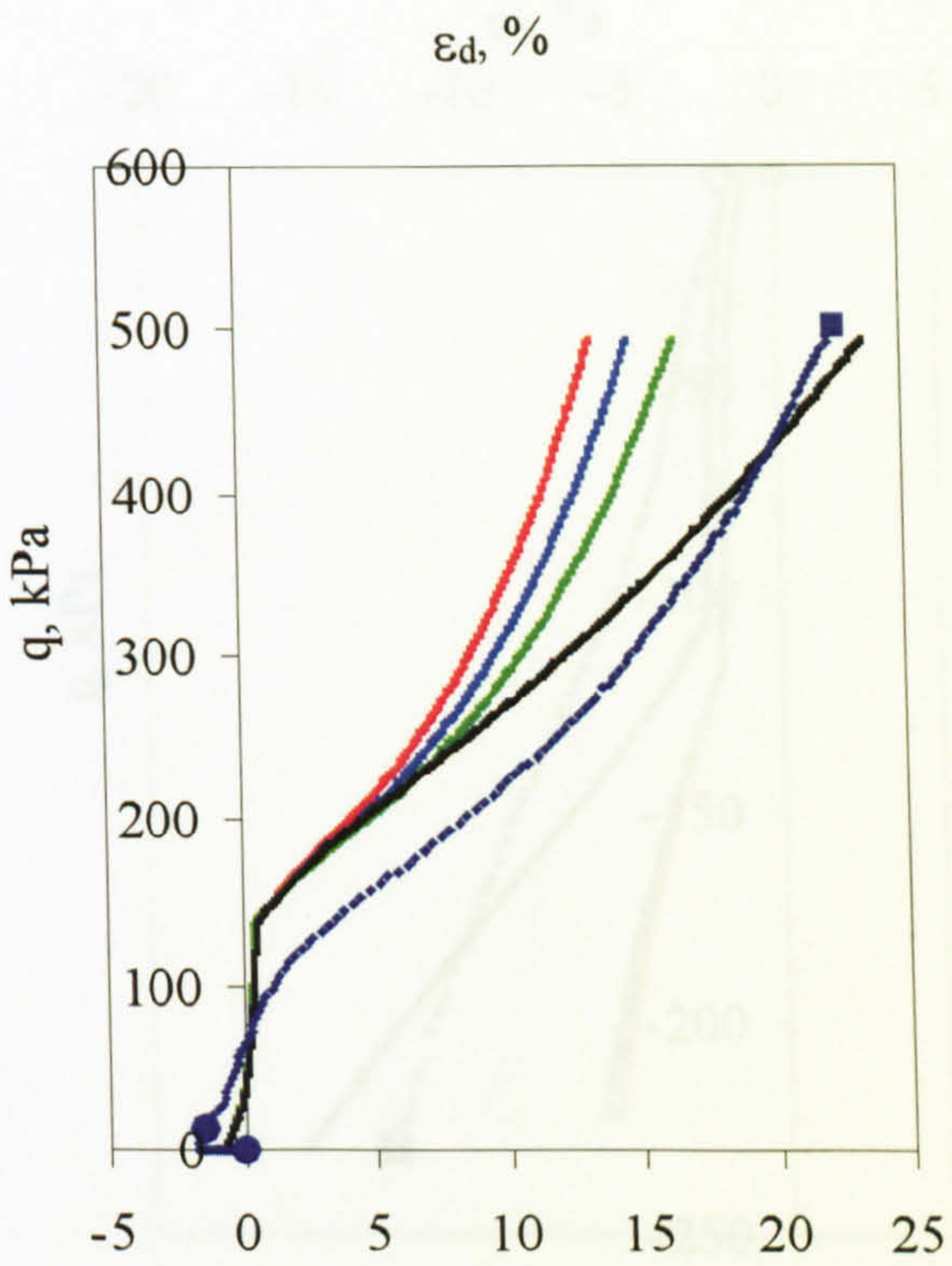

(b)

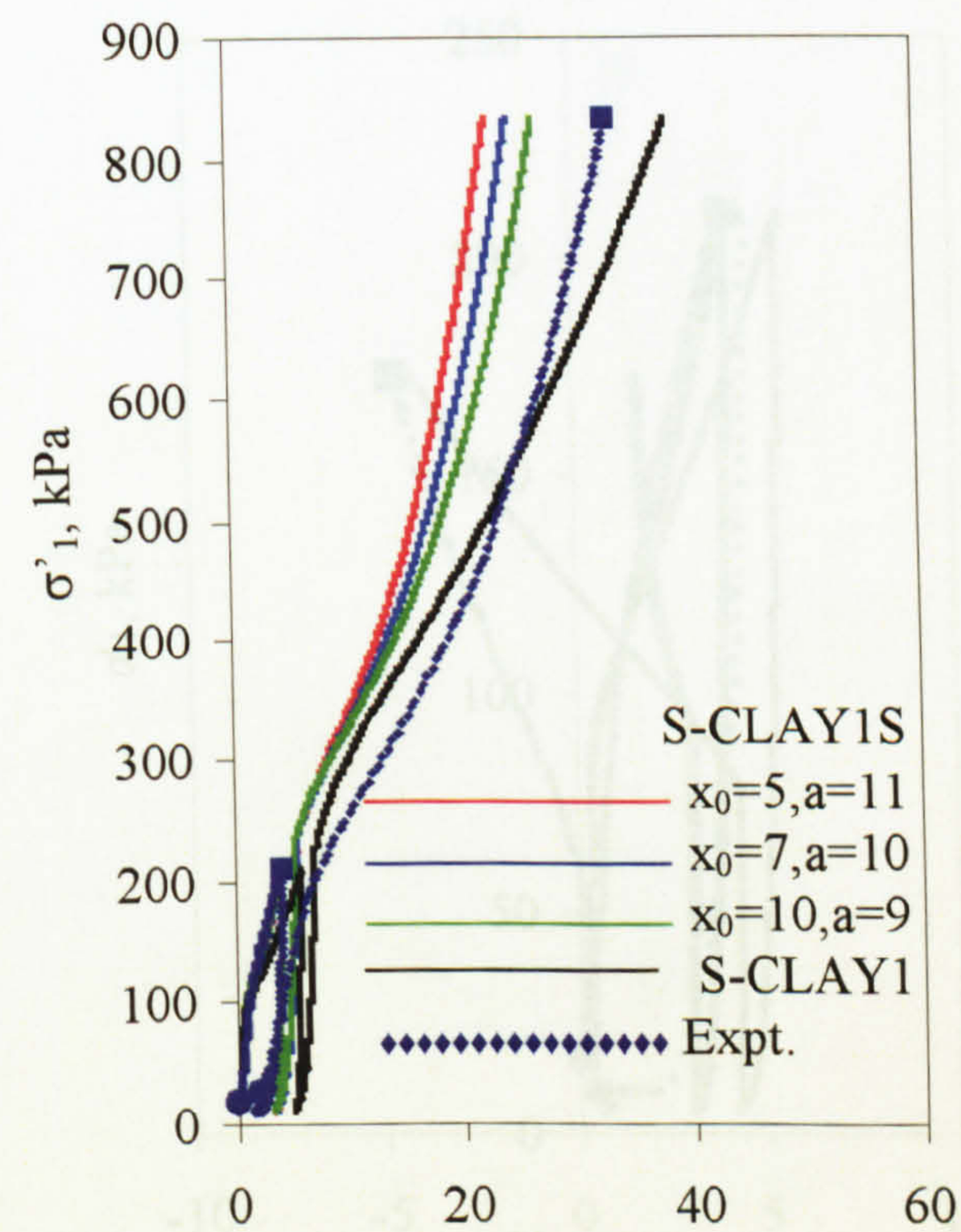

(c)

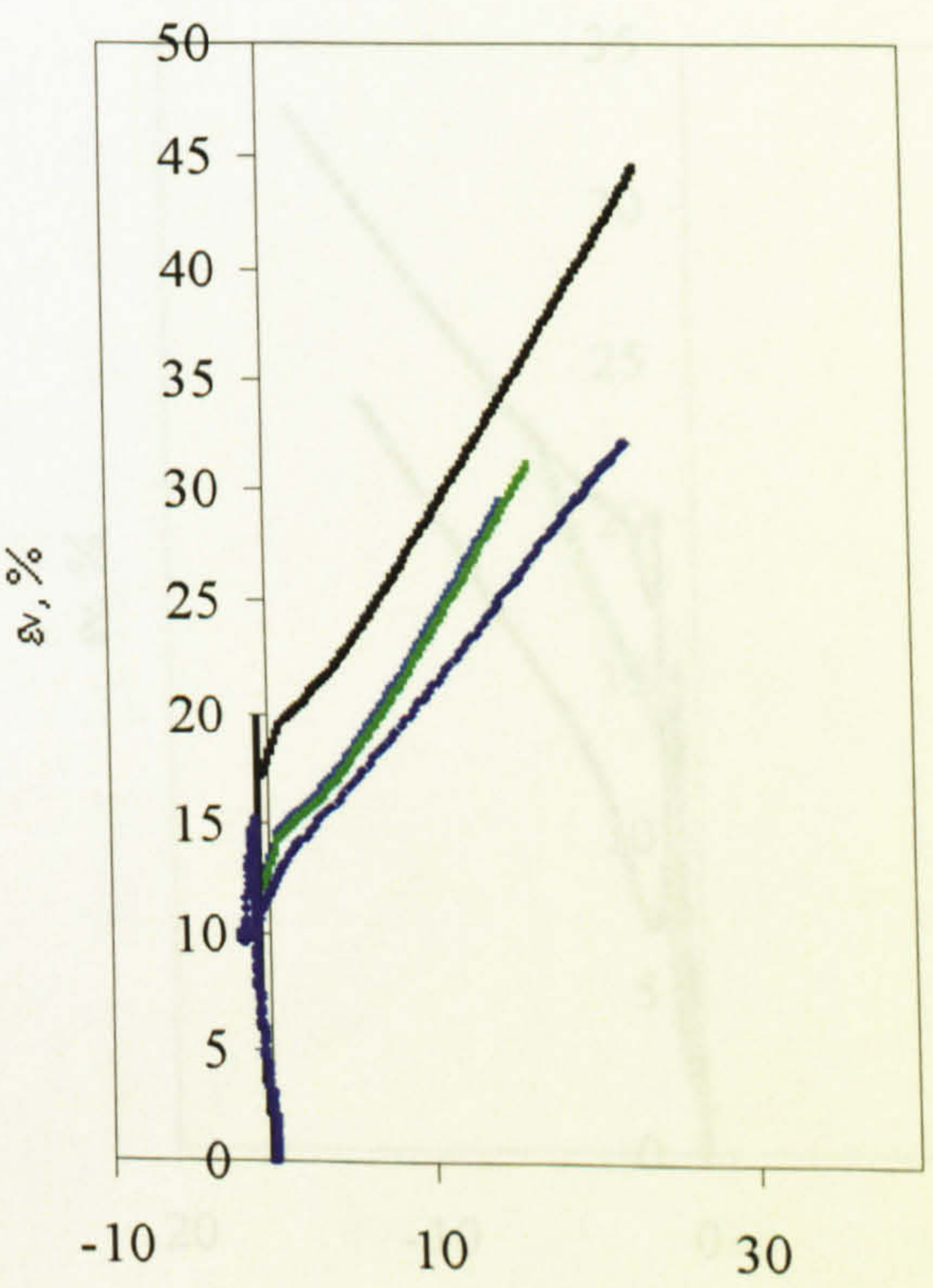

(d)

Figure 9.5. Simulations of Test B3 ($\eta_1 = 0$, $\eta_2 = 1.01$); (a) compression behaviour, (b) deviatoric stress-strain behaviour, (c) axial stress-strain behaviour (d) strain path.

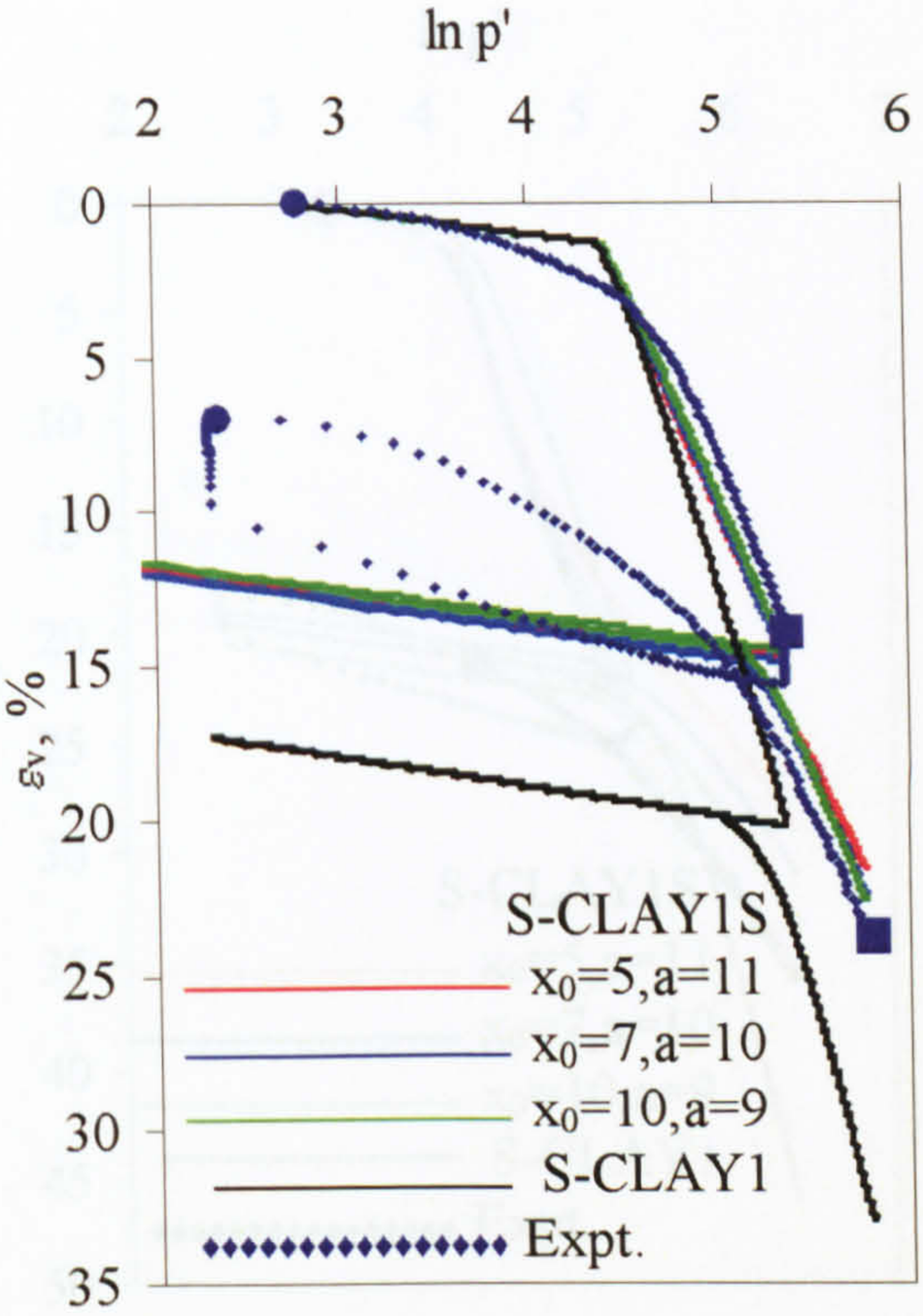

(a)

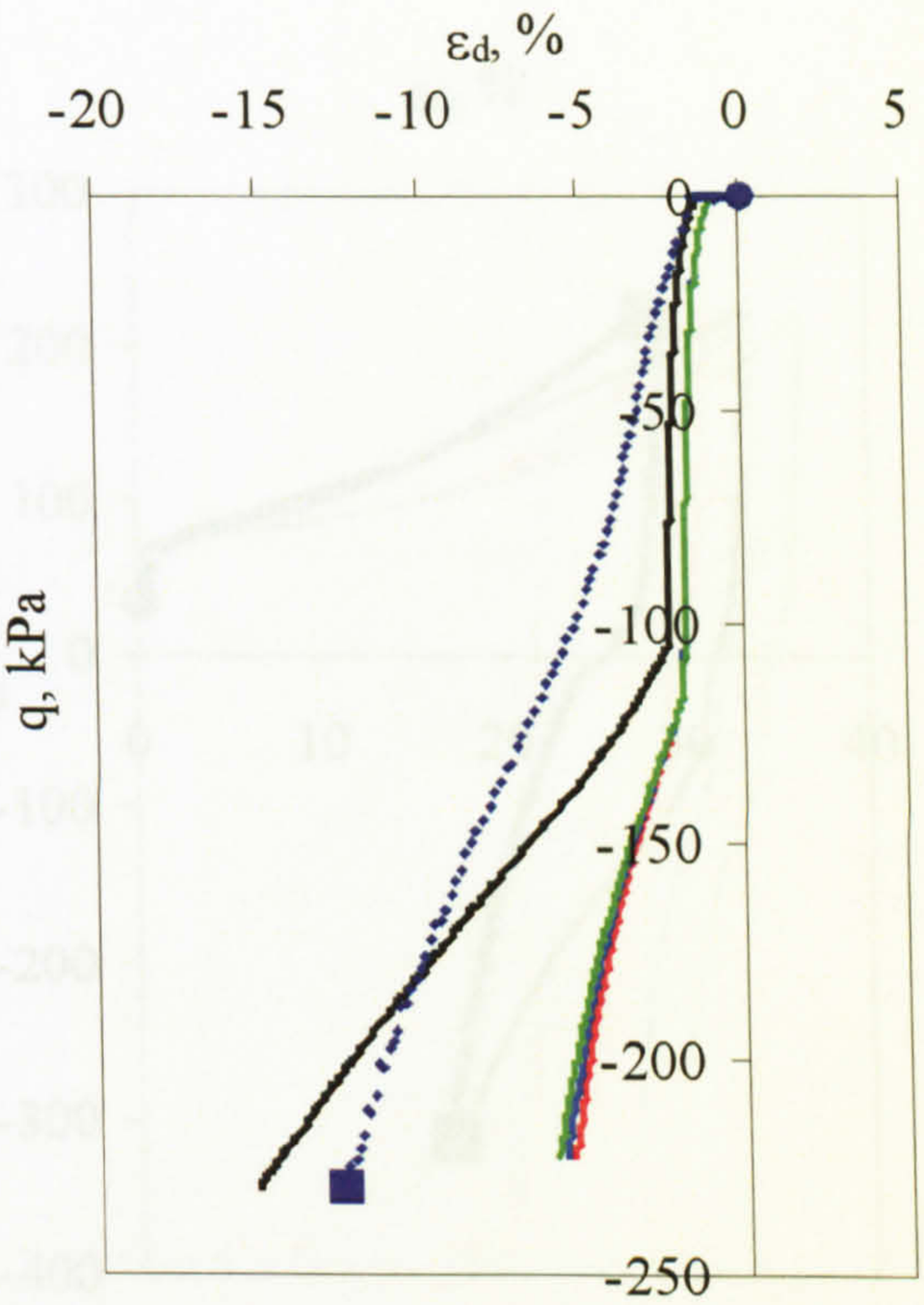

(b)

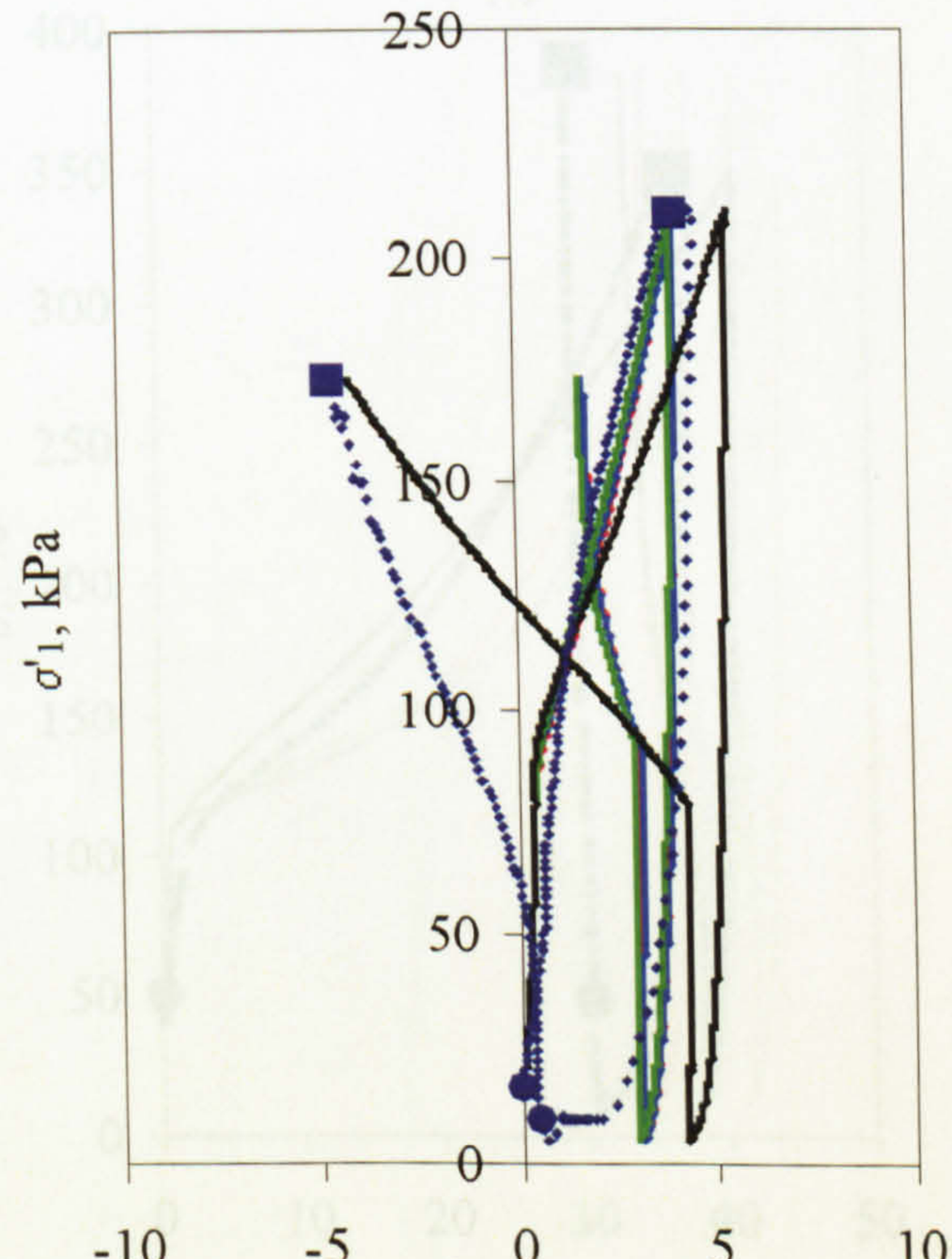

(c)

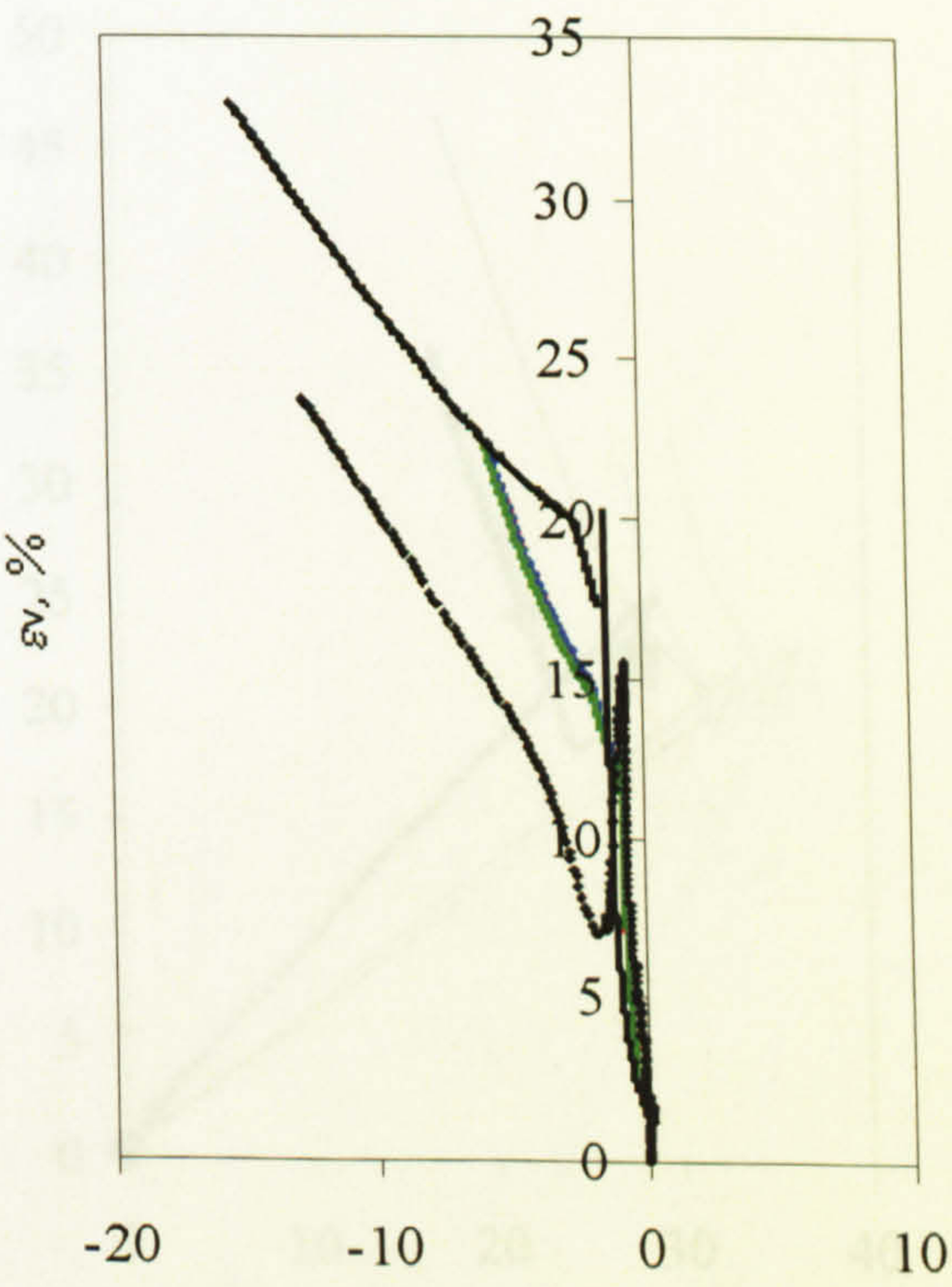

(d)

Figure 9.6. Simulations of Test B6 ($\eta_1 = 0$, $\eta_2 = -0.70$); (a) compression behaviour, (b) deviatoric stress-strain behaviour, (c) axial stress-strain behaviour (d) strain path.

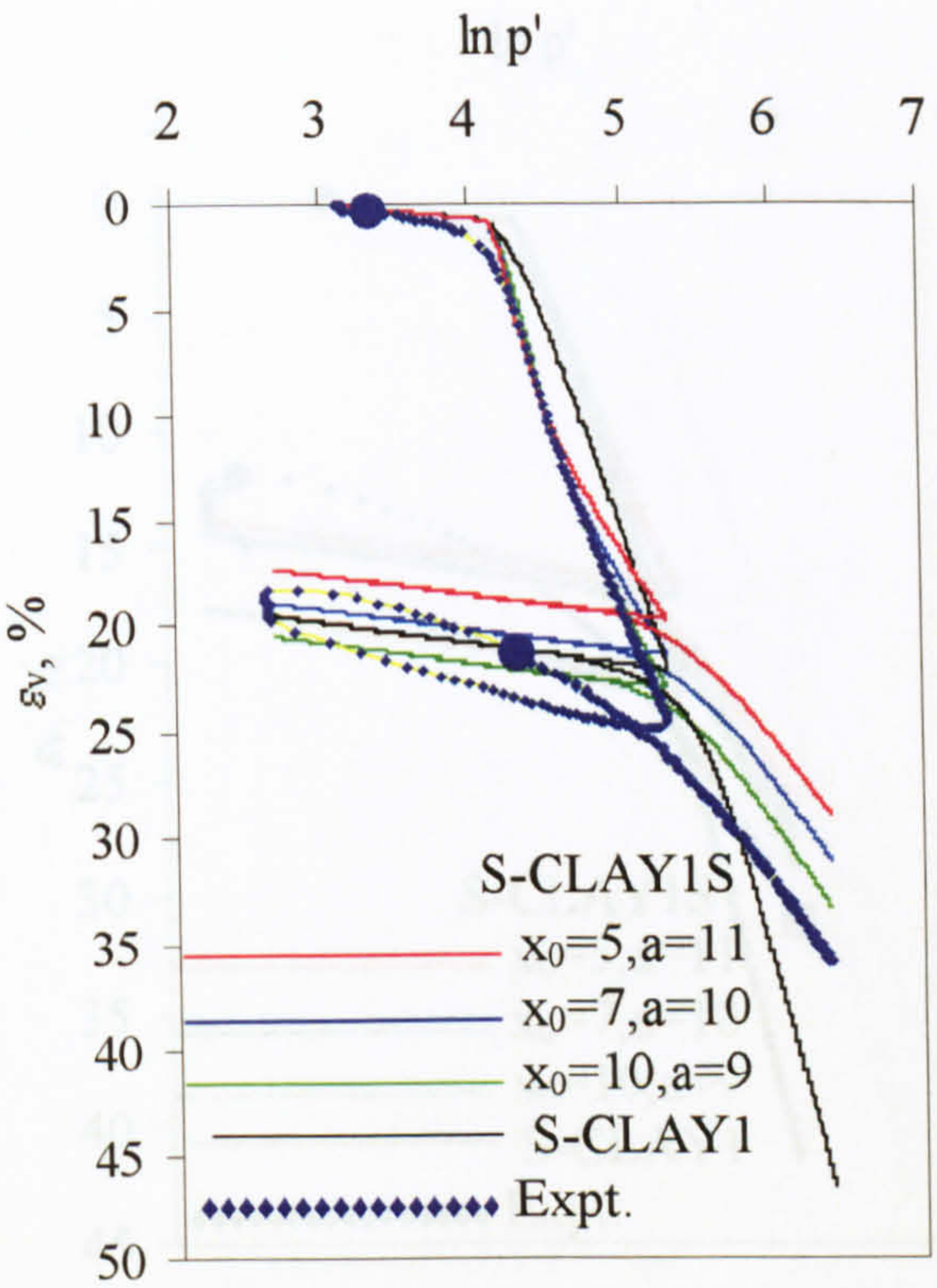

(a)

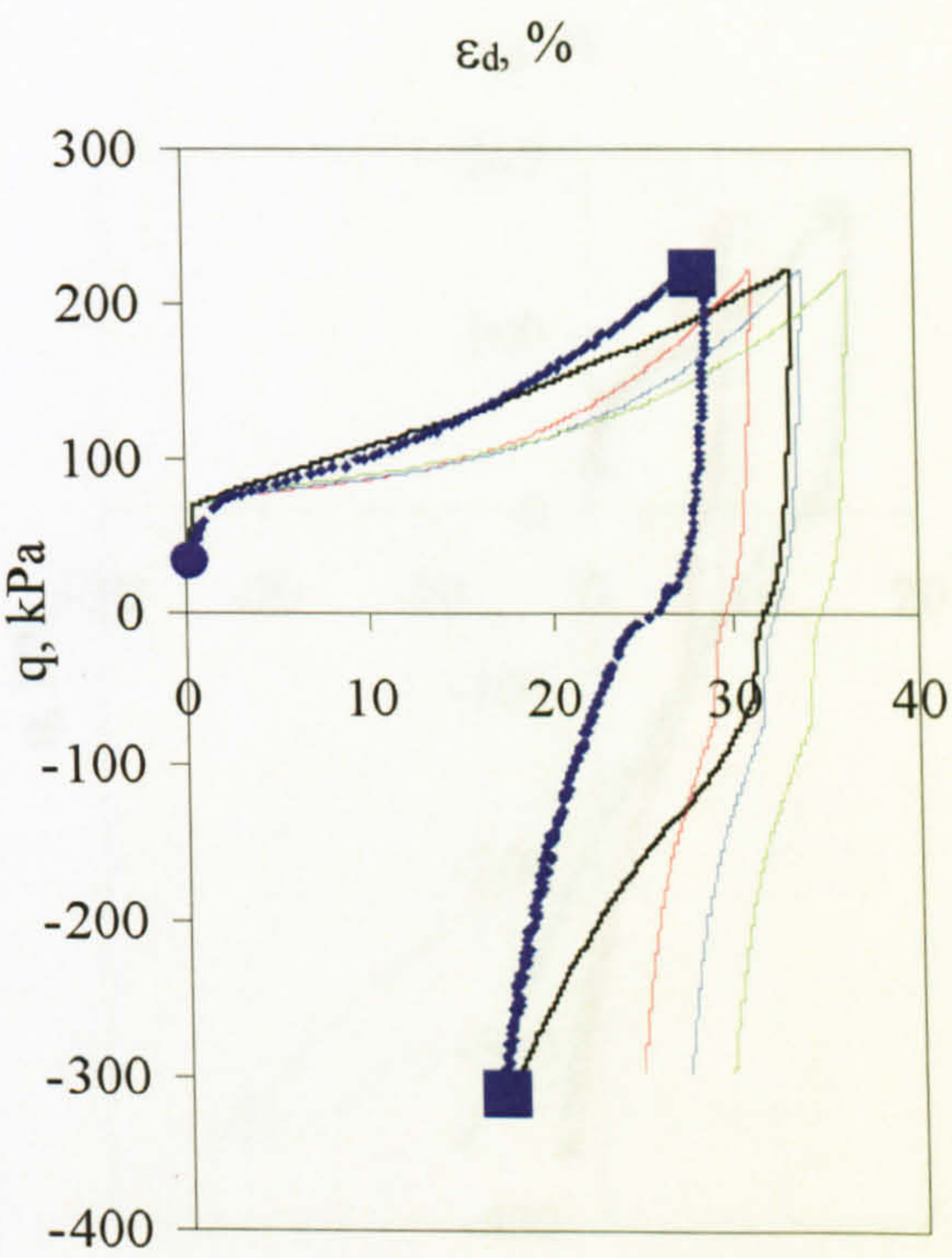

(b)

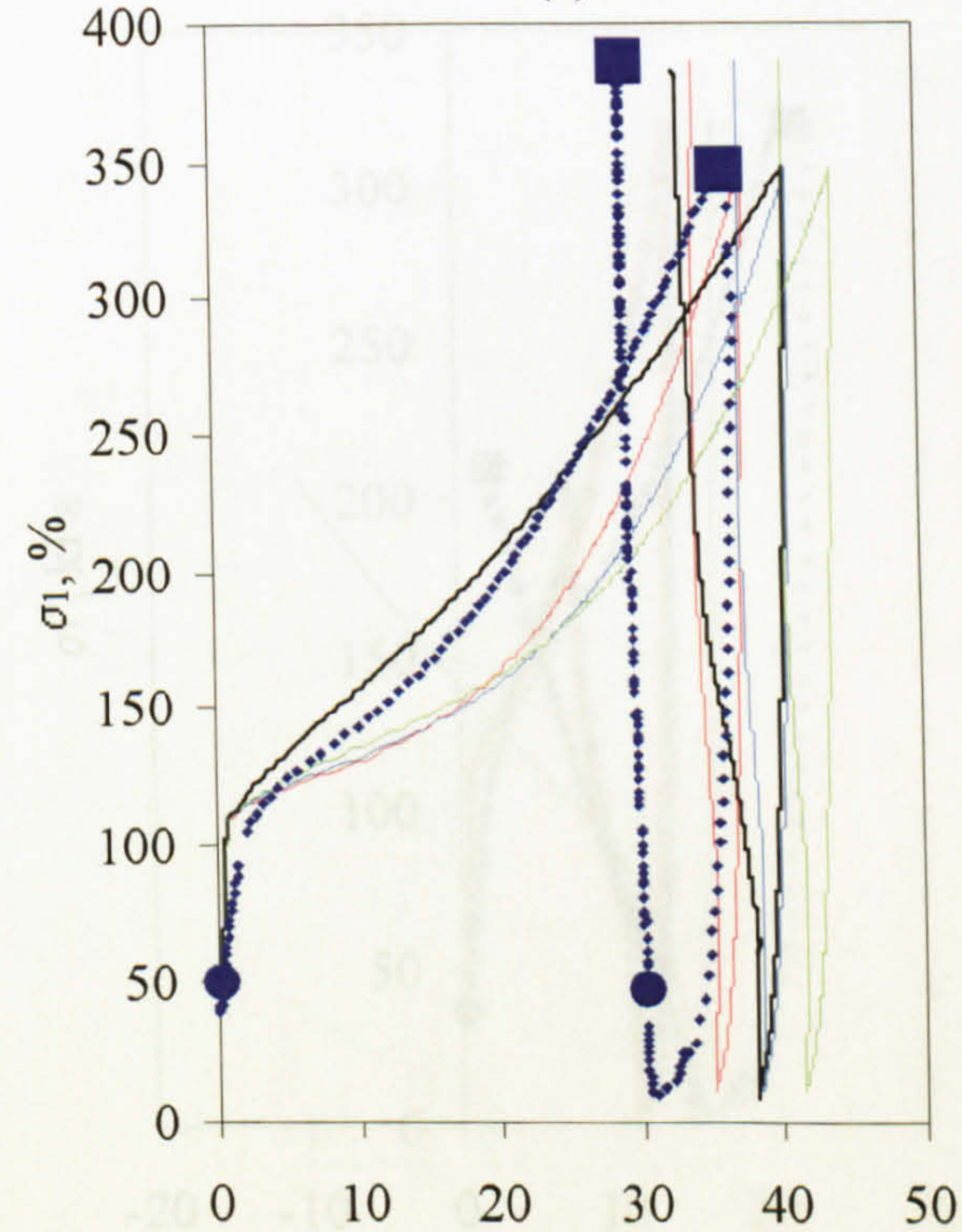

(c)

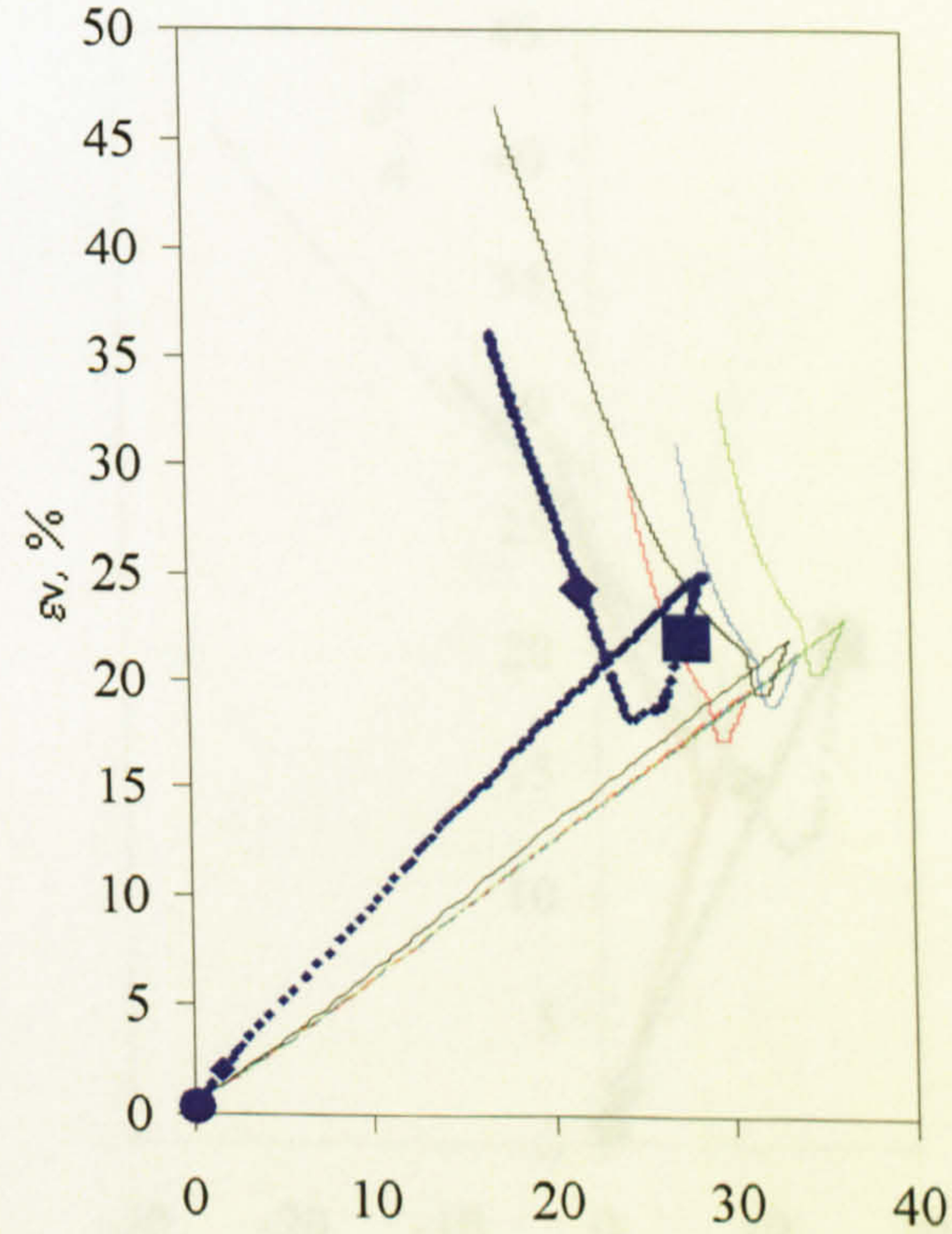

(d)

Figure 9.7. Simulations of Test C2 (η_1 = 1.10, η_2 = -0.50); (a) compression behaviour, (b) deviatoric stress-strain behaviour, (c) axial stress-strain behaviour (d) strain path.

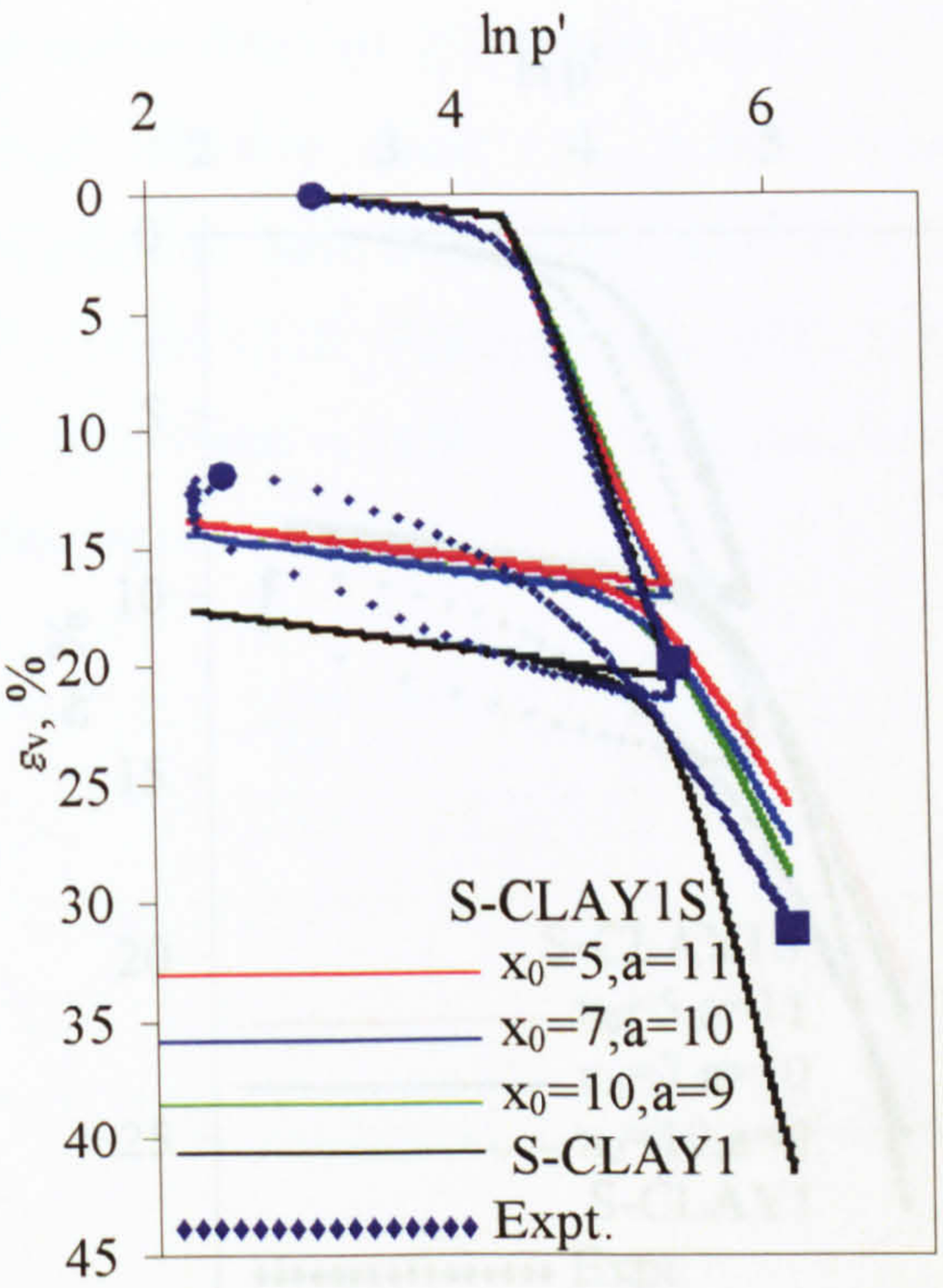

(a)

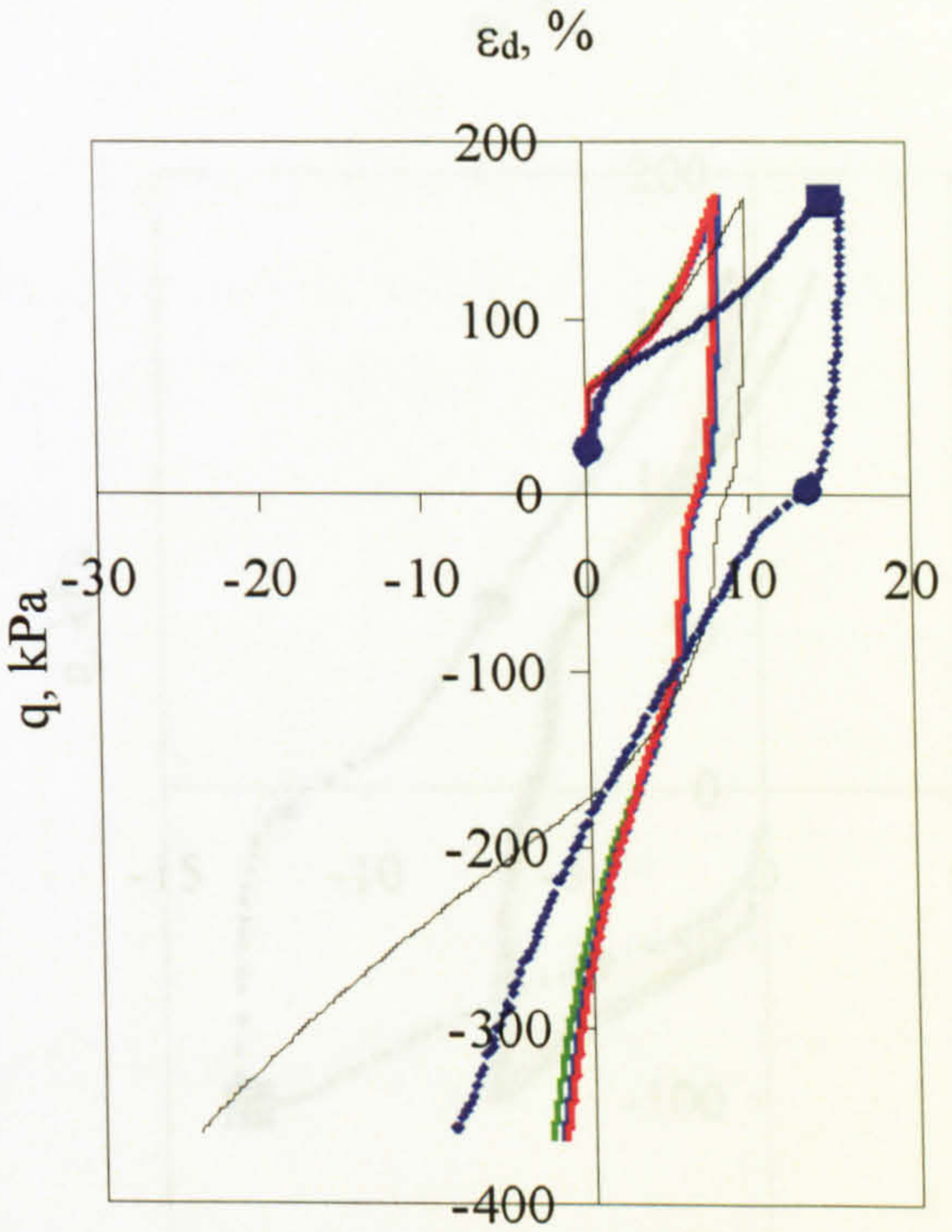

(b)

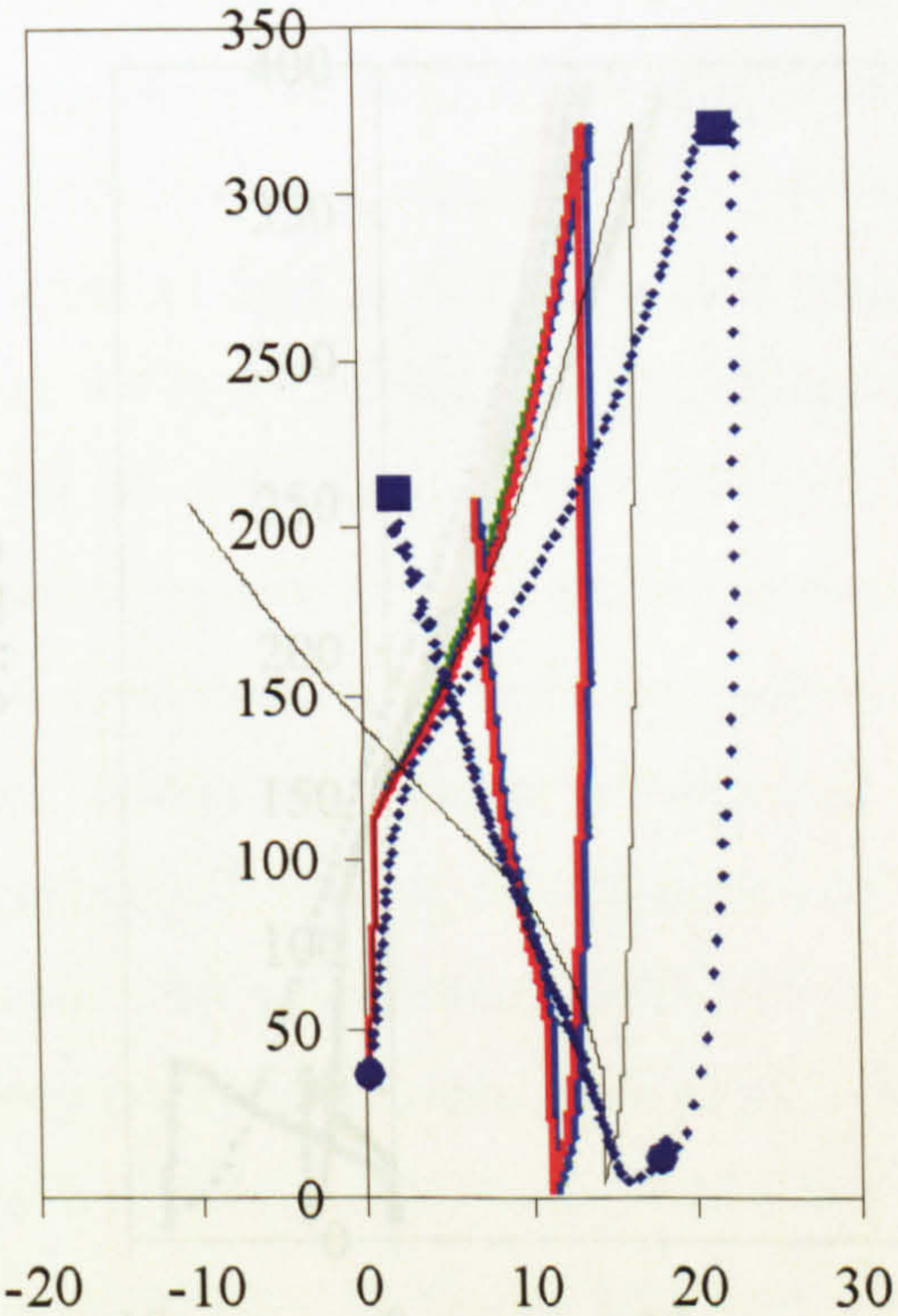

(c)

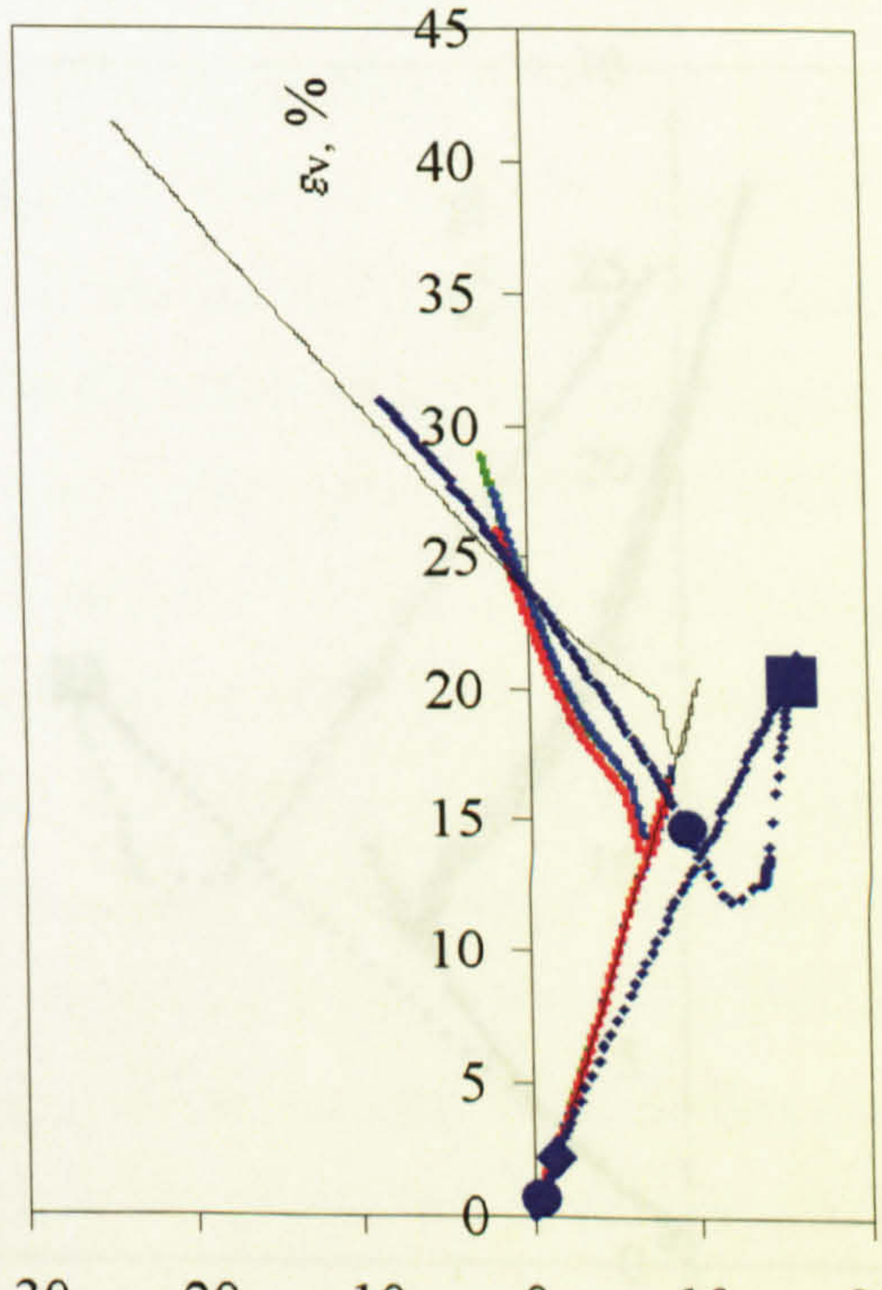

(d)

Figure 9.8. Simulations of Test C5 (η_1 = 0.80, η_2 = -0.80); (a) compression behaviour, (b) deviatoric stress-strain behaviour, (c) axial stress-strain behaviour (d) strain path.

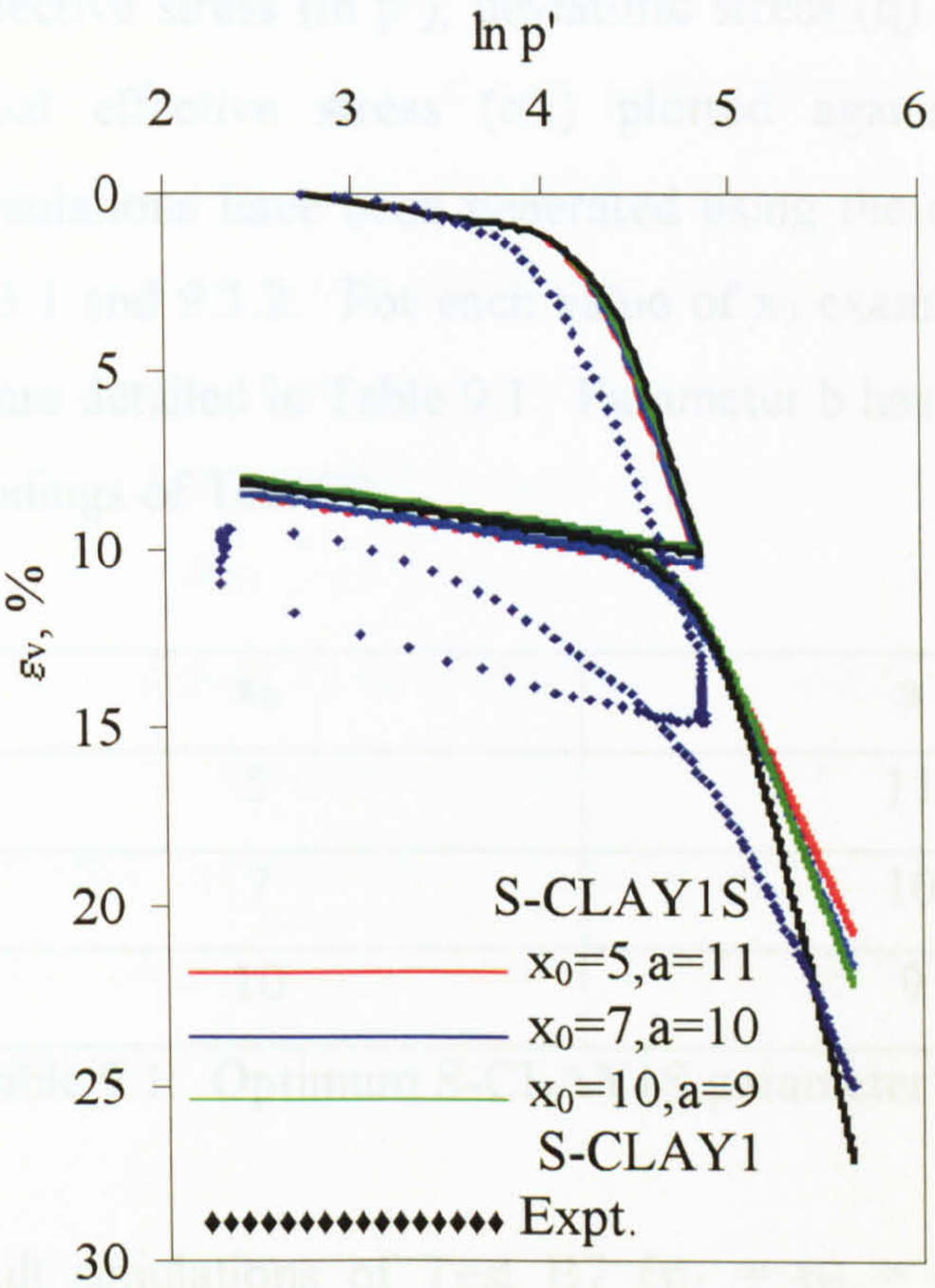

(a)

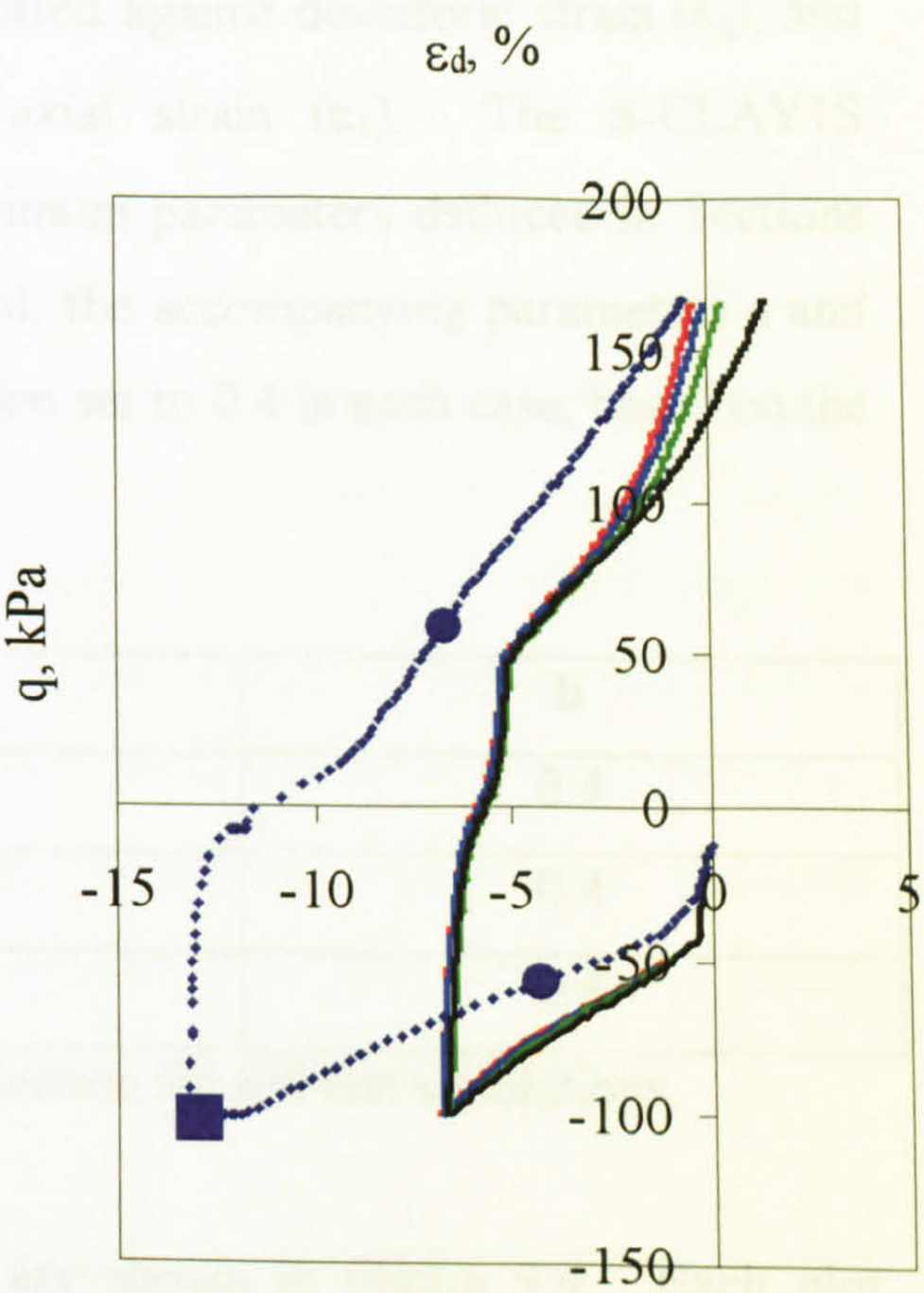

(b)

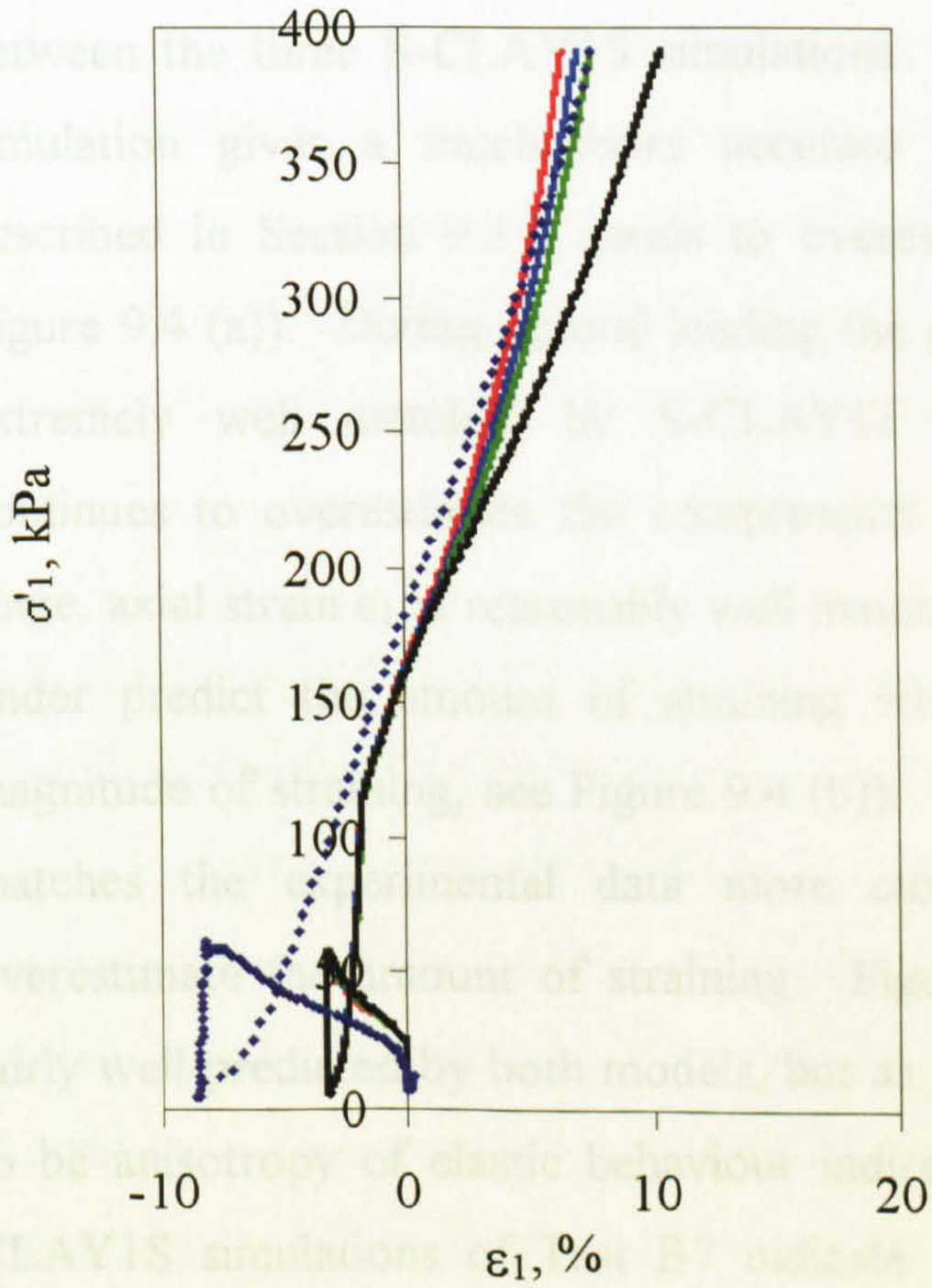

(c)

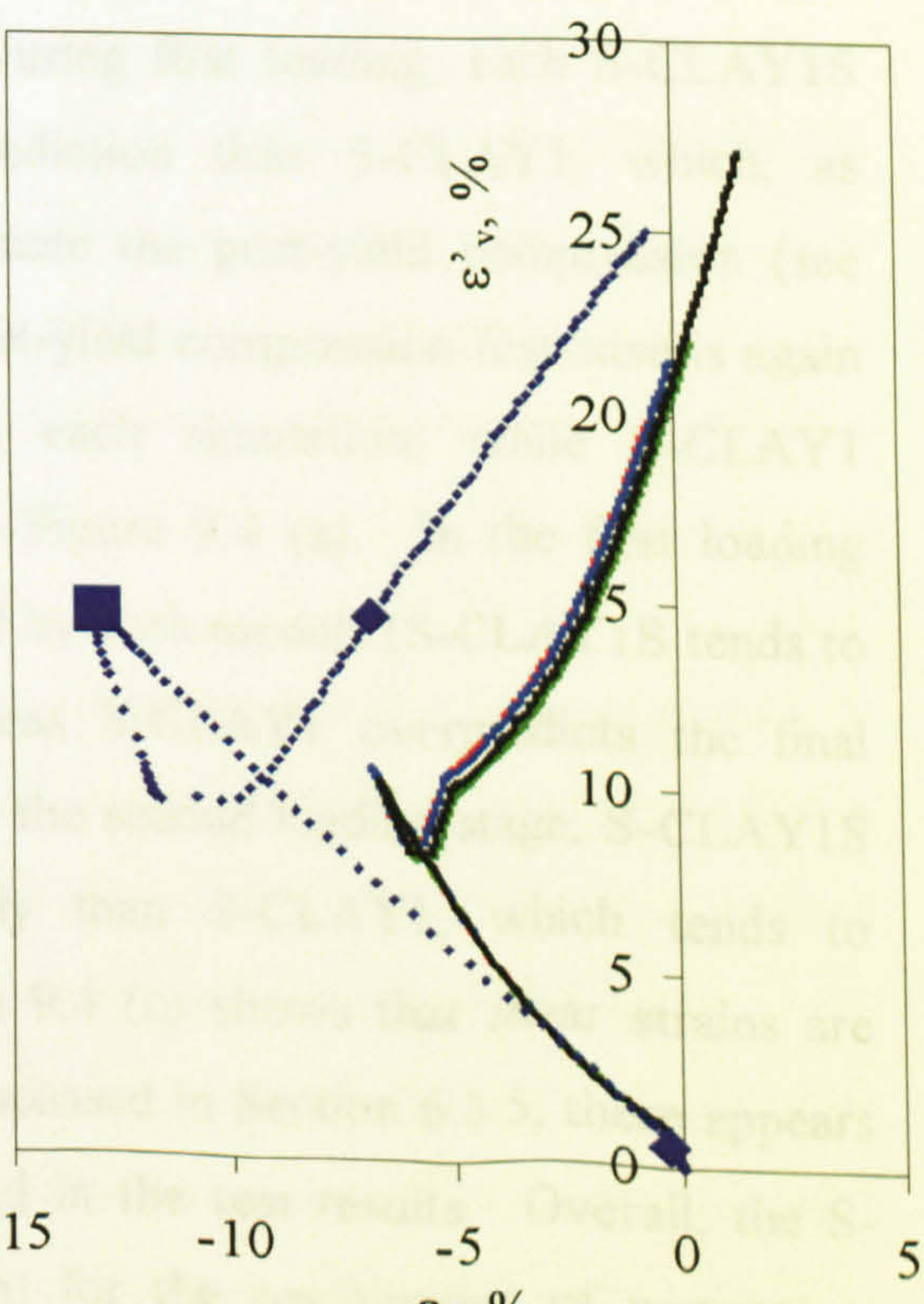

(d)

Figure 9.9. Simulations of Test C4 (η_1 = -0.80, η_2 = 0.60); (a) compression behaviour, (b) deviatoric stress-strain behaviour, (c) axial stress-strain behaviour (d) strain path.

effective stress (ln p'), deviatoric stress (q) plotted against deviatoric strain (ε_d), and axial effective stress (σ'_1) plotted against axial strain (ε_1). The S-CLAY1S simulations have been generated using the optimum parameters deduced in Sections 9.3.1 and 9.3.2. For each value of x_0 examined, the accompanying parameters a and b are detailed in Table 9.1. Parameter b has been set to 0.4 in each case, based on the findings of Test C2.

x_0	a	b
5	11	0.4
7	10	0.4
10	9	0.4

Table 9.1. Optimum S-CLAY1S parameter selection for full test simulations.

Full simulations of Test B7 ($\eta_1 = \eta_2 = 0$) are shown in Figure 9.4. Each plot indicates that in both the first and second loading stages, there is very little difference between the three S-CLAY1S simulations. During first loading, each S-CLAY1S simulation gives a much more accurate prediction than S-CLAY1, which, as described in Section 9.3.1, tends to overestimate the post-yield compression (see Figure 9.4 (a)). During second loading the post-yield compression response is again extremely well matched by S-CLAY1S in each simulation, while S-CLAY1 continues to overestimate the compression in Figure 9.4 (a). In the first loading stage, axial strain ε_1 is reasonably well matched by both models (S-CLAY1S tends to under predict the amount of straining whereas S-CLAY1 overpredicts the final magnitude of straining, see Figure 9.4 (b)). In the second loading stage, S-CLAY1S matches the experimental data more closely than S-CLAY1, which tends to overestimate the amount of straining. Figure 9.4 (c) shows that shear strains are fairly well predicted by both models, but as discussed in Section 6.3.5, there appears to be anisotropy of elastic behaviour indicated in the test results. Overall, the S-CLAY1S simulations of Test B7 indicate that for the combination of parameters shown, the model predictions are significantly improved over S-CLAY1.

Test B3 involved an isotropic first loading stage ($\eta_1 = 0$), followed by unloading and reloading in triaxial compression at $\eta_2 = 1.01$ and corresponding S-CLAY1 and S-

CLAY1S simulations are shown in Figure 9.5. During the second stage, each S-CLAY1S simulation shows a significant improvement over S-CLAY1 in terms of predicted post-yield volumetric strain ε_v, as shown in Figure 9.5 (a). S-CLAY1 substantially overpredicts compression in the second stage, due to the continued assumption of a λ value that is inappropriately high. Figure 9.5 (a) shows that S-CLAY1S matches the shape of the compression curve very well. Figures 9.5 (b) and (c) show that post-yield deviatoric and axial strains in the second loading stage are well predicted by both models, but towards the end of the second loading stage the S-CLAY1S simulations closely approximate the observed stress-strain behaviour, whereas the S-CLAY1 predictions increasingly overpredict the amount of strain. Both models significantly underestimate pre-yield axial and deviatoric strains. Figure 9.5 (d) shows that the strain path is matched very well by S-CLAY1S.

Test B6 involved isotropic loading ($\eta_1 = 0$) followed by unloading and reloading in triaxial extension at $\eta_2 = -0.70$. Comparisons of post-yield behaviour during second loading shown in Figure 9.6 are undermined by the fact that the yield point in the data is poorly predicted by both models. However, after yield has occurred, the S-CLAY1S model simulations appear to predict the soil behaviour very accurately. This is again in contrast to the S-CLAY1 simulations, which notably overestimate the amount of volumetric, deviatoric and axial, straining (see Figures 9.6 (a), (b) and (c)).

Full simulations of Test C2 are shown in Figure 9.7 where the first loading stage is in triaxial compression ($\eta_1 = 1.10$) and the second loading stage is in triaxial extension at $\eta_2 = -0.50$. As previously described, the S-CLAY1S simulations show marked improvement over S-CLAY1 during first loading stage, particularly where $x_0 = 10$. During second loading, the improvement achieved by S-CLAY1S is much more significant. Figure 9.7 (a) shows that the S-CLAY1 simulation gives a highly inaccurate prediction of post-yield compression in the second loading stage. Each S-CLAY1S simulation is in excellent agreement with the observed data. Each of the three S-CLAY1S simulations are similar, due to significant loss of structure during the first loading stage (rendering changes in model parameters less significant during second loading), and the apparent mismatch during second loading is mainly due to

mismatching from the first loading stage. In terms of deviatoric and axial strain, Figures 9.7 (b) and (c) show that the best match to the data in the second loading stage is obtained in the simulations where $x_0 = 10$. Figure 9.7 (d) indicates that any mismatches in either model during second loading cannot be attributed to problems with the flow rule as the strain path direction is in very good agreement with the data for both models.

Simulations of Test C5 are shown in Figure 9.8, where $\eta_1 = 0.80$ and $\eta_2 = -0.80$. In the first loading stage, the experimental data are very well matched by S-CLAY1, although this is partly due to the fact that the observed value of λ is almost coincident with λ_{K0}. Each of the three S-CLAY1S simulations underestimate the post-yield compression in the first loading stage, as shown in Figure 9.8 (a). In comparison to Tests C2 and C3, the S-CLAY1S model shows relatively little difference between the three simulations at this stress ratio. In terms of deviatoric and axial strains, all simulations underestimate post-yield straining during the first loading stage, although S-CLAY1 gives slightly better predictions than S-CLAY1S. During the second loading stage, S-CLAY1 significantly overestimates the post-yield volumetric strain (Figure 9.8 (a)), despite closely approximating the yield point. In each of the plots in Figure 9.8, S-CLAY1S predicts the behaviour during second loading very well, since the predicted rate of straining is much slower due to preceding destructuration during the first loading stage. The simulations suggest that the data is best matched where $x_0 = 10$.

Test C4 involved first loading in triaxial extension ($\eta_1 = -0.80$) and second loading in triaxial compression at $\eta_2 = 0.80$, as shown in Figure 9.9. During first loading, both S-CLAY1 and S-CLAY1S give very similar predictions, partly because this test stage is largely dominated by changes in anisotropy. In the second loading stage, S-CLAY1S gives more accurate predictions, particularly in terms of volumetric strains (see Figure 9.9 (a)). S-CLAY1S has again accounted for the fact that a significant amount of destructuration has occurred during first loading, while S-CLAY1 continues to predict a rate of compression that is unrealistically rapid. The progress of deviatoric and axial strain is well matched by S-CLAY1S in the second loading stage (see Figures 9.9 (b) and (c)), particularly where $x_0 = 10$. The pattern of

straining shown in Figure 9.9 (d) shows that during first loading, all simulations initially match the post-yield strain path very well. However, the predicted effects of evolving anisotropy, in particular clockwise rotation of the yield curve, means that the predicted gradient of the strain path increases. This is not reflected by the experimental data, suggesting that there may be remaining inaccuracies in the yield curve shape or the flow rule assumption. A similar effect can be seen during the second loading stage in Figure 9.9 (d), where the gradient of the predicted strain path increasingly departs from that of the experimental curve.

9.4 Conclusion

With the inclusion of the effects of destructuration, the S-CLAY1S model has been shown to be an improvement on S-CLAY1 in predicting the behaviour of Bothkennar clay under a wide variety of loading conditions. This is because S-CLAY1S has the ability to make satisfactory predictions on the behaviour of the natural soil, with a suitable choice of λ_i and destructuration parameters x_0, a and b. Simulations suggest that the value of x_0 for Bothkennar clay is likely to be about 10 and therefore Bothkennar clay exhibits a significant degree of initial bonding. This explains why S-CLAY1, where simulations were generated using λ_{K0}, generally overpredicted post-yield strains during first loading stages at $\eta_l < \eta_{K0}$ and significantly overestimated post-yield strains during second loading stages, where much of the soil structure had already been destroyed. Optimum values for parameters a and b, in the case where $x_0 = 10$, are $a = 9$ and $b = 0.4$.

CHAPTER 10: CONCLUSIONS AND RECOMMENDATIONS

10.1 Conclusions

Experimental test results from Bothkennar clay have provided important information on natural clay behaviour. Constitutive model simulations of these tests have shown that the S-CLAY1 and S-CLAY1S models generally show improved predictions over Modified Cam Clay (MCC), although modifications and additional components will be necessary in order to model natural clay behaviour more accurately. Further testing, perhaps on other natural clays will be necessary in order to fully validate the models.

Pre-yield behaviour

Results from isotropic loading tests on vertically oriented samples suggested that pre-yield behaviour was anisotropic. In particular, results from isotropic loading and unloading test stages showed evidence of cross-anisotropy of elastic behaviour. Subsequent isotropic reloading suggested that this elastic anisotropy still existed and was relatively unchanged. It may therefore be more resistant to change than anisotropy of plastic behaviour.

On horizontally oriented samples pre-yield behaviour was monitored in the axial direction and in two radial directions. Results from these tests again suggested that pre-yield behaviour is anisotropic and that this anisotropy of elastic behaviour does not appear to change significantly during subsequent plastic straining.

At present, the S-CLAY1 and S-CLAY1S models do not incorporate anisotropy of pre-yield behaviour. In order to model fully generalized anisotropic elastic behaviour, 21 elastic parameters would be necessary. However, if the elastic behaviour of the soil is cross-anisotropic and can be assumed to remain unchanged, as suggested in the test results, then only 5 elastic constants would be necessary to model this behaviour.

Test results suggested that elastic behaviour was more non-linear than is predicted by S-CLAY1 and S-CLAY1S. This weakness of classical elasto-plastic models (such as MCC) is well known. An alternative form of model would be required in order to model this complexity of small strain behaviour (occurring inside the yield surface of models such as MCC, S-CLAY1 and S-CLAY1S).

Critical state behaviour and Lode angle dependency

Conventional drained shear tests on vertical samples showed that the value of the critical state stress ratio in triaxial compression (M_C) was much greater than in triaxial extension (M_E). This is a widely reported feature of clay behaviour which is incorporated in both the S-CLAY1 and S-CLAY1S models and can be represented in generalized form by making the value of M a function of the Lode angle of the tensor $\underline{\sigma}_d - p'\underline{\alpha}_d$.

On similar tests involving horizontal samples the value of the critical state stress ratio in triaxial compression was again greater than that in triaxial extension, but in both cases the measured value of critical state stress ratio was different from corresponding tests on vertical samples. This suggests an additional degree of complexity in the clay behaviour with behaviour at the critical state still showing some dependency on a previous state of anisotropy. This is in contrast to one of the main assumptions of the S-CLAY1 and S-CLAY1S models. It was noted however, that it was difficult to make a clear distinction of true critical state in the experimental tests, since both M_C and M_E were measured at peak conditions, which may not be representative of the true critical state.

Yielding

Bothkennar clay exhibits a gradual onset of yielding, which is in contrast to the abrupt transition from elastic to plastic behaviour predicted by S-CLAY1 and S-CLAY1S. This is a weakness in all classical elasto-plastic models. From the experimental data, yield points are reasonably clear in the first loading stages, but are less obvious during second loading stages. Precise yield points were particularly difficult to detect in second loading stages which involved a significantly different

stress ratio from that in the first loading stage. This was thought to be due to the effects of evolving anisotropy, causing post-yield stress strain curves to be more rounded at the onset of yield.

In general, yield points for both vertical and horizontal samples were reasonably well matched by S-CLAY1 and S-CLAY1S and both models showed general improvement over Modified Cam Clay in this respect. Yield points from the first loading stages on vertical samples were obtained and the S-CLAY1 yield curve was fitted to these. The yield data showed that the in-situ state of Bothkennar clay is anisotropic. The orientation of the yield curve fitted to the data did not match well with the orientation predicted in the procedure given by Wheeler et al. (2003b) for normally consolidated or lightly overconsolidated clays with a K_0 strain history. This can be attributed to plastic straining (and further change of yield curve orientation) during in-situ unloading to an overconsolidated state (even though the soil was lightly overconsolidated).

Tests on horizontal samples again provided a set of yield points from first loading stages. This information allowed a new section of the initial location of the yield surface to be explored. The shape of this section of the yield surface was again consistent with the predictions of S-CLAY1, and the size and orientation were found to be very consistent with predictions based on information obtained on the yielding of vertically oriented samples.

Post-yield stress-strain behaviour

The gradient of the post yield compression curve (λ) is highly dependent on the stress ratio η. This is thought to be linked to the process of destructuration (in conjunction with consolidation). The apparent value of λ increases at higher stress ratios, associated with large amounts of plastic shear strains contributing to destructuration (in addition to the considerable amount of plastic volumetric strains also contributing to destructuration). During second loading stages, apparent values of λ were generally lower than in the first loading stages (regardless of the value of η). This was thought to be a result of a reduced rate of destructuration with much of

the soil bonding having been destroyed during the first loading stages. In some tests, where destructuration had been particularly large during a first loading stage, the value of λ approached its intrinsic value λ_i towards the end of the second loading stage.

Due to the absence of destructuration features in both S-CLAY1 and MCC, and the assumption of post-yield compression gradient λ_{K0}, these models tend to overpredict the magnitude of plastic volumetric strains in first loading stages at low values of η and underestimate the amount of plastic volumetric strains in first loading stages at high values of η. This latter outcome is particularly marked in second loading stages when the rate of destructuration has slowed due to the loss of bonding occurring in the previous loading stage. Model predictions are significantly better in S-CLAY1S which incorporates an initial degree of soil bonding, an intrinsic post-yield compression gradient λ_i and a destructuration law to determine the rate at which bonding is destroyed.

Measurement of post-yield principal strain behaviour on horizontal samples showed that the initial cross-anisotropy of the soil could be removed by continued yielding. The eventual convergence of the two measured radial strains suggested that a new form of cross-anisotropic fabric had emerged. The type of behaviour is qualitatively predicted by S-CLAY1, but MCC cannot predict changes in fabric and is therefore much less accurate. The measured differences between the two radial strains were often predicted with poor accuracy. This could be a weakness of the S-CLAY1 model or may be partly due to experimental error when mounting the radial callipers.

At low to moderate stress ratios the use of the associated flow rule in S-CLAY1 and S-CLAY1S is a good assumption. However, at high stress ratios in both triaxial compression and triaxial extension, the models grossly overpredict the magnitude of shear strain. This cannot be attributed exclusively to any slight error in the estimation of the critical state stress ratio since the effects were seen in simulations at stress ratios significantly lower than critical state. It seems likely, therefore, that the soil response may be significantly non-associated at high stress ratios.

Creep

It was noted that during rest periods, volumetric and axial strains continued to develop even though the stresses were held constant. This could have been due to incomplete primary consolidation (perhaps as a result of loading the samples too rapidly). Another possibility is that this phenomenon is due to creep strains and work is now in progress to develop an elasto-viscoplastic version of S-CLAY1 which incorporates creep and anisotropy.

10.2 Recommendations

Despite the advances in modelling the behaviour of a natural clay achieved by S-CLAY1 and S-CLAY1S, a number of aspects of modelling behaviour must be improved further.

- Tests showed that pre-yield behaviour was significantly anisotropic. This suggests the need for anisotropic elastic laws within S-CLAY1 and S-CLAY1S. The possibility that unchanging cross-anisotropic pre-yield behaviour exists means that only five elastic constants would be necessary (three more than is presently used in S-CLAY1 and S-CLAY1S).
- A generalized form of Lode angle dependency is required. It is possible that this may be in the form of the value of M dependent on $\underline{\sigma}_d$ - p'$\underline{\alpha}_d$. In addition, further testing will be required to examine the influence of anisotropy at a critical state (in both triaxial compression and triaxial extension).
- A non-associated flow rule should be considered, particularly to account for the inaccurate predictions at high stress ratios in triaxial compression and triaxial extension.
- Constitutive modelling of creep strains should be incorporated into the S-CLAY1 models.
- Aspects of natural clay behaviour such as anisotropy and destructuration should be incorporated in finite element analyses applications for use in practical engineering solutions.

References

Adachi, T., Oka, F., Hirata, T., Hashimoto, T, Pradhan, T.B.S., Nagaya, J. and Mimura, M. (1979). Triaxial and torsional hollow cylinder tests of sensitive natural clay and an elasto-viscoplastic constitutive model. Proc. 6th ARCSMFE, Vol. 1, 117-120.

Adachi, T., Oka, F., Hirata, T., Hashimoto, T., Nagaya, J., Mimura, M., and Pradhan,T.B.S. (1995). Stress-strain and yielding characteristics of eastern Osaka clay, Soils and Foundations, 35, 3: 1-13, 1995.

Al-Tabbaa, A. and Muir Wood, D. M. (1989). An experimentally based bubble model for clay. Proceedings of the 3rd International Symposium on Numerical Models in Geomechanics, pp.90-99, Elsevier.

Allman, M.A and Atkinson, J.H. (1992). Mechanical properties of reconstituted Bothkennar soil. *Géotechnique*, Vol., 42 No.2, 289-302.

Amorosi, A. and Rampello, S. (1998). The influence of natural soil structure in the mechanical behaviour of a stiff clay. The Geotechnics of hard soils – soft rocks, (Eds. Evangelista and Picarelli), Balkema, Rotterdam.

Atkinson, J.H. and Richardson, D. (1985). Elasticity and normality in soil – experimental examinations. Géotechnique 35, No. 4, 443-449.

Atkinson, J.H., Richardson, D., and Robinson, P.J. (1987). Compression and extension of K_0 normally consolidated kaolin clay. ASCE Journal of Geotechnical Engineering, 113, No. 12, 1468-1482.

Atkinson, J.H., Richardson, D. and Stallebrass, S.E. (1990). Effect of recent stress history on the stiffness of overconsolidated soil. Géotechnique 40, No. 4, 531-540.

Bai, X. and Smart, P. (1997). Change in microstructure of kaolin in consolidation and undrained shear. Géotechnique 47, No. 5, 1009-1017.

Banerjee, P.K. and Yousif N.B. (1986). A plasticity model for the mechanical behaviour of anisotropically consolidated clay. Int. J. for Num. Anal. Meth. in Geomechanics 10, 521-541.

Baudet, B.A. and Stallebrass, S.E. (2004). A constitutive model for structured clays. Géotechnique 54, No. 4, 269-278.

Bishop, A.W. and Wesley, L.D. (1975). A hydraulic triaxial apparatus for controlled stress path testing. *Geotechnique*, Vol. 25, 657-670.

Bjerrum, L. (1967). Engineering geology of normally consoldiated Norwegian marine clays. Géotechnique 17, No. 1, 49-69.

Boudali, M., Leroueil, S. and Murthy, B.R.S. (1994). Viscous behaviour of natural soft clays. *Proc. 13th Int. Conf. on Soil Mechanics and Foundation Engineering*, New Delhi, 1: 411-416.

Broms, B.B. and Casbarian, A.O. (1965). Effects of rotation of the principal stress axes and of the intermediate principal stress on the shear strength. Proc. 6th ICSMFE, Montreal, Vol. 1, 179-182.

Burland, J.B. (1990). On the compressibility and shear strength of natural clays. Géotechnique 40, No. 3, 327-379.

Christoulas, S., Kalteziotis, N., Tsiambaos, G. and Sabatakakis, N. (1987). Engineering geology of soft clays. Examples from Greece. Bulletin of Public Works Research Centre: Embankments on soft clays, 1-31.

Clayton, C.R.I., Hight, D.W. and Hopper, R.J. (1992). Progressive destructuring of Bothkennar clay: implications for sampling and reconsolidation procedures. Géotechnique 42, No. 2, 220-240.

Clayton, C.R.I., and Khatrush, S.A. (1986). A new device for measuring local axial strains on triaxial specimens. Geotechnique, Vol. 36, No.4, 593-597.

Clayton, C.R.I, Khatrush, S.A., Bica, A.V.D., Siddique, A. (1989). The use of Hall effect semiconductors in geotechnical instrumentation. *Geotechnical Testing Journal*, GTJODJ, Vol. 12, No.1, 69-76.

Collins, K. and McGown, A. (1974). The form and function of microfabric features in a variety of natural soils. Géotechnique 24, No. 3, 223-254.

Crawford, C.B. (1964). Interpretation of the consolidation test. ASCE Journal of Geotechnical Engineering, Vol. 90 (SM5), 87-102.

Cudny, M. (2003). Simple multi-laminate model for soft soils incorporating structural anisotropy and destructuration. In P.A. Vermeer, H.F. Schweiger, M. Karstunen & M. Cudny (ed.), *Proc. Int. Workshop on Geotechnics of Soft Soils: Theory and Practice, Noordwijkerhout.* VGE

Dafalias, Y.F., (1987). An anisotropic critical state clay plasticity model. Constitutive laws for engineering materials: theory and application, C.S. Desai et al . (eds.), Vol. 1, 513-521.

Das, B.M. (1990). Principles of Geotechnical Engineering (2nd Edition), PWS Kent.

Davies, M.C.R., and Newson, T.A. (1993). A critical state constitutive model for anisotropic soil. Predictive soil mechanics (Eds. G.T. Houlsby and A.N. Schofield), 219-229, London: Thomas Telford.

Díaz-Rodriguez, J. A., Leroueil, S. and Aleman, J.D. (1992). Yielding of Mexico City Clay and other natural clays. ASCE Journal of Geotechnical Engineering, 118, No. 7 981-995.

Dodd, C. (2000). Private communication.

Garga, V.K. and Kahn, M.A. (1991). Laboratory evaluation of K_0 for overconsolidated clays, Can. Geotech. J. 28, 650-659.

Gens, A (1982). Stress-strain and strength characteristics of a low plasticity clay. Ph.D thesis, London University.

Gens, A. and Nova, R. (1993). Conceptual bases for a constitutive model for bonded soils and weak rocks. Proc. Int. Symp. Hard Soils-Soft Rocks, Athens.

Gens, A. and Potts, D.M. (1987). Critical state models in computational geomechanics. Engineering Computation, 5: 178-197.

Géotechnique Symposium-in-Print (1992) Vol. 42. No. 2.

Gibson, R.E. and Henkel, D.J. (1954). Influence of duration of tests at constant rate of strain on measured shear strength. *Géotechnique*, Vol. 4, No. 1, 6-15.

Graham, J. and Houlsby, G.T. (1983). Anisotropic elasticity of a natural clay. *Geotechnique*, Vol.33 165-180.

Graham, J., Lew, K.V., and Noonan, M.L., (1983). Yield states and stress-strain relationships in a natural plastic clay. Canadian Geotech. Journal 20, No.3 502-516.

Graham, J. and Li., E.C.C. (1985). Comparison of natural remolded plastic clay. ASCE Journal of Geotechnical Engineering, 111, No. 7, 1985 865-881.

Head, K.H. (1990). Manual of soil laboratory testing, Vol.3.

Hight, D.W., Böese, R., Butcher, A.P., Clayton, C.R.I. and Smith, P.R. (1992). Disturbance of Bothkennar clay prior to laboratory testing. *Géotechnique*, Vol.42 No.2, 199-219.

Hird, C.C. and Yung, P. (1987). Discussion. *Geotechnique*, Vol. 37 No.3, 413-414.

Holtz, R. and Kovacs, W.D. (1981). An Introduction to Geotechnical Engineering. Prentice-Hall, pp. 733-735.

Janbu, N. (1985). Twenty-fifth Rankine Lecture: Soil models in offshore engineering. *Géotechnique*, Vol. 35, No.3, 239-282.

Jardine, R.J. (1992). Some observations on the kinematic nature of soil stiffness. Soils and Foundations, Vol. 32, No.2, 111-124.

Jardine, R.J., Symes, M.J. and Burland, J.B. (1984). The measurement of soil stiffness in the triaxial apparatus. Géotechnique 34, No. 3, 323-340.

Jardine, R.J., St. John H.D., Hight, D.W. and Potts, D.M. (1991). Some practical applications of a non-linear ground model. *Proc. 10th Eur. Conf. Soil Mech., Florence* 1, 223-228.

Kamei, T. and Nakase, A. (1989). Undrained shear strength anisotropy of K_0-overconsolidated cohesive soils. Soils and Foundations Vol. 29 No.3 141-151.

Karstunen M. and Koskinen, M. (2004). Anisotropy and destructuration of Murro clay. In: Advances in Geotechnical Engineering. The Skempton Conference, London 29-31 March 2004. Thomas Telford. Vol. 1 476-486.

Karstunen, M and Wheeler, S.J. (2002). Discussion of: Voyiadjis, G.Z. and Song, C.R. (2000). Finite strain, anisotropic Modified Cam Clay model with plastic spin. 1: Theory. *Journal of Engineering Mechanics ASCE*, 128: 497-498.

Kenney, T.C., Moum, J., and Berre, T. (1967). An experimental study of bonds in a natural clay. Proc. Geotech. Conf., Oslo, Vol. 1, 65-69.

Kirkgard, M.M and Lade, P.V. (1993). Anisotropic three-dimensional behaviour of a normally consolidated clay, *Can. Geotech. J.* 30, 848-858.

Korhonen, K-H. and Lojander, M. (1987). Yielding of Perno clay. Proc. 2nd Int. Conf. on Constitutive Laws for Engineering Materials, Tucson, Arizona 1987. Vol. 2: 1249-1255. Elsevier.

Koskinen, M. (2001). M.Sc. Thesis, Helsinki University of Technology.

Koskinen, M., Karstunen, M. and Wheeler, S.J. (2002a). Modelling destructuration and anisotropy of a natural soft clay. In P. Mestat (ed.), *Proc. 5th European Conf on Numerical Methods in Geotechnical Engineering (NUMGE 2002), Paris:* 11-20. Presses de l'ENPC.

Koskinen, M., Zentar R. and Karstunen, M. (2002b). Anisotropy of reconstituted POKO clay. In G.N. Pande & S Pietruszczak (ed.), Proc. 8th Int. Symp. on Numerical Models in Geomechanics (NUMOG VIII), Rome, 99-105. A.A. Balkema.

Koskinen, M., Karstunen, M. and Wheeler, S.J. (2002). Modelling destructuration and anisotropy of a natural soft clay. In P. Mestat (ed.), *Proc. 5th European Conf on*

Numerical Methods in Geotechnical Engineering (NUMGE 2002), Paris: 11-20. Presses de l'ENPC.

Kuganenthira, N., Zhao, D., and Anandarajah, A. (1996). Measurement of fabric anisotropy during triaxial shearing. Géotechnique, 46, No. 4, 657-671.

Leonards, G.A. and Altschaeffl, A.G. (1964). Compressibility of clay. ASCE, J. of SMFD, Vol. 90 (SM5): 133-155.

Leroueil, S. (1997). Critical state soil mechanics and the behaviour of real soils, Symp. on Recent Developments in Soil and Pavement Mechanics", Rio de Janeiro, June 1997.

Leroueil, S., Lerat, P., Hight D.W. and Powell, J.J.M. (1992). Hydraulic conductivity of a recent estuarine silty clay at Bothkennar. Géotechnique 42, No. 2, 275-288.

Leroueil, S., Magnan, J-P. and Tavenas, F. (1990). Embankments on soft clays, Ellis Horwood, Chichester.

Leroueil, S. and Vaughan, P.R. (1990). The general and congruent effects of structure in natural soils and weak rocks. Géotechnique 40, No. 3, 452-467.

Lewin, P.I. and Allman, M.A. (1993). Three-dimensional tests on reconstituted Bothkennar soil. Predictive soil mechanics 436-448, Thomas Telford, London.

Liu, M.D. and Carter, J.P. (2000). Modelling the destructuring of soils during virgin compression, Géotechnique 50, No. 4, 479-483.

Liu, M.D. and Carter, J.P. (2002). A structured Cam Clay model, Canadian Geotechnical Journal 39, 1313-1332.

Lojander, M. (2000). Private communication.

Menkiti, C.O. (1995). Behaviour of clay and clayey-sand, with particular reference to principal stress rotation. PhD. Thesis, Imperial College of Science, Technology and Medicine, University of London.

Mesri, G. and Godlewski, P.M. (1977). Time and stress-compressibility interrelationship, *Proc. ASCE, Journal of the Geotechnical Engineering Division,* Vol. 103 (GT5): 417-430.

Mesri, G. and Hayat, T.M. (1993). The coefficient of earth pressure at rest, Can. Geotech. J., 30, 647-666.

Mitchell, J.K. (1976). Fundamentals of soil behaviour, John Wiley, New York.

Muir Wood (1990). Soil Behaviour and Critical State Soil Mechanics. Cambridge University Press.

Nash, D.F.T., Sills, G.C. and Davison, L.R. (1992a). One dimensional consolidation testing of soft clay from Bothkennar. Géotechnique 42, No. 2, 163-181.

Nash, D.F.T., Powell, J.J.M. and Lloyd, I.M. (1992b). Initial investigations of the soft clay test site at Bothkennar. Géotechnique 42, No. 2, 163-181.

Näätänen, A. and Lojander, M. (2000). Modelling of anisotropy of Finnish clays. Proc. 7th Finnish Symposium on Mechanics, Tampere, Finland.

Näätänen, A., Wheeler, S.J., Karstunen, M. and Lojander, M. (1999). Experimental investigation of an anisotropic hardening model for soft clays. In M. Jamiolkowski, R. Lancellotta & D. Lo Presti (ed.), *Proc. 2nd Int. Symp. on Pre-Failure Deformation Characteristics of Geomaterials, Torino,* Vol. 1: 541-548. A.A. Balkema.

Neher, H.P., Cudny, M., Wiltafsky, C. & Schweiger, H.F. (2002). Modelling principal stress rotation effects with multilaminate type constitutive models for clay. In G.N. Pande & S. Pietruazczak (eds.), Proc. 8th Int. Symp. on Numerical Geomechanics (NUMOG VIII), Rome: 41-47. A.A. Balkema.

Neher, H.P., Vermeer, P.A. and Bonnier, P.G. (2001). Strain-rate effects in soft soils, modelling and application. In C.F. Lee, C.K. Lau, C.W.W. Ng, A.K.L. Kwong, P.L.R. Pang, J.-H. Yin and Z.Q. Yue (ed.), *Proc. 3rd Int. Conf. on Soft Soil Engineering, Hong Kong:* 361-367. A.A. Balkema.

Newson, T.A., Davies, M.C.R. and Bondok, A.R.A. (1997). Selecting the rate of loading for drained stress path triaxial tests. *Geotechnique*, Vol. 47, No.5, 1063-1067.

Pande, G.N. and Sharma, K.G. (1983). Multilaminate model of clays – a numerical evaluation of the influence of rotation of principal stress axes. *International Journal for Numerical and Analytical Methods in Geomechanics*, Vol. 7: 397-418.

Paul, M.A, Peacock, J.D. and Wood, B.F. (1992). The engineering geology of the Carse clay of the National Soft Clay Research Site, Bothkennar. Géotechnique 42, No. 2, 183-196.

Pennington, D.S., Nash, D.F.T and Lings, M.L. (1997). Anisotropy of G_0 shear stiffness of Gault Clay. Géotechnique 47, No. 3, 391-399.

Rolo, R. (2003). The anisotropic stress-strain strength behaviour of brittle sediments. PhD Thesis, University of London.

Roscoe, K.H. and Burland, J.B. (1968). On the generalised stress-strain behaviour of "wet" clay. Engineering Plasticity 553-609. Cambridge University Press.

Roscoe, K.H., Schofield, A.N. and Wroth, C.P. (1958), "On the yielding of soils", Géotechnique No. 8,22-53.

Rouainia, M. and Muir Wood, D. (2000). A kinematic hardening model for natural clays with loss of structure. Géotechnique 50, No. 2, 153-164.

Schmertmann, J.H. (1991). The mechanical aging of soils. *Journal of Geotechnical Engineering*, ASCE, Vol. 117 (9): 1288-1330.

Shibata, T. and Karube, D. (1979). Influence of the variation of the intermediate principal stress on the mechanical properties of normally consolidated clays. Proc. 6th ARCSMFE, Vol. 1, 225-234.

Smith, P.R., Jardine, R.J. and Hight, D.W. (1992). The yielding of Bothkennar clay. Géotechnique 42, No. 2, 257-274.

Stallebrass, S.E. (1990). Modelling small strains for analysis in geotechnical engineering. *Ground Engineering, Vol. 22 :* 26-29.

Stallebrass, S.E. and Taylor, R.N. (1997). The devlopment and evaluation of a constitutive model for the prediction of ground movements in overconsoldated clay. Géotechnique 47, No.2 235-253.

Stolle, D.F.E., Bonier, P.G. and Vermeer, P.A. (1997). A soft soil model and experiences with two integration schemes. Num. Methods in Geomechanics 123-128, Eds – G.N. Pande and S. Pietruszczak.

Tavenas, F. (1981). Some aspects of clay behaviour and their consequences on modelling techniques. Laboratory shear strength of soil, Special Technical Publication, No. 740, American Society for Testing and Materials, 667-677.

Tavenas, F. and Leroueil, S. (1977). Effects of stresses and time on yielding of clays. Proc. 9th ICSMFE, Tokyo, Vol. 1, 319-326.

Tavenas, F., Leroueil, S., La Rochelle, P., & Roy, M. (1978). Creep behaviour of an undisturbed, lightly overconsolidated clay. Canadian Geotechnical J., 15 (3), 402-423.

Vermeer, P.A. (1978). A double hardening model for sand. Géotechnique 28, No. 4, 413-433.

Wheeler, S.J., (1997), "A rotational hardening elasto-plastic model for clays". Proc. of XIV ICSMFE, Hamburg, Vol.1: 431-434. Rotterdam: A.A. Balkema.

Wheeler, S.J., Cudny, M., Neher, H.P. and Wiltafsky, C. (2003a). Some developments in constitutive modelling of soft clays. In P.A. Vermeer, H.F.

Schweiger, M. Karstunen and M Cudny (eds.), Proc. Int. Workshop on Geotechnics of Soft Soils: Theory and Practice, Noorwijkerhout, 3-22.

Wheeler, S.J., Karstunen, M. and Näätänen, A. (1999). Anisotropic hardening model for normally consolidated soft clay. In G.N. Pande, S. Pietruszczak and H.F. Schweiger (ed.), *Proc. 7th Int. Symp. on Numerical Models in Geomechanics (NUMOG VII), Graz:* 33-40. A.A. Balkema.

Wheeler, S.J., Näätänen, A., Karstunen, M. & Lojander, M. (2003b). An anisotropic elastoplastic model for soft clays. Canadian Geotechnical J., 40, 403-418.

Whittle A.J. and Kavvadas, M.J. (1994). Formulation of MIT-E3 constitutive model for overconsolidated clays. J. Geotech. Eng., 120(1): 173-198.

Wiltafsky, C., Messerklinger, S. and Schweiger, H.F. (2002). An advanced multilaminate model for clay. Proc. 8th Int. Symp. Numerical Models in Geomechanics (NUMOG), Rome, Italy, 2002.

Yin, J.-H. and Graham, J. (1999). Elastic viscoplastic modelling of the time-dependent stress-strain behaviour of soils. *Canadian Geotechnical Journal* 36: 736-745.

Yong R.N. and Sheeran, D.E., (1973). Fabric unit interaction and soil behaviour. Proc. Int. Symp. Soil Structure, Gothenburg, 176-183.

Yu, Y. and Axelsson, K. (1994). Constitutive modelling of Swedish cohesive soils accounting for anisotropy", Computer Methods and Advances in Geomechanics, Siriwardane & Zaman, Balkema, Rotterdam.

Zdravkovic L. (1996), Stress-strain-strength anisotropy of a granular medium under general stress conditions; PhD thesis, Imperial College, University of London

Zentar, R., Karstunen, M., Wiltafsky, C., Schweiger, H.F., and Koskinen, M. (2002a). Comparison of two approaches for modelling anisotropy of soft clays. In Proceedings of the 8th International Symposium on Numerical Models in Geomechanics (NUMOG VIII), Rome. 10–12 April, Edited by G.N. Pande and S. Pietruszczak. A.A. Balkema, Rotterdam. 115–121.

Zentar, R., Kartstunen, M., Wheeler, S.J. (2002b). Influence of anisotropy and destructuration on undrained shearing of natural clays. Proc 5th European Conf. on Numerical Methods in Geotechnical Engineering (NUMGE 2002), Paris 4-6 September. Eds. P. Mestat, Presses de l'ENPC, Paris 21-25.

Zienkiewicz, O.C. and Pande, G.N. (1977). Time-dependent multilaminate model of rocks – a numerical study of deformation and failure of rock masses. *International Journal for Numerical and Analytical Methods n Geomechanics* 1(3): 219-347.

Zytynski, M., Randolph, M.F., Nova, R. and Wroth, C.P. (1978). On modelling the unloading-reloading of soils. Int. J. for Numerical and Analytical Methods in Geomechanics, 2, 87-94.

LIST OF SYMBOLS

a	destructuration parameter in S-CLAY1S model
a	radius of soil sample
A	destructuration scaling parameter in Rouainia and Muir Wood (2000) model
A	area of sample
A_e	Anisotropy coefficient (Kuganenthira et al., 1996)
b	destructuration in S-CLAY1S model
b	ratio of deviatoric stresses
b	destructuration parameter in Rouainia and Muir Wood (2000) model
c_u	undrained shear strength
C_c	compression index
C_α	creep index
c_{ur}	remolded vane strength
c_v	coefficient of consolidation
d	sample diameter
$\underline{D}^e$	elastic compliance matrix
e	void ratio
E_h	stiffness in horizontal direction
E_v	stiffness in vertical direction
f	yield curve function
F	deviator force
g	plastic potential
G_s	specific gravity
G'	shear stiffness
G_{hh}	shear stiffness in horizontal pane
G_{vh}	shear stiffness in vertical pane
h	sample height
h_1	destructuration constant for plastic shear strains in Gens and Nova (1993) model
h_2	destructuration constant for plastic volumetric strains in Gens and Nova (1993) model
I_P	plasticity index
J	cross-anisotropic elastic parameter
k	soil constant in Dafalias (1987) model
K	ratio of radial stress to axial stress in triaxial test
K_0	earth pressure coefficient at rest
K_{0nc}	value of K_0 for normally consolidated soil
m_i	zeroes of Bessel function (first kind and zero order)
M_C	critical state stress ratio in triaxial compression
M_E	critical state stress ratio in triaxial extension
M_{CH}	critical state stress ratio in triaxial compression (horizontal sample)
M_{EH}	critical state stress ratio in triaxial extension (horizontal sample)
N_i	location of intrinsic compression line at p' = 1kPa
p'	mean effective stress in triaxial stress space
p'_c	preconsolidation stress
p'_m	yield curve size in S-CLAY1 and S-CLAY1S
p'_{mi}	intrinsic yield curve size in S-CLAY1S
p'_0	yield curve size in Modified Cam Clay

p'_y	yield stress
q	deviator stress in triaxial stress space
s_h	electrical conductivity in horizontal direction (Kuganenthira et al., 1996)
s_v	electrical conductivity in vertical direction (Kuganenthira et al., 1996)
s'	mean effective stress in plane strain
S_t	sensitivity
t'	shear stress in plane strain
T_v	time factor
u	pore pressure/back pressure
$\bar{u}$	average excess pore pressure
v	specific volume
V	sample volume
w_L	liquid limit
w_P	plastic limit
x	soil constant in Dafalias (1987) model
x	degree of bonding in S-CLAY1S and in Gens and Nova (1993) models
Y_1, Y_2, Y_3	yield surfaces (Smith et al., 1992)
α	yield curve orientation in S-CLAY1 and S-CLAY1S models
$\underline{\alpha}_d$	fabric tensor
$\alpha_x, \alpha_y, \alpha_z$	fabric tensor components
α_{K0}	yield curve orientation due to one-dimensional loading history in S-CLAY1 and S-CLAY1S models
α_s	rotation of yield curve at start of load increment in Davies and Newson (1993) model
β	constant controlling relative influence of shear and volumetric strains in change of anisotropy in S-CLAY1 and S-CLAY1S
$\gamma_{xy}, \gamma_{yz}, \gamma_{zx},$	shear strains
Δp^*	anisotropy variable in Davies and Newson (1993) model
$\varepsilon_a, \varepsilon_1$	axial strain
ε_d	shear strain
$\underline{\varepsilon}_d$	deviatoric strain tensor
ε_n	nominal (engineering) strain
$\varepsilon_x, \varepsilon_y, \varepsilon_z$	normal strains
ε_v	volumetric strain
ε_{vpr}	volumetric strain calculated from sum of normal strains
κ^*	swelling line gradient (non-structured soil in Rouainia and Muir Wood, 2000)
ν_{hh}	Poisson's ratio in horizontal plane
ν_{vh}	Poisson's ratio in vertical plane
λ	post-yield compression gradient
λ_i	post-yield compression gradient (non-structured soil)
λ_{K0}	post-yield compression gradient corresponding to one-dimensional loading history
λ^*	post-yield compression gradient (non-structured soil in Rouainia and Muir Wood, 2000)
Λ	scalar multiplier

η	stress ratio = q/p'
η_{K0}	value of η for one-dimensional conditions
η_0	yield curve orientation in Banerjee (1986) model
η_s	stress ratio at start of load increment in Davies and Newson (1993) model
μ	constant controlling overall rate of change of anisotropy in S-CLAY1 and S-CLAY1S
σ'_c	effective cell pressure in drained shearing tests
$\underline{\sigma}'_d$	deviatoric stress tensor
σ'_n	normal effective stress
σ'_r	radial effective stress
σ'_x	in-situ horizontal effective stress
σ'_y	in-situ vertical effective stress
σ'_z	in-situ horizontal effective stress
σ'_1	major principal effective stress
σ'_2	intermediate principal effective stress
σ'_3	minor principal effective stress
ϕ'_C	Mohr-Coulomb friction angle in triaxial compression
ϕ'_E	Mohr-Coulomb friction angle in triaxial extension
ϕ'_{ult}	ultimate friction angle (Zdravkovic, 1996)
θ	Lode Angle
τ	shear stress
$\tau_{xy}, \tau_{yz}, \tau_{zx},$	shear stresses
ζ	soil constant for rate of loading (Newson et al. 1997)
χ_d	target orientation due to plastic volumetric strains in S-CLAY1 and S-CLAY1S
χ_v	target orientation due to plastic volumetric strains in S-CLAY1 and S-CLAY1S

SUPERSCRIPTS

e	elastic
p	plastic

SUBSCRIPTS

X	horizontal direction in the ground
Y	vertical direction in the ground
Z	horizontal direction in the ground
x, z	radial directions in the triaxial apparatus
y	axial (vertical) direction in the triaxial apparatus

APPENDIX A

S-CLAY1 and S-CLAY1S partial derivatives

Partial derivatives for the S-CLAY1 and S-CLAY1S models:

S-CLAY1:

$$\frac{\partial f}{\partial p'} = -2\alpha(q - \alpha p') + \left(M^2 - \alpha^2\right)(2p' - p'_m)$$

$$\frac{\partial f}{\partial q} = 2(q - \alpha p')$$

$$\frac{\partial f}{\partial p'_m} = -p'\left(M^2 - \alpha^2\right)$$

$$\frac{\partial f}{\partial \alpha} = -2p'(q - \alpha p') + 2p'\alpha(p'_m - p')$$

$$\frac{\partial p'_m}{\partial \varepsilon_v^p} = \frac{(v p'_m)}{\lambda - \kappa}$$

$$\frac{\partial \alpha}{\partial \varepsilon_v^p} = \mu\left(\frac{3\eta}{4} - \alpha\right)$$

$$\frac{\partial \alpha}{\partial \varepsilon_d^p} = \mu\beta\left(\frac{\eta}{3} - \alpha\right)$$

S-CLAY1S:

$$\frac{dx}{d\varepsilon_v^p} = -ax$$

$$\frac{dx}{d\varepsilon_d^p} = -abx$$

APPENDIX B

Graphical construction in yield point identification

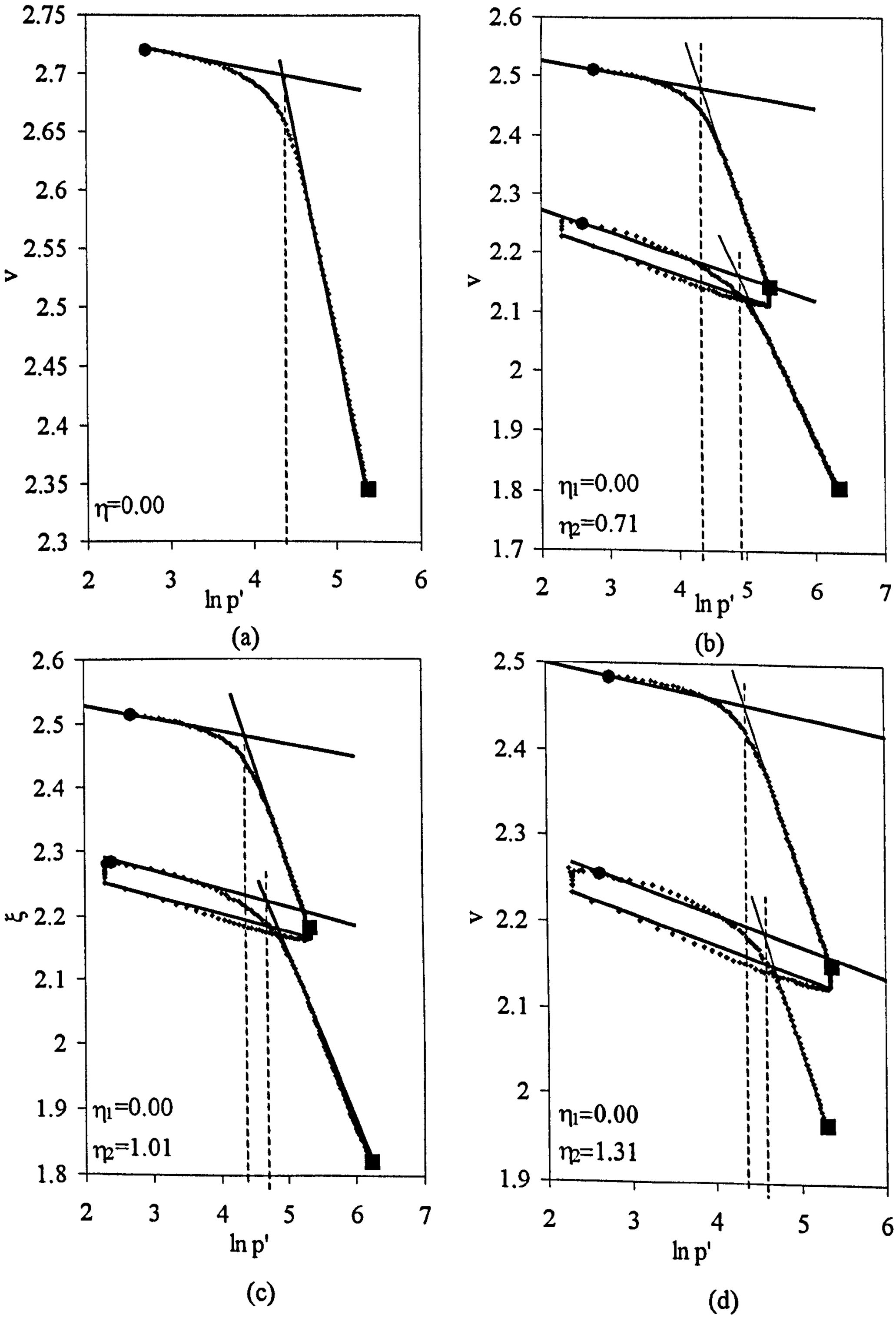

Figure B.1. Yield points from Test Series B. (a) Test B1, (b) Test B2, (c) Test B3, (d) Test B4.

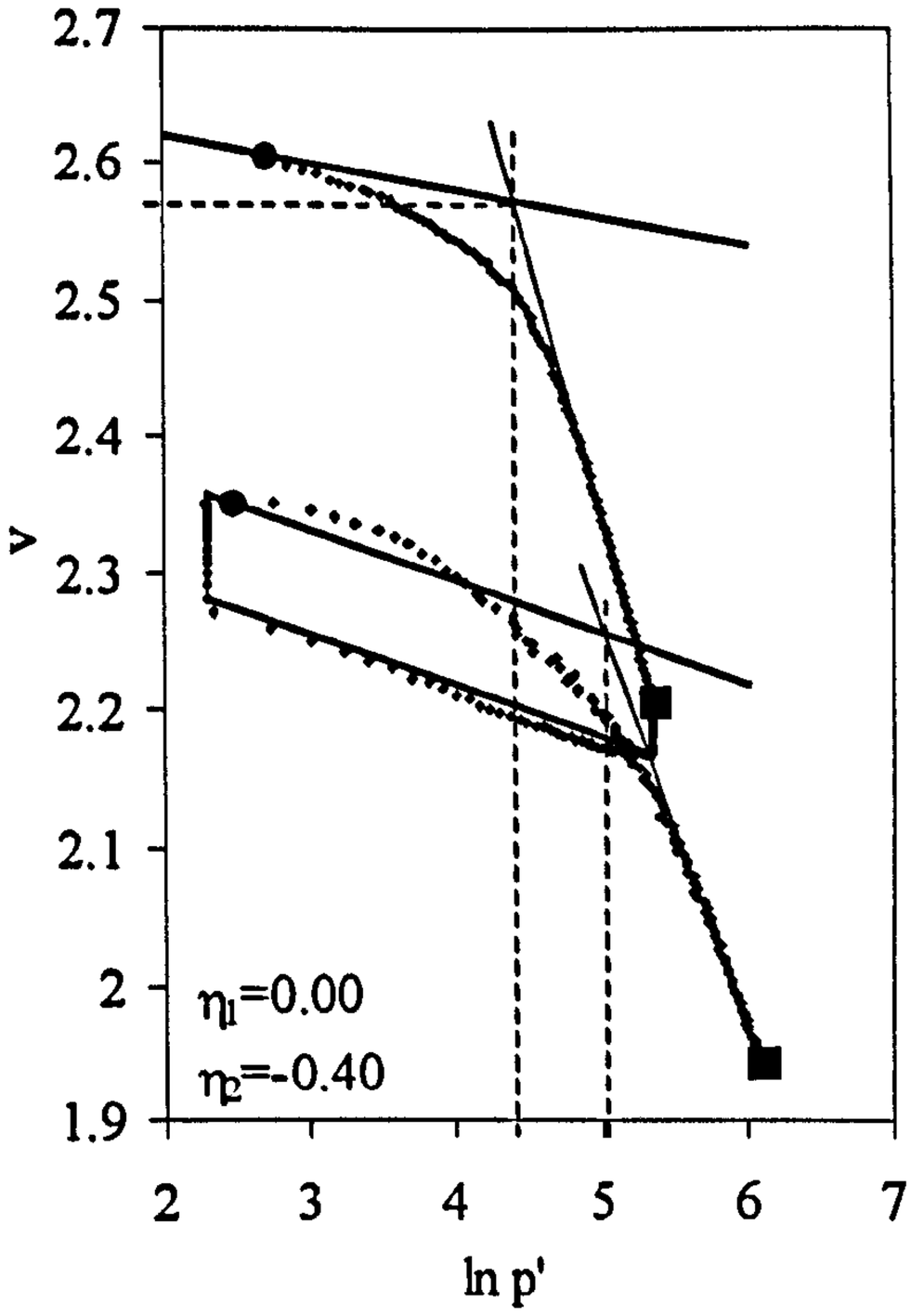

(e)

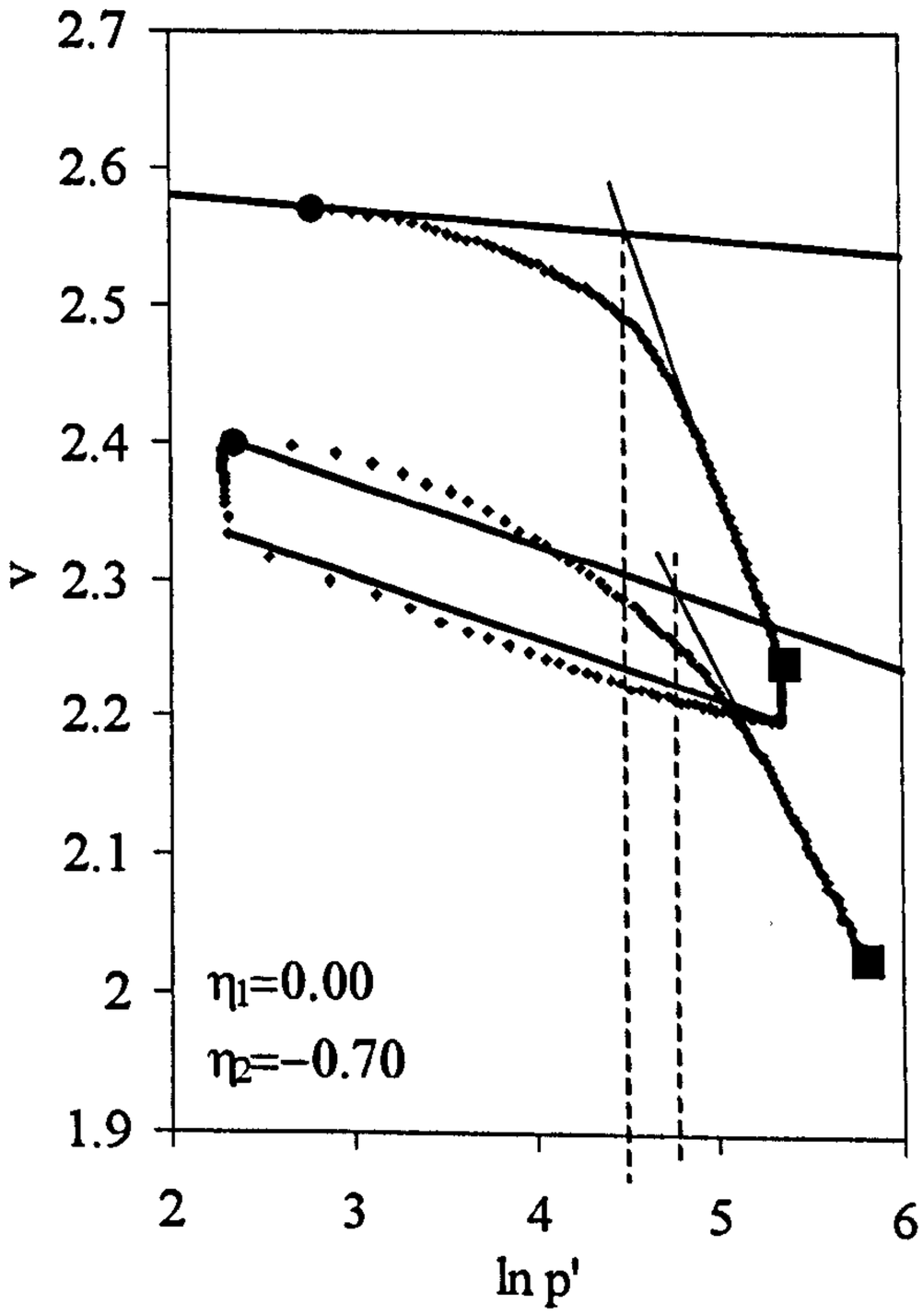

(f)

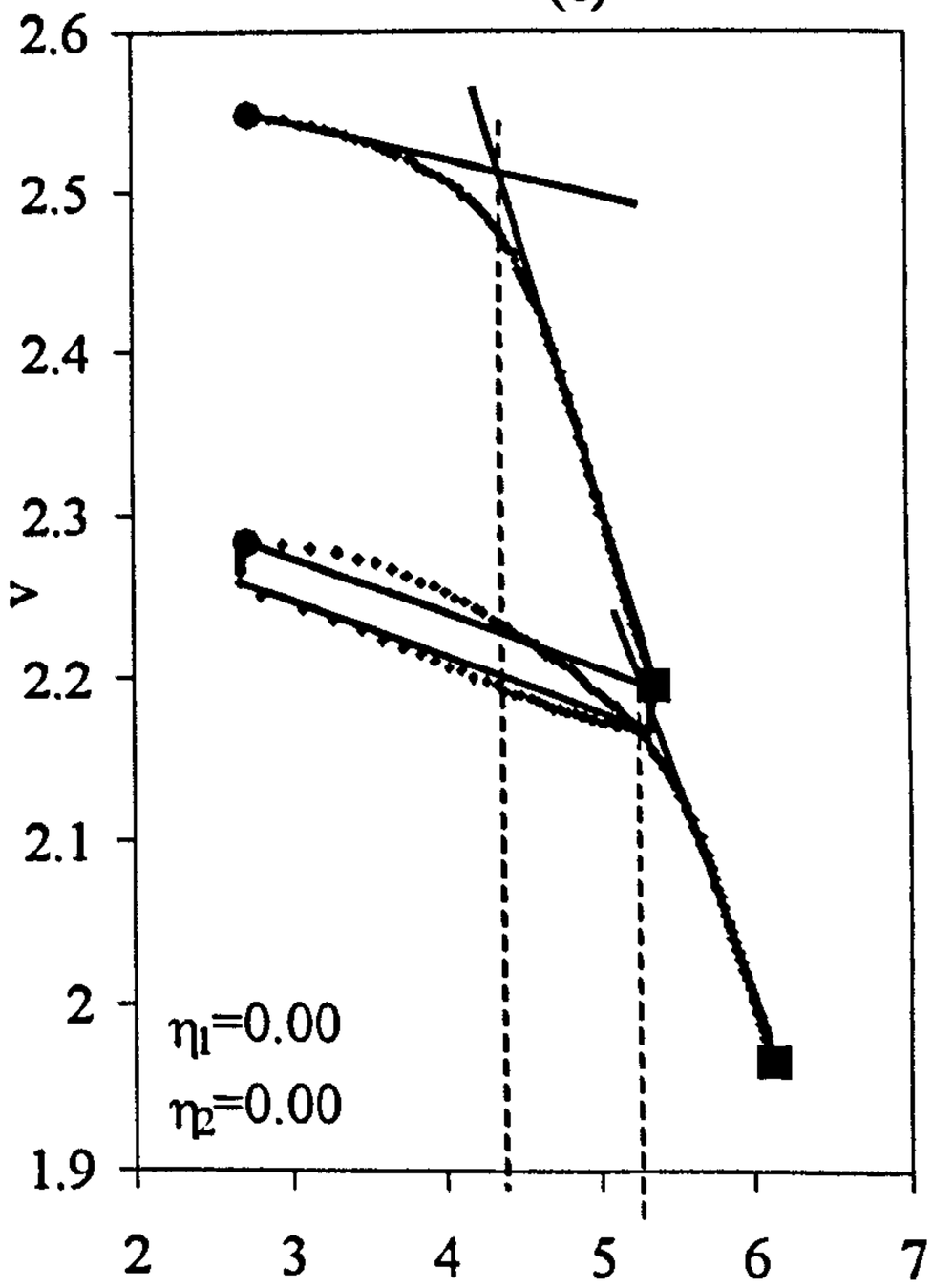

(g)

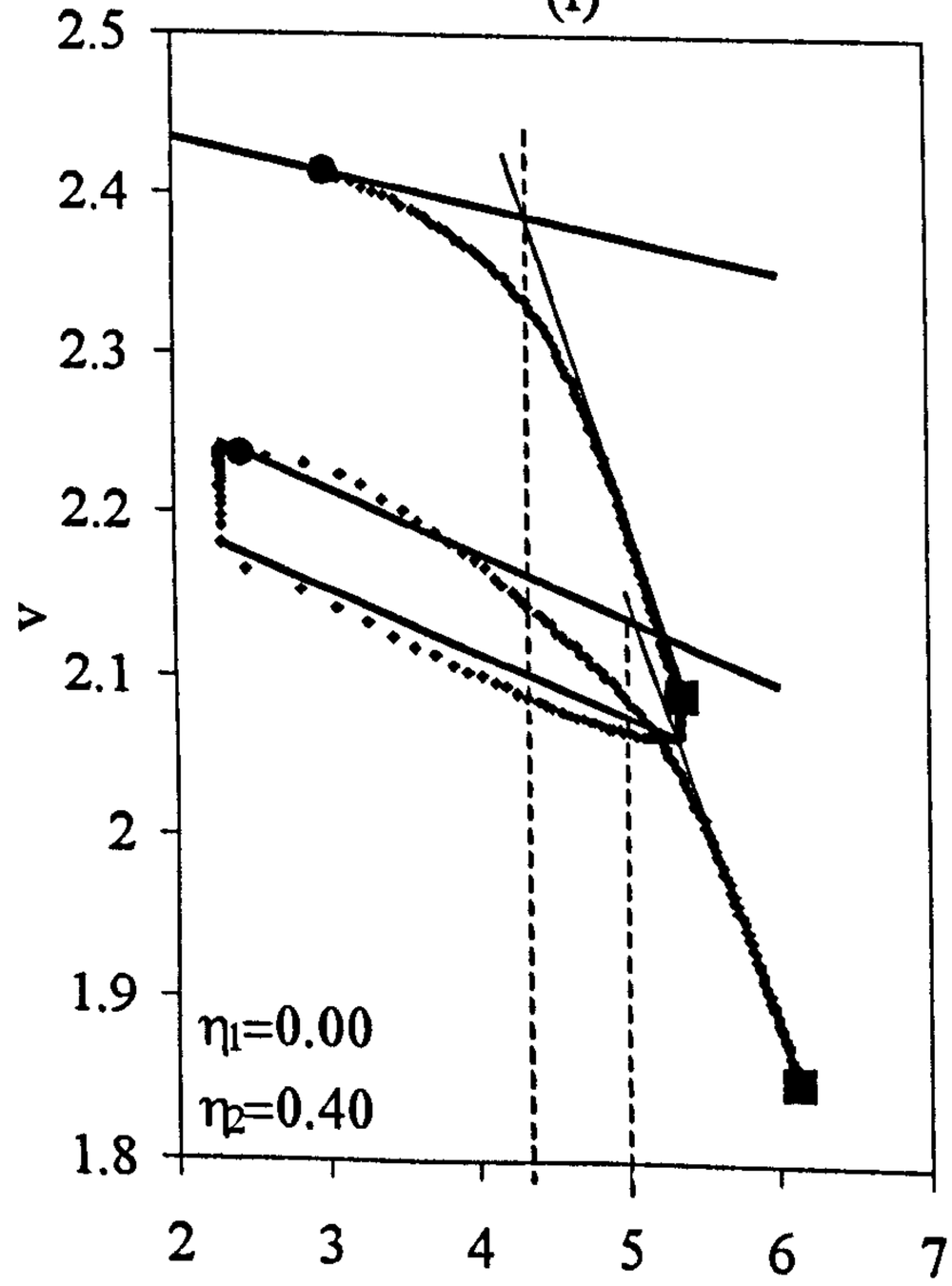

(h)

Figure B.1. Yield points from Test Series B. (e) Test B5, (f) Test B6, (g) Test B7, (h) Test B8.

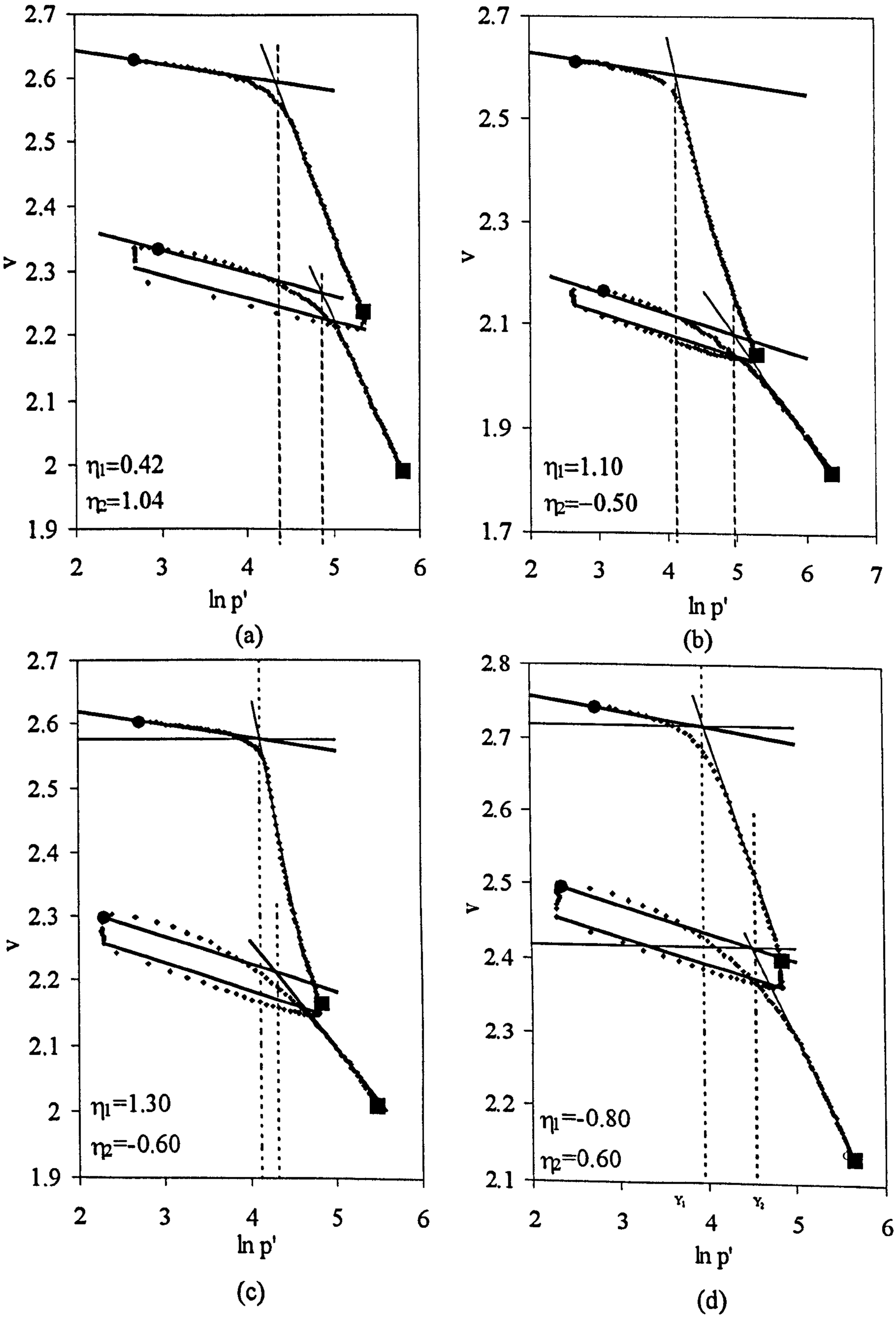

Figure B.2. Yield points from Test Series C. (a) Test C1, (b) Test C2, (c) Test C3, (d) Test C4.

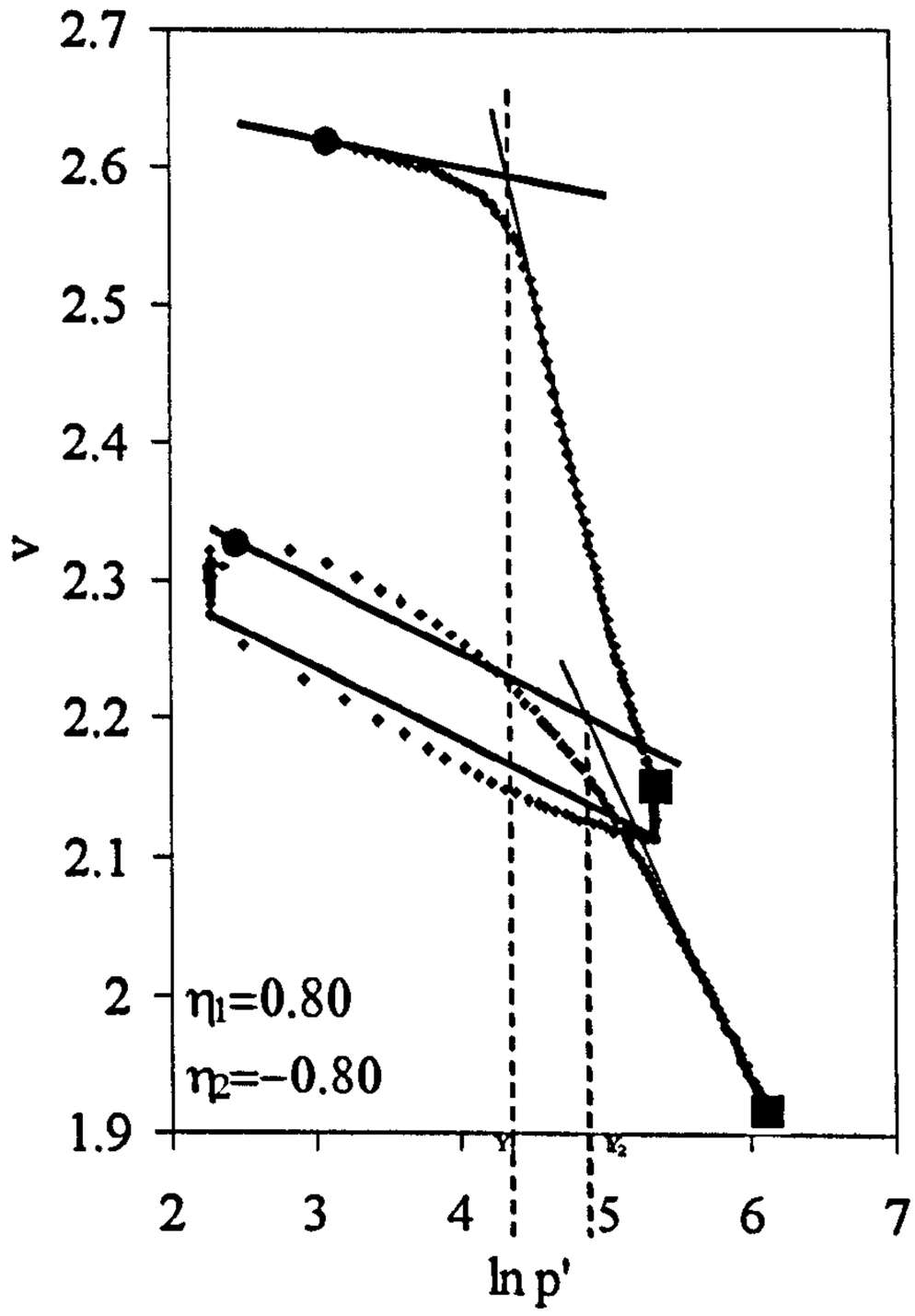

(e)

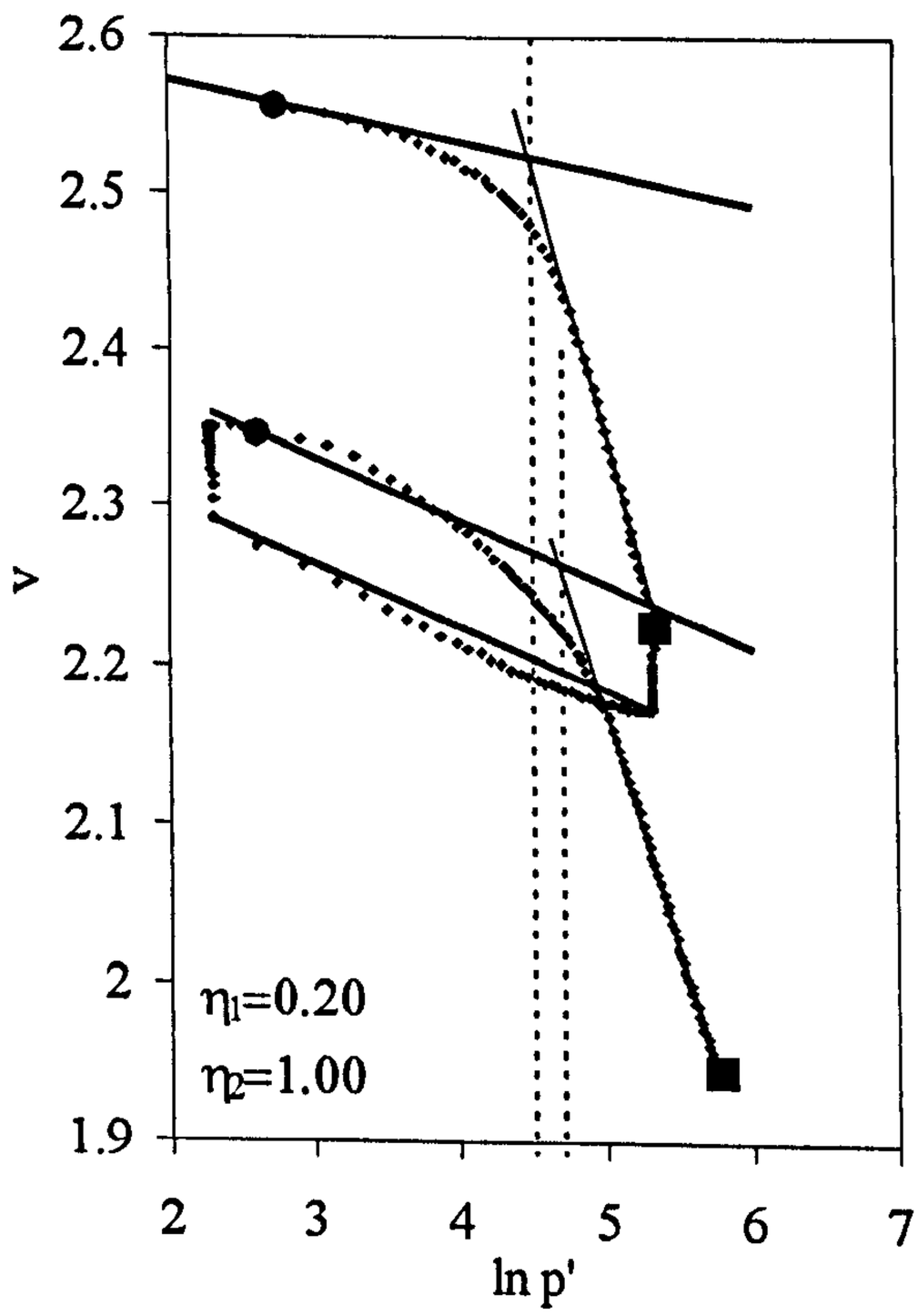

(f)

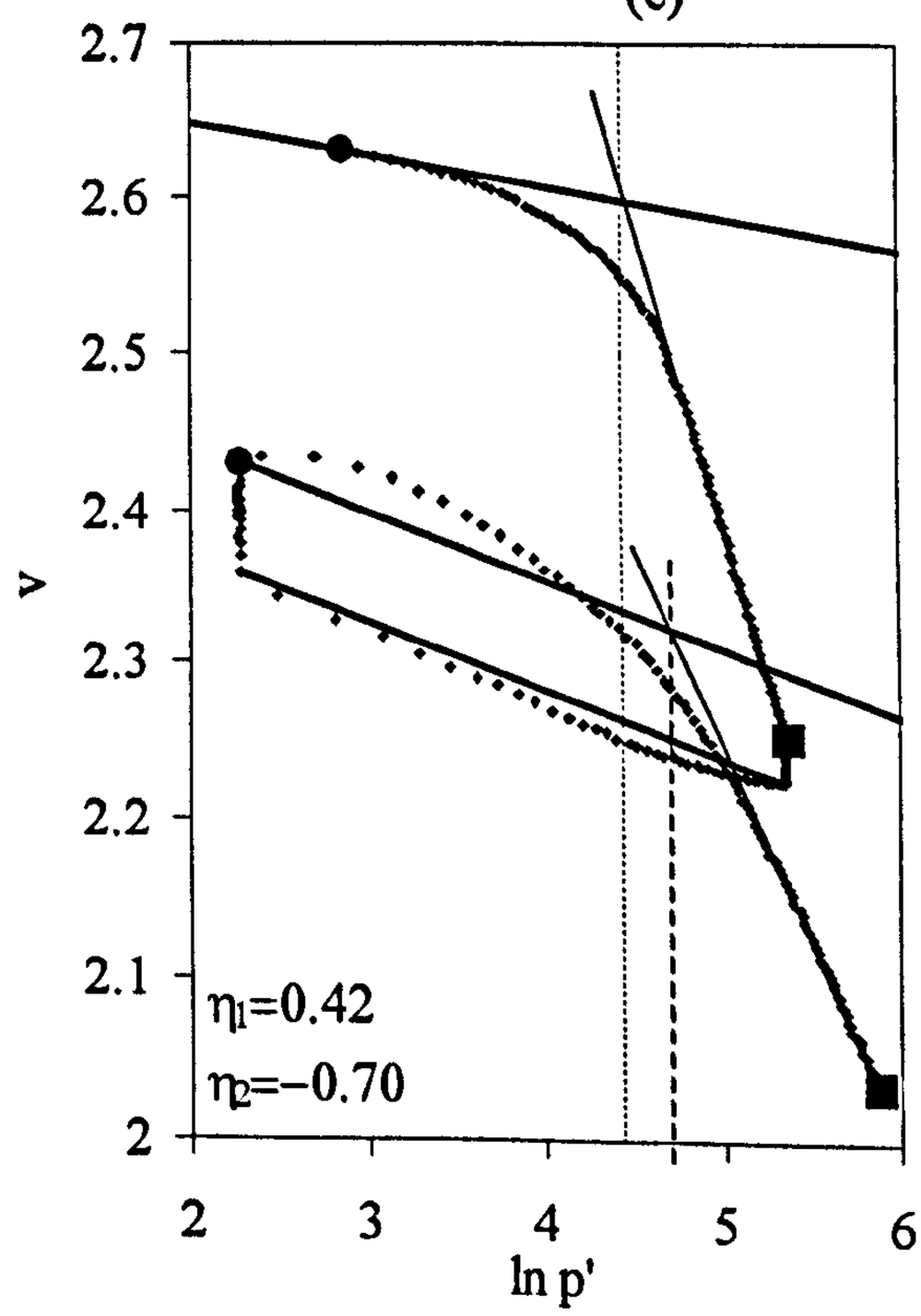

(g)

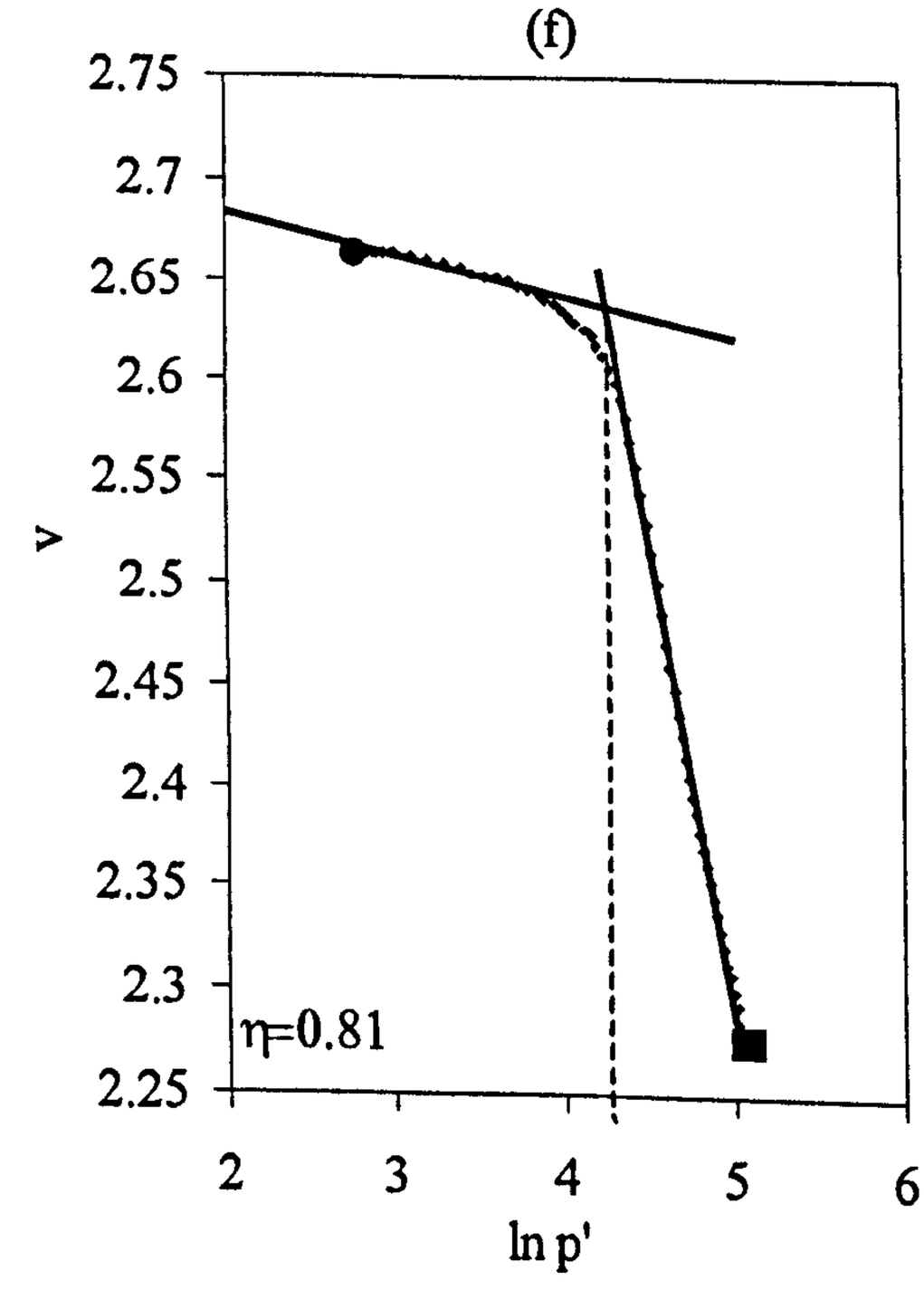

(h)

Figure B.2. Yield points from Test Series C. (e) Test C5, (f) Test C6, (g) Test C7, (h) Test C9.

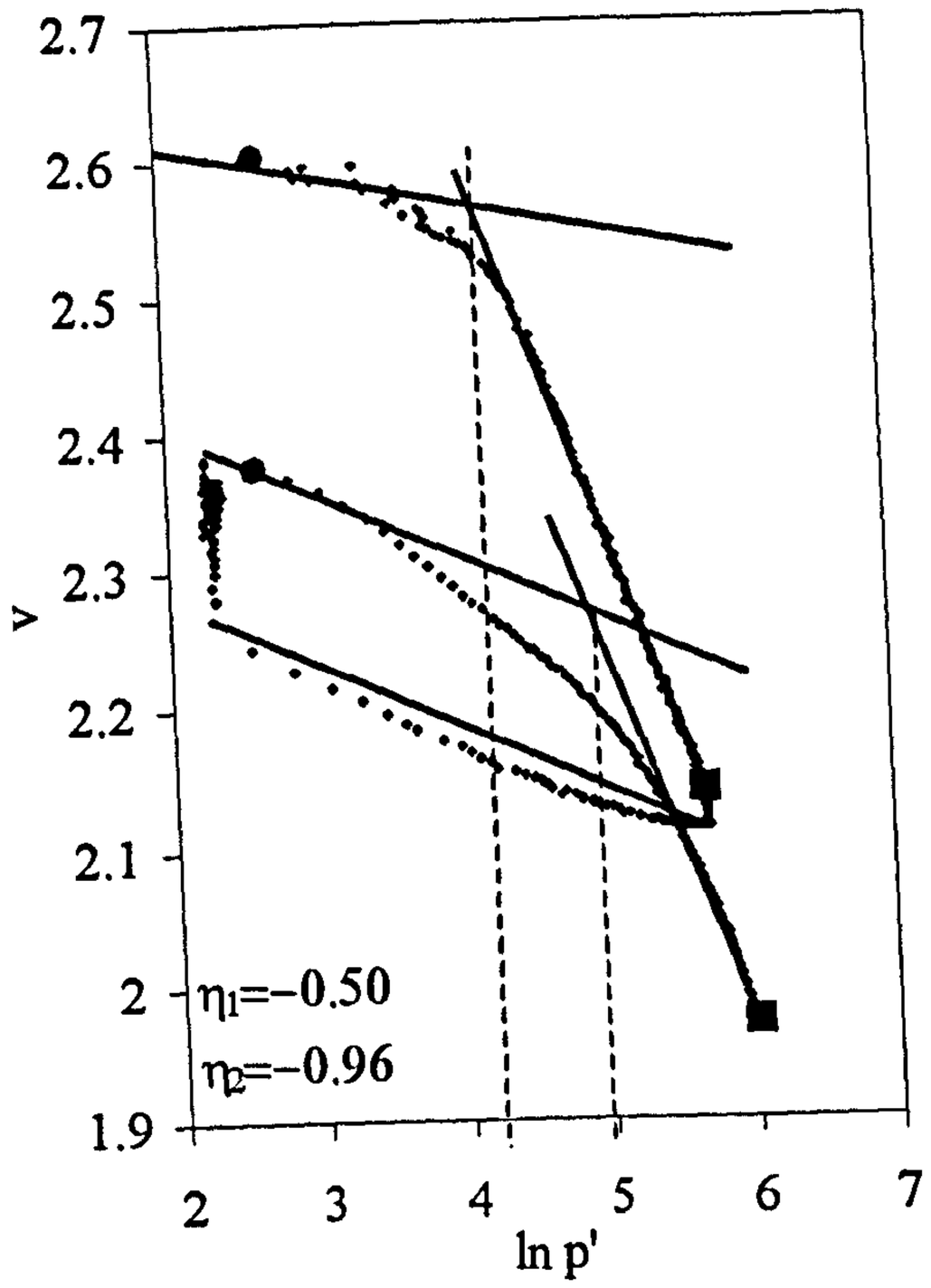

(j)

Figure B.2. Yield points from Test Series C. (j) Test C10.